AFGL-TR-83-0046
ENVIRONMENTAL RESEARCH PAPERS, NO. 838

Proceedings of the Air Force Geophysics Laboratory Workshop on Natural Changes of Large Space Structures in Near Earth Polar Orbit: 14-15 September 1982

Editors:

R. C. SAGALYN
U. S. INAMATELLI
I. MICHAEL

25 January 1983

This report has been reviewed by the ESD Public Affairs Office (PA) and is releasable to the National Technical Information Service (NTIS).

This technical report has been reviewed and is approved for publication.

Alva T. Stair, Jr.

DR. ALVA T. STAIR, Jr
Chief Scientist

Qualified requestors may obtain additional copies from the Defense Technical Information Center. All others should apply to the National Technical Information Service.

COMPONENT PART NOTICE

THIS PAPER IS A COMPONENT PART OF THE FOLLOWING COMPILATION REPORT:

(TITLE): Proceedings of the Air Force Geophysics Laboratory Workshop on Natural Charging of Large Space Structures in Near Earth Polar Orbit: 14-15 September 1982.

(SOURCE): Air Force Geophysics Lab., Hanscom AFB, MA.

TO ORDER THE COMPLETE COMPILATION REPORT USE AD-A134 894.

THE COMPONENT PART IS PROVIDED HERE TO ALLOW USERS ACCESS TO INDIVIDUALLY AUTHORED SECTIONS OF PROCEEDINGS, ANNALS, SYMPOSIA, ETC. HOWEVER, THE COMPONENT SHOULD BE CONSIDERED WITHIN THE CONTEXT OF THE OVERALL COMPILATION REPORT AND NOT AS A STAND-ALONE TECHNICAL REPORT.

THE FOLLOWING COMPONENT PART NUMBERS COMPRISE THE COMPILATION REPORT:

AD#:	TITLE:
AD-P002 100	An Overview of Charging of Large Space Structures in Polar Orbit.
AD-P002 101	Ionospheric Characteristics: A Review.
AD-P002 102	Is There a Good Way to Model Spacecraft Charging in the Presence of Space-Charge Coupling, Flow, and Magnetic Fields?
AD-P002 103	Charged Particle Effects on Space Systems.
AD-P002 104	Space Shuttle Charging Results.
AD-P002 105	STS-3/OSS-1 Plasma Diagnostics Package (PDP) Measurements of Orbiter-Generated $\underline{V} \times \underline{B}$ Potentials and Electrostatic Noise.
AD-P002 106	Electron Beam Experiments and Other Observations from STS-3.
AD-P002 107	Floating Potentials and the Hot Plasma Generated by an Electron-Beam-Emitting Rocket in the Ionosphere.
AD-P002 108	The Worst Case Charging Environment.
AD-P002 109	Estimates of Precipitating Electron Power Flux from Simultaneous DMSP Auroral Image and ISEE-1 AKR Observations.
AD-P002 110	Environmental Interactions of Polar Orbiting Satellites.
AD-P002 111	Interactions Between a Large Body and Its Environment in a Low Polar Orbit.
AD-P002 112	Observations of Differential Charging with Meteosat.
AD-P002 113	Laboratory and Space Measurements of Materials.
AD-P002 114	Space Electron Induced Discharge Coupling into Satellite Electronics.
AD-P002 115	The Interaction of Large Space Structures With the Near Earth Environment.
AD-P002 116	Shuttle Orbiter Charging in Polar Earth Orbit.
AD-P002 117	Potential Barriers and Multiple Root Effects in Spacecraft Charging.
AD-P002 118	Mechanisms that Limit Potentials on Ionospheric Satellites.

COMPONENT PART NOTICE (CON'T)

AD#:	TITLE:
AD-P002 119	The Importance of Neutrals, Transient Effects, and the Earth"s Magnetic Field on Sheath Structure.
AD-P002 120	The Threshold Temperature Effect in High-Voltage Spacecraft Charging.
AD-P002 121	Models of the Ionospheric Environment.
AD-P002 122	Polar Code Development.
AD-P002 123	High Voltage Solar Array Models and Shuttle Tile Charging.
AD-P002 124	Sheath Shapes: A 3-D Generalization of the Child-Langmuir Sheath Model for Large High-Voltage Space Structures in Dense Plasmas.
AD-P002 125	Space Systems Environmental Interactions Technology Program.
AD-P002 126	Summary of Experimental Results.
AD-P002 127	Questions that Need to be Answered.
AD-P002 128	Requirements for Validating System Models.

Unclassified

SECURITY CLASSIFICATION OF THIS PAGE (When Data Entered)

REPORT DOCUMENTATION PAGE		READ INSTRUCTIONS BEFORE COMPLETING FORM
1. REPORT NUMBER AFGL-TR-83-0046	2. GOVT ACCESSION NO. AD-A134894	3. RECIPIENT'S CATALOG NUMBER
4. TITLE (and Subtitle) PROCEEDINGS OF THE AIR FORCE GEOPHYSICS LABORATORY WORKSHOP ON NATURAL CHARGING OF LARGE SPACE STRUCTURES IN NEAR EARTH POLAR ORBIT: 14-15 September 1982		5 TYPE OF REPORT & PERIOD COVERED Scientific. Interim.
		6. PERFORMING ORG. REPORT NUMBER ERP No. 825
7 Editors: R. C. Sagalyn * D. E. Donatelli I. Michael		8. CONTRACT OR GRANT NUMBER(s) **
9 PERFORMING ORGANIZATION NAME AND ADDRESS Air Force Geophysics Laboratory (PH) Hanscom AFB Massachusetts 01731		10 PROGRAM ELEMENT, PROJECT, TASK AREA & WORK UNIT NUMBERS 76611101 62101F
11. CONTROLLING OFFICE NAME AND ADDRESS Air Force Geophysics Laboratory (PH) Hanscom AFB Massachusetts 01731		12. REPORT DATE 25 January 1983 13 NUMBER OF PAGES 415
14 MONITORING AGENCY NAME & ADDRESS(if different from Controlling Office)		15 SECURITY CLASS. (of this report) Unclassified 15a DECLASSIFICATION/DOWNGRADING SCHEDULE

16. DISTRIBUTION STATEMENT (of this Report)

Approved for public release; distribution unlimited.

17. DISTRIBUTION STATEMENT (of the abstract entered in Block 20, if different from Report)

18. SUPPLEMENTARY NOTES

*Boston College Physics Dept.
Chestnut Hill, MA 02167

**Work done in the Workshop by Boston College was supported by AF Contract F19628-81-K-0011

19. KEY WORDS (Continue on reverse side if necessary and identify by block number)

Natural charging	Shuttle environment interactions
Polar orbit	Charged particle effects
Spacecraft charging	Low earth orbit (LEO)
Differential charging	Auroral electrons
Large space structures	

20. ABSTRACT (Continue on reverse side if necessary and identify by block number)

A two-day workshop on the natural charging of large space structures was held on 14-15 September 1982 at the Air Force Geophysics Laboratory. The workshop reviewed the causes and effects of vehicle charging in near earth orbit and the problems encountered in developing models or codes to adequately deal with the charged vehicle environment. The meeting will also help determine the areas into which future research should be directed. The proceedings of the workshop presented here include written contributions by the speakers in each of the four sessions. The topics covered are: (1) the general

DD FORM 1 JAN 73 1473 EDITION OF 1 NOV 65 IS OBSOLETE

Unclassified

SECURITY CLASSIFICATION OF THIS PAGE (When Data Entered)

20. Abstract (Continued)

characteristics of the near-earth environment and their effects on large space structures; (2) causes and effects of spacecraft charging as shown experimentally and theoretically; and (3) modeling of space structures in a charging environment.

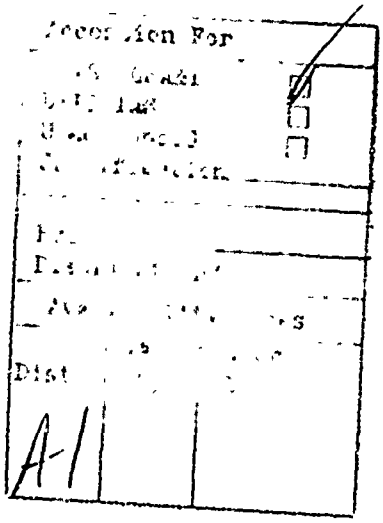

Summary

A workshop on Natural Charging of Large Space Structures in Near Earth Polar Orbits, sponsored by the Air Force Geophysics Laboratory and Boston College, was held on 14 and 15 September, 1982, at AFGL. Many of the specialists in the area of spacecraft charging problems assembled to discuss the necessity and/or possibility of developing realistic, effective codes describing the interaction of low earth orbiting systems with the environment. The workshop consisted of four sessions: (1) tutorial lectures on the characteristics of the near-earth environment and its effects on large space structures; (2) experiments examining and interpreting spacecraft charging and the environment causing it; (3) theoretical interpretation of spacecraft charging and the environment in which it occurs; (4) modeling space structures in a charging environment.

Topics covered in four tutorial lectures are: a review of environmental effects that may cause spacecraft charging (E. C. Whipple, Jr.); a general overview of the ionosphere (F. J. Rich); the difficulties in attempting to model the spacecraft environment and the effects that lead to charging (J. G. Laframboise); and the effects of charged particles on space systems (N. J. Stevens). The panel sessions consisted of invited presentations with time allotted for discussion after each one. Summaries of each session were presented by the session chairmen in the last half of the final session.

The proceedings consist of the written contributions of the individual speakers. Some have chosen to include summaries of their presentation while others have submitted complete papers. In the few cases where speakers did not submit written texts for inclusion in the proceedings, summaries are included. They

were written by and attributed to the reporters assigned to the particular speakers, making use of transcripts of the tape-recorded presentations. The proceedings are divided into five chapters based on the four sessions of the workshop and a fifth summary chapter. However, papers are not listed in the order in which they were presented. In some instances the editors felt that a certain paper was better suited to a session other than the one in which it was presented. The ordering of the proceedings reflects this.

With the Air Force committed to the space Shuttle and the future utilization of space platforms and other large space structures, it is imperative that problems associated with the interactions of these structures with their environment be resolved. There are considerable differences of opinion among specialists in this area concerning the nature and magnitude of the problems and the feasibility of developing realistic models or codes to deal with them. The discussion of these problems at this workshop will assist in defining the future role of the Air Force in their resolution.

Preface

The insight and organization of the workshop's co-chairmen, Rita C. Sagalyn and Allen G. Rubin, brought together many of the specialists in the area at AFGL to address the various aspects of the spacecraft charging problems. The coordination of the event itself was attended to by Delia E. Donatelli of Boston College with the assistance of Mary Outwater of AFGL. Frances Labo of AFGL handled registration and local information and, with Karen Flaherty of AFGL, attended to many of the details prior to and during the meeting. They were assisted by Jean James and Diane Riehl of Regis College. M. Patricia Hagan of Emmanuel assumed responsibility for printing the programs and transcribing the tape recorded material. The audio and video equipment and the tape recording were the responsibility of Alice McGinty of AFGL with the equipment handled by Airmen L. Carpenter, M. Schwarzman, and Debra Douglass.

The workshop was supported in part by Boston College under Air Force Contract F19628-81-K-0011.

The Editors

Contents

Contents

PROCEEDINGS OF THE AIR FORCE GEOPHYSICS LABORATORY WORKSHOP ON NATURAL CHARGING OF LARGE SPACE STRUCTURES IN NEAR EARTH POLAR ORBIT: SEPTEMBER 14-15, 1982

1. An Overview of Charging of Large Space Structures in Polar Orbit

by

E. C. Whipple, Jr.
Center for Astrophysics and Space Science
University of California at San Diego
La Jolla, Calif. 92109

1. INTRODUCTION

This paper gives an overview of some of the important questions regarding charging effects on large space structures in the polar ionosphere. The ionosphere as a rule is a rather benign environment as far as charging of spacecraft is concerned. The ionospheric plasma is relatively cool and dense in comparison with other plasmas in space. The plasma density ranges from values on the order of 10^6 /cm^3 down to values as low as or even below 10^2 /cm^3, with temperatures well below 1 eV (11600° K). However, there can be large fluxes of energetic electrons in the polar ionosphere. This subject is a matter of concern because these auroral fluxes could charge a spacecraft to large potentials.

(Received for publication 18 January 1983)

Figures 1 and 2 show how two important length scales vary in the ionosphere. Figure 1 shows that the Debye length ranges from about 1 mm to a few cm. The electrostatic sheath thickness around a charged object is on the order of a few Debye lengths. Thus, in the ionosphere the Debye length is very small compared to a large space structure. Figure 2 shows typical electron and proton gyroradii

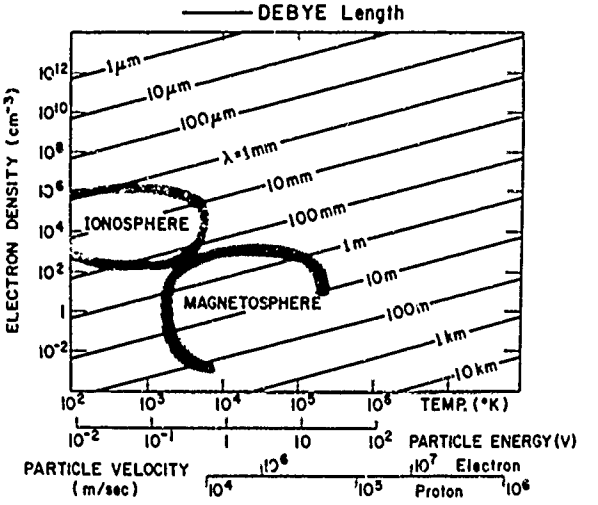

Figure 1. The Debye Length as a Function of Electron Density and Temperature

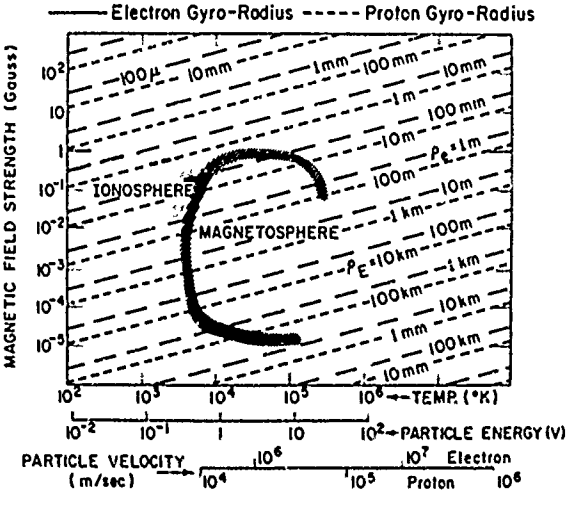

Figure 2. The Electron and Proton Gyroradii as Functions of Magnetic Field Strength and Temperature

in the ionosphere. Again, the electron gyroradius is small, on the order of a few cm to 1 m. The proton gyroradius is larger, up to tens of meters in size, and thus can be comparable to the dimensions of large space structures.

The charging of objects in the ionosphere is characterized by extreme anisotropy in the charging currents. The ion current is dominated by the motion of the spacecraft in its motion through the plasma and hence the ion current occurs largely on the leading surfaces of such an object. The electron current does not vary as strongly as the ion current but it is affected both by the $\underline{V} \times \underline{B}$ effect and by the wake effect which cause the current to vary with position on the spacecraft surface. The photoemission current varies with surface orientation with respect to sunlight. These variations are illustrated in Figures 3 through 5 which show measured currents on Explorer 8 as a function of angular position on the spacecraft surface.[1] Figure 3 shows how the ion current peaks strongly as the detector looks in the direction of motion of the spacecraft. Figure 4 shows the electron current (both photoemission current and collected plasma current) as a function of position, again indicating the dependence of the current on orientation. Finally, Figure 5 shows the total current as a function of angle.

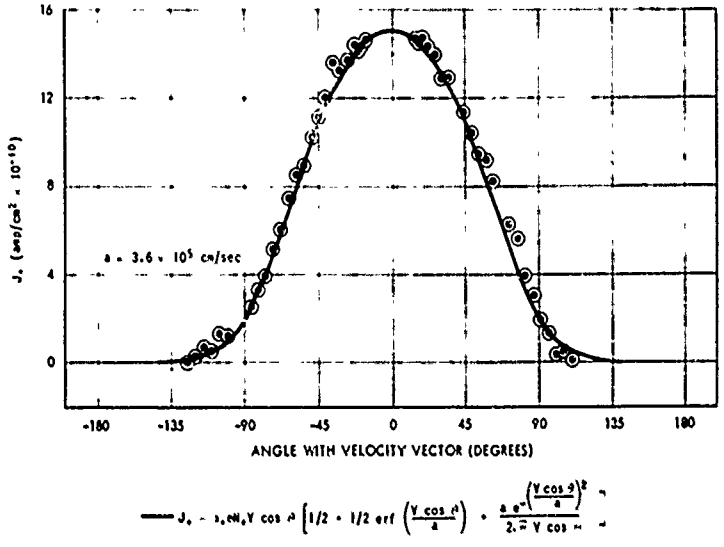

Figure 3. Ion Current as a Function of Angular Position Measured on the Explorer 8 Spacecraft Surface (from Ref. 1)

1. Bourdeau, R.E., Donley, J.L., Serbu, G.P., and Whipple, E.C. (1961) Measurements of sheath currents and equilibrium potential on the Explorer 8 satellite, J. Astronaut Sci. 8:65.

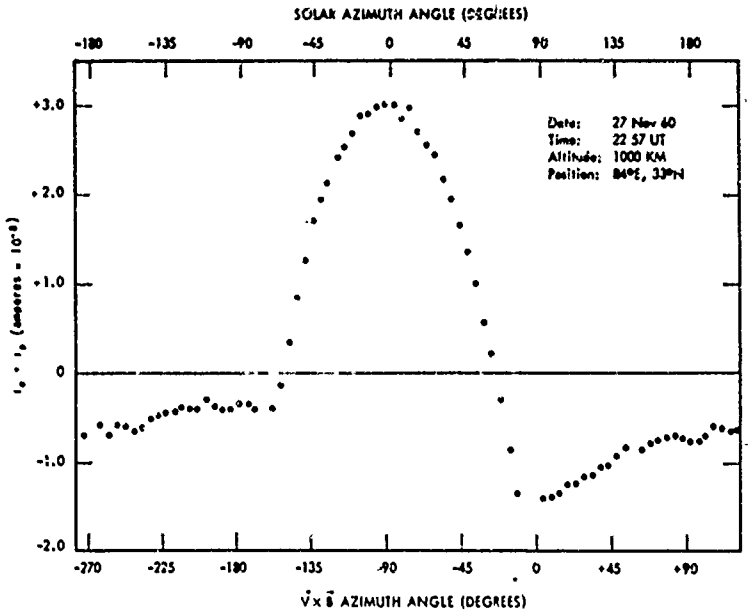

Figure 4. Electron Current as a Function of Angular Position Measured on the Explorer 8 Spacecraft Surface (from Ref. 1)

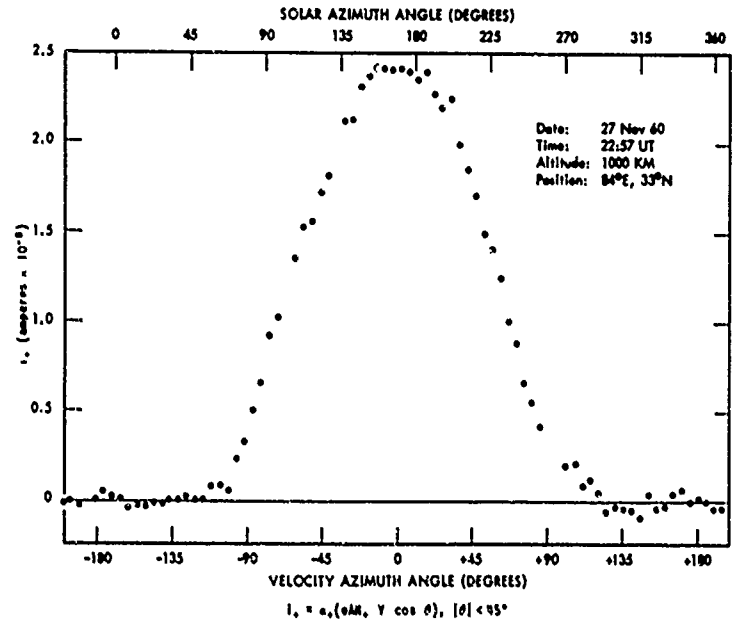

Figure 5. Total Current as a Function of Angular Position Measured on the Explorer 8 Spacecraft Surface (from Ref. 1)

2. POSSIBILITY OF LARGE POTENTIALS IN THE POLAR IONOSPHERE

Katz and Parks[2] studied the possible charging effects of large electron fluxes in the auroral ionosphere on a spacecraft. They took an energetic electron flux of 2×10^{-4} A/m^2 at an energy of 5 keV and examined its effect on an orbiting sphere in an ionospheric plasma with a density of 10^5/cm^3 at a temperature of about 0.1 eV. In their model, the large negative current due to the energetic electrons was balanced primarily by the positive current due to ion collection. The significant result they obtained was that the sphere would charge to large negative potentials approaching the energy of the auroral electrons. This occurred because the increase in ion current necessary to balance the electron current was limited by the sheath thickness. The sheath thickness grows slowly with the potential drop across the sheath when the Debye length is small and hence a large potential drop is required to obtain the necessary ion current.

This result is illustrated in Figure 6, which shows how the equilibrium potential of the sphere increases with its radius. In regions where the plasma density is low, the potentials are correspondingly greater. A more precise calculation must include secondary electron currents and photoemission, but in principle it is possible to have large potentials in regions where large energetic electron fluxes occur. It is therefore important to know the frequency of occurrence of large fluxes of energetic electrons in the polar ionosphere.

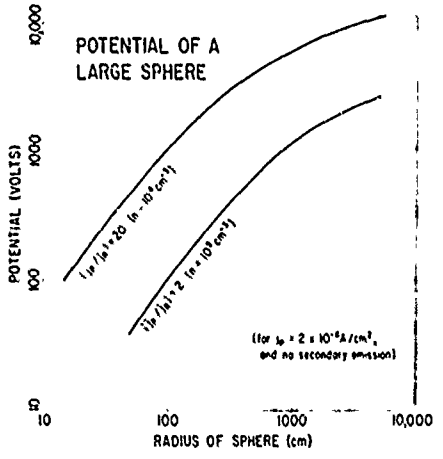

Figure 6. The Potential of a Sphere as a Function of its Radius for Two Values of the Plasma Density

2. Katz, I., and Parks, D.E. (1982) Space Shuttle Orbiter Charging, AIAA 20th Aerospace Sci. Mtg., Orlando, Florida, Jan., 1982.

3. SHEATH APPROXIMATIONS

A sheath is a region of significant space charge adjacent to a surface. The thickness of a sheath can be used to estimate the increase in cross-section for current collection by a charged body. The paper by Katz and Parks[2] modified the sheath approximation of Langmuir and Blodgett,[3] by using the streaming energy of the ions in place of the thermal energy of the plasma. Figure 7 shows how the cross-section for current collection varies with the potential across the sheath. Similar extensions of the Langmuir-Blodgett work have been obtained by Al'pert[4] and by Parker.[5] Parker has compared the currents obtained with the spherical diode sheath approximation of Langmuir and Blodgett with a self-consistent numerical calculation. Figure 8 shows that the self-consistent current (marked "S. C.") can be as much as 50 percent higher than the spherical diode sheath approximation for a range of potentials. The difference is probably due to so-called "pre-sheath" acceleration which the sheath approximation does not allow for. The two curves do seem to be approaching the same slope asymptotically.

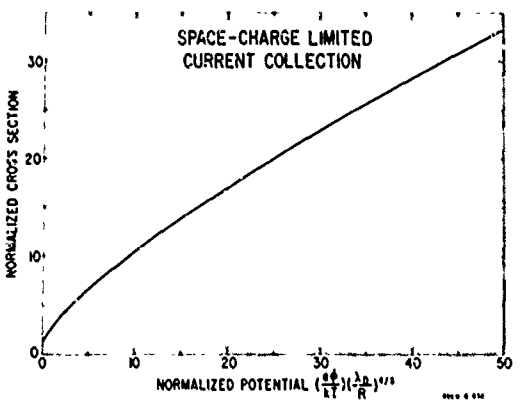

Figure 7. The Cross-section for Current Collection as a Function of the Potential Across the Sheath

3. Langmuir, I., and Blodgett, K. (1924) Currents limited by space charge between concentric spheres, Phys. Rev. 24:99.

4. Al'pert, Ya. L., Gurevich, V., and Pitaevskii, L. P. (1965) Space Physics With Artificial Satellites, Consultants Bureau, New York, pp. 186-210.

5. Parker, L. W. (1980) Plasmasheath-photosheath theory for large high-voltage space structures, Prog. Astron. Aeron. 71:477.

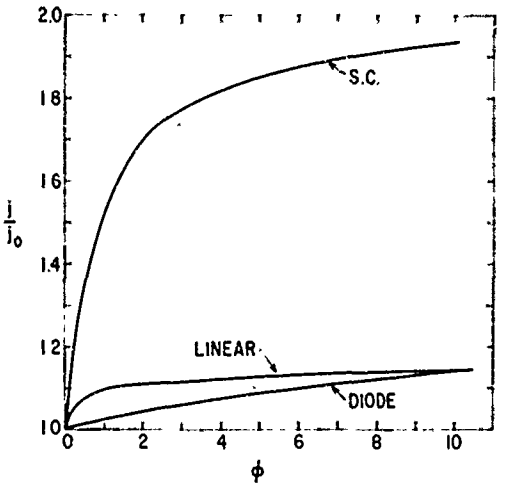

Figure 8. Comparison of Three Methods for Calculating Currents for a Range of Sheath Potentials

It would be useful to have an accurate sheath approximation, whose limitations were well-understood, for describing ion collection by a large body in a streaming plasma.

4. THE WAKE

The plasma wake behind a moving body is a region depleted unequally of both ions and electrons because of the small thermal velocities of the ions compared to the streaming velocity. Electrons can readily penetrate this region until the negative space charge from the excess electrons builds up the negative potential to a value such that they also are depleted. This acts as a negative potential barrier for electron collection on the rear surfaces of the spacecraft.

Figure 9, taken from Samir and Wrenn,[6] shows how the electron current measured on Explorer 31 varied with angle, with 0^{o} corresponding to the ram direction. The electron current at lower altitudes is depleted by as much as two orders of magnitude on the back surface compared to the front surface, with smaller depletions at higher altitudes. The back-to-front current ratio is shown in Figure 10 as a function of the mean ion mass. The altitude dependence of the current ratio of Figure 9 is in reality a dependence on the mean ion mass which

6. Samir, U., and Wrenn, G. L. (1969) The dependence of charge and potential distribution around a spacecraft on ionic composition, Planet. Space Sci. 17:693.

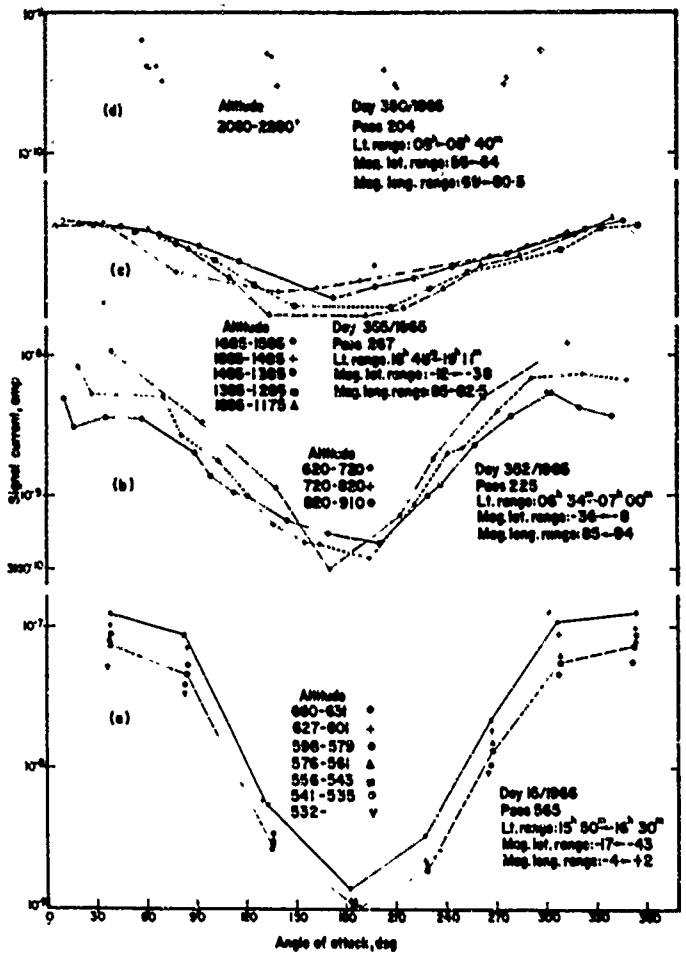

Figure 9. The Altitude Dependence of the Electron Current as a Function of Angular Position From the Ram Direction as Measured on Explorer 31. Reprinted with permission from Planet. Space Sci., 17, Copyright 1969, Pergamon Press Ltd.

decreases with altitude, as the dominant ion changes from oxygen to helium and then to hydrogen.

It is difficult to calculate the height of this negative potential barrier in the wake which controls the rear-surface electron current, although Samir's data show that it varies linearly with the square of the ion Mach number (see Whipple[7]). However, it should also depend on the Debye length.

7. Whipple, E. C. (1981) Potentials of surfaces in space, Rep. Prog. Phys. 44:1197.

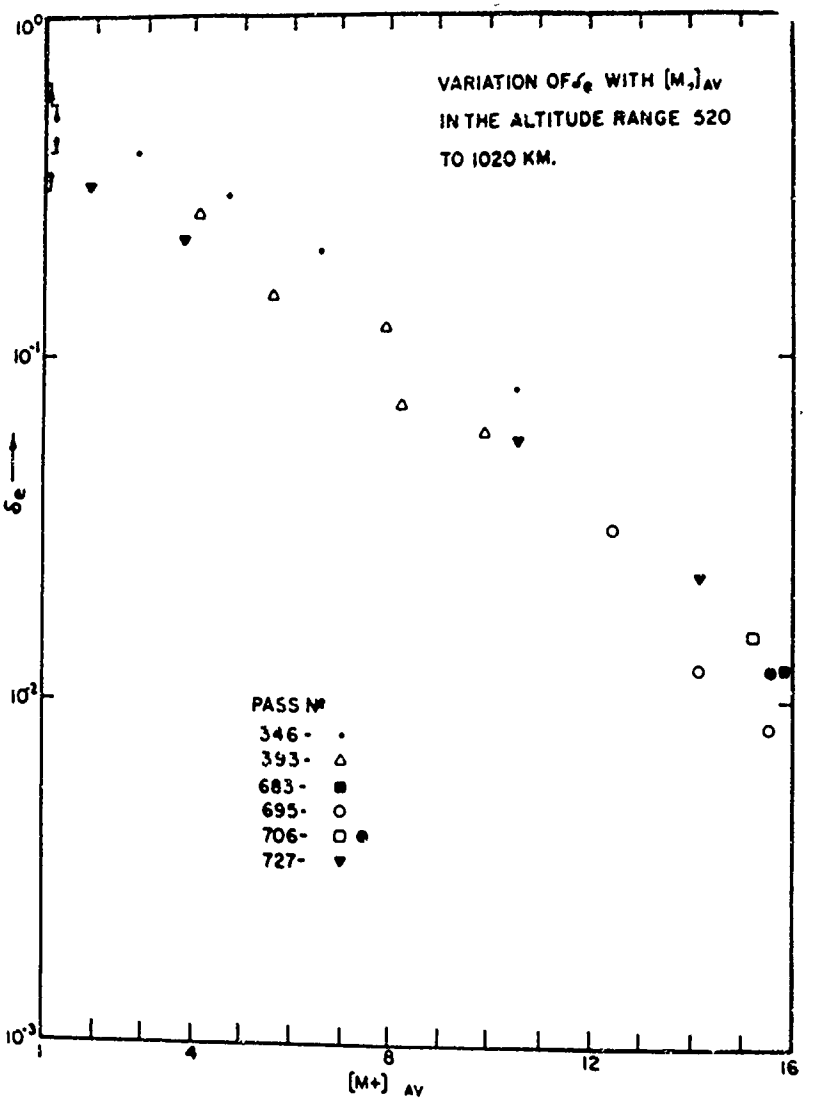

Figure 10. The Back-to-front Current Ratios From the Data of Figure 9 as a Function of Mean Ion Mass

Another effect of the wake is that insulating portions of a body that are situated on the back side of the body may charge to large negative potentials. Figure 11, from Parker[8] shows potential contours around an insulating cylinder immersed in a streaming plasma, with an ion Mach number equal to 4. The

8. Parker, L.W. (1978) Differential charging and sheath asymmetry of nonconducting spacecraft due to plasma flows, J. Geophys. Res. 83:4873.

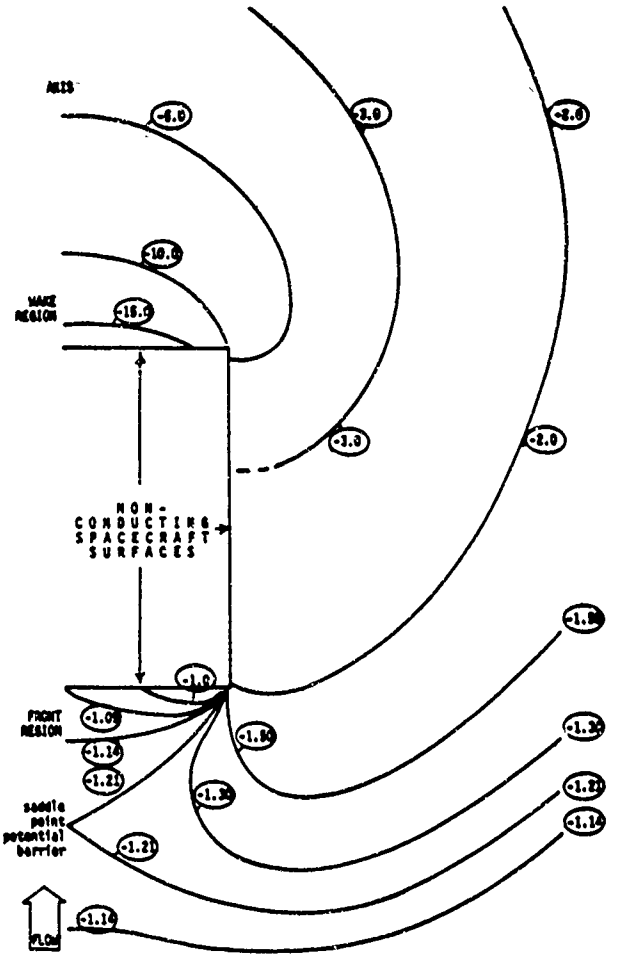

Figure 11. Potential Contours Around an Insulating Cylinder Immersed in a Streaming Plasma With an Ion Mach Number of 4. (Reprinted from the Journal of Geophysical Research)

potentials are indicated in units of (kT/e). The rear surface charges to a potential that is more than an order of magnitude larger than (kT/e).

5. $\underline{V} \times \underline{B}$ EFFECT

A body moving across a magnetic field experiences an electric field given by $\underline{V} \times \underline{B}$. In the reference frame of the moving body this is a real electric field that interacts with a conducting body by inducing electric charges at the body's

surface. This is illustrated in Figure 12, which shows such a body moving in the ionosphere. The electric field in the region of space around the body is indicated by the equipotential contours. At a great distance from the body, the equipotential contours are straight, indicating a uniform electric field, but in the body's vicinity the contours are distorted by the conductor's presence. The conducting body itself is at a given potential, but the potential difference between the body and the adjacent plasma depends on the position at which the potential difference is taken. This variation in potential difference occurs not because the body potential varies, but because the reference potential in the adjacent plasma varies with position.

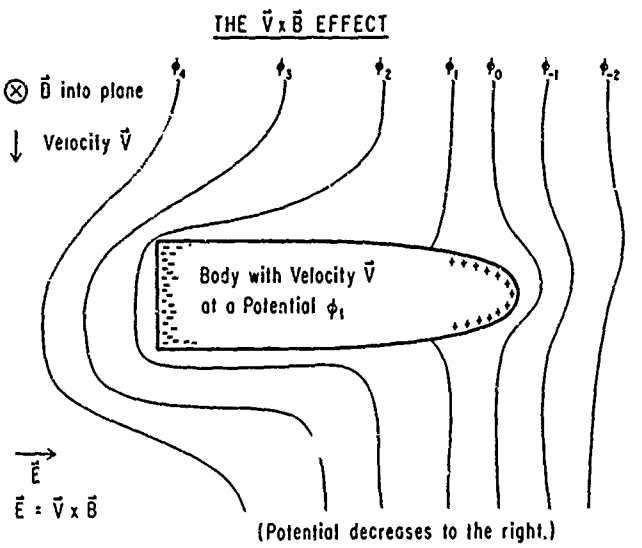

Figure 12. Equipotential Contours Around a Body Moving Across a Magnetic Field

Since the current collected by a surface in a plasma depends on the potential difference with respect to the plasma, it follows that the current density to the body will vary with position on the body's surface. The end of the body that is more positive with respect to the adjacent plasma will tend to collect electrons, whereas the negative end will collect ions. Since the electron current density is higher than the ion current density for a given potential difference because of the smaller mass of the electron, the current balance condition that determines the equilibrium potential will drive the body to a potential so that only a small area

will be at a positive potential with respect to the adjacent plasma, as illustrated in the figure.

The variation in collected current to such a body means that a current flows along the body from the negative to the positive end, as illustrated in Figure 13. In equilibrium, this current path must close through the plasma. There has been almost no work on this problem of how this current returns through the plasma. The current loop must disturb the plasma, with the disturbance being proportionately greater for larger structures. It is important to understand this interaction and to know how the distant plasma responds to the presence of a large structure.

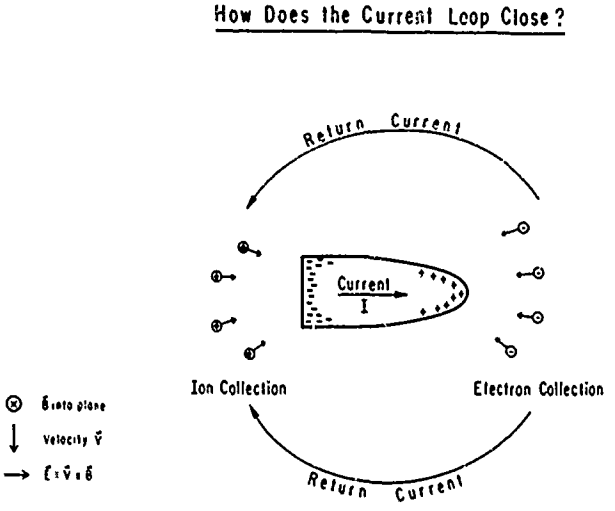

Figure 13. Current Flow as a Result of Variation in Collected Current Along a Body Moving in Space

6. DISTANT PLASMA BEHAVIOR

In a uniform, unmagnetized plasma far from a spherical charged body, the electrostatic potential varies asymptotically as the inverse square of the distance from the body. This behavior is obtained from the so-called "plasma solution" where the asymptotic forms of the ion and electron densities are found in terms of the potential and distance, and then quasi-neutrality of the plasma is invoked. Physically, both the ion and electron densities involve terms depending on the potential, such as the Boltzmann factor, $\exp(\pm Ve/kT)$, and solid angle factors depending on the distance, $(1 - r_p^2/r^2)$, where r_p is the radius of the body. In

the limit as r approaches infinity, the potential V approaches 0, and to first order the potential enters the density terms linearly. This gives the first-order asymptotic variation of the potential as r^{-2}.

The appropriate boundary condition to use in a numerical scheme where a boundary at a finite distance is necessary is a floating condition, where the potential is related to the potential gradient. Laframboise[9] has discussed the application of such boundary conditions and gives examples of calculations showing how the accuracy of the solutions to Poisson's equation depends on the distance of the boundary. Parker and Sullivan[10] have also discussed this boundary condition.

The corresponding asymptotic behavior for the plasma around a body moving through a magnetized plasma is not known. Parker and Murphy[11] discussed the motion of electrons in the plasma about a charged sphere and showed that the electron gyrocenters would themselves drift in a spiral about the body. Linson[12] argued that turbulent diffusion would enable the electrons to cross the magnetic field lines. Figure 14, from Linson's paper, shows the variation of collected electron current versus potential on a charged sphere under various assumptions. The upper curve is an upper limit based on the Langmuir-Blodgett sheath approximation. The lower curve represents the currents derived from the work of Parker and Murphy. The intermediate curves represent the possible effects of turbulence in increasing the collected current. The parameter q_c is the critical value of the ratio of the square of the plasma frequency to the electron gyrofrequency. At a value of this parameter on the order of unity, the plasma is unstable to the growth of turbulence.

7. BEAM EMISSION AND POTENTIAL MODIFICATION

The mechanism for electron collection by moderately or highly positively charged moving bodies in the ionosphere is not well understood. However, some data on this question has been obtained from electron beam emission experiments carried on vehicles in the ionosphere (Winckler[13]). The plasma response to

9. Laframboise, J.G. (1966) Theory of Spherical and Cylindrical Langmuir Probes in a Collisionless, Maxwellian Plasma at Rest, Rep. No. 100, University of Toronto Institute for Aerospace Studies.

10. Parker, L.W., and Sullivan, E.C. (1974) Iterative Methods for Plasma-Sheath Calculations--Application to Spherical Probe, NASA TN D-7409.

11. Parker, L.W., and Murphy, B.L. (1967) Potential buildup on an electron-emitting ionospheric satellite, J. Geophys. Res. 72:1631.

12. Linson, L.M. (1969) Current-voltage characteristics of an electron-emitting satellite in the ionosphere, J. Geophys. Res. 74:2368.

13. Winckler, J.R. (1980) The application of artificial electron beams to magnetospheric research, Rev. Geophys. Space Phys. 18:659.

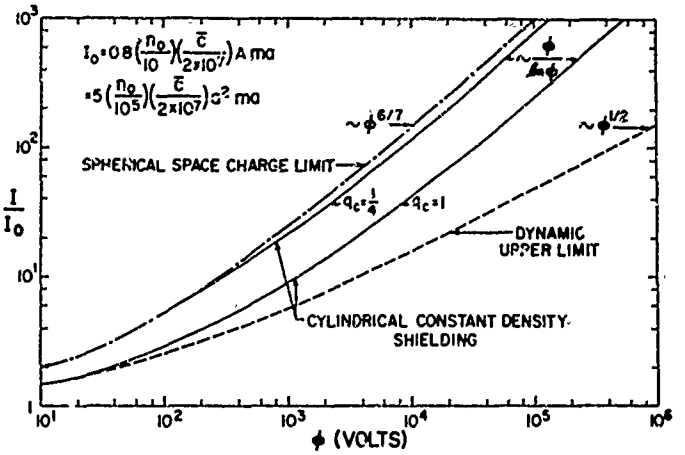

Figure 14. Comparison of Three Methods for Determining the Collected Electron Current as a Function of Potential on a Charged Sphere. (Reprinted from the Journal of Geophysical Research)

electron beam emission experiments appears to be quite different in the ionosphere than it is in the low density magnetosphere. Both ion and electron beam experiments have been carried out in the magnetosphere on the ATS-5, ATS-6, and SCATHA satellites. These experiments have shown that emission of a plasma containing both ions and electrons is required to fully discharge the conducting and dielectric surfaces on spacecraft (Purvis and Bartlett[14]). There has been no evidence of any kind of a beam plasma discharge in these beam emission experiments at synchronous altitudes.

Cohen et al[15] have shown that charging a vehicle by ion beam emission in the ionosphere is consistent with the return current consisting of ions collected from the ionospheric plasma. However, electron beam experiments in the ionosphere have yielded vehicle potentials much lower than the beam energy.[13,16] (A possible exception is the Jacobson and Maynard[17] result.) Anomalously high

14. Purvis, C.K., and Bartlett, R.O. (1980) Active control of spacecraft charging, Prog. Astron. Aeron. 71:299.

15. Cohen, H.A., Sherman, C., and Mullen, E.G. (1979) Spacecraft charging due to positive ion emission: an experimental study, Geophys. Res. Lett. 6:515.

16. Arnoldy, R.L., and Winckler, J.R. (1981) The hot plasma environment and floating potentials of an electron-beam-emitting rocket in the ionosphere, J. Geophys. Res. 86:575.

17. Jacobson, T.A., and Maynard, N.C. (1980) Evidence for significant spacecraft charging by an electron accelerator at ionospheric altitudes, Planet. Space Sci. 28:291.

return electron currents have kept vehicle potentials low. A beam plasma discharge may have occurred in some of these experiments, but the evidence for this is not yet convincing, although the data showed that there were a large number of heated electrons in the vicinity of the vehicle. These heated electrons were produced by a variety of processes, probably including collisional ionization of the ambient and vehicle-produced neutral gases, secondary electron production, and the effects of waves and instabilities excited in the surrounding plasma.

8. NEUTRAL ATOM AND MOLECULE IMPACT EFFECTS

Recent data from the plasma diagnostics package on the space shuttle flight STS-3 showed a faint, sub-visual glow on the leading surfaces of the spacecraft. The glow was attributed to the effects of impact of neutral atomic oxygen atoms on the surfaces at a kinetic energy of about 5 eV (Williamson et al[18]). Other kinds of neutral particle impact effect have been seen by Hanson et al[19] on the AE-C satellite where ion sputtering was inferred to have occurred because of neutral atom and molecule impact, and on the Pioneer Venus Orbiter,[20] which showed a change in the Langmuir Probe current at periapsis that correlated well with the neutral atmospheric density.

The data from the Pioneer Venus Orbiter can be qualitatively explained by the secondary emission of electrons from the spacecraft and from the probe itself, caused by the impact of neutral CO_2 molecules. These molecules are the dominant constituent at the peripasis altitude of about 150 km in the Venus atmosphere, and the impact energy at the satellite orbital speed is about 22 eV. Figure 15 illustrates the secondary emission process that is thought to occur in the vicinity of the leading surface of the spacecraft that is exposed to the streaming neutral gas. As the probe voltage is swept, contributions to the current from the ionospheric plasma and from the secondary electrons can be distinguished. The observed current/voltage behavior is suggestive of a probe-barrier interaction.[21]

Effects of neutral particle impact on the charging of vehicles in the ionosphere have been ignored almost completely in the past. Although the effects are usually

18. Williamson, P.R., Banks, P.M., Raitt, W.J., Baker, K.D., Sojka, J.J., Inan, U., Obayashi, T., and Taylor, W.W.L. (1982) Vehicle charging and potential: first results from the OSS-1 mission on STS-3, Spring AGU Mtg., Philadelphia, Pa.

19. Hanson, W.B., Sanatani, S., and Hoffman, J.H. (1981) Ion sputtering from satellite surfaces, J. Geophys. Res. 86:11350.

20. Brace, L.H. (1981) Private Communication.

21. Parker, L.W. (1982) Private Communication.

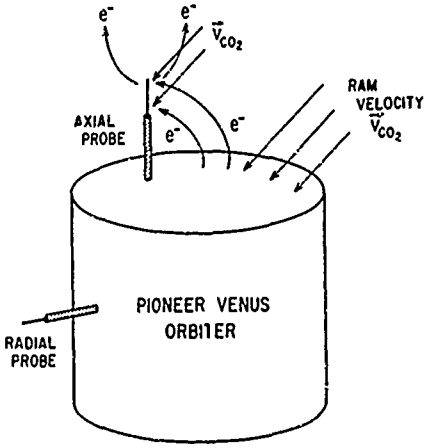

Figure 15. Model for a Secondary Emission Process at the Leading Surface of a Spacecraft Exposed to a Streaming Neutral Gas

small, they should be kept in mind as potentially important for large structures at lower altitudes in the ionosphere where the neutral density is relatively large.

9. CONCLUDING QUESTIONS

We close with a list of important unanswered questions:

(1) What is the size and frequency of occurrence of large, energetic electron fluxes in the auroral ionosphere?

(2) Can a good sheath approximation be developed to describe ion collection by a large body in a streaming plasma?

(3) Is there an easy way to calculate the magnitude of the potential barrier in the wake of a spacecraft in the ionosphere?

(4) For large structures where the $\underline{V} \times \underline{B}$ effect leads to large induced currents, how does the current path return through the plasma?

(5) What is the asymptotic (that is, distant) behavior of the plasma around a large, moving structure in the ionosphere?

(6) What is the mechanism for electron collection by moderately or highly positively charged bodies in the ionosphere?

References

1. Bourdeau, R.E., Donley, J.L., Serbu, G.P., and Whipple, E.C. (1961) Measurements of sheath currents and equilibrium potential on the Explorer 8 satellite, J. Astronaut Sci. 8:65.
2. Katz, I., and Parks, D.E. (1982) Space Shuttle Orbiter Charging, AIAA 20th Aerospace Sci. Mtg., Orlando, Florida, Jan., 1982.
3. Langmuir, I., and Blodgett, K. (1924) Currents limited by space charge between concentric spheres, Phys. Rev. 24:99.
4. Al'pert, Ya.L., Gurevich, V., and Pitaevskii, L.P. (1965) Space Physics With Artificial Satellites, Consultants Bureau, New York, pp. 186-210.
5. Parker, L.W. (1980) Plasmasheath-photosheath theory for large high-voltage space structures, Prog. Astron. Aeron. 71:477.
6. Samir, U., and Wrenn, G.L. (1969) The dependence of charge and potential distribution around a spacecraft on ionic composition, Planet. Space Sci. 17:693.
7. Whipple, E.C. (1981) Potentials of surfaces in space, Rep. Prog. Phys. 44:1197.
8. Parker, L.W. (1978) Differential charging and sheath asymmetry of nonconducting spacecraft due to plasma flows, J. Geophys. Res. 83:4873.
9. Laframboise, J.G. (1966) Theory of Spherical and Cylindrical Langmuir Probes in a Collisionless, Maxwellian Plasma at Rest, Rep. No. 100, University of Toronto Institute for Aerospace Studies.
10. Parker, L.W., and Sullivan, E.C. (1974) Iterative Methods for Plasma-Sheath Calculations--Application to Spherical Probe, NASA TN D-7409.
11. Parker, L.W., and Murphy, B.L. (1967) Potential buildup on an electron-emitting ionospheric satellite, J. Geophys. Res. 72:1631.
12. Linson, L.M. (1969) Current-voltage characteristics of an electron-emitting satellite in the ionosphere, J. Geophys. Res. 74:2368.

13. Winckler, J.R. (1980) The application of artificial electron beams to magnetospheric research, Rev. Geophys. Space Phys. 18:659.

14. Purvis, C.K., and Bartlett, R.O. (1980) Active control of spacecraft charging, Prog. Astron. Aeron. 71:299.

15. Cohen, H.A., Sherman, C., and Mullen, E.G. (1979) Spacecraft charging due to positive ion emission: an experimental study, Geophys. Res. Lett. 6:515.

16. Arnoldy, R.L., and Winckler, J.R. (1981) The hot plasma environment and floating potentials of an electron-beam-emitting rocket in the ionosphere, J. Geophys. Res. 86:575.

17. Jacobson, T.A., and Maynard, N.C. (1980) Evidence for significant spacecraft charging by an electron accelerator at ionospheric altitudes, Planet. Space Sci. 28:291.

18. Williamson, P.R., Banks, P.M., Raitt, W.J., Baker, K.D., Sojka, J.J., Inan, U., Obayashi, T., and Taylor, W.W.L. (1982) Vehicle charging and potential: first results from the OSS-1 mission on STS-3, Spring AGU Mtg., Philadelphia, Pa.

19. Hanson, W.B., Sanatani, S., and Hoffman, J.H. (1981) Ion sputtering from satellite surfaces, J. Geophys. Res. 86:11350.

20. Brace, L.H. (1981) Private Communication.

21. Parker, L.W. (1982) Private Communication.

Contents

2. Ionospheric Characteristics: A Review

by

F. J. Rich
Air Force Geophysics Laboratory
Space Physics Division
Hanscom AFB, Mass.. 01731

This paper discusses low, mid, and high latitude ionospheric characteristics.

1. INTRODUCTION

The ionosphere is the ionized component of the earth's atmosphere. We generally consider the ionosphere to lie between 60 and 1000 km altitudes. On the bottomside, the ionosphere is bounded by high recombination rates and low production rates of ionization. On the topside, the ionosphere is bounded only by gravity and the earth's magnetic field. Since H^+ is gravitationally unbound, the topside of the ionosphere does not have a distinct boundary. For convenience, we will define the ionosphere as those regions of the near-earth environment where the density of ions (or electrons) with temperatures less than 1 eV, or 13,000 ^oK, is greater than 1.0/cm^3.

The ionosphere is important to spacecraft charging because the thermal ions and electrons can provide a significant current to a spacecraft surface (see Figure 1). For approximate calculations of current balance the emitted photoelectron distribution is a two-component Maxwellian electron gas with temperatures of ~ 2 eV and ~ 20 eV. In a pure vacuum, solar UV radiation causes

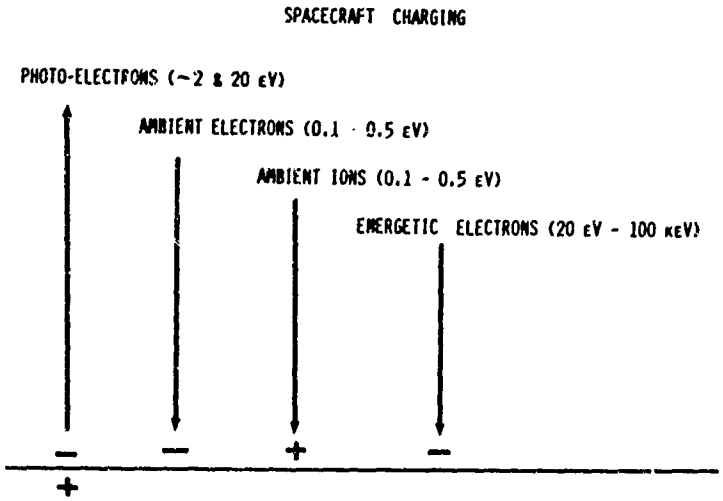

Figure 1. Sources of Currents to and From a Spacecraft in the Ionosphere

photoelectrons to be emitted from spacecraft surfaces and the spacecraft charges positively. In low earth orbit, the ambient electrons flow to the spacecraft to yield a vehicle charge of 0 to -1 V in sunlight and -1 to -2 V in shadow. The ambient ions also provide a small current to the spacecraft surface. However, because a spacecraft traveling 7.8 km/sec is supersonic with respect to the ions, the ionospheric ions can only be collected on the forward or ram side of the spacecraft. The only times that spacecraft charges greater than a few volts are likely is when either there are larger fluxes of energetic particles than ambient particles, or when the spacecraft is actively emitting or absorbing electrons or ions. The first is a high latitude effect. The latter can occur any place.

2. LOW- AND MID-LATITUDE IONOSPHERE

In general the ionosphere is approximately in a state of balance between physical processes that create ionization in a unit volume and processes that remove ionization from that unit volume. Figure 2 shows the various terms. The most common source of production is photoionization of neutral gas by solar radiation and the most common loss process is recombination. If the ionosphere were created by one frequency of photon and had one loss process, the ionosphere would be a single layer of ionization with exponential decreases in density with distance from a peak density altitude. This static layer model is known as a

IONOSPHERIC PLASMA

PRODUCTION		LOSS	
SOURCE	REGION	PROCESS	REGION
COSMIC RAYS, X-RAYS	D	RECOMBINATION	D,E,F
EUV	E	CHARGE EXCHANGE	F
UV	F	TRANSPORT (V AND H)	F
PARTICLE PRECIPITATION	D,E,F		
TRANSPORT	F		

Figure 2. Sources of Production of Charged Particles in the Ionosphere and Processes Causing Losses of Charged Particles From the Ionosphere

Chapman layer.[1] Since there are many processes occurring simultaneously, the ionosphere is not described as a simple Chapman layer. However, since certain processes dominate at certain altitudes, an ionospheric model with four Chapman layers is a reasonable first-order approximation of the ionosphere.

If the solar UV flux is specified and the solar zenith angle is specified, density profiles such as Figure 3 can be calculated with good accuracy from a superposition of Chapman layers, at least at low altitudes. Above 300 km altitude, the mean free path of ionospheric particles becomes long enough that transport along magnetic field lines becomes an important phenomenon. Below 300 km, transport is important only if the ions and electrons are pushed through magnetic fields by the neutrals. Since the collision frequencies for ion-neutral and electron-neutral interactions are different, movement of ionospheric plasma through the magnetic field results in electric currents, such as the equatorial electrojet and the mid-latitude S_q current system shown in Figure 4. Near the equator, the rise of the neutral atmosphere due to solar heating pushes the ionospheric plasma upward. Since the ionospheric plasma cannot return to lower latitudes in an ordinary convective motion, the plasma slides down magnetic field lines.[2] This is the equatorial fountain effect, shown in Figure 5. The result is that plasma density between ~ 200 and ~ 500 km altitudes near the equator is less than the density a few degrees to either side of the equator.

There are many processes occurring in the mid and low-latitude ionosphere that make it impossible to calculate the plasma density exactly. The processes, other than solar UV and recombination, generally yield a second-order variation to the plasma density. The various processes affecting the mid- and low-latitude

1. Banks, P.M., and Kockart, G. (1973) Aeronomy: Part A and Part B, Academic Press, New York.

2. Hanson, W.B., and Moffet, J. (1966) Ionization and transport effects in the equatorial F region, J. Geophys. Res. 71:5559-5572.

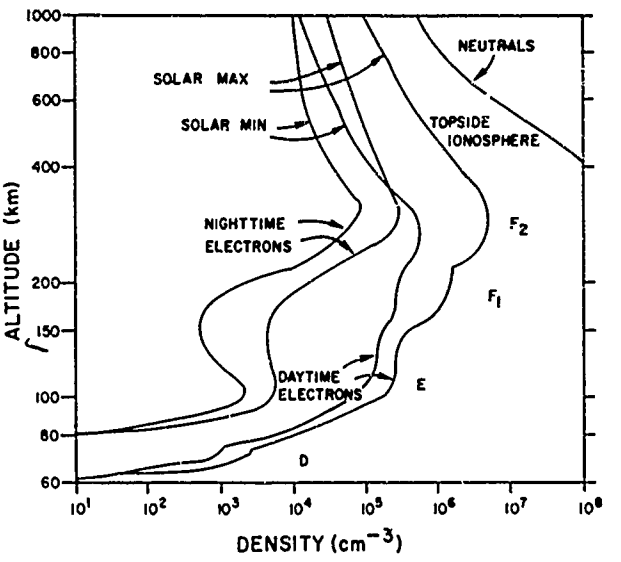

Figure 3. Day and Night Midlatitude Electron Density Profiles for Solar Maximum and Solar Minimum

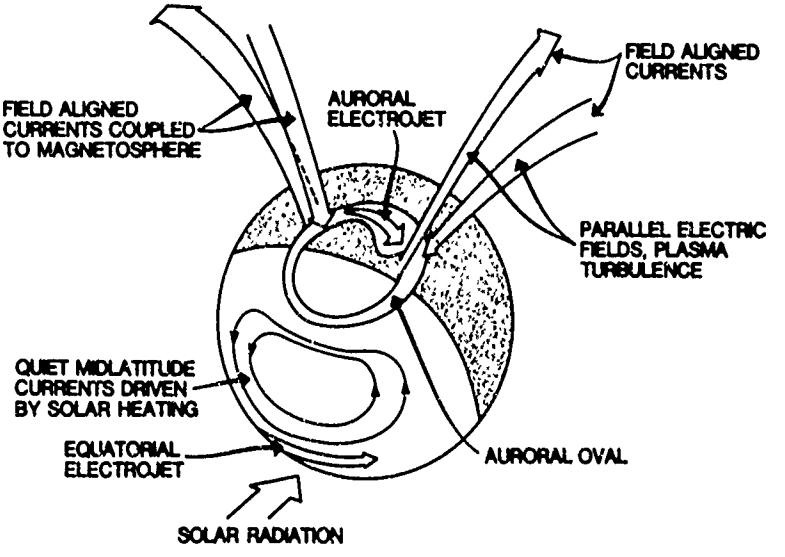

Figure 4. Electrical Coupling Between the Magnetosphere, Ionosphere, and Atmosphere

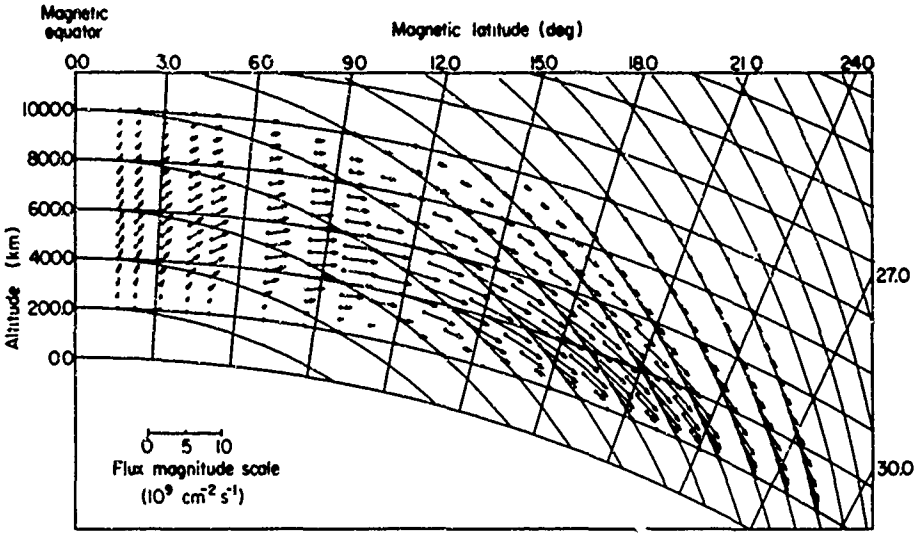

Figure 5. The "Equatorial Fountain." Vector plot of electron flux in the meridian plane, in a theoretical steady-state model of the equatorial F region. The motions are due to the combined action of plasma diffusion along magnetic field lines and electromagnetic drift across field lines, produced by an assumed distribution of eastward electric field. The magnetic field lines are shown every 200 km above the equator [Hanson and Moffett (1966)]. (Reprinted from the Journal of Geophysical Research)

ionosphere generally have small spatial gradients. The result is that the low- and mid-latitude density profiles change very slowly with latitude and local time, except at sunrise and sunset. At high latitudes, the processes other than solar UV ionization and recombination loss are stronger, have smaller spatial scale sizes and have greater temporal variations. Figure 6 demonstrates the difference between the polar ionosphere and the mid- and low-latitude ionosphere. It shows the plasma density observed at 840 km altitude by the polar-orbiting DMSP/F2 satellite over two orbits.

The dominant component of the ionosphere between 300 and 1000 km altitudes is O^+. Above the peak density of the F2 region the O^+ density decreases with a height with a scale length of 200-400 km. Above 1000 km altitude, the dominant ion becomes H^+. Due to its low mass, H^+ is not gravitationally bound to the earth. If the earth did not have a magnetic field, H^+ would free-flow away from the earth. At mid- and low-latitude, the magnetic field confines the ionospheric H^+. This region of trapped ionospheric H^+ is called the plasmasphere, and is shown in Figure 7. Depending on the context of a discussion, either the transition from O^+ to H^+ can be called the top of the ionosphere, or the plasmasphere

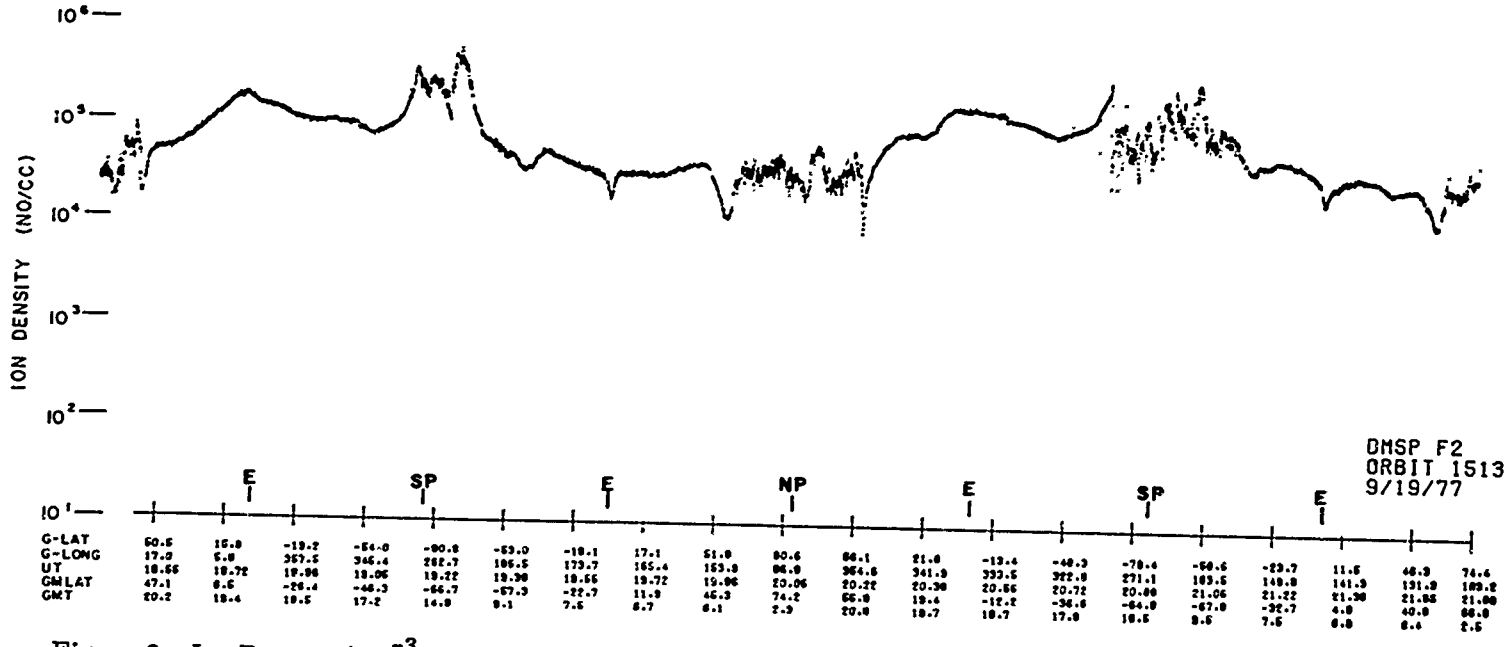

Figure 6. Ion Density (cm^{-3}) Measured Along the Orbital Path of the Defense Meteorology Satellite Program (DMSP) F2 Satellite

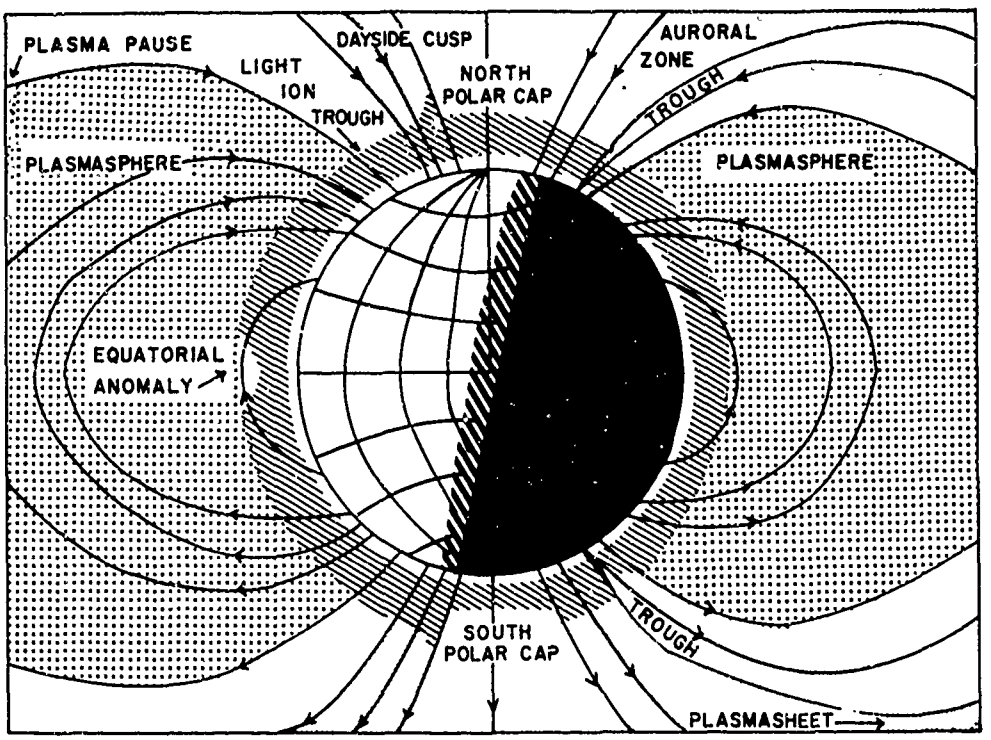

Figure 7. The Ionosphere and Inner Magnetosphere Including the Plasmasphere

can be called a part of the ionosphere. The edge of the plasmasphere, called the plasmapause, is defined by the rate at which H^+ can fill a tube of magnetic flux and the strength of the magnetospheric convection electric field which drives flux tubes away from the near-earth region. Generally the plasmapause is found along the magnetic field line that passes through the earth near 60^o magnetic latitude, or $L = 4 = (\cos 60^o)^{-2}$. The plasma density inside the plasmapause is 10^2 to 10^4, and outside it is 10^1 to 10^{-1} cm^{-3} at altitudes greater than 3000 km. Figure 8 shows several examples of the plasmapause observed by GEOS-1.[3]

3. HIGH-LATITUDE IONOSPHERE

In order to understand the high-latitude ionosphere, it is necessary to understand the interaction of the near-earth environment with the solar environment.

3. Decreau, P.M.E., Beghin, C., and Parrot, M. (1982) Global characteristics of the cold plasma in the equatorial plasmapause region as deduced from the GEOS 1 mutual impedance probe, J. Geophys. Res. 87:695-712.

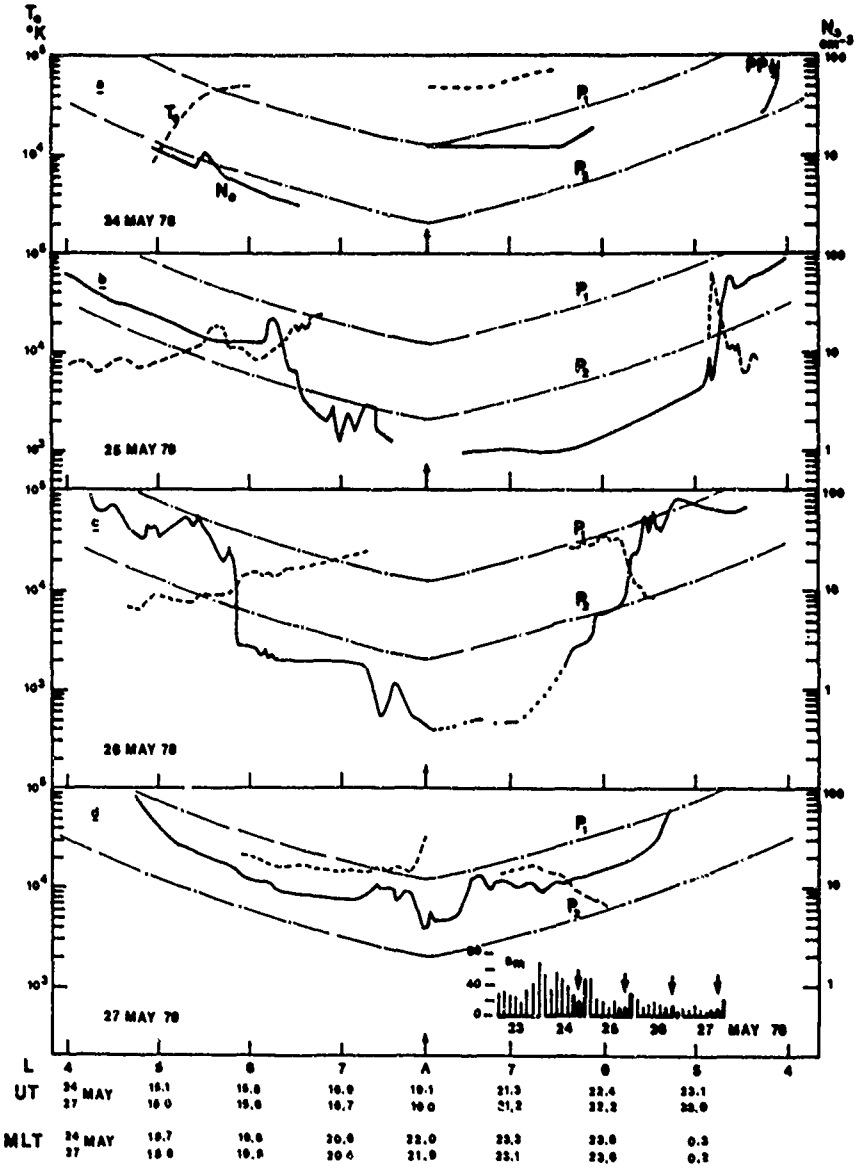

Figure 8. The Plasmapause as Observed at High Altitudes by the GEOS Spacecraft. (Reprinted from the Journal of Geophysical Research)

At the interface between the chromosphere and the corona of the sun, plasma is heated to temperatures of a few million ^{o}K or a few hundred eV and given a radially outward bulk flow velocity of ~ 1000 km/sec, which is highly supersonic with respect to the ions. The plasma pulls magnetic field lines away from the

sun. The magnetic field lines are bent into a spiral formation, shown in Figure 9, as the sun rotates while the supersonic flow of plasma, known as the solar wind, travels radially outward and passes the earth. At the distance of the earth, the plasma temperature is roughly unchanged due to electron conduction of heat from the inner corona, but the flow speed is decreased to ~ 400 km/sec. The earth's magnetic field acts as a blunt object in the pathway of the supersonic flow. There is a shock front 12-20 earth radii in front of the earth as the solar wind slows to flow around the earth's environment. The boundary between the solar wind and the terrestrial environment is called the magnetopause and is sharply defined at the noon side and dusk and dawn flanks of the terrestrial environment. The terrestrial environment inside the magnetopause is the magnetosphere. The interaction of the solar wind and the earth's magnetic field causes magnetic field lines that in a vacuum would cross the equatorial plane at distances greater than four earth radii ($L \geq 4$) to be pushed inward on the dayside and pulled outward on the nightside as shown in Figure 10. At high latitudes ($L \geq 20$), the earth's magnetic field lines are drawn behind the earth to distances of greater than 200 earth radii and may be connected to the solar magnetic field being carried by the solar wind. This region of stretched out magnetic field is called the geomagnetic tail. In the geomagnetic tail, there is a slab of hot, semi-trapped plasma called the plasma sheet. The source of the plasma sheet is often assumed to be the solar wind, although it is not known how the plasma crosses the magnetopause. It is also possible that the plasma sheet is populated (at least in part) by ionospheric plasma that has been heated by unknown mechanisms. The plasma sheet connects to the earth in the auroral regions.

The auroral region is a band of disturbed ionosphere at high latitudes. The band is approximately 6° wide formed into a circumpolar ring centered approximately 3° toward midnight from the magnetic pole and 25° to 50° in diameter. The auroral region is characterized by particles entering the ionosphere, scattering off the neutral atmosphere between 100 and 500 km altitude and causing enhanced ionization. The incoming particles are predominantly electrons, but some ions also are entering the ionosphere. The ionization and recombination processes involving the incoming particles result in visible light emissions that are characteristic of the aurora. In much of the auroral zone, the spectrum of the incoming particles indicates that they are electrons with energies of ~ 1 keV and isotropic in the downcoming hemisphere of pitch angles. Since particles trapped on field lines with mirror points below 500 km altitude are quickly lost to the atmosphere, some process or processes in the plasma sheet must rapidly [illegible] the pitch angle of particles to provide a steady source of particles [illegible] ionosphere. The isotropic incoming electrons cause

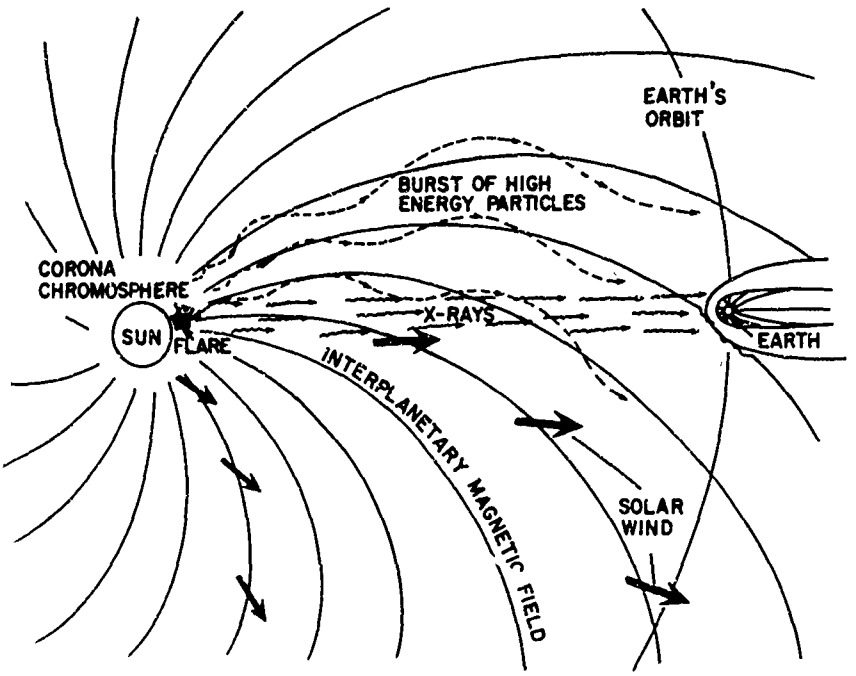

Figure 9. The Solar-terrestrial Environment

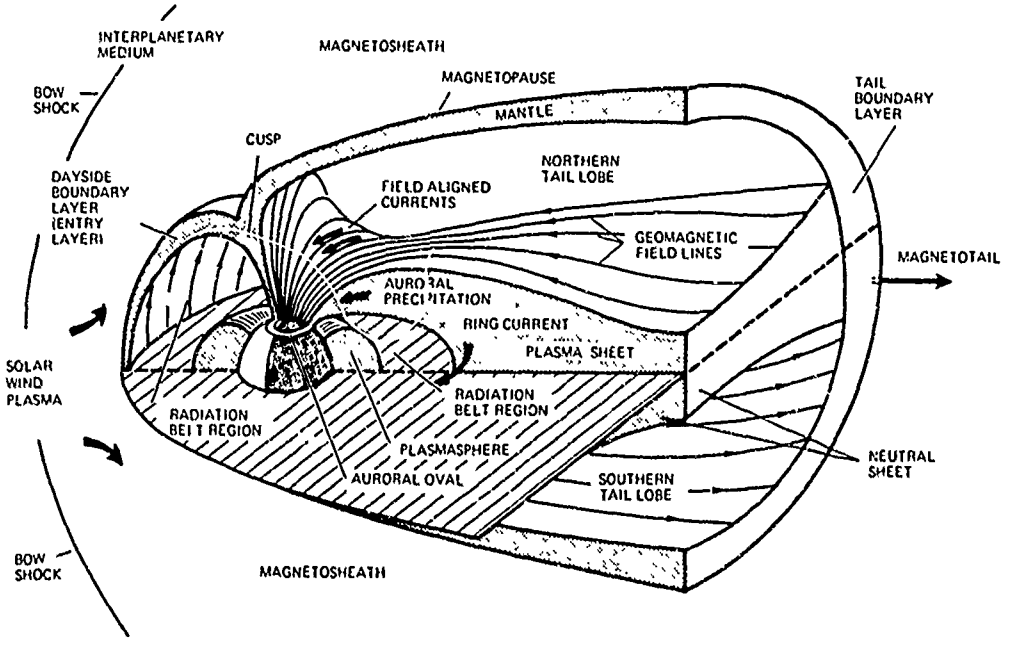

Figure 10. The Magnetosphere Shown as a Cut-away Schematic

a barely visible or sub-visual, spatially uniform emission known as the diffuse aurora. The bright, spatially distinct auroral features of arcs, bands, rays, and curtains are generally caused by electrons that have a Maxwellian energy distribution of ~ 1 keV plus an acceleration along the magnetic field of several keV. The degree of acceleration is often spatially distributed across a latitudinal distance of ~ 100 km. At the center of the region (where the bright visual features are often found), the acceleration is maximum and it smoothly decreases with latitudinal distance from the center. Due to the shape of such a feature on spectrograms, this feature is called an "inverted-V". Such features are often spatially uniform for a great distance in the direction along the auroral oval. These accelerated particles also come from the plasma sheet and are accelerated into the ionosphere at altitudes of 2,000 to 12,000 km.

The equatorward boundary of the auroral zone can be defined as the equatorward edge of precipitating particles. This also is assumed to define the field line that forms the inner edge of the plasma sheet. Figure 11 shows the equatorward edge of the auroral zone in magnetic latitude/magnetic local time coordinates as defined by the DMSP satellite's particle detector.[4] The area of high latitude ionosphere affected by auroral particles increases with the intensity of auroral activity as given by the K_p index. This implies that the plasma sheet moves earthward during high activity, and particle observations at geosynchronous orbit confirm this inward movement.

It has been stated that the ionosphere is like the screen of a television set. The ionosphere at high latitudes produces images of physical processes elsewhere. In a television set, the processes occur in the modulation circuit and the electron gun. In the solar-terrestrial environment, the processes occur on the magnetopause and in the magnetosphere. At the magnetopause on the dayside, geomagnetic flux tubes are broken open by magnetic merging with solar wind magnetic flux tubes. The flux tubes are pulled across the polar regions into the geomagnetic tail where the geomagnetic ends of flux tubes break away from the solar wind flux tubes and rejoin at both ends to the earth. In the geomagnetic tail, the flux tubes move earthward to a distance of 4 to 12 earth radii in the midnight sector and then slide around the earth until they are once again on the magnetopause in the noon sector. These motions are seen in the ionosphere as plasma drifts from noon to midnight across the polar cap and back to noon along the auroral oval. Such motion in a magnetic field is equivalent to an electric field and the streamlines of motion are equivalent to equipotential surfaces[5] as shown

4. Hardy, D.A., Burke, W.J., and Gussenhoven, M.S. (1982) DMSP optical and electron measurements in the vicinity of polar cap arcs, J. Geophys. Res. 87:2413-2430.

5. Heppner, J.P. (1977) Empirical models of high-latitude electric fields, J. Geophys. Res. 82:1115-1125.

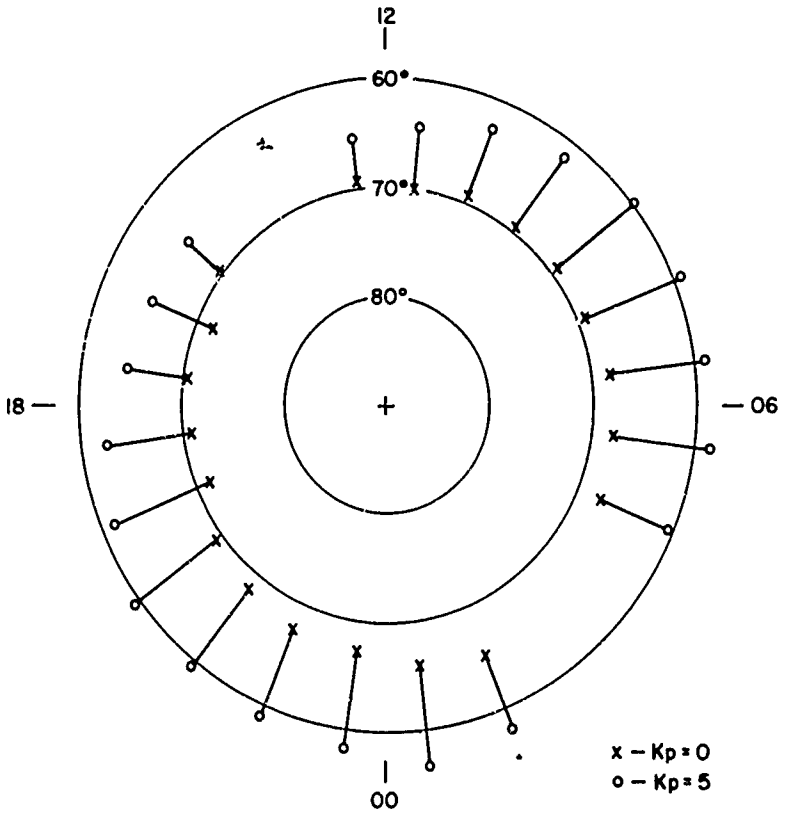

Figure 11. The Equatorward Boundary of Precipitating Electrons Determined From Detectors on DMSP Satellites for Very Quiet (K_p = 0) and Active (K_p = 5) Geomagnetic Conditions. The coordinate system is invariant latitude and magnetic local time

in Figure 12. If the ionosphere were a perfect projection of magnetosphere plasma motion and that motion was simple, Figure 12a would be a good representation of the expected high-latitude plasma circulation pattern. In fact, there are several complicating factors. First, the earth rotates and a co-rotation electric field term is shown in Figure 12b. Next, the ionosphere is not a uniform region of electrical conductivity. Figure 12c shows the addition of a simple variation in ionospheric conductivity and Figure 12d is the sum of all three effects. The real variation in the ionosphere is complex due to a complex spatial pattern of particle precipitation. Figure 13 shows a statistically averaged conductivity pattern based on solar UV and particle precipitation observed by Atmospheric Explorer.[6]

6. Spiro, R.W., Reiff, P.H., and Maher, L.J. (1982) Precipitating electron energy flux and auroral zone conductances--an empirical model, J. Geophys. Res. 87:8215.

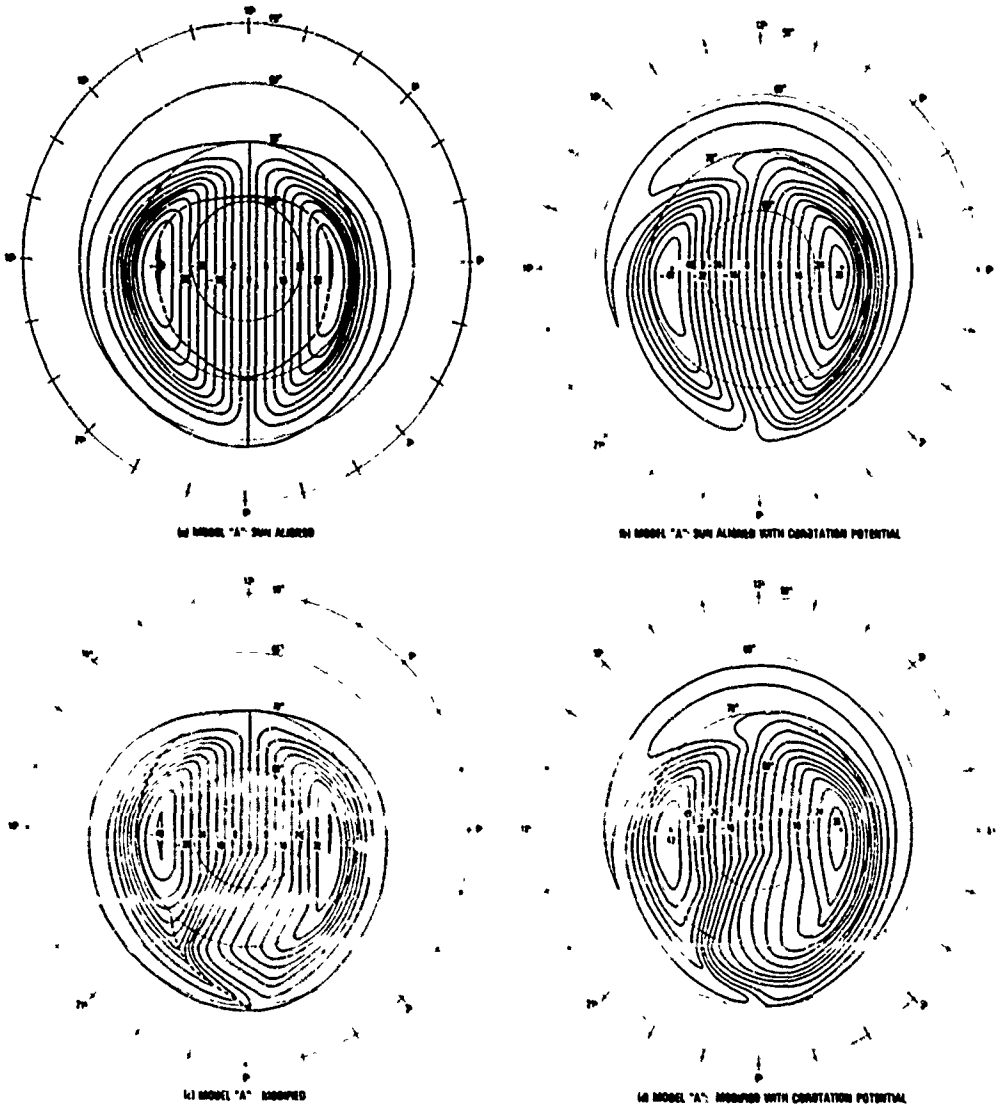

Figure 12. Convection Patterns Based on Model A (4-keV Contour Intervals). (a) Sun-aligned pattern. The dashed line shows the location of the polar cap boundary. (b) Sun-aligned pattern with corotation added. (c) Model A pattern modified to fit nightside observations. The Harang discontinuity is indicated with a dashed line. (d) Model A pattern modified to fit nightside observations with corotation added. (Reprinted from the Journal of Geophysical Research)

The motion of ionospheric plasma at high latitudes moves plasma between high and low production regions. In addition, the motion of plasma by an electric field causes a differential flow between the plasma and the neutral atmosphere.

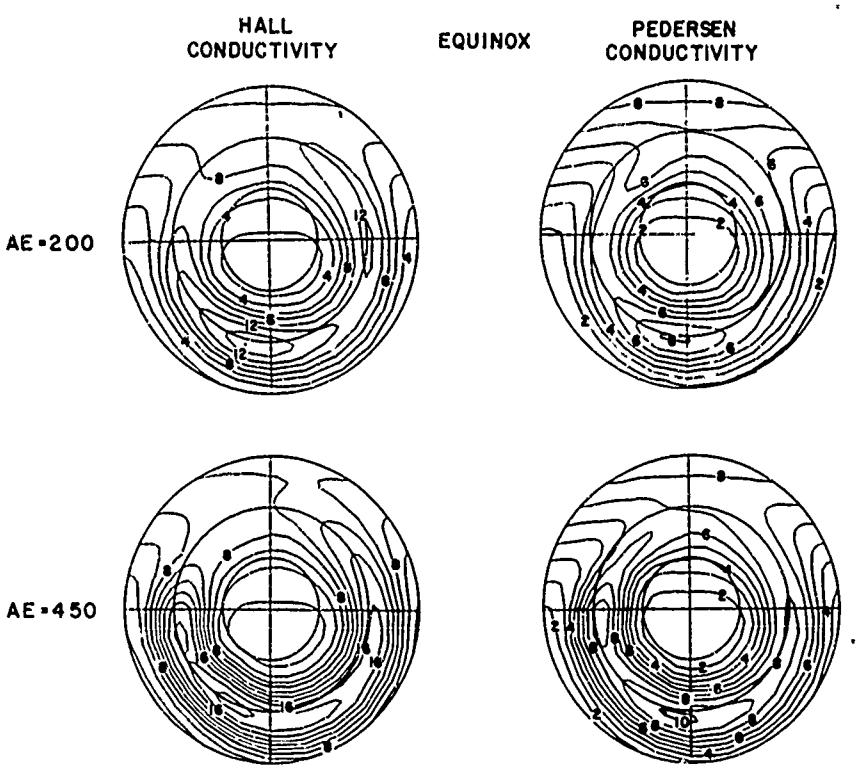

Figure 13. The Height Integrated Hall and Pedersen Conductivity in the High Latitude Ionosphere From Solar UV Plus Average Particle Flux Based on Atmospheric Explorer Data for Two Levels of Geomagnetic Activity. The diagram assumes that the geographic and geomagnetic coordinates are co-located

The differential flow results in an enhanced collision rate that changes the chemical processes related to charge exchange and recombination. The overall effect is that differential flow tends to decrease the total plasma density, especially at altitudes above the production region.[7] Also, the differential flow can have a very significant effect upon the ratio of various ionic components of the ionosphere. Figures 14 and 15 show typical high latitude height profiles of the ionosphere for conditions of no plasma flow and strong plasma flow respectively.

Another effect on the ionospheric density, especially above 400 km altitude, is the polar wind. At all latitudes, H^+ ions tend to flow up magnetic field lines. At mid-latitudes, the flux tubes close near the earth and trap a significant population of H^+. The result is that H^+ flows upward at diffusive speeds of less than

7. Sojka, J.J., Raitt, W.J., Schunk, R.W., Rich, F.J., and Sagalyn, R.C. (1982) Observations of the diurnal dependence of the high-latitude F region ion density by DMSP satellites, J. Geophys. Res. 87:1711-1718.

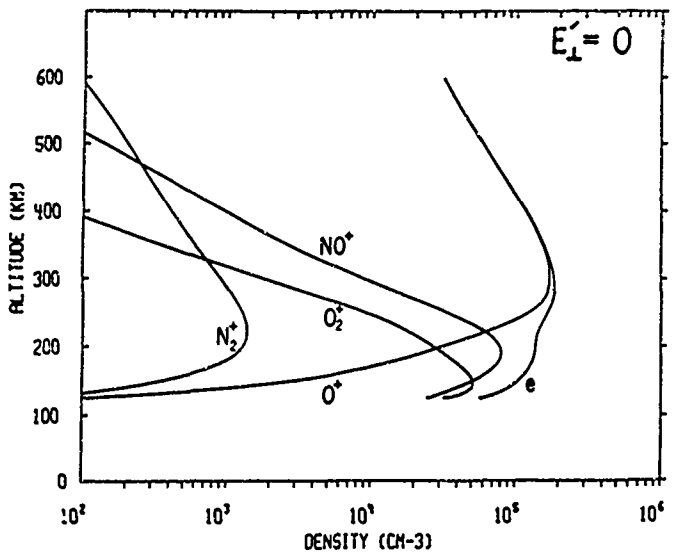

Figure 14. A Typical Density Profile in the Post-sunset, High-latitude Ionosphere When the Convection Electric Field is Zero

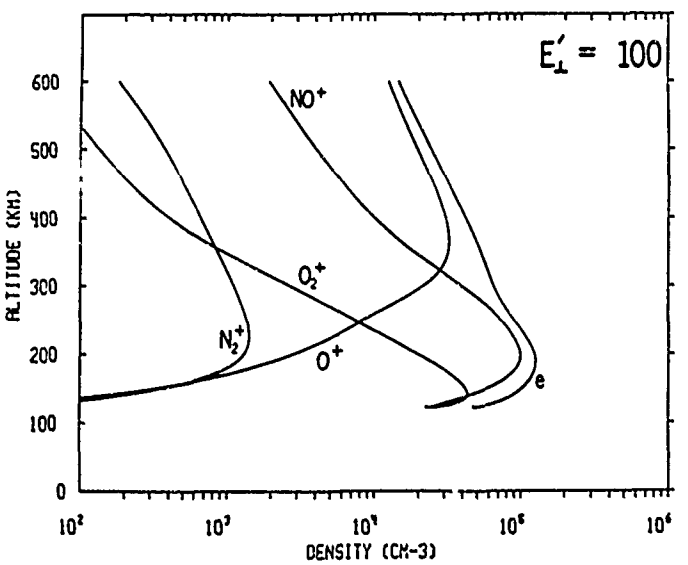

Figure 15. Same as Figure 14 Except the Convection Electric Field is 100 mV/m. This increases the collision rate between ions and neutrals due to the differential bulk motions

1 km/sec such as curve (a) or (b) in Figure 16. At high latitudes, the random velocity of H^+ is converted into streaming velocity as the ions move up the rapidly expanding flux tubes. The streaming velocity may approach the sonic velocity of H^+ as in curves (d), (e), or (f) of Figure 16 or become supersonic as in curves (g) or (h). The upward flow of H^+ has a significant effect on the density profile as shown in Figure 17. Since H^+ would be the dominant ion above ~ 1000 km altitude in the absence of flow out of the ionosphere, the presence of outward flow decreases the total density at high altitudes in the high latitude ionosphere. The shaded section of Figure 17 represents a range of typical 0^+ profiles. Figure 18 shows a measured profile of the total density at high altitude and high latitude. From 1500 to 2000 km altitude, the measured ionosphere has a very small scale height similar to the shaded 0^+ profile range in Figure 17. Above 2000 km altitude, the measured profile[8,9] is similar to the H^+ profile (h) in Figure 17. (For further detail, see chapter 24, "Models of the Ionospheric Environment" by R.W. Schunk.)

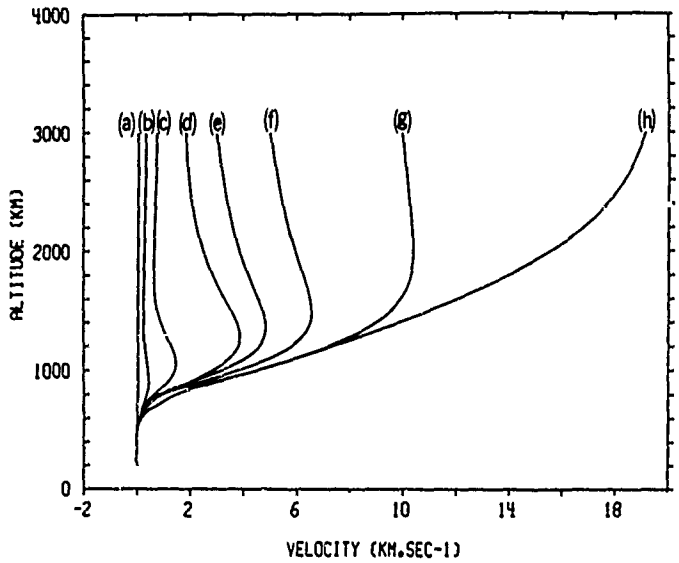

Figure 16. Various Possible Flow Velocity Profiles for the Outflow of H^+ From the High-latitude Ionosphere

8. Lysak, R.L., and Hudson, M.K. (1979) Coherent anomalous resistivity in the region of electrostatic shocks, Geophys. Res. Letts. 6:661-663.

9. Mozer, F.S., Cattell, C.A., Temerin, M., Torbert, R.B., Von Glinski, S., Woldorff, M., and Wyant, K.J. (1979) The dc and ac electric field, plasma density, plasma temperature, and field-aligned current experiments on the S3-3 satellite, J. Geophys. Res. 84:5875-5884.

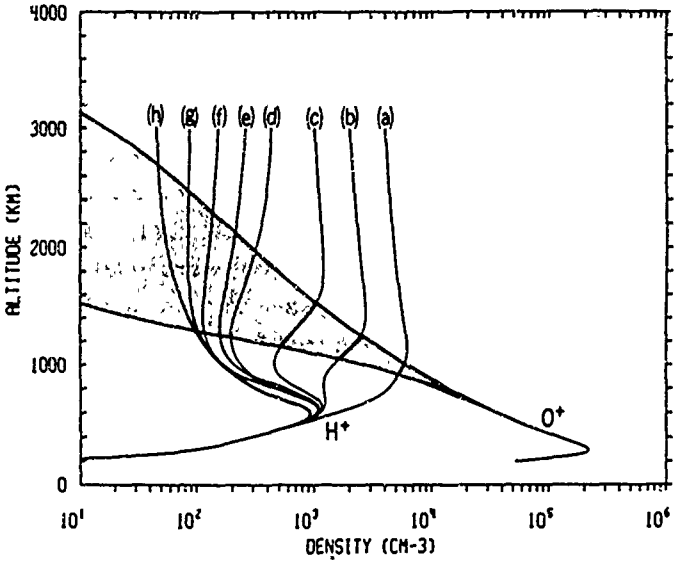

Figure 17. Various H^+ Density Profiles That Result From the Outflow Profiles in Figure 16. The shaded 0^+ range of profiles represents a typical range of scale heights

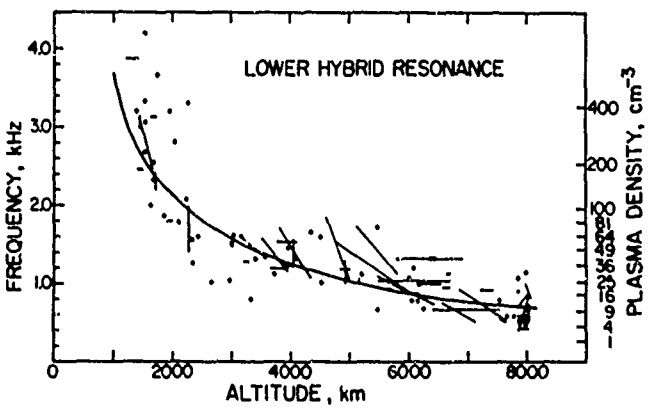

Figure 18. A Plot of the Lower Hybrid Resonance Frequency as a Function of Altitude[9] With the Calculated LHR Frequency Based on a Dipole Field Model at Invariant Latitude 70° and on the Density Profile $n = 1.34 \times 10^7 h^{-1.55}$

At high latitudes, electrical currents flow along magnetic field lines from the magnetosphere to the ionosphere and back again. These field-aligned

currents are a significant element in the solar-terrestrial interaction.[10] There are two ways to explain the field-aligned currents. First, given that the solar-terrestrial interaction generates the electric field shown in Figure 12 and that the ionosphere is a conductor, electric currents must flow in the ionosphere. Where there is a divergence in the ionospheric current, current flows up or down field lines to maintain current continuity. Alternatively the field-aligned currents could be considered a primary result of the solar-terrestrial interaction. The current across the polar cap from the dawn sector to the dusk sector could be an element of the Chapman-Ferraro current system in the magnetosphere that forms the magnetopause. The electric field is then required to keep the currents flowing. The horizontal ionospheric currents flow primarily at altitudes of 100 to 120 km.

The distribution of field-aligned currents was unknown until satellite magnetometers mapped out the magnetic field deflection caused by the currents flowing along the field lines.[10] The distribution given in Figure 19 is a statistical average based on observations at 800 km altitude. The current into the ionosphere on the morningside and out on the afternoon/evening-side is called Region 1 and is often considered to be directly related to the solar-terrestrial interaction. The current just equatorward of Region 1 is called Region 2 and is oppositely directed. The Region 2 current is often considered to be a response to Region 1 currents. There are reported observations of Region 1 currents without Region 2 current, but not the reverse. Without Region 2 currents, the ionospheric currents connecting the morning and evening Region 1 currents will flow at mid-latitudes as well as at high latitudes. With Region 2 currents present, almost all of the ionospheric currents related to the field-aligned current system flow in the high latitude ionosphere.

The charge carriers for the field-aligned current are almost exclusively electrons. The current into the ionosphere is carried by thermal electrons flowing sub-sonically out of the ionosphere. The current out of the ionosphere is carried by precipitating electrons. The regions of currents into the ionosphere often are in regions of precipitating electrons, but the net flux of electrons is upward. There are observations of ion fluxes into and out of the ionosphere but the ion fluxes are insignificant for carrying the current. In regions where electrons are accelerated into the ionosphere, ions have been observed to be flowing out of the ionosphere due to the same electrostatic potential drop along the field lines.

10. Iijima, T., and Potemra, T.A. (1978) Large-scale characteristics of field-aligned currents associated with substorms, J. Geophys. Res. 83:599-615.

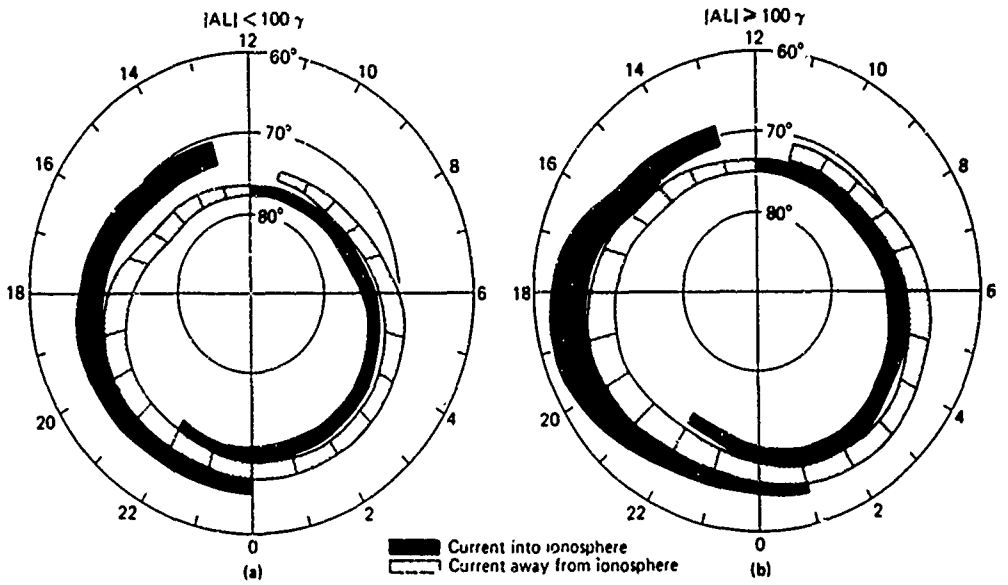

Figure 19. A Summary of the Distribution and Flow Directions of Large-scale Field-aligned Currents Determined From (a) Data Obtained From 439 Passes of Triad During Weakly Disturbed Conditions ($|AL| < 100\ \gamma$) and (b) Data Obtained From 366 Triad Passes During Active Periods ($|AL| \geq 100\ \gamma$)

In general, there are precipitating particles entering all parts of the auroral oval at all times and most parts of the polar cap most of the time. Figure 20 shows a typical observation of the precipitating electron detector on the DMSP satellite.[4] The space between the dashed and solid vertical lines is the latitudinal width of the equatorward edge of the auroral precipitation region. The auroral precipitation region is $\sim 10^{\circ}$ wide on both the morning and evening side. Most of the region is filled with the diffuse-auroral type electrons ($E \sim 1$ keV). There are several regions of accelerated, precipitating electrons. These regions of more energetic particles have latitudinal widths from 10 km to $\sim$ 300 km. The polar cap region is dominated by a very low energy ($E \leq 200$ eV) electrons near 78° latitude and within one hour of local time of noon.

As mentioned earlier, the precipitating electrons create ionization by repeated interactions with neutrals until the initial energy of the incoming particle has been dissipated. The altitude range where each precipitating particle has its maximum interaction with the neutral atmosphere is characteristic of the energy of the precipitating particle. For 10 keV electrons, the interaction is mostly in the altitude range of 95 to 140 km. For the winter high latitude region where the solar ionization is negligible compared to the particle-induced ionization, the flux

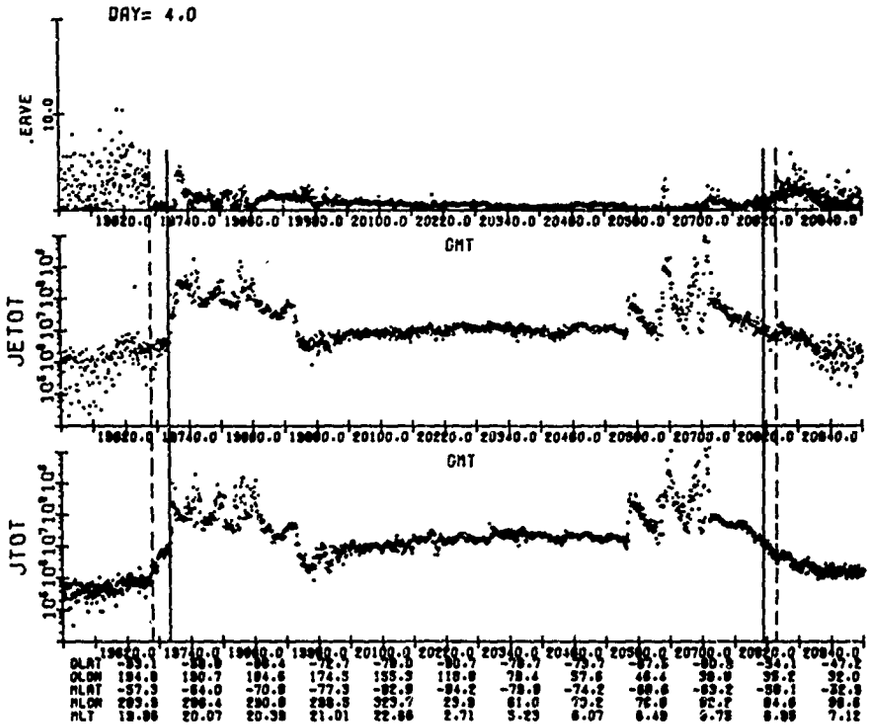

Figure 20. A Typical Data Set From a Polar Pass of the Precipitating Electron Detector (SSJ/3) From the DMSP/F2 Satellite. Total particle flux (cm^{-2} sec^{-1} $ster^{-1}$), energy flux (keV cm^{-2} sec^{-1} $ster^{-1}$) and average energy (keV) are plotted

profile of precipitating particles maps directly into a height profile of ionization assuming a steady state process. In other regions, the same transfer function between precipitation and ionization profiles can be applied after subtracting the solar component of ionization. The major difficulty in applying the transfer function is the time for the ionization to come to equilibrium with the precipitation. At 100 km altitude, the time to achieve equilibrium is milliseconds; at 150 km altitude, the time is seconds; and at 250 km, it is minutes.

Several of the ionospheric features related to precipitation can be seen in Figure 21, which shows the altitude-density profile in the vicinity of Chatanika, Alaska. Between 64° and 67° invariant latitude, there are five patches of enhanced plasma.[11] The patches are latitudinally narrow. (From other observations, it is reasonable to assume that the patches extend great distances in

11. Kelley, M. C., Vickrey, J. F., Carlson, C. W., and Torbert, R. (1982) On the origin and spatial extent of high-latitude F-region irregularities, J. Geophys. Res. 87:4469-4475.

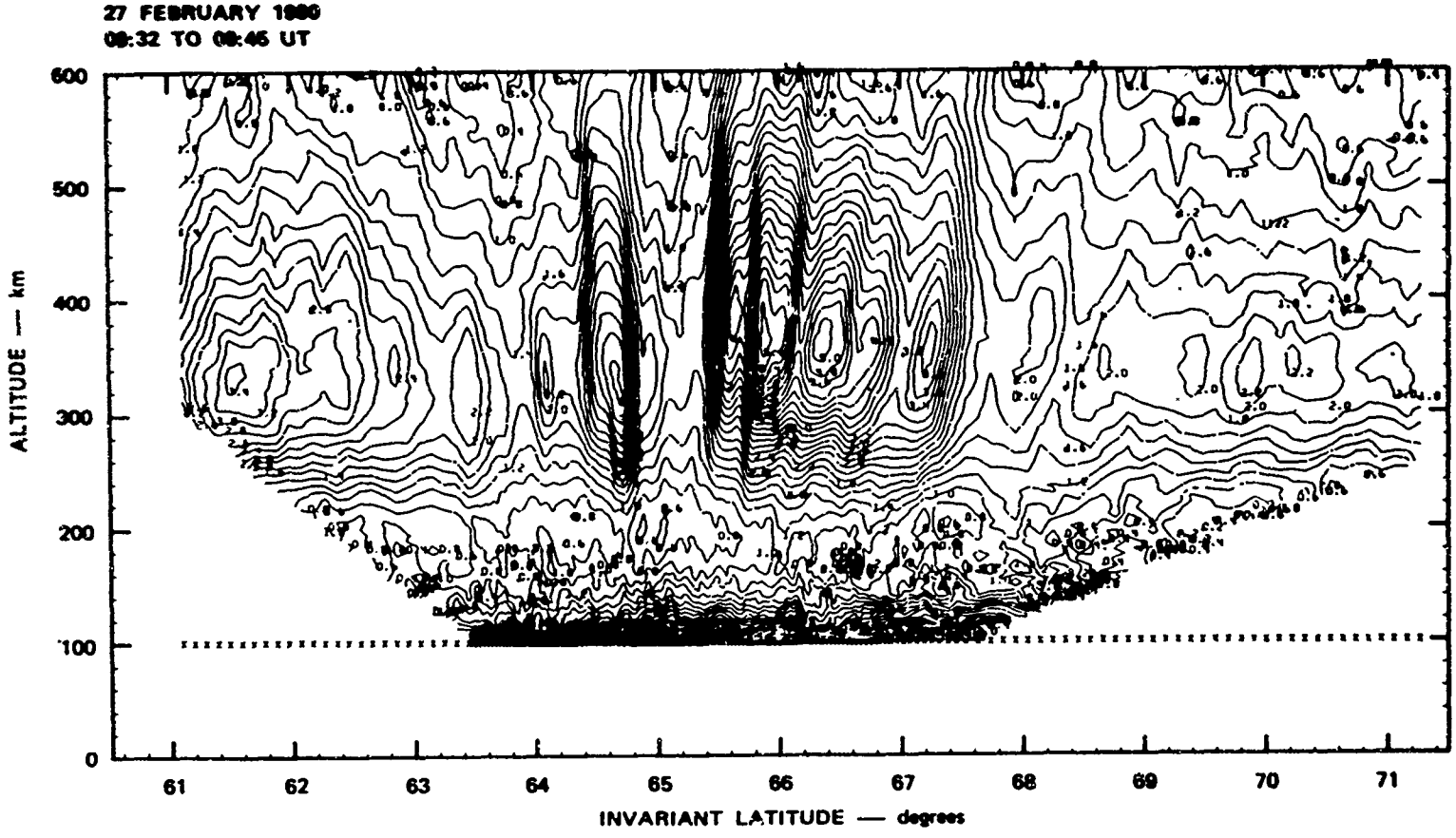

Figure 21. Altitude/latitude Variation of Electron Density in the Midnight Sector Auroral Zone Measured by the Chatanika Radar. The contour interval is 2×10^4 cm^{-3}

longitude.) The narrowness of the ionization is typical of the narrowness of an enhanced precipitation region. The lack of a plasma enhancement below 200 km indicates either that the precipitating electrons were exclusively low energy (E $\leq$ 100 eV), or that the observation shown was made after the precipitation had stopped. Correlated observations, which are not shown here, indicate that the enhanced ionization is due to precipitation occurring minutes to hours prior to this observation and at some distance north of the field of view of the radar. The enhanced ionization drifted into the field of view under the influence of the convection electric field. Ionization below 200 km altitude dissipated by recombination within seconds to minutes after the patches departed the production region. The ionization above 200 km has a lifetime against recombination of minutes to hours. Thus, the thermal plasma in the high-latitude ionosphere is spatially irregular due to the spatial and temporal irregularity of the precipitating electrons, but is also irregular at spacecraft altitudes due to bulk motions of the ionosphere through the precipitating regions.

The degree of enhanced ionization in the polar cap region is often minimal compared to the auroral oval. Both the flux and energy of electrons precipitating into the polar cap are significantly less than in the auroral oval. As discussed above, there may be some enhancements of ionization due to plasma drifting into the polar cap from the auroral zone. In addition there are times when the flux of precipitating electrons is very significant in the polar cap. The DMSP data shown in Figure 22 represent a time of high precipitating flux in the polar cap.[12] Near 24420 seconds GMT, the energy of these precipitating electrons exceeds 1 keV. In this case, the polar ionospheric density is enhanced significantly due to local ionization from the precipitating electrons.

The strong fluxes of precipitating electrons occasionally seen in the polar cap are associated with visual features called polar cap arcs. Figure 23 shows sketches of four classes of polar cap visual features based on DMSP imagery. (Only the section of the auroral oval visual features adjacent to the polar cap features are shown.) Figure 23(a) shows a sun-aligned arc that joins the auroral features at midnight and extends toward noon. Figure 23(b) shows visual features in the region normally considered as the polar cap, but may in fact be a poleward expansion of the auroral oval from the dawn and/or dusk flanks of the polar cap. Figure 23(c) shows arcs across the polar caps that join the auroral oval at locations other than noon or midnight. Figure 24 shows a wide-spread region of complex visual features in the polar region observed from the ground together

12. Gussenhoven, M.S., Hardy, D.A., and Burke, W.J. (1981) DMSP/F2 electron observations of equatorward auroral boundaries and their relationship to magnetospheric electric fields, J. Geophys. Res. 86:768-778.

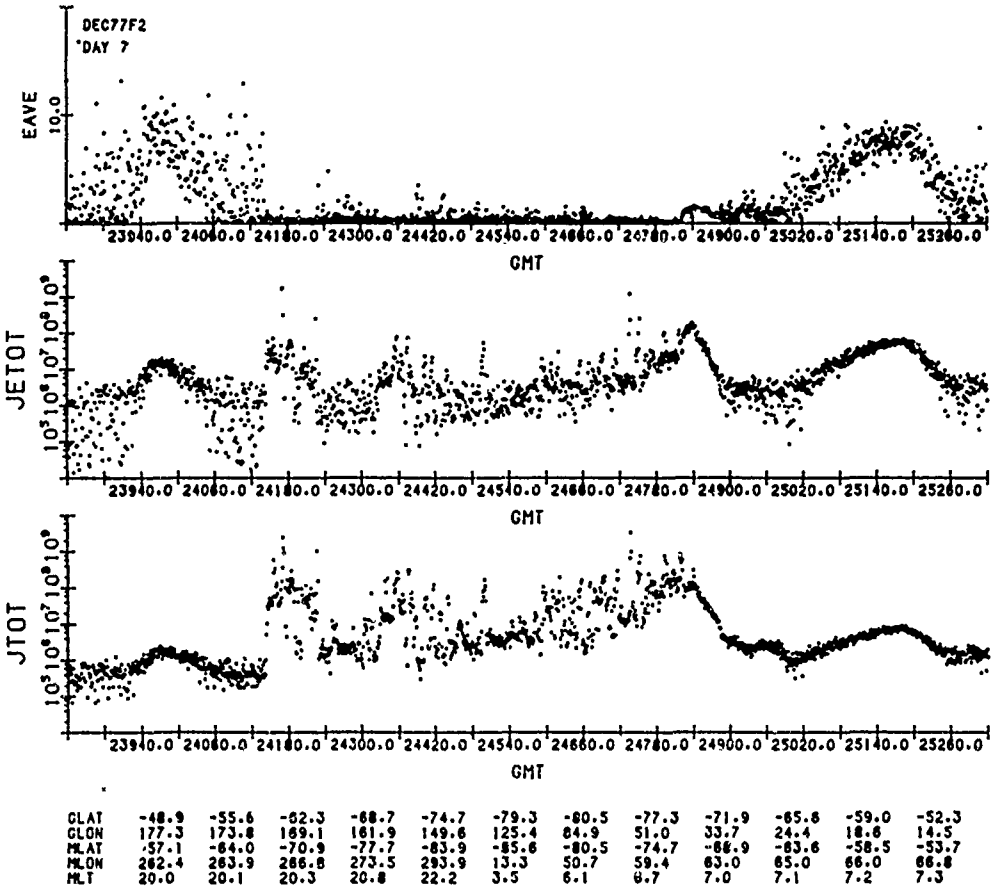

GLAT	-48.9	-55.6	-62.3	-68.7	-74.7	-79.3	-80.5	-77.3	-71.9	-65.6	-59.0	-52.3
GLON	177.3	173.8	169.1	161.9	149.6	125.4	84.9	51.0	33.7	24.4	18.6	14.5
MLAT	-57.1	-64.0	-70.9	-77.7	-83.9	-85.6	-80.5	-74.7	-68.9	-63.6	-58.5	-53.7
MLON	262.4	263.9	266.8	273.5	293.9	13.3	50.7	59.4	63.0	65.0	66.0	66.8
MLT	20.0	20.1	20.3	20.8	22.2	3.5	6.1	6.7	7.0	7.1	7.2	7.3

Figure 22. A Polar Pass of the DMSP SSJ/3 Detector Showing High Fluxes of Precipitating Electrons in the Polar Cap Region

with the simultaneous DMSP particle data that shows the particles causing the visual features.

The density of the ionospheric plasma at high latitudes, especially the polar cap, can be lower than a standard background level would indicate. In the absence of precipitation-induced production, the density is often assumed to be influenced only by solar UV production and standard recombination rates. At high latitudes the convective action of plasma (Figure 12) can combine with the rotation of plasma with the earth about the geographic pole to give regions of plasma that are out of the solar or particle-induced ionization production regions for abnormally long times. In these regions, recombination continues and abnormally low ionospheric densities are observed. The regions most affected by this stagnation of plasma motion with respect to the production regions are the evening sector

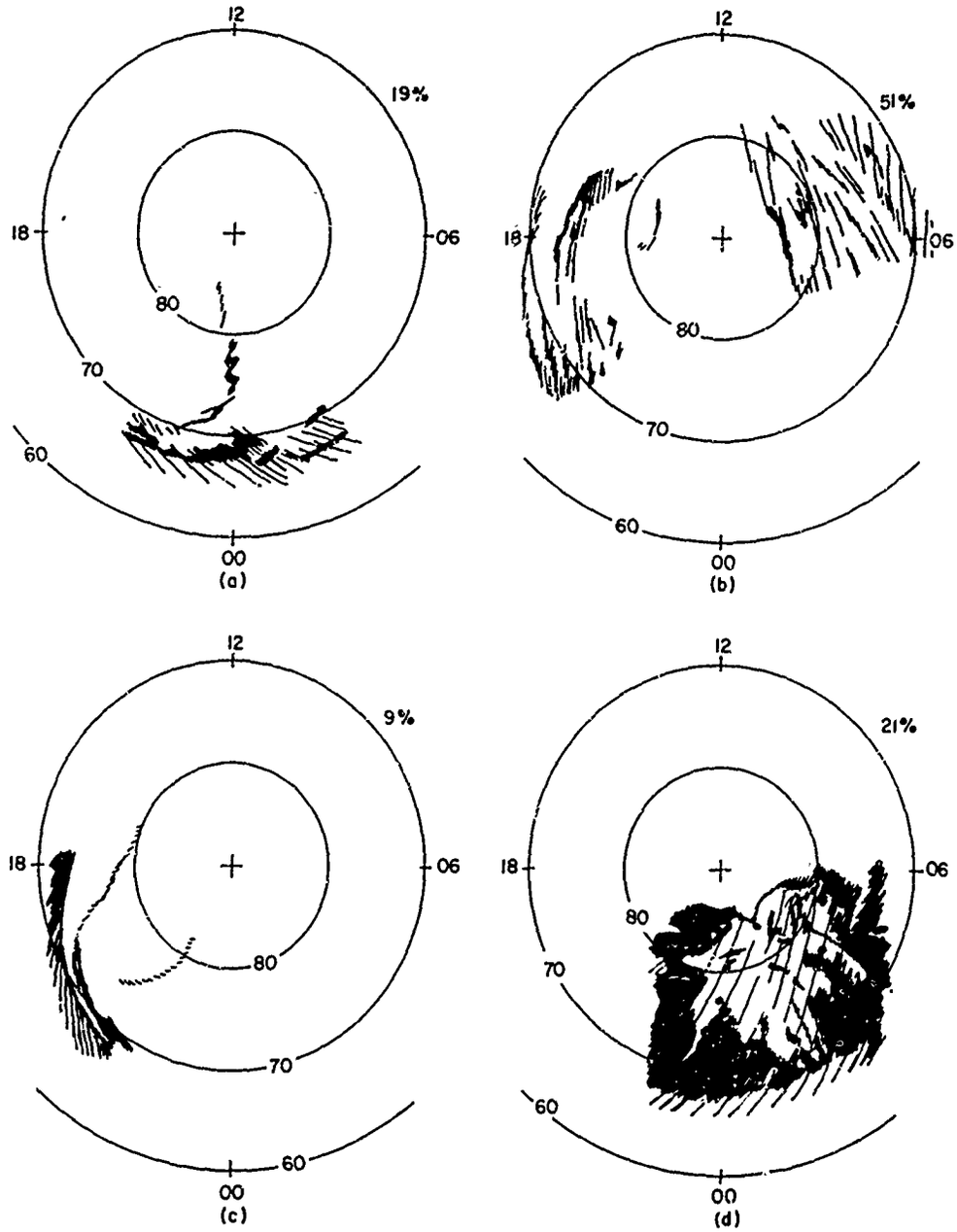

Figure 23. The Four Classes of Visual Polar Cap Ionospheric Features and the Relative Distribution of the Four Classes. Sketches are based on DMSP imagery; only auroral oval visual features near the polar cap feature are shown

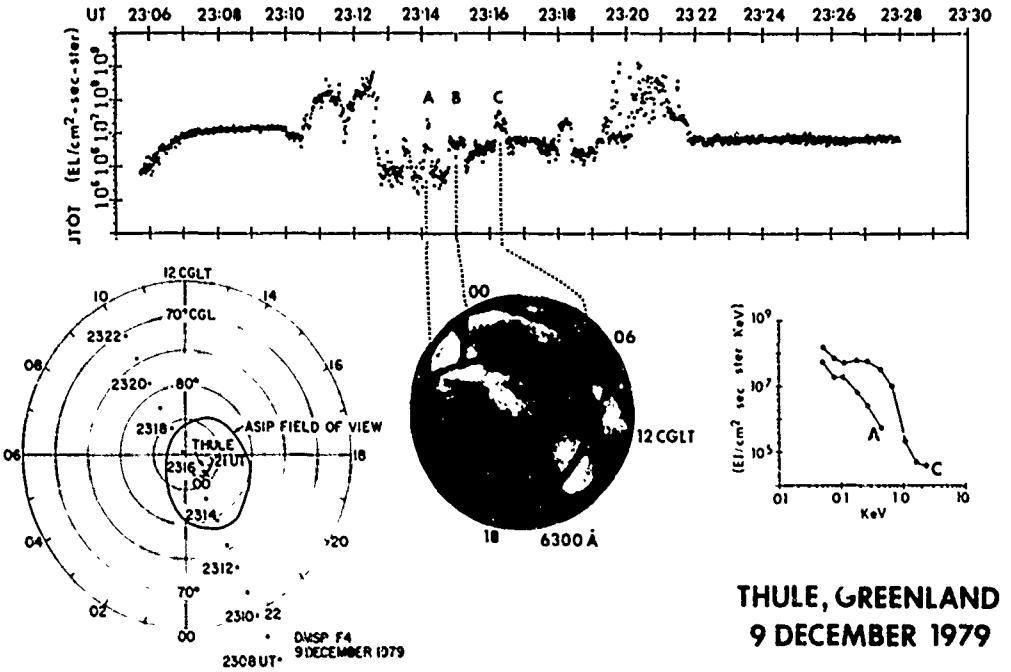

Figure 24. Simultaneous Observation of Polar Cap Ionospheric Visual Features From Ground Observations and DMSP Precipitating Electron Observations

ionosphere on the equatorward edge of the auroral zone and the polar cap ionosphere near midnight during the winter season. Since the magnetic pole is offset from the geographic pole by 11^{o}, the relative influence of high latitude ionosphere/magnetosphere convection about the magnetic pole and co-rotation about the geographic pole has a diurnal effect. Figure 25 shows the thermal plasma density observed by two DMSP satellites on the same day 12 h apart. In magnetic latitude/magnetic local time coordinates, both satellites follow the same path across the pole. The F2 satellite passed when the high-latitude ionosphere was strongly affected by plasma stagnation and the F4 satellite passed when the ionospheric density was not decreased by plasma stagnation. Other observations of the stagnation-induced depletion show densities at 840 km altitude of less than $10^{3}/cm^{3}$.

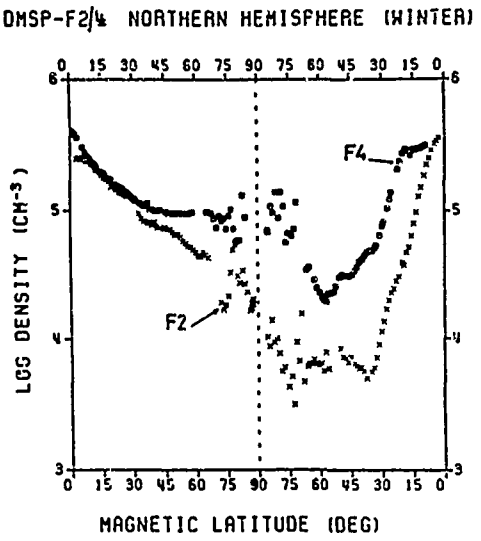

Figure 25. Thermal Ion Densities for Two Passes Along the Same Path in Geomagnetic Coordinates by Two DMSP Satellites 12 Hours Apart on a Geomagnetically Quiet Winter Day. Differences are due to the constructive and destructive interference between the corotation pattern and the geomagnetic convection pattern

4. CONCLUSION

Since the ionosphere is an ionized gas, charges can freely flow to and from a space vehicle in the ionosphere. An inert body in the ionosphere will generally develop a negative potential of a few times the thermal energy of the plasma or -1 to -2 V. For certain types of space vehicles that actively disturb the ambient ionized gas (for example, solar panels with exposed potentials, plasma guns, etc.), other potential levels are possible. For a relatively passive vehicle, the largest negative charge will occur where there is a large flux of energetic electrons with a small flux of thermal ions and without a flux of emitted photoelectrons or secondary electrons to neutralize the charge. For a space vehicle in the altitude range of 200 to 1000 km altitude, these conditions occur best in the winter auroral zone. If the large flux of energetic electrons is encountered within ~ 100 sec of the onset of the flux into the ionosphere, the charging will be greater since the thermal plasma density will not have risen to the equilibrium levels caused by the energetic particles. For a space vehicle at altitudes greater than 1000 km, charging is possible any time energetic particle fluxes are encountered in the high latitude region.

References

1. Banks, P.M., and Kockart, G. (1973) Aeronomy: Part A and Part B, Academic Press, New York.
2. Hanson, W.B., and Moffet, J. (1966) Ionization and transport effects in the equatorial F region, J. Geophys. Res. 71:5559-5572.
3. Decreau, P.M.E., Beghin, C., and Parrot, M. (1982) Global characteristics of the cold plasma in the equatorial plasmapause region as deduced from the GEOS 1 mutual impedance probe, J. Geophys. Res. 87:695-712.
4. Hardy, D.A., Burke, W.J., and Gussenhoven, M.S. (1982) DMSP optical and electron measurements in the vicinity of polar cap arcs, J. Geophys. Res. 87:2413-2430.
5. Heppner, J.P. (1977) Empirical models of high-latitude electric fields, J. Geophys. Res. 82:1115-1125.
6. Spiro, R.W., Reiff, P.H., and Maher, L.J. (1982) Precipitating electron energy flux and auroral zone conductances--an empirical model, J. Geophys. Res. 87:8215.
7. Sojka, J.J., Raitt, W.J., Schunk, R.W., Rich, F.J., and Sagalyn, R.C. (1982) Observations of the diurnal dependence of the high-latitude F region ion density by DMSP satellites, J. Geophys. Res. 87:1711-1718.
8. Lysak, R.L., and Hudson, M.K. (1979) Coherent anomalous resistivity in the region of electrostatic shocks, Geophys. Res. Letts. 6:661-663.
9. Mozer, F.S., Cattell, C.A., Temerin, M., Torbert, R.B., Von Glinski, S., Woldorff, M., and Wyant, K.J. (1979) The dc and ac electric field, plasma density, plasma temperature, and field-aligned current experiments on the S3-3 satellite, J. Geophys. Res. 84:5875-5884.
10. Iijima, T., and Potemra, T.A. (1978) Large-scale characteristics of field-aligned currents associated with substorms, J. Geophys. Res. 83:599-615.

11. Kelley, M.C., Vickrey, J.F., Carlson, C.W., and Torbert, R. (1982) On the origin and spatial extent of high-latitude F-region irregularities, J. Geophys. Res. 87:4469-4475.

12. Gussenhoven, M.S., Hardy, D.A., and Burke, W.J. (1981) DMSP/F2 electron observations of equatorward auroral boundaries and their relationship to magnetospheric electric fields, J. Geophys. Res. 86:768-778.

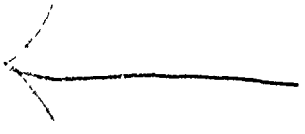

Contents

3. Is There a Good Way to Model Spacecraft Charging in the Presence of Space-Charge Coupling, Flow, and Magnetic Fields?

by

J. G. Laframboise
Physics Department
York University
Toronto, Ontario, Canada M3J 1P3

Abstract

The development of realistic numerical simulations of spacecraft-environment interactions in low-orbit conditions appears likely to be a more difficult task than it has been in high-orbit conditions. At the same time, carefully chosen combinations of existing simulation methods show some promise of being able to cope with this situation, at least in two dimensions and possibly in three dimensions. Simple large-voltage symmetric-sheath probe theories, which have been used to provide preliminary estimates of spacecraft voltages, contain serious limitations for use in making more precise calculations.

1. INTRODUCTION: LOW-ORBIT PLASMA ENVIRONMENT

The physical properties of the plasma that surrounds a spacecraft in low Earth orbit are very different than in (or near) geostationary orbit. As a result,

the task of modeling spacecraft-environment interactions is very different in these two regions. Three important differences are as follows.

In geostationary orbit:

(a) the Debye length is usually several tens of meters. Therefore space-charge coupling is small, and is frequently ignored entirely, or linearized approximations for it are used[1] when calculating potentials near spacecraft of "ordinary" size (up to a few meters).

(b) average particle gyroradii are usually at least a few tens of meters. Therefore magnetic field effects are negligible for calculating particle orbits, near spacecraft of "ordinary" size.

(c) circular orbit speed is usually much less than average particle random speeds. Therefore ambient particle velocity distributions can usually be assumed isotropic. This greatly simplifies calculations of ambient-particle current deposition on spacecraft surfaces. The most usual exception to this occurs when the velocity distributions themselves contain anisotropies.

However, in low orbit, none of the above are true; space-charge coupling, magnetic-field effects, and ion flow effects are all important. As a result, modeling of spacecraft-environment interactions in low orbit appears likely to be a much more difficult task than it has been in high orbit. In particular, numerical calculation of ion orbits appears to be essential for doing realistic low-orbit spacecraft-charging calculations, and until now, ion orbit calculations have been generally considered to be too expensive in three dimensions for widespread use.

We now examine magnetic-field effects, ion flow effects, and space-charge coupling effects in more detail. Table 1 shows representative values of characteristic lengths and speeds important in low-orbit conditions. An important effect of magnetic fields in these conditions is to alter the collection of ambient electrons on spacecraft surfaces, and the re-emission of secondary electrons from them. Because the average gyroradius of high-energy auroral electrons is comparable to Shuttle dimensions, only a moderate amount of anisotropy in the deposition of these electrons onto Shuttle surfaces is likely. However, the average gyroradius of secondary electrons is much smaller. This implies that escape of secondaries will be strongly inhibited on surfaces that are nearly parallel to the direction of the magnetic field $\vec{B}$ (Figure 1). In this situation such surfaces may charge to large (negative) voltages even if surfaces perpendicular to the magnetic field do not.

---

1. Laframboise, J.G., and Prokopenko, S.M.L. (1977) Numerical simulation of spacecraft charging phenomena, in: Proc. Spacecraft Charging Technology Conference, C.P. Pike and R.R. Lovell, Eds., Report No. AFGL-TR-77-0051, Air Force Geophysics Laboratory, Massachusetts; Report No. NASA TMX-73537, Lewis Research Center, Cleveland, Ohio, pp. 309-318, AD A045459.

Table 1. Low-Earth-Orbit Conditions[2]

(a) CHARACTERISTIC LENGTHS		
Ambient Debye length:		$\lesssim$ 1 cm
Thickness of 1 kV and 5 kV spherically-symmetric sheath[3] around a sphere of radius 3 m:		2.5 m and 5.8 m
Thickness of 1 kV and 5 kV planar Child-Langmuir sheath:		5.0 m and 17 m
Particle gyroradii:		
ambient electrons (0.1 eV)	2 cm	
secondary electrons (3 eV)	13 cm	
auroral electrons (10 keV)	4 m	
ions (0^+; 0.1 keV)	3 m in "rest" frame	
	27 m* in spacecraft frame (larger inside a high-voltage sheath)	
(b) CHARACTERISTIC SPEEDS		
Ion thermal speed:	1 km/sec	
Spacecraft speed:	$\lesssim$ 8 km/sec, depending on orbit	
Electron thermal speed:	100 km/sec, for ambient electrons	

*Partic motions do not depend on the frame of reference in which they are viewed. The transformation from rest frame to spacecraft frame produces a $\vec{V} \times \vec{B}$ electric field ≤ 0.35V/m where $\vec{V}$ = spacecraft velocity and $\vec{B}$ = magnetic induction; electric fields inside a 1 kV sheath are ~ 200 V/m.

For a larger object (size >> 4 m), deposition of auroral electrons will also become anisotropic, with both collection and escape of electrons now being inhibited on surfaces nearly parallel to $\vec{B}$. This suggests that high-voltage charging of such surfaces may be more likely on objects of intermediate size than on either larger or smaller ones. In the calculation of Parks and Katz,[4,5] the tendency toward high-voltage charging increased with spacecraft size because in their model, ion collection increased less rapidly with spacecraft size than did electron collection. To resolve this question will probably require detailed numerical simulation.

Also evident from Table 1 is the large value of the ion speed ratio (spacecraft speed/ion most-probable thermal speed) in low-orbit conditions. In these

References 2 to 5 will not be listed here. See References, page 74.

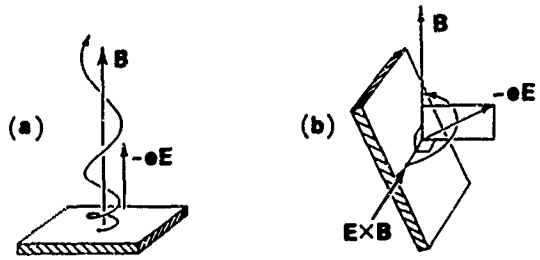

Figure 1. Effect of Surface Orientation on Escape of Secondary or Backscattered Electrons. In a, the spacecraft surface is perpendicular to the magnetic field $\vec{B}$, and the emitted electrons, which experience an electric force $-e\vec{E}$ directed away from the surface, all escape. In b, the spacecraft surface is nearly parallel to $\vec{B}$, and almost all of the emitted electrons return to the surface, even though they still experience an electric force directed away from it. Note that the component of $\vec{E}$ perpendicular to $\vec{B}$ results only in an $\vec{E} \times \vec{B}$ drift parallel to the surface

conditions, ion collection on downstream surfaces will be inhibited. If a surface is simultaneously downstream and nearly parallel to the magnetic field, then the tendency for high-voltage charging to occur on it will be greatly increased (Figure 2).

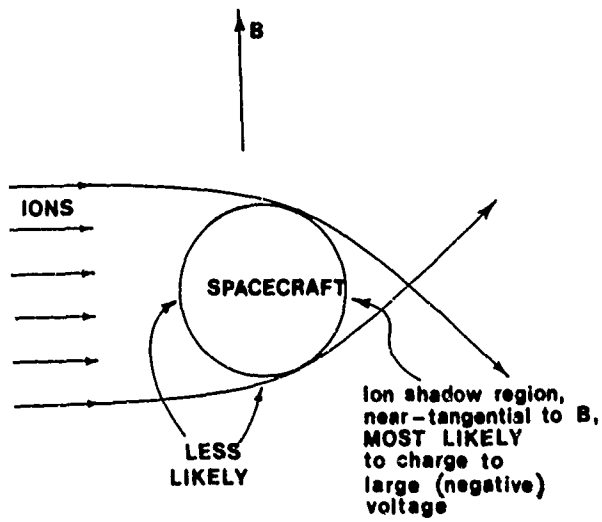

Figure 2. Spacecraft Simultaneously in a Collisionless Ion Flow and a Magnetic Field $\vec{B}$

The very small value of the ambient Debye length, which is also listed in Table 1, indicates that space-charge coupling is strong in low-orbit conditions. This suggests that the "barrier effect" will be very much less pronounced in low-orbit than in geostationary-orbit conditions. The barrier effect is the tendency of a highly-charged region on one side of a spacecraft to produce electric fields that "wrap around" the spacecraft and produce barriers which control the potentials of other surfaces on it.[6-13] On the other hand, Table 1 also indicates that sheath thickness can become comparable to Shuttle dimensions when the surface voltage is large,[14] so barrier effects may still occur to some extent. Whenever a sheath exists outside a surface, its total charge balances that of the surface, so the potential disturbance due to a charged spot will decrease with distance like the potential of a dipole rather than a source at distances larger than about one sheath thickness. Clearly, space charge will at least strongly modify any tendency for barriers to form, especially around larger surface features. In

---

6. Fahleson, U. (1973) Plasma-vehicle interactions in space - some aspects on present knowledge and future development, in: Photon and Particle Interactions with Surfaces in Space, R.J.L. Grard, Ed., D. Reidel, Dordrecht, Holland, pp. 563-569.

7. Whipple, Jr., E.C. (1976) Observation of photoelectrons and secondary electrons reflected from a potential barrier in the vicinity of ATS 6, J. Geophys. Res. 81(4):715-719.

8. Prokopenko, S.M.L., and Laframboise, J.G. (1977) Prediction of large negative shaded-side spacecraft potentials, in: Proc. Spacecraft Charging Technology Conference, C.P. Pike and R.R. Lovell, Eds., Report No. AFGL-TR-77-0051, Air Force Geophysics Laboratory, Massachusetts; Report No. NASA TMX-73537, Lewis Research Center, Cleveland, Ohio, pp. 369-387, AD A045459.

9. Prokopenko, S.M.L., and Laframboise, J.G. (1980) High-voltage differential charging of geostationary spacecraft, J. Geophys. Res. 85(A8):4125-4131.

10. Katz, I., Parks, D.E., Wang, S., and Wilson, A. (1977) Dynamic modeling of spacecraft in a collisionless plasma, in: Proc. Spacecraft Charging Technology Conference, C.P. Pike and R.R. Lovell, Eds., Report No. AFGL-TR-77-0051, Air Force Geophysics Laboratory, Massachusetts; Report No. NASA TMX-73537, Lewis Research Center, Cleveland, Ohio, pp. 319-330, AD A045459.

11. Besse, A.L., and Rubin, A.G. (1980) A simple analysis of spacecraft charging involving blocked photoelectron currents, J. Geophys. Res. 85(A5):2324-2328.

12. Purvis, C. (1982) Evolution of spacecraft charging technology, Paper AIAA-82-0273, Amer. Inst. Aeron. Astron. 20th Aerospace Sciences Mtg., January 1982, Orlando, Florida.

13. Laframboise, J.G., Kamitsuma, M., and Godard, R. (1982) Multiple floating potentials, 'Threshold-temperature' effects, and 'Barrier' effects in high-voltage charging of exposed surfaces on spacecraft, in: Proc. Internat. Symp. on Spacecraft Materials in Space Environment, Report No. ESA SP-178, European Space Agency, Paris, pp. 269-275.

14. Mandell, M.J. (1982) Private communication.

retrospect, the most important benefit obtained from three-dimensional (NASCAP)[10,15] simulations up to now has probably been the ability to make detailed barrier-effect predictions, so it is not clear at present whether three-dimensional simulation for low-orbit conditions will prove equally valuable. If barrier effects in low orbit turn out to be unimportant, the most likely justification for three-dimensional simulation will be the need to make accurate calculations of ion focusing effects. Some calculations of ion focusing effects in two and three dimensions are presented by Parker in another paper given at this Conference.

In the remaining sections of this paper, we discuss various numerical simulation techniques that may be applicable to the calculation of low-orbit charging of large spacecraft. In Sections 2 and 3, we discuss methods for time-dependent simulation and "quasistatic" simulation, respectively. In Section 4, we discuss methods for performing ion density and flux calculations within simulation programs of the types discussed in Section 3. In Section 5, we discuss the limitations of simple, large-voltage spherically-symmetric sheath theories which have been used to estimate spacecraft potentials. Section 6 contains some concluding remarks.

2. TIME-DEPENDENT SIMULATION METHODS

The auroral plasma is known to contain spatial variations having characteristic sizes down to a few kilometers, and may contain variations down to a few hundred meters. If objects several hundred meters in size are to be orbited through the auroral zone in the future, time-dependent modeling of their sheaths may therefore become necessary. Katz and Parks[5] have estimated 10^6 V/sec for typical charging rates in the auroral plasma. For a spacecraft orbiting at 8 km/sec, this suggests that a 10 kV charging equilibrium can be reached in ~100 m travel distance, or about 0.01 sec. This is less than the above-mentioned minimum hypothesized size of auroral features, but not by a large factor. Also, temporal variations of auroral features are believed to exist (R. Schunk, paper presented at this Conference) on time scales down to 0.1 sec, corresponding to 800 m spacecraft travel distance, or about 100 m ion travel distance (Table 1).

From a variety of viewpoints, it therefore appears that true time-dependent modeling, as opposed to the "quasistatic" treatments generally used in

15. Katz, I., Cassidy, J.J., Mandell, M.J., Schnuelle, G.W., Steen, P.G., and Roche, J.C. (1979) The capabilities of the NASA charging analyzer program, in: Spacecraft Charging Technology - 1978, NASA Conference Publication 2071; Report No. AFGL-TR-79-0082, AD A084626, Air Force Geophysics Laboratory, Massachusetts, pp. 101-122.

geostationary-orbit charging modeling and also in low-orbit sheath and wake modeling, may eventually become necessary. Quasistatic modeling means the calculation of a steady-state situation, or a succession of steady-state situations separated in time by appropriate increments of surface charging. We discuss quasistatic modeling approaches in Section 3. Here we list three possible methods for time-dependent modeling.

(a) PARTICLE-IN-CELL

Description: a random number generator produces "particles" at upstream boundaries or elsewhere. These are "followed" numerically as time advances. Electric fields involved are calculated self-consistently at every time step.

Advantages: relatively simple to code; works reliably.

Disadvantages: very subject to discretization noise, therefore expensive. In one and two dimensions, typically $\sim 10^2$ and $\sim 10^4$ particles are needed, respectively, to produce "reasonable" accuracy. This suggests that in three dimensions, $\sim 10^6$ particles will be needed. This seems likely to force some hard choices between realism of the simulation geometry and accuracy of the results. One basic inefficiency of this method is that it does not use information about values of the velocity distribution function f on particle orbits.

(b) DIRECT VLASOV DIFFERENCING

Description: integrates a finite-difference approximation of the time-dependent Vlasov equation to generate new values of f at spatial grid nodes after each time step. In effect, this method starts a new particle orbit at every grid node every time step.

Comments: traditionally crippled by numerical diffusion, but new antidiffusive algorithms exist. Examples of one-dimensional and two-dimensional calculations using these algorithms have been published.[16-19]

(c) VELOCITY-SPACE INTEGRATION OF f USING MULTIPLE-WATERBAG AND TETRAHEDRAL-INTERPOLATION METHODS

Description: The multiple-waterbag method[20] approximates real velocity distributions by stepwise-constant ones. It follows only those particle orbits that

16. Boris, J.P., and Book, D.L. (1976) Solution of continuity equations by the method of flux-corrected transport, Methods Comput. Phys. 16:85-129.
17. Zalesak, S.T. (1979) Fully multidimensional flux-corrected transport algorithms for fluids, J. Comput. Phys. 31:335-362.
18. Rowland, H.L. (1980) Strong turbulence effects on the kinetic beam-plasma instability, Phys. Fluids 23:508-517.
19. Smith, R.A. (1982) Vlasov simulation of plasma double layers, Physica Scripta 25:413-415.
20. Berk, H.L., and Roberts, K.V. (1970) The Water-Bag Model, Methods Comput. Phys. 9:88-134.

are on the step locations (waterbag boundaries) in phase space. It starts new orbits on waterbag boundaries when necessary to preserve a realistic approximation of boundary shapes. A newer method, which is essentially a higher-order replacement for this, uses a finite-element approach to perform linear tetrahedral (or hypertetrahedral) interpolations[21-23] between particle locations in phase space, rather than making the assumption of stepwise-constancy, in order to find f values as a function of phase-space (velocity and position) coordinates. These f values are then integrated over velocity to find number densities for substitution into Poisson's equation.

Advantage: unlike standard particle-in-cell, these methods use information about f on particle orbits.

Comment: the standard multiple-waterbag method has been used only on problems involving two phase-space dimensions, but the tetrahedral interpolation method circumvents this restriction.

3. QUASISTATIC SIMULATION METHODS

Although time-dependent modeling of low-orbit charging may eventually become necessary (Section 2), quasistatic modeling is sufficient for obtaining spacecraft charging response to steady-state or slowly-varying environments. In quasistatic modeling,[1] particle transit times through the spacecraft sheath are assumed to be small compared to time scales of external changes, including those due to charging of spacecraft surfaces, spacecraft rotation, eclipse passage, or changes of the plasma environment. This leads to the following calculation scheme: a distribution of surface potentials is chosen. Poisson's equation for the electric potential and the time-independent Vlasov equations for the charged-particle distributions (coupled unless the Debye length is large) are then solved to provide net surface charging rate as a function of surface position. Using this information, the surface potentials are updated. This process is repeated until a steady-state floating condition is attained or in order to follow external changes.

The essential difference between this process and time-dependent modeling is that at every iterative step (or time-step), a time-independent sheath solution, for a given set of surface potentials, is calculated. Whether or not this method

21. Buneman, O. (1979) Vectorization and parallelism in Stanford's 3D, EM particle code, MFECC Buffer 3(7):7-12. Magnetic Fusion Energy Computer Center Monthly Bulletin, Livermore, California.

22. Buneman, O. (1980) Tetrahedral finite elements for interpolation, SIAM J. Sci. and Stat. Comput. 1:223-248.

23. Hockney, R.W., and Eastwood, J.W. (1981) Computer Simulation Using Particles, McGraw-Hill, New York.

is better than time-dependent modeling, even for steady-state problems, depends on how difficult this sheath solution is to calculate. For geosynchronous-orbit problems, in which space-charge coupling is very weak, quasistatic modeling has been the preferred method; see, however, remarks made by Isensee and Maassberg.[24] The low-orbit situation is very different (section 1). However, a large body of previous work on steady-state sheath and wake solutions is applicable. We now list methods for quasistatic simulation, including those used in this previous work.

(a) TREAT IONS AS NEUTRALS.[25,26]

Advantage: permits a simple shadowing calculation of ion density in wake; does not require numerical integration of ion orbits.

Disadvantage: for O^+, ion directed energy in the spacecraft reference frame is only 4 eV, so this treatment is invalid in a high-voltage sheath.

(b) PRETEND THAT ION VELOCITY COMPONENT IN FLOW DIRECTION IS UNCHANGED, AND THEREFORE ION ENERGY GAIN IN SHEATH GOES ENTIRELY INTO TRANSVERSE MOTION.

Advantage: permits a "front-to-back marching" calculation of ion density which is almost as simple as (a). Somewhat more realistic than (a).

Disadvantage: no physical basis for making such an approximation except when ion deflections are very small. Invalid in a high-voltage sheath.

(c) POISSON ITERATION.[27-34]

Advantage: the basic exact method for obtaining self-consistent sheath and wake solutions.

Disadvantage: convergence becomes very poor when Debye length << object size.[35-38]

Comment: The treatments of Davis and Harris,[27] Maslennikov and Sigov,[28,29] Call,[30] and Martin[3] all make the "mesothermal" approximation: ion thermal speed << spacecraft speed << electron thermal speed, so that the method described in Section 4(a) can be used to calculate ion densities and fluxes. They also assume that the surface potential is large and negative ($e\phi_s/kT_e$ <<-1, where e is the elementary charge, ϕ_s is surface potential, k is Boltzmann's constant, and T_e is electron temperature), so that the electron density is well-approximated by the usual Boltzmann factor.

(d) POISSON ITERATION WITH ONE SPECIES "FROZEN". (Ref. 30, p. 57)

Description: assume a potential distribution. Calculate ion and electron densities. Use the resulting space-charge distribution to calculate a new potential. If the ion density calculation is the more expensive, then recalculate only the

Because of the large number of references cited above, they will not be listed here. See References, page 74.

electron density in the new potential, reusing the previous ion density to recalculate the potential again. Repeat until convergence. Then calculate a new ion density and proceed as before. Repeat all steps until convergence.

Advantage: partly overcomes difficulty of (c).

(e) METHOD (d) PLUS USE OF PARKER[39] KEY-POINT METHOD.

Description: when calculation of density distribution of a charged species requires expensive numerical orbit integration, do it only at every third or fourth grid interval in each coordinate direction, and use an appropriate interpolating function at intermediate grid points.

Advantage: greatly improves economy of other methods listed.

(f) QUASINEUTRAL ITERATION.[40-43]

Description: iterate toward equality of ion and electron densities rather than toward solution of Poisson's equation. The Grabowski-Fischer[41] calculations showed sideways deflection of cylinder wakes by magnetic fields.

Advantage: overcomes difficulty of (c).

Disadvantage: invalid in sheath and inner part of wake.

(g) CHILD-LANGMUIR ITERATION.[44]

Description: hold Child-Langmuir length (proportional to $T_i^{-1/4} N_i^{-1/2}$ where T_i and N_i are ion temperature and number density) constant while progressively decreasing Debye length (proportional to $T_i^{1/2} N_i^{-1/2}$) as iteration proceeds.

Advantage: partly overcomes difficulty of (c).

(h) QUASINEUTRAL ITERATION WITH MATCHING TO "INNER" SOLUTION AT SHEATH EDGE.

Advantage: overcomes difficulty of (f).

Disadvantage: untried, not well formulated.

---

39. Parker, L.W. (1973) Computation of Ion Collection by a Rocket-Mounted Mass Spectrometer in the Limit of Vanishing Debye Number, Report No. AFCRL-TR-73-0735, Contract F19628-73-C-0065, Air Force Geophysics Laboratory, Hanscom AFB, Massachusetts, AD A783625.

40. Al'pert, Ya.L., Gurevich, A.V., and Pitaevskii, L.P. (1965) Space Physics with Artificial Satellites, Consultants Bureau, New York.

41. Grabowski, R., and Fischer, T. (1975) Theoretical density distribution of plasma streaming around a cylinder, Planet. Space Sci. 23:287-304.

42. Isensee, U., Lehr, W., and Maassberg, H. (1981) A numerical model to calculate the wake structure of a spacecraft under ionospheric conditions, Adv. Space Res. 1:409-412.

43. Parrot, M.J.M., Storey, L.R.O., Parker, L.W., and Laframboise, J.G. (1982) Theory of cylindrical and spherical Langmuir probes in the limit of vanishing Debye number, Phys. Fluids (in press).

44. Cooke, D. (1982) Private communication.

(i) QUASINEUTRAL FRONT-TO-BACK MARCHING, IGNORING ION DIRECTION REVERSALS.[42]

Description: noniterative. Marching takes place from one plane to another, all such planes being perpendicular to the ambient ion drift velocity vector.

Advantage: fast, economical.

Disadvantages: invalid in sheath and inner wake, same as (f). Numerous reversals may occur in a high-voltage sheath.

(j) OUTSIDE-IN MARCHING.[45,46]

Description: noniterative. In this method, quasineutrality is not assumed. A leading equipotential surface must be specified on which the ion density has its ambient value and the potential has a given, very small value. Marching then proceeds inward from one equipotential surface to another. The innermost chosen equipotential resulting from this procedure then represents the object, assuming that the latter is an equipotential.

Advantage: fast, economical.

Disadvantage: object shape cannot be specified in advance but is generated indirectly by the choice of the shape of the leading equipotential.

(k) USE OF ANALYTIC POTENTIAL-DEPENDENT APPROXIMATIONS FOR SPACE-CHARGE DENSITIES, ESPECIALLY FOR ATTRACTED PARTICLES.[47,48]

Advantage: fast, economical.

Disadvantages: ignores ion focusing effects on space-charge densities. Accuracy may be unpredictable except in cases very similar to others already treated exactly.

Additional Comments: Essentially a way to "parameterize" exact calculations already done. Some comparisons between results calculated using exact space charge and certain previously-used analytic space charge approximations are presented by Parker in another paper given at this Conference. The NASCAP-LEO program[47,48] uses a hybrid calculation method in which the potential

---

45. Walker, E.H. (1965) Plasma sheath and screening around a stationary charged sphere and a rapidly moving charged body, in: Interactions of Space Vehicles with an Ionized Atmosphere, S.F. Singer, Ed., Pergamon, Oxford, pp. 61-162.

46. Walker, E.H. (1973) Plasma sheath and screening of charged bodies, in: Photon and Particle Interactions with Surfaces in Space, R.J.L. Grard, Ed., D. Reidel, Dordrecht, Holland, pp. 73-89.

47. Katz, I., Mandell, M.J., Schnuelle, G.W., Parks, D.E., and Steen, P.G. (1980) Plasma collection by high-voltage spacecraft at low earth orbit, Paper AIAA-80-0042, Amer. Inst. Aeron. Astron. 18th Aerospace Sciences Mtg., January 1980, Pasadena, California.

48. Mandell, M.J., Katz, I., Steen, P.G., and Schnuelle, G.W. (1980) The effect of solar array voltage patterns on plasma power losses, IEEE Trans. Nucl. Sci. NS-27.

distribution is obtained by solving a Poisson equation that contains an analytic space-charge-density approximation. Then the resulting equipotential surface at potential $\phi = kT_e/e$ is located, and ion fluxes onto spacecraft surfaces are found by integrating ion orbits inward from this "sheath edge"; the ions are started with thermal velocity normal to this surface, and are accelerated by the sheath electric fields.

(l) HYBRID METHOD OF ILLIANO AND STOREY.[49]

Description: used infinite-ion-speed-ratio computer program of Call (1969) to obtain self-consistent potential distribution; then used finite-ion-speed-ratio program of Fournier[32,33] with this potential to calculate ion fluxes onto surfaces.

Advantage: may improve economy of other methods.

Disadvantage: becomes inaccurate when ion speed ratio is small.

(m) ZERO-TEMPERATURE (SHARP SHEATH EDGE) APPROXIMATION FOR COLD REPELLED-SPECIES (ELECTRON) POPULATION.[35,50,51]

Description: iterates toward the condition of zero electric field at the sheath edge by moving the sheath edge in or out until convergence (Figure 3). The sheath edge is the problem domain boundary. One-dimensional (radially-symmetric) calculations of this type were done by Laframboise;[35] two- and three-dimensional ones have been presented by Parker[50] and Cooke et al.[51] Further details and results are given by Parker in another paper presented at this Conference.

Advantages: may save large amounts of computer time by restricting problem domain. Can be used in the presence of a hot electron population and of ion flow. Calculated sheath edge will automatically move downstream on aft side of spacecraft.

Additional Comment: some features of the NASCAP-LEO computer program, described briefly in Section 3(k), resemble some features of this method.

---

49. Illiano, J.M., and Storey, L.R.O. (1974) Apparent enhancement of electron temperature in the wake of a spherical probe in a flowing plasma, Planet. Space Sci. 22:873-878.

50. Parker, L.W. (1981) Trajectory-Controlled Space-Charge-Sheath Computer Models; Application to Large High-Voltage Solar Arrays in Dense Plasmas, NASA Johnson Space Center Contract Report No. NAS 9-15934.

51. Cooke, D., Parker, L.W., and McCoy, J.E. (1981) Three-dimensional space charge model for large high-voltage satellites, in: Spacecraft Charging Technology 1980, NASA Conference Publication 2182; Report No. AFGL-TR-81-0270, Air Force Geophysics Laboratory, Massachusetts, pp. 957-978, AD A114426.

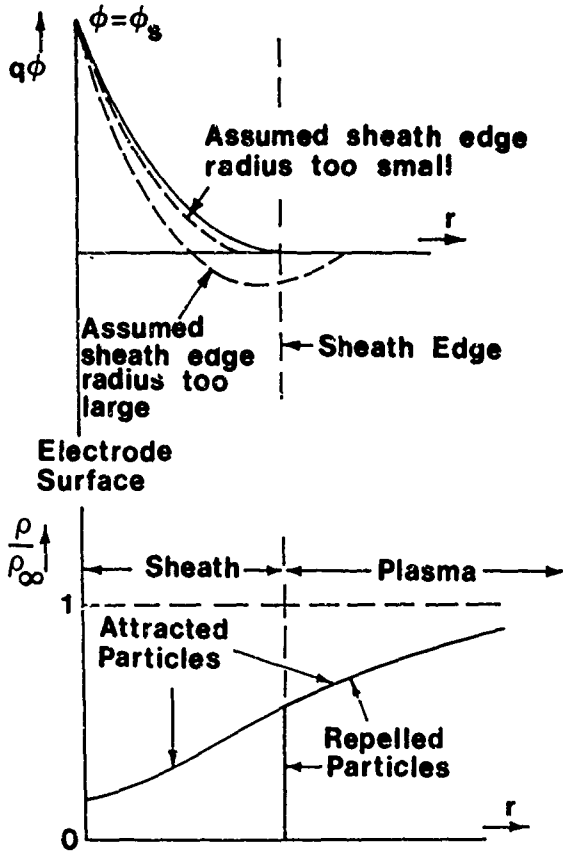

Figure 3. Potential ϕ and Space-Charge-Density ρ as Functions of Radius r Near an Electrode Surface in the Limit of Zero-Temperature Repelled Particles (having charge q) (after Laframboise[35])

4. ION DENSITY AND FLUX CALCULATIONS

Most of the quasistatic methods listed in Section 3 involve using numerical orbit integration to calculate ion space-charge density distributions and current densities (fluxes) deposited onto spacecraft surfaces, in the presence of given time-independent electric potential distributions. In this section we present what appear to be the most appropriate methods for calculating ion densities and fluxes, depending on the value of the ion speed ratio S_i = (spacecraft speed/ion most probable thermal speed). The methods described in Sections 4(c) or 4(d) may also be required for calculating electron densities and fluxes, depending on the level of accuracy desired in such calculations.

(a) $S_i = \infty$: OUTSIDE-IN ORBIT-FOLLOWING.[3,27-30,34]

In this type of calculation, the ion orbits are assumed parallel at the upstream boundary of the computation domain, and are integrated in the same direction as the ions actually move. Densities and fluxes are calculated by monitoring the changes in area of particle flux tubes defined by neighboring orbits. The assumption $S_i = \infty$ is only approximate for real situations and can lead to spurious singularities in densities or fluxes at points where orbits cross. Another possible difficulty is that if the orbits chosen are too far apart initially, two neighboring orbits may eventually go off in very different directions, making calculations of flux or density between them impossible or unrealistic. On the other hand, if they are initially too close together, inaccuracies in calculating either orbit may obscure the small differences that one is trying to calculate. A method for circumventing this difficulty, based on differential orbit perturbations, is described by Laframboise et al,[52] Section 7.

(b) $S_i \gg 1$: OUTSIDE-IN WITH DISTRIBUTION SAMPLED OR WITH DIFFERENTIAL PERTURBATIONS.

An ion distribution with large but finite speed ratio can be approximated by a superposition of a small number of infinite-speed-ratio distributions ("beams") with slightly differing speeds and/or directions, appropriately weighted. Alternatively, the differential perturbation technique mentioned in connection with (a) can be extended to include large but finite speed ratios (Ref. 52, Section 7). Whether either of these approaches is advantageous is not clear because the approach described below in (c) for $S_i \sim 1$ still works well up to $S_i = 10$ (L. W. Parker[53]).

(c) $S_i \sim 1$: INSIDE-OUT ORBIT-FOLLOWING.[32-34]

In this method, one finds ion (or electron) density at each grid point [or at selected grid points; see Section 3(e)] by integrating particle orbits from such a point backward to a domain boundary where the velocity distribution function value on each orbit is assumed known. The total number of orbits that must be followed is large but may not be prohibitive (Fournier,[32,33]; Parker[34]).

(d) $S_i = 0$: PHASE-SPACE BOUNDARY TRACKING.[7,54-57]

If the velocity distribution function f at infinite distance is isotropic, then the values of f on orbits passing through any finite point are known for all orbits which "connect backwards to infinity", and have not originated at a solid surface (for orbits originating at a solid surface, the situation will be more complicated if the surface emits particles and either is not at uniform potential or emits nonisotropically). In such a situation, knowledge of the phase-space boundary

---

Because of the large number of references cited above, they will not be listed here. See References, page 74.

that separates these two types of orbit provides all of the information required to calculate densities and fluxes, at least for particles originating in the ambient plasma. This result has been used to calculate currents collected by electrostatic probes in collisionless plasmas (Bernstein and Rabinowitz[58]; Laframboise[35]; see also references cited by Parrot et al[43]).

5. LIMITATIONS ON THE USE OF SIMPLE LARGE-VOLTAGE SPHERICAL-PROBE THEORY[59,40] OR CYLINDRICAL-PROBE THEORY[60] TO ESTIMATE SPACECRAFT POTENTIALS

These theories have often been used to estimate current collection and sheath thickness for spherical and cylindrical electrodes (probes) at large voltages. They assume that the surrounding plasma is collisionless and nondrifting, that the ion and electron temperatures are both small compared to the voltage change across the probe sheath, and that the surface potential of the electrode is uniform. They have often been used in situations where they may be inappropriate, because no better theory has been available. Here we point out three effects that are not included in these theories and that may be important in many situations in which they have been used. This situation is one example of a variety of long-standing deficiencies that still exist in basic "probe theory".

The following three effects are ignored in some or all of the above-mentioned theories.

(a) Turning points in ion radial motion may exist, because of initial ion circumferential motions at the sheath edge. This is ignored in the theories of Langmuir and Blodgett.[59,60] In their theories, all ions entering the sheath are assumed to move radially inward toward the origin. This approximation can lead to serious errors whenever the radial variation of potential becomes less steep than that of an inverse-square dependence. When this happens, the angle between the inward direction and the velocity vector of an attracted particle (ion) increases continuously as the ion moves inward. Eventually a turning-point must be reached at which the ion will reverse its radial motion and begin to move outward. When a significant fraction of the ions entering the sheath do this, space-charge density and current collection are both altered.

---

58. Bernstein, I.B., and Rabinowitz, I.N. (1959) Theory of electrostatic probes in a low-density plasma, Phys. Fluids 2:112-121.
59. Langmuir, I., and Blodgett, K.B. (1924) Currents limited by space charge between concentric spheres, Phys. Rev. 23:49.
60. Langmuir, I., and Blodgett, K.B. (1923) Currents limited by space charge between coaxial cylinders, Phys. Rev. 22:347.

Turning-point effects turn out to be much more serious in cylindrical than in spherical sheaths. For spherical probes, exact theories including ion thermal motion effects reduce to the results given by radially-inward-motion theories, in the limit when ion temperature $T_i \rightarrow 0$ in the exact theories (Laframboise,[35] Figures 27a and 28). However, for cylindrical probes, this does not happen, and the resulting error is large (Sonin[61,62]; Sonin et al[63]; and Laframboise,[35] Figure 53). This difference arises because the asymptotic dependence of the sheath potential at large radii is at least as steep as an inverse-square in the spherical case, but is less steep than an inverse-square in the cylindrical case (Laframboise,[35] pp. 36-37 and Table 2).

This is a surprising difference, and illustrates the inadequacy of existing theories for treating more complicated shapes, such as that of the Shuttle. Would a zero-ion-thermal-motion theory provide the correct limit of finite-ion-thermal-motion theories in the limit when $T_i \rightarrow 0$? At present, the answer to this question is unknown.

(b) Surface potentials may be very nonuniform (Section 1), with some surfaces (especially those downstream and parallel to the magnetic field vector $\vec{B}$) much more likely to charge to large voltages than others. Such a situation would destroy the symmetry of the electric field, thus violating an assumption made in these simple theories, even if the spacecraft shape were symmetric.

(c) In low-orbit conditions, most ions will enter the spacecraft sheath from its upstream side. This will create asymmetries in the space-charge distribution and hence in the sheath potential distribution, even if the spacecraft is, say, a conductive sphere. The consequences of this have been investigated by Makita and Kuriki[64,65] who measured total current collected by spherical and cylindrical

---

61. Sonin, A.A. (1965) The Behaviour of Free Molecule Cylindrical Langmuir Probes in Supersonic Flows, and their Application to the Study of the Blunt Body Stagnation Layer, University of Toronto, Institute for Aerospace Studies, Report No. 109.

62. Sonin, A.A. (1966) Free-molecule Langmuir probe and its use in flowfield studies, AIAA Jour. 4:1588-1596.

63. Sonin, A.A., Graf, K., Laframboise, J.G., and deLeeuw, J.H. (1965) The ion collection of free molecular cylindrical Langmuir probes in flowing plasmas, in: Proc. 7th Internat. Conf. on Phenomena in Ionized Gases, Gradevinska Knjiga Publishing House, Belgrade, Yugoslavia, pp. 53-57.

64. Makita, H., and Kuriki, K. (1977) Comparative study of spherical and cylindrical drift probes, Proc. 10th International Symposium on Rarefied Gas Dynamics, J. Leith Potter, Ed., p. 1007, Progress in Astronautics and Aeronautics, Vol. 51, Amer. Inst. of Astronaut. and Aeronaut., New York.

65. Makita, H., and Kuriki, K. (1978) Current collection by spherical Langmuir probes drifting in a collisionless plasma, Phys. Fluids 21:1279.

probes mounted on a rotating arm in a collisionless plasma. They achieved speed ratios up to about 1.5, and ratios of probe radius to Debye length between 0.4 and 15 for spheres and between 0.03 and 1.5 for cylinders, that is, precisely in the ranges in which large departures from symmetric-sheath-theory predictions might be expected (Godard[66], pp. 47-49; Godard and Laframboise[67]). Their results show dramatic departures from predictions made by such theories.

6. DISCUSSION: CONCLUSIONS

The development of realistic numerical spacecraft-charging simulations for low-orbit conditions appears likely to be a more difficult task than for geosynchronous-orbit conditions. On the other hand, existing numerical methods, used as efficiently as possible and in appropriate combinations, show some promise of ability to cope with this situation, at least in two dimensions and possibly in three dimensions. Some hard choices between realism of the simulation geometry and accuracy of results may be necessary.

If time-dependent simulation proves necessary, it is not clear at present which of the methods described in Sections 2(b) or 2(c) is best. If quasistatic simulation proves sufficient, combinations of the methods described in Sections 3(d), 3(e), 3(g), 3(l), and 3(m) appear likely to be most effective. Within a quasistatic calculation, the best method for calculating ion densities and fluxes depends on the value of the ion speed ratio S_i (Section 4). Simple, large-voltage symmetric-sheath theories often used to provide preliminary estimates of sheath sizes and spacecraft potentials (for example, Parks and Katz,[4] and Katz and Parks[5]) contain serious limitations for use in making more precise calculations (Section 5).

Acknowledgments

We are grateful to D. Cooke, I. Katz, M.J. Mandell, L.W. Parker, and E.C. Whipple for valuable discussions and comments.

---

66. Godard, R. (1975) A Symmetrical Model for Cylindrical and Spherical Collectors in a Flowing Collisionless Plasma, Ph.D. Thesis, York University, Toronto, Canada (available from the author).

67. Godard, R., and Laframboise, J.G. (1983) Total current to cylindrical collectors in collisionless plasma flow, Planet. Space Sci. (in press).

References

1. Laframboise, J.G., and Prokopenko, S.M.L. (1977) Numerical simulation of spacecraft charging phenomena, in: Proc. Spacecraft Charging Technology Conference, C.P. Pike and R.R. Lovell, Eds., Report No. AFGL-TR-77-0051, Air Force Geophysics Laboratory, Massachusetts; Report No. NASA TMX-73537, Lewis Research Center, Cleveland, Ohio, pp. 309-318, AD A045459.

2. deLeeuw, J.H. (1967) A brief introduction to ionospheric aerodynamics, in: Proc. 5th Internat. Symp. on Rarefied Gas Dynamics, C.L. Brundin, Ed., Academic Press, New York, pp. 1561-1586.

3. Martin, A.R. (1974) Numerical solutions to the problem of charged particle flow around an ionospheric spacecraft, Planet. Space Sci. 22:121-141.

4. Parks, D.E., and Katz, I. (1981) Charging of a large object in low polar earth orbit, in: Spacecraft Charging Technology 1980, NASA Conference Publication 2182/Report No. AFGL-TR-81-0270, Air Force Geophysics Laboratory, Massachusetts, pp. 979-989, AD A114426.

5. Katz, I., and Parks, D.E. (1982) Space shuttle orbiter charging, Paper AIAA-82-0119, Amer. Inst. Aeron. Astron. 20th Aerospace Sciences Mtg., January 1982, Orlando, Florida.

6. Fahleson, U. (1973) Plasma-vehicle interactions in space - some aspects on present knowledge and future development, in: Photon and Particle Interactions with Surfaces in Space, R.J.L. Grard, Ed., D. Reidel, Dordrecht, Holland, pp. 563-569.

7. Whipple, Jr., E.C. (1976) Observation of photoelectrons and secondary electrons reflected from a potential barrier in the vicinity of ATS 6, J. Geophys. Res. 81(4):715-719.

8. Prokopenko, S.M.L., and Laframboise, J.G. (1977) Prediction of large negative shaded-side spacecraft potentials, in: Proc. Spacecraft Charging Technology Conference, C.P. Pike and R.R. Lovell, Eds., Report No. AFGL-TR-77-0051, Air Force Geophysics Laboratory, Massachusetts; Report No. NASA TMX-73537, Lewis Research Center, Cleveland, Ohio, pp. 369-387, AD A045459.

9. Prokopenko, S.M.L., and Laframboise, J.G. (1980) High-voltage differential charging of geostationary spacecraft, J. Geophys. Res. 85(A8):4125-4131.

10. Katz, I., Parks, D.E., Wang, S., and Wilson, A. (1977) Dynamic modeling of spacecraft in a collisionless plasma, in: Proc. Spacecraft Charging Technology Conference, C.P. Pike and R.R. Lovell, Eds., Report No. AFGL-TR-77-0051, Air Force Geophysics Laboratory, Massachusetts; Report No. NASA TMX-73537, Lewis Research Center, Cleveland, Ohio, pp. 319-330, AD A045459.

11. Besse, A.L., and Rubin, A.G. (1980) A simple analysis of spacecraft charging involving blocked photoelectron currents, J. Geophys. Res. 85(A5):2324-2328.

12. Purvis, C. (1982) Evolution of spacecraft charging technology, Paper AIAA-82-0273, Amer. Inst. Aeron. Astron. 20th Aerospace Sciences Mtg., January 1982, Orlando, Florida.

13. Laframboise, J.G., Kamitsuma, M., and Godard, R. (1982) Multiple floating potentials, 'Threshold-temperature' effects, and 'Barrier' effects in high-voltage charging of exposed surfaces on spacecraft, in: Proc. Internat. Symp. on Spacecraft Materials in Space Environment, Report No. ESA SP-178, European Space Agency, Paris, pp. 269-275.

14. Mandell, M.J. (1982) Private communication.

15. Katz, I., Cassidy, J.J., Mandell, M.J., Schnuelle, G.W., Steen, P.G., and Roche, J.C. (1979) The capabilities of the NASA charging analyzer program, in: Spacecraft Charging Technology - 1978, NASA Conference Publication 2071; Report No. AFGL-TR-79-0082, AD A084626, Air Force Geophysics Laboratory, Massachusetts, pp. 101-122.

16. Boris, J.P., and Book, D.L. (1976) Solution of continuity equations by the method of flux-corrected transport, Methods Comput. Phys. 16:85-129.

17. Zalesak, S.T. (1979) Fully multidimensional flux-corrected transport algorithms for fluids, J. Comput. Phys. 31:335-362.

18. Rowland, H.L. (1980) Strong turbulence effects on the kinetic beam-plasma instability, Phys. Fluids 23:508-517.

19. Smith, R.A. (1982) Vlasov simulation of plasma double layers, Physica Scripta 25:413-415.

20. Berk, H.L., and Roberts, K.V. (1970) The water-bag model, Methods Comput. Phys. 9:88-134.

21. Buneman, O. (1979) Vectorization and parallelism in Stanford's 3D, EM particle code, MFECC Buffer 3(7):7-12. Magnetic Fusion Energy Computer Center Monthly Bulletin, Livermore, California.

22. Buneman, O. (1980) Tetrahedral finite elements for interpolation, SIAM J. Sci. and Stat. Comput. 1:223-248.

23. Hockney, R.W., and Eastwood, J.W. (1981) Computer Simulation Using Particles, McGraw-Hill, New York.

24. Isensee, U., and Maassberg, H. (1981) Particle-in-cell simulation of the plasma environment of a spacecraft in the solar wind, Adv. Space Res. 1:413-416.

25. Taylor, J.C. (1967) Disturbance of a rarefied plasma by a supersonic body on the basis of the Poisson-Vlasov equations - I(II), Planet. Space Sci. 15:155-187(463-474).

26. Kiel, R.E., Gey, F.C., and Gustafson, W.A. (1968) Electrostatic potential field of an ionospheric satellite, AIAA Journal 6:690.

27. Davis, A.H., and Harris, I. (1961) Interaction of a charged satellite with the ionosphere, Proceedings 2nd International Symposium on Rarefied Gas Dynamics, L. Talbot, Ed., Academic Press, New York, p. 691.

28. Maslennikov, M.V., and Sigov, Yu.S. (1965) A discrete model for the study of the flow of a rarefied plasma about a body, Soviet Phys. Doklady 9:1063.

29. Maslennikov, M.V., and Sigov, Yu.S. (1969) Rarefied plasma stream interaction with a charged body, Proc. 6th International Symposium on Rarefied Gas Dynamics, L. Trilling and H.Y. Wachman, Eds., Vol. 2, Academic Press, New York, pp. 1671-1680.

30. Call, S.M. (1969) The Interaction of a Satellite With the Ionosphere, Plasma Lab., Columbia Univ., New York, Report 46.

31. McDonald, P.W., and Smetana, F.O. (1969) Results of a numerical experiment to determine the current collected by a charged cylinder in a collisionless plasma stream, in: Proc. 6th Internat. Symposium on Rarefied Gas Dynamics, L. Trilling and H.Y. Wachman, Eds., Vol. 2, Academic Press, New York, pp. 1627-1636.

32. Fournier, G. (1971) Ecoulement de Plasma Sans Collisions Autour d'un Cylindre en Vue d'Applications Aux Sondes Ionosphériques, Office Nat. d'Etudes et de Rech. Aerosp., Chatillon, France, Publication 137.

33. Fournier, G. (1971) Positively biased ionospheric probes, Phys. Letters 34A:241.

34. Parker, L.W. (1977) Calculation of sheath and wake structure about a pillbox-shaped spacecraft in a flowing plasma, in: Proc. Spacecraft Charging Technology Conference, C.P. Pike and R.R. Lovell, Eds., Report No. AFGL-TR-77-0051, Air Force Geophysics Laboratory, Massachusetts; Report No. NASA TMX-73537, Lewis Research Center, Cleveland, Ohio, pp. 331-366, AD A045459.

35. Laframboise, J.G. (1966) Theory of Spherical and Cylindrical Langmuir Probes in a Collisionless, Maxwellian Plasma at Rest, University of Toronto, Institute for Aerospace Studies, Report 100 (available from the author).

36. Parker, L.W. (1970) Theory of the External Sheath Structure and Ion Collection Characteristics of a Rocket-Borne Mass Spectrometer, Report No. AFCRL-71-0105, Contract F19628-70-C-0053, Air Force Geophysics Laboratory, Massachusetts, AD A720833.

37. Parker, L.W., and Sullivan, E.C. (1969) Boundary conditions and iterative procedures for plasma sheath problems, in: Proc. 6th Internat. Symp. on Rarefied Gas Dynamics, L. Trilling and H.Y. Wachman, Eds., Academic Press, New York, pp. 1637-1641.

38. Parker, L.W., and Sullivan, E.C. (1974) Iterative Methods for Plasma-Sheath Calculations - Application to Spherical Probe, NASA Technical Note TN D-7409.

39. Parker, L.W. (1973) Computation of Ion Collection by a Rocket-Mounted Mass Spectrometer in the Limit of Vanishing Debye Number, Report No. AFCRL-TR-73-0735, Contract F19628-73-C-0065, Air Force Geophysics Laboratory, Hanscom AFB, Massachusetts, AD A783625.

40. Al'pert, Ya.L., Gurevich, A.V., and Pitaevskii, L.P. (1965) Space Physics with Artificial Satellites, Consultants Bureau, New York.

41. Grabowski, R., and Fischer, T. (1975) Theoretical density distribution of plasma streaming around a cylinder, Planet. Space Sci. 23:287-304.

42. Isensee, U., Lehr, W., and Maassberg, H. (1981) A numerical model to calculate the wake structure of a spacecraft under ionospheric conditions, Adv. Space Res. 1:409-412.

43. Parrot, M.J.M., Storey, L.R.O., Parker, L.W., and Laframboise, J.G. (1982) Theory of cylindrical and spherical Langmuir probes in the limit of vanishing Debye number, Phys. Fluids (in press).

44. Cooke, D. (1982) Private communication.

45. Walker, E.H. (1965) Plasma sheath and screening around a stationary charged sphere and a rapidly moving charged body, in: Interactions of Space Vehicles with an Ionized Atmosphere, S.F. Singer, Ed., Pergamon, Oxford, pp. 61-162.

46. Walker, E.H. (1973) Plasma sheath and screening of charged bodies, in: Photon and Particle Interactions with Surfaces in Space, R.J.L. Grard, Ed., D. Reidel, Dordrecht, Holland, pp. 73-89.

47. Katz, I., Mandell, M.J., Schnuelle, G.W., Parks, D.E., and Steen, P.G. (1980) Plasma collection by high-voltage spacecraft at low earth orbit, Paper AIAA-80-0042, Amer. Inst. Aeron. Astron. 18th Aerospace Sciences Mtg., January 1980, Pasadena, California.

48. Mandell, M.J., Katz, I., Steen, P.G., and Schnuelle, G.W. (1980) The effect of solar array voltage patterns on plasma power losses, IEEE Trans. Nucl. Sci. NS-27.

49. Illiano, J.M., and Storey, L.R.O. (1974) Apparent enhancement of electron temperature in the wake of a spherical probe in a flowing plasma, Planet. Space Sci. 22:873-878.

50. Parker, L.W. (1981) Trajectory-Controlled Space-Charge-Sheath Computer Models; Application to Large High-Voltage Solar Arrays in Dense Plasmas, NASA Johnson Space Center Contract Report No. NAS 9-15934.

51. Cooke, D., Parker, L.W., and McCoy, J.E. (1981) Three-dimensional space charge model for large high-voltage satellites, in: Spacecraft Charging Technology 1980, NASA Conference Publication 2182; Report No. AFGL-TR-81-0270, Air Force Geophysics Laboratory, Massachusetts, pp. 957-978, AD A114426.

52. Laframboise, J.G., Kamitsuma, M., Prokopenko, S.M.L., Chang, Jen-Shih, and Godard, R. (1982) Numerical Simulation of Spacecraft Charging Phenomena at High Altitude, Final Report on Grant AFOSR-76-2962, York University.

53. Parker, L.W. (1982) Private communication.

54. Parker, L.W., and Whipple, Jr., E.C. (1967) Theory of a satellite electrostatic probe, Ann. Phys. 44:126-161.

55. Whipple, Jr., E.C., and Parker, L.W. (1969) Effects of secondary electron emission on electron trap measurements in the magnetosphere and solar wind, J. Geophys. Res. 74:5763-5774.

56. Laframboise, J.G., and Parker, L.W. (1973) Probe design for orbit-limited current collection, Phys. Fluids 16:629-636.

57. Laframboise, J.G., Prokopenko, S.M.L., Kamitsuma, M., and Godard, R. (1981) Results from a two-dimensional spacecraft-charging simulation and comparison with a surface photocurrent model, in: Spacecraft Charging Technology 1980, NASA Conference Publication 2182; Report No. AFGL-TR-81-0270, Air Force Geophysics Laboratory, Massachusetts, pp. 709-716, AD A114426.

58. Bernstein, I.B., and Rabinowitz, I.N. (1959) Theory of electrostatic probes in a low-density plasma, Phys. Fluids 2:112-121.

59. Langmuir, I., and Blodgett, K.B. (1924) Currents limited by space charge between concentric spheres, Phys. Rev. 23:49.

60. Langmuir, I., and Blodgett, K.B. (1923) Currents limited by space charge between coaxial cylinders, Phys. Rev. 22:347.

61. Sonin, A.A. (1965) The Behaviour of Free Molecule Cylindrical Langmuir Probes in Supersonic Flows, and their Application to the Study of the Blunt Body Stagnation Layer, University of Toronto, Institute for Aerospace Studies, Report No. 109.

62. Sonin, A.A. (1966) Free-molecule Langmuir probe and its use in flowfield studies, AIAA Jour. 4:1588-1596.

63. Sonin, A.A., Graf, K., Laframboise, J.G., and deLeeuw, J.H. (1965) The ion collection of free molecular cylindrical Langmuir probes in flowing plasmas, in: Proc. 7th Internat. Conf. on Phenomena in Ionized Gases, Gradevinska Knjiga Publishing House, Belgrade, Yugoslavia, pp. 53-57.

64. Makita, H., and Kuriki, K. (1977) Comparative study of spherical and cylindrical drift probes, Proc. 10th International Symposium on Rarefied Gas Dynamics, J. Leith Potter, Ed., p. 1007, Progress in Astronautics and Aeronautics, Vol. 51, Amer. Inst. of Astronaut. and Aeronaut., New York.

65. Makita, H., and Kuriki, K. (1978) Current collection by spherical Langmuir probes drifting in a collisionless plasma, Phys. Fluids 21:1279.

66. Godard, R. (1975) A Symmetrical Model for Cylindrical and Spherical Collectors in a Flowing Collisionless Plasma, Ph.D. Thesis, York University, Toronto, Canada (available from the author).

67. Godard, R., and Laframboise, J.G. (1983) Total current to cylindrical collectors in collisionless plasma flow, Planet. Space Sci. (in press).

Contents

4. Charged Particle Effects on Space Systems

by

W. N. Hall
Air Force Geophysics Laboratory
Hanscom AFB, Mass. 01731

based on a presentation by

N. J. Stevens*
NASA Lewis Research Center
Cleveland, Ohio 44135

Abstract

There is a growing tendency to plan space missions that will incorporate very large space power systems. These space power systems must function in a space plasma environment that can impose operational limitations. As the power output increases, the operating voltage must also increase and this voltage, exposed at solar array interconnects, interacts with the local plasma. The implications of such interactions are considered here. The available laboratory data for biased array segment tests are reviewed to demonstrate the basic interactions considered. A data set for a test of a floating high voltage array illuminated in a solar simulator test is used to generate approximate relationships for positive and negative current collection from plasma. These relationships are applied to a hypothetical 100 kW power system operating in a 400 km, near-equatorial, orbit. It is found that discharges from the negative regions of the array are the most probable limiting factor for array operation.

*Now with Hughes Aircraft Company, Space and Communications Group, Los Angeles, California 90009.

1. INTRODUCTION

This report concerns the interactions that can occur between the space charged-particle environments and the spacecraft that must function in that environment. The interactions of concern are illustrated in Figure 1, which shows a typical large spacecraft. This spacecraft has two large solar array wings and a central body. For convenience, I have divided the interactions into two categories: the first, called spacecraft passive, involves interactions such as spacecraft charging in which the environment acts on the spacecraft and the second, called spacecraft active, involves interactions caused by the spacecraft, for example, high voltage space power systems. It must be recognized that space is not a vacuum, but contains significant charged-particle fluxes that can induce anomalous behavior in satellite system operations. Hence, these interactions are important and must be considered in system designs.

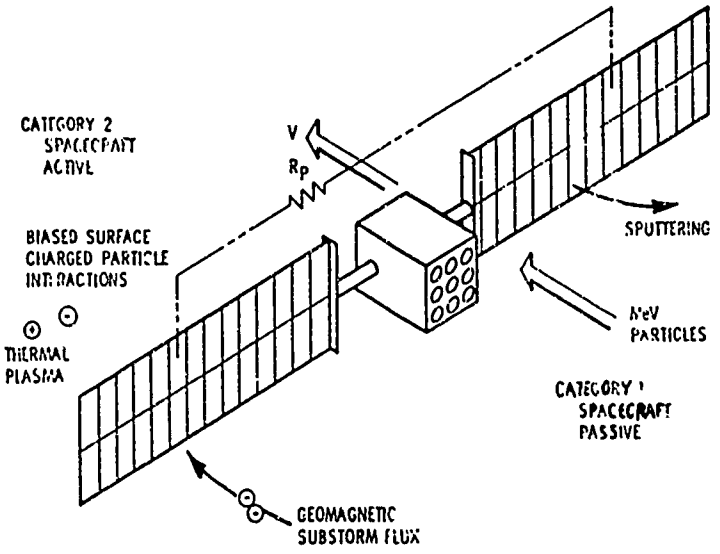

Figure 1. A Typical Spacecraft System With Some Possible Environmental Interactions

1.1 Spacecraft-Passive Interactions

The first category of environmental interactions deals with charged particle environments acting on spacecraft surfaces. The most important of these interactions is geomagnetic substorm environments charging geosynchronous satellite

surfaces to a point where discharges can occur, disrupting systems operations. This spacec. aft charging phenomenon was first noticed in the early 1970's as a series c. electronic switching anomalies that seemed to occur predominantly in the satellite local midnight-to-dawn quadrant. While these switching events were irritating, they were not harmful and were generally ignored. It was the failure of a satellite in the early seventies that triggered the interest in this environmental effect.

It was found, from ATS-5 data (1969), that plasma clouds were injected periodically into geosynchronous orbits at local midnight. These plasma clouds were generated from solar wind particles accelerated down the neutral sheet into the Earth's magnetic field. At altitudes near synchronous orbit, the particles separated according to their energies and produced a plasma cloud. Satellites would move into this cloud and become charged to substantial negative values. It is believed that the differential charging caused by surfaces shadowed from the sun could reach breakdown thresholds. The transients introduced by the discharges were believed to couple into the electrical harness and cause the switching.

The Spacecraft Charging At High Altitudes (SCATHA) satellite, P-78-2, was built and launched specifically to evaluate the effect of substorm environments on satellite system operation. One of the more significant results of this mission is summarized in Figure 2. This shows the relationship between surface charging (from Surface Potential Monitor data) and recorded system discharge transients. Transients observed between local 2200 to 0700 hours occurred when the satellite surfaces were charged. The satellite data also indicated that transients were observed when the satellite was in the local noon position. These transients are believed to be caused by electron penetration of the interior, charging cables and interior dielectrics to the point of discharge. Hence, these data indicate two possible discharge transient mechanisms; exterior surface discharges due to substorm differential charging and high energy particle penetration of spacecraft causing interior surface charging and subsequent discharges.

1.2 Spacecraft-Active Interactions

The topic of this presentation is the anticipated behavior of large space systems proposed for lower Earth orbits - those compatible with the Space Shuttle operations. The systems can also interact with space environments in a manner that can influence their operational behavior. Because it is the spacecraft moving through the environment that causes the interactions, they are referred to as "spacecraft active" or category 2 interactions.

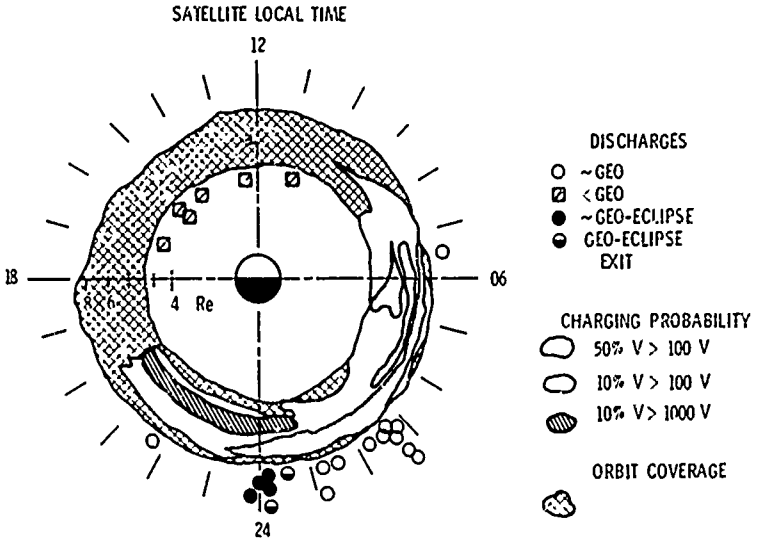

Figure 2. SCATHA Spacecraft Charging/Discharging Data. Distribution in altitude and local time of the probability of charging greater than a threshold value and local time of recorded system discharge transients

One of these category 2 interactions is the motion of the large body through the Earth's magnetic field, which can produce electric fields that induce additional stresses in the body (see Figure 3). These stresses can introduce distortions in sensitive antennas and other parts of these proposed low-density structures. While this is a serious concern and must merit attention in the design of such structures, the discussion will be limited to high voltage space power systems. This technology is more fully developed and can be used to illustrate the reasons for low-Earth orbit environmental interactions.

2. NASA MISSION PLANNING

For the past several years, NASA has been studying mission plans calling for extremely large satellites to be placed in low Earth orbits by the Shuttle.[1-4] The

1. (1976) Outlook for Space, NASA SP-386.
2. Johnson, R.D., and Holbrow, C., Eds. (1977) Space Settlements, A Design Study, NASA SP-413.
3. Bekey, I. (1979) Big COMSATS for big jobs at low user costs, Astron. and Aeron. 17:42-56.
4. Snoddy, W.C. (1981) Space platforms for science and applications, Astron. and Aeron, 19:28-36.

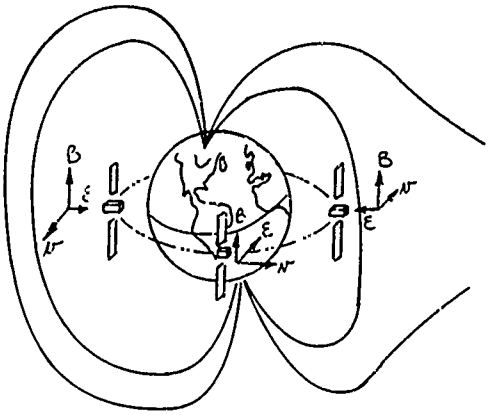

Figure 3. Motion-Induced Electric Fields Generated in a Large Spacecraft in Low-Latitude Orbit

planners were freed from the constraints imposed by expendable launch vehicle shrouds; satellite dimensions grew to tens of meters while power generation requirements rose to hundreds of kilowatts.

Now that the Space Transportation System (that is, the Shuttle) is operational, there is an effort underway to place these large structures in orbit in the near future. One possibility could be a manned space platform capable of conducting Earth-oriented studies, space science investigations, or space manufacturing experiments. Although plans are not completed, the mission could involve an expandable platform concept; initially a simplified station that can be expanded in the future. The platform would probably be placed in an orbit similar to Skylab (400 to 500 km) so that it could be serviced by the Shuttle, while high enough to minimize reboost cost and have an adequate mission life. Array power generating capabilities are postulated as being between 50 and 100 kW.

The generation of large amounts of power requires very large solar arrays since the nominal solar array power density is on the order of 100 W/m^2. Hence, a 50 kW array would require area of 500 m^2. This area implies long cabling to bring power to the user. If the system is operated at a nominal voltage of 30 to 60 V, currents on the order of 1000 A would be required. Currents of this magnitude can produce either significant cable harness losses (I^2R) or unacceptable increases in weight if the cable loss is reduced by thicker conductor sectional areas.[5] In addition, large currents flowing in the array can generate magnetic

5. Stevens, N. J. (1979) Interactions between spacecraft and the charged-particle environment, Spacecraft Charging Technology - 1978, NASA CP-2071/ AFGL-TR-79-0082, pp. 268-294.

fields that could interact with the earth's field. This increases the drag on the system and shortens its mission life. The alternative to large currents is to increase the operating voltages, thereby reducing currents. However, the Skylab array used the highest operational voltages in space to date, when, for short periods of time, it was configured to operate at 100 V.[6] The operation of power systems at these elevated voltages (operating voltages in the range from 200 to 1000 V are considered) can give rise to interactions with the space plasma environment that must be considered in designing these systems.

The interactions of concern are illustrated in the high-voltage space power system shown in Figure 1. This system consists of two large solar array wings surrounding a central body or spacecraft. The solar arrays are assumed to be assembled in what is called standard construction techniques, as shown in Figure 4. This means that the cover slides do not completely shield the metallic interconnects from the environment. These cell interconnects are at various voltages depending on their location in the array circuits. Hence, the interconnects can act as plasma probes, attracting or repelling charged particles. At some location on the array, the generated voltages will be equal to the space plasma potential. Since the electrons are more mobile than the ions, more of the array will float at a voltage that is negative with respect to the space plasma than will float at a voltage that is positive with respect to the space potential. Cell interconnects at voltages above this space plasma potential will collect electrons, while those at voltages below the space potential will collect ions. The voltage distribution in the interconnects relative to space must be such that these electron and ion currents are equal (that is, the net current collected is zero).[7]

This flow of particles can be considered to be a current loop through space that is in parallel with the operational systems and, hence, is a power loss. In addition, the cover glass used on the solar cells must also have a zero net current collection. This interaction with the space plasma forces the cover glass to a small negative potential and can produce large voltage gradients in the gap region between solar cells. This can give rise to arcing conditions or transient breakdowns to space.

The severity of these plasma interactions depends upon the array operational voltages and the charged-particle environments. The operating voltage will be determined from power system studies, but will probably be less than 1000 V. The charged-particle environment is determined by the orbital altitude (see Figure 5).

---

6. Woosley, A.P., Smith, O.B., and Nassen, H.W. (1974) Skylab technology electrical power system, ASME Paper 74-129.

7. Chen, F.F. (1965) Electric probes, in: Plasma Diagnostic Techniques, R.H. Huddlestone and S. Leonard, Eds. - Pure & Applied Physics, Vol. 21, Academic Press, pp. 113-119.

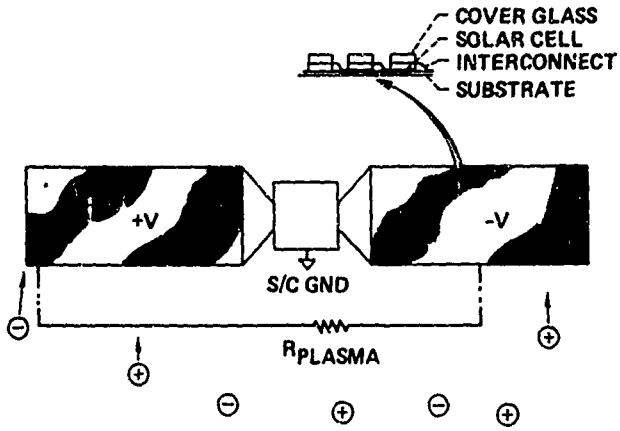

Figure 4. Spacecraft With a High-Power Solar Array Power System Showing Standard Construction Technique of Uncovered Metal Interconnect Between Individual Solar Cells

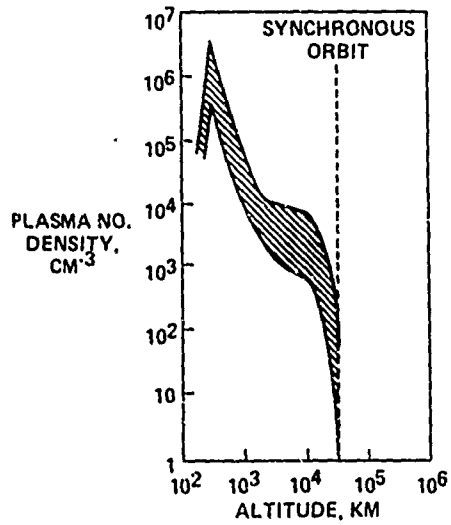

Figure 5. Variation of the Charged-Particle Environment With Altitude Near the Equator

Only the low energy or thermal plasma environment should be of concern at the projected operational voltages, since the array voltage is too low to influence the higher energy environmental particles. This plasma environment has particles

with temperatures of about 1 eV and densities that vary from a maximum of about $3 \times 10^6/cm^3$ at 300 km to between 1 and $10/cm^3$ at geosynchronous altitudes. Hence, plasma interactions should be more severe at the lower altitudes than at synchronous.

These possible interactions between space power systems and plasma environments have been discussed previously in general terms. In the next section, the basic phenomena are reviewed and later will be applied to a power system directed towards the assumed space platform.

3. REVIEW OF BIASED ARRAY TESTS

3.1 Ground Simulation Data

Tests of small segments of solar arrays biased by laboratory power supplies while exposed to simulated plasmas in vacuum facilities have been conducted over the past ten years.[8-16] There has also been a similar test conducted in space.[17] Regardless of the size of the array segment (areas from 100 to 13,600 cm^2 have been tested) the results are quite similar. In this section, the test procedure and the pertinent results are summarized.

---

8. Cole, R.W., Ogawa, H.S., and Sellen, Jr., J.M. (1968) Operation of Solar Cell Arrays in Dilute Streaming Plasmas, NASA CR-72376.
9. Knauer, W., Bayless, J.R., Todd, G.T., and Ward, J.W. (1970) High Voltage Solar Array Study, NASA CR-72675.
10. Herron, B.G., Bayless, J.R., and Worden, J.D. (1972) High voltage solar array technology, AIAA Paper 72-443.
11. Kennerud, K.L. (1974) High Voltage Solar Array Experiments, NASA CR-121280.
12. Stevens, N.J. (1973) Solar Array Experiments on the SPHINX Satellite, NASA TMX-71458.
13. Domitz, S., and Grier, N.T. (1974) The interaction of spacecraft high voltage power systems with the space plasma environment, Power Electronic Specialists Conference, IEEE, N.J., pp. 62-69.
14. Stevens, N.J., Berkopec, F.D., Purvis, C.K., Grier, N.T., and Staskus, J.V. (1978) Investigation of high voltage spacecraft system interactions with plasma environments, AIAA Paper 78-672.
15. McCoy, J.E., and Konradi, A. (1981) Sheath effects observed on a 10-meter high voltage panel in simulated low Earth orbit plasmas, Spacecraft Charging Technology - 1980, NASA CP-2182; AFGL-TR-81-0270, AD A114426.
16. Stevens, N.J. (1981) Review of Biased Solar Array-Plasma Interaction Studies, NASA TM-82693.
17. Grier, N.T., and Stevens, N.J. (1981) Plasma interaction experiment (PIX) satellite results, Spacecraft Charging Technology - 1980, NASA CP-2182/AFGL-TR-81-0270, AD A114426.

These plasma interaction tests are typically conducted in an experimental arrangement shown schematically in Figure 6. The vacuum chamber is capable of pumping to background pressures of 10^{-6} Torr or less. The plasma environment is created by ionizing a neutral or inert gas (such as, nitrogen, argon, or helium). The plasma parameters (plasma number density and particle temperatures) are usually determined with either cylindrical or spherical Langmuir probes. The solar array segment (Figure 7) is mounted in this chamber electrically isolated from the tank ground. A high voltage power supply is connected to one or both ends of the array through an isolated feedthrough in the tank wall. A current sensing instrument is placed between the power supply and the tank wall to measure any coupling current between the segment and tank ground through the plasma environment. This lead is shielded to minimize extraneous currents. A surface voltage probe (such as manufactured by TREK) is used to sense the voltage on the array during the test. Hence, a surface voltage profile and a leakage current measurement are obtained as functions of applied positive or negative voltage for a given plasma environment. It should be pointed out that the tank ground (at the wall) is not necessarily the plasma potential. This plasma potential is determined from the probe readings and this potential must be added to, or subtracted from, the applied bias voltage to interpret the test data. It is very important to make this correction at low bias voltages, since the plasma potential can be in the range of ±20 V.

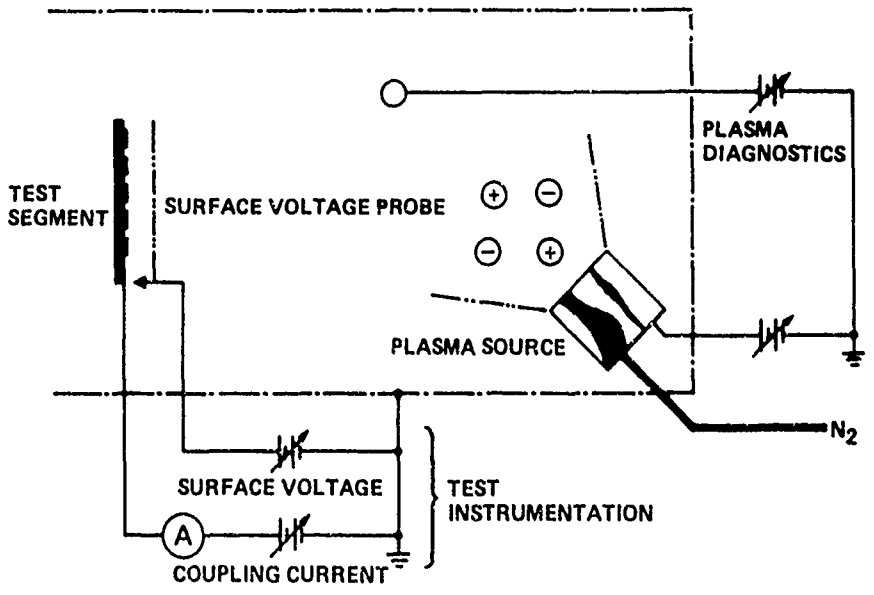

Figure 6. Schematic of Ground Simulation Tests of Behavior of Biased Solar Array Panel Segments in a Plasma Environment

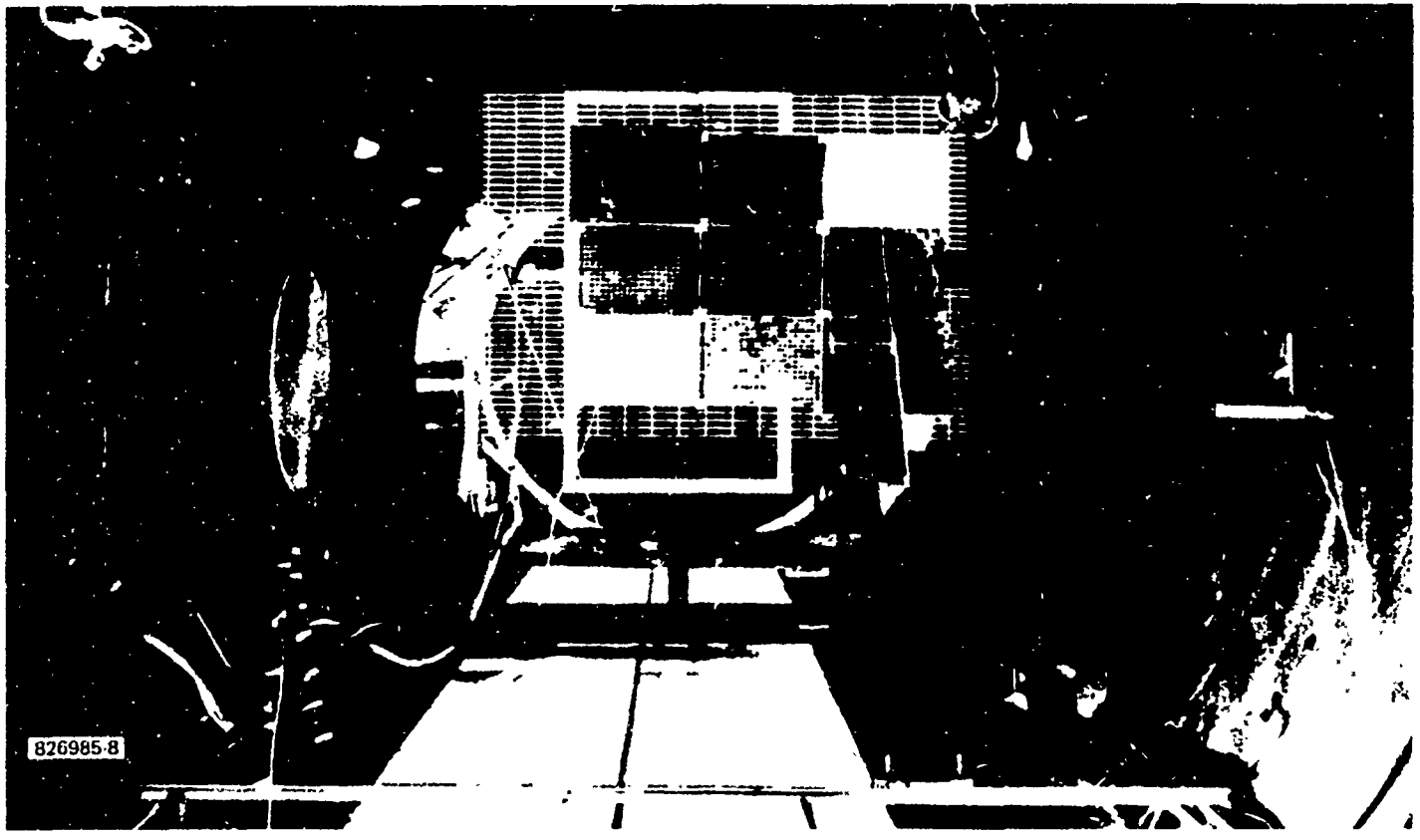

Figure 7. Array of Nine Solar Panel Segments Used for Tests in a Plasma Environment, Shown Here Being Placed in a NASA/Lewis Research Center Test Chamber for Tests of Biased Panels. It was later tested at NASA/Johnson Space Center with a solar simulator producing self-generated panel voltages

Typical results for a 100 cm^2 solar array segment biased positively and negatively are shown in Figures 8 through 11. With positive bias voltage, (Figure 8) the current collection starts at relatively low values, increasing slowly until a bias of about 100 V is reached. At this point, there is an increase in current collection of orders of magnitude. Above about +250 V, the current tends to increase linearly with voltage. The surface voltage probe traces (Figure 9) indicate why this behavior occurs. At the low applied biases, the voltage is confined to the gap region between the cells. The cover glass maintains its required zero current balance with the plasma by a slightly negative surface voltage and the superposition of the fields resulting from these voltages results in shielding the bias voltage from the plasma. At bias values greater than 100 V, the shielding appears to break down. The bias field now is stronger and starts to encompass the cover glass. This accelerates electrons from the plasma into the cover glass creating secondary-emitting electrons. The surface voltage must now change to maintain a zero current balance at the glass surface. This surface voltage assumes a value which is about 50 V less than the bias voltage. Hence,

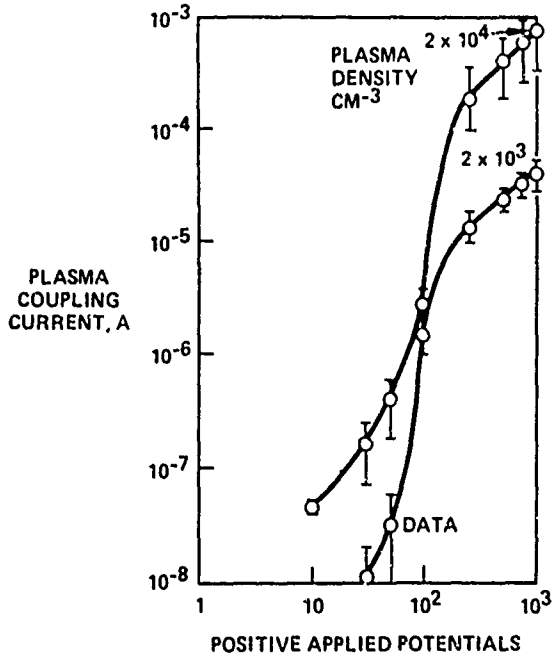

Figure 8. Current Collected by a 100 cm^2 Solar Panel, Biased With Positive Applied Potentials, in a Plasma Environment

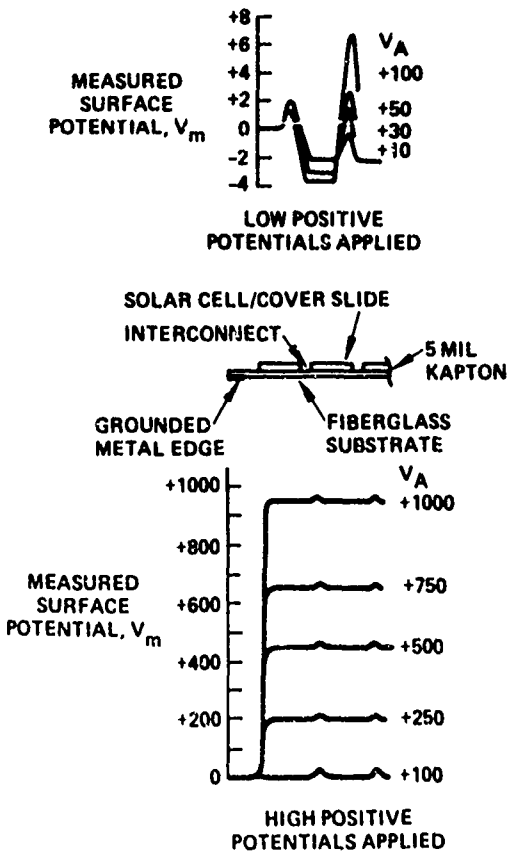

Figure 9. Surface Voltage Probe Measurements of a 100 cm^2 Solar Panel, Biased With Positive Applied Potentials, in a Plasma Environment

at this transition, called "snapover",[18] the collecting area is increased to the full segment area, causing the change in coupling currents. Empirically, the data can be modeled as cylindrical probe collection at positive bias voltages up to 100 V and spherical probe collection (with the bias reduced by 100 V) at positive values greater than 100 V.[16]

For negative bias voltages (Figure 10) the data indicate that the coupling current increases slowly and then transitions into an arc or breakdown, signified by a rapid rise in current that trips off the laboratory power supply. Since at other times, we have used the supply to bias metallic probes negatively without causing breakdowns, it must be assumed that the arcing results from the

18. Purvis, C.K., Stevens, N.J., and Berkopec, F.D. (1977) Interaction of Large, High Power Systems with Operational Orbit Charged-Particle Environments, NASA TMX-73867.

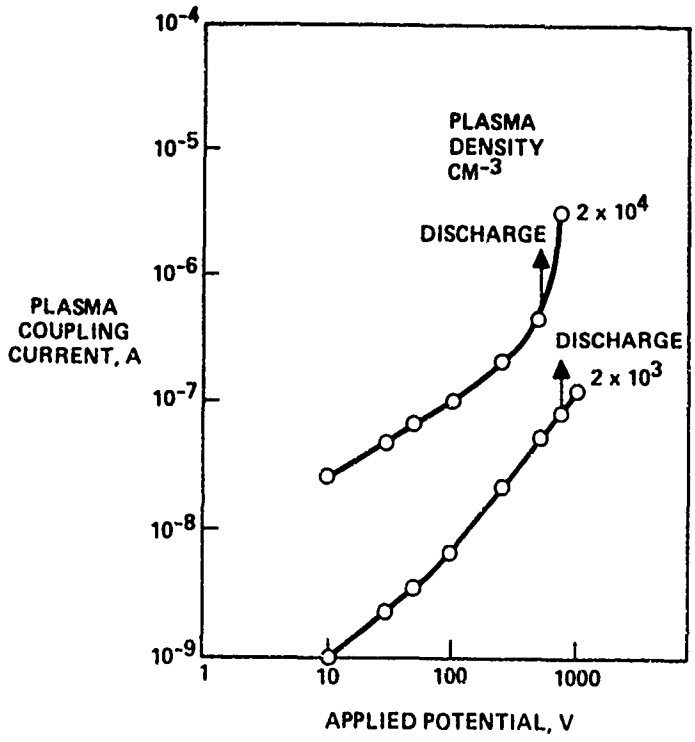

Figure 10. Current Collected by a 100 cm^2 Solar Panel, Biased With Negative Potentials, in a Plasma Environment

interaction between the negatively biased conductor (cell interconnects), the dielectrics (cover slides) and the plasma environment. The surface voltage probe traces (Figure 11) indicate that it is the gap region between cells that is the probable cause for the breakdown. As the bias voltage is made more and more negative, the fields resulting from the cover glass voltage confine the bias field to this limited area. It is known that a negative conductor confined by a less negative dielectric is prone to breakdown and this appears to be happening here.

Both the positive and negative bias voltage effects described above are plasma-density dependent phenomena. For positive bias voltages, both the low and high voltage collection changes in direct proportion to the density.[11, 14] However, the transition remains at about 100 V. The only condition that seems to influence the transition appears to be the area of the segment relative to the area of the dielectric and/or conductive boundaries. The data obtained in support of the PIX flight seemed to indicate a higher transition voltage,[17] probably due to the use of a small segment mounted on a large plate. The negative bias breakdown

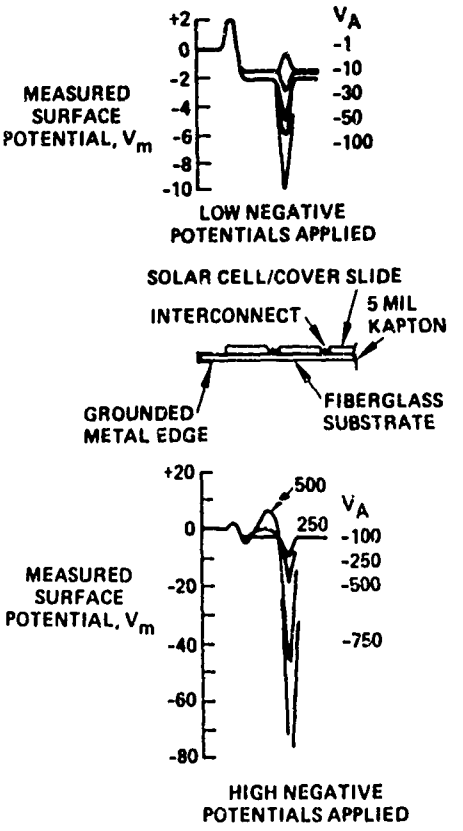

Figure 11. Surface Voltage Probe Measurements of a 100 cm^2 Solar Panel, Biased With Negative Applied Potentials, in a Plasma Environment

thresholds as a function of plasma density are shown in Figure 12. Extrapolated to the peak space plasma density environment (about 300 km), this breakdown value is uncomfortably low (about 300 V negative relative to the space plasma potential).

The phenomena described above seem to be independent of the interconnect configuration and array size. Both the standard interconnect configuration and wrap-around configurations have been tested. Array sizes varied from 100 to 400, to 1000, to 13,600 cm^2 with similar results. The higher positive bias voltage results for the larger panels can be questioned, however, since the tank walls can interact with bias voltage sheaths and distort the results.

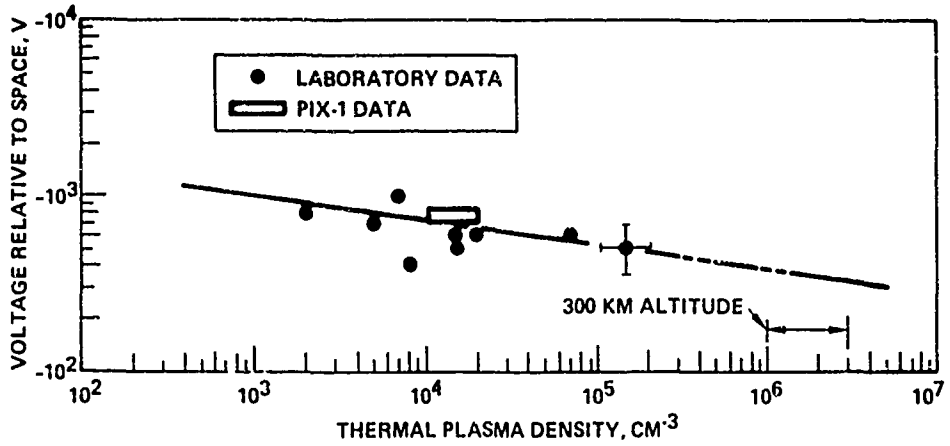

Figure 12. Variation With Plasma Density of the Voltage Threshold at Which Negatively Biased Solar Array Segments Encounter Arcing or Breakdown

3.2 Space Flight Data

Biased solar array experiments have been conducted in space. The first Plasma Interaction Experiment (PIX-1) was launched as an auxiliary payload experiment on the Landsat C mission in 1978. The experiment remained attached to the Delta launch vehicle second stage and operated for 4 h in a 900 km polar orbit. The experiment consisted of an experiment plate with a 100 cm^2 solar array and a 10 cm^2 button-on-kapton experiments, and an electronics enclosure with a 10 cm^2 button isolated on the exterior (see Figure 13). The bias power supply would step through a preprogrammed voltage series (to ± 1000 V) applying voltage to either the solar array or the button-on-kapton experiment. The isolated button was always biased and acted as the control for the experiment. Electrometers were used to measure the current independently to each of the three experiments. Data was retrieved in real time only so that only about half of the data was available for analysis.

Typical results from this experiment are shown in Figure 14. These data show reasonable agreement with ground simulation data and demonstrate that "snapover" and arcing at negative voltages are real phenomena. This experiment showed that flight experiments of this high voltage-space plasma interaction must be designed carefully. At ' ~ high positive voltages (greater than 500 V), the ion collection capability was not sufficient to balance the electron current collection and the potential of the Delta was driven slightly negative (believed to be -30 V maximum). This resulted in the need for post-flight ground tests to interpret the data.

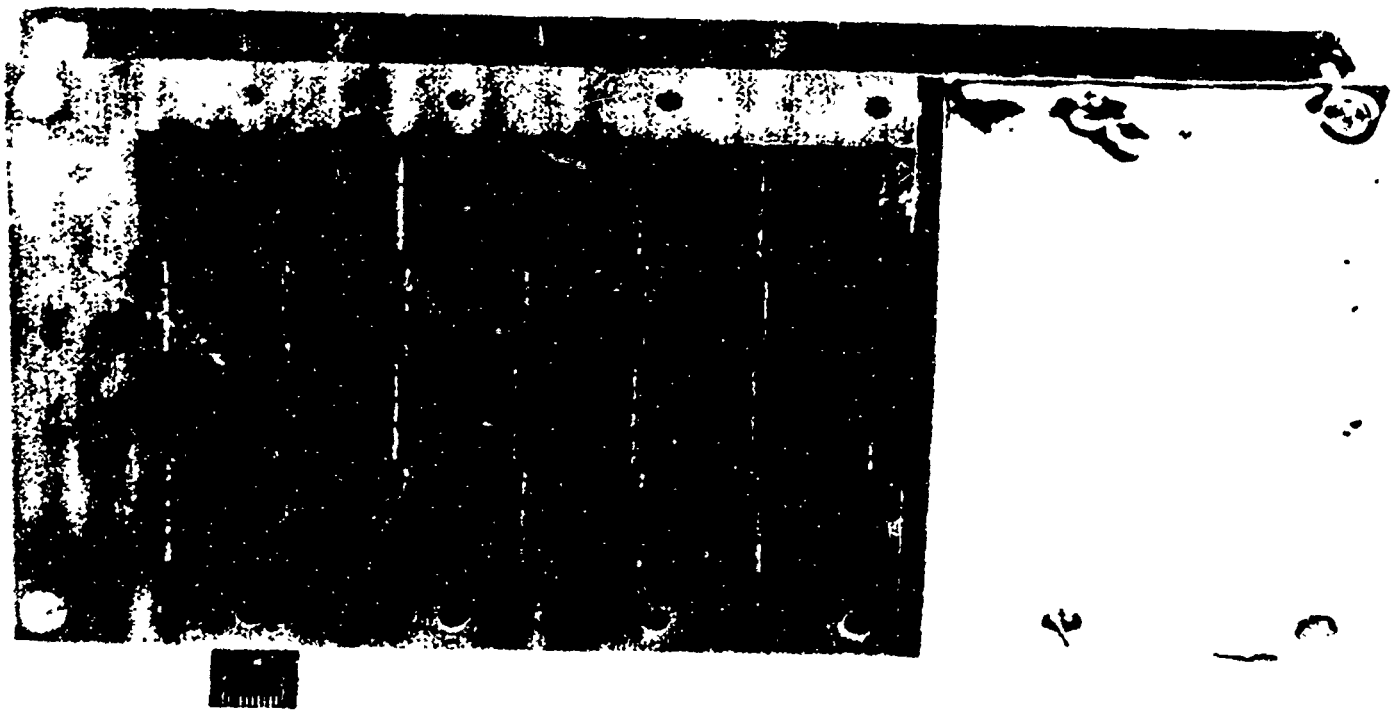

Figure 13. PIX-1 Experiment Plate

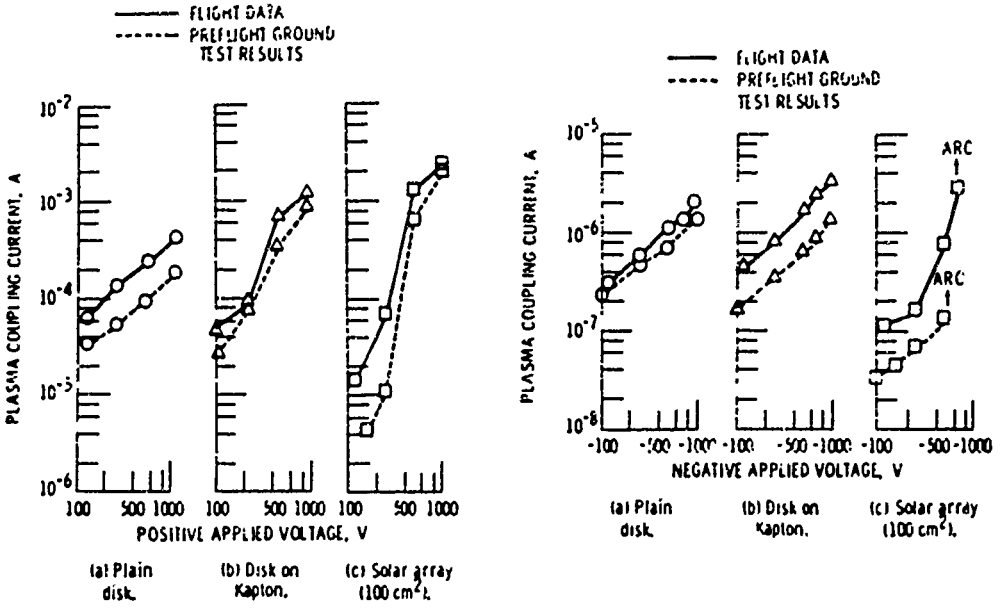

Figure 14. Comparison of Current Collected vs Bias Voltage for PIX-1 Experiment Results and Ground Simulation Results

A secondary auxiliary payload experiment is currently being assembled for launch on the IRAS mission in January, 1983. This experiment (PIX-2) is primarily directed towards investigating scaling with array area of solar array interactions in a 900 km polar orbit. The experiment consists of a 2000 cm^2 solar array panel divided into four parts. This panel can be biased (to ± 1000 V) as separate parts or collectively to determine the influence of biased portions adjacent to each other. To ease post flight data interpretation, an electron emitter has been included in this experiment. This should compensate for lack of ion collection area. A data retrieval system has been included so that all of the flight data can be obtained.

4. TESTS OF FLOATING ARRAYS IN A SOLAR SIMULATOR

Small segments of solar arrays with bias voltages provided by external power supplies can be used to study the phenomena of plasma interactions with high voltage solar arrays. However, the concepts developed must still be tested with self-generated voltages using solar simulators. Unfortunately, there have been relatively few such tests, primarily because a large solar array is required to

generate the high voltages needed, and therefore, a large facility (with large solar simulators) is required to obtain interaction data without wall effects. Even the small amount of data available is incomplete. For this paper, the results obtained with a nine-solar-panel array in the Johnson Space Center (JSC) facility[19] are used to provide a basis for predicting performance of large space power systems in a space environment.

The nine-panel array is shown in Figure 7. This array is made up of surplus flight solar array panels with no attempt made to try to match panel characteristics. There were seven panels (1400 cm^2 each) originally assembled in the late 1960s for the Space Electric Rocket Test (SERT-2) project and two panels, 1950 cm^2 each, assembled in the early 1970s for the Space Plasma High-Voltage Interaction Experiment (SPHINX) project. This nine-panel array was used in a series of tests conducted at both JSC and Lewis Research Center (LeRC) to evaluate the influence of facilities on plasma interactions.[19] While at JSC, a series of floating tests were also made using the solar simulator. Since the panels were not matched and the solar simulator did not uniformly illuminate all nine panels, the results must be viewed as an approximation to the desired test data. Furthermore, not all of the plasma properties were reported, so approximations for the particle energies and the plasma potential in the chamber had to be made.

The test was run with the array in an open circuit condition but with the capability of measuring each panel voltage and the current between each panel. The plasma density was stated to be 2×10^4 cm^{-3}. After correcting for the assumed value of the plasma potential (10 V), the distribution of open circuit voltages per panel is shown in Figure 15. The slope of the voltage for each panel is not the same, due to the non-uniformity of the panels. In this configuration the array open-circuit voltage was about 248 V or slightly less than the 260 V obtained without the plasma. This is either due to a fluctuation in the solar simulator or, more probably, a slight loading of the array by leakage through the plasma. As shown in Figure 15, the array floats from slightly positive to predominantly negative. This is the expected distribution due to the higher mobility of electrons, compared to ions. It is interesting to note that the average value of the positive voltage panel is about 10 percent of the overall voltage, which is the assumption usually made in computing power system interactions with plasma environments.

The following empirical approximations for current collection[16] were used to compute the coupling currents:

19. Grier, N. T. (1980) Experimental Results on Plasma Interactions with Large Surfaces at High Voltages, NASA TM-81423.

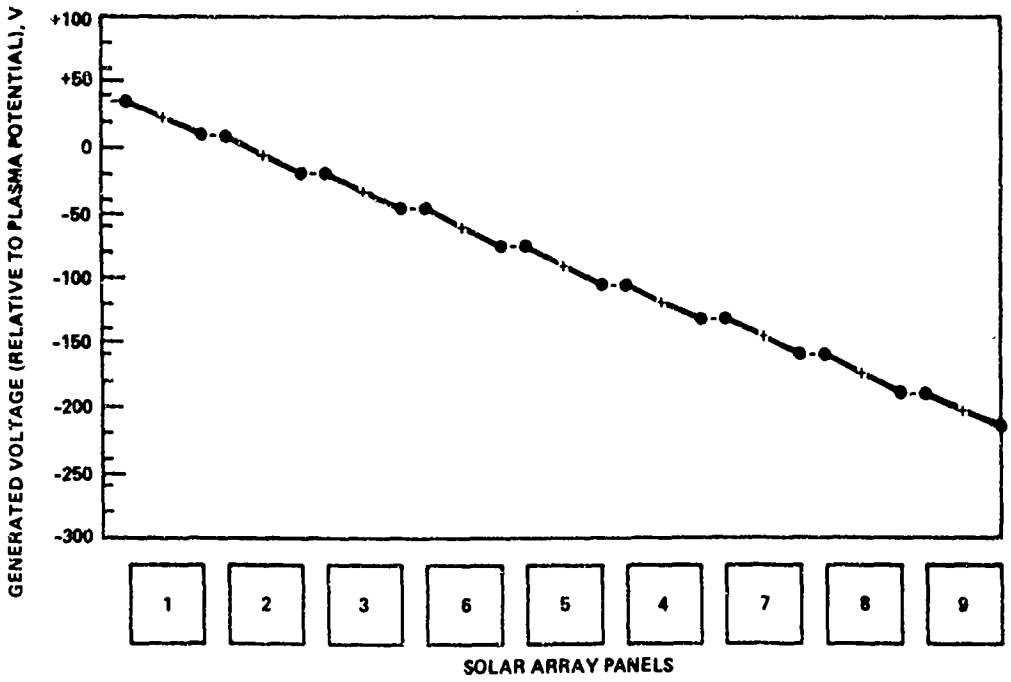

Figure 15. Open Circuit Voltage Distribution of Nine Series-Connected Solar Panel Segments Exposed to a Solar Simulator in a Plasma Environment

$$I_- \propto j_{eo} A_{int} \sqrt{1 + \frac{V+}{E_e}}$$

$$I_+ \propto j_{io} A_{int} \left[1 + \frac{V-}{E_i}\right]$$

where

j_{eo} and j_{io} are the thermal electron and ion current densities (A/cm^2),

A_{int} is the interconnect area (cm^2),

V+ and V- are the positive and negative average panel voltage (volts) (relative to plasma potential), and

E_e and E_i are the electron and ion energies (eV) .

The relationships were iterated until the electron coupling current was approximately equal to the ion current. The results are shown in Figure 16 along with the stated measured values. The agreement is reasonable. The agreement obtained here may be fortuitous in view of the many approximations made. If the behavior of high voltage solar array systems is to be understood, then it is

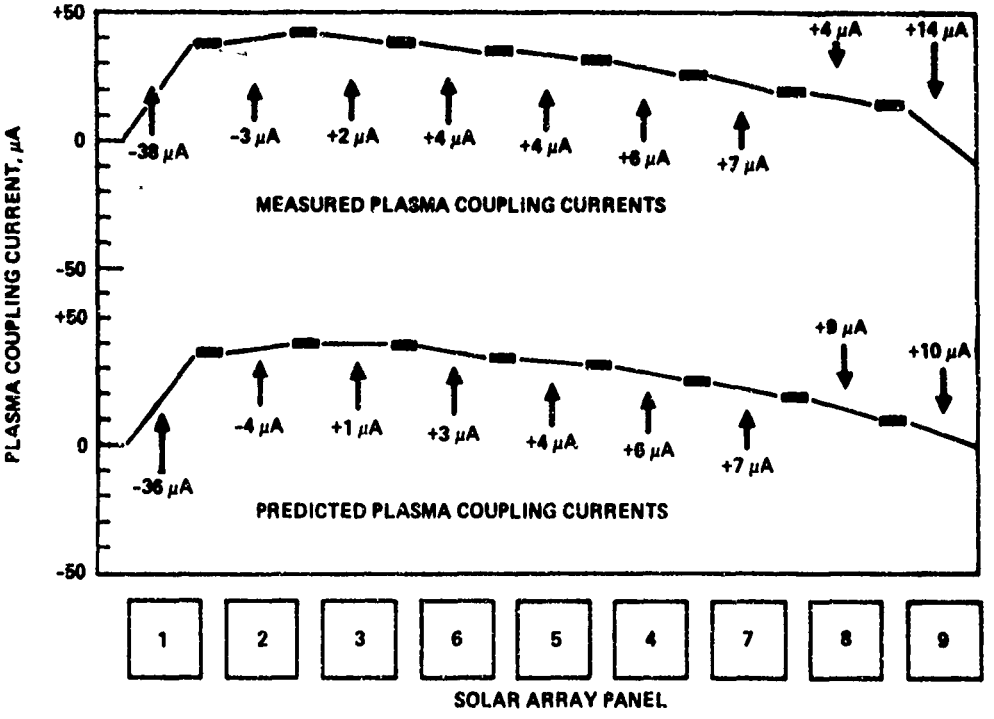

Figure 16. Comparison of Measured and Predicted Plasma Coupling Currents for Nine Series-Connected Solar Panel Segments Exposed to a Solar Simulator in a Plasma Environment

mandatory that a well-conceived, complete set of experiments be conducted. These experiments must include bias voltage tests and self-generated voltage tests with the capability of achieving positive voltages above the snap-over condition. This would answer questions on the negative voltage breakdown phenomena as well.

5. APPLICATION TO SPACE POWER SYSTEMS

To illustrate the impact of plasma interactions on a high voltage large space power system, consider a 100 kw generator, made up of 10 modules of 10 kw each, operating in a 400 km, near-equatorial orbit (see Figure 17). It is assumed that the modules are connected electrically in parallel to avoid a single point failure that could occur with a series connection. Each of the modules is assumed to operate at a load voltage, V_L, and a load current, I_L. The 100 kw power output of the system would then be available to the using system at a voltage, V_L,

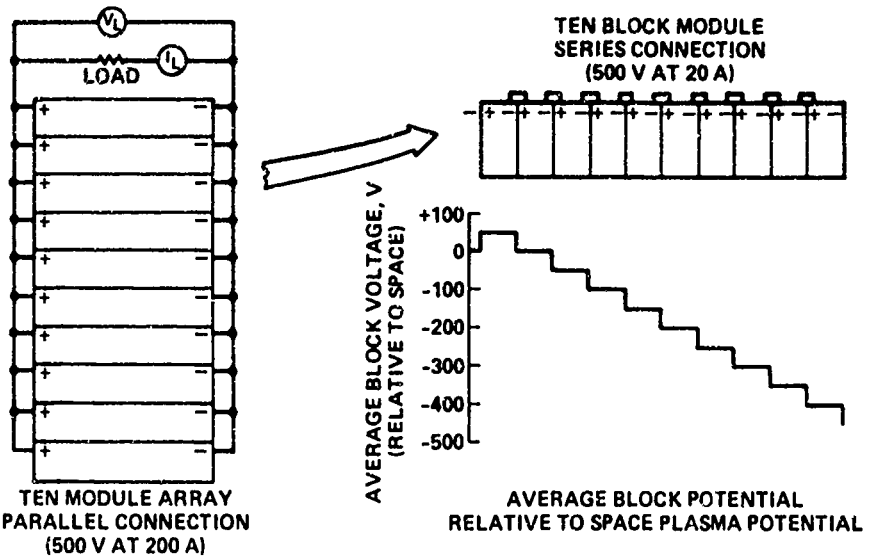

Figure 17. Arrangement of a Model 100 kW Solar Array Space Power System

and current, 10 (I_L). Furthermore, each of the modules is assumed to be built up from ten 1-kW solar array blocks connected in series. Each block would then generate a current I_L at an average voltage of 0.1 (V_L). Relative to the space plasma potential, approximately one block would be at a positive potential while the other nine would be negative (see Figure 17). The plasma environmental parameters for the 400 km orbit are given in Table 1.[18] The implications that could arise from the environment measurements made on the third shuttle flight will be discussed later in this section.

The plasma coupling or drainage current can be computed for the 10 kw module operating at an average load voltage of 500 V and producing a load current of 20 A. Each block would generate 1 kW of power at an average voltage of 50 V. The relationships derived in the previous section are used to compute the positive and negative coupling currents for this module, which is assumed to be typical for the system. The results are summarized in Table 2. These results indicate that the currents do not balance and that another iteration should be made. But the average loss, on the order of 15 mA, represents a possible power loss of about 0.1 percent. This is such a negligible loss that refining the computations is considered to be a waste of time. This is true only when the positive voltage stays below snapover conditions (that is, less than 100 V).

What is of concern is that the blocks that are at negative voltages relative to the space plasma potential approach the breakdown threshold. This can have more serious consequences than the coupling current losses; a block discharging to

Table 1. Environment at 400 km Orbit

Plasma Characteristics:		
	Electrons:	$n_e = 2 \times 10^{11}/m^3$
		$E_e = 0.22$ eV
	Ions (O_{16}^+):	$n_i = 2 \times 10^{11}/m^3$
		$E_i = 0.09$ eV
Spacecraft Orbital Velocity:		77 km/sec
Plasma Current Densities:		
	Isotropic - Electron:	$j_{eo} = 2.4 \times 10^{-3}$ A/m^2
	Ion:	$j_{io} = 9.4 \times 10^{-6}$ A/m^2
	Ram - Ion:	$j_{io} = 2.6 \times 10^{-4}$ A/m^2

Table 2. Summary of Plasma Coupling Currents for a Module

Block No.	Av. Potential (Rel. Space) (V)	Plasma Coupling Current (mA)	
1	+ 50	-10.	-10.4 mA
2	0	- 0.4	
3	- 50	+ 0.6	+20.4 mA
4	-100	+ 1.1	
5	-150	+ 1.7	
6	-200	+ 2.3	
7	-250	+ 2.8	
8	-300	+ 3.4	
9	-350	+ 4.0	
10	-400	+ 4.5	
Assumed Operating Conditions: Module: $V_{op} = 500$ V $I_{op} = 20$ A Block: $V_{op} = 50$ V $I_{op} = 20$ A			

space can disrupt the whole power system output. Based on discharge pictures obtained in ground tests on small, biased solar array segments, [16,18] it appears that the whole segment area is not involved in a given discharge. Hence, it appears that only a finite area of a large solar array could be involved in any single discharge. The location of this finite area within the power system 1 kW block then becomes critical to evaluating the effect of discharges on system performance. If discharges occur in such a location that there are parallel paths within the block that will allow the module to continue to be a power generator, then one could expect a ripple impressed on the dc voltage (see Figure 18). Since the breakdown threshold is not an absolute value and since there are ten modules in this power system, there should be considerable randomness in the breakdowns and the resulting overall ripple.

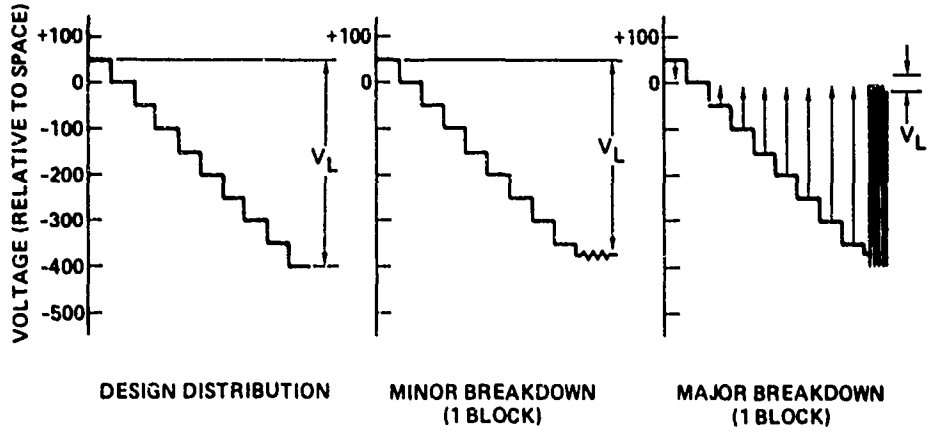

Figure 18. Effects of Discharges or Breakdowns on a Model 100 kW Solar Array Space Power System

The worst case would occur when the discharge occurs in the series portion of the block. If the output of a whole block is involved, then the module output will also have a transient behavior since all blocks are in series. The cycle could be relatively long (on the order of seconds) causing the system output to approach zero volts, temporarily shutting off the array (see Figure 18). The randomness would be caused by the breakdowns in each module and by the, as yet unknown, lifetime influence on breakdown thresholds. In essence this would be analogous to a dead cell in a battery causing the whole module voltage to collapse and then try to build up again. Such a power system would be worthless.

The data obtained on environmental measurements on the third shuttle flight[20,21] compound the difficulties imposed by possible plasma interactions. It has been found that the plasma environment around the shuttle in sunlight is approximately 10 times more dense than previous measurements would indicate, due to photoemission from the surfaces. Furthermore, this dense environment seemed to stay with the shuttle, for at least the 8 days of the mission. If this phenomenon holds true for all altitudes and for extended periods of time, then the plasma surrounding the large power system could also be more dense than previously considered. A factor of 10 increase in plasma density would increase the coupling current losses to about 1 percent, which may still be unimportant. The discharge threshold would be reduced significantly by such an increase and more blocks would be involved in discharge transients. This is a much more serious interaction problem.

The above considerations apply to cases where the environment is assumed to be isotropic. Such conditions do not always exist in low Earth orbits and there can be significant change during the orbit (see Figure 19). At certain times, the active area of the array faces into the orbital velocity direction ("ram"). Under such condition the ion currents are increased (ram velocity is larger than ion thermal velocities), causing the array to float more positive relative to the space plasma potential. This will increase the coupling currents and reduce the discharge tendency. When the active area faces away from the orbital velocity direction ("wake"), there is a deficiency of ions and the system will float more negative, increasing the discharge probability. Finally, the system will enter eclipse each orbit. This eclipse is long enough to allow the array to cool down significantly. Upon re-entry to sunlight, the cold solar array system would generate higher than normal (up to twice) voltage until the temperature returns to normal, enhancing the likelihood of discharge. Unfortunately, the system would be entering the ram condition upon leaving eclipse, so for a short period of time, both power losses and discharges could be a concern.

The conditions described above apply to a large space power system operating in a 400 km, near-equatorial orbit. If the system were placed at a lower altitude (for example, 300 km), then the plasma density would be higher, which would increase the coupling losses and probability of discharge. At a higher altitude, high energy particle damage to solar arrays must be considered. Operating in a polar orbit

20. Banks, P.M., Williamson, P.R., and Raitt, W.J. (1983) Results from the charged particle beam experiments on the space shuttle, AIAA Paper 83-0307.

21. Shawhan, S.D., Anderson, R.R., D'Angelo, N., Frank, L.A., Gurnett, D.A., Murphy, G.B., Owens, H.D., Reasoner, D., Stone, N., Brinton, H., and Fortna, D. (1983) Beam-plasma interactions and orbiter environment measurements with PDP on STS-3, AIAA Paper 83-0308.

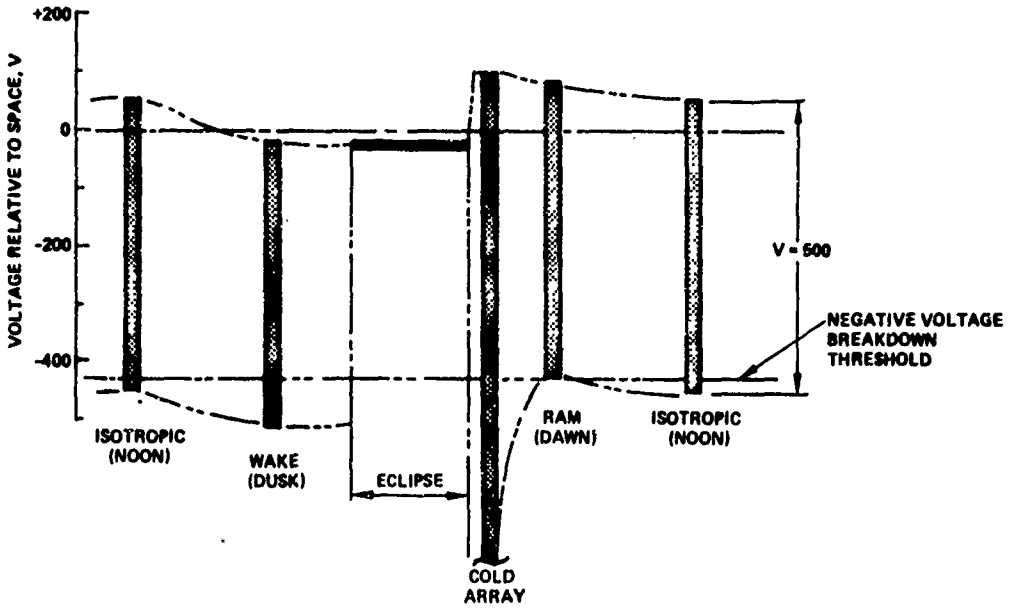

Figure 19. Variation of the Voltage Output of the Model 100 kW Solar Array Space Power System During a Low-Latitude Orbit Revolution

environment brings in a variable plasma environment along with possible auroral electron flux interactions. In spite of all this, a plasma environment is not prohibitive to operations of space power systems, provided the possible interactions are considered and accounted for in system designs. The alternative of lower system design voltage operations is not necessarily safe, nor conducive to power system growth.

To answer a few questions, I will say that there is an add-on Power Extension Package (PEP) solar panel system proposed for the shuttle. The PEP array has been tested by Lockheed and NASA/Johnson in the Johnson Chamber. Some of the data in the Johnson chamber indicate instabilities between 100 and 200 V in their data collection. So, they are being driven down to lower and lower voltages.

I think Johnson's original intention was to operate at something like 50 or 60 V. It's a 25-kW package. They would, of course, love to get it up higher. The solar electric propulsion people were talking about 200-V systems, and that would probably be the highest voltage you can find anywhere.

6. CONCLUDING REMARKS

Future plans for NASA missions call for large space platforms operating in low Earth orbits. These platforms require large space power systems capable of generating up to a few hundred kilowatts of power. At these levels, the operating voltage must be increased above those values commonly used in today's power systems. However, the increased voltage can result in interactions with the space plasma environment that can influence the operating characteristics of the power system.

Tests in ground simulation facilities in which small solar array segments were biased to positive and negative voltages in a plasma environment have shown that interactions can be detrimental. When positive voltages are applied, electron currents can be collected that become proportional to the panel area at voltages greater than +100 V. Under negative bias voltages, arcing, or breakdown, can occur. This arcing threshold depends upon the plasma density and can be as low as -300 V in a simulated 300 km orbit plasma environment. Relatively few tests have been conducted in which an array capable of generating high voltages was operated in a plasma environment under solar simulation conditions. One such test of a nine-block, 13,600 cm^2 array has shown that the array would float electrically such that one block would have an average positive voltage that would be 10 percent of the overall voltage, with the other eight blocks progressively more negative. This test indicated that array behavior could be approximated by considering the interaction with separate blocks at an average voltage.

This approach was applied to a 10 kW array that was considered to be part of a 100 kW space power system operating at 500 V. Ten 10-kW arrays, each in parallel, made up this system. It was found that, under normal quiescent conditions, the power drain due to the electron coupling current would be negligible. However, the arcing in the negative voltage regions could seriously disrupt the system operations by either introducing a ripple on the output or terminating operations depending on the severity and location of the breakdowns. The orbital variations ranging through ram, wake and eclipse conditions generally tend to make the situation worse. Finally, the evidence from early shuttle experiments that indicates that large space structures could create their own plasma environment tends to make plasma interactions even more critical.

For the past 12 years the advantages and disadvantages of large space power system operations at elevated bus design voltages have been argued and discussed. There are obvious advantages to the use of high design voltage in space and the possible hazard of such operations with standard array technology has been demonstrated. These interactions are not insurmountable, but can be overcome

given adequate understanding of the phenomena. What is needed is a systematic investigation to determine why discharges occur and how to prevent them. This would require test programs involving large arrays with self-generated voltages and a flight experiment to prove that all the interactions can be minimized.

References

1. (1976) Outlook for Space, NASA SP-386.
2. Johnson, R.D., and Holbrow, C., Eds. (1977) Space Settlements, A Design Study, NASA SP-413.
3. Bekey, I. (1979) Big COMSATS for big jobs at low user costs, Astron. and Aeron. 17:42-56.
4. Snoddy, W.C. (1981) Space platforms for science and applications, Astron. and Aeron. 19:28-36.
5. Stevens, N. (1979) Interactions between spacecraft and the charged-particle environment, Spacecraft Charging Technology - 1978, NASA CP-2071/ AFGL-TR-79-0082, AD A084626, pp. 268-294.
6. Woosley, A.P., Smith, O.B., and Nassen, H.W. (1974) Skylab technology electrical power system, ASME Paper 74-129.
7. Chen, F.F. (1965) Electric probes, in: Plasma Diagnostic Techniques, R.H. Huddlestone and S. Leonard, Eds. - Pure & Applied Physics, Vol. 21, Academic Press, pp. 113-119.
8. Cole, R.W., Ogawa, H.S., and Sellen, Jr., J.M. (1968) Operation of Solar Cell Arrays in Dilute Streaming Plasmas, NASA CR-72376.
9. Knauer, W., Bayless, J.R., Todd, G.T., and Ward, J.W. (1970) High Voltage Solar Array Study, NASA CR-72675.
10. Herron, B.G., Bayless, J.R., and Worden, J.D. (1972) High voltage solar array technology, AIAA Paper 72-443.
11. Kennerud, K.L. (1974) High Voltage Solar Array Experiments, NASA CR-121280.
12. Stevens, N.J. (1973) Solar Array Experiments on the SPHINX Satellite, NASA TMX-71458.
13. Domitz, S., and Grier, N.T. (1974) The interaction of spacecraft high voltage power systems with the space plasma environment, Power Electronic Specialists Conference, IEEE, N.J., pp. 62-69.

14. Stevens, N.J., Berkopec, F.D., Purvis, C.K., Grier, N.T., and Staskus, J.V. (1978) Investigation of high voltage spacecraft system interactions with plasma environments, AIAA Paper 78-672.

15. McCoy, J.E., and Konradi, A. (1981) Sheath effects observed on a 10-meter high voltage panel in simulated low Earth orbit plasmas, Spacecraft Charging Technology - 1980, NASA CP-2182/AFGL-TR-81-0270, AD A114426.

16. Stevens, N.J. (1981) Review of Biased Solar Array-Plasma Interaction Studies, NASA TM-82693.

17. Grier, N.T., and Stevens, N.J. (1981) Plasma interaction experiment (PIX) satellite results, Spacecraft Charging Technology - 1980, NASA CP-2182/ AFGL-TR-81-0270, AD A114426.

18. Purvis, C.K., Stevens, N.J., and Berkopec, F.D. (1977) Interaction of Large, High Power Systems with Operational Orbit Charged-Particle Environments, NASA TMX-73867.

19. Grier, N.T. (1980) Experimental Results on Plasma Interactions with Large Surfaces at High Voltages, NASA TM-81423.

20. Banks, P.M., Williamson, P.R., and Raitt, W.J. (1983) Results from the charged particle beam experiments on the space shuttle, AIAA Paper 83-0307.

21. Shawhan, S.D., Anderson, R.R., D'Angelo, N., Frank, L.A., Gurnett, D.A., Murphy, G.B., Owens, H.D., Reasoner, D., Stone, N., Brinton, H., and Fortna, D. (1983) Beam-plasma interactions and orbiter environment measurements with PDP on STS-3, AIAA Paper 83-0308.

Contents

5. Space Shuttle Charging Results

by

W. J. Raitt, CASS, UMC 34
Utah State University
Logan, Utah 84322

1. INTRODUCTION

The vehicle charging and potential experiment (VCAP) was accepted by NASA as part of the OSS-1 payload to be flown on a test flight of the space shuttle. The VCAP eventually flew on the third shuttle flight at the end of March, 1982. This shuttle flight, designated STS-3, flew a circular orbit with an inclination of 37°, an altitude of 250 km, and an orbital plane approximately dawn/dusk.

The VCAP experiment consisted of four plasma diagnostic instruments, two of which were duplicated, a fast pulse electron generator (FPEG) and a digital control and interface unit. Thermal plasma measurements to establish vehicle potential and the properties of the thermal plasma environment of the orbiter were made by a spherical retarding potential analyzer (SRPA) and a Langmuir probe for ions and electrons respectively. Return currents to the orbiter were measured by two current probes and vehicle potential changes by two charge probes. The charge and current probes (CCP1 and CCP2) were physically one unit, and two of these units were flown with the greatest spatial separation possible on an ESA shuttle pallet. The FPEG emitted electrons with beam currents of either

50 mA or 100 mA at a beam energy of 1 keV, and a beam divergence of approximately 5°. The instrument was mounted on the port side of the pallet and oriented to emit electrons parallel to the orbiter z-axis (that is, straight out of the bay). An important feature of the FPEG is its ability to switch the electron beam on and off in a time of about 100 nsec resulting in the capability of pulsing the beam from essentially a dc emission to frequencies of hundreds of kilohertz. The DCIU provided an interface to the OSS-1 command and data handling system, and also included three microprocessors to control and monitor instrument behavior. The location of the VCAP units on the shuttle pallet is shown in Figure 1.

The prime objective of the VCAP experiment was to study the electrical charging of the orbiter under conditions of passive orbiting, and under conditions of active charge emission by an electron generator. These measurements were to be made under a wide variety of conditions, such as orientation to the B vector, ram vector, solar direction, varying ambient plasma density, and sunlit/darkness conditions. In order to better understand the mechanisms of vehicle charging, experiments were also made on the interaction of the beam with its environment. Experiments t. measure wave and particle fields around the beam were made in collaboration with the University of Iowa plasma diagnostics package experiment. Visual imaging of the beam was performed using low light TV and optical photography.

2. FLIGHT OPERATIONS

The STS-3 flight was an orbiter test flight primarily designed to study the thermal properties of orbiter systems. Therefore, we had little control of vehicle attitude, an important parameter because of the guiding of the FPEG electrons by the geomagnetic field. Thus, in general, for pitch angles less than about 45° the beam would impact either part of the vehicle or part of the payload, while for smaller pitch angles the beam could escape from the vehicle.

The prime vehicle attitude was nose-sun, which was held for about 80 h. Since the thermal test put no constraint on the other two axes, we were able to have a roll at twice the orbital rate initiated, phased so that the z-axis was parallel to the earth's axis at the ascending and descending nodes of the orbit. This resulted in the minimum pitch angle at all orbital positions consistent with the thermal requirement to maintain the nose of the orbiter pointing towards the sun.

The plasma diagnostic instruments were left on for the entire flight to accumulate passive charging results. The FPEG was activated to perform a 5-min charge and capacitance sequence and a 5-min wave stimulation sequence about 50 times during the flight to accumulate measurements over a wide variety of vehicle

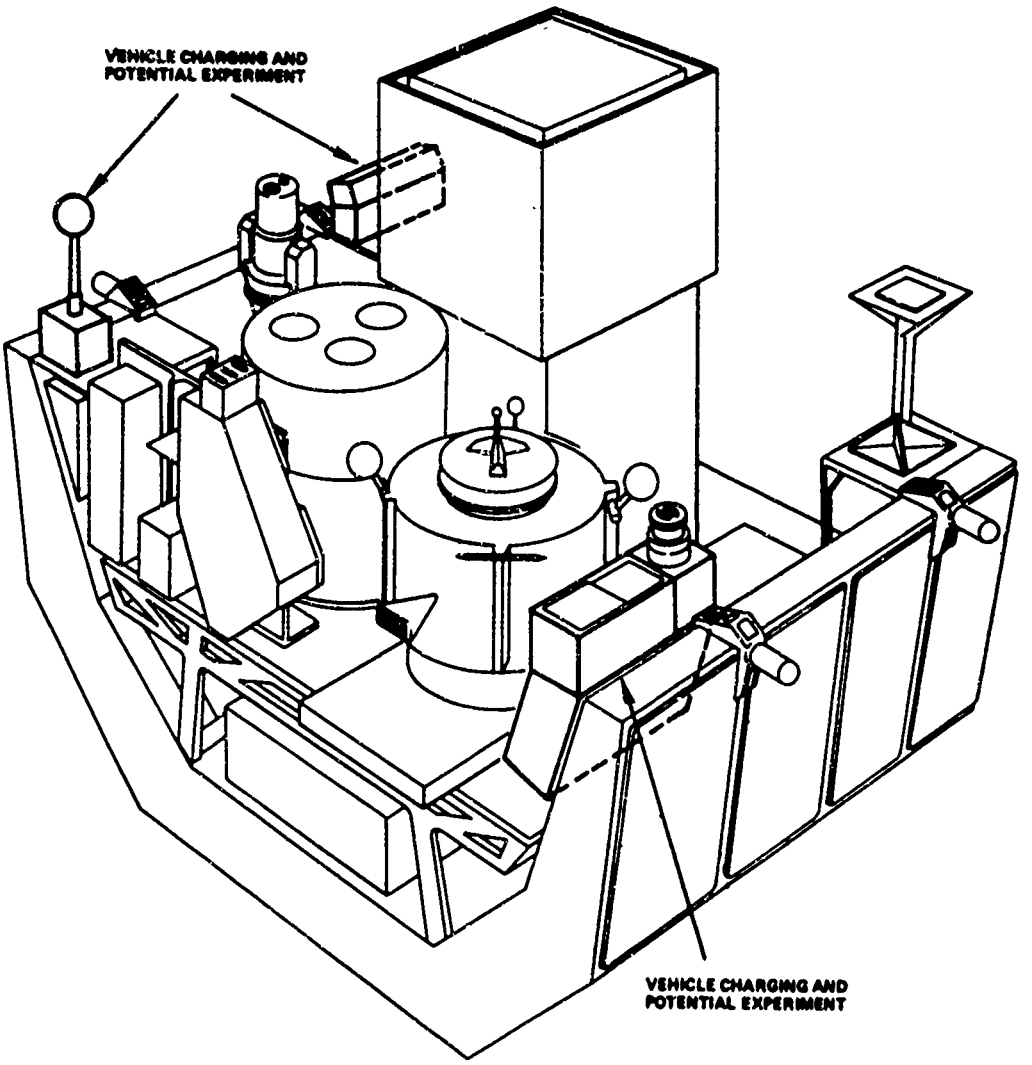

Figure 1. Diagram of OSS-1 Pallet Showing the Locations of VCAP Instruments. The cluster of instruments at the right consists of the FPEG, CCP1 and the Digital Control and Interface Unit. CCP2 is in the far left corner and the SRPA at the left front of the pallet

attitudes and locations. There were four periods when the crew activated the FPEG to provide a stimulus for the PDP beam search activities. In addition to these pre-planned activities, the ground system was sufficiently flexible to enable numerous real-time FPEG activities to be scheduled into the flight operations.

3. PASSIVE CHARGING OBSERVATIONS

It was not clear at which equilibrium voltage relative to the ionosphere the space shuttle would settle because of the large area of the vehicle covered by insulating material and the limited, localized area of conducting surface of the main engine nozzles. Furthermore, the electrical properties of the surfaces of the engine nozzles were indeterminate since the engines had been used to achieve orbit. The localization of the clean area was expected to have an effect on the passive electrical potential through the possibility of the engines being in the wake when the shuttle orbited in "airplane mode" and the generation of electrical potentials between the engines and various parts of the structure through $\underline{V} \times \underline{B}$ induced electric fields.

We have analyzed the variation of vehicle potential for two standard attitudes using the Langmuir probe current-voltage characteristics. In both nose-sun and tail-sun, the vehicle potential at the location of the probe varies between about -1.5 V and -3 V relative to the ambient plasma. In both cases it was not possible to get complete orbital coverage because of deep wake effects seen as the Langmuir probe goes into the wake of parts of the orbiter structure. In addition, nose-sun was a prime time for FPEG operations and measurements were disturbed by electron emission at intervals of the order of one hour. Because the Langmuir probe has a limited sweep range, the potential during passive orbiting could exceed the measured extreme of 3 V negative. However, studies of the probe characteristics show that the difference between the real and measured extreme is not likely to exceed 0.5 V.

In both attitudes we see a regular fluctuation of vehicle potential at the orbital period. This is thought to be due to variation in the electrical potential difference $(\underline{V} \times \underline{B}) \cdot \underline{L}$, where $\underline{L}$ is the vector between the Langmuir probe and the engine nozzles. Calculations of this quantity do show qualitative agreement with the observed measured vehicle potential variations. The variation of the vehicle potential for 3 h of the tail-sun attitude is shown in Figure 2A, and the variation of $(\underline{V} \times \underline{B}) \cdot \underline{L}$ is shown in Figure 2B. Exact agreement is not expected because of the influence of other factors on vehicle potential, such as ram direction, day/night and solar vector direction.

On the STS-3 flight it was not possible to investigate the effect of having the engine nozzles directly in the vehicle wake because of the restricted attitudes available on the flight.

In summary, we do not see excessive excursions of vehicle potential for passive orbiting at latitudes below 37° and 250 km altitude. The $\underline{V} \times \underline{B}$ induced electric field is significant and could cause potential fluctuations as much as

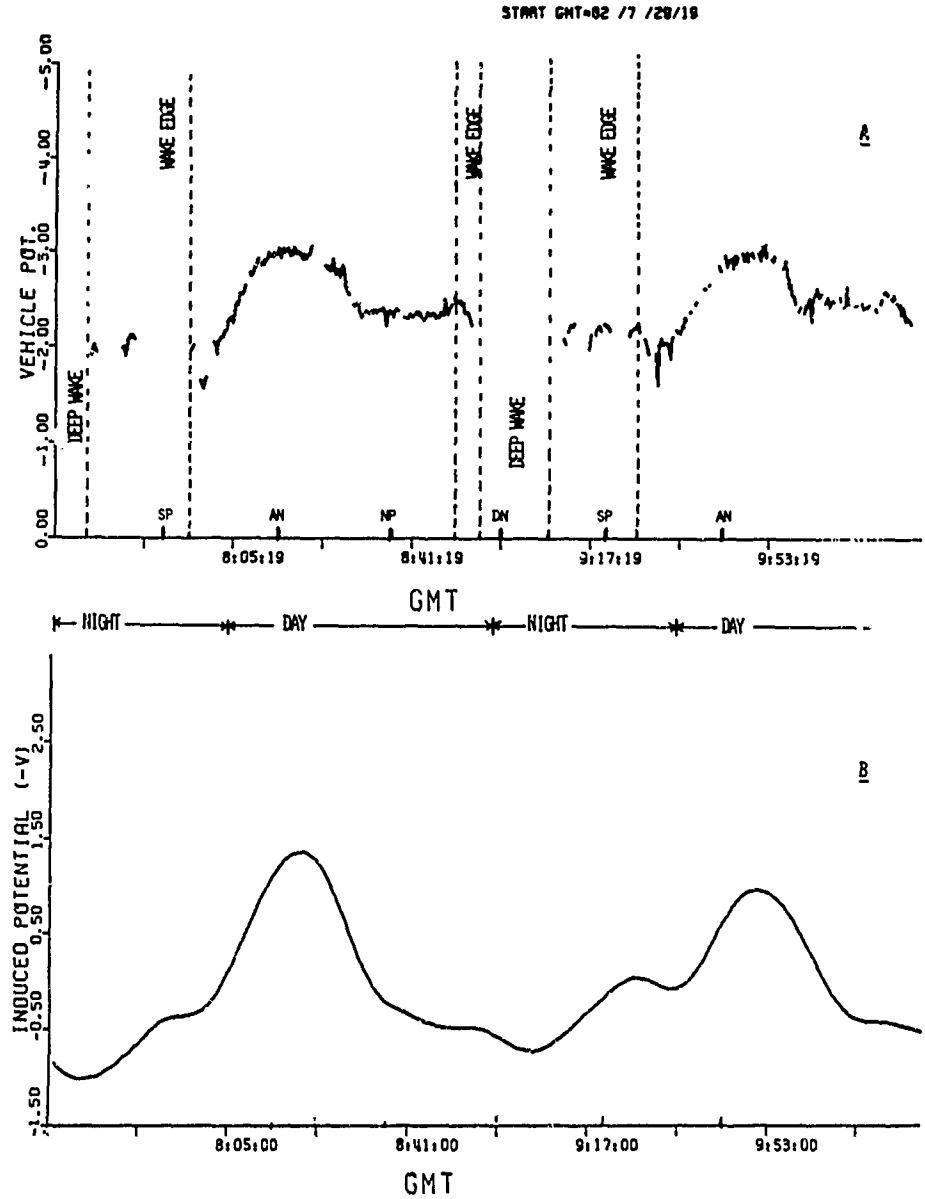

Figure 2. A: Variation of the Vehicle Potential at the Location of the Langmuir Probe During a 3-h Segment of the Tail-Sun Attitude. AN and DN indicate the ascending and descending nodes of the orbit, and NP and SP indicate the north and south points respectively. B: Computed, induced electric potential difference between the location of the Langmuir probe and the engine nozzles due to the motion of the vehicle through the geomagnetic field for the same period as the measurements in the upper panel

± 8 V relative to the engine nozzles and therefore to the ambient plasma, at locations near the forward end of the payload bay.

4. ACTIVE CHARGING OBSERVATIONS

The routine vehicle charging observations were obtained by executing a preprogrammed sequence of FPEG operations which included electron emissions to study both capacitative charging of the shuttle and steady state current balance. This report will only address some observations of the latter effect. The FPEG charge and capacitance sequences were timed to coincide with different orbital conditions, for example, day/night, high latitude/low latitude. Because of our limited control of vehicle attitude, the pitch angle of the electron beam is not always low enough for the beam to escape from the vehicle. The general rule for the nose-sun attitude was that at extreme latitudes in the northern and southern hemispheres, the pitch angle was near 90°, while at low latitudes the pitch angle was generally less than 45°. Since all orbiter roll rates were integrally related to the orbital period, the variation of attitude around the orbit remained the same from orbit to orbit for given primary attitudes.

The steady state charging measurements were obtained from 52-sec beam pulses which formed part of the charge and capacitance sequence referred to earlier. Data have been studied from the charge probes (QD1 and QD2) and the return current probes (CD1 and CD2). Six such data sequences were studied, two near midday, one near midnight, two near dusk, and one near dawn. The dawn and dusk data correspond to low electron beam pitch angles while the midday/midnight data correspond to electron beam pitch angles near 90°.

When the pitch angle is low and the beam can escape from the vehicle there is clearly a large difference in charging between day and night. For a morning case (L. T. = 06:00) shown in Figure 3, the vehicle charges to only about +8 V, while for an evening case (L. T. = 19:10) shown in Figure 4, when it is dark the vehicle charging exceeds the +40 V limit of the high sensitivity range of the charge probe. The signals from the current probes are very sensitive to wake effects. The positions of the orbiter and the ram and geomagnetic field vectors are shown schematically in the figures. The actual pitch (P) and azimuth (A) angles in the coordinate system indicated are also shown on the figures.

In the three cases when the pitch angle was near 90°, and the beam would have hit the vehicle, very little charging is seen during daytime cases; but at night, even under these circumstances, the charge and current probes indicate that the vehicle charges up to about +40 V. The time history of the nighttime charging for 90° pitch angles is quite different; a slow charging is seen with a

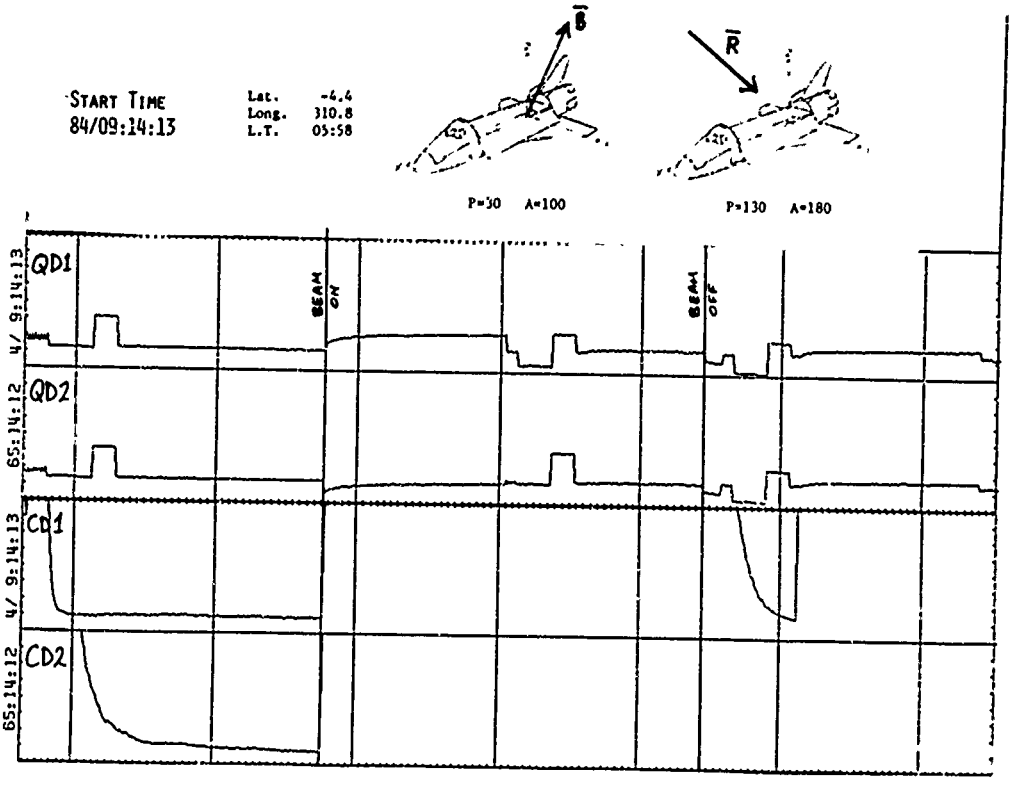

Figure 3. Plots of the CCP1 and CCP2 Outputs for Part of a Charge/Capacitance FPEG Sequence for a Condition of Low Pitch Angle and Sunlit Orbit. The top panel shows sketches of the geomagnetic field (B) and ram (R) vectors relative to the shuttle, the actual pitch and azimuth angles are listed below the sketches. The center panel is a plot of the outputs of charge probes 1 & 2. The scale covers the range of -8V to +40V potential difference across the probe dielectric material. The lower panel shows the output of the return current probes 1 & 2 for the same time as the charge probe data. The duration of the 52-sec beam is shown on the figure. The fluctuation in the charge probe signals after about 26 sec are due to changes in the bias on probes. The start time of the data plots is given in the upper panel as DD/HH:MM:SS GMT. The tic marks on the horizontal axes are at 1-sec intervals

time constant of tens of seconds. It is possible that this results from a charge build-up on part of the vehicle tiled surface or on the charge probe dielectric that are being impacted by the electron beam. These cases are shown in Figures 5, 6, and 7, respectively.

In summary, there is clearly substantial charging of the vehicle at night beyond +40 V when the beam can escape impact with the vehicle. We have not seen a strong ram angle effect on vehicle charging in this data set, however if,

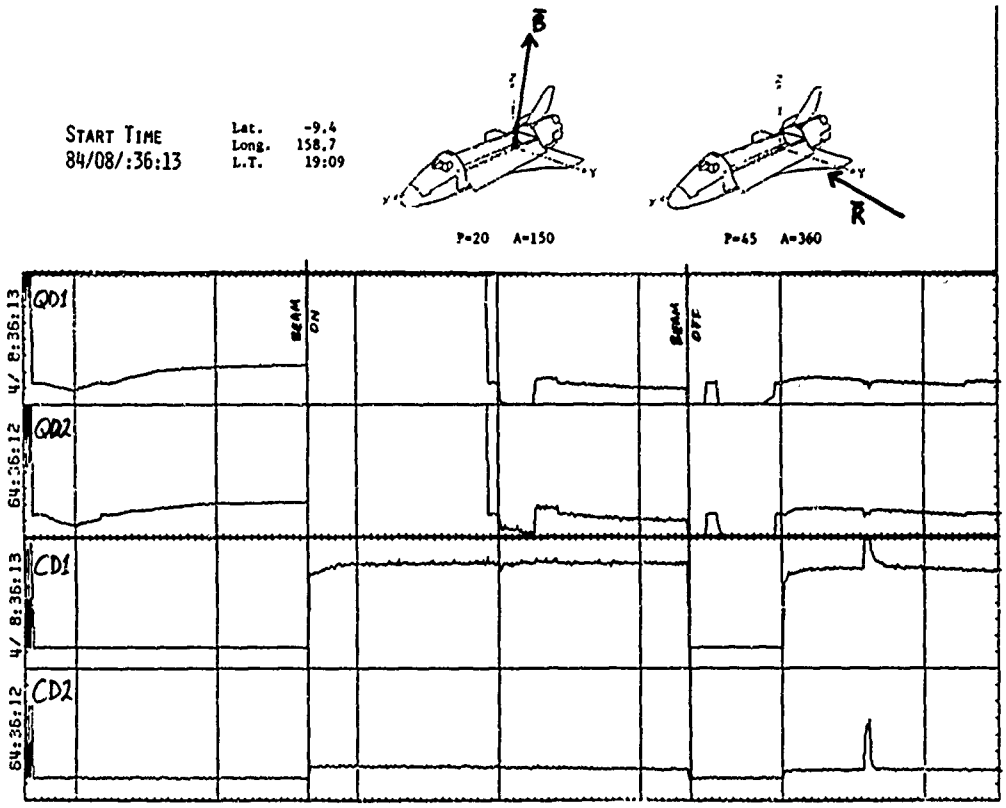

Figure 4. Plots of CCP1 and CCP2 Outputs for Part of a Charge/Capacitance FPEG Sequence for a Condition of Low Pitch Angle and Dark Orbit. The format of the plot is the same as Figure 3

as the passive observations suggest, the engine nozzles collect the return current, we have not yet seen any attitudes to preclude this.

The reasons for the much increased night-time charging are not clear since the ambient ionospheric density does not show more than a factor of 10 change between night and day. There is some evidence from the SRPA data that the orbiter may be generating its own plasma cloud by photo-ionization of outgassing material during the day and disappearing at night when the photo-ionization ceases. The mechanism to cause the plasma to move with the vehicle is not obvious, however, even if the locally generated plasma does not move with the vehicle and is tied to the geomagnetic field lines once it is generated, it could still be collected by the orbiter as it moves through the newly generated plasma. At this stage of the data analysis it is not possible to do more than suggest the possibility of this phenomenon. Further work on the rate of production of local

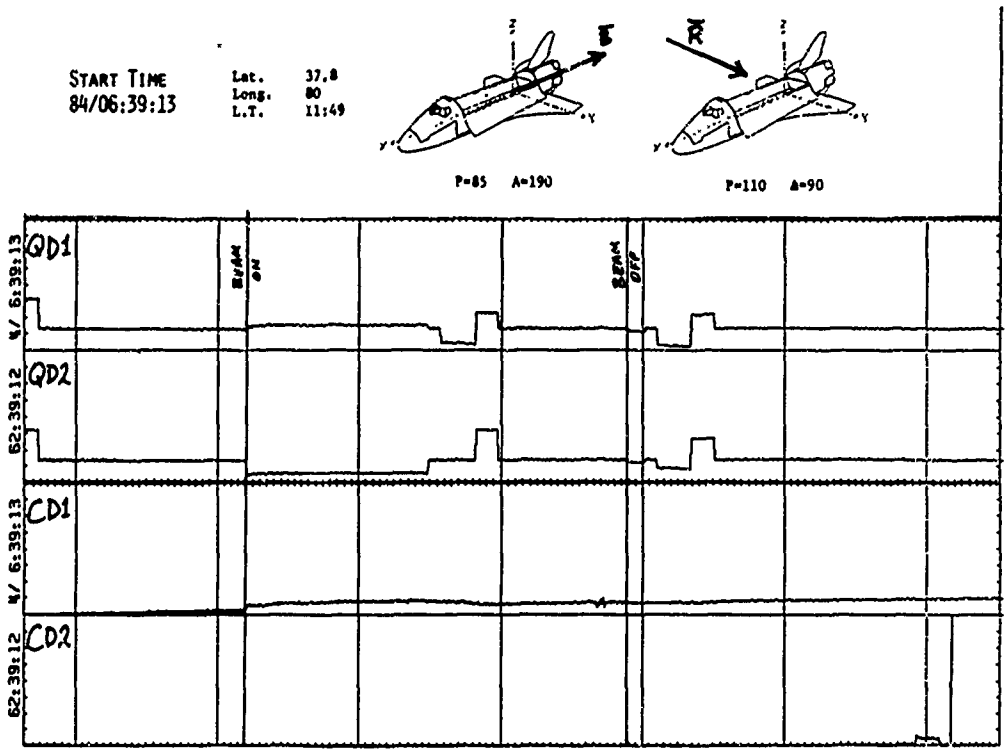

Figure 5. Plots of CCP1 and CCP2 Outputs for Part of Charge/Capacitance FPEG Sequence for a Condition of Near 90° Pitch Angle at Local Noon. The format of the plot is the same as Figure 3

plasma, its dynamic behavior and the interpretation of the SRPA data needs to be done before a more definite statement can be made.

The effects of beam emission are more complex, involving effects of geomagnetic field and ram vector orientation. However, there does seem to be little charging during the daytime when a 100 mA, 1 keV beam is emitted to escape from the vehicle. At night there is generally more charging of the vehicle to electric potentials greater than +40 V relative to the surroundings if it is assumed that the surface of the charge probe does not become charged to a significantly different potential from the ambient plasma.

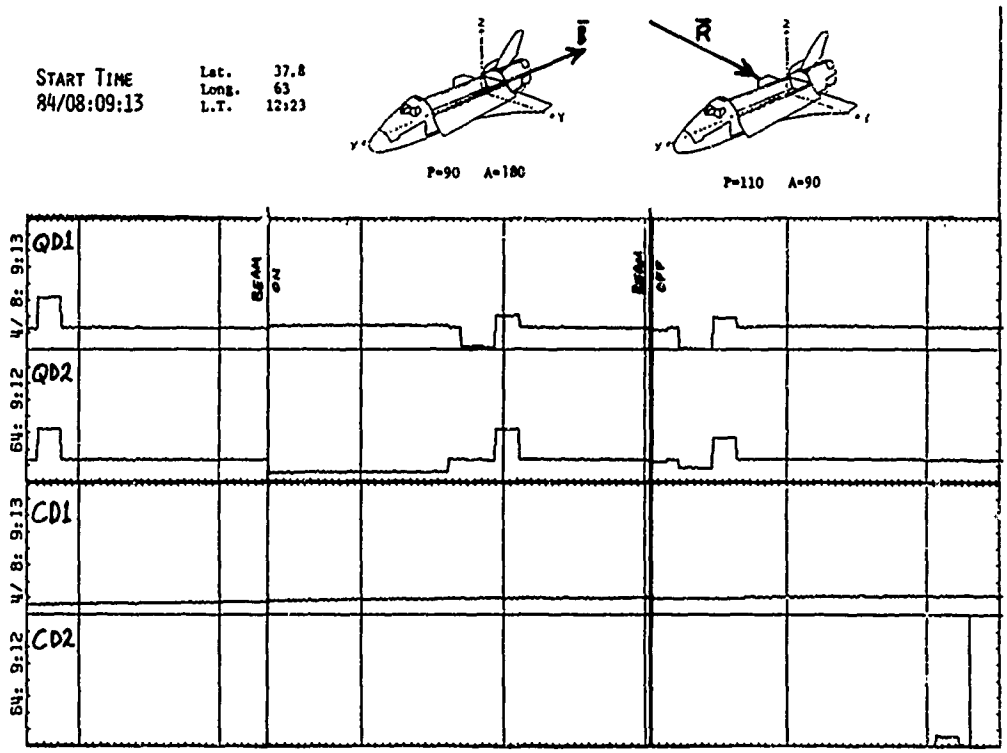

Figure 6. Plots of CCP1 and CCP2 Outputs for Part of a Charge/Capacitance FPEG Sequence for a Condition of Near 90^{O} Pitch Angle at Local Noon Showing a High Degree of Repeatability With the Data Shown in Figure 5. The format of the plot is the same as Figure 3

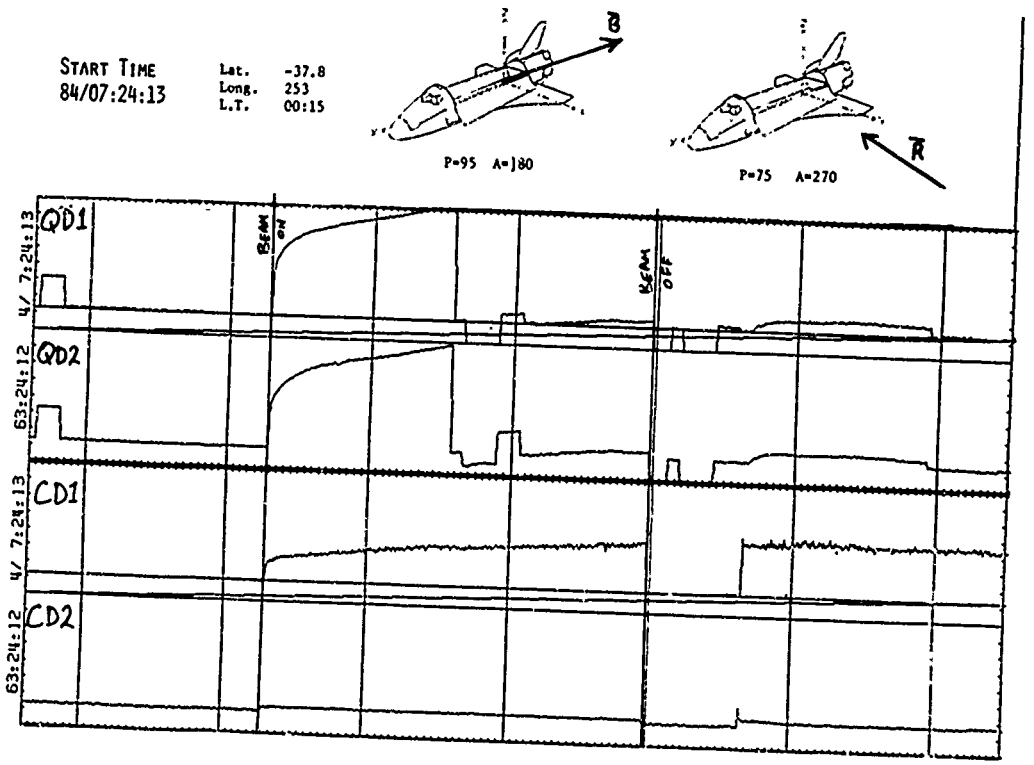

Figure 7. Plots of CCP1 and CCP2 Outputs for Part of a Charge/Capacitance FPEG Sequence for a Condition of Near 90° Pitch Angle and Local Midnight. The format of the plot is the same as Figure 3

5. CONCLUSION

The results in this report represent the analysis of a small amount of the OSS-1/VCAP data available. This limited study has, however, been beneficial in guiding our future studies of vehicle charging and the associated beam-plasma and vehicle plasma environment studies that play an important part in determining the vehicle charge balance. The data so far studied show that for the STS-3 orbit there is no anomalous vehicle charging during passive orbiting, but the effects of $\underline{V} \times \underline{B}$ induced electric fields can be seen.

Acknowledgments

The work described in this report was supported by NASA contract NAS5-24455, Principal Investigator Dr. P. M. Banks. The charge and current probe instrument was developed by Dr. P. R. Williamson. Thanks are also due to Dr. J. J. Sojka for help in reconstructing the vehicle attitude and L. Jensen, C. L. Chidester, and D. E. Siskind for programming assistance in handling the OSS-1 data.

6. STS-3/OSS-1 Plasma Diagnostics Package (PDP) Measurements of Orbiter-Generated $\underline{V} \times \underline{B}$ Potentials and Electrostatic Noise

by

S. D. Shawhan
G. B. Murphy
Department of Physics and Astronomy
The University of Iowa
Iowa City, Iowa 52242

The Plasma Diagnostics Package (PDP) was flown as part of the OSS-1 pallet on the Space Shuttle flight STS-3 in March 1982. During this eight-day mission, the PDP was operated in its pallet position and on the Remote Manipulator System (RMS). PDP measurements included dc electric and magnetic fields; ac magnetic fields to 100 kHz; ac electric fields to 800 MHz and at S-band; energetic ions and electrons from 2.5 eV to 50 keV; total electron flux; the ion mass spectrum, energy distribution, and streaming direction; the electron density and temperature, and the neutral pressure. A detailed list of the measurement parameters is shown in Table 1.

The STS-3 attitude was chosen to meet the thermal flight test objectives. It was discovered that charging characteristics and the intensity of observed electrostatic noise, both of which are discussed below, were Orbiter-attitude dependent. Figure 1 illustrates the approximate geometry of the nose-to-sun twice-orbital rate roll attitude--the condition under which the following observations were made.

Table 1. OSS-1 PDP Instrumentation and Measurements

- Low Energy Proton and Electron Differential Energy Analyzer (LEPEDEA)
  - Nonthermal electron and ion energy spectra and pitch angle distributions for particle energies between 2 eV and 50 keV
- AC Magnetic Wave Search Coil Sensor
  - Magnetic fields with a frequency range of 10 Hz to 30 kHz
- Total Energetic Electron Fluxmeter
  - Electron flux 10^9-10^{14} electrons/cm^2 sec
- AC Electric and Electrostatic Wave Analyzers
  - Electric fields with a frequency range of 10 Hz to 1 GHz
- DC Electrostatic Double Probe With Spherical Sensors
  - Electric fields in one axis from 2 mV/m to 2 V/m
- DC Triaxial Fluxgate Magnetometer
  - Magnetic fields from 12 milligauss to 1.5 gauss
- Langmuir Probe
  - Thermal electron densities between 10^4 and 10^7 cm^{-3}
  - Density irregularities with 10-m to 10-km scale size
- Retarding Potential Analyzer/Differential Velocity Probe
  - Ion number density from 10^2 to 10^7 cm^{-3}
  - Energy distribution function below 16 eV
  - Directed ion velocities up to 15 km/sec
- Ion Mass Spectrometer
  - Mass ranges of 1 to 64 atomic mass units
  - Ion densities from 20 to 2×10^7 ions cm^{-3}
- Pressure Gauge
  - Ambient pressure from 10^{-3} to 10^{-7} torr

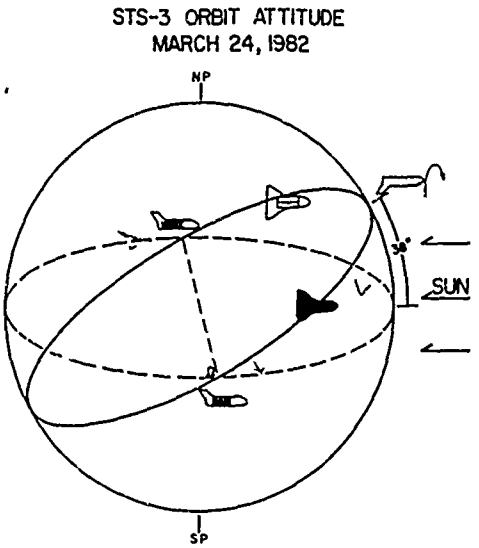

Figure 1. Approximate Geometry of the Nose-to-Sun Roll Attitude

The PDP measured the common-mode potential between two spherical probes mounted on 0.5-m booms and Orbiter ground. This potential difference is consistent with the motional potential $\underline{V} \times \underline{B} \cdot \underline{L}$, where $\underline{L}$ is the distance between the Orbiter conducting engine fairings and the PDP on the pallet or on the RMS. On STS-3, the most positive potential was ~ 4 V near sunset with the PDP in the velocity wake direction; the most negative potential was ~ 3 V near sunrise with the PDP in the velocity ram direction. Figure 2 shows a comparison between this measured potential and a crude $\underline{V} \times \underline{B} \cdot \underline{L}$ model as described in the caption. Firing the 1 kV 100 mA electron gun*, significantly enhances spacecraft positive potential to levels beyond the instrumentation range (> 8V). Preliminary indications are that thruster firings also enhance the Orbiter potential.

Additional measurements indicate, however, that at a time when the PDP electric field sensors may indicate fairly low $\underline{V} \times \underline{B} \cdot \underline{L}$ potentials (close to zero V), the PDP electron energy analyzer indicates a significant flux of 10 to 30 eV electrons. These energized electrons are also orbit-periodic and seem to depend on the Orbiter's attitude. These particle detectors may be the only way of accurately measuring the potential of the Orbiter and its sheath with respect to the ambient plasma.

*The FPEG was designed and built by Dr. John Raitt of Utah State University and Dr. Peter Banks of Stanford University.

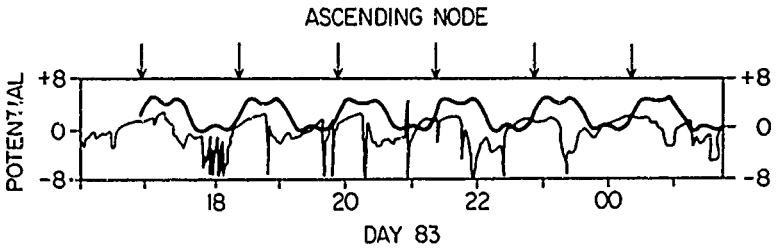

Figure 2. Potential as Measured by the PDP (light line) vs V × B · L Model (heavy line). B is modeled as a simple dipole; V is modeled from the Figure 1 orbit geometry and L is the vector from the SME fairings to the PDP. The model is offset upward by 2 V for easier comparison. Note relative amplitude and periodicity agree well but detailed structure does not. The large excursions in the data can always be associated with FPEG operation or thruster firings

Ac electric fields from 30 Hz to 178 kHz are also observed and vary by ~ 70 dB over an orbit with field strengths up to 0.1 V/m at the spectral peak of ~ 0.3 kHz with the PDP in the velocity ram direction. Figure 3 shows the relevant geometry and samples of the data. At thruster firing periods, the higher frequencies in the 10^3 to 10^5 kHz range are significantly attentuated, whereas the 10^1 to 10^3 range is enhanced; when the payload bay doors were closed, the electric field noise was attentuated to receiver noise levels at all frequencies. It is thought that this electrostatic noise is generated in the Orbiter wake at frequencies near the ion plasma frequency (~ 50 kHz) and below in the ion acoustic mode. The highest frequencies ~ 200 kHz are Doppler-shifted short wavelengths (~ 0.1 m); the lowest frequencies are probably characteristic of several thermal ion Larmor radii (~ tens of meters). In the ram direction, all frequencies can reach the PDP. In the wake orientation, the high frequencies may be attenuated across the wake region so that only the longer wavelength lower frequencies are detected. With thruster firings, the ion density may be significantly lower, which lowers the ion plasma frequency and thus lowers the upper Doppler-shifted frequency. This electrostatic noise generation may cause significant drag on large space structures.

Work in progress includes a detailed look at correlation between short-term potential variations and thruster firings, evaluation of more data from the particle analyzer and correlation of results with the FPEG/VCAP experiment. The PDP will fly again on Spacelab-2 (November 1984 launch) and a number of experiments are being designed to investigate further the phenomena discovered on this mission.

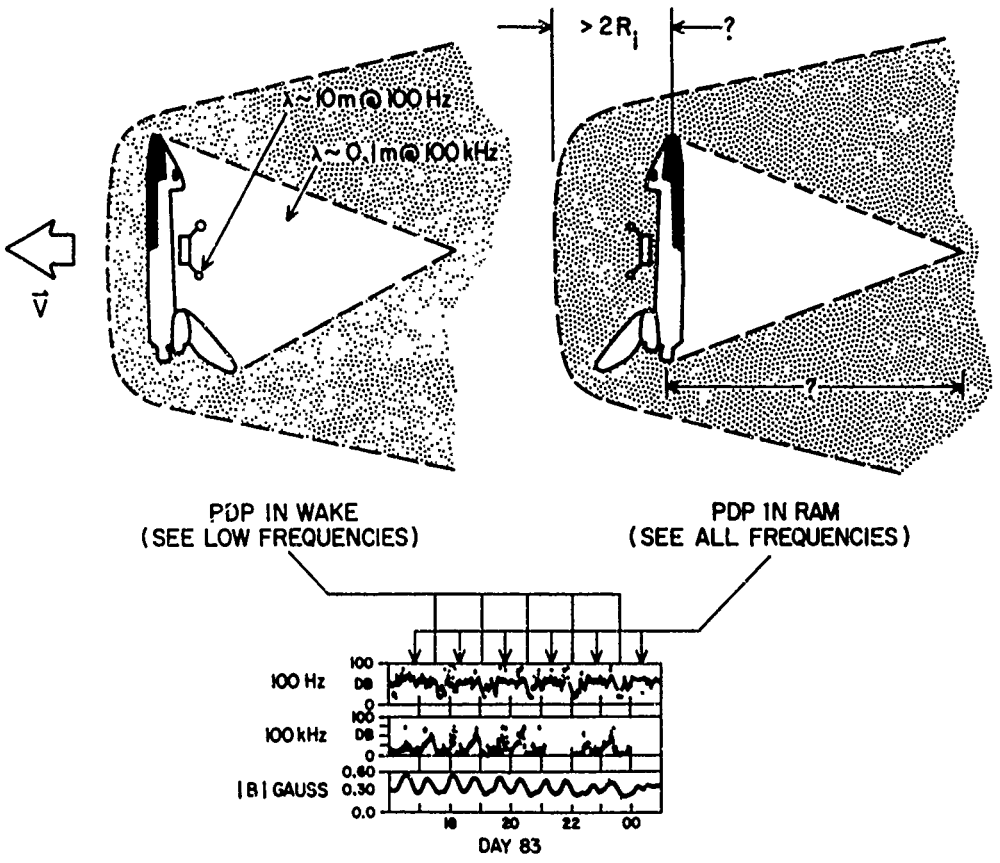

Figure 3. Relevant Plasma Diagnostics Package Geometry and Samples of Data

Acknowledgment

This work was performed under NASA contract with Marshall Space Flight Center NAS8-32807.

Contents

7. Electron Beam Experiments and Other Observations from STS-3

by

P. M. Banks
Space, Telecommunications, and Radioscience Laboratory
Stanford University
Stanford, Calif. 94305

1. INTRODUCTION

The Vehicle Charging and Potential Experiment (VCAP) experiment was one of six major experiments flown on the OSS-1 pallet aboard STS-3 in March, 1982. The VCAP flight objectives were both scientific and technological and included studies of natural electrical charging of the Orbiter, the effects of artificial electron beam emissions on the Orbiter electrical characteristics, and measurements of plasma phenomena. To determine plasma conditions, wave phenomena associated with pulsed and dc electron beam operations, the nature of the plasma environment within the payload bay, the feasibility of making ionospheric measurements from the Orbiter, and the characteristics of vehicle return currents to different parts of the Orbiter were measured.

The results of observations of vehicle charging phenomena are described in greater detail in a paper by Prof. W. J. Raitt. In this paper, we give primary emphasis to the electron beam experiments as deduced from optical observations

made with the aid of onboard photographic and TV cameras. In addition, a few results of measurements from the University of Iowa Plasma Diagnostics Package (PDP) are discussed.

The electron beam experiments aboard STS-3 were made using the VCAP Fast Pulse Electron Generator (FPEG) described in W.J. Raitt's paper. In the course of the STS-3 flight, many different emission sequences were undertaken at a variety of pitch angles and with many different plasma environmental conditions.

For the results discussed here, FPEG was operated by the STS-3 crew (Col. J. Lousma, Col. G. Fullerton) from an aft flight deck control panel. Since maximum electron beam luminosity was desired for the optical observations of beam propagation characteristics, a 100 mA beam current was used in each of four observing sessions undertaken when the vehicle was in total darkness. In these sessions successive 1-min FPEG firings were initiated by the crew. Both black and white and color photographs, as well as TV recordings, were made during each session. Further information about these observations is given in Banks, et al. [1]

Diagnostic information about plasma waves, electron and ion energy spectra, electric fields, ion composition, and vehicle charging was available from the PDP during three of the four optical recording sessions. In two instances the PDP was deployed away from the payload bay using the STS remote manipulator arm. In one case, plasma observations were made with the PDP located in its normal latched position on the OSS-1 pallet in the payload bay.

2. RESULTS

Both photographic and TV recordings of the FPEG electron beam proved successful, even though the atmospheric pressure at flight altitude (240 km) was substantially lower than in laboratory measurements conducted prior to flight with similar instruments. The recordings show that the electron beam exits FPEG as a narrow, bright column with little evidence for beam divergence in the first 0.5 m. Figure 1 shows this beam as detected with an onboard STS-3 low light level TV. In this figure the beam is seen to the right of a triangular S-band antenna that is directly illuminated by the FPEG filament. The trajectory of the beam at this time is directed up and towards the rear of the vehicle with impact upon the rear of the port engine pod. The magnetic field deduced from other

1. Banks, P.M., Williamson, P.R., and Raitt, W.J. (1982) Observations of vehicle glow on STS-3 (submitted to Geophys. Res. Lett.).

Figure 1. View of the FPEG Electron Beam During the Flight of the OSS-1 Pallet on STS-3. Stars and vehicle glow are visible in the background. General illumination in the payload bay arises from the FPEG filament. The bright object next to the beam is an S-band antenna also lit by the filament. The beam itself has a bright vertical core that rapidly diffuses above the height of the antenna

information agrees with this behavior. It is directed almost exactly transverse to the Orbiter in the vehicle horizontal plane.

A different view of the electron beam a few minutes prior to the results of Figure 1 is given in Figure 2, taken from the portside aft TV camera looking towards the cabin. In this case the beam can be seen to a greater distance. The white object seen in the left background is the remote manipulator arm, illuminated by the FPEG filament light.

Two separate electron beam effects are apparent in the two figures. First, bending of the beam occurs as a result of the geomagnetic Lorentz force. Since the Orbiter attitude varied substantially during each observing session, the beam wandered considerably, yielding a variety of results on the PDP and optical records. In fact, in some pitch angle orientations there is clear evidence for the impact of the electron beam on the surfaces of the Orbiter lying aft of the OSS-1 pallet. One series of video images, for example, shows a well-defined intersection of the beam with the Orbiter's vertical stabilizer. As time passes, the direction of the geomagnetic field with respect to the Orbiter changes and the beam-induced luminosity moves across the port side of the vertical stabilizer and eventually impacts the port engine pod. This latter situation is illustrated by

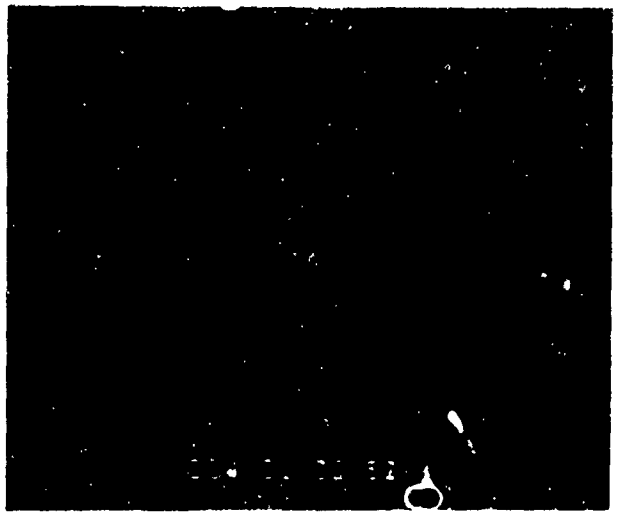

Figure 2. View of the FPEG Electron Beam as Seen From an Aft TV Camera. The S-band antenna is in the foreground, while the vertically erected remote manipulator arm is seen to the left center. The beam trajectory is such as to bring the electrons in a helical path towards the camera. Considerable beam divergence seems to be present, but the location of the camera may overemphasize this effect

Figure 3, taken during a period when the earth's airglow could be seen in the background. At this time the electron beam was bent so that a full impact occurred on the port engine pod, yielding a luminescence that competes in intensity with the previously mentioned vehicle glow. This observation, together with the tail intersection results, leads to the conclusion that the FPEG electron beam is not a simple helix emanating from FPEG, but rather appears to be a cylindrical shell of electrons having a radius approximately equal to the electron gyroradius for the pitch angles involved. Such a behavior implies considerable scattering of the primary electron beam and the presence of a confining electrostatic potential well around the beam volume defined roughly by the circumscribing helical trajectory set by classical single particle motion.

The second important feature of the electron beam images is the extent to which there appears to be extensive divergence. From two different TV camera positions (Figures 1 and 2) it seems that the beam opens out much more rapidly than is accounted for by the 5° intrinsic beam geometry. This may be due to an internal electrostatic effect whereby the electron beam is neutralized by expanding to a larger radius whose size is set by the requirement that the density of beam

Figure 3. General View of the STS-3 Payload Bay at Nighttime. The broad light seen at the lower center and upper right of the figure arises from internal reflection within the spacecraft. The earth's airglow layer at about 100-km altitude is well resolved, as are individual stars. Vehicle glow occurs on the upper portion of the tail, while the FPEG filament illuminates most of the payload bay. The bright light seen on the aft bulkhead and the port engine pod is caused by the FPEG electron beam impacting the vehicle. It is suggested that a similar brightening of the vehicle surface may occur in regions of sufficiently intense auroral precipitation

electrons be equal to or less than the ambient ion density. Since the ion density at night is low, we expect that substantial beam expansion may be present. In addition, since the ambient density of ions in the payload bay is very sensitive to the vehicle ram angle, it is possible that the beam spreading may depend upon the vehicle attitude. Studies of this effect will be undertaken in the near future.

Studies of the TV images reveals no variations or fluctuations within the electron beam within the time scale set by the individual 30-Hz TV framing rate. During one session a water dump took place, and there was an expectation that the beam image would be intensified or show some features associated with ice crystals. Examination of the TV data at this time, however, shows no particular effects which can be connected to this event.

Observations of plasma phenomena during the dc electron beam operations show many different effects similar to those seen in laboratory experiments. Of

particular interest is the effect electron beam impact on the Orbiter surfaces has upon the PDP measurements of the electron and ion energy spectra. At times when no impact occurs and the beam propagates away from the vehicle, the PDP sees a full electron energy spectrum extending from low energies up to the FPEG maximum energy of 1 keV. In addition, there is a characteristic energization of ions, giving a substantial flux of ions with energies extending from 5 to 25 eV. Intense electrostatic waves are also measured at the same time.

When the beam impacts the vehicle surfaces, substantial distortion of the electron energy spectrum is noted and the hot ions go away altogether. This result indicates that the energization of the ions is a sensitive feature of the beam formation and may be associated with the beam structure.

Other features of interest in the TV and photographic images include the frequent firing of Reaction Control System (RCS) jets and the glow of vehicle surfaces originating from an unknown vehicle-surface interaction. The RCS events appear as the rapid expansion of a glowing cloud emanating from the jets involved. From PDP and VCAP measurements, it appears that such clouds are associated with vehicle charging of a limited scale. Such results imply the presence of RCS-associated plasma clouds enveloping the vehicle for periods of several seconds.

The vehicle glow observations give an interesting, and perhaps important, clue to the way atomic oxygen atoms of the thermosphere interact with a rapidly moving space vehicle. Based on measurements, it appears that the source lies in molecular emission from one or more species originating in interaction of the atmospheric gas with the surface materials of the Orbiter. The excited molecules emanating from the windward surface have a typical decay time of several milliseconds. If this gas flow is related to the flux of impinging atmospheric gas, its density will be substantially enhanced through accommodation at the vehicle surface and subsequent re-emission at a temperature much lower than that of the thermosphere.

As a final note, the TV observations show that the electron beam was able to create a broadband optical luminosity on the surface of the Orbiter. Based upon our knowledge of the FPEG beam current and the surface area over which it had spread by the time it reached the Orbiter surfaces, it appears possible that the vehicle may exhibit an appreciable luminosity within regions of auroral precipitation. In a particular sense, Orbiter surfaces offer a new type of viewing screen for auroral particles. It is not known whether this means of detecting energetic particles might provide useful scientific information about small scale-features in auroras.

3. FUTURE MEASUREMENTS

Both the VCAP and PDP experiments are scheduled to be flown aboard Spacelab-2 in early 1985. Many of the experiments first tried on STS-3 will be repeated to gather data in a new regime of environmental conditions. In addition, because Spacelab-2 will have a higher orbital inclination, it will be possible to obtain information about the effects of auroral particles upon the potential and return currents of the Orbiter. In addition, active electron emissions will be undertaken with the FPEG to assess the extent to which the combination of electron impact from natural sources can be modified by active electron emission from the payload bay to achieve electrical control of the vehicle potential.

Another interesting feature of Spacelab-2 will be the release of the PDP. During this time, special FPEG sequences will be used to assess the characteristics of the electron beam to greater distances from the Orbiter than was possible using the RMS on STS-3. It is expected that both electrostatic and electromagnetic waves will be observed, perhaps providing a measure of the extent to which pulsed electron beams can generate VLF radio waves in the ionosphere.

Acknowledgments

This work was supported by the National Aeronautics and Space Administration under Contract NAS 24455 from Goddard Space Flight Center. The extensive efforts of the VCAP project team, both at Utah State University and Stanford University, are gratefully acknowledged.

8. Floating Potentials and the Hot Plasma Generated by an Electron-Beam-Emitting Rocket in the Ionosphere

by

J. R. Winckler
School of Physics and Astronomy
University of Minnesota
Minneapolis, Minn. 55455

This paper summarizes some recent experimental results concerning the potentials of a large vehicle emitting a powerful electron beam in the ionosphere. Many such experiments have been conducted in the last decade (see Winckler[1]) and these experiments indicate that if a constant electron beam is emitted in the ionosphere from a large rocket or other space vehicle, a return current may be drawn from the ionospheric plasma that will stabilize the potential of the vehicle in the range of a few tens of volts to perhaps several hundred volts. Ejecting an electron beam of for example, tens of kilovolts and tenths of an ampere of current, creates a very hot plasma medium near the vehicle, in which electron current may be drawn freely transverse to the magnetic field as well as parallel to the magnetic field. It is known that part of this current flows directly to the rocket body from the very hot turbulent plasma around the rocket and that part of the current flows from the region around the beam itself as the beam passes out away from the rocket and creates another very hot plasma region. Positive potentials

1. Winckler, J.R. (1980) The application of artificial electron beams to magnetospheric research, Rev. Geophys. Space Phys. 18:659-682.

are difficult to measure, and retarding potential analyzers, electron energy spectrometers, and other devices have not so far given convincing values for the positive excursions of the vehicle during beam ejection. The figures quoted above are estimates but it seems that very high potentials are not achieved even with very large currents. The above comments refer to the E and F regions of the ionosphere. For vehicles at considerably higher altitudes the situation may be quite different, but there is very little experience there with the potentials of vehicles ejecting electron beams. It would seem that the best way to measure vehicle potentials in the positive range while ejecting electron beams would be with a tethered probe anchored in a distant region away from the vehicle where the medium is undisturbed. Such experiments are in progress but the results are not yet available.

In a recent paper, Arnoldy and Winckler[2] examined the potentials of a large rocket emitting a 40 kV electron beam at approximately 0.1 A during the period just following the turn-off of the electron gun. This situation is particularly interesting for the problems of the floating potentials of large passive vehicles because it illustrates the extremes that may be encountered if the vehicle is immersed in a very hot plasma medium. The Arnoldy and Winckler results apply to the Echo 3 experiment conducted in April 1974 but are generally applicable to other similar experiments. The detailed analysis given in the above paper will be summarized briefly here. During the Echo 3 experiment, observations were made with an energy spectrometer of the positive ions normally present in the ionosphere. Typical spectra are shown in Figure 1. In the upper panel before the gun pulse the ion spectrum shows an approximate Maxwellian form with a sharp lower limit of about 1 V, which reflects the normal negative 1-V floating potential of the passive vehicle. The example shown in the upper panel is of particular interest because during the energy sweep that passes in time from left to right a short gun pulse occurred. Following the gun pulse the ion Maxwellian spectrum was observed with a lower limit at approximately 4 V showing that the floating potential of the vehicle had quickly dropped to a larger negative value. After a short time as shown in the lower panel the Maxwellian spectrum returned to its pre-gun pulse condition with a minimum energy of about 1 eV corresponding to the normal floating potential of the vehicle. These negative vehicle potentials can be well measured by observing the spectrum of positive ions during rocket flights in the ionosphere. This has been clearly demonstrated also by experiments at synchronous orbit (DeForest[3]). The Echo 3 result is well

2. Arnoldy, R.L., and Winckler, J.R. (1981) The hot plasma environment and floating potentials of an electron-beam-emitting rocket in the ionosphere, J. Geophys. Res. 86:575.

3. DeForest, S.E. (1972) Spacecraft charging at synchronous orbit, J. Geophys. Res. 77:651.

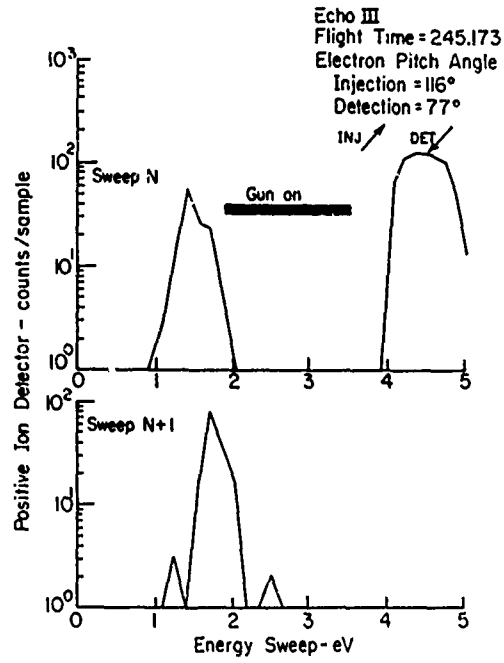

Figure 1. Atmospheric Ion Spectra in the Ionosphere (T ~ 1400°K). Upper panel, left, normal; right, shifted Maxwellian after end of gun pulse. Lower panel, normal, after recovery

documented because the spectrum of the hot plasma electrons was carefully measured with energy analyzers with the results shown in Figure 2. The spectra are measured during an after short gun pulses, and we see that during a gun pulse an intense hot spectrum exists near the vehicle. The spectrum decays away with a time constant of about 50 msec due in part to the motion of the rocket away from the disturbed region and due also to the cooling of the plasma following gun turn-off. As discussed by Arnoldy and Winckler the spectrum shown for the hot electrons during pulsing can easily provide the required total return current to the rocket skin of about 0.1 A. An interesting fact is that in a few milliseconds after gun turn-off the spectrum dropped very little, which means that the flux reaching the rocket skin was still approximately the same as during beam emission, namely about 0.1 A. This means then that the rocket potential will be driven negative rapidly and that the incident current must have been balanced by an electron secondary emission caused by the bombardment of the rocket skin with the hot thermal spectrum.

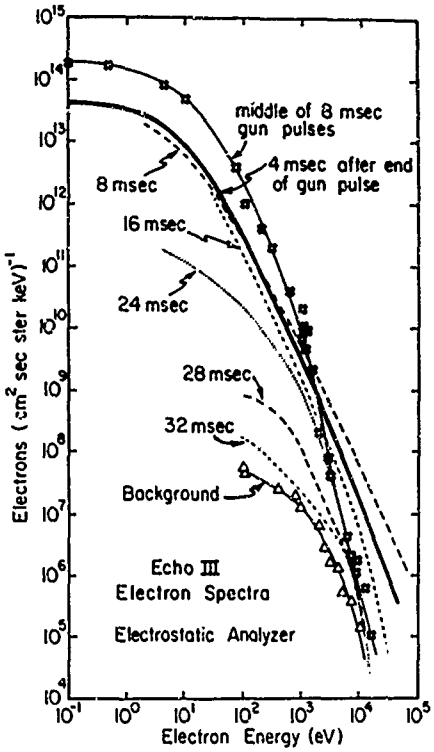

Figure 2. The Hot Plasma Electron Spectra During and After Gun Pulse Injection

A time history of the floating potential of the vehicle is shown in Figure 3. We see the large positive excursion during the gun pulse and at gun turn-off the payload potential snaps quickly negative and then recovers to its normal floating value of about 1 V negative. These results were all obtained with the thermal ion spectrometer. An interesting effect occurs at about 10 msec after gun turn-off provided the electron beam is ejected downward towards the atmosphere. In this case the electron beam mirrors and scatters and a large intensity is reflected back up, passes by the rocket and again produces a temporary heating of the plasma, which again drives the vehicle potential negative. It is interesting to speculate as to the mechanism by which the plasma is heated. This may be due to an inherent collective plasma process such as a beam plasma interaction in the primary beam or in the return electron current to the vehicle payload. Thus it is quite surprising that the primary beam after passing downward to the atmosphere and returning from a distance of perhaps 150 km, still has high enough energy density to produce a hot plasma by collective processes. An alternative

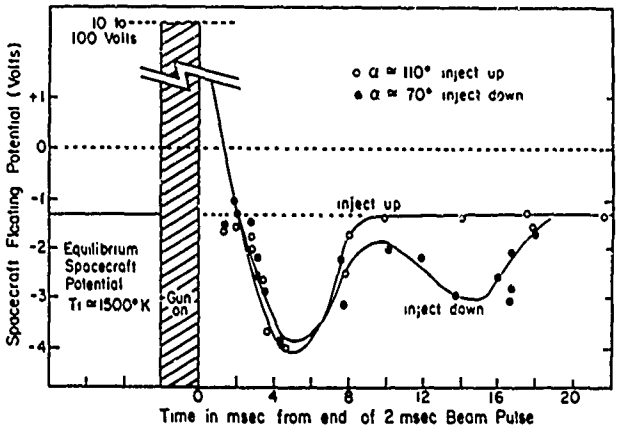

Figure 3. Floating Potentials of the Echo 3 Rocket Following Beam Cut-off, Derived From Positive Ion Measurements. Note the "quick echo" effect for downward injections

is that the plasma may be heated by collisions. This process may well contribute at lower altitudes. Nevertheless, the sensitivity of the rocket negative potential to the presence of fluxes of high energy electrons is clearly demonstrated by these experiments and confirms the experiences at large distances, for example at synchronous orbit, where during magnetic substorm activity and during satellite eclipse negative potentials of up to 10 kV have been observed.[3]

In the recent Echo 5 experiment very powerful beams of up to 40 keV energy and 0.8 A of electron current were emitted into the ionosphere in the altitude range of 150 to 250 km. Again it was found that these very large currents were successfully neutralized by an equally large return current drawn from the ionosphere, accompanied by a very large plasma heating. The plasma heating is always accompanied by the emission of characteristic atmospheric spectral lines particularly close to the skin of the rocket and to a lesser extent in the region of the beam as it spirals away from the payload. Many of the results of Echo 5 confirm the findings with Echo 3. In Figure 4 we show the altitude dependence of the electron intensity at two discrete energies, namely 0.5 keV characteristic of the hot plasma and 8 keV characteristic perhaps of beam electrons degraded and scattered back into the detector systems. The Echo 5 results in Figure 4 show that the altitude dependence of these two components is completely different. The 8 keV electrons decrease with increasing altitude and the intensity finally levels above 150 km, an effect which is almost certainly due simply to scattering by the atmosphere. The leveling at 150 km is a result of the emission of gases for the attitude control system, leakage and other sources.

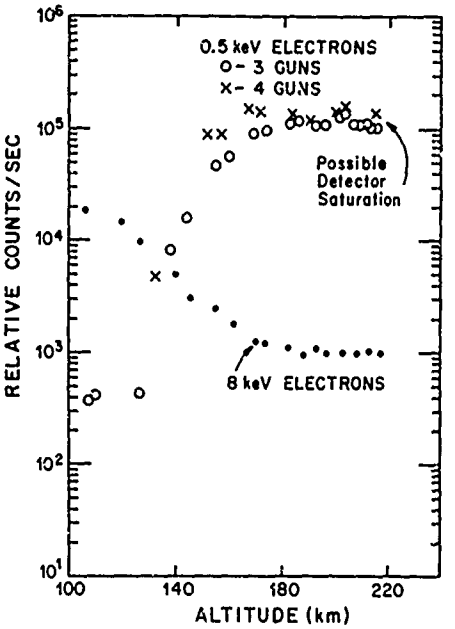

Figure 4. Altitude Dependence of Two Components of the Very Hot Plasma Surrounding the Echo 5 Rocket. The 8 keV electron flux decreases with decreasing density, and is probably scattered and degraded beam particles. The 0.5 keV electrons increase with decreasing density as if due to a collective process in the hot plasma

On the other hand the 0.5 keV hot plasma electrons actually increase their flux with altitude very markedly. The detectors saturate at the indicated plateau value because of the very large beam currents that were used on Echo 5. It appears that this component of the plasma electrons may well be due to a beam plasma interaction and that these electrons are generated by a collective process, for example, by fluctuating electric fields near the rocket or in the beam region which create enough potential drops to accelerate the ambient electrons to further ionize the medium and to produce a kind of cascade or discharge. Another surprise with the Echo 5 experiment was the finding of positive ions accelerated during gun pulsing as shown in Figure 5. Prior to the ejection one sees the usual spectrum of thermal ions that falls off very rapidly in the neighborhood of 10 eV and has a shape characteristic of the normal ionospheric oxygen and nitrogen positive ions. During gun pulsing however, a new high energy component appears with a maximum in the spectrum near 1 keV and furthermore an enhanced

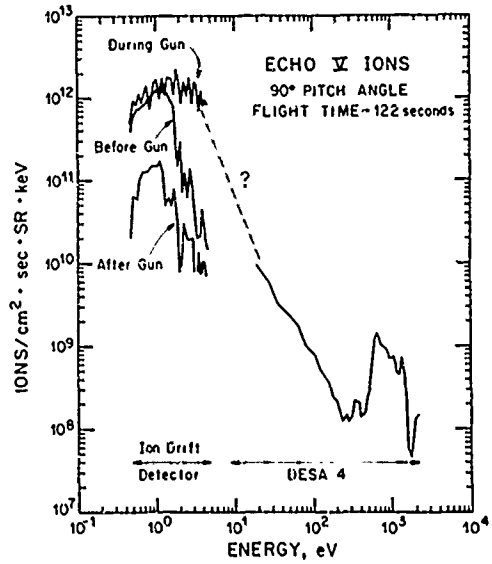

Figure 5. Ion Spectra Before, During and After Gun Pulsing. These ions give evidence for negative rocket potentials of up to 1 kV, and also of atmospheric ion depletion by the large residual positive charge following gun turn-off

intensity in the electron volt range near the thermal energy: Just after gun turn-off the thermal ion flux drops to a very low value, much lower than normal, and then slowly recovers in a time of several seconds as the rocket drifts through the ionosphe.:. An investigation is under way to determine the acceleration mechanism for these positive ions during gun pulsing when the vehicle potential is nominally positive. The answer seems to be that in the Echo series the gun is really not a dc gun but is pulsed by the relatively unfiltered output of the dc-dc converter system. The power drive is a 500-Hz system, which when rectified, gives a 1-kHz quasi-square wave with a finite rise time and a faster but finite decay time. Thus, there is a substantial off time in the interstitial region between each 1-msec pulse. The presence of kilovolt ions during beam ejection may mean that during these brief periods between gun pulses of perhaps 0.1 msec duration the payload potential is quickly driven negative by the very hot plasma surrounding it and the ambient ions are accelerated to the payload in a relatively tight sheath region of perhaps 1 m in extent. The negative potential of the vehicle probably corresponds to the peak in the spectrum seen around 1 kV in Figure 5 but the ion spectrum also includes a very large thermal flux and behaves in this sense analogous to the electron thermal flux during beam injection when the payload

potential is positive. One is impressed by the rapidity with which changes in payload potential can occur and one supposes that the plasma frequency represents the upper limit to the speed of change with due consideration to the free space capacity of the vehicle structure. This may make large changes like those encountered on Echo 5 of perhaps a kilovolt possible in some tens of microseconds.

The Echo 5 experiment, which was launched into the polar ionosphere in November 1979, ejected currents of up to 0.8 A. Thus, a 1-sec gun pulse sent up to 4/5 C of charge off to infinity in the electron beam. Given the charge density of the ionosphere, this is a huge amount of charge to accommodate. It is not at all clear how the ionosphere becomes neutral again. The large decrease in thermal ion content shown in Figure 5 just after gun pulsing may reflect the effect of the positive charge contained in a large volume of the ionosphere resulting from the charge carried away by the beam. Positive ions may be repelled both transversely and along the field line with the result observed as a drop in flux. It is not known why the thermal ion flux drops to such a low level and yet maintains its spectral shape more or less at the thermal value of a few electron volts. It may simply be in accord with thermalizing processes that prevail during the beam ejection and the charge neutralization processes in the ionosphere.

Acknowledgments

This work has been supported by the National Aeronautics and Space Administration under Grant NSG 5088 to the University of Minnesota.

The plasma results from the Echo 5 experiment result from the Arnoldy measurements (U. of New Hampshire) and will be reported in detail at a later date.

References

1. Winckler, J.R. (1980) The application of artificial electron beams to magnetospheric research, Rev. Geophys. Space Phys. 18:659-682.
2. Arnoldy, R.L., and Winckler, J.R. (1981) The hot plasma environment and floating potentials of an electron-beam-emitting rocket in the ionosphere, J. Geophys. Res. 86:575.
3. DeForest, S.E. (1972) Spacecraft charging at synchronous orbit, J. Geophys. Res. 77:651.

Contents

9. The Worst Case Charging Environment

by

D. A. Hardy
Air Force Geophysics Laboratory
Hanscom AFB, Mass. 01731

Whether a spacecraft will charge in the auroral zone is crucially dependent on the magnitude of the current to the spacecraft from the precipitating and backscattered electrons and on how that current is distributed over the electron spectrum. To provide theorists and modelers with some initial inputs on this aspect of the spacecraft charging problem a survey was conducted to find examples of electron precipitation where the total integral number flux over the electron spectrum exceeded 10^{10} electrons/cm^2 sec sr and the average energy of the electrons was approximately equal to or exceeded 1 keV. The data surveyed were from the zenith looking cylindrical electrostatic analyzer flown on board the F2 satellite of the Defense Meteorological Satellite Program. The detector measures the flux of electrons in 16 energy channels spanning the energy range from ~ 50 eV to 20,000 eV once per second. The detector was used by the Air Weather Service as a monitor of the location of the equatorward boundary of auroral electron precipitation. As such, the detector was operated almost continuously. The data were surveyed for all passes of the satellite between September 1977 and December 1978. This comprises approximately 10,000 passes over the auroral zone. From these passes spectra were chosen for three passes to give worst

case examples. In the following sections an overview of each of the three passes is given followed by a description of the spectra taken from each pass.

I. DAY 263, 1977 01:54 TO 02:19 UT

Figure 1 shows an overview of the south pole auroral pass between 01:54 and 02:19 UT on day 263, 1977. In the figure plotted from top to bottom are the average energy in keV, the integral energy flux over the 16 channels of the detector in units of keV/cm^2 sec sr and the integral number flux in units of electrons/cm^2 sec sr. The bottom of the figure is annotated at 2-min intervals with the universal time in seconds and the geographic, geomagnetic, and magnetic local time coordinates of the satellite all mapped down the magnetic field line to 110 km. The pass of interest occurred during a period of intense activity with Kp in the 3-h period including the pass having a value of 6- and having been in the range from 6- to 6 for the previous 12 h. The period of interest is the 1-min interval between 01:54 and 01:55 UT during which both the integral flux and energy flux exceeded 10^{10} keV/cm^2 sec sr respectively and average energies reached values as high as 10 keV.

From the interval we selected three spectra. The spectra chosen had integral number fluxes or integral energy fluxes exceeding the 10^{10} level and displayed no obvious temporal or spatial aliasing. The three spectra were for the 1-sec intervals beginning at 01:54:13, 01:54:50, and 01:54:54. The differential number flux spectra are plotted in Figures 2, 3, and 4. In all cases the differential number flux was calculated with corrections being made for dead time effects in the detector electronics. The second and third spectra are both roughly monotonically decreasing over the energy range of the detector with integral number fluxes of $\sim 2 \times 10^{10}$ electrons/cm^2 sec sr and integral energy fluxes between 10 and 20 erg/cm^2 sec sr.

If isotropy is assumed for the precipitating electrons the total downward number fluxes are 6.28×10^{10} and 7.04×10^{10} electrons/cm^2 sec, equivalent to currents of $\sim$ 101 and 113 μA/m^2, and the total energy fluxes are 60.3 and 42.7 erg/cm^2 sec. Typically between 30 and 50 percent of the total flux precipitating into the ionosphere is returned either as secondary backscattered or mirrored electrons. If an average value of 40 percent is chosen then the net currents carried by the two spectra are 61 and 68 μA/m^2 respectively. It is important to remember that the critical assumption made in these calculations is that the flux is isotropic for the precipitating electrons. If there is any significant field alignment for the electrons in any portion of the spectrum then these values are only upper bounds on the current and total energy flux. In

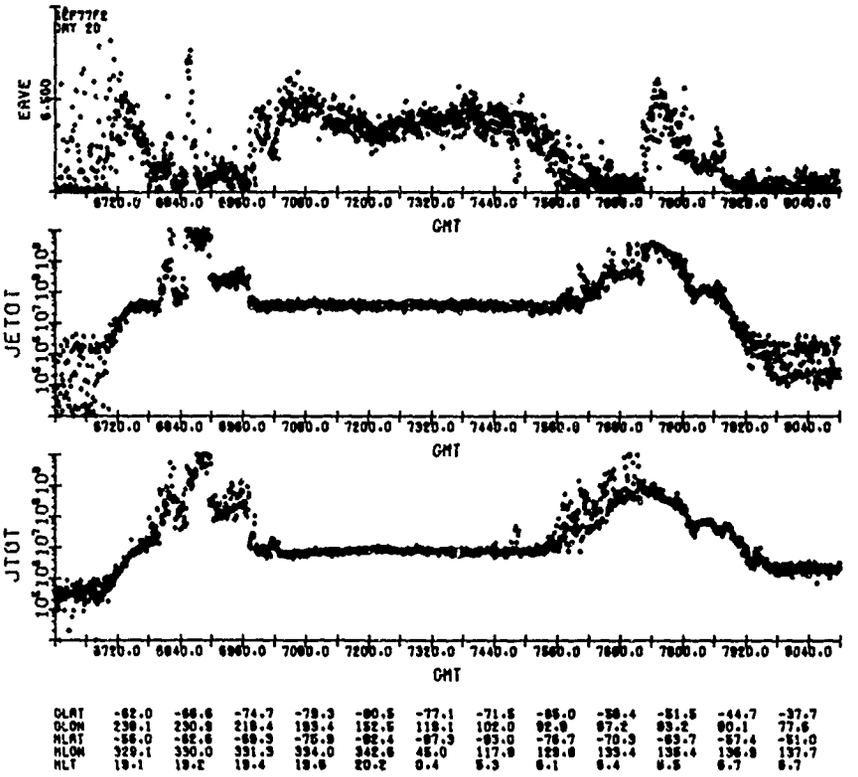

Figure 1. Average Energy, Integral Energy Flux, and Integral Number Flux for the South Pole Auroral Pass Between 01:54 and 02:19 on Day 263, 1977

Table 1 the values of the differential flux in each of the 16 channels are listed in units of e/cm^2 sec sr eV. The 16 channels are centered in energy at approximately 47, 73, 112, 267, 412, 638, 973, 1000, 1535, 2355, 3580, 5500, 8000, 13,200, and 20,400 eV as one goes from channels 1 to 16. The table also gives the percentage of the total integral number flux and integral energy flux that is carried in the energy band centered on each channel. One notes from the table that for the second and third spectra a small fraction of the integral number flux is carried by electrons with energies above 1 keV (15.5 and 4.8 percent respectively). In the two cases this would correspond to net current from electrons with energies above 1 keV of 9.5 and 3.3 $\mu A/m^2$ respectively. It should be noted that the greater than 1 keV electrons carry a much larger portion of the total energy flux; in the case of these two spectra, 64.3 and 44.5 percent.

The third spectrum from the day 263 pass is very different from the two discussed above. The integral flux in this case is only 4.9×10^9

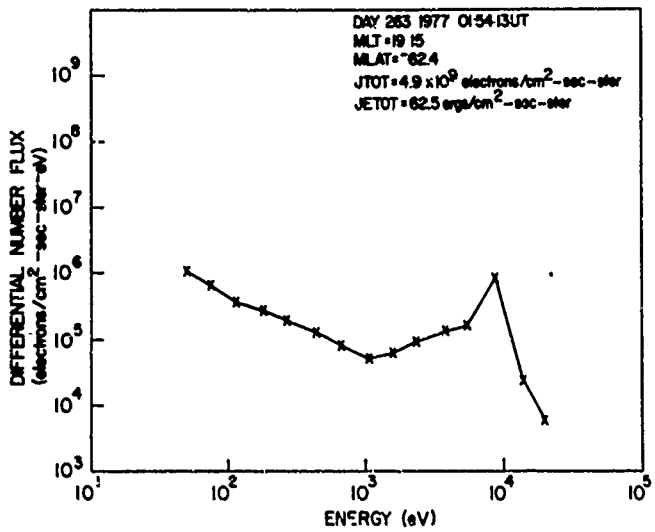

Figure 2. Differential Number Flux for the 1-sec Interval Beginning 01:54:13 on Day 263, 1977

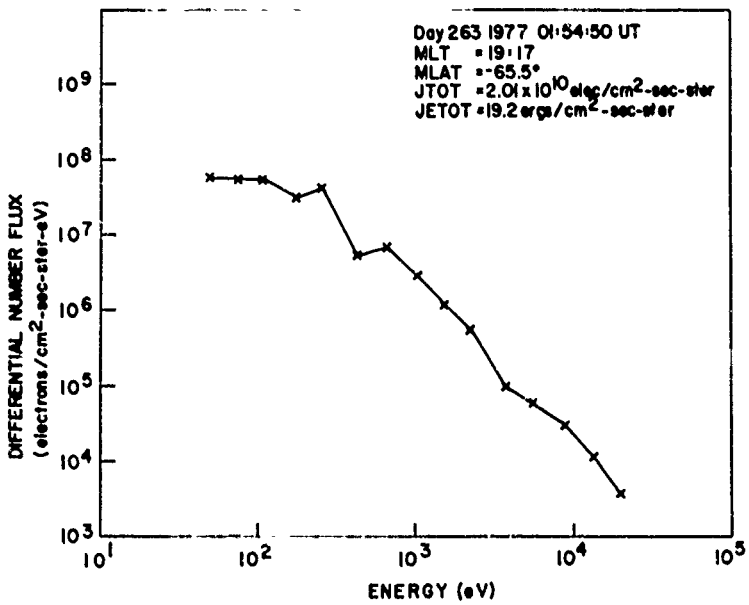

Figure 3. Differential Number Flux for the 1-sec Interval Beginning 01:54:50 on Day 263, 1977

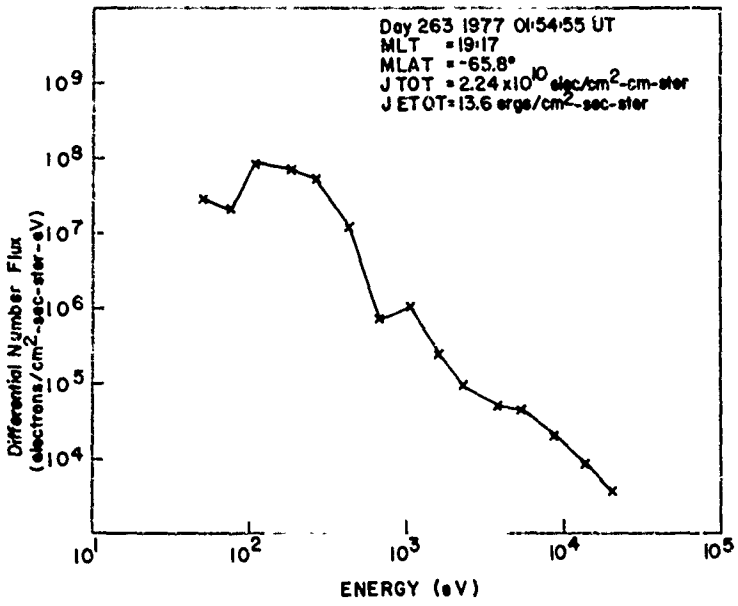

Figure 4. Differential Number Flux for the 1-sec Interval Beginning 01:54:54 on Day 263, 1977

electrons/cm^2 sec sr, compared to 2×10^{10} electrons/cm^2 sec sr for the previous case. Unlike the other two spectra, however, almost all this flux is carried by electrons with energy above 1 keV (~ 97 percent). The spectrum shows a prominent peak at ~ 9 keV with the channel at 9 keV carrying over 70 percent of the entire flux. Making the same assumptions made for the previous two spectra, we find that this spectrum carries a net current of ~ 14.9 μA/m^2. The peak in the spectrum indicates acceleration by a parallel electric field that would tend to produce field aligned fluxes such that the total current would be less than the estimate. As for the two previous spectra, the differential flux values are listed in Table 1.

The spectrum in Figure 2 is typical in shape if not in intensity of those found in "inverted-V" events. In some events in fact the peak appears to be beyond the 20,000 eV upper limit of the detector. It is probable, therefore, to assume that events take place with the electrons having spectra as seen in Figure 3 but with the peak appearing between 20 and 30 keV.

Table 1. Day 263

Channel	Differential Number Flux	Percent Integral Flux	Percent Energy Flux
	10:54:13 UT		
1	1.05×10^6	0.55	0.004
2	6.62×10^5	0.41	0.005
3	3.76×10^5	0.41	0.007
4	2.79×10^5	0.44	0.013
5	1.94×10^5	0.50	0.021
6	1.31×10^5	0.53	0.036
7	8.13×10^4	0.51	0.053
8, 9	6.25×10^4	0.59	0.097
10	6.13×10^4	0.77	0.192
11	9.19×10^4	2.06	0.736
12	1.33×10^5	4.35	2.58
13	2.62×10^5	13.90	9.61
14	8.52×10^5	71.2	80.51
15	2.59×10^4	2.90	5.00
16	6.09×10^3	0.78	2.44
	01:54:50 UT		
1	5.52×10^7	7.15	0.61
2	5.40×10^7	8.06	1.04
3	5.35×10^7	14.05	2.61
4	3.20×10^7	12.26	3.77
5	4.30×10^7	27.00	11.97
6	5.30×10^6	5.24	3.83
7	6.95×10^6	10.65	11.84
8, 9	2.8×10^6	6.48	11.46
10	1.22×10^6	3.76	10.04
11	5.30×10^5	2.88	11.17
12	9.45×10^4	0.75	4.81
13	5.82×10^4	0.75	6.97
14	2.90×10^4	0.59	9.00
15	1.07×10^4	0.29	6.78
16	3.82×10^3	0.01	4.04
	01:54:54 UT		
1	2.87×10^7	3.33	0.45
2	2.06×10^7	2.76	0.56
3	8.65×10^7	20.42	5.93
4	7.30×10^7	25.11	12.12
5	5.57×10^7	31.36	21.89
6	1.27×10^7	11.27	12.95
7	6.87×10^5	0.94	1.65
8, 9	1.02×10^6	2.11	5.87
10	2.48×10^5	0.69	2.78
11	8.87×10^4	0.44	2.64
12	5.00×10^4	0.36	3.60
13	4.30×10^4	0.50	7.26
14	2.08×10^4	0.38	9.06
15	8.60×10^3	0.21	7.64
16	3.75×10^3	0.11	5.57

2. DAY 46, 1978 10:16 TO 10:41 UT

In Figure 5 the data for the pass of interest are plotted in the same format as Figure 1. Here again primary interest is in an interval as the satellite was passing over the evening side of the oval when both the integral number and energy fluxes exceeded the 10^{10} level; in this case the interval between 10:20:30 and 10:21:00 UT. This pass again occurred during a period of high activity with a Kp value for the interval including the pass of 7+ and an hourly AE value of -1675 γ. The two spectra studied in more detail were measured at 10:20:40 and 10:20:41 UT.

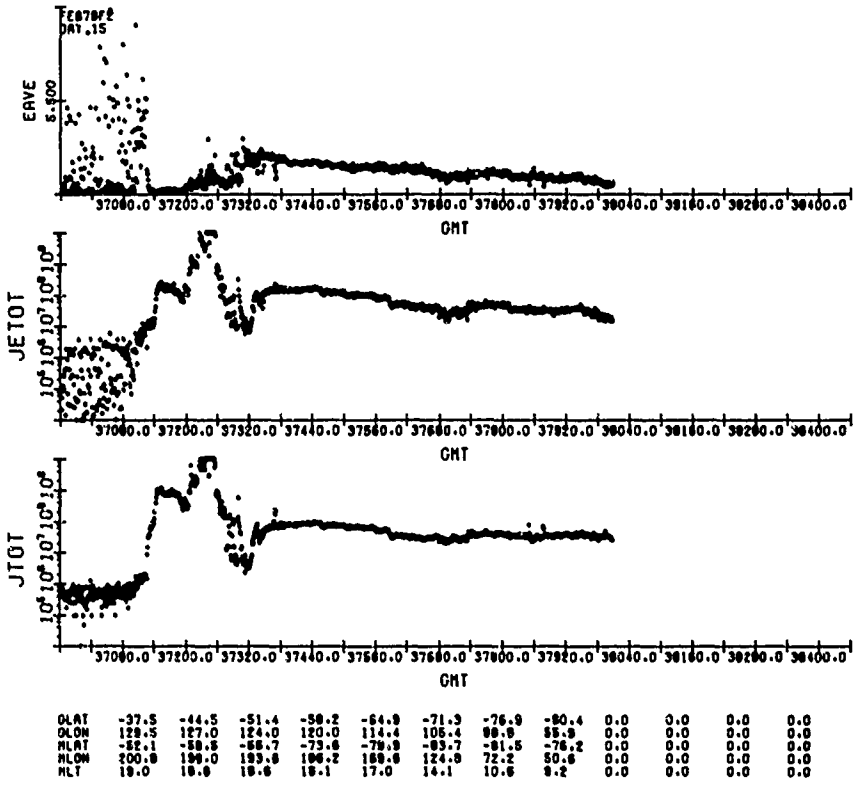

GLAT	-37.5	-44.5	-51.4	-58.2	-64.9	-71.3	-76.9	-80.4	0.0	0.0	0.0	0.0
GLON	128.5	127.0	124.0	120.0	114.4	106.4	98.8	95.9	0.0	0.0	0.0	0.0
MLAT	-52.1	-58.5	-65.7	-73.6	-79.9	-83.7	-81.5	-76.2	0.0	0.0	0.0	0.0
MLON	200.8	196.0	193.6	190.2	188.6	124.8	72.2	50.6	0.0	0.0	0.0	0.0
MLT	19.0	18.8	18.6	18.1	17.0	14.1	10.6	9.2	0.0	0.0	0.0	0.0

Figure 5. Average Energy, Integral Energy Flux, and Integral Number Flux for the Auroral Pass Between 10:16 and 10:41 on Day 46, 1978

The differential number flux spectra are plotted in Figures 6 and 7 and the values and percentages are shown in Table 2. The two spectra are harder than the first two spectra discussed in the previous section. For these two spectra,

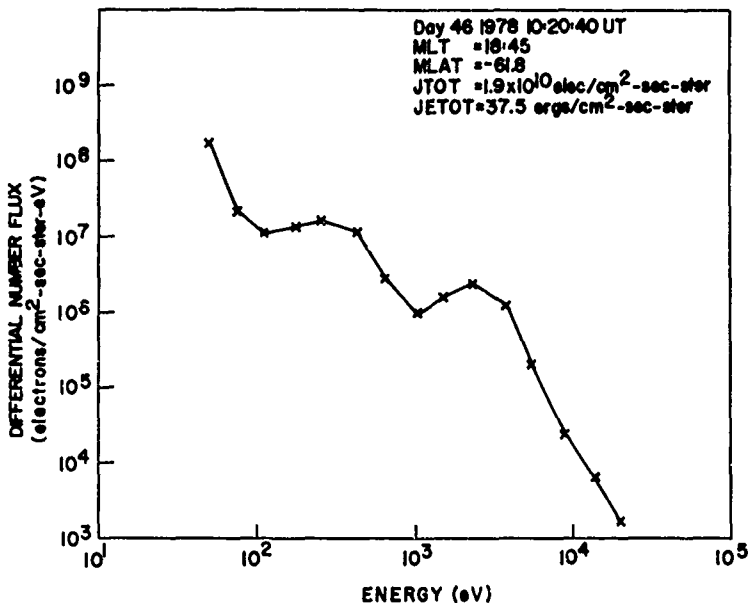

Figure 6. Differential Number Flux for the 1-sec Interval Beginning 10:20:40 on Day 46, 1978

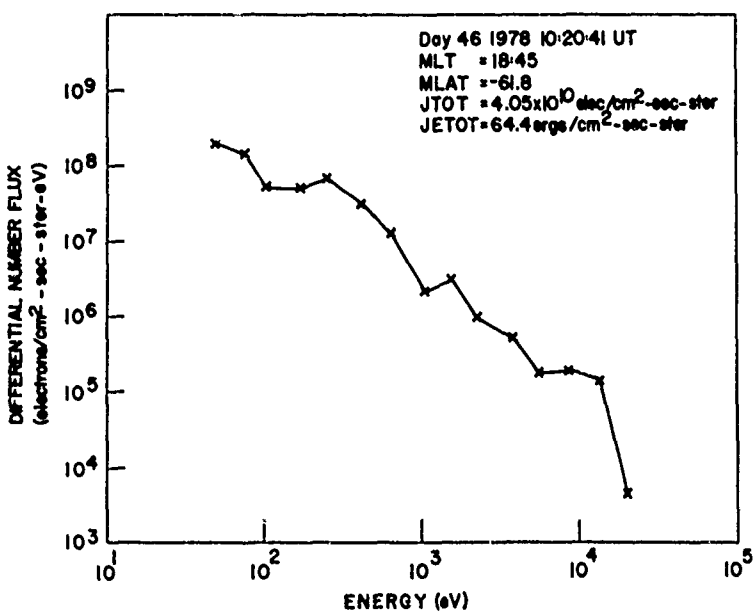

Figure 7. Differential Number Flux for the 1-sec Interval Beginning 10:20:41 on Day 46, 1978

Table 2. Day 46

10:20:40 UT			
Channel	Differential Number Flux	Percent Integral Flux	Percent Energy Flux
1	1.76×10^8	24.08	1.01
2	2.15×10^7	3.39	0.21
3	1.10×10^7	3.08	0.28
4	1.37×10^7	5.55	0.83
5	1.61×10^7	10.71	2.31
6	1.18×10^7	12.40	4.39
7	2.80×10^6	4.53	2.45
8 } 9	9.19×10^6	2.25	1.93
10	1.70×10^6	5.57	7.21
11	2.43×10^6	14.08	26.31
12	1.26×10^6	10.64	32.98
13	2.11×10^5	2.89	13.00
14	2.55×10^4	0.55	4.04
15	6.47×10^3	0.19	2.09
16	1.67×10^3	0.06	0.90

10:20:41 UT			
Channel	Differential Number Flux	Percent Integral Flux	Percent Energy Flux
1	1.93×10^8	12.34	0.63
2	1.44×10^8	10.62	0.83
3	5.15×10^7	6.73	0.75
4	4.82×10^7	9.20	1.71
5	6.37×10^7	19.81	5.30
6	3.07×10^7	15.12	6.62
7	1.23×10^7	9.38	6.25
8 } 9	2.15×10^6	2.46	2.63
10	3.10×10^6	4.75	7.62
11	9.87×10^5	2.68	6.14
12	5.07×10^5	2.01	7.69
13	1.82×10^5	1.17	6.50
14	1.93×10^5	1.96	17.81
15	1.49×10^5	2.03	28.13
16	4.57×10^3	0.07	1.44

approximately 36 and 17 percent of the integral number flux and 89 and 78 percent of the integral energy flux are carried by electrons with energies above 1 keV. Using the same assumptions used in the previous section the total precipitating electron fluxes are 5.97×10^{10} and 1.27×10^{11} electrons/cm^2 sec corresponding to currents of 96 and 204 μA/m^2. Net currents are estimated at 58 and 123 μA/m^2 over the entire spectrum and 21 μA/m^2 for both if only the portion of the spectrum with energies above 1 keV is considered. It is unclear from the spectral shape whether the electrons composing these spectra have been acted on by

a field-aligned potential; therefore, the degree to which the electrons are field-aligned is again uncertain.

3. DAY 122, 1978 10:30 TO 10:55 UT

The data for the pass from which the last spectra were chosen is shown in Figure 8 where again the region of interest is on the evening side of the oval. In this pass there are several periods in the interval from 10:32 to 10:35:30 UT in which the integral and energy flux both simultaneously exceed 10^{10}. Again, geomagnetic activity is high with Kp = 7 in the 3-h period covering the pass. The hourly AE average was over 1000 γ. The two spectra chosen were from 10:34:18 (see Table 3) and 10:35:04 (see Figures 9 and 10) with integral number fluxes of 2.07×10^{10} and 2.87×10^{10} electrons/cm^2 sec sr and integral energy fluxes of 53.6 and 51.4 ergs/cm^3 sec sr respectively. The two differ significantly in shape and in how the energy and flux are distributed over the spectrum. For the spectrum at 10:34:18, ~ 39 percent of the integral number flux and ~ 91 percent of the integral energy flux is carried by electrons with energies above 1 keV. By contrast, in the second spectrum only ~ 13 percent of the integral number flux and ~ 78 percent of the integral energy flux are carried by electrons with energies exceeding 1 keV. Making the same assumption as in the previous case the total precipitating currents are 105 and 145 μA/m^2, the estimated total net currents are 63 and 87 μA/m^2, and the estimated net current for electrons with energies above 1 keV are 25 and 19 μA/m^2. Again, the absence of a strong peak in the distribution function makes uncertain the extent to which the electrons comprising the spectra were accelerated by parallel electric fields and therefore the degree of field alignment.

Several concluding points must be made concerning the spectra presented above. First, the data presented were only from DMSP F2 passes in 1978. Although the year does span a wide range in activity, the orbit of the F2 satellite limited observations to magnetic local times between roughly 1500 and 2300 h on the evening side of the oval and 0400 to 1100 h on the morning side of the oval. To insure that this limitation did not exclude particularly intense events occurring in the post-midnight sector a preliminary survey was also conducted on the data from the DMSP F4 satellite and from the P78-1 satellite. Both satellites carried identical detectors to those flown on the F2 satellite. The F4 satellite was in a sun-synchronous orbit in 1000 to 2200 hours meridian and the P78-1 satellite was in a sun-synchronous orbit in the noon-midnight meridian. Both satellites routinely passed into the post-midnight sector. To date no examples of spectra more intense than those presented above have been found in either of the data

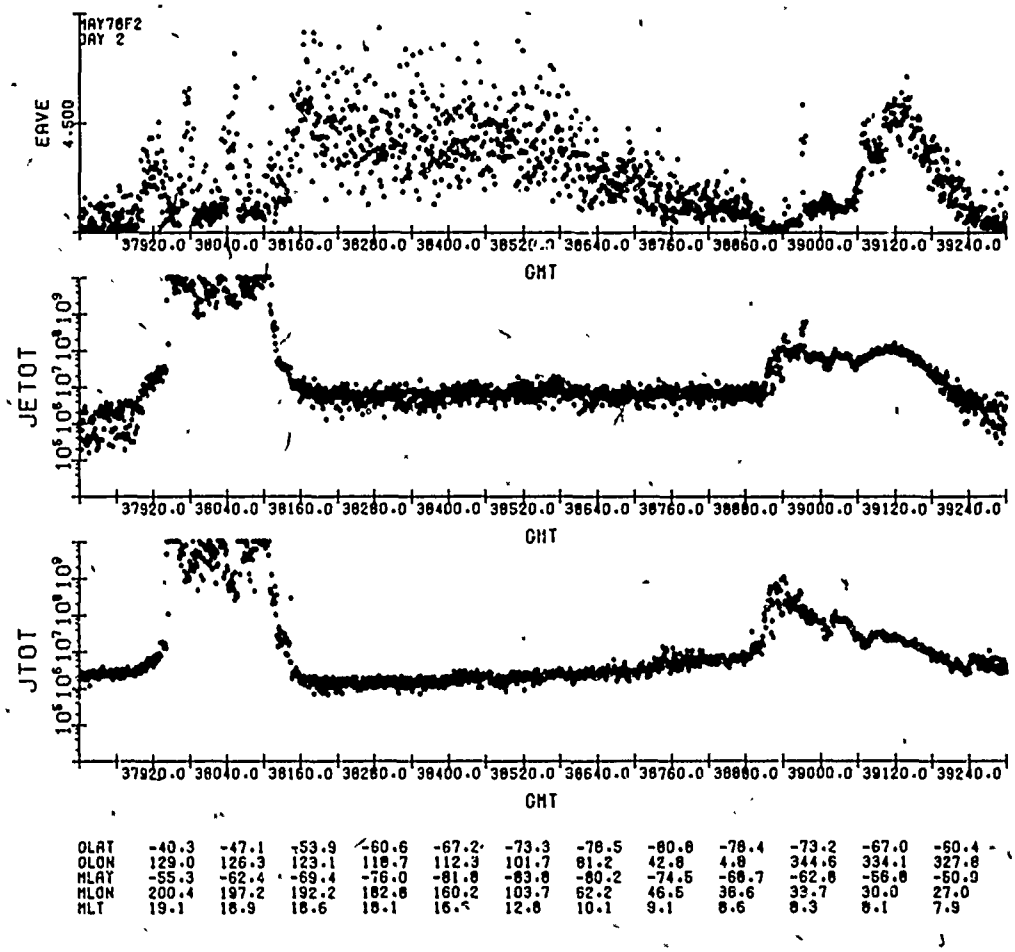

GLAT	-40.3	-47.1	-53.9	-60.6	-67.2	-73.3	-78.5	-80.8	-78.4	-73.2	-67.0	-60.4
GLON	129.0	126.3	123.1	118.7	112.3	101.7	81.2	42.8	4.8	344.6	334.1	327.8
MLAT	-55.3	-62.4	-69.4	-76.0	-81.8	-83.8	-80.2	-74.5	-68.7	-62.8	-56.8	-50.9
MLON	200.4	197.2	192.2	182.8	160.2	103.7	62.2	46.5	36.6	33.7	30.0	27.0
MLT	19.1	18.9	18.6	18.1	16.[illegible]	12.8	10.1	9.1	8.6	8.3	8.1	7.9

Figure 8. Average Energy, Integral Energy Flux, and Integral Number Flux for the Auroral Pass Between 10:32 and 10:35:30 on Day 122, 1978

sets. Second, the lack of pitch angle is a severe limitation on determination of the flux to the satellite due to the possibility of significant field alignment of the fluxes over part or all of the spectrum. To overcome this problem the P78-1 data are being surveyed for similar intense events. On the P78-1 satellite there are two sets of electrostatic analyzers as on the DMSP satellite but with look directions in the spin plane of the satellite and with the look direction for the two detectors set 90° apart. The satellite rotates at 11 rpm with each detector recording four spectra/sec. Using the data from the satellite, the degree of field alignment can be determined and the actual net current calculated. Also, higher energy electron detectors are included as part of the P78-1 satellite payload so that the spectrum can be specified at energies beyond the 20,000 eV

Table 3. Day 122

10:34:18 UT			
Channel	Differential Number Flux	Percent Integral Flux	Percent Energy Flux
1	9.51×10^7	11.93	0.38
2	3.95×10^7	5.70	0.27
3	2.26×10^7	5.80	0.40
4	1.97×10^7	7.34	0.83
5	2.35×10^7	14.30	2.35
6	1.16×10^7	11.16	3.06
7	3.03×10^6	4.50	1.85
8, 9	1.94×10^6	4.35	2.85
10	1.70×10^6	5.07	5.02
11	1.41×10^6	7.49	10.67
12	1.07×10^6	8.31	19.58
13	9.46×10^5	11.88	40.54
14	9.05×10^4	1.79	10.03
15	7.28×10^3	0.19	1.65
16	1.51×10^3	0.04	0.59

10:35:04 UT			
Channel	Differential Number Flux	Percent Integral Flux	Percent Energy Flux
1	1.29×10^8	11.70	0.53
2	1.37×10^8	14.32	0.99
3	6.17×10^8	11.39	1.15
4	2.59×10^7	6.97	1.15
5	2.20×10^7	9.65	2.29
6	1.82×10^7	12.61	4.92
7	1.68×10^7	18.01	10.72
8, 9	2.50×10^5	4.04	3.82
10	6.38×10^5	1.38	1.97
11	1.81×10^5	0.69	1.43
12	2.26×10^5	1.26	4.29
13	2.43×10^5	2.20	10.88
14	3.17×10^5	4.53	36.68
15	5.45×10^4	1.05	12.88
16	1.63×10^4	0.35	6.43

upper limit of the J sensor. Third, in the data surveyed so far, a complete spectrum was obtained only once per second. This limited the search to auroral events with dimensions of approximately 7 km or greater. The spectrum for any event of smaller dimension would be aliased. Since discrete arcs in the auroral zone typically have widths of approximately 1 km, the intensity of electron precipitation into such forms cannot be determined from the data used so far. With the higher sampling frequency on the P78-1 satellite this problem is only

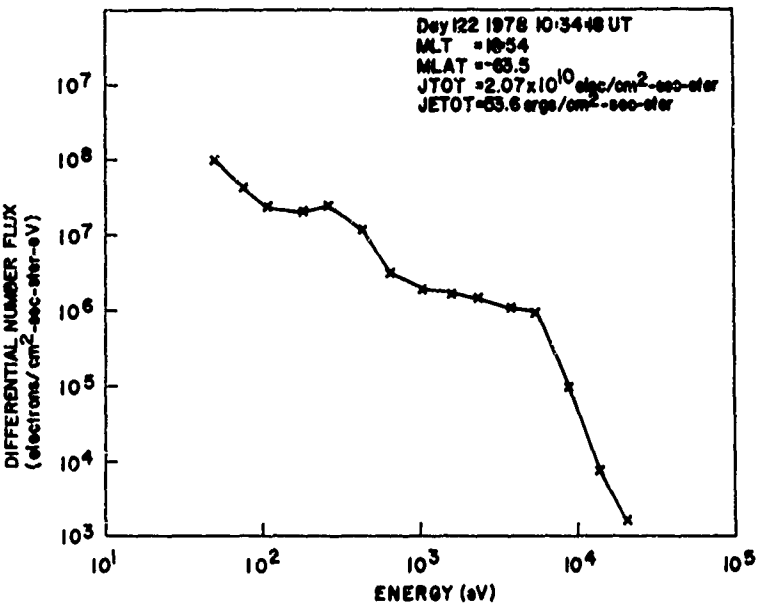

Figure 9. Differential Number Flux for the 1-sec Interval Beginning 10:34:18 on Day 122, 1978

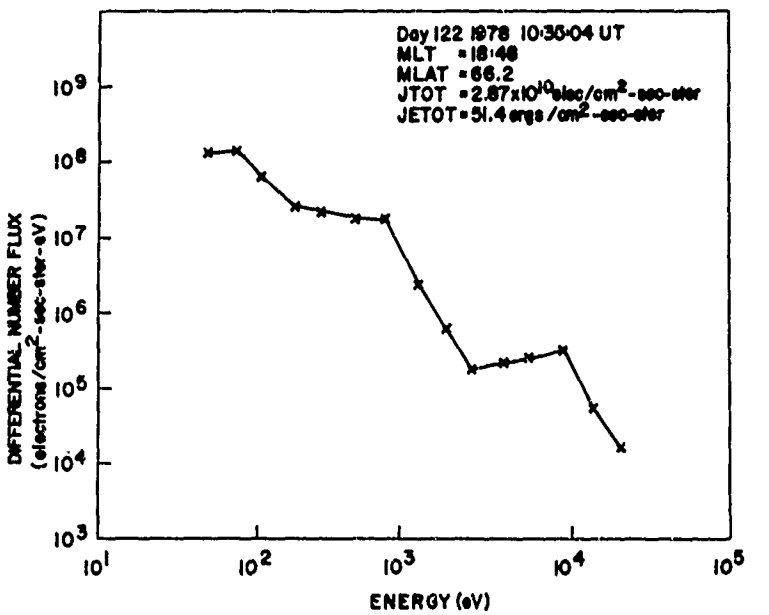

Figure 10. Differential Number Flux for the 1-sec Interval Beginning 10:35:04 on Day 122, 1978

partially solved since in this data set the pitch angle is involved. As will be shown next there is convincing evidence that intense precipitation events carrying very large currents take place in the auroral zone on a spatial scale of a kilometer or less. Lastly, the detection of extremely intense events is limited by instrument design. Detectors of auroral plasma are typically designed with sensitivities such that for typical levels of auroral precipitation count rates of 100 to 1000/sec are recorded. If a spectrum like that shown in Figure 2 were carrying 100 $\mu A/m^2$ in the peak rather than 10 $\mu A/m^2$ this would correspond to a count rate of $\sim 3 \times 10^6$ counts/sec. The electronics in detectors typically require 1-μsec dead time between each count recorded. For a count rate of 3×10^6 the electronics would be unable to respond and only a very low count rate will be read out.

4. S3-2 OBSERVATIONS

As mentioned above there is good evidence that intense current structures exist on spatial dimensions of a kilometer or less. This evidence comes from data recorded by the S3-2 satellite. The S3-2 satellite carried a triaxial fluxgate magnetometer. The magnetometer recorded 32 vector measurements of the field each second providing a spatial resolution of approximately 200 m per measurement. In Figure 11, approximately 8 sec of data from the magnetometer are plotted. The three traces at the top of the figure give the difference between the magnetometer measurements and the model field plotted in geomagnetic coordinates. The histogram in the center of the plot gives the derived currents and the stick diagrams at the bottom provide information on the orientation of the ambient electric field. The figure shows that in the 1/4 sec prior to 42497.8 sec UT the east-west component of ΔB decreased by approximately 300 γ while the other two components remained relatively unchanged. Under such circumstances the infinite current sheet approximation can be used to calculate the current producing the deviation. There are actually two slopes observed in the 1/4-sec period corresponding to an average current of 135 $\mu A/m^2$. This is a current out of the ionosphere that would correspond to precipitating electrons. In the interval shown in the figure there are other significant currents, though due to deviation in the other components their magnitude is more uncertain.

The S3-2 satellite also carried an electron spectrometer. The spectrometer again measured only one spectrum per second so that no definitive information was provided on the characteristics of the electrons producing these currents. While these data confirm that very large currents exist in the auroral zone they do not insure that the types of spectra shown in this paper and such small scale

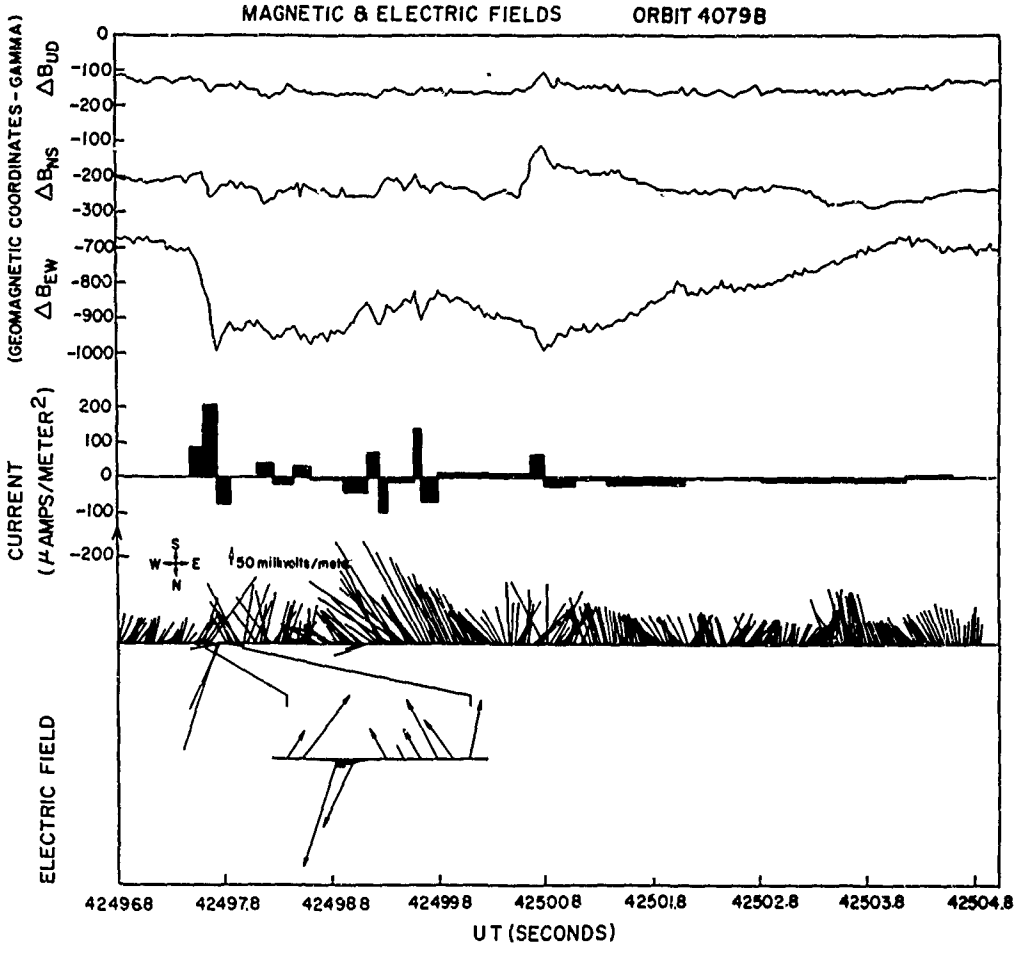

Figure 11. Magnetic and Electric Field Measurements During an 8-sec Interval Measured by the S3-2 Satellite

intense currents are related, that is, they do not insure that the assumption of isotropy is valid.

In conclusion data have been presented showing the most intense spectra seen in the auroral zone and evidence that very large net currents exist. Work is underway to refine and extend these results to provide improved inputs for modelers and theorists.

10. Estimates of Precipitating Electron Power Flux from Simultaneous DMSP Auroral Image and ISEE-1 AKR Observations

by

N. A. Saflekos
R. E. Sheehan
Department of Physics
Boston College
Chestnut Hill, Mass. 02167

This report describes the first attempt to associate the area of discrete aurora observed in a DMSP image with simultaneous measurements of auroral kilometric radiation (AKR) power flux at 178 and 311 kHz. It is generally believed that fluxes of 1 to 10 keV electrons produce discrete auroral arcs and AKR. Recent theories of AKR generation restrict the frequency range of AKR to a narrow band near the electron gyrofrequency. The requirements for AKR generation summarized by Grabbe[1] indicate that there must be a region of reduced plasma density related to the condition $\omega_{pe} < 0.2\ \omega_{ce}$, where ω_{pe} and ω_{ce} are the electron plasma frequency and gyrofrequency, respectively. Although AKR at a particular frequency can be generated only in a thin layer, the rapid change in ω_{ce} with altitude allows an extended source region from about 1.3 to 3.1 R_E geocentric (2000 to 14,000 km altitude) for an AKR frequency range of 50 to 700 kHz. The frequency has an inverse relationship with altitude so that the highest frequencies are generated at the lowest altitudes. The downgoing electromagnetic

1. Grabbe, C. (1981) Auroral kilometric radiation: A theoretical review, Rev. Geophys. Space Phys. 19:627.

waves are then reflected back at the right-hand cutoff, which effectively blocks their observation at the earth's surface.

Simultaneous auroral and AKR observations are shown in Figures 1 and 2, respectively. Figure 1 is a sketch of the aurora (shown in black) seen during orbit 12,573 of the DMSP F-1 satellite over the northern hemisphere on 15 February 1979. The solid vertical lines represent the image border, and the dotted line running between them is the ground track. The satellite scanned the portion of the image shown here from top to bottom in about 4 min from an altitude of about 800 km. The 'x' on the ground track is the satellite location at 0854 UT. Dashed lines are corrected geomagnetic (CG) latitudes and local times at 110-km altitude.

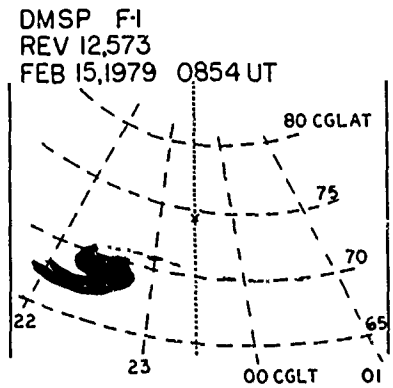

Figure 1. Sketch of North Pole DMSP F-1 Image, Orbit 12573 on 15 February 1979. Area of intense aurora shown in black is located at 2200 to 2300 corrected geomagnetic local time (CGLT) and 67 to 70° corrected geomagnetic latitude (CGLAT). "X" on center line image shows satellite location at 0854 UT

Figure 2 shows a portion of the ISEE-1 survey plot of the Electric Spectrum Analyzer (ESA) on 15 February 1979 (courtesy of R.R. Anderson). The vertical dashed line indicates time of the DMSP image in Figure 1. The amplitude scales for each frequency are approximately logarithmic with a base value of 0.1 μV/m and a full scale range of about 110 dB. For the frequencies shown here the bandwidths are approximately ±7.5 percent of the center frequencies. The solid area represents the average intensity in a 144-sec interval and the line above the solid area is the peak intensity in the 144-sec interval.

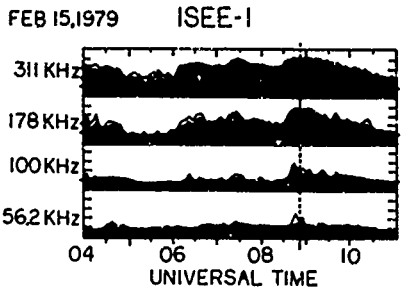

Figure 2. Survey Plot From ISEE-1 Electric Spectrum Analyzer on 15 February 1979 (Courtesy of R. R. Anderson). Dashed line indicates time of DMSP image shown in Figure 1. Dynamic range of amplitude scales is approximately 110 dB (see text)

During 0600 to 1200 UT on 15 February 1979 the planetary Kp index values were 4- and 3+, and the AE index (Figure 3) showed a sharp increase from about 250 to 400 nT at approximately 0840 UT. The auroral feature in the DMSP image appears to be a westward traveling surge or bulge typically seen after a substorm onset. This is consistent with the AE increase beginning at about 0840 UT and the increased AKR intensities observed after 0830 UT. The sharpest jump in AKR intensity is seen in the 178 kHz channel. ISEE-1 was located at about 14 R_E geocentric over the northern hemisphere at 30° latitude (solar magnetic) and 0200 MLT, a favorable position for observing AKR emitted from the auroral zone in the night sector.

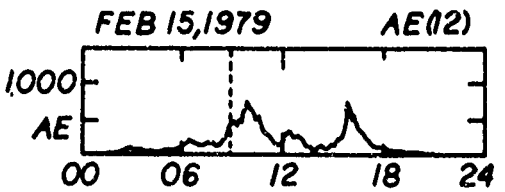

Figure 3. Auroral Electrojet (AE) Indices on 15 February 1979 [from World Data Center (WDC C-2), Data Book No. 5, April, 1982]. Dashed line indicates time of DMSP image in Figure 1

Theories of AKR generation and satellite images of auroras can be combined to yield estimates of the input power required to account for observed AKR intensities. Grabbe[1] summarized the frequency condition for AKR generation by the following equation

$$\omega_{ce} + \frac{\omega_{pe}^2}{\omega_{ce}} < \omega < \omega_{ce} + k_z V_b \quad , \tag{1}$$

where ω is radiation frequency, k_z is the component of the wave vector parallel to the magnetic field, and V_b is the velocity of the electron beam producing the radiation. With $\omega = 2\pi\nu$, and $k_z = k \cos\theta$, where k is the amplitude of the total wave vector, Eq. (1) becomes

$$\nu_{ce} + \frac{\nu_{pe}^2}{\nu_{ce}} < \nu < \nu_{ce} + V_b \frac{\nu}{c} \cos\theta \quad . \tag{2}$$

Representative quantities in Eq. (2) are $\nu_{pe} = 0.2\ \nu_{ce}$, as mentioned above, $V_b = 0.1c$, corresponding to 2.6 keV electrons, and $\theta = 60^o$. These substitutions yield

$$\begin{aligned} &1.04\ \nu_{ce} < \nu < \nu_{ce} + .05\ \nu \\ &1.04\ \nu_{ce} < \nu < 1.05\ \nu_{ce} \quad . \end{aligned} \tag{3}$$

Equation (3) specifies a narrow range of AKR frequencies at a given altitude. Similarly, a range of AKR frequencies implies that the condition is met over some altitude range. Since the plasma frequency requirement indicates a region of reduced plasma density, the AKR frequency range can be used to determine the altitude range of plasma depletion. By equating the area of discrete aurora observed in a DMSP image with the cross section of flux tubes carrying energetic electrons, we can estimate the total volume of the AKR source region.

Figure 1 suggests an auroral extent of roughly 1/2 hour in local time and 3^o in latitude centered at 68.5^o CGLAT. From Figure 2 we see that the most intense AKR is at 178 and 311 kHz. For the relatively low altitudes considered here, a dipole field model may be used to plot the electron gyrofrequency and AKR frequency range given by Eq. (3) as a function of radial geocentric distance along the field line passing through 68.5^o lat at 110 km (Figure 4). The center

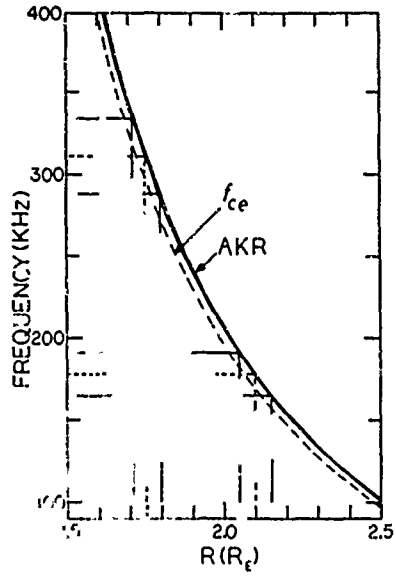

Figure 4. Plot of Electron Gyrofrequency f_{ce} (Dashed Curve) and the Allowed AKR Frequency Band (Solid Curves) vs Geocentric Radial Distance Along a Dipole Field Line Originating at $\lambda_m = 68.5^o$. Horizontal dashed and solid lines along the frequency scale indicate the center frequencies and bandpasses, respectively, of the 178- and 311-kHz channels of the ISEE-1 ESA. Vertical lines above the distance scale indicate the height range of these frequencies as determined from the allowed AKR frequencies

frequencies at 178 and 311 kHz and their bandpasses are indicated to the right of the frequency scale. When these frequencies are projected over to the AKR curve and down to the radial distance scale, the corresponding altitude ranges are determined. Thus, radiation from the 311-kHz channel originates from ~ 1.7 to $1.8\ R_E$ ($\sim$4500 to 5100-km altitude), and the 178-kHz channel originates from ~ 2.05 to $2.15\ R_E$ (6700 to 7300-km altitude).

Based on calculations of the Poynting flux from the survey plot (Figure 2), the estimated radiated power passing the satellite is 1.80×10^{-10} erg/cm^2 sec Hz at 311 kHz and 9.94×10^{-11} erg/cm^2 sec Hz at 178 kHz. Multiplying by bandwidths of 4.67×10^4 Hz and 2.67×10^4 Hz at 311 and 178 kHz, respectively,

the power in the 311-kHz channel is approximately 8.39×10^{-6} erg/cm^2 sec and in the 178-kHz channel approximately 2.65×10^{-6} erg/cm^2 sec.

If, after multiple reflections, the radiation escapes isotropically into the hemisphere above the source, and the distance from the source to the receiver is known, the total radiated power can be calculated. At the ISEE-1 distance of approximately 13 R_E, the area of the hemisphere centered at the source is $2\pi(13R_E)^2 = 4.32 \times 10^{20}$ cm^2. Thus, the total power emitted by the source in the 311 kHz channel is 8.39×10^{-6} erg/cm^2 sec $\times 4.32 \times 10^{20}$ cm^2 = 3.62×10^{15} erg/sec. The power in the 178-kHz channel is 2.65×10^{-6} erg/cm^2 sec $\times 4.32 \times 10^{20}$ cm^2 = 1.14×10^{15} erg/sec.

If inverted V electrons precipitating along flux tubes are responsible for AKR, the theoretical efficiency of converting particle energy to AKR is about 1 percent. This requires the particle energy input to be 3.62×10^{17} erg/sec at 311 kHz and 1.14×10^{17} erg/sec at 178 kHz. Since this energy passes through the cross sectional area of the flux tube at the generation altitude, the necessary precipitating power density is $(3.62 \times 10^{17}$ erg/sec$)/(5.21 \times 10^{15}$ cm$^2) = 69.5$ erg/cm^2 sec at 311 kHz and $(1.14 \times 10^{17}$ erg/sec$)/(9.13 \times 10^{15}$ cm$^2) = 12.4$ erg/cm^2 sec at 178 kHz.

Our estimates of the altitude range of the source and the input power density necessary to drive the AKR rest on two sets of assumptions. The altitude range at a given frequency (Figure 4) depends on the field model employed, in our case a pure dipole, and the allowed AKR frequency band. The frequency condition of Eq. (3) was theoretically derived, but it appears to adequately explain all known AKR properties. The AKR band in Figure 4 was calculated from reasonable parameter values. As the plasma frequency decreases, the lower limit of the band would approach the gyrofrequency, while the upper limit would be raised by increasing the electron energy or decreasing θ. Even with extreme parameter values the altitude ranges in Figure 4 would still be the order of several tenths of R_E.

The power estimates depend on the accuracy of the ISEE-1 power flux calibration, the area of the source region and its distance from ISEE, and the solid angle filled by radiation from the source. The distance from ISEE to the source would not vary appreciably if the source were distributed throughout the nightside auroral oval instead of concentrated in the patch seen in Figure 1. The final power densities are probably overestimated because the source area could be larger than that seen in the DMSP image and the solid angles of emission are probably smaller than the 2π steradians used in the calculations.

11. Environmental Interactions of Polar Orbiting Satellites

by

W. J. Burke
Air Force Geophysics Laboratory
Hanscom AFB, Mass. 01731

Addressed are

~~In this workshop we are addressing~~ questions concerning how large, and/or high-power, polar-orbiting spacecraft will interact with auroral environments. This paper discusses some experiences of spacecraft charging, vehicle shadowing, and current leakage encountered by AFGL measuring systems on small, polar-orbiting satellites. Because spacecraft charging at ionospheric altitudes does not seriously threaten the operation of present systems this subject has not received the widespread attention given to it at geostationary altitudes. As a matter of economics it is desirable to transfer as much as possible of what we have learned about spacecraft interactions at geostationary orbit to the auroral oval. Economics must not however blind us to the real differences between the two problems.

The environment at auroral latitudes in the ionosphere differs from that encountered at geostationary altitude in at least two major aspects.

(1) There is a large reservoir of high-density, cold plasma that tends to mitigate charging effects by providing a large source of charged particles from which neutralizing currents may be drawn. However, since Debye lengths in the ionosphere are measured in centimeters as opposed to hundreds of meters at

geostationary altitude, effective current collecting areas may be severely limited. Significant wake effects behind large structures will introduce new problems with differential charging. Rubin and Besse discuss these effects in more detail in their paper in this volume.

(2) Between the magnetic equator and the ionosphere, auroral electrons frequently undergo field-aligned accelerations of several kilovolts.[1] The degree to which auroral, as opposed to plasma sheet, electrons deviate from isotropy is a complex function of the electron's energy and the potential distribution along magnetic field lines.[2] In such environments, measurable fluxes of energetic protons are usually absent.[3,4]

It is anticipated that polar-orbiting shuttles will encounter the most severe charging environments in the vicinity of westward-traveling surges. These phenomena occur in the midnight sector during the expansion phases of substorms. Substorm onsets are frequently marked by the sudden brightening of the equatorward-most arc.[5] This is followed by a bulging and rapid poleward expansion of active arcs in the midnight sector.[6] For observers on the ground in the evening sector the bulge appears on the eastward end of arcs and moves quickly toward the western horizon. Using DMSP satellite imagery and electron flux measurements Meng and coworkers[7] constructed a composite morphology of westward traveling surges shown in Figure 1. Bright arcs emanate to the west (A) and to the east from the equatorward and poleward edges of the bulge region, respectively. A myriad of arc-like structures are embedded in the bulge region (C), while nonuniform diffuse auroral precipitation (D) is found to the east of the bulge and equatorward of the B arc.

Differential spectra typical of downcoming electrons in the vicinity of surges are shown on the left side of Figure 1. In region A, to the west (evening side) of

1. Mozer, F.S., Cattell, C.A., Hudson, M.K., Lysak, R.L., Temerin, M., and Torbert, R.B. (1980) Satellite measurements and theories of low altitude auroral particle acceleration, Space Sci. Rev. 27:155.
2. Lin, C.S., and Hoffman, R.A. (1979) Characteristics of the inverted-V event, J. Geophys. Res. 84:1514.
3. Frank, L.A., and Ackerson, K.L. (1971) Observation of charged particle precipitation into the auroral zone, J. Geophys. Res. 76:3612.
4. Frank, L.A., and Ackerson, K.L. (1972) Local time survey of plasma at low altitudes over the auroral zone, J. Geophys. Res. 77:4116.
5. Akasofu, S.-I. (1964) The development of the auroral substorm, Planet Space Sci. 12:273.
6. Akasofu, S.-I., Kimball, D.S., and Meng, C.-I. (1965) The dynamics of the aurora, II, Westward travelling surges, J. Atmos. Terr. Phys. 27:173.
7. Meng, C.-I., Synder, A.L., and Kroehl, H.W. (1978) Observations of auroral westward travelling surges and electron precipitations, J. Geophys. Res. 83:575.

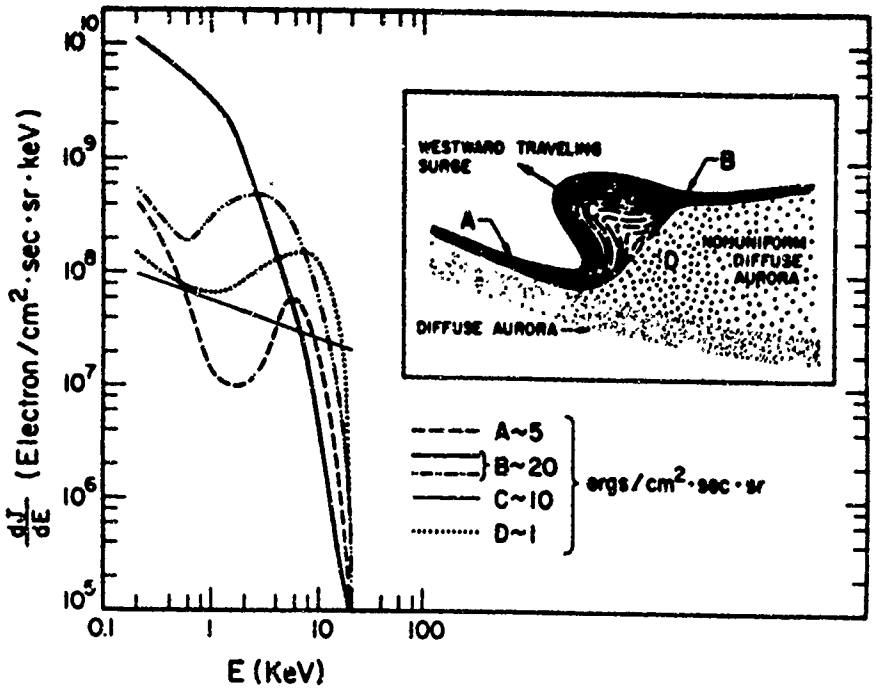

Figure 1. The Morphology of Auroral Illumination and Precipitating Electron Spectra in the Vicinity of Westward Traveling Surges (Ref. 7)

the bulge, spectra are similar to those measured over quiet-time arcs. However, the "monoenergetic beams" shift to higher than quiet-time values. This indicates that stronger field-aligned potentials occur during substorm periods. In the region of the poleward arc (region B) two spectral types are measured. One has a shape similar to that found in the diffuse aurora (D) but with lower mean energy. The second spectral type is characterized by electrons with energies of 100 eV and differential flux levels of $10^{11}/cm^2$ sec sr keV. The spectral shapes indicate that field-aligned accelerations in regions B and D are not significant. Within region C electron spectra are relatively flat, sometimes out to the high-energy measuring limit of DMSP spectrometers. If, as suggested by the "worst-case" study of SCATHA's environment,[8] severe charging most strongly correlates with fluxes of electrons with energies in the several tens-of-keV regime, then region C electrons may present the most severe charging environment for polar-orbiting shuttles.

At geostationary altitude, negative spacecraft potentials are readily inferred from charging peaks measured in low-energy channels of positive ion detector

8. Mullen, E.G., and Gussenhoven, M.S. (1982) High-Level Spacecraft Charging Environments Near Geosynchronous Orbit, AFGL-TR-82-0063, AD A118791.

systems. In the ionosphere, spacecraft potentials of up to a few volts are directly measured by Langmuir probe sweeps. Most polar orbiting satellites have measuring systems that concentrate on electrons rather than positive ions. Thus, there are few direct measurements of "worst-case" charging events in the ionosphere. The INJUN 5 satellite did have some capability. We will concentrate on measurements taken in the northern, evening sector of the ionosphere during a substorm. In terms of the diagram shown in Figure 1 the satellite probably passed over an auroral arc characteristic of region A.

The INJUN 5 satellite was launched in November 1968 into a polar orbit with an apogee, perigee, and inclination of 2560 km, 677 km, and 81°, respectively. The satellite was magnetically aligned. Its scientific complement included two LEPEDEA (Low Energy Proton Electron Differential Energy Analyzers), which in the northern auroral zones detected particles with pitch angles near 0° and 90°. Each sensor required 2 sec to compile a 117-point spectrum of both positive ions and electrons with energies between 50 eV and 15 keV. The University of Iowa's color spectrograms based on LEPEDEA measurements are well known.[3] Unfortunately, information readily transmitted through color coding does not reproduce in black and white. The reader is referred to Plates 1 and 2 of Frank and Ackerson[4] (also to Plate 1 of Frank[9]) for ion and electron measurements taken in the late evening sector during a substorm on Rev 1487. The energy-time spectrogram based on electron count rates of the uplooking LEPEDEA shows that after leaving the polar cap the satellite encountered three inverted-V events before passing through the diffuse auroras. While passing through the second inverted-V, electron count rates peaked at energies greater than 10 keV, and as discussed below, spacecraft charging was most severe. The integral flux of electrons with energies between 50 eV and 15 keV at pitch angles 0° and 90° are given in Figure 2.[9] At these angles the directional flux was $1 - 2 \times 10^9$ electrons/cm^2 sec sr. The pitch angle distribution of electrons was never isotropic but did not go more than a factor of 3 away from isotropy.

The spectrogram based on count rates from the uplooking positive detector shows that during this pass no measurable energetic proton fluxes were detected except near the equatorward boundary of diffuse auroral precipitation.[4] It is possible that positive ion detectors looking at other pitch angles would see greater fluxes.

Two AFGL experiments were also on board INJUN 5.[10] They were spherical electrostatic analyzers (SEA) placed on the ends of 5-foot-long booms. Due to

9. Frank, L.A. (1975) Magnetospheric and auroral plasmas: a short survey of progress, Rev. Geophys. Space Phys. 13:974.

10. Burke, W.J., Donatelli, D.E., and Sagalyn, R.C. (1978) INJUN 5 observations of low-energy plasma in the high-latitude topside ionosphere, J. Geophys. Res. 83:2047.

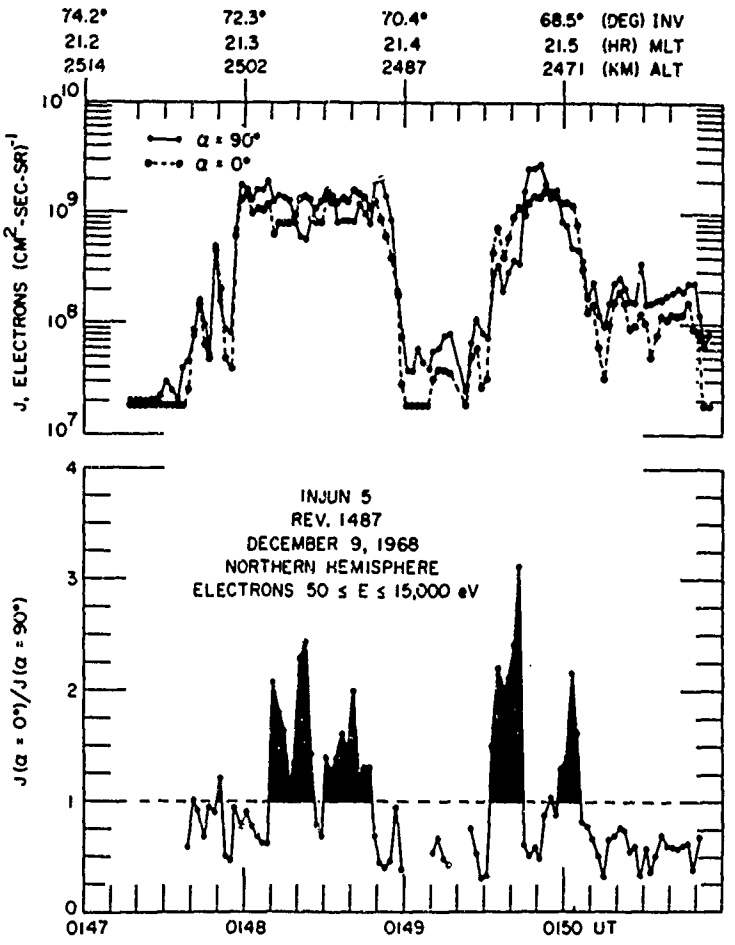

Figure 2. Directional Fluxes of Electrons With Energies Between 50 eV and 15 keV at Pitch Angles of Approximately 0° and 90° Measured Over the Northern Auroral Oval During INJUN 5 Rev. 1487. The anisotropy of these fluxes is indicated in the bottom trace (Ref. 9)

the satellite's magnetic alignment they were always well outside the satellite's wake. Schematics of the ion and electron SEA's, given in Figure 3, show that both detectors consist of 1-in. diameter solid collectors surrounded by two wire-mesh grids. The potentials of the collectors of the ion and electron probes were set at -2000 V and +100 V, respectively. The outer grid of the ion SEA is grounded and the inner grid is held at +28 V with respect to satellite ground, thus filtering ions with energies less than 28 V. The electron sensor grids are electrically connected and operate sequentially in two modes, each of 15.9-sec duration. In Mode 1 the grids are set at +6 V. This positive resting bias was

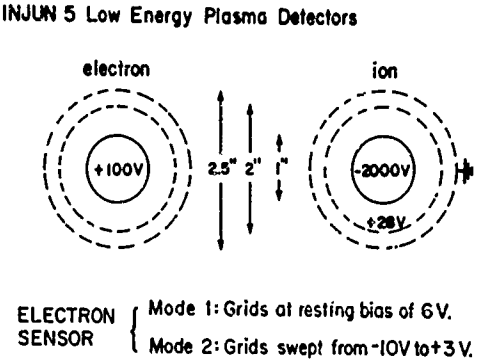

Figure 3. Schematic of the Electron and Ion Spherical Electrostatic Analyzers on INJUN 5 (Ref. 10)

intended to counteract expected negative satellite potentials. In Mode 2 the grids are swept from -10 to +3 V. Operating in these modes, we are normally able to measure the ambient electron temperature and density, the satellite potential, and the omnidirectional flux of ions with energies greater than 28 eV.

The SEA measurements for Rev 1487 are given in Figure 4. Prior to 0147 UT the satellite was in sunlight and the measurements were contaminated by sensor-related photoelectron currents. The times of the inverted-V events detected by the LEPEDEA are marked for reference. Attention is directed to measurements taken at the time of the second (10 keV) inverted-V event. We note that at this time it is impossible to distinguish between Mode 1 and Mode 2 electron measurements. This is because the collection of ambient ionospheric electrons is completely suppressed by the satellite potential. The measured flux of 2×10^9 electrons/cm^2 sec is in good agreement with that of the LEPEDEA (Figure 2). From the electron SEA measurements an upper bound of -6 V (because of the +6 Mode 1 grid bias) may be set on the vehicle potential.

During this period the omnidirectional ion flux, the upper trace in Figure 4, varied rapidly between 4×10^6 and 8×10^8/cm^2 sec. The lower value is a default level indicating that the current to the ion sensor was negative. That is, the flux of electrons with $E > 2$ keV, the ion-collector potential, exceeded the total ion flux with $E > 28$ eV. The peak flux of 8×10^8/cm^2 sec is due to ambient ions being accelerated to the sensor by a spacecraft potential < -28 V. A value of -50 V can be set as a tentative lower bound on the potential. There are 117 positive-ion energies sampled in the range $50 \text{ eV} \leq E \leq 15$ keV. It is unlikely that an ion flux of 8×10^8/cm^2 sec would pass undetected. If the ion current were highly directional it is possible that a misdirected LEPEDEA would not see the streaming ions. The SEA provides no directional information.

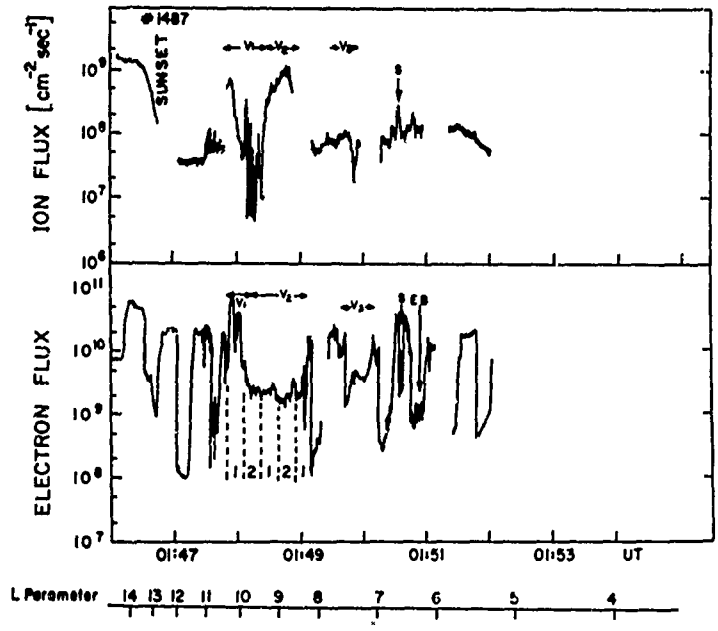

Figure 4. Omnidirectional Fluxes of Ions and Electrons Measured by the AFGL Spherical Electrostatic Analyzers During Rev. 1487. The times during which INJUN 5 passes through inverted-V events are marked for reference

The satellite potential adjusts itself so that the total current to the vehicle is zero. The precipitating electron flux is $\sim 2.5 \times 10^9/\text{cm}^2$ sec. In the absence of an electron flux to the ion sensor the measured ion flux would be equal to the electron flux. The electron flux to the negatively biased ion sensor collector (-2 kV) is

$$\phi_{e,i} = 2.5 \times 10^9 \, e^{-qV/kT_e} \, ,$$

where $\phi_{e,i}$ is the hyperthermal electron flux to the ion sensor, V = 2000 V and kT_e = 10 keV. Thus, $\phi_{e,i} = 2 \times 10^9/\text{cm}^2$ sec. Thus, the measured ion flux should be $\phi_{net} = 2.5 \times 10^9 - \phi_{e,i} = 5 \times 10^8/\text{cm}^2$ sec. Given the uncertainty in the precipitating electron temperature in the above equation, this number compares favorably with the measured ion flux of $8 \times 10^8/\text{cm}^2$ sec.

The second topic concerns vehicle shadows. Several speakers at this workshop have pointed to the wake region as a possible locus of severe charging or ion focusing. The parametrization of the ratio of ram-to-wake ionic currents

measured by driftmeters on S3-2 has been discussed by Samir and coworkers.[11] Some caution must be exercised in applying these results to polar-orbiting shuttles. The most ion-depleted region near low inclination shuttles should be in the anti-ram direction. This is not necessarily true at high latitudes for shuttles in polar orbit. Besides the driftmeters S3-2 was also equipped to measure ambient electric fields using a double probe system.[12] Typically, auroral electric fields have intensities of a few tens of mV/m. On occasion meridionally directed electric fields with intensities of several hundred mV/m have been measured in the altitude range 250 to 1550 km.[13,14] The $\vec{E} \times \vec{B}$ plasma drifts produced by such fields are zonal, that is, at right angles to the satellite's velocity. In commonly used units the magnitude of the drift is

$$V(m/s) = 10\, E(mV/m)/B(G) \quad .$$

For a magnetic field in the polar ionosphere of 0.4 G and an electric field strength of 200 mV/m the $\vec{E} \times \vec{B}$ drift speed is 5 km/sec. This is a significant fraction of the satellite velocity of 7.5 km/sec. There are several occasions when the double probe measured intense electric fields and the driftmeter was facing toward the nominal ram direction. Unpublished measurements show that under these circumstances currents to one or several sensors fell below the level of detectability. Because of strong $\vec{E} \times \vec{B}$ drifts, sensors looking $\sim 40^{\circ}$ away from the nominal ram direction were in the satellite's effective wake.

A final topic that we touch upon briefly concerns satellite current leakage. Our unsought-for-experience was gained while trying to analyze ionospheric plasma measurements from the first SSIE[15] (Special Sensor for Ions and Electrons) flown on the DMSP/F2 spacecraft. As sketched in Figure 5 the SSIE

11. Samir, U., Wildman, P.J., Rich, F., Brinton, H.C., and Sagalyn, R.C. (1981) About the parametric interplay between ionic Mach number, body size and satellite potential in determining the ion depletion in the wake of the S3-2 satellite, J. Geophys. Res. 86:11161.

12. Burke, W.J., Hardy, D.A., Rich, F.J., Kelley, M.C., Smiddy, M., Shuman, B., Sagalyn, R.C., Vancour, R.P., Wildman, P.J.L., and Lai, S.T. (1980) Electrodynamic structure of the late evening sector of the auroral zone, J. Geophys. Res. 85:1179.

13. Rich, F.J., Burke, W.J., Kelley, M.C., and Smiddy, M. (1980) Observations of field-aligned currents in association with strong convection electric fields at subauroral latitudes, J. Geophys. Res. 85:2335.

14. Burke, W.J. Electric fields, Birkeland currents and electron precipitation in the vicinity of discrete auroral arcs, in Physics of Auroral Arc Formation, ed. by S.-I. Akasofu and J.R. Kan, Geophysics Monograph 25, American Geophysical Union, Washington, D.C., 164-172.

15. Smiddy, M., Sagalyn, R.C., Sullivan, W.P., Wildman, P.J.L., Anderson, P., and Rich, F. (1978) The Topside Ionosphere Plasma Monitor SSIE for the Block 5D/Flight 2 DMSP Satellite, AFGL-TR-78-0071, AD A058503.

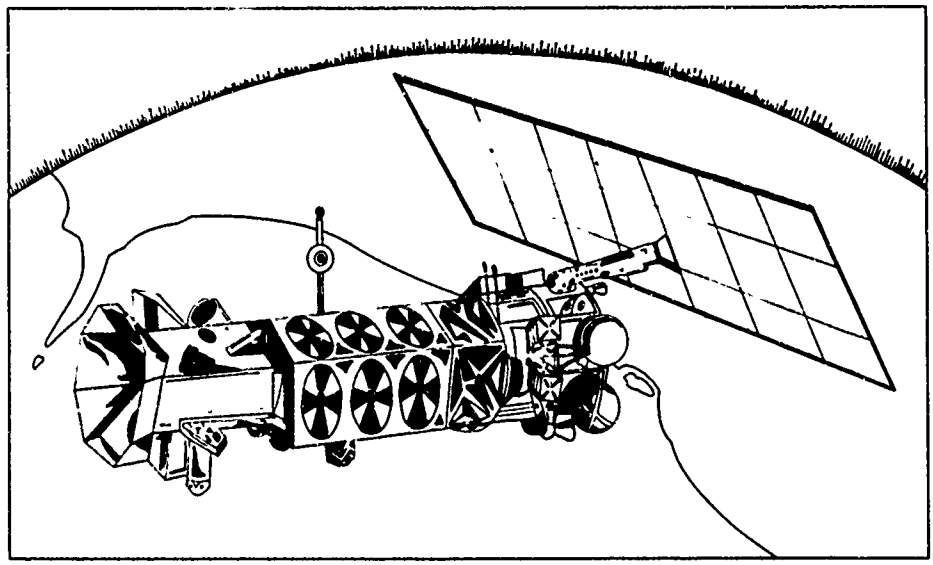

Figure 5. Schematic of AFGL Electron and Ion Probes (SSIE) on DMSP/F2 (Ref. 11)

consists of boom-mounted spherical and planar electrostatic analyzers. The gridded spherical analyzer operates in a two-mode sequence, similar to that of INJUN 5, to measure the density and temperature of ionospheric electrons. The planar sensor is a retarding potential analyzer designed to measure the densities and temperatures of the ionic components. This sensor has a surface normal directed along the direction of the 3-axis stabilized satellite's velocity. The satellite was launched into an orbit in the 0700 to 1900 local time meridian. The orbital plane then drifted at a rate of 1 h/yr toward later local times.

Data retrieved during the early post-launch period showed the ion sensor to be working as expected. However, except during the extreme positive excursions of the electron sensor sweep only unexpectedly low currents were measured. Housekeeping data indicated nominal sensor operations. It was not until the orbit precessed enough to carry the satellite occasionally into the Earth's shadow that the mystery resolved itself. Within the Earth's shadow the electron sensor provided densities and temperatures in ranges that were expected from previous satellite measurements. The villains were, of course, +28 V connectors exposed on the backs of solar panels. Although the collecting areas of the exposed positive potentials were small they were sufficient to attract enough electrons to drive the satellite potential to almost -28 V. The problem was fixed by spraying dielectric

sealants on the backs of the DMSP/F4 solar panels. The experience does provide a salutary warning that in going to high-power space systems special care must be taken to anticipate and close off all possible current paths between the satellite and the environmental plasma.

References

1. Mozer, F.S., Cattell, C.A., Hudson, M.K., Lysak, R.L., Temerin, M., and Torbert, R.B. (1980) Satellite measurements and theories of low altitude auroral particle acceleration, Space Sci. Rev. 27:155.
2. Lin, C.S., and Hoffman, R.A. (1979) Characteristics of the inverted-V event, J. Geophys. Res. 84:1514.
3. Frank, L.A., and Ackerson, K.L. (1971) Observation of charged particle precipitation into the auroral zone, J. Geophys. Res. 76:3612.
4. Frank, L.A., and Ackerson, K.L. (1972) Local time survey of plasma at low altitudes over the auroral zone, J. Geophys. Res. 77:4116.
5. Akasofu, S.-I. (1964) The development of the auroral substorm, Planet Space Sci. 12:273.
6. Akasofu, S.-I., Kimball, D.S., and Meng, C.-I. (1965) The dynamics of the aurora, II, Westward travelling surges, J. Atmos. Terr. Phys. 27:173.
7. Meng, C.-I., Synder, A.L., and Kroehl, H.W. (1978) Observations of auroral westward travelling surges and electron precipitations, J. Geophys. Res. 83:575.
8. Mullen, E.G., and Gussenhoven, M.S. (1982) High-Level Spacecraft Charging Environments Near Geosynchronous Orbit, AFGL-TR-82-0063, AD A118791.
9. Frank, L.A. (1975) Magnetospheric and auroral plasmas: a short survey of progress, Rev. Geophys. Space Phys. 13:974.
10. Burke, W.J., Donatelli, D.E., and Sagalyn, R.C. (1978) INJUN 5 observations of low-energy plasma in the high-latitude topside ionosphere, J. Geophys. Res. 83:2047.
11. Samir, U., Wildman, P.J., Rich, F., Brinton, H.C., and Sagalyn, R.C. (1981) About the parametric interplay between ionic Mach number, body size and satellite potential in determining the ion depletion in the wake of the S3-2 satellite, J. Geophys. Res. 86:11161.
12. Burke, W.J., Hardy, D.A., Rich, F.J., Kelley, M.C., Smiddy, M., Shuman, B., Sagalyn, R.C., Vancour, R.P., Wildman, P.J.L., and Lai, S.T. (1980) Electrodynamic structure of the late evening sector of the auroral zone, J. Geophys. Res. 85:1179.
13. Rich, F.J., Burke, W.J., Kelley, M.C., and Smiddy, M. (1980) Observations of field-aligned currents in association with strong convection electric fields at subauroral latitudes, J. Geophys. Res. 85:2335.

14. Burke, W.J. Electric fields, Birkeland currents and electron precipitation in the vicinity of discrete auroral arcs, in Physics of Auroral Arc Formation, ed. by S.-I. Akasofu and J.R. Kan, Geophysics Monograph 25, American Geophysical Union, Washington, D.C., 164-172.

15. Smiddy, M., Sagalyn, R.C., Sullivan, W.P., Wildman, P.J.L., Anderson, P., and Rich, F. (1978) The Topside Ionosphere Plasma Monitor SSIE for the Block 5D/Flight 2 DMSP Satellite, AFGL-TR-78-0071, AD A058503.

Contents

12. Interactions Between a Large Body and its Environment in a Low Polar Orbit

by

R. Grard
K. Knott
A. Pedersen
Space Science Department of ESA/ESTEC
Noordwijk, The Netherlands

Abstract

The parameters that characterize the high latitude ionosphere are reviewed. The electron current density collected by a surface is evaluated in typical environments and is compared to the emitted flux of photoelectrons. The polarity and order of magnitude of the relative surface potentials are tentatively estimated for various situations: sunlight, shadow, and eclipse. Other types of interactions encountered by large structures, such as magnetic induction effect and plasma instability triggering, are also discussed.

1. INTRODUCTION

During the past decade, the study of interactions between a body and its space environment has been exclusively focused on phenomena associated with the static electricity that may develop on the surface of satellites orbiting in the

outer magnetosphere of the Earth, for example, at geostationary altitude. The matter is important and the emphasis is justified: electrostatic charging can cause severe malfunctions to on-board electronic equipment and the geostationary orbit is used by a large number of application spacecraft. Accordingly, this topic has been the subject of dedicated experimental space programs,[1] major specialized conferences[2,3] and countless publications, as can be realized from the reference list of review papers such as those written by Garrett[4] and Whipple.[5]

Markedly different is the level of attention that has been devoted to the intrinsic situation of a rocket or a spacecraft in an ionospheric plasma. This environment is reputedly not conducive to interferences and the findings that may clarify some aspects of the interaction, such as the structure of the wake or the surface sputtering by molecular impact, could be considered somewhat academic. However, the advent of the space shuttle, the future prospects of manned space activities and the development planning of large orbiting structures have renewed interest in the environmental problems that characterize the ionosphere.

This paper reviews some of the basic mechanisms that govern the interactions between a large body and the ionospheric environment, especially in a polar orbit. First, the parameters that describe the space plasma are recapitulated; then the density of the random currents of ions and electrons collected by a body at a reference altitude of 2000 km are compared to the flux of charged particles extracted from its surface by photoemission for example, to establish the polarity and order of magnitude of electrostatic charging. Phenomena that result from the electromotive force induced by the motion of a large structure across the Earth's magnetic field are presented, and the artificial generation of various instabilities triggered by the associated plasma disturbance are discussed.[6]

---

1. Stevens, J.R., and Vampola, A.L., Eds. (1978) Description of the Space Test Program P78-2 Spacecraft and Payloads, SAMSO TR-78-24, AD A061324.
2. Pike, C.P., and Lovell, R.R., Eds. (1977) Proceedings of the Spacecraft Charging Technology Conference, NASA TMX-73537, AFGL-TR-77-0051, AD A045459.
3. Finke, C.F., and Pike, C.P., Eds. (1978) Spacecraft Charging Technology 1978, NASA Conference Publication 2071, AFGL-TR-79-0082, AD A084626.
4. Garrett, H.B. (1981) The charging of spacecraft surfaces, Rev. Geophys. Space Phys. 19:577.
5. Whipple, Jr., E.C. (1981) Potentials of surfaces in space, Rep. Prog. Phys. 44:1197.
6. Banks, P., Ed. (1980) The Tethered Satellite System, Center for Atmospheric and Space Sciences, Utah State University, NASA Contract NAS8-3383.

2. THE IONOSPHERIC PLASMA

At altitudes less than about 800 km the electron density distribution is primarily a function of solar illumination and, in first approximation, does not otherwise display any marked latitudinal dependence. Above 1500 km, however, the features of the space plasma are clearly related to those of the whole magnetosphere, as illustrated in the noon-midnight meridian cross-section of Figure 1.

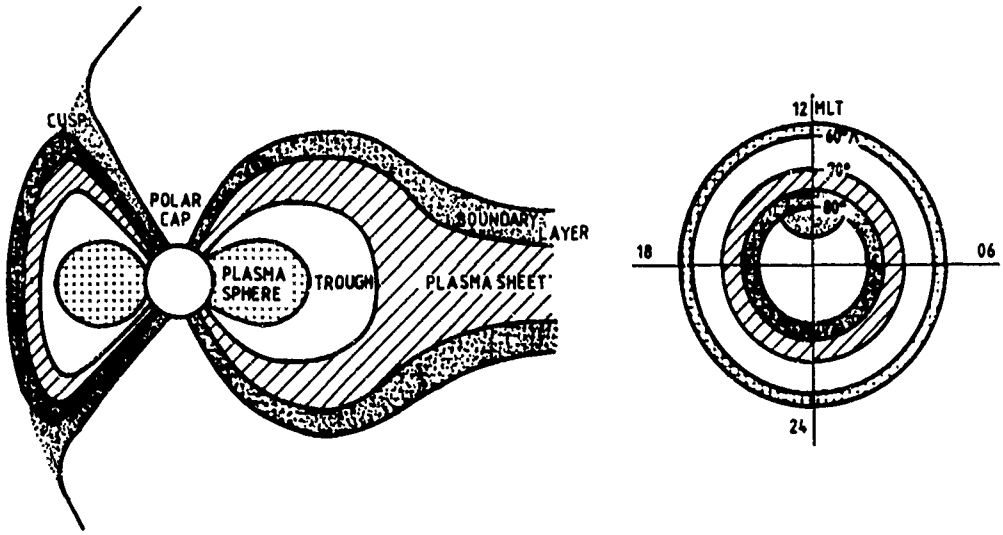

Figure 1. Schematic Cross-section of the Magnetosphere in the Noon-midnight Meridian Plane (Not to Scale) and Approximate Mapping of These Regions in the Ionosphere [Magnetic Local Time (MLT) vs Invariant Latitude Λ]

Several plasma regions can be identified along a low-altitude polar orbit ($\simeq$ 1000 km). The plasmasphere is bounded by an invariant magnetic latitude of 60°. In the mid-latitude ionosphere the plasma is relatively dense and cold ($\lesssim$ 1 eV). The plasma trough lies between the plasmapause and the auroral zone, which is linked to the plasma sheet and the boundary layer. The regions at higher latitudes, the polar cap and cusp, are connected to open magnetic field lines and to the magnetopause.

Outside the plasmasphere and at altitudes below 3000 km, the probability of observing a plasma density less than $100/cm^3$ is of the order of 0.12 as measured with the Alouette satellites;[7] values as low as 8 to $30/cm^3$ are not exceptional.

7. Nelms, G. L., and Chapman, J. H. (1970) The high latitude ionosphere: results from the Alouette/Isis topside sounders in The Polar Ionosphere and Magnetospheric Processes, G. Skovli, Ed., Gordon and Breach, New York, p. 233.

In the boundary layer and in the plasma sheet, electron populations with respective mean kinetic energies of the order of 0.1 and 1 keV have been detected with HEOS-2 from the magnetopause and outer magnetosphere down to the ionosphere.[8] During magnetically disturbed conditions, an increased precipitation of high energy particles at the auroral latitude causes an enhancement of ionospheric ionization by collision. Densities of the order of $10^4/cm^3$ are typical at an altitude of 1000 km.[9]

The ionospheric electron thermal energy is relatively invariant with latitude and a typical value of 0.3 eV can be assumed.[10]

3. CHARGED PARTICLE EXCHANGE BETWEEN A BODY AND ITS ENVIRONMENT

The density n of the plasma encountered by a spacecraft in a circular polar orbit at a reference altitude of 2000 km can vary by at least 3 orders of magnitude, as illustrated in Table 1.

Table 1. Orders of Magnitude of Plasma Parameters at Various Latitudes for an Altitude of About 2000 km. The approximate magnitude of the surface potential is also indicated for different degrees of solar irradiation

Latitude	n (cm^3)	$e\phi_e$ (eV)	J_e ($\mu A/m^2$)	Surface potential (V)		
				Eclipse	Shadow	Sunlight
Mid-latitude	10^4	0.3	150	-1	-1	-1
Trough, polar cap						
typical	100	0.3	1.5	-1	+2	+4
minimum	10	0.3	0.15	-1	+5	+8
Auroral zone						
ionospheric	10^3	0.3	15	-1	0	+1
plasma sheet	10?	1000	8	-3000?	0	+1

8. Formisano, V. (1980) HEOS-2 observations of the boundary layer from the magnetopause to the ionosphere, Planet Space Sci. 28:245.

9. Thomas, J.O., and Andrews, M.K. (1970) The polar exospheric plasma, in The Polar Ionosphere and Magnetospheric Processes, G. Skovli, Ed., Gordon and Breach, New York, p. 225.

10. Bauer, S.J. (1970) Temperature and composition studies in the polar ionosphere, in The Polar Ionosphere and Magnetospheric Processes, G. Skovli, Ed., Gordon and Breach, New York, p. 161.

The electrons from ionospheric origin have a relatively low energy ($e\phi_e < 1$ eV); those which are observed in the auroral zone during disturbed conditions and which are precipitated from the plasma sheet are much more energetic ($e\phi_e \simeq$ 1 keV). The random electron current density, J_e, can be as low as a fraction of 1 $\mu A/m^2$ or larger than 100 $\mu A/m^2$.

The equilibrium potential of a body in eclipse is reached when the ambient electron and ion currents collected by its surface are equal; it is a matter of common knowledge that the polarity of this potential is negative and that its magnitude is a direct function of the electron mean kinetic energy.[4] This potential is therefore of the order of -1 V, except possibly at the auroral latitude and during disturbed conditions. If the flux of electrons that are precipitating from the plasma sheet predominates over that of electrons that are created in the ionosphere by photoionization or by collisions, the potential may reach negative values of the order of 1 kV. This situation however, if it is met, should not last for more than 2 min at a time, since this is the duration required for a spacecraft to cross a zone that extends over 10^o in latitude.

The photoelectron current density emitted from a surface in sunlight is of the order of 20 $\mu A/m^2$ under nominal solar irradiation.[11] At a 2000-km altitude and at latitudes higher than 60^o, a surface will develop a positive charge and will reach a potential larger than that of its immediate environment by a few volts.

A surface in shadow, that is, not directly exposed to the sun, is still illuminated by the earth albedo; it is indeed estimated that about 30 percent of the sun's energy is reflected in the short wavelength range by the clouds, the atmosphere and the surface of the Earth. It may therefore be anticipated that a moderate photoemission level, of the order of .6$\mu A/m^2$, will prevent a surface in shadow from acquiring a negative charge in the polar ionosphere.

4. MAGNETIC INDUCTION EFFECTS

The electric field measured by a satellite in motion with respect to the ambient plasma is given by the vector product of the orbital velocity and magnetic field ($\vec{E} = \vec{V} \times \vec{B}$). The magnitude of the electric field is shown in Figure 2 for two types of low circular orbit. The strength of the field is constant for a satellite orbiting in the magnetic equatorial plane; it is maximum at the magnetic poles for a satellite moving in a magnetic meridian plane.

---

11. Grard, R.J.L. (1973) Properties of the satellite photoelectron sheath derived from laboratory measurements, J. Geophys. Res. 78:2885.

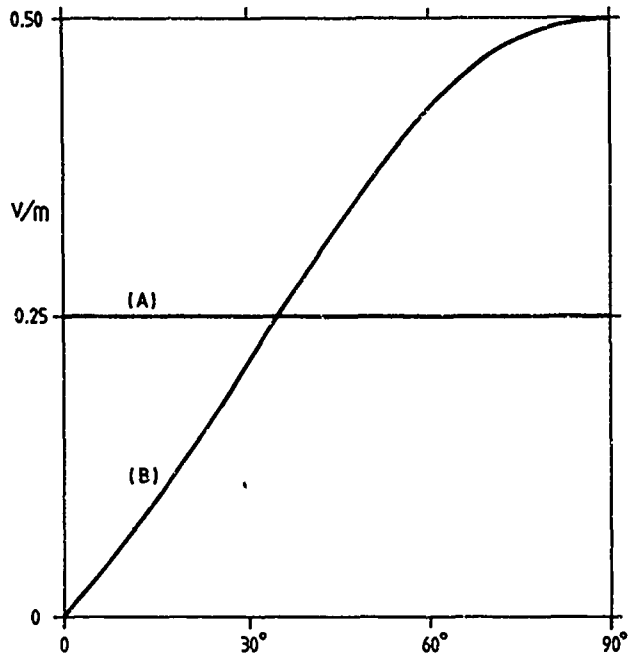

Figure 2. Electric Field Induced in a Structure Along a Low Altitude Circular Orbit: (A) in the Magnetic Equatorial Plane and (B) in a Magnetic Meridian Plane

The induced voltage will never be larger than 10 V if the dimensions of the structure do not exceed 20 m. However, voltage differences of several kV are possible if, for example, a 10-km long tether is unrolled.

Figure 3 illustrates how the electric equilibrium is reached when two electrically connected bodies are moving with respect to a magnetized plasma. The current-voltage characteristics (I vs ϕ) of each of the two bodies are represented by the curves labelled I_1 and I_2; the individual floating potentials are respectively ϕ_{F1} and ϕ_{F2}. The potentials reached by the two bodies ϕ_1 and ϕ_2, when they are linked by a conductive tether of length L, are such that $I_1 = I_2 = I_o$ and $EL = \phi_2 - \phi_1$.

In the example shown in Figure 3, body number 2 has the most stable potential because it is positively biased and it has the largest conductive surface area ($dI_2/d\phi > dI_1/d\phi$). The stability of a surface element held at a positive or a negative potential can be further improved by the artificial emission of ions or electrons, respectively.

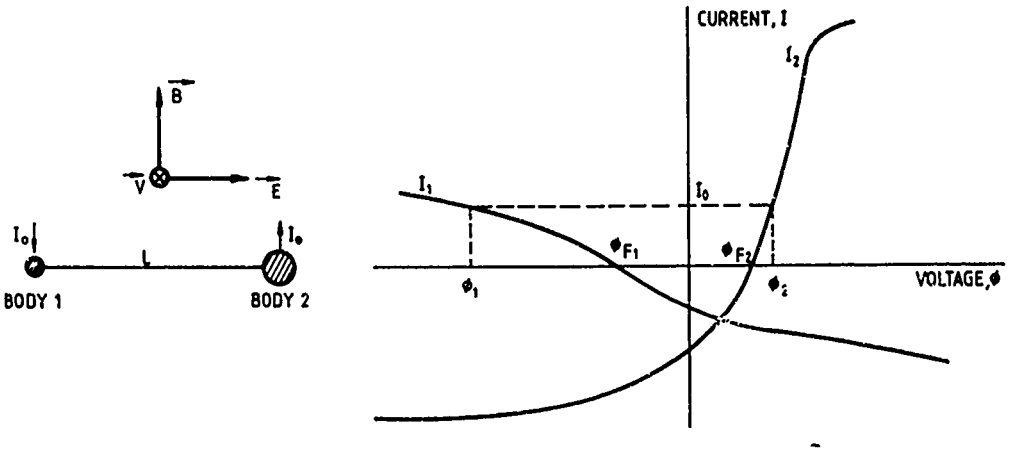

Figure 3. The Equilibrium Potential of a Two-body System in Motion With Respect to the Ambient Plasma; the Tether Provides the Electric Connection Between the Two Bodies but is Insulated From the Plasma Environment

5. PLASMA DYNAMIC ASPECTS

The plasma dynamics phenomena associated with a large orbiting body have been investigated by Drell et al,[12] and Chu and Gross;[13] the study of a tethered satellite system as a shuttle facility has cast a new light on the importance of these problems.[6]

The currents emitted and collected by different elements of a large polarized body spread along separated field lines; these charged sheets are commonly called Alfvèn wings. The current loop closes at a distance that is a function of the size of the body and of the efficiency of cross-field diffusion, as illustrated in Figure 4.

The two flux tubes form a transmission line across which the potential induced in the body is applied. One magnetic field line is in contact with the orbiting structure for a time which is limited to L/V, where L is the size of the body and V is the orbital velocity. This transient signal has a duration of the order of a few milliseconds, which limits the lowest frequency of the signal that can be excited to about 100 Hz.

The field-aligned currents also disturb the velocity distribution of the ambient charged particles. Electrostatic and electromagnetic waves may be triggered if the current intensity is sufficiently large.

---

12. Drell, S.D., Foley, H.M., and Ruderman, M.A. (1965) Drag and propulsion of large satellites in the ionosphere: an Alfvèn propulsion engine in space, J. Geophys. Res. 70:3131.

13. Chu, C.K., and Gross, R.A. (1966) Alfvèn waves and induction drag on long cylindrical satellites, AIAA J. 4:2209.

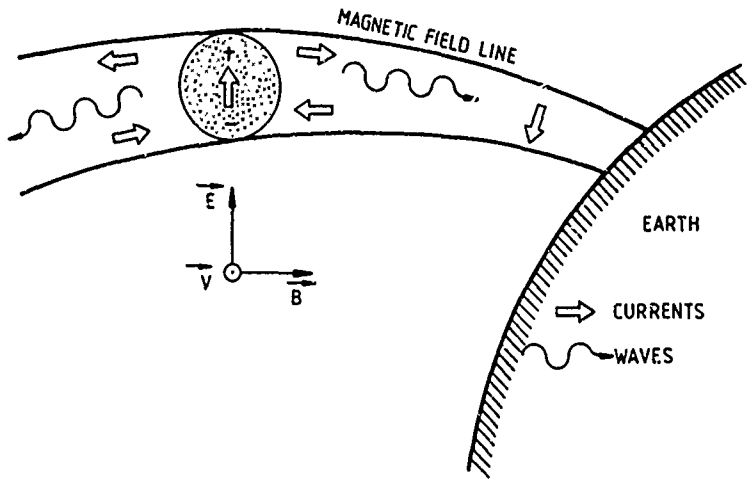

Figure 4. Dynamic Interaction Between a Large Orbiting Structure and the Magnetized Plasma Environment

It must be noted, parenthetically, that a number of simple active experiments can be performed from a large orbiting structure that can be used as an antenna for radiating very low frequency waves, for example. This property may have interesting applications for specialized communication purposes.

6. CONCLUSION

The electrostatic charging problems encountered by a spacecraft on a low polar orbit may not be as drastic as those met by geostationary satellites. However, high surface potentials may develop in eclipse, at altitudes above 2000 km, when the spacecraft crosses the magnetically conjugate zone of the plasma sheet. In-situ measurements of the thermal and energetic (1 keV) plasma fluxes will assess the importance of this threat and the probability of its occurrence. The magnitude of differential charging between sunlit and shadowed surfaces is somewhat limited by the Earth albedo.

Phenomena specific to large structures are generated by the interaction with the environment. The effect of potential differences induced by magnetic induction must be considered with care for bodies with dimensions of several hundred meters; large negative potentials will accelerate ambient particles and be responsible for ion surface bombardment, for example. Other dynamic processes, such as the triggering of plasma wave instabilities, do not cause any practical drawback but present inherently interesting scientific aspects.

References

1. Stevens, J.R., and Vampola, A.L., Eds. (1978) Description of the Space Test Program P78-2 Spacecraft and Payloads, SAMSO TR-78-24, AD A061324.
2. Pike, C.P., and Lovell, R.R., Eds. (1977) Proceedings of the Spacecraft Charging Technology Conference, NASA TMX-73537, AFGL-TR-77-0051, AD A045459.
3. Finke, C.F., and Pike, C.P., Eds. (1978) Spacecraft Charging Technology 1978, NASA Conference Publication 2071, AFGL-TR-79-0082, AD A084626.
4. Garrett, H.B. (1981) The charging of spacecraft surfaces, Rev. Geophys. Space Phys. 19:577.
5. Whipple, Jr., E.C. (1981) Potentials of surfaces in space, Rep. Prog. Phys. 44:1197.
6. Banks, P., Ed. (1980) The Tethered Satellite System, Center for Atmospheric and Space Sciences, Utah State University, NASA Contract NAS8-3383.
7. Nelms, G.L., and Chapman, J.H. (1970) The high latitude ionosphere: results from the Alouette/Isis topside sounders in The Polar Ionosphere and Magnetospheric Processes, G. Skovli, Ed., Gordon and Breach, New York, p. 233.
8. Formisano, V. (1980) HEOS-2 observations of the boundary layer from the magnetopause to the ionosphere, Planet Space Sci. 28:245.
9. Thomas, J.O., and Andrews, M.K. (1970) The polar exospheric plasma, in The Polar Ionosphere and Magnetospheric Processes, G. Skovli, Ed., Gordon and Breach, New York, p. 225.
10. Bauer, S.J. (1970) Temperature and composition studies in the polar ionosphere, in The Polar Ionosphere and Magnetospheric Processes, G. Skovli, Ed., Gordon and Breach, New York, p. 161.
11. Grard, R.J.L. (1973) Properties of the satellite photoelectron sheath derived from laboratory measurements, J. Geophys. Res. 78:2885.

12. Drell, S.D., Foley, H.M., and Ruderman, M.A. (1965) Drag and propulsion of large satellites in the ionosphere: an Alfvèn propulsion engine in space, J. Geophys. Res. 70:3131.

13. Chu, C.K., and Gross, R.A. (1966) Alfvèn waves and induction drag on long cylindrical satellites, AIAA J. 4:2209.

13. Observations of Differential Charging with Meteostat

by

A. D. Johnstone
G. L. Wrenn
Department of Physics and Astronomy
University College London

The behavior of the geosynchronous Meteosat spacecraft in the Earth's shadow throws new light on the topic of the influence of secondary electron emission on differential charging, which could assist our understanding of these processes in more general situations.

Meteosat F1, a geosynchronous meteorological satellite operated by the European Space Agency, suffered from a number of non-damaging operational anomalies that were attributed to electrostatic discharges caused by differential charging. The second flight model F2 was modified in several ways to reduce its susceptibility to arcing. In addition, two new sensors were included in the payload to monitor the plasma environment and to detect the electrical effects of discharges. Since launch in June 1981 the spacecraft has experienced only a few anomalies attributable to arcing and no electrostatic discharges have been detected by the monitor although that could be a matter of sensitivity. So far the only evidence for the spacecraft charging to significant potentials occurs during eclipse and comes from the plasma environment monitor.

The plasma environment monitor, an SSJ/3 electron detector provided by AFGL, consists of a pair of channel electron multiplier detectors with electrostatic analyzers that step in parallel through the energy ranges 50 eV to 1 keV and 1 to 20 keV. They were mounted to view at 45° to the spacecraft spin axis to avoid exposure to direct sunlight. Since the spin rate is 100 rpm and the detector integration period is 12.5 sec, no information is obtained about the pitch angle distribution. Using data from both detectors, a 16-point energy spectrum is obtained in 100 sec.

Its typical behavior during an eclipse is shown in Figure 1. The most obvious feature, and a most unusual one, is the sharp peak in the energy spectrum at an energy that increases from below the bottom of the instrument's energy range up to the energy channel centered at 640 eV. The width of the peak is much less than the spacing between adjacent steps in the detector spectrum. If we make the assumption that the energy of the peak increases uniformly and maintains the same intensity then the full width at half maximum can be calculated to be 50 eV.

The only explanation of the peak to come to mind is that it is the result of secondary emission from an adjacent spacecraft surface at a more negative potential than the detector, which is grounded to the spacecraft frame. These secondary electrons are attracted by the potential of the detector and collected before they can escape from the spacecraft.

Their escape from the spacecraft depends on its potential, which can be estimated from the shift in electron velocity distribution as it charges up. In practice, because the ambient electron distribution varies, frequently a clearer indication of the spacecraft potential is obtained at the exit from eclipse when the spacecraft rapidly returns to a small positive potential. In Figure 1 there is an increase in intensity over the entire energy range above the secondary emission peak as the spacecraft emerges into the sunlight once more. Figure 2 compares the energy distribution before and after this transition in spectra obtained 5 min apart. The ordinate of the plot is J(E)/E, which is proportional to phase space density. The "before" or dark spectrum is shifted almost uniformly to lower energies by an average of 4.7 keV relative to the "after" or sunlit spectrum implying that the detectors were at a potential of -4.7 kV relative to space. If this potential extends over a distance of the order of a Debye length, which is greater than 200 m in these conditions, then the electric field between the two spacecraft surfaces, say 0.5 m and 650 V apart, could well dominate and direct secondary electrons to the surface at the more positive potential.

Since the charging process here is controlled by secondary emission there should be differences in the response as the electron intensity and spectrum changes. Figure 3 shows an example of an eclipse where no negative charging

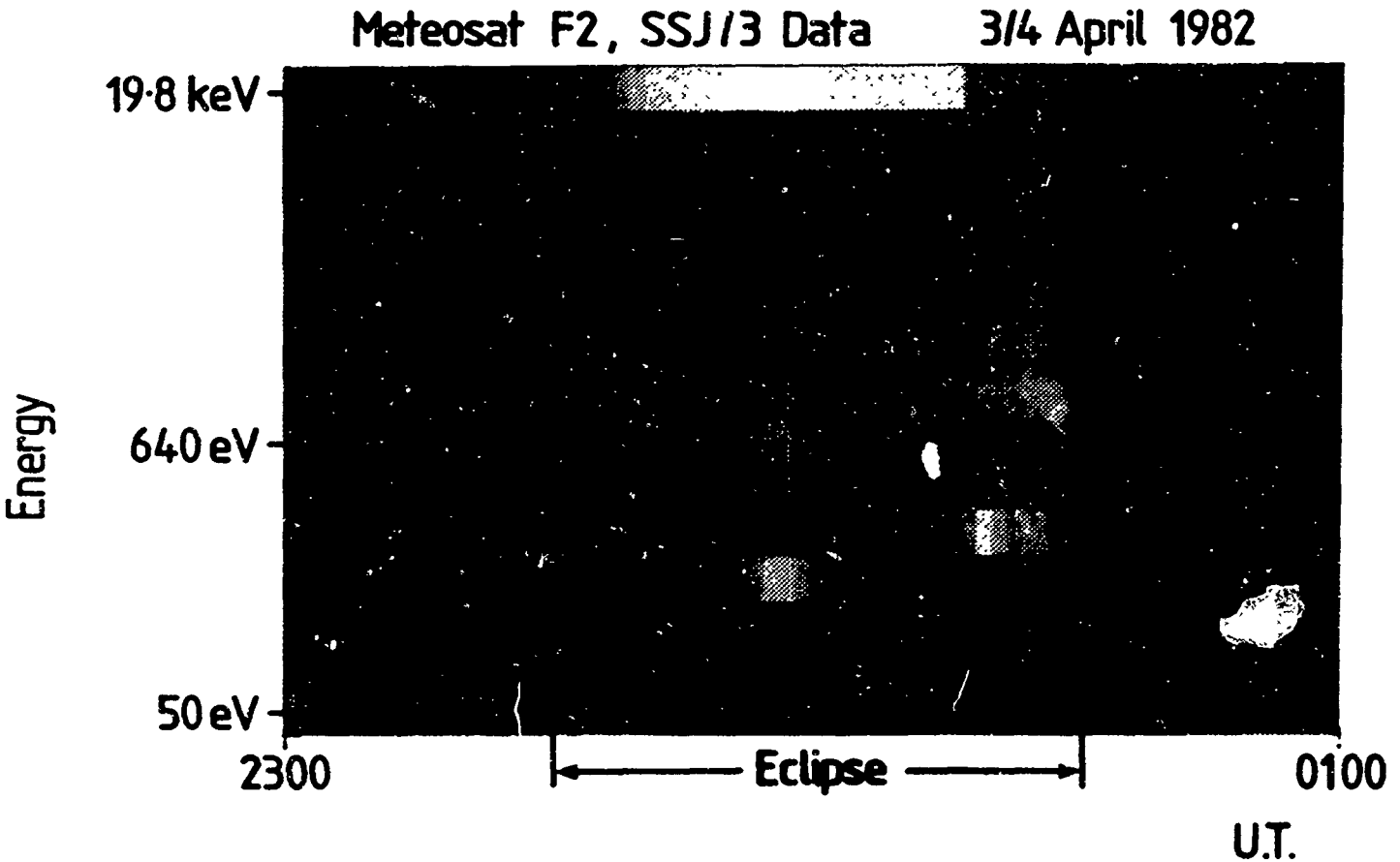

Figure 1. An Energy/Time Spectrogram of Log (Electron Intensity/(cm^2 sr keV·sec)) for a 2-h Period Centered on an Eclipse. Black indicates high intensity. The spacecraft immediately charges negatively when the eclipse begins. The sharp peak in the spectrum at a gradually increasing energy is the result of secondary emission from a surface at a more negative potential

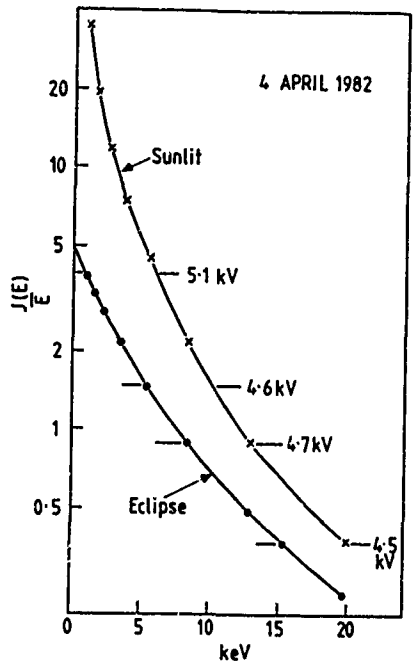

Figure 2. Two Spectra Taken 5 min Apart, Before and After the End of the Eclipse in Figure 1. The ordinate is proportional to phase space density in units of $cm^{-2}\ sr^{-1}\ sec^{-1}$. If the ambient electron spectrum is the same in both cases then the horizontal separation indicates the potential difference

occurred, and where there is no sign of the peak that results from differential charging. The spectrum remains nearly constant throughout the eclipse and with no sign of a change in potential as the spacecraft comes out of eclipse. In Figure 4 the spectrum at the beginning of this eclipse is compared with the spectrum at the beginning of the eclipse in Figure 1. In the energy channels up to and including the one at 2.3 keV the electron intensity in the second, non-charging, case is actually slightly greater. At higher energies the electron intensities in the first example are much higher. The essential difference between the two spectra is that in the charging example there are many more high energy electrons. There may, of course, be differences in other particle distributions not measured by the instrument on Meteosat that are responsible for the difference in behavior. However, the same change is found in another example (Figure 5) where the electron spectrum hardens during an eclipse and charging begins. The spectrogram shows that the secondary emission peak signalling the occurrence of

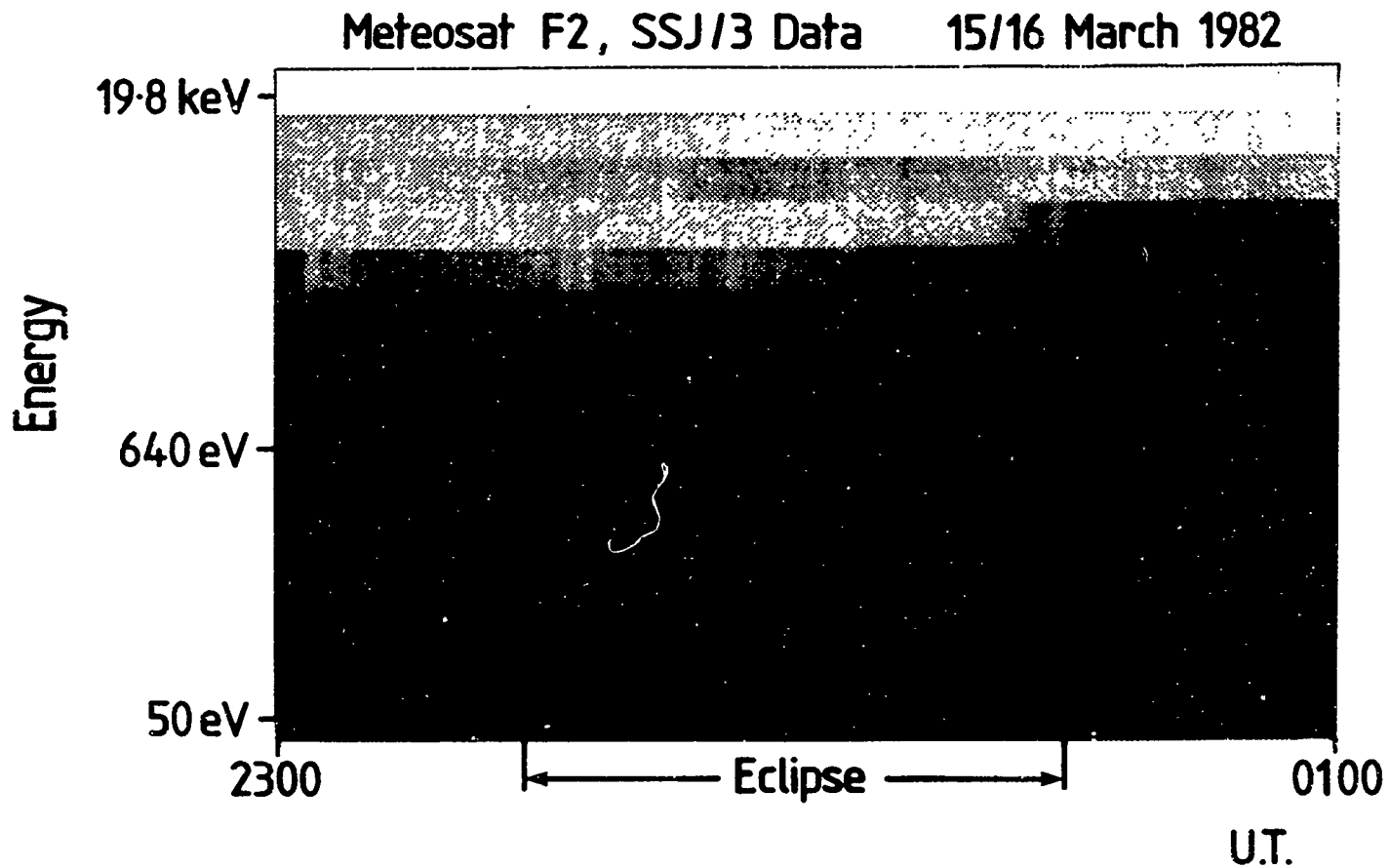

Figure 3. A Spectrogram of an Eclipse (Similar to that in Figure 1) During Which There was no Change in Spacecraft Potential

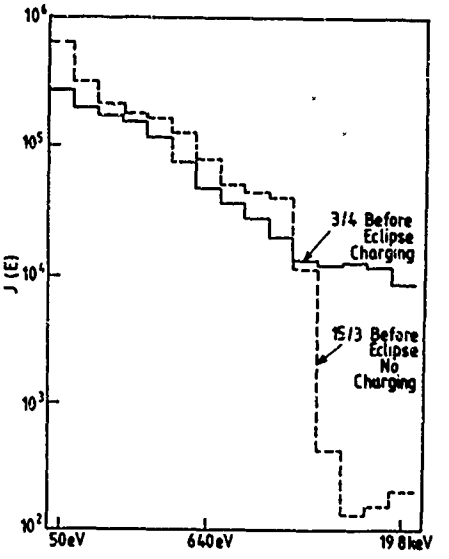

Figure 4. A Comparison of Spectra Taken Before the Eclipses in Figure 1 (3/4) and Figure 3 (15/3)

charging appears when the intensity at high energies increases. The change in spectrum responsible for the onset of charging is illustrated in Figure 6 with two spectra, one taken before the eclipse, and the other immediately after to avoid any possible effect of charging. These two spectra are therefore taken some time before and after the actual transition but are still close to the actual spectra as the spectrogram in Figure 5 shows. Again it shows that charging is initiated by an increase in the intensity of high energy electrons.

The situation during the eclipse of Figure 1 is summarized in Figure 7. On the spacecraft there are two surfaces, one at a potential of -5.3 kV, and the other, on which the detector is mounted, at a potential of -4.7 kV. The difference in potential is the result of different secondary emission characteristics for the two surfaces. A number of interesting conclusions can be drawn from these observations.

Figure 5 shows what seems to be the first observed example of a change from a triple to single root current/voltage characteristic predicted by several authors[1] (Figure 8) when, as the consequence of a small or gradual change in the ambient spectrum, there is a large change in the spacecraft potential. The extra high energy electrons produce little secondary emission and start to charge

1. Prokopenko, S.M.L., and Laframboise, J.G. (1980) J. Geophys. Res. 85:4125.

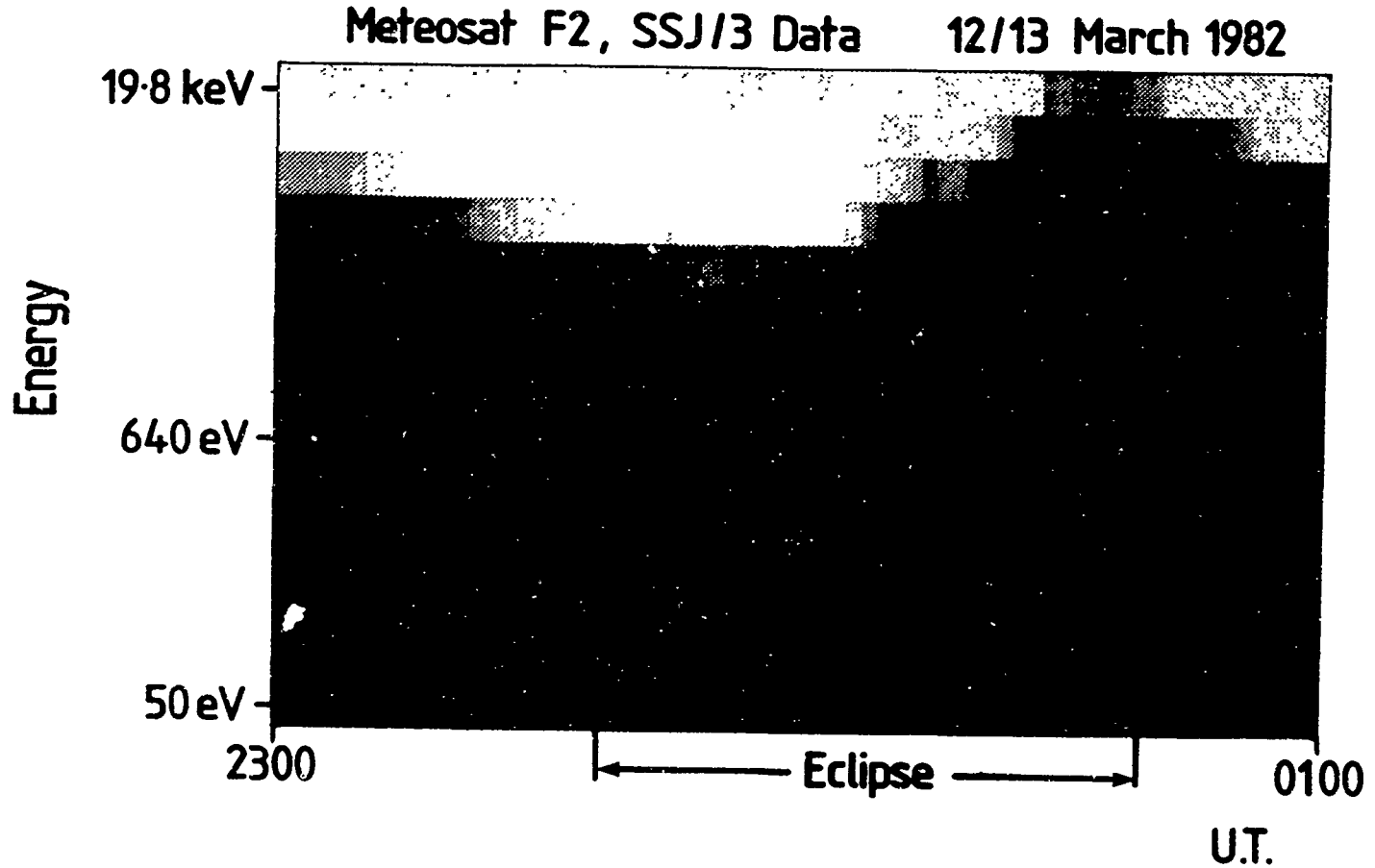

Figure 5. In This Eclipse Charging Starts Towards the End of the Eclipse When the High Energy Intensity Increases

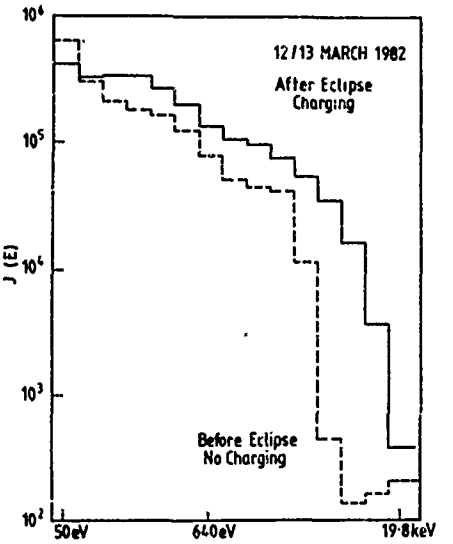

Figure 6. A Comparison of Spectra Taken Before (Dashed Line) and After (Solid Line) the Eclipse in Figure 5

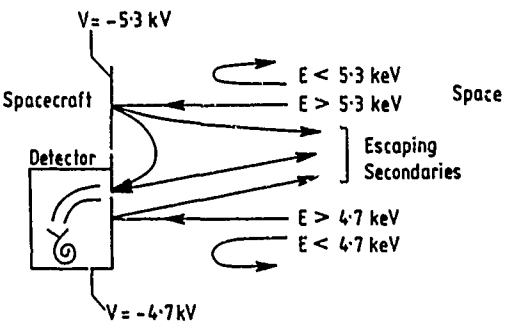

Figure 7. A Diagram Illustrating the Types of Electron Trajectory Thought to be Responsible for the Observations in Figure 1

the spacecraft negatively. This immediately reduces the flux of electrons in the 50 eV to 1 keV energy range at the spacecraft surface that produce the most secondary emission. The resulting reduction in the outward flux of secondary electrons sends the spacecraft even more negative.

The charging process can be described more precisely with reference to the three current/voltage characteristics for the spacecraft shown in Figure 8. The top one shows the characteristics, including the photoemission current that is

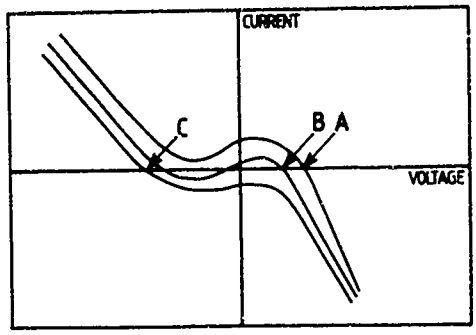

Figure 8. Three Schematic Current/ Voltage Characteristics for a Geosynchronous Spacecraft. The top one corresponds to the sunlit situation; the middle one to an eclipse when the spacecraft remains at a low potential; the bottom one causes the spacecraft to charge negatively in eclipse

applicable to the spacecraft before it enters eclipse. The only root at A (where the net current to the spacecraft is zero) is at a small positive voltage. Removing the photoemission current when going into eclipse gives the middle characteristic that has three roots, the central one being unstable. The spacecraft makes a gradual transition to the positive root at B. As the spectrum changes, with the addition of more high energy electrons, the characteristic takes the shape of the lower characteristic which only has a single root at C for current balance at a high negative potential to which the spacecraft quickly goes. Thus a gradual small change in the electron spectrum leads to a sudden large change in the spacecraft potential.

The behavior of the secondary emission peak shows how differential charging is controlled by the secondary emission properties of the surfaces involved.

The shape of a typical secondary emission yield curve is shown in Figure 9. The yield is greater than unity from a primary energy of 50 eV up to nearly 700 eV in this case. The initial difference between the two spacecraft surfaces occurs because their respective yields are different. The surface with the lower secondary emission yield will charge negatively more quickly. When the difference exceeds 50 V, the more positive surface, on which the detector is mounted, acts as the first dynode in an electron multiplier so that the net emission of electrons from the more positive surface is actually increased. This differs from the situation envisaged by Katz and Mandell[2] where they assume that the effect of

2. Katz, I., and Mandell, M.J. (1982) J. Geophys. Res. 87:4533.

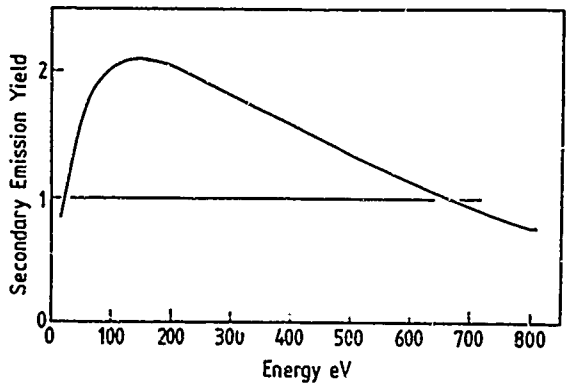

Figure 9. A Typical Secondary Emission Yield Curve

differential charging potentials is to suppress secondary emission from the positive surface and to aid the escape of the electrons from the negative surface. They do not include the current of electrons from the negative to positive surface. If secondary emission from the positive surface were suppressed in this case no differential potentials could build up. Eventually the potential difference builds up to the point where the yield from the impact of secondaries on the positive surface drops back towards unity. Further increases in the voltage difference are then pegged by the decrease in the secondary emission yield with energy. A current balance is then obtained for both surfaces simultaneously. The balance for the most negative surface depends on the ambient plasma distribution and its secondary emission characteristics. The additional factor to be taken into account in the current balance of the more positive surface is the electron multiplication of the impact of secondary electrons from the more negative surface that holds the potential difference close to the second crossover in the secondary emission yield curve of the more positive surface.

Acknowledgments

We would like to thank Dr. J.G. Laframboise for clarifying our understanding of current/voltage characteristics with multiple roots.

It is a pleasure to acknowledge the efforts of Mr. A. Huber and Dr. D. Parsignault at Emmanuel College, Dr. P. Rothwell at AFGL and Mr. D. Hoge at

the ESA Earth Observations Programme Office, Toulouse, who arranged for the plasma environment monitor to be installed on Meteosat 2 at very short notice.

The work at Mullard Space Science Laboratory has been supported by ESA Contract No. 4715/81/F/CG.

Contents

14. Laboratory and Space Measurements of Materials

by

J. F. Fennell
P. F. Mizera
M. S. Leung
Space Sciences Laboratory
The Aerospace Corporation
P. O. Box 92957
Los Angeles, Calif. 90009

(Spacecraft Charging at High Altitude)

Abstract

The SCATHA data has shown that several dielectric materials responded to the space environment differently than was expected prior to launch. For example, there was a marked increase in the bulk conductivity of Kapton samples that were exposed to the sun in the space vacuum. Teflon accumulated a permanent charge, which resulted in a potential difference that increased with time between it and the satellite frame. A quartz "cloth" thermal control material was observed to charge to higher levels on orbit than was obtained in pre-launch laboratory tests. Some of the differences between the expected and observed data have been explained by laboratory tests that more accurately model the space environment.

1. INTRODUCTION

The electrical properties of spacecraft insulating materials undergo drastic changes when exposed to the particle and radiation environments in space.[1,2,3] The ability to predict how these changes occur as a function of time is needed to extend the reliability and mission life of spacecraft. In-situ space measurements from the SCATHA satellite have shown that the electrical conductivity of Kapton changed dramatically in the near-geosynchronous orbit.[3] Similarly, the charge retention of Teflon and the ability of quartz cloth thermal blankets to charge up in the near synchronous environment must be understood before using these materials on new spacecraft. A laboratory program was initiated to understand and measure the changes in Kapton[4,5] and the quartz cloth charging[1] that are caused by exposure to the space environment. The permanent charge buildup in Teflon appears to be a result of bulk charging by high energy (> 50 keV) electrons in the radiation belts.[2,3,6,7] These results are summarized in this paper to bring the last few years experiences and findings together in one place. The emphasis is placed on the Kapton studies, which are more recent.

2. OBSERVATIONS

The Satellite Surface Potential Monitor (SSPM) was an experiment payload flown on the P78-2 (SCATHA) satellite[8,9] to study the electrical behavior of typical spacecraft insulating materials in the space environment. The P78-2 satellite is a spin-stabilized satellite with its spin axis normal to the satellite-sun line. There are several material samples on board. Two Kapton samples are mounted in such a way that they rotate into and out of the sun. A third Kapton sample plus silvered Teflon and quartz fabric samples were mounted in the shadow of the spacecraft. For a description of the SSPM experiment and experimental technique the reader is referred to the Mizera[10] article.

The first discrepancy between some laboratory results and observation was the measurement of a relatively high level of charging on the quartz fabric. This fabric was mounted on Teflon backed with silver. A small hole was cut in the Teflon to expose the electric field from the fabric to a back side sensor.[10] A typical example of the SSPM sample geometry is shown in Figure 1.

Figure 2 shows the charging levels of the quartz fabric and other materials during a natural charging event on 24 April 1979. The fabric charged to over 3 kV. Laboratory measurements by Belanger and Eagles,[11] prior to SCATHA's

Because of the large number of references cited above, they will not be listed here. See References, page 212.

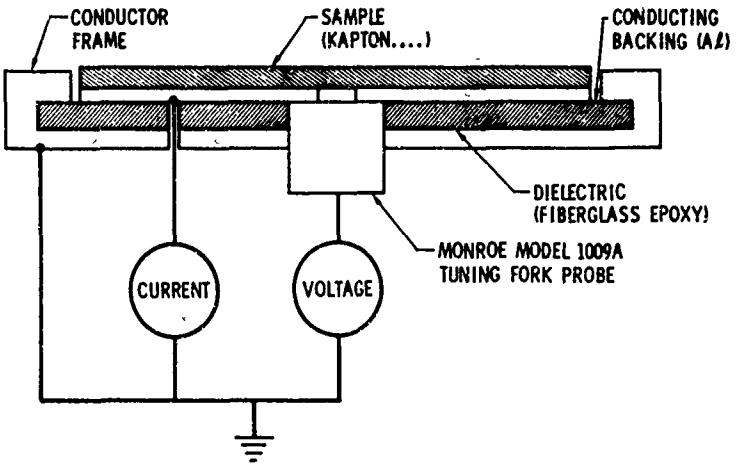

Figure 1. Schematic View of an SSPM Sample (Aluminized Kapton) Mounted on a Copper-Clad Fiberglass Board to Collect Current. The conducting backing is removed over the Monroe electrostatic field meter to permit a back surface measurement (from Ref. 1)

launch, had indicated that this material would not charge significantly above a few hundred volts in the space environment. There were also tests which indicated the fabric would indeed charge to high levels.[12] There were some doubts about both results, so that at the launch of SCATHA the science community was split in its opinion concerning whether the actual samples being flown would charge or not.

A laboratory test program was set up to find out why there was such a difference between quartz fabric charging on orbit and in the Belanger and Eagles[11] study (Mizera et al.[1]). Figure 3 shows the charging response of the quartz fabric when irradiated by a 6-keV electron beam of different current densities. As seen in the figure, there is a relationship between charging level and beam current. The lower current beams charged the sample to higher voltage for a longer period. The 0.08 nA/cm^2 beam that charged the sample to the higher value was about two orders of magnitude lower in current than the beams used in the Belanger and Eagles[11] study.

It was found that the charging level of the quartz fabric initially rose to a relatively high value with the rate of charging greater for higher incident current.

12. Stevens, N.J., Berkopec, F.D., Staskus, J.V., Blech, R.A., and Narciso, S.J. (1977) Testing of typical spacecraft materials in a simulated substorm environment, in Proceedings of the Spacecraft Charging Technology Conference, Pike and Lovell, Eds., NASA Publ. TMX-73537 and U. S. Air Force Publ. AFGL-TR-77-0051, AD A045459.

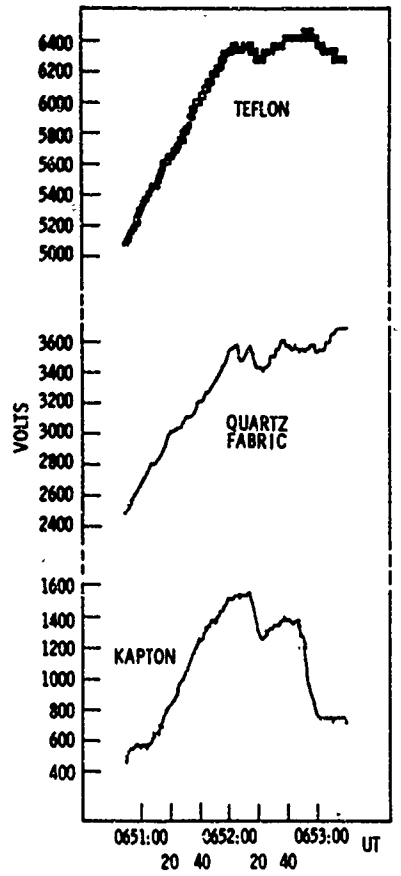

Figure 2. Kapton, Teflon, and Quartz Fabric Charging Levels on the SCATHA (P78-2) Satellite During the 24 April 1979 Charging Event (From Ref. 2)

Then, the charging level decreased to a steady-state value of a few hundred volts with the most rapid decrease occurring for the higher incident currents. Thus, Belanger and Eagles'[11] results were correct for the steady state but didn't show that the charging and discharge rate were very sensitive to incident current density. With the very low current densities experienced in the natural environment, such as the 0.1 nA/cm^2 estimated for the 24 April event, [1] the quartz fabric can charge to high levels relative to the satellite ground for significant periods of time.

Another feature of the early SCATHA SSPM results was the observation that the Teflon samples showed a potential offset after only a few days on orbit. By

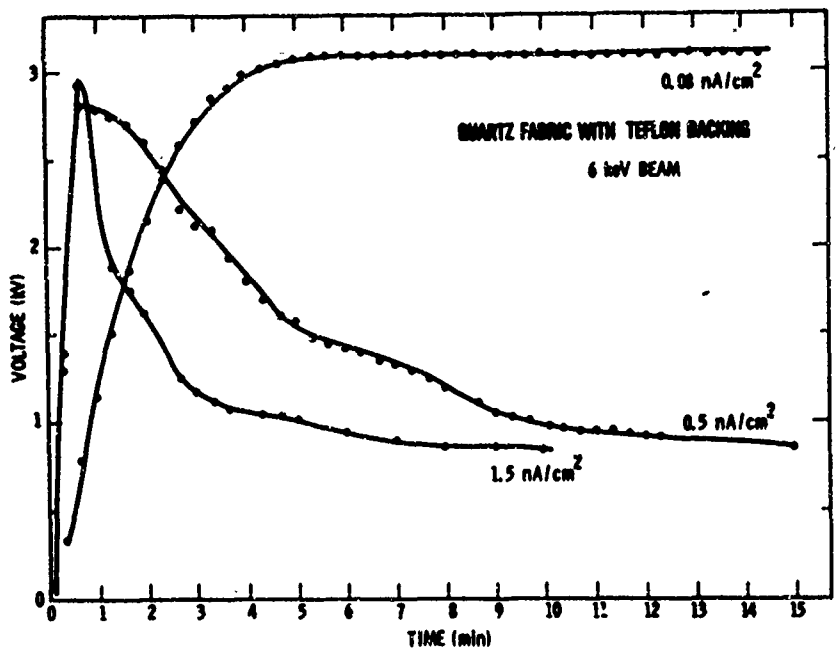

Figure 3. Typical Response of a Quartz Fabric Sample With Silvered Teflon Backing Under Laboratory Electron Irradiation (From Ref. 4)

the time of the 24 April charging event shown in Figure 2, the Teflon sample showed a -2000 V offset. This offset voltage was not due to surface charging. The Teflon bulk charge buildup was studied, using the SCATHA SSPM data, by plotting its potential as a function of time as shown in Figure 4. The data were taken at local noon where the probability of surface charging is a minimum.[2] There is an obvious gradual increase in the minimum potential with time. On top of this gradual increase are superimposed rather large short duration potential jumps. These occur over a period of about a day. Some are associated with satellite attitude maneuvers and others were caused by large energetic particle enhancements.[3]

Recent calculations of the levels of potential expected from imbedded energetic electrons in Teflon give results that are in agreement with the observed potentials.[6] Some early laboratory studies[13] were suggestive of a model for Teflon discharge events in which the charges from a charge deposition layer would flow

13. Yadlowsky, E.J., Hazelton, R.C., and Churchill, R.J. (1979) Characterization of electrical discharges on teflon dielectrics used as spacecraft thermal control surfaces, in Spacecraft Charging Technology-1978, Finke and Pike, Eds., available as NASA Conference Publication 2071 or Air Force Publ. AFGL-TR-79-0082, AD A084626, p. 632.

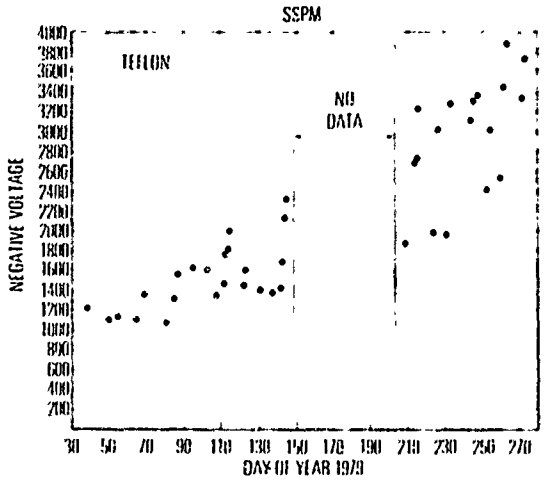

Figure 4. Teflon Potentials in Volts Taken When the P78-2 Satellite was Near Local Noon. These variations in voltages are not due to surface charging (from Ref. 2)

through a localized channel to the back surface. Reagan et al.[6] indicated they do not expect the electric field inside the Teflon potential to reach dielectric breakdown levels but that micrometeorites or heavy cosmic rays penetrating the material may create a breakdown channel.

Another effect which has been estimated for Teflon is the radiation induced conductivity enhancement.[14] Calculations, based on measured energetic electron dose rates, show that the conductivity of Teflon can be enhanced over its intrinsic conductivity by substorm and magnetic storm increases in the particle fluxes. This would cause a modulation of the Teflon potential by such magnetospheric events.

At times other than magnetospheric storms and when the Teflon is shadowed, its resistivity is very large and the embedded charges from electrons with energy $\lesssim$ 150 keV cannot easily migrate. So, they build up, increasing the potential until the electric fields are strong enough to pull the charge out of the material as fast as it is produced. As Figure 4 shows, such an equilibrium was not reached after ~ 250 days on orbit.

The last material change noted, so far, on orbit was the ever decreasing level of charging of some of the Kapton samples.[2,3] This was first noted by

14. Reagan, J.B., Nightingale, R.W., Gaines, E.E., Meyercroft, R.E., and Imhof, W.L. (1981) The role of energetic particles in the charging/discharging of spacecraft dielectrics, in Spacecraft Charging Technology 1980, Stevens and Pike, Eds., NASA Conference Publication 2182 or Air Force Publication AFGL-TR-81-0270, AD A114426, p. 74.

comparing the charging levels of Kapton during three similar charging events separated in time by several months. These data are shown in Figure 5. The Kapton -1 and -2 samples are on the sides of the spacecraft and are exposed to the sun every spin period.[10,8] The charging levels of these samples are compared with the potential of an isolated gold-plated conductor as a reference.

The potential of the samples relative to satellite ground increases as the samples rotate into the satellite shadow (shaded portions of curve) and decreases to a very small value in sunlight. The maximum potential reached by the gold was the same, within 30 percent, for the three events while the Kapton potentials varied by orders of magnitude. The gold sample data suggests that the three charging events were of the same magnitude. For example, the bulk currents through the samples were within a factor of 2 over the events but the Kapton-2 sample potential decreased from $\sim |100|$ volts to $<|10|$ volts from the 24 April 1979 event to the 10 June 1980 event. The shadowed Kapton (No. 3) sample on the top of the satellite retained its normal charging properties during these periods.

Figure 6 shows the measured bulk currents for the 10 June 1980 and 28 March 1979 events and unilluminated laboratory values for the charged sample. The bulk current measured on orbit was more than 3 orders of magnitude greater than the laboratory values. The June 1980 current, at low potential, is nearly a factor of 3 larger than the later March 1979 value at $\sim$ 1.7 kV potential. This suggested that solar illumination of the Kapton samples on the sides of the vehicle had caused a conductivity increase and that the level of conductivity was probably continuously increasing with time. This was tested by comparing the Kapton voltage to the gold sample voltage for a large body of data (from 7 February 1979 to 17 February 1980). This is shown in Figure 7 where each point represents the ratio of the maximum Kapton voltage to the maximum gold voltage for each 24-h period. Gold was assumed to be a space stable reference and any trends in the ratio were attributed to changes in the Kapton characteristics, specifically its conductivity. Figure 7a shows the result for the smaller Kapton sample ($\sim$ 160 cm^2) and Figure 7b shows the result for the large area sample ($\sim$ 830 cm^2). The solid line is an exponential regression line with the slope shown. The two Kapton samples show the same trend; they attained an ever lower maximum potential with increasing time. The e-folding time for the decrease in the ratio is $\sim$ 92 days.[15] The fact that both samples behaved the same would indicate that these changes in the Kapton bulk conductivity are representative of Kapton itself. At the same time, the shadowed Kapton sample on the top of the satellite showed no such conductivity changes.

15. Mizera, P.F. (1981) Charging results from the satellite surface potential monitor, J. Spacecraft and Rockets 18:506.

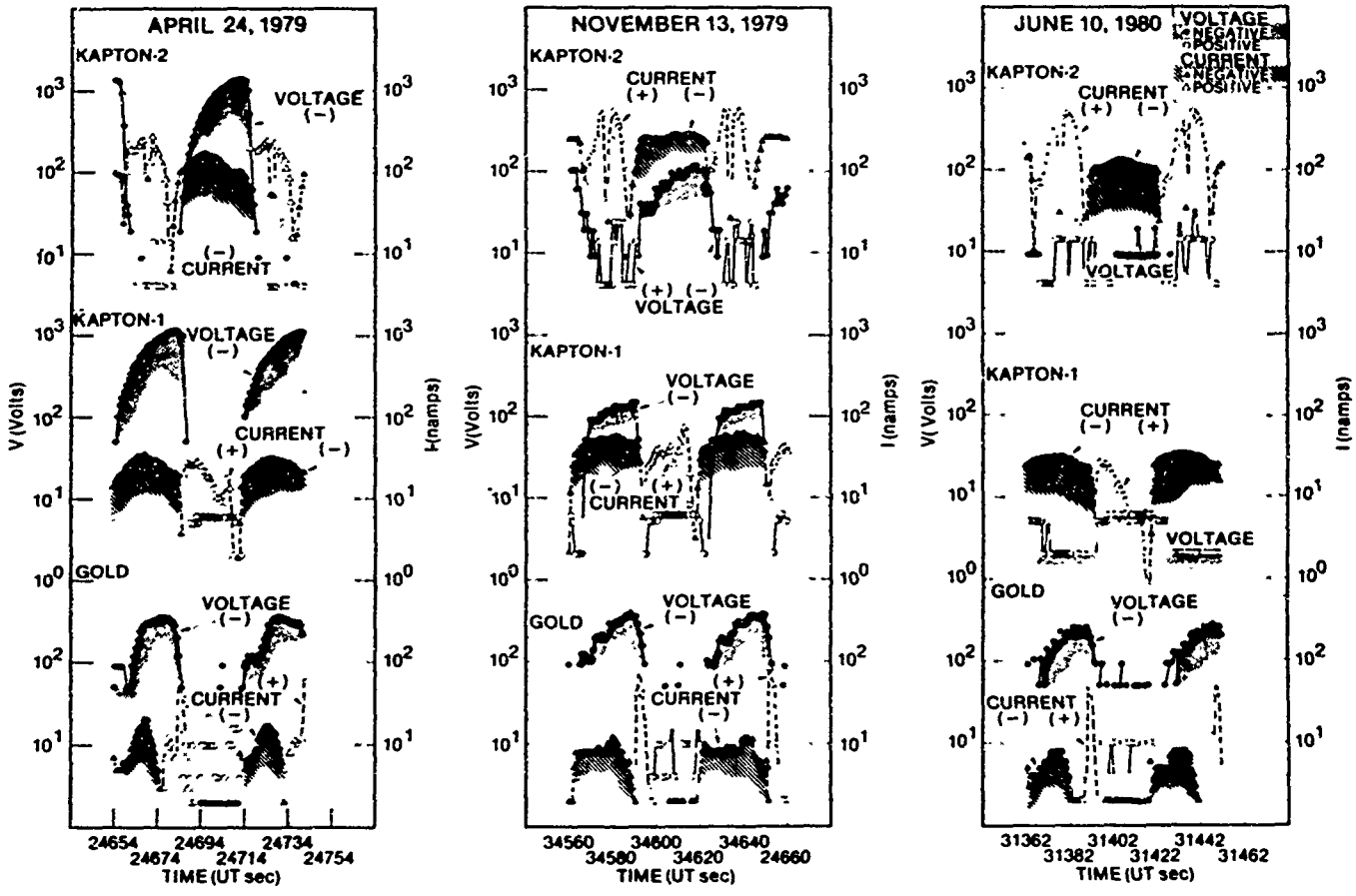

Figure 5. Three Charging Events Taken Early, 9 Months, and 16 Months After Launch. Gold serves as a reference voltage with time. The Kapton-1 and Kapton-2 are 180° apart; hence, one charges while the other discharges (see Ref. 1)

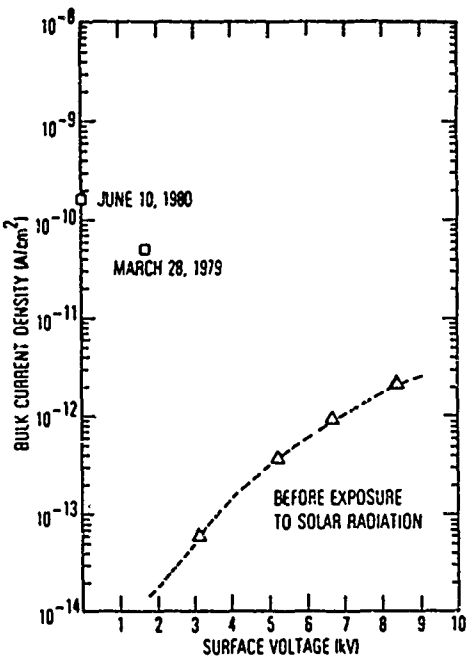

Figure 6. Bulk Kapton Current Measured on Orbit (10 June 1980 and 28 March 1979) and in the Laboratory (See Ref. 5)

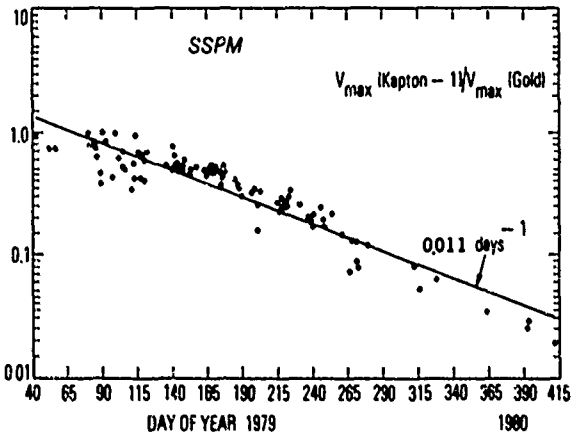

Figure 7a. Logarithmic Ratios of Kapton to Gold Conductor Voltage with Time. Both samples were on the SSPM-1 instrument mounted on the P78-2 bellyband with 50 percent solar exposure. Early ratios were normalized to 1

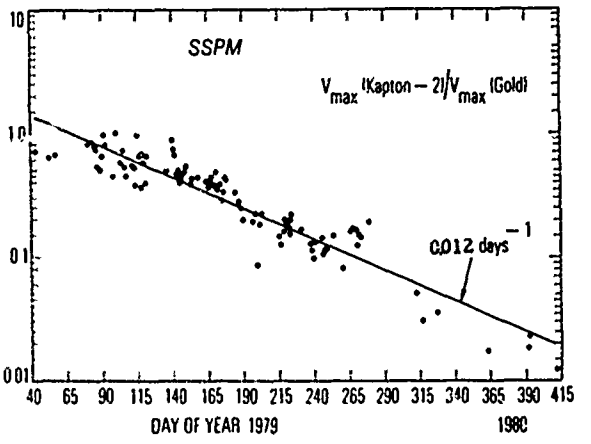

Figure 7b. Same Format as Figure 7a, but Using Voltages From the Large Area Kapton Flown on the SSPM-2 (See Ref. 1)

Such results had been suggested by some early laboratory tests,[16,17] in which the conductivity of Kapton was seen to rise with increased temperature, with increasing voltage impressed on the sample, and with exposure to light from a sun simulator. The dark conductivity of Kapton was found to increase by ~ 2 orders of magnitude in the first hour, after exposure to a "one sun" illumination, and then the rate of increase slowed with extended exposure. Similar results were also obtained with the Teflon and quartz fabric but the conductivity increases were orders of magnitude less than those of Kapton. Adamo and Nanevicz[17] also examined the photoconductivity of Kapton as a function of UV wavelength and found its increase in conductivity to be greatest for light with 450 to 524 nm wavelengths. This result is shown in Figure 8.

After the SCATHA Kapton results were seen, measurements were made at the Aerospace Corp. laboratories[4,5] using samples identical to the SCATHA samples in a duplicate SSPM instrument. The tests were carried out using simulated solar and particle radiation (for a description of the test equipment see Mizera et al;[1] Leung et al;[5] and Leung and Broussard[18]). The bulk dark

16. Coffey, H.T., Nanevicz, J.E., and Adamo, R.C. (1978) Photoconductivity of High Voltage Space Insulating Materials, Final Report, NASA Contract NAS3-18912, Stanford Research Institute, Menlo Park, Calif.

17. Adamo, R.C., and Nanevicz, J.E. (1977) Conductivity effects in high-voltage spacecraft insulating materials, in Proceedings of the Spacecraft Charging Technology Conference, Pike and Lovell, Eds., available as AFGL-TR-77-0051, AD A045459, or NASA TMX-73537, p. 669.

18. Leung, M.S., and Broussard, R.M. (1982) Summary of laboratory charging results on spacecraft dielectrics, AIAA Paper 82-0114, 20th Aerospace Sci. Mtg., Orlando, Fla.

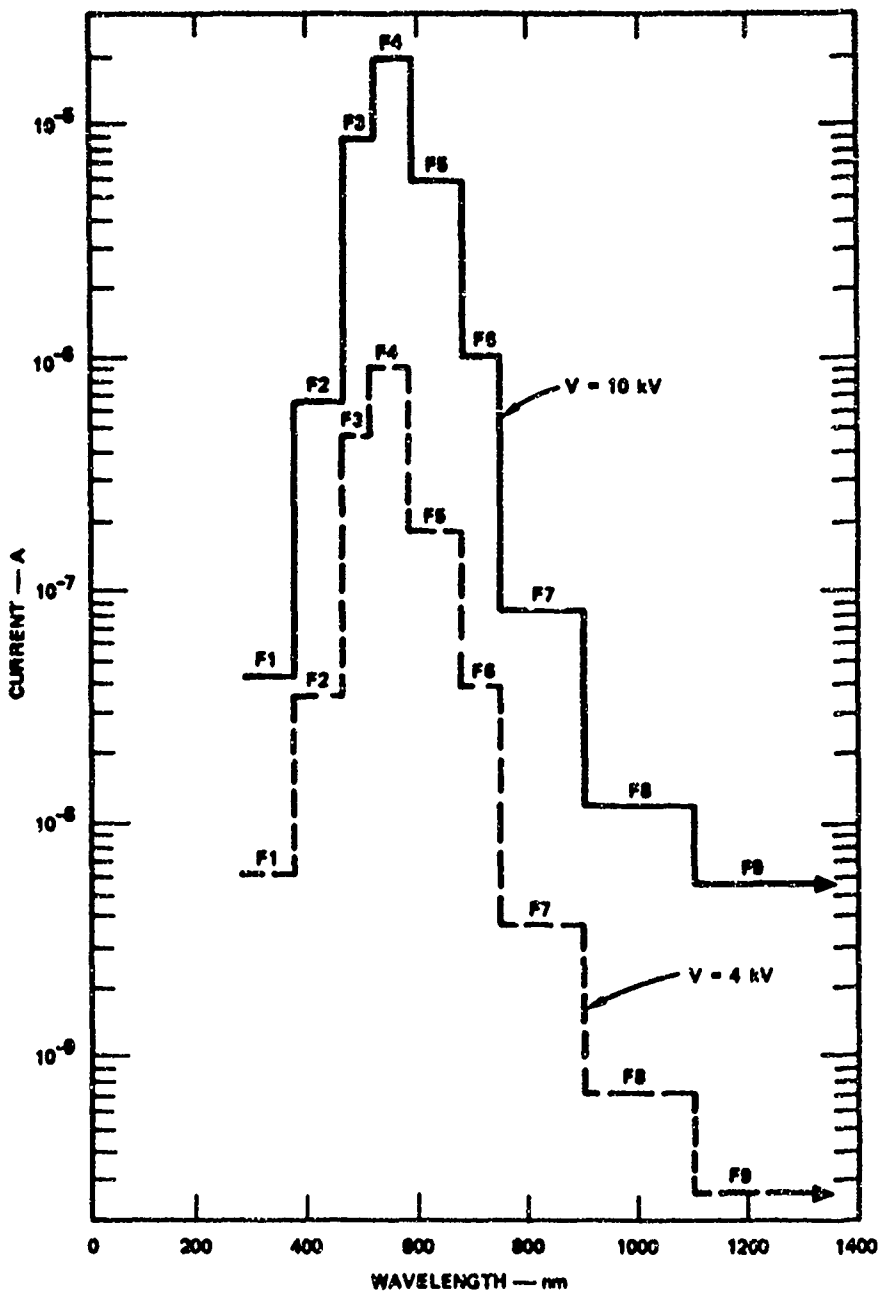

Figure 8. Normalized Bulk Photocurrents in Kapton V (5 Mil) at 22°C (See Ref. 17)

current of Kapton was measured as a function of the surface potential using both biased electrodes in contact with the surface and an electron beam to charge the surface. Figure 9 shows that both techniques gave the same result and thus the results are not dependent on electrode configuration. The Aerospace tests[1,4] confirmed the SRI results,[16,17] which showed that the bulk dark current of Kapton was about 3 orders of magnitude higher after UV exposure than before.

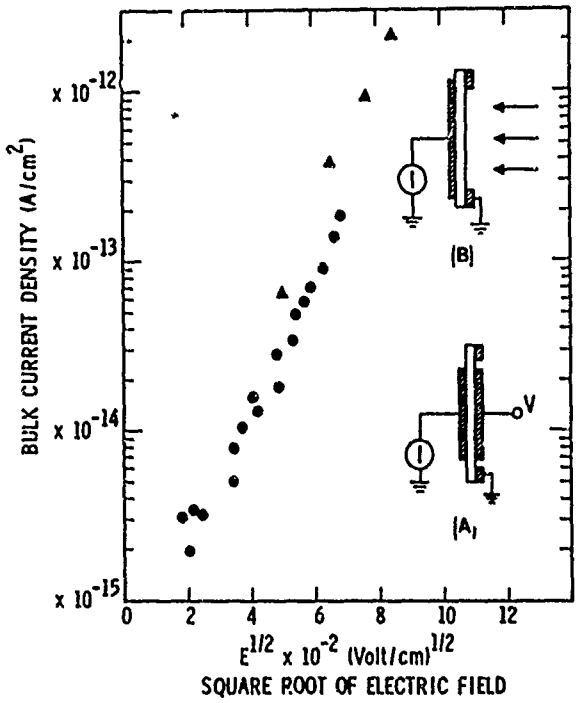

Figure 9. A Semilog Plot of the Bulk Current vs the Square Root of the Electric Field for Aluminized Kapton. The slope is approximately 1.0×10^{-2} $(cm/V)^{1/2}$. The dots represent the data points collected using a metal/insulator/metal structure shown in measurement scheme (A). The triangles are obtained by measurement scheme (B) in which the biasing electrode is replaced by an electron beam and surface potential of the sample is controlled by the beam energy (see Ref. 4)

It should be noted here that we do not mean the instantaneous photoconductivity of the material during UV exposure but an enhancement in the dark conductivity of the material after it has been illuminated. Exposure to UV for a short time caused a permanent change in the dark bulk conductivity as long as the material was in vacuum.

This dark conductivity enhancement was reduced if the sample was exposed to air.[1,5] This is shown in Figure 10 where the bulk dark current versus voltage profile is plotted for; (1) the unilluminated sample, (2) a sample that was exposed to "one sun" for 60 min, and (3) the sample after it was exposed for an additional 28 min. After the second illumination and dark current measurement, the sample was exposed to atmosphere for 15 min and then a new dark conductivity profile was run in vacuum [curve (4) in Figure 10]. This was followed by sample illumination for 45 min [curve (5)] whereupon the dark current again increased to the previous [curve (3)] value. Thus, exposure to air partially "quenched" the conductivity enhancement, but illumination by "one sun" UV in vacuum caused the dark current to increase again.

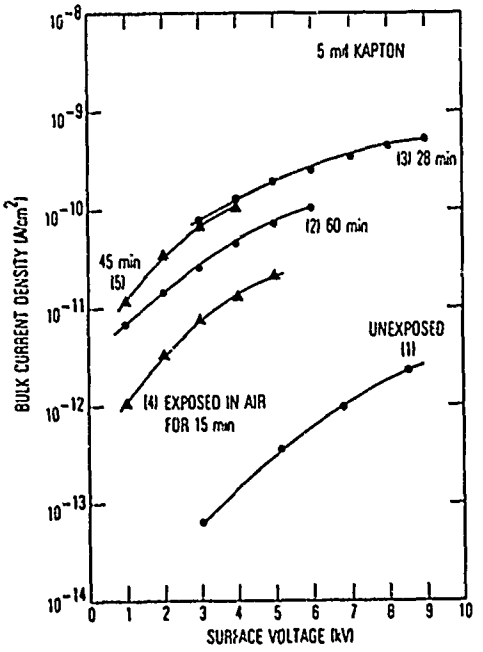

Figure 10. Laboratory Simulation of the Photo-induced Enhancement of Kapton Conductivity (See Ref. 5)

Why does the Kapton dark conductivity permanently increase in a vacuum after exposure to UV and why does it quench when exposed to air? Is this important in low altitude orbits? The partial answers to these questions are given by the laboratory tests. As mentioned earlier, Adamo and Nanevicz[17] showed that the Kapton photoconductivity was enhanced most effectively by light in the 450- to 524-nm wavelength range. Mizera et al[2] did a similar test, but for dark conductivity, with a spare SSPM and showed that indeed the largest bulk current was provided when both 2-mil and 5-mil Kapton samples had been exposed to "solar" light through a filter with a peak transmission near 502 nm. A shorter wavelength light (425 nm) produced the smallest response and the 560-nm wavelength an intermediate response. Figure 11 shows the Kapton spectral response versus wavelength and the response of the filters used in the Mizera et al[2] study. The strongest response was obtained for the shortest wavelengths that just started to penetrate the material causing the "... formation of electrically active centers in the bulk of the material...", as noted by Leung et al.[5] Apparently this same wavelength produces both the maximum photoconductivity and permanent conductivity change in Kapton.

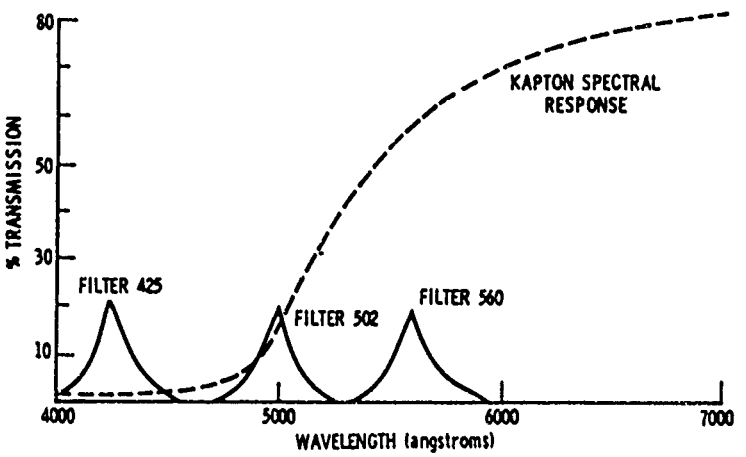

Figure 11. Absorption Spectra of 5-mil Kapton and Selected Filters (See Ref. 5)

To study the photochemistry that had occurred in the Kapton, Leung et al[5] exposed the samples to various gases after their dark conductivity had been raised by UV illumination. Argon, dry N_2, and dry air were used. Only dry air caused a quenching of the enhanced conductivity. Based on this result the

authors suggested that oxygen was responsible for the quenching. This could be very important at Shuttle altitudes where oxygen is the dominant constituent. The residual atmosphere may quench the Kapton photo-induced conductivity enhancement and keep the conductivity low. Only on-orbit tests or good laboratory simulations will reveal the answer.

3. SUMMARY

We have seen that the plasma and solar UV environment acted on dielectric materials to produce effects that were not clearly understood prior to the SCATHA program. Previously, only the thermal and optical properties of Kapton and Teflon materials were of concern. With the knowledge that these dielectrics charge up in the space plasma and can discharge causing spurious system responses,[8,19-21] it became important to consider their electrical properties. The pre-SCATHA satellite data laboratory tests did not uncover all the important properties of such materials. The orbital data bore out some of the laboratory results and showed differences from others.

The charging of the quartz fabric to high levels during impulsive charging events, lasting minutes to hours, was a surprise. The fact that the material responded the same way in the laboratory, when the proper simulation was performed, showed that the "worst case environment" testing normally used can be misleading. In the future one must be careful to verify first that the worst case test doesn't hide the response we are looking for.

The testing of the Teflon materials before launch did not uncover the bulk charging of the material by energetic electrons (> 50 keV) because such energies were not used in the tests and only surface charging was considered. The SCATHA results show that bulk charging can be equally important for Teflon. Recent calculations by Reagan et al[14,6] show that most of the Teflon response is to energetic electrons. In fact, a significant number of discharges on the SCATHA satellite are suspected of being the result of bulk charging[22,23] as are some anomalies on other spacecraft.[7] At the time of early SCATHA satellite data, some test results became available which indicated that energetic electrons can penetrate into the interior of spacecraft and charge highly resistive dielectrics there. Then arcing can occur and cause system upsets.[24] Thus, bulk charging of highly resistive materials must be considered wherever exposure to intense fluxes of very energetic electrons is possible.

Because of the large number of references cited above, they will not be listed here. See References, page 212.

Finally, the permanent conductivity enhancement of Kapton by solar UV exposure could reduce charging of vehicle surfaces composed of this material. The question of whether the oxygen densities experienced on orbit ($< 10^{10}$ cm^{-3} above 200-km altitude) could quench the photo-induced conductivity has not been studied yet and may be important at shuttle altitudes.

Acknowledgment

This work was supported by the U.S. Air Force Systems Command's Space Division under Contract F04701-82-C-83.

References

1. Mizera, P.F., Leung, M.S., and Kan, H.K.A. (1981) Laboratory and Space Results from the SSPM Experiments, The Aerospace Corp., TOR-0081 (6505-02)-03, El Segundo, Calif.

2. Mizera, P.F., and Boyd, G.M. (1982) A summary of spacecraft charging results, AIAA Paper 82-0268, 20th Aerospace Sci. Mtg., Orlando, Fla.

3. Mizera, P.F. (1982) Changes in Electrical Properties of Spacecraft Dielectrics, The Aerospace Corp., TOR-0082(2505-20)1, El Segundo, Calif.

4. Leung, M.S., and Kan, H.K.A. (1981) Laboratory study of the charging of spacecraft materials, J. of Spacecraft and Rockets, 18:10.

5. Leung, M.S., Tueling, M.B., and Schnauss, E.R. (1981) Effects of secondary electron emission on charging, in Spacecraft Charging Technology, NASA CP-2182, or AFGL-TR-81-0270, AD A114426, p. 163.

6. Reagan, J.B., Mayarott, E.E., Gaines, E.E., Nightingale, R.W., Filbert, P.C., and Imhof, W.L. (1982) Space charging currents and their effects on spacecraft systems, in Proceedings of Tenth International Symposium on Discharges and Electrical Insulation in Vacuum.

7. Vampola, A.L. (1983) Thick dielectric charging on high altitude satellites, AIAA Paper 83-0166, 21st Aerospace Sci. Mtg., Reno, Nev.

8. Stevens, J.R., and Vampola, A.L. (1978) Description of Space Test Program P78-2 Spacecraft and Payload, The Aerospace Corp., SAMSO TR-78-24, El Segundo, Calif.

9. Fennell, J.F. (1982) Description of P78-2 (SCATHA) satellite and experiments, in The IMS Source Book, Russell and Southwood, Eds., Am. Geophysical Union, Washington, D.C., p. 65.

10. Mizera, P.F. (1980) Natural and artificial charging: results from the satellite surface potential monitor flown on P78-2, AIAA Paper 80-0334, 18th Aerospace Sci. Mtg., Pasadena, Calif.

11. Belanger, V.J., and Eagles, A.E. (1977) Secondary emission conductivity of high purity silica fabric, in Proceedings of the Spacecraft Charging Technology Conference, Pike and Lovell, Eds., available as AFGL-TR-77-0051, AD A045459 or NASA TMX-73537, p. 655.

12. Stevens, N.J., Berkopec, F.D., Staskus, J.V., Blech, R.A., and Narciso, S.J. (1977) Testing of typical spacecraft materials in a simulated substorm environment, in Proceedings of the Spacecraft Charging Technology Conference, Pike and Lovell, Eds., NASA Publ. TMX-73537 and U. S. Air Force Publ. AFGL-TR-77-0051, AD A045459.

13. Yadlowsky, E.J., Hazelton, R.C., and Churchill, R.J. (1979) Characterization of electrical discharges on teflon dielectrics used as spacecraft thermal control surfaces, in Spacecraft Charging Technology-1978, Finke and Pike, Eds., available as NASA Conference Publication 2071 or Air Force Publ. AFGL-TR-79-0082, AD A084626, p. 632.

14. Reagan, J.B., Nightingale, R.W., Gaines, E.E., Meyercroft, R.E., and Imhof, W.L. (1981) The role of energetic particles in the charging/discharging of spacecraft dielectrics, in Spacecraft Charging Technology 1980, Stevens and Pike, Eds., NASA Conference Publication 2182 or Air Force Publications AFGL-TR-81-0270, AD A114426, p. 74.

15. Mizera, P.F. (1981) Charging results from the satellite surface potential monitor, J. Spacecraft and Rockets, 18:506.

16. Coffey, H.T., Nanevicz, J.E., and Adamo, R.C. (1978) Photoconductivity of High Voltage Space Insulating Materials, Final Report, NASA Contract NAS3-18912, Stanford Research Institute, Menlo Park, Calif.

17. Adamo, R.C., and Nanevicz, J.E. (1977) Conductivity effects in high-voltage spacecraft insulating materials, in Proceedings of the Spacecraft Charging Technology Conference, Pike and Lovell, Eds., available as AFGL-TR-77-0051, AD A045459, or NASA TMX-73537, p. 669.

18. Leung, M.S., and Broussard, R.M. (1982) Summary of laboratory charging results on spacecraft dielectrics, AIAA Paper 82-0114, 20th Aerospace Sci. Mtg., Orlando, Fla.

19. McPherson, D.A., Cauffman, D.P., and Schober, W.R. (1975) Spacecraft charging at high altitudes: SCATHA satellite program, J. Spacecraft and Rockets 12:621.

20. Rosen, A., Ed. (1976) Spacecraft charging by magnetospheric plasmas, Vol. 47, Progress in Astronautics and Aeronautics, AIAA and MIT press publ., Cambridge, Mass.

21. Garret, H.B., and Pike, C.P., Eds. (1980) Space systems and their interactions with earth's space environment, Prog. in Astronautics and Aeronautics, Volume 71, AIAA, New York.

22. Koons, H.C. (1980) Electrical discharges on the P78-2 satellite (SCATHA), AIAA Paper 80-0333, 18th Aerospace Sci. Mtg., Pasadena, Calif.

23. Koons, H.C. (1982) Summary of environmentally induced electrical discharges on the P78-2 (SCATHA) satellite, AIAA Paper 82-0263, 20th Aerospace Sci. Mtg., Orlando, Fla.

24. Wenaas, P., Treadaway, M.J., Flanagan, T.M., Mallon, C.E., and Denson, R. (1979) High-energy electron-induced discharges in printed circuit boards, IEEE Trans. on Nuclear Sci. NS-26:5152.

Contents

15. Space Electron-Induced Discharge Coupling into Satellite Electronics

by

J. Wilkenfeld
IRT Corp.
San Diego, Calif. 92100

1. INTRODUCTION

The USAF and NASA began the Spacecraft Charging at High Altitude (SCATHA) program because indirect evidence indicated that discharges induced by space electrons in spacecraft dielectrics could generate sufficient electromagnetic energy to cause spacecraft malfunction or failure. The ultimate cause must be related to the coupling of energy from the discharge into circuits that then malfunction: either an upset (uncommanded change of state) or electrical burnout of components, occurs.

Designers, manufacturers, and program offices responsible for ensuring that spacecraft perform according to specifications in the charging environment will find the important findings of the SCATHA program in the Spacecraft Charging Requirements Appendix (SCRA) to MIL-STD 1541, Electromagnetic Compatibility Requirements for Space Systems (Ref. 1). The draft of this document contains

1. Holman, A. B. (1982) Spacecraft Charging Standard Report, USAF Space Division Contract F04701-80-C-0009.

information that designers need to develop spacecraft that are resistant to electron-induced discharges. Of most relevance to the design of spacecraft are Sections 50.2, Design; 50.3, Analysis; and 50.4, Testing.

To evaluate the electromagnetic susceptibility of circuits in his design, a manufacturer must calculate or experimentally determine a set of "pin specifications". These "pin specifications" are the signal characteristics of the transients induced by a space-electron-induced discharge at each circuit input/output interface or box pin. These specifications are typically expressed as voltage/current waveforms or as an amount of energy between a given pin and the box or circuit common or ground. The design margin is adequate if the electron-induced-discharge induced energy on each pin is low enough so that no significant change is caused in circuit performance; for example, a change in state for a digital circuit, or an unacceptable shift in operating characteristics for an analog circuit are significant changes. The specific components of a circuit and its function determine what is acceptable and what is unacceptable. If enough energy is coupled into the circuit, then one or more parts may suffer irreversible failure or burnout.

A calculation of "pin specifications" for particular circuits in a given satellite requires two kinds of information. First, a description of the source term is needed. For an electron-induced discharge, this is a discharge waveform typically specified in terms of the current induced on the surface of the spacecraft. Second, a coupling model is needed. This is an electromagnetic model representing the spacecraft structure and cable bundle. The discharges become source terms in such a model and the impedance between pins and common are the loads. The model is exercised to obtain the response generated by a discharge at each pin to determine the "pin specification" and the electron-induced-discharge safety margin. Various approaches have been taken to develop the coupling model. These include adaptation of electromagnetic compatibility codes such as SEMCAP,[2] and modeling the spacecraft structure and cable bundle as a series of lumped elements. The result is then solved by a transient circuit analysis code.[3] Simplifications are inevitably made in such models because of the complexity of real spacecraft. Such simplifications lead to deviations between prediction and measurement of more than 6 dB. Often, discrepancies of 20 dB or more occur, even in predictions of the results of electrical testing where the source characteristics and injection locations are known.

2. Inouye, G., et al (1978) Voyager spacecraft electrostatic discharge immunity verification tests, paper presented at the Symposium on the Effects of the Ionosphere on Space and Terrestrial Systems, January 1978, Arlington, Va.

3. Rudie, N. (1980) Principles and Techniques of Radiation Hardening, Vol. 3, Chapter 28, 2nd Ed.

Section 5.2.4 of the SCRA provides a discharge specification, that is, a set of current waveforms for different materials scaled according to material area. These waveforms are based primarily on the results of ground test data in which the replacement currents generated in planar, grounded samples exposed to monoenergetic electrons were measured. These data are summarized in Ref. 4. The limited amount of detailed discharge data from the P78-2 (SCATHA) spacecraft was not used in the discharge model.

Section 50.2.3 of the SCRA suggests ways to reduce electron-induced-discharge coupling by various techniques, such as enclosure of sensitive electronics inside a Faraday cage, shielding individual wires or cable bundles, and closing structural penetrations to prevent leakage of externally generated electromagnetic fields into spacecraft interiors. Such techniques are well known, because they are also applied in spacecraft design to reduce EMI and nuclear-weapon induced EM effects such as Systems Generated Electromagnetic Pulses. Typically, such combinations of shielding will reduce the coupling of EM energy into individual spacecraft wires by 40 dB or more.

Section 50.4 also contains a recommended set of electron-induced-discharge qualification test procedures. These current injection tests were designed to simulate the replacement currents generated by the type of discharges summarized in Ref. 4. The rationale for their development is described in Ref. 5. As the analysis uncertainties in calculating "pin specifications" are typically greater than allowable design margins, some sort of testing is mandated to show that a spacecraft will survive the charging environment without significant overdesign with its concomitant penalties of weight, complexity, and cost.

Unfortunately, there is an increasing body of evidence that the discharge models embodied in the SCRA are an overly severe model of what actually happens on orbit. This is critical, because these models define the threat against which proposed satellites must be designed, constructed, and tested to survive. This evidence includes:

(1) Limited data from spacecraft in orbit, especially the P78-2, that the differential potentials and discharge amplitudes seen are much less than expected from ground tests (Refs. 5,6).

4. O'Donnell, E.E., and Beers, B.L. (1982) Characteristics of Electrostatic Discharge on Spacecraft Materials, SAI Report.

5. Koons, H.C. (1982) Summary of Environmentally Induced Electrical Discharges on the P78-2 (SCATHA) Satellite, Aerospace Corp., Report SSL-83(3505-30-1).

6. Adamo, R.C., and Materrese, J.R. (1982) Transient pulse monitor (TPM) data from the SCATHA/P78-2 spacecraft, paper presented at the AIAA 20th Aerospace Science Meeting, Orlando, Fla., 11-14 January 1982.

(2) Confirmation of the P78-2 observations based on 3-dimensional analytic modeling of spacecraft-like objects exposed to realistic charging environments using the NASCAP code (Ref. 7).

(3) Recent ground test data in which the charged particle environment is more accurately simulated (Refs. 8-10).

(4) Relative immunity of recently designed spacecraft to electron-induced discharges.

In this paper, the discharge models presented in the Spacecraft Charging Requirements Appendix will be used with simple, but reasonable, coupling models to determine how severe the electron-induced discharge threat to spacecraft ought to be and then to compare the results of these calculations to the limited on-orbit data. The calculations are presented in a form by which the efficiency of various design approaches is explicitly demonstrated. In particular, we address the question: given the correctness of the discharge models, do reasonable amounts of structural and cable shielding (40 dB or so) limit the "pin specifications" to safe levels?

The approach taken in the rest of this paper is:

(1) The discharge models in the Spacecraft Charging Requirements Appendix are taken as truly representative of those that occur in spacecraft dielectrics in the magnetospheric charging environment.

(2) The coupling of external electron-induced-discharge induced transients through the spacecraft skin and shielded wires is calculated for a variety of discharge source terms, and assuming reasonable values for EM field attenuation by the structure and wire shields.

(3) The energy coupled into individual wires is compared to the upset and burnout threshold for two common types of semiconductor digital logic used in spacecraft.

(4) The results are evaluated for system consequences.

7. Stevens, N.J. (1981) Analytical modeling of satellites in geosynchronous environments, in Spacecraft Charging Technology, 1980, NASA Conference Publication 2182, AFGL-TR-81-0270, AD A1.4426.

8. Coakley, P., et al (1982) Charging and discharging characteristics of spacecraft dielectrics exposed to low and mid energy electrons, IEEE Trans. Nucl. Sci. NS-29.

9. Staskus, J.V., and Roche, J.C. (1981) Testing of a spacecraft model in a combined environment simulator, IEEE Trans. Nucl. Sci. NS-28:4509.

10. Treadaway, M., et al (1979) The effect of high energy electrons on the charging of spacecraft dielectrics, IEEE Trans. Nucl. Sci. NS-26:5102.

2. MIL-STD 1541 SPACECRAFT CHARGING REQUIREMENTS ANALYSIS DISCHARGE MODEL

The discharge model in the Spacecraft Charging Requirements Appendix is based on a review of the available discharge data presented in Ref. 4. The majority of these data were based on the measured response of planar samples exposed to low energy ($E \leq 30$ keV) electrons at fluences of about 1 nA/cm^2. The primary measurement is the replacement current flowing in a low impedance ($\leq 1\ \Omega$) ground return. Note that this is primarily a measure of the response induced by the discharge. Some workers[11,12] measured the currents flowing in the body of simple 3-D objects covered with representative dielectrics on the end exposed to electrons. Such body currents ($\vec{K}_n$), flowing normal to the spacecraft surface, are proportional to one of the source terms, the tangential magnetic field ($\vec{H}_t$). The body current couples electromagnetic energy into spacecraft interiors. Nanevicz et al[13] measured external electron-induced-discharge generated electric and magnetic fields.

The worst case responses produced by electron-induced discharges occur when electrons are physically expelled or blown off from the discharging surface of the spacecraft. The fraction of such charge blown off[12] for the charging conditions described above is typically 25 to 75 percent of the total charge involved in a discharge. The rest of this charge recombines with adjacent image charge by dielectric punchthrough or by edge flashover. The latter two discharge modes produce a much smaller object response if measured in terms of the body replacement currents generated.

It was observed that discharge induced replacement currents for grounded planar samples approximately follow a series of scaling laws:

$$I_p = C_1 A^{C_2} \quad , \tag{1}$$

$$t_o = C_1' A^{C_2'} \quad , \tag{2}$$

where I_p is the peak replacement current generated by the discharge of a dielectric of area A, and t_o is the current pulse width at half maximum. For analysis purposes, the pulse shape is reasonably well approximated by an isosceles

11. Wilkenfeld, J., et al (1981) Development of Electrical Test Procedures for Qualification of Spacecraft Against EID, Vol. I, NASA CR-165590.
12. Treadaway, M.J., et al (1980) Experimental Verification of an ECEMP Spacecraft Discharge Coupling Model, SGEMP-J-5083, Computer Sciences Corp.
13. Nanevicz, J., et al (1981) Electromagnetic fields produced by simulated spacecraft discharges, in Spacecraft Charging Technology, NASA CR-2182, AFGL-TR-81-0270, AD A114426.

triangle. The constants C_1, C_2, C_1', and C_2' are material dependent. O'Donnell and Beers[4] have provided a best fit for these parameters, which are given in Table 1. For comparison, various experimental data for Kapton are plotted in Figure 1 along with the specification curves and other (Refs. 14, 15) "best" fits. Table 2 presents a summary of discharge pulse characteristics for Kapton, Teflon, Mylar, and fused quartz for dielectric areas ranging from 1 to 10^4 cm^2, taken to be representative of those found on spacecraft. In fact, the solar array panels of current generation communications satellites are covered with fused quartz cover slips spanning even larger areas.

Table 1. Discharge Parameters for Equations 1 and 2

Material	I_p(A)		t_o(nsec)	
	C_1	C_2	C'_1	C'_2
Kapton	3.8	0.482	10.4	0.669
Teflon	5.146	0.516	8	0.511
Mylar	8.359	0.509	7.7	0.461
Fused Quartz	0.81	0.6		

The replacement currents measured on grounded samples represent an upper bound for blowoff discharge coupling. Typically, during a discharge, which occurs over times of 0.01 to several microseconds, a spacecraft in the magnetosphere is effectively isolated from it, because the magnetosphere cannot instantaneously supply replacement charge. Thus, a better ground test simulation is to couple the test object to ground through a large resistance, such as 10^5 to 10^6 Ω (so-called high impedance coupling). The resistance provides for a dc connection to the external environment. However, the RC time constant, where C is the capacitance of the test object to the tank, about 100 pf, is long compared to the discharge pulse width. The test object is essentially isolated during the discharge. Then, space charge limiting of the blown-off electrons occurs. Most of these return to the test object. Figure 2 shows measured and

14. Balmain, K. (1978) Scaling laws and edge effects for polymer surface discharges, in Spacecraft Charging Technology, 1978, AFGL-TR-79-0082, AD A084626.

15. Inouye, G. (1981) Implications of Arcing Due to Spacecraft Charging on Spacecraft EMI Margins of Immunity, NASA CR-165442.

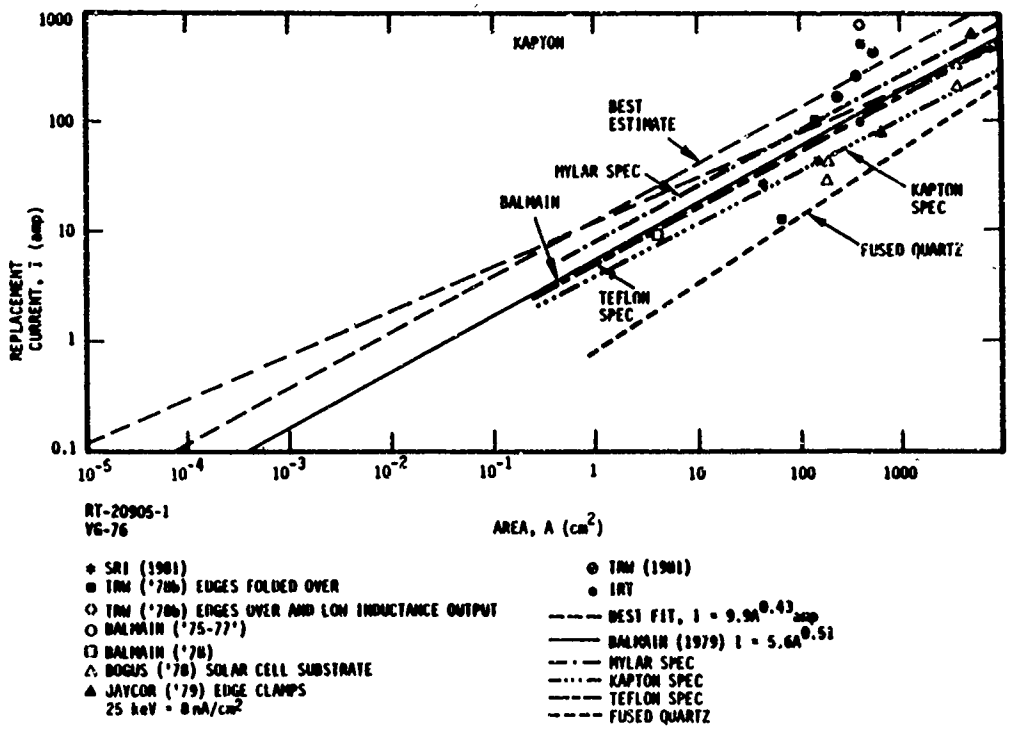

Figure 1. Electron-induced-discharge Replacement Current vs Area for Common Spacecraft Dielectrics. The experimental data are for Kapton samples

Table 2. Typical Discharge P··lse Characteristics

Material	I_p(A)				t_o(nsec)			
	1 cm²	100 cm²	1000 cm²	10^4 cm²	1 cm²	100 cm²	1000 cm²	10^4 cm²
Kapton	3.8	35	106	521	10.4	225	1052	4909
Teflon	5.1	54.4	182	597	8	84	272	882
Mylar	8.4	87	281	907	7.7	64	186	537
Fused Quartz	0.81	12.8	51.1	203				

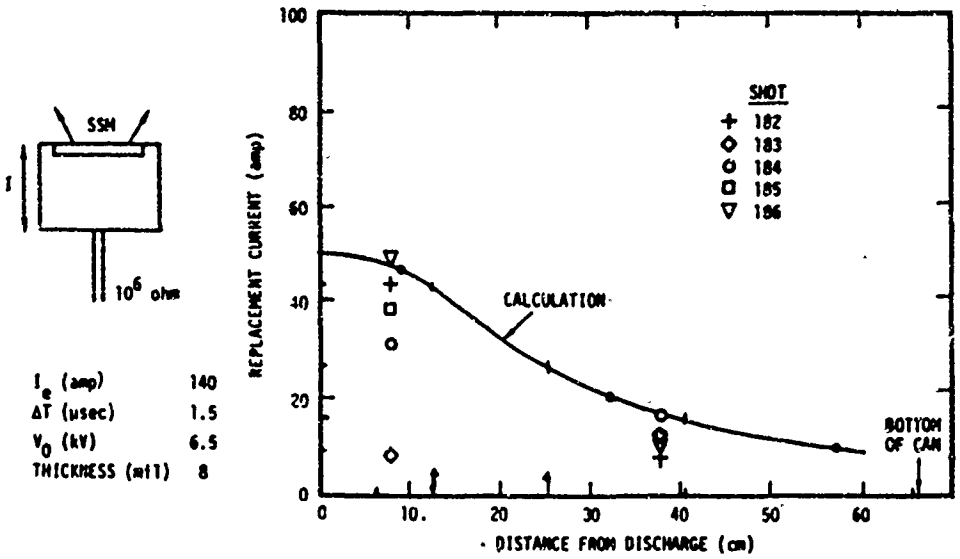

Figure 2. Calculated and Experimentally Measured Peak Replacement Currents vs Distance for SSM on a Simple Canister; High Impedance (Ref. 3)

predicted replacement currents induced on the side of a 91 cm wide by 61 cm high right circular cylinder as a function of distance from the top of the cylinder. The estimated emission current, 131 A, is based on replacement current measurements for the same object grounded to the test tank. Note that the magnitude of the replacement currents induced on the side are reduced by factors of 3 or more. However, for a worst case response, it is satisfactory to take the replacement currents measured with the test object grounded. These replacement currents are comparable to the emission current.

The only published measurements of electron-induced-discharge induced electric fields are those of Nanevicz et al.[13] They measured the electric field components normal to discharging surfaces of about 150 cm^2 in area at distances of 30 cm or more from the sample along a ground plane parallel to and in line with the sample. Peak electric fields were $\leq$ 48 kV/m and pulse widths were typically several hundred nsec.

3. COUPLING MODEL

An electron-induced discharge in external spacecraft dielectrics will produce transient electric and magnetic fields. These include normal electric fields above the dielectric surface and tangential magnetic fields. $\vec{E}_n$ at the surface is

Table 3. Characteristics of Logic Families

Logic Family	Power Supply (Volts)	Typical Gate Quiescent Power Dissipation (mW)	Typical Propagation Delay (nsec)	Typical Signal Line DC Noise Immunity (Volts)				Typical Signal Line Impedance (Ohms)		Logic Voltage Swing (Volts)	Typical Energy Noise Immunity on Signal Line (Joules $\times 10^{-9}$)	
				Low		High						
				Min	Typ #	Min	Typ #	Low	High		Low	High
DTL	5	5	30	0.7	1.2	0.7	3.8	50	1.7k	4.5	3	1.5
TTL	5	15	10	0.4	1.2	0.4	2.2	30	140	3.5	4	2.5
HTL	15	30	85	5.0	7.5	4.0	7.0	140	1.6k	13	48	7
SCL	-5.2	25	2	N.A.	0.25	N.A.	0.17	7	7	0.8	N.A.	N.A.
CMOS	5	0.000025	45	1.5	2.2	1.5	3.4	*600	**1.2k	5	3	1.5
CMOS	10	0.00010	16	3.0	4.2	3.0	6.0	*300	**600	10	10	5
CMOS	15	0.00023	12	4.5	6.5	4.5	9.0	*250	**450	15	22	13

#Typical values are from experimental results of testing a small sample quantity of parts and may not reflect the manufacturer's specifications.

*Defined at 30% of V_{DD}
**Defined at 70% of V_{DD}
} dc resistance

proportional to the induced surface charge, while $\vec{H}_t$ is proportional to the skin currents. These fields can couple into external wires. They can also excite apertures in the skin that permit penetration of fields into the interior. These interior electric and magnetic fields can then couple into spacecraft wiring. If the induced transients are sufficiently large, they can cause upset, that is, an uncommanded change of state or burnout. Upset thresholds for representative logic device families are given in Table 3 in the column labeled "Typical Energy Noise Immunity on Signal Lines". It can be seen that for most types of devices, only a few nanojoules of energy are needed to produce upset. If more energy is input to a semiconductor junction, it can be irreversibly damaged so that it will not function. The energy required ranges from 10 nJ for microwave diodes to several hundred nanojoules and above for various logic families shown in Figure 3. The energies quoted are those that must be input to the device.

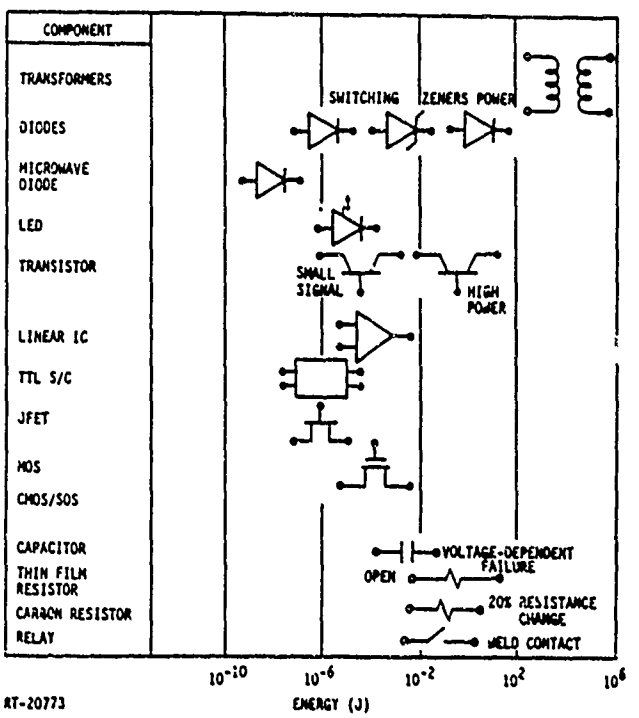

Figure 3. Parts Permanent Damage Threshold Energy for 100-nsec Square Pulses

Even if the exact spatial and temporal characteristics of the electron induced discharge fields are known, the details of the coupling process depend on a number of factors. These include:

(1) The detailed characteristics of the spacecraft skin including material composition, thickness, and dimensions, and the size and location of openings relative to the discharge site;

(2) The wire length, internal orientation, location relative to openings, distance from ground planes, presence of wires or cable bundle shielding, and relative location in a cable bundle;

(3) The nature of the interface circuits attached to either end of the wire.

To estimate the energy coupled into interior circuits by electron-induced discharges quantitatively, a generic approach is taken. The essence of this approach, shown graphically in Figure 4, is:

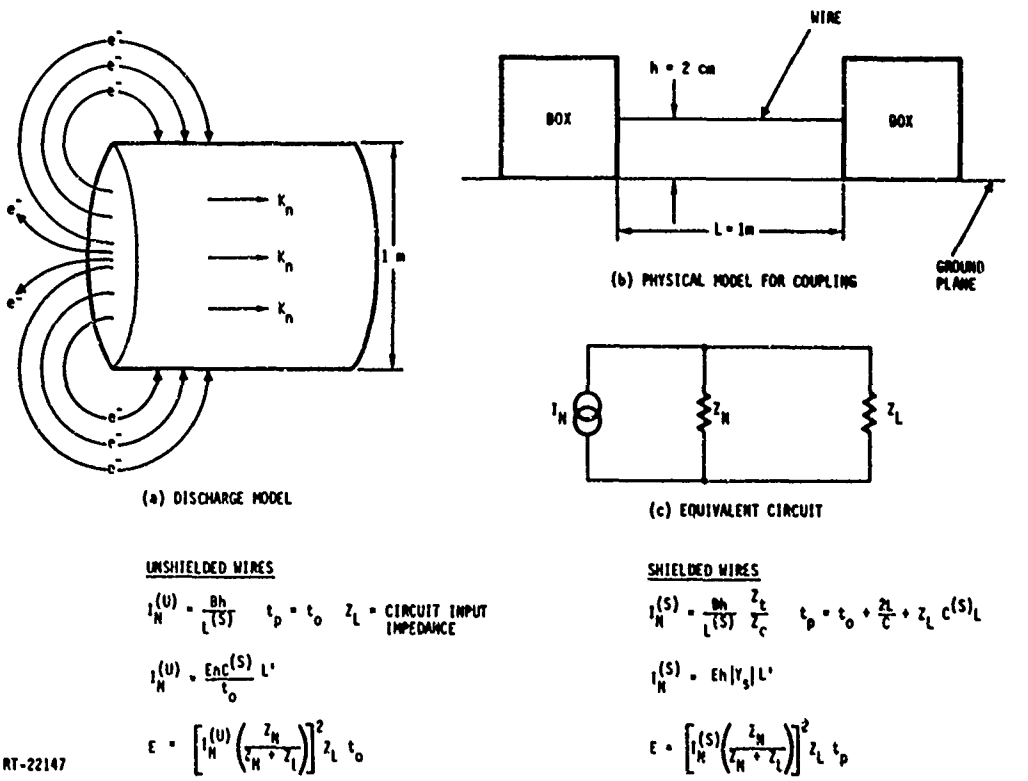

Figure 4. Coupling Model

(1) It is assumed that the external electric and magnetic fields are attenuated by a given fraction by the spacecraft skin but are otherwise unchanged. Representative shielding by poor to good Faraday cages, which will, of necessity, have some gaps, range from 10 to 26 dB. For computation, a value of 20 dB is assumed.

(2) To calculate coupling to unshielded wires, or the shields of shielded wires, a model wire is assumed. It is 1 m long and lies 2 cm above a ground plane. A cursory review of several spacecraft wiring harnesses indicates that these are reasonable values.

(3) Two modes of coupling were considered. One is through the voltage in the wire immersed in a changing magnetic induction field ($\vec{B}$). The strength of this coupling is proportional to the integrated scalar product of the time rate of change of $\vec{B}$ and the area enclosed by the circuit formed by the wire of interest, connected boxes, and the ground plane. The second mode of coupling is the current source generated between two conductors with a capacitance $C^{(s)}$ when the voltage V between them changes with time. For a conductor a distance h above a ground plane, $V \simeq E_n h$, where E_n is the normal electric field near the surface of the ground plane.

(4) For shielded wires, the magnetic field is assumed to couple into the center conductor primarily through the transfer impedance Z_t, while the electric field couples through the transfer admittance Y_t.

The "pin specification" for the interface circuit is calculated using the procedure developed by Clement.[16] The cable and the load on the end of the wire away from the circuit of interest are replaced by a Norton equivalent impedance Z_n whose magnitude is the series combination of the cable capacitance and its characteristic impedance. The load presented by the interface circuit Z_l is approximated by the typical signal line impedance for the most sensitive state, as shown in Table 3. For TTL, this is taken as 140 Ω while for 5 V CMOS it is 1.2 kΩ. The currents coupled into the cable by the fields are replaced by a Norton equivalent current source.

The peak magnitude of the Norton equivalent current source I_n is given by:

$$I_N = \frac{Bh}{L^{(s)}} \quad , \tag{3}$$

16. Clement, D. M., et al (1979) The development of SGEMP pin specifications, IEEE Trans. Nucl. Sci. NS-26:4912; Clement, D. M. (1981) SGEMP User's Manual, Vol. III, Chap. 2, Defense Nuclear Agency (Draft).

for $\dot{B}A$ coupling and

$$I_N = \frac{C^{(s)}EhL'}{t_o} \tag{4}$$

for $C\dot{V}$ coupling, where B and E are the peak values of the penetrating magnetic induction and electric fields, h is the height of the cable above ground, equal to 2 cm in our model, L' is an effective cable length essentially equal to the real cable length (1 m) for the case of interest, t_o is the pulse rise time given by Eq. (2), and $C^{(s)}$ and $L^{(s)}$ are the capacitance and inductance per unit length of the cable. For a wire over a ground plane, $C^{(s)}$ is given by:

$$C^{(s)} = 2\pi\epsilon_o / \cosh^{-1}(h/a) \quad , \tag{5}$$

and

$$L^{(s)} = [c^2 C^{(s)}]^{-1} = \frac{\mu_o}{2\pi} \cosh^{-1}(h/a) \quad , \tag{6}$$

where c is the velocity of light = 3×10^8 m/sec, and a is the wire radius. Typical values of $C^{(s)}$ are about 10 - 25 pf/m. The model calculations were made for a shielded AWG 20 wire. In this case, a is the shield radius and $C^{(s)}$ = 16.7 pf/m. $L^{(s)}$ = 0.66 μH/m.

The energy E coupled into the interface circuit for an unshielded wire is given by

$$E = \left[I_N \left(\frac{Z_N}{Z_N + Z_L} \right) \right]^2 Z_L t_p \quad , \tag{7}$$

where the Norton equivalent impedance Z_n is approximated by

$$Z_n = Z_c \left[1 + \left(\frac{vt_o}{L} \right)^2 \right]^{1/2} \tag{8}$$

where Z_c is the characteristic impedance of the cable (or shield) forming a transmission line with the ground plane, L the cable length = 1 m, and v the velocity of propagation = 3×10^8 m/sec for a wire over a ground plane. For an

AWG 20 shielded wire over a ground plane, $Z \simeq 5.97$ kΩ for t_o = 100 nsec and 59.7 kΩ for t_o = 1 μsec. For the case of interest, $t_p \equiv t_o$, and I_n is given by Eq. (3) or (4).

Table 4 presents calculations for the electron-induced-discharge induced $\dot{B}$ A coupling of the discharge fields into CMOS and TTL input circuits using the coupling model described above. The parametric variations by material and discharge area are based on source terms given in Table 2. To obtain the internal B field required to calculate I_N with Eq. (3), the following procedure was used. The peak currents of Table 2 were converted to surface currents K_s by assuming that they flow uniformly on the body of the model spacecraft as shown in Figure 3. Then,

$$K_s = I_p/\pi D \quad , \tag{9}$$

where D is the cylinder diameter. D was taken to be 1 m, comparable to the diameter of the P78-2, but somewhat smaller than the corresponding centerbody dimension for a current generation communication satellite. The magnitude of the corresponding tangential magnetic induction field B_t is then $B_t = \mu_o K_s$, where $\mu_o = 4\pi \times 10^{-7}$, the permeability of free space.

In computing the internal B_t, assumptions were made about the attenuation of B_t by the spacecraft skin. We have taken B_t (interior)/B_t (exterior) = 1/10, or -20 dB, based on the limited amount of quantitative evidence available.

Table 4. Predicted Discharge Energy (nJ) Coupled Into 5 V CMOS and TTL Through an Unshielded AWG 20 Wire 1 m Long, 2 cm Above Ground Plane

	5 V CMOS (Z = 1.2 kΩ, NM = 1.5 nJ)			TTL (Z = 140Ω, NM = 2.5 nJ)		
Material	1 cm^2	100 cm^2	1000 cm^2	1 cm^2	100 cm^2	1000 cm^2
Kapton	0.025	255	14.8 μJ	0.014	33.7	1.78 μJ
Teflon	0.025	212	9.4 μJ	0.018	35.0	1.23 μJ
Mylar	0.067	358	14.7 μJ	0.049	62.4	2.04 μJ
SiO_2	0.0011	14.9	840	$6.4 \cdot 10^{-4}$	2.3	109

An additional 20 db of electromagnetic shielding as per recommendation in MIL-STD 1541 SCRA would reduce coupled energy by a factor of 100.

Proper shielding wires reduces the energy coupled by a factor of 10^4 - 10^6.

There are no available empirical scaling laws relating the magnitude of external E fields produced by external discharges to the discharge area. However, an estimate of the energy coupled into our model circuit can be made from the data presented in Ref. 13. These measurements showed peak fields of about 48 kV/m and rise times of ~ 100 nsec for discharges in dielectrics of area 155 cm^2. Using Eqs. (4), (5), and (7) one finds that E $\simeq$ 9.1 nJ for the TTL circuit and 70 nJ for the 5 V CMOS circuits if a 20 dB attenuation of the external E field is assumed. Comparing these numbers with those presented in Table 3, and allowing for area scaling (Energy $\propto A^{3/2}$), these values are comparable to the calculated $\dot{B}A$ energy coupled into circuits by discharges in SiO_2, but much less than that generated by the other dielectrics.

The numbers presented in Table 3, and in the calculation for E field coupling, are for unshielded wires, or for coupling onto the shields of shielded ones. Many spacecraft wires, especially those carrying low-level, high-frequency signals to sensitive circuits must be shielded. In this case, an extra step is necessary to calculate I_n on the center conductor of a shielded wire.

The magnetic field coupling is primarily through the transfer impedance. For a shielded wire, the Norton equivalent current source on the center conductor is reduced from the value calculated with Eq. (3), by the ratio of the transfer impedance to the characteristic impedance of the shielded wire. Typical transfer impedances for the shielded wires used in spacecraft range from 0.01 to 1Ω/m (Ref. 17). A Z_t of 1Ω/m corresponds to a shielding effectiveness of 35 dB. The characteristic impedance of shielded wires ranges from about 10Ω to about 100Ω. Thus, the Z_t/Z_c ratio is certainly less than 0.1. More representative values are less than 0.01. As the power input to the interface circuit is proportional to I_N^2, the presence of wire or cable bundle shielding will reduce the energy input to a circuit by a factor of 100 or more.

Similarly, the current induced on the center conductor of a shielded wire (I_s) is approximately given by

$$I_c = Eh|Y_t|L' \quad . \tag{10}$$

According to Ref. 18, Y_t, the magnitude of the transfer admittance, is given by:

$$|i\omega C_{12}| = |i\omega S C_1 C_2| \quad , \tag{11}$$

17. Rudie, N.J., et al Flash X-Ray Testing of GPS Block II Spacecraft Cables and Connectors, to be published as an AFWL Technical Report.

18. Vance, E. (1978) Coupling to Shielded Cables, Wiley-Interscience, New York, Chapter 5.

C_1 is the internal shielded wire capacitance, C_2 is the capacitance from shield to ground, and s is about 10^8 for small coaxial cables or shielded wires. If we take $\omega \sim t_o^{-1}$, the ratio for the Norton current drivers for shielded to unshielded wires is proportional to sC_1. Typical values of C_1 are 20 to 74 pf/m for shielded wires. Thus, the E field attenuation ratio is ~ 0.004. As the energy input is proportional to I_N^2, shielding reduces the E field coupling by factors of 10^5, so that it becomes negligible.

4. DISCUSSION

We have used a relatively simple coupling model, and the discharge parameters given in the SCRA document to estimate the severity of the problem posed by electron-induced discharges. The calculations are probably worst case for the following reasons:

(1) An ideal cable orientation relative to penetration points for the entry of discharge energy is assumed. Good EM design dictates the routing of cable bundles away from such points.

(2) No account is taken of the fact that there may be interface devices in front of the input to sensitive circuits to protect them against transients. This is especially true for spacecraft hardened against nuclear weapon EM effects.

(3) The discharge currents given in Table 2 are worst case. As Figure 2 shows, space charge limiting of emission will reduce body currents by factors of 3 or more. This in turn reduces the energy coupled into interior cables by factors of 10.

The model calculations indicate that discharges occurring in dielectrics of moderate areas (~ 100 cm^2) are capable of producing numerous upsets in interior unshielded wires, while those occurring over larger areas can produce burnout of unprotected sensitive circuits. The key is the degree of electromagnetic shielding provided. For a well shielded satellite, with 40 dB or more of shielding against the penetration of exterior fields into wires, even large area discharges will not produce burnout, but are certainly capable of producing circuit upset if such circuits are not otherwise protected.

One may ask how these findings compare with on-orbit flight experience. There is little direct data available. It has been reported in the literature that a correlation exists between the occurrence of switching anomalies and the presence of substorms capable of producing significant spacecraft charging (Ref. 7). On the other hand, there is little indication (except possibly for the failure of a DSCS-II satellite) that external electron-induced discharge has caused catastrophic failure.

As of October 1981, the P78-2 satellite had suffered only one observed anomaly that could be attributed to electron-induced discharge. Given the charging environment at the time of occurrence, this anomaly has been attributed to ECEMP (electron caused electromagnetic pulse); that is, as the result of a discharge occurring in an interior dielectric or isolated conductor. The P78-2 was designed to provide at least 40 dB of electromagnetic shielding through the consistent use of cable shields and the enclosure of sensitive electronics in a Faraday cage. In fact, most of the observed anomalous switching behavior has been seen in older spacecraft such as DSP where sensitivity to the need for careful shielding to prevent coupling of non-system generated transients into circuits may not have been as high as at present.

The only available quantitative evidence on discharge magnitudes is available by inference from two experiments on the P78-2. These are the transient pulse monitor or TPM and the SC1-8B experiment, the transient pulse shape analyzer.

Adamo and Materrese[6] state that nearly all of the pulses sensed by the TPM have been produced on the low Z and high Z antennas; these are basically unshielded wires placed outside the shielded P78-2 cable bundle; that is, outside the Faraday cage of the vehicle. The largest analyzed signals observed on these antennas were recorded during a day when the external particle environment was conducive to producing a high degree of external differential charging. Approximately 8 nJ and 70 nJ were coupled into the low Z and high Z antennas, respectively. While these energies are sufficient to cause circuit upset, they represent energy coupled into unshielded exterior wires. Using unshielded wires outside a spacecraft would represent extremely poor design practice - and may represent a possible source for electron-induced discharge transients observed in older vehicles. If a reasonable degree of shielding were added to such wires (say 20 dB), then the energy coupled into them would be reduced by a factor of 100. The electron-induced discharge energies would then be below the upset threshold for semiconductor logic.

The SC1-8B has detected a variety of signals on both internal and external vehicle sensors that have dominant frequencies between 5 and 32 MHz and peak amplitudes of up to 30 V into a 50Ω load. According to Koons,[5] only 34 of 4640 pulses analyzed cannot be associated with normal vehicle commands or ion and electron beam operations. The largest analyzed transient was seen on a wire inside the spacecraft cable harness, which is exterior to the vehicle center body. On the same day a signal seen on an internal sensor, a loop around the CDU, was nearly an order of magnitude lower in amplitude. This probably shows the effect of the Faraday cage in reducing the penetration of internal fields into the spacecraft interior. The transient signal shown in Figure 7 of Ref. 5 for this event,

when integrated, represents an energy of 5 to 10 nJ. However, the peak voltage level (< 3 V) is probably insufficient to cause a change of state.

Thus, the limited amount of evidence available from the P78-2 (including that for the external charging experiment, the Satellite Surface Potential Monitor) imply that the on-orbit discharges are less severe than those seen in monoenergetic ground tests on which the discharge specification in the SCRA is based. However, the data base in extremely limited.

It appears that the limited amount of flight experience available supports the conclusion that external electron-induced discharges should not be a significant problem in a properly designed spacecraft. While electron-induced discharges may produce circuit upset, burnout is not likely to be a problem. However, if the discharge models contained in the model calculations are correct, then 40 dB of shielding may be inadequate to prevent discharge-transient-induced upset produced by the discharge of very large exterior dielectric areas. On the other hand, if the magnitude of on-orbit electron-induced discharge is much smaller than expected from the ground tests, the need for shielding and interface protection is diminished. A designer of a large current-generation spacecraft following the threat specification on the SCRA might have to add additional shielding or extra interface protection to ensure protection against these levels. If the discharge specification is too severe, then this will have a significant and unnecessary impact on the weight, complexity and cost of spacecraft design. Testing spacecraft to the levels recommended in the SCRA also presents considerable technical difficulty and risk, which increases program costs. On the other hand, such testing seems mandatory given the uncertainties in the analysis tools used to calculate pin specs. Hence, it is important to improve our knowledge of the nature of on-orbit electron-induced discharge. At present, the best means of doing this is by analyzing as much P78-2 data as possible, supplemented by ground tests with the best possible particle and photon environment simulations that simulate coupling into spacecraft.

References

1. Holman, A.B. (1982) Spacecraft Charging Standard Report, USAF Space Division Contract F04701-80-C-0009.
2. Inouye, G., et. al. (1978) Voyager spacecraft electrostatic discharge immunity verification tests, paper presented at the Symposium on the Effects of the Ionosphere on Space and Terrestrial Systems, January 1978, Arlington, Va.
3. Rudie, N. (1980) Principles and Techniques of Radiation Hardening, Vol. 3, Chapter 28, 2nd Ed.
4. O'Donnell, E.E., and Beers, B.L. (1982) Characteristics of Electrostatic Discharge on Spacecraft Materials, SAI Report.
5. Koons, H.C. (1982) Summary of Environmentally Induced Electrical Discharges on the P78-2 (SCATHA) Satellite, Aerospace Corp., Report SSL-83(3505-30-1).
6. Adamo, R.C., and Materrese, J.R. (1982) Transient pulse monitor (TPM) data from the SCATHA/P78-2 spacecraft, paper presented at the AIAA 20th Aerospace Science Meeting, Orlando, Fla., 11-14 January 1982.
7. Stevens, N.J. (1981) Analytical modeling of satellites in geosynchronous environments, in Spacecraft Charging Technology, 1980 NASA Conference Publication 2182, AFGL-TR-81-0270, AD A114426.
8. Coakley, P., et al (1982) Charging and discharging characteristics of spacecraft dielectrics exposed to low and mid energy electrons, IEEE Trans. Nucl. Sci. NS-29.
9. Staskus, J.V., and Roche, J.C. (1981) Testing of a spacecraft model in a combined environment simulator, IEEE Trans. Nucl. Sci. NS-28:4509.
10. Treadaway, M., et al (1979) The effect of high energy electrons on the charging of spacecraft dielectrics, IEEE Trans. Nucl. Sci. NS-26:5102.
11. Wilkenfeld, J., et al (1981) Development of Electrical Test Procedures for Qualification of Spacecraft Against EID, Vol. I, NASA CR-165590.

12. Treadaway, M.J., et al (1980) Experimental Verification of an ECEMP Spacecraft Discharge Coupling Model, SGEMP-J-5083, Computer Sciences Corp.

13. Nanevicz, J., et al (1981) Electromagnetic fields produced by simulated spacecraft discharges, in Spacecraft Charging Technology, NASA CR-2182, AFGL-TR-81-0270, AD A114426.

14. Balmain, K. (1978) Scaling laws and edge effects for polymer surface discharges, in Spacecraft Charging Technology, 1978, AFGL-TR-79-0082, AD A084626.

15. Inouye, G. (1981) Implications of Arcing Due to Spacecraft Charging on Spacecraft EMI Margins of Immunity, NASA CR-165442.

16. Clement, D.M., et al (1979) The development of SGEMP pin specifications, IEEE Trans. Nucl. Sci. NS-26:4912; Clement, D.M. (1981) SGEMP User's Manual, Vol. III, Chap. 2, Defense Nuclear Agency (Draft).

17. Rudie, N.J., et al Flash X-Ray Testing of GPS Block II Spacecraft Cables and Connectors, to be published as an AFWL Technical Report.

18. Vance, E. (1978) Coupling to Shielded Cables, Wiley-Interscience, New York, Chapter 5.

Contents

16. The Interaction of Large Space Structures with the Near-Earth Environment

by

U. Samir*
Department of Geophysics & Planetary Sciences
Tel-Aviv Univ. Israel,
and
Space Physics Research Laboratory
Univ. of Michigan,
Ann Arbor, Mich. 48100

1. INTRODUCTION

The interaction between natural plasmas and satellites orbiting the planets is one aspect of the more general problem of the interaction between collisionless plasma flows and bodies in the solar system. Examples of body-plasma interactions relevant to the solar system are given in Table 1. The detailed structures, that is, the detailed particle and field distributions in space and time around the bodies, are expected to differ for different types of interactions. However, the basic patterns could be similar since the basic physical processes acting in such interactions are probably similar. Planetary magnetospheres and shocks for example are to be seen as effects whose cause is the interaction between the body (planet's intrinsic and/or induced magnetic field) and plasma (solar wind).

*On Sabbatical leave as Senior NRC Associate at the Space Science Laboratory, NASA/MSFC, Huntsville, Ala.

Table 1. Examples of Body-Plasma Interactions in the Solar System

(A)	(1) Solar wind with planetary magnetic fields (for example, Earth). (2) Solar wind and a planetary ionosphere (for example, Venus). (3) Solar wind with non-magnetized bodies (for example, the Moon).
(B)	Planetary magnetospheres with natural satellites (for example, Jupiter/Io, Saturn/Titan).
(C)	Solar wind with comets.
(D)	Dust particles of different size and origin with the interplanetary medium.
(E)	Artificial satellites and large space platforms with planetary ionospheres/ magnetospheres, and with the solar wind.

The interaction yields cavities whose structure is quite complicated even for bodies that do not have an intrinsic magnetic field. Potential and density gradients, plasma oscillations and instabilities are created around the body. Acceleration mechanisms and time dependent phenomena are most probably responsible for various structural patterns that exist in the wake and elsewhere around the body. In a more general way, the question of the filling of the wake can be viewed as an example of an "expansion of a plasma into a vacuum".

For bodies having an intrinsic magnetic field (such as the Earth, Jupiter, and Saturn) or bodies having an atmosphere/ionosphere (for example, Venus), shocks ahead of the "body" are known to exist. In solar-planetary interactions the wake zone is often referred to as the "night-side"; "dark-side", "shadow-zone", or "anti-solar region".

Problems involved in body-plasma interactions extend to astrophysical plasma physics where the "body" may be a system and the "flow" is the galactic medium. Basic physical processes relevant to body-plasma interactions within the solar system could apply to larger cosmic systems. However, such an assumption should be tested and verified both theoretically and experimentally. Hence, it is quite clear that the complex problems involved in body-plasma interactions are of basic importance to space plasma physics.

Sound scientific work in this area will require in-situ experiments, laboratory simulations, and theoretical work. It would be most effective if these efforts were conducted simultaneously. Space geophysicists in the U.S.A. in the last two decades have devoted very little effort to the systematic study of body-plasma interactions for a variety of body and plasma parameters. This is true even for the more practical and specific case of satellite-ionosphere/magnetosphere

interactions. With a little extra experimental effort and cost, artificial satellites could have been instrumented to yield important information relevant to body-plasma interactions (Table 2). In the past the interest in satellite-ionosphere and satellite-magnetosphere interaction was restricted to spacecraft charging and, to a lesser extent, to wake and sheath effects. While the latter has practical (technological) applications to measurements performed by probes mounted on rockets and satellites, a wider view could have been adopted combining technological and scientific objectives simultaneously. It is perhaps ironic that even for the practical case of wakes and sheaths around probes and satellites orbiting in the terrestrial ionosphere, there are important questions that are not yet answered in a physically meaningful way.

Table 2. Aspects of the Interaction Between a Satellite and the Terrestrial Ionosphere

(1) Per se.
(2) As a "model" for various aspects of the interaction between planets and the solar wind and particularly between natural satellites with planetary magnetospheres (utilizing the concept of "qualitative scaling").
(3) As a test of the validity, quality, and range of applicability of thermal particle and field measurements performed in-situ.
(4) In the context of spacecraft charging.
(5) For testing theoretical models (physical assumptions and mathematical procedures).

The advent of the Shuttle with its wide range of capabilities provides a long awaited opportunity to perform controlled and carefully conceived in-situ experiments on "body-plasma" interactions that are of both scientific and technological interest, supported by laboratory and theoretical simulations. The technology being developed for advanced missions offers opportunities not readily available in the past two decades of space exploration. The author and N.H. Stone[1] have discussed new experimental approaches applicable for the Shuttle era. While it remains surprising that space geophysicists did not emphasize this area of scientific and technological endeavor in the past, it is possible now to utilize the

1. Samir, U., and Stone, N.H. (1980) Shuttle era experiments in the area of plasma flow interactions with bodies in space, Acta Astronautica.

Spacelab as a near-earth plasma laboratory and launch an extensive scientific and technological program of investigation. Experimental work, both in-situ and by laboratory simulation, together with a theoretical effort, should take place.

Capabilities such as tethered satellites, small throw-away detector packages and plasma diagnostic packages mounted on remote manipulators or booms could be utilized. In this way the scope of the investigations can be significantly expanded to encompass a wide range of questions relevant to the interaction of large bodies, that is, large space structures, in space.

The preliminary stage preceding such a scientific and technological program is the quantitative determination of the Spacelab environment and its charging effects. This stage is now in progress, and preliminary results were already discussed in this meeting, by Banks and Raitt, and by Shawhan and Murphy. It should be re-emphasized that it is possible to perform experimental work of both scientific and technological interest simultaneously, and that such an effort should be supported by an extensive theoretical effort.

2. DISCUSSION OF RESULTS

2.1 Morphological Studies

We restrict the discussion to satellite-ionosphere interactions and focus on results from parametric in-situ and theory-experiment investigations. In recent years the study of the distribution of thermal ions and electrons around ionospheric satellites focused on parametric rather than morphological investigations. The parametric studies were supported by a theoretical effort aiming at testing the validity and range of applicability of assumptions used in the theoretical models. Results regarding earlier theory-experiment comparisons are given in Gurevich and Dimant,[2] Al'pert,[3] and Samir and Stone.[1] The measurements used in recent studies came from the NASA Atmosphere Explorer C and E satellites and from the U.S.A.F. satellite S3-2. Results of such studies were used by Whipple[4] and by Garrett[5] in reviewing the present knowledge of spacecraft potential and charging mechanisms.

2. Gurevich, A.V., and Dimant, Ya.S. (1975) Flow of a rarefied plasma around a disc, Geomagnetism and Aeronomy 15(2):183.
3. Al'pert, Ya.L. (1976) Wavelike phenomena in the near earth plasma and interaction with man made bodies, Handbuch der Physik S. Flugge, Ed., Geophysics III V:217.
4. Whipple, E.C. (1981) Potentials of surfaces in space, Rep. Prog. Phys. 44:1197.
5. Garrett, H.B. (1981) The charging of spacecraft surfaces, Rev. Geophys. Space Phys. 19(4):577.

From basic measurements of ion and electron densities, temperatures, and the values of spacecraft potential with respect to local ambient, it was possible to obtain plots of the angular distribution of charge and potential around the spacecraft at fixed distances from the surface of the spacecraft. Information on ion mass allowed the current and potential around the satellite to be examined vs ionic Mach number. Some examples are shown in Figures 1 through 4.

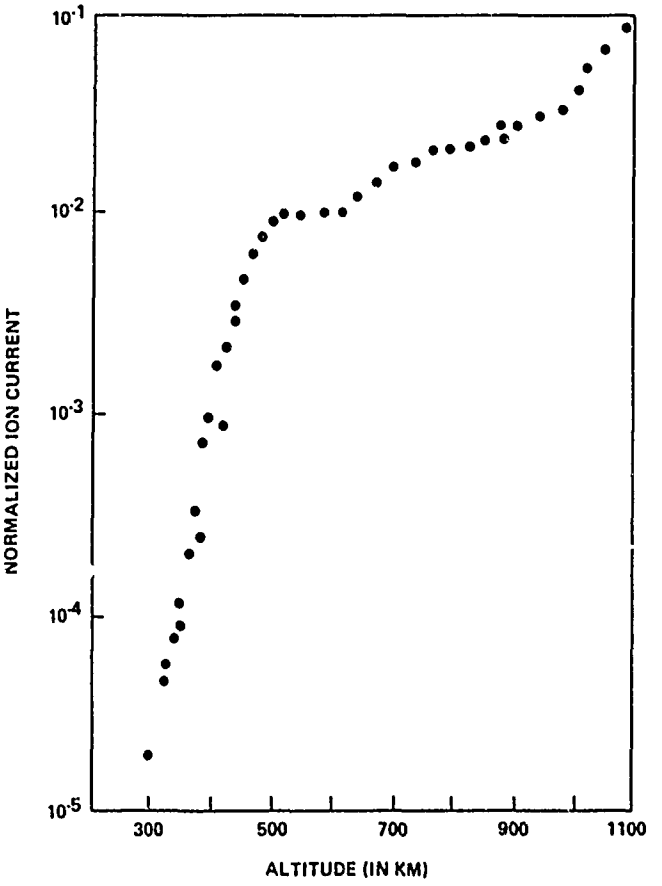

Figure 1. The Variation of Normalized Ion Current α = [I_+ (wake)/I+ (front)] With Altitude in the Altitude Range 300 to 1100 km (S3-2 Measurements)

As seen in Figures 1 and 2, and, as could have been expected, the ion depletion in the wake is more severe than the electron depletion. Hence, the wake region behind the satellite is depleted unequally of both ions and electrons. A

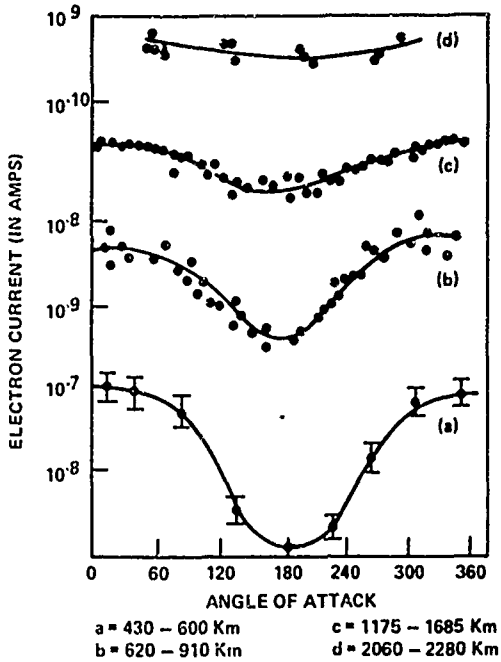

Figure 2. Variation of Electron Current (in Amperes) With Angle of Attack (θ) for the Altitude Ranges: (a) 430 to 600 km, (b) 620 to 910 km, (c) 1175 to 1685 km, and (d) 2060 to 2280 km Based on the Ariel I, Explorer 31, and Atmosphere Explorer C Measurements

negative potential well is thus created that acts selectively on the electrons and the ions.

Often, the practical problem of computing the spacecraft potential is solved by assuming that the potential distribution in the wake does not affect the total ion collection since most of the ions are collected by the front part of the moving body. While this can be considered as a reasonable zeroth approximation for ion collection it is not valid for electrons. Nor is it valid for ions if plasma oscillations and instabilities are indeed generated in the edges of the wake and ion acceleration mechanisms contribute significantly to the wake filling process. Theoretical evidence that supports the existence of instabilities in the wake boundaries was given by Gurevich et al,[6] Gurevich and Pitaevsky,[7] Al'pert[3] and

6. Gurevich, A.V., Pariskaya, L.V., and Pitaevsky, L.P. (1973) Sov. Phys. JETP 36(2):274.

7. Gurevich, A.V., and Pitaevsky, L.P. (1975) Non-linear dynamics of a rarefied ionized gas, Prog. Aerospace Sci. 16(3):227.

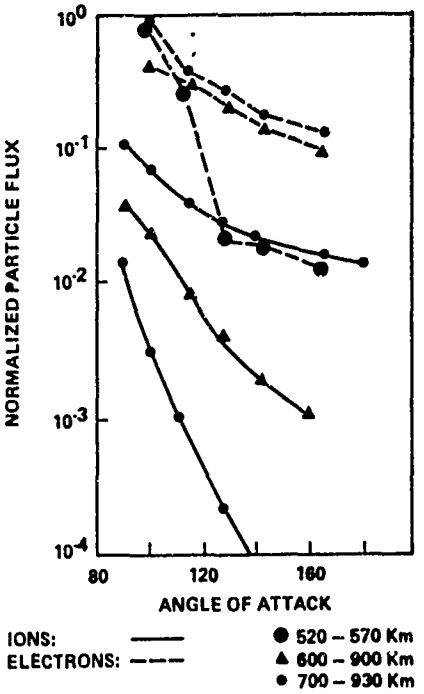

Figure 3. Variation of Normalized Ion and Electron Currents With Angle of Attack. Ions-solid line, electrons-dashed line for the altitude ranges: 520 to 570 km (●); 600 to 900 km (Δ); 700 to 930 km (·), based on Explorer 31 and Atmosphere Explorer C measurements

more recently (though in a different context) by Singh and Schunk.[8] Singh and Schunk studied the collisionless expansion of an H^+ - O^+ plasma into a "vacuum" because of its relevance to the polar wind, but this problem is similar in principle to that of an expansion of a plasma into the wake zone of any large structure orbiting in the near-earth environment or the "night-side" of a planet or moon that does not have a significant intrinsic magnetic field (for example, our moon, Venus).

Figure 3 shows the variation of normalized ion current [$I_+ (\theta)/I_+$ (ambient)], and normalized electron current [$I_e (\theta)/I_e$ (ambient)] in the wake of the Explorer 31 satellite.[9] These variations are shown for several altitude ranges. The

8. Singh, N., and Schunk, R.W. (1982) Numerical calculations relevant to the initial expansion of the polar wind, J. Geophys. Res. 87(A11):9154.

9. Samir, U. (1981) Bodies in flowing plasmas: spacecraft measurements, Adv. Space Res. 1:373.

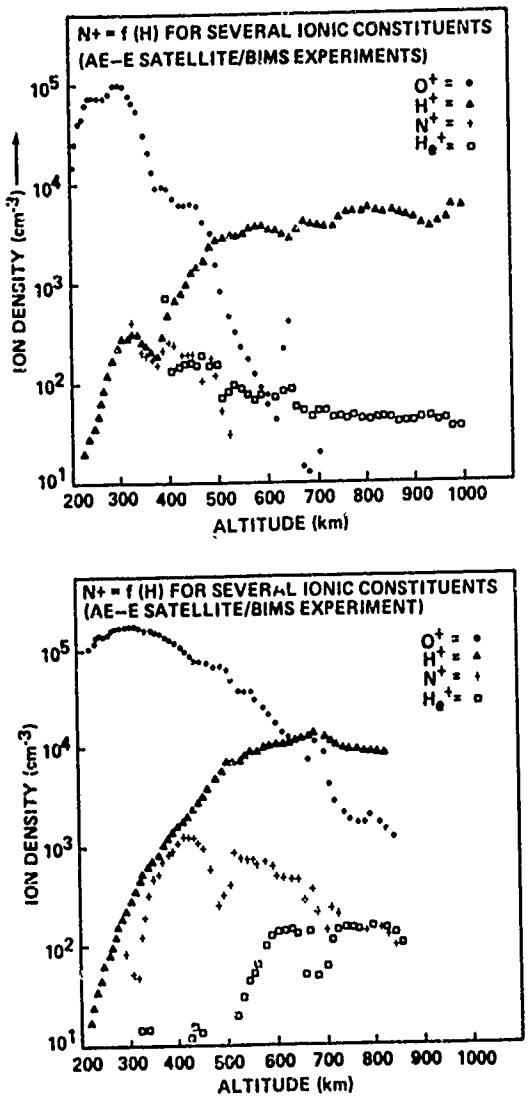

Figure 4. The Variation of Ion Density With Altitude for (O^+), (N^+), (H^+), and (He^+) Ions Based on AE-E Measurements

result shows quantitatively the difference between I_+ and I_e and, as expected (qualitatively) the difference increases as we proceed further into the wake region (that is, for larger values of the angle of attack θ). It is interesting to note that even close to the "terminator" ($\theta \sim 90^o$) the ion and electron currents differ appreciably.

2.2 Parametric Studies

To understand the physical processes involved in the filling-in of the wake region, and the structure of the near and far environment of the body (that is, the entire "sheath" zone), one must examine the variations of I_+, I_e, and $\phi = f(\gamma, \theta)$ with characteristic plasma parameters such as the ion-acoustic Mach number, average and specific ion composition, ratio of body-size to ambient Debye length, and spacecraft potential (with respect to local plasma potential). Examples of normalized current variation in the wake with average mass and ionic Mach numbers are shown in Figures 5 and 6.

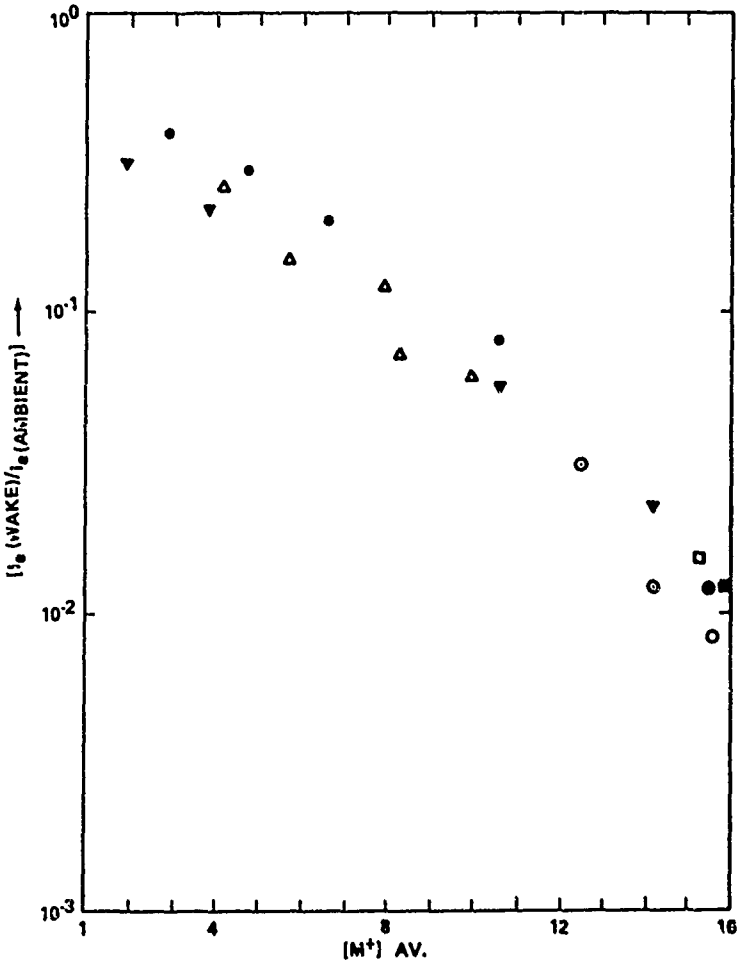

Figure 5. Variation of [I_e (wake)/I_e (ambient)] With Average Ionic Mass ($[M_+]_{av}$) Based on Measurements From the Explorer 31 Satellite

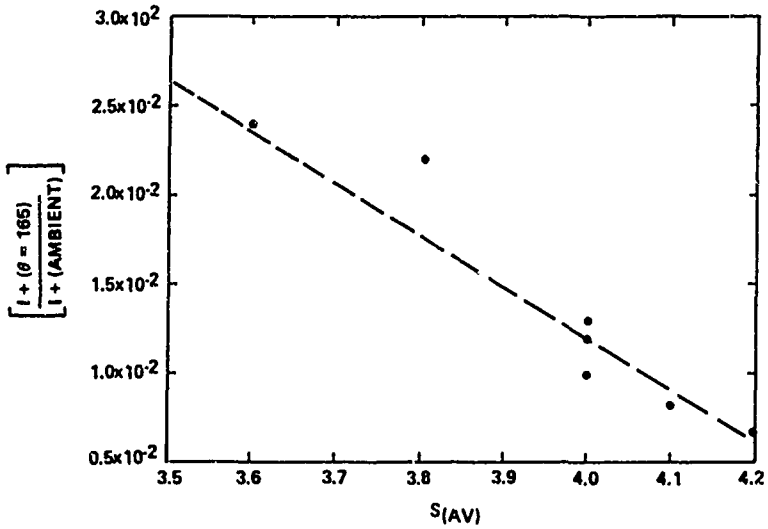

Figure 6. Variation of [I_+ ($\theta = 165^o$)/I_+ (ambient)] With Average Ionic Mach Number (S_{av}) Based on Measurements From the Explorer 31 Satellite

Surprising as it may be (and indeed it is!) the in-situ data available at the present time for the purpose of plasma-body interactions is meager, fragmentary, and restricted to the very near vicinity of the spacecraft. Obviously, this situation is not satisfactory. As mentioned earlier, this situation calls for new investigations utilizing the Shuttle/Spacelab facility, including capabilities such as tethered satellites, ejectable probe packages, and plasma diagnostic packages mounted and/or ejected from booms (for example, from remote manipulator-type arms). There can be no doubt that prior to relying on large space structures orbiting in space (space stations) as carriers of equipment of any kind, their entire interaction with the near-earth environment needs to be understood and known quantitatively. Experiments that have significance to both basic space physics and astrophysics should be conducted simultaneously (see Table 1).

Figure 7 shows the variation of normalized ion density [N_+ ($\theta = 160^o$)/ N_+ ($\theta = 90^o$)] with $R_D = Ro/\lambda_D$. This result is based upon measurements by the Atmosphere Explorer C satellite and gives a quantitative measure of the importance of body size (R_o) normalized by the ambient Debye length (λ_D) in determining the amount of ion depletion in the wake (Samir and Stone[1] and the references therein). Ratios of $R_D \approx 2 \times 10^2$ are of scientific interest to a wide range of body-plasma interactions (see Tables 1 and 2) as well as to the interaction of large space structures with the terrestrial space plasma, another example of the possibility of combining scientific and technological objectives.

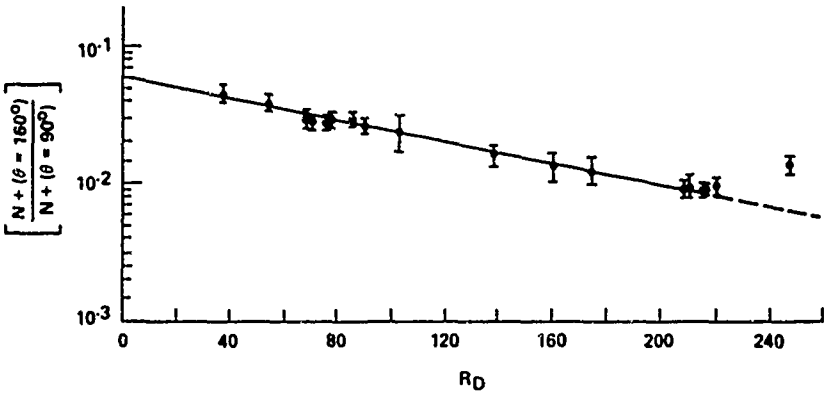

Figure 7. Variation of [N_+ ($+160^{\circ}$)/N_+ (ambient)] With Normalized Body Size ($R_D = R_o/\lambda_D$) Based on Measurements From the Atmosphere Explorer C Satellite

One more example of a parametric study is given in Figure 8. Here, the variation of [I_+ (wake)/I_+ (ambient)] is shown as a function of the electron temperature T_e for various values of the concentration ratio, [N (O^+)/N (H^+)]. While it is not the objective of this paper to go into detailed physical analyses, it is apparent that the above results are connected to the assumption of non-interacting streams filling in the wake zone.[3,6,7,10]

Among the more recent parametric studies performed by using relatively small samples of in-situ observations is the work of Samir et al,[11] which used measurements from the U.S. Air Force satellite S3-2. In this study it was possible to distinguish between the influence of normalized body size, $R_d = R_o/\lambda_D$, and normalized potential, $\phi_N = e\phi s/kT_e$, on the current ratio, α = [I_+ (wake)/I_+ (ram)], for the range $10 < |\phi_N| < 18$. However, uncertainty remains regarding the competition between R_D and $S(H^+)$ and $S(O^+)$, the oxygen and hydrogen ionic Mach numbers, respectively, in determining the distribution of ions near the satellite surface. From this investigation it became clear that care should be exercised in using the average Mach number, and average ionic mass, rather than using the specific ionic Mach numbers for each constituent.[11]

In summary, it is essential that parametric investigations be continued through both in-situ measurements and laboratory simulation work. Although

10. Gurevich, A.V., Pitaevsky, L.P., and Smirnova, V.V. (1969) Ionospheric aerodynamics, Space Sci. Rev. p. 805.

11. Samir, U., Wildman, P.J., Rich, F., Brinton, H.C., and Sagalyn, R.C. (1981) About the parametric interplay between ionic mach number, body-size and satellite potential in determining the ion depletion in the wake of the S3-2 satellite, J. Geophys. Res. 86(A13):11161.

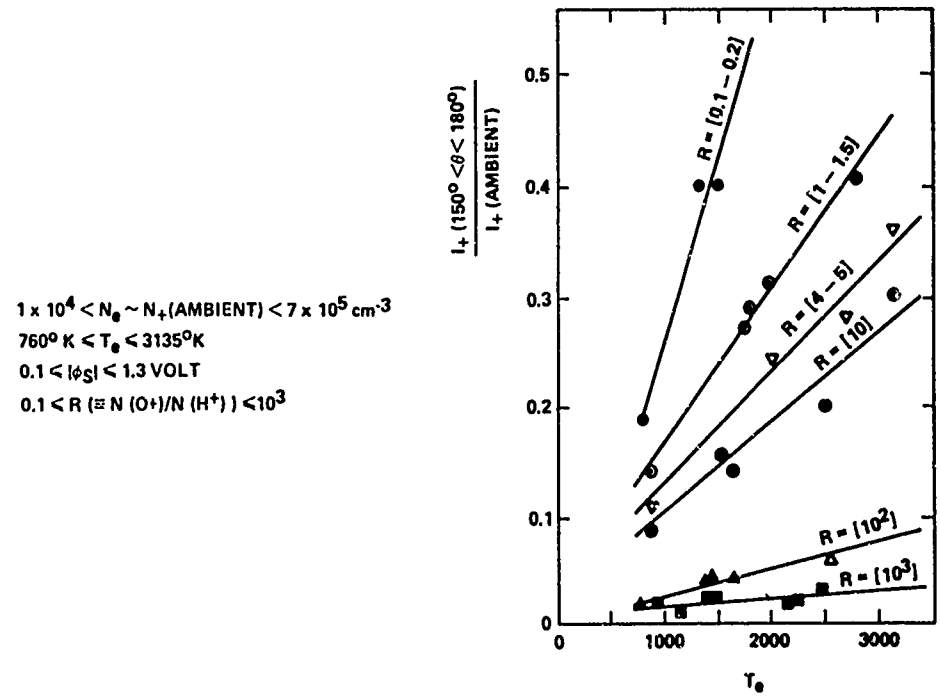

Figure 8. Variation of [I_+ ($150^\circ \leq \theta \leq 180^\circ$)/ I_+ (ambient)] With Electron Temperature (T_e) for Several Ratios of R = [$N(O^+)/N(H^+)$] Based on Measurements From the Atmosphere Explorer C Satellite

the latter aspect was not discussed in the present meeting the importance of laboratory studies is eminent. The importance of laboratory studies regarding the "aerodynamics of bodies in a rarefied ionized gas with applications to spacecraft environmental dynamics" are discussed in Stone;[12,13] Stone and Samir;[14] and Stone, Samir, and Wright,[15] which also provide an extensive bibliography.

12. Stone, N.H. (1981) The plasma wake of mesosonic conducting bodies, Part 1: An experimental parametric study of ion focusing by the plasma sheath, J. Plasma Phys. 25(3):351.
13. Stone, N.H. (1981) The plasma wake of mesosonic conducting bodies, Part 2: An experimental parametric study of the mid-wake ion density peak, J. Plasma Phys. 26(3):385.
14. Stone, N.H., and Samir, U. (1981) Bodies in flowing plasmas: laboratory simulation studies, Adv. Space Res. 1:361.
15. Stone, N.H., Samir, U., and Wright, Jr., K.H. (1982) Laboratory studies of bodies in collisionless mesosonic plasma streams, Proc. of the 1982 International Conference on Plasma Physics, Goteborg, Sweden, 9-15 June, p. 9b:6.

2.3 Theoretical Studies

In addition to morphological studies (Figures 1 through 4) and parametric studies (Figures 5 through 8) theory-experiment comparison studies were also performed (see, for example, Refs. 10, 3, and 16). Discussions relevant to the latter in the context of spacecraft charging were given by Whipple;[4] Parker;[17] Garrett;[5] and to some degree by the S-cubed group and L. Parker in the present meeting.

Comparing theoretical models with experimental results (in-situ and laboratory) and different theoretical models among themselves is essential for determining the validity and range of applicability of physical assumptions used in the theoretical models. This is particularly so when very elaborate computer codes are used in solving the Vlasov-Poisson equations in a self-consistent manner for cases of interest to general wake studies and to spacecraft charging of large structures orbiting the earth.

In principle it makes no difference whether the structure of a wake is looked at as a problem of the expansion of a plasma into a vacuum, which is a basic problem of interest in space plasma physics and plasma astrophysics, or whether a more practical view is adopted for the purposes of spacecraft charging studies. Indeed, the boundary conditions are not the same; (because the surface properties at specific locations on the spacecraft, body geometry and so forth, differ) but in either case the same basic time-dependent Vlasov and Poisson equations should be solved in a self-consistent way.

Comparison of theoretical models with in-situ measurements for an (O^+) dominated plasma show a difference of at least 2 to 3 orders of magnitude for the maximum rarefaction zone on the wake axis. For several simplified models the discrepancy is even larger. Recent studies, for example, Samir and Fontheim,[16] have shown that even the use of the self-consistent steady-state computer code of Parker,[18] which solves the Vlasov-Poisson equations numerically, does not remove the discrepancy. An example of such a comparison is given in Figure 9 for $S_{av} = 7.7$; $\phi N\,[(e\phi s)/kT_e] = -8.4$, and $R_D = 162$. For this case, which represents a "large body" applicable to large structures orbiting in space, the measured value of [I_+ ($\theta = 160$)/I_+ (ambient)] exceeds the computed value by a factor of 600. It is reasonable to assume that for [I_+ ($\theta = 180$)/I_+ (ambient)], the discrepancy is even larger. The status of other theory-experiment comparisons is no better.

16. Samir, U., and Fontheim, E.G. (1981) Comparison of theory and in-situ observations for electron and ion distributions in the near wake of the Explorer 31 and AE-C satellites, Planet. Space Sci. 29(9):975.

17. Parker, L.W. (1982) Private communication.

18. Parker, L.W. (1976) Computation of Collisionless Steady-State Plasma Flow Past a Disc, NASA Report CR-144159.

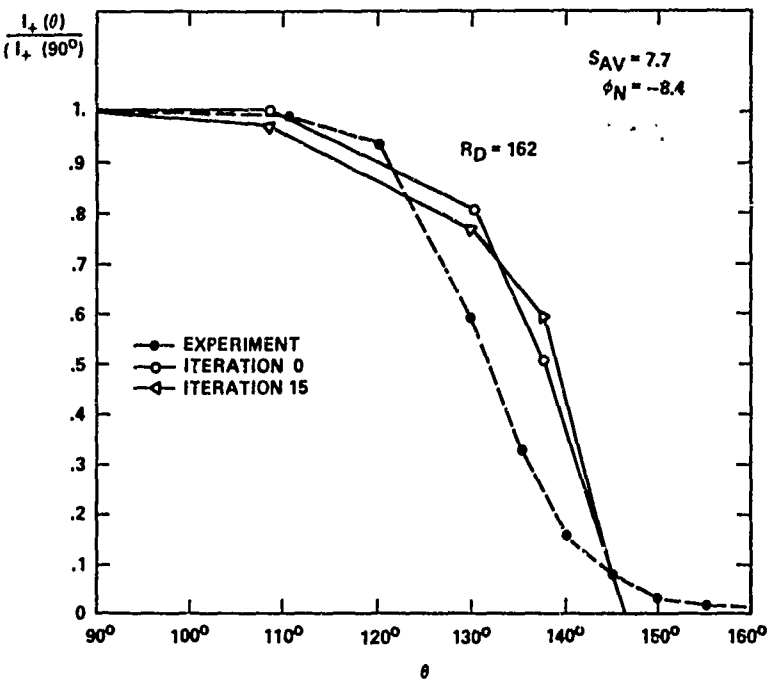

Figure 9. Variation of Computed and Experimental Values of $[I_+(\theta)/I_+(90)]$ With Angle of Attack (θ), for $90^o \leq \theta \leq 160^o$. The computations are based on Parker's model[18] and the measurements are from the Atmosphere Explorer C satellite. Iteration -0 refers to the "neutral particle" approximation

A similar conclusion is drawn from the comparison between theory and the Explorer 31 electron measurements, where the theory also significantly overestimates the electron depletion.[16] This suggests that the discrepancies may be due to the use of a steady-state theory and a single ion equation (using a mean ion mass). It was suggested that improved agreement between theory and experiment may be obtained by the use of the time-dependent Vlasov-Poisson equations with separate equations for the various ion species. Parker[17] believes that body geometry factors are responsible for the discrepancy. If Parker's steady-state model does not yield a better agreement for the maximum wake zone it is difficult to see how simplified models can be applied. Since plasma oscillations and instabilities can be generated by the motion of a spacecraft (or any other body in space) it is recommended that the theoretical models now being developed should attempt to solve the time dependent problem for several ionic species and for several values of the concentration ratio, $[N(H^+)/N\ (\text{total})]$.

Gurevich et al[6] and Gurevich and Pitaevsky[7] discussed the existence of strong acceleration of ions during the free expansion of a plasma. The application to the filling-in of the wake created in body-plasma interactions was specifically emphasized.

More recently Singh and Schunk,[8] discussed the characteristics of the expansion of a plasma into a vacuum and, like Gurevich et al, found it to be strongly dependent on the concentration ratio $[N(H^+)/N(O^+)]$ for an $H^+ - O^+$ plasma. In other words, it is of critical importance whether H^+ is a minor or a major constituent of the plasma. Both Gurevich et al[6] and Singh and Schunk[8] predict that upon the expansion of a plasma into a vacuum the ions are accelerated by a self-consistent electric field that arises during the expansion. The Russian computations (and similarly, those of Singh and Schunk) show that as a result of the acceleration a considerable portion of the light ions (for example, H^+ in an O^+, H^+ plasma) acquire energies on the order of $10^2 - 10^3$ (kT_e/e). This implies that even if the H^+ relative concentration in the plasma is very small, these ions contribute significantly to the distribution of charge and potential in the wake region. Therefore, it is possible that zeroth approximation calculations of current collection for spacecraft charging may not be practically applicable. It is the author's impression that except for Gurevich et al,[6] and more recently Singh and Schunk,[8] who emphasized the importance of such an accelerating mechanism to space plasma physics, the computer codes written for wake theory in the context of the natural charging of satellites and large structures in space have not taken notice of this physical process. If, as predicted by Gurevich et al, the average energy of the H^+ ions on the boundary of the quasineutral zone behind the body for $[N(H^+)/N\ (total)]$ is about (5 to 8) kTe/e (that is, energies of the order of 1 to 1.5 eV), then this process cannot be ignored.

Singh and Schunk[8] state in their paper that they are studying numerically the collisionless expansion of an $H^+ - O^+$ plasma into a vacuum because of the relevance to the polar wind. They suggest that the energization of ionospheric ions through the process of plasma expansion could be one of the mechanisms for creating the energetic ion population of ionospheric origin in the magnetosphere.

Again, we see that studying the complex of phenomena involved in the interaction between a large structure orbiting in space motivated by practical objectives may reveal physical processes that are of a much wider range of interest.

Now, with the advent of space shuttle, such studies can be performed in a controlled way for the benefit of both science and technology.

Acknowledgment

I thank Nobie Stone and Ken Wright for reading the paper and for their comments. This paper was written while the author was a senior NRC associate at the Space Science Laboratory, NASA/MSFC, Huntsville, Ala.

References

1. Samir, U., and Stone, N.H. (1980) Shuttle era experiments in the area of plasma flow interactions with bodies in space, Acta Astronautica.
2. Gurevich, A.V., and Dimant, Ya.S. (1975) Flow of a rarefied plasma around a disc, Geomagnetism and Aeronomy 15(2):183.
3. Al'pert, Ya.L. (1976) Wavelike phenomena in the near earth plasma and interaction with man made bodies, Handbuch der Physik S. Flugge, Ed., Geophysics III V:217.
4. Whipple, E.C. (1981) Potentials of surfaces in space, Rep. Prog. Phys. 44:1197.
5. Garrett, H.B. (1981) The charging of spacecraft surfaces, Rev. Geophys. Space Phys. 19(4):577.
6. Gurevich, A.V., Pariskaya, L.V., and Pitaevsky, L.P. (1973) Sov. Phys. JETP 36(2):274.
7. Gurevich, A.V., and Pitaevsky, L.P. (1975) Non-linear dynamics of a rarefied ionized gas, Prog. Aerospace Sci. 16(3):227.
8. Singh, N., and Schunk, R.W. (1982) Numerical calculations relevant to the initial expansion of the polar wind, J. Geophys. Res. 87(A11):9154.
9. Samir, U. (1981) Bodies in flowing plasmas: spacecraft measurements, Adv. Space Res. 1:373.
10. Gurevich, A.V., Pitaevsky, L.P., and Smirnova, V.V. (1969) Ionospheric aerodynamics, Space Sci. Rev. p. 805.
11. Samir, U., Wildman, P.J., Rich, F., Brinton, H.C., and Sagalyn, R.C. (1981) About the parametric interplay between ionic mach number, body-size and satellite potential in determining the ion depletion in the wake of the S3-2 satellite, J. Geophys. Res. 86(A13):11161.
12. Stone, N.H. (1981) The plasma wake of mesosonic conducting bodies, Part 1: An experimental parametric study of ion focusing by the plasma sheath, J. Plasma Phys. 25(3):351.

13. Stone, N.H. (1981) The plasma wake of mesosonic conducting bodies, Part 2: An experimental parametric study of the mid-wake ion density peak, J. Plasma Phys. 26(3):385.

14. Stone, N.H., and Samir, U. (1981) Bodies in flowing plasmas: laboratory simulation studies, Adv. Space Res. 1:361.

15. Stone, N.H., Samir, U., and Wright, Jr., K.H. (1982) Laboratory studies of bodies in collisionless mesosonic plasma streams, Proc. of the 1982 International Conference on Plasma Physics, Goteborg, Sweden, 9-15 June, p. 9b:6.

16. Samir, U., and Fontheim, E.G. (1981) Comparison of theory and in-situ observations for electron and ion distributions in the near wake of the Explorer 31 and AE-C satellites, Planet. Space Sci. 29(9):975.

17. Parker, L.W. (1982) Private communication.

18. Parker, L.W. (1976) Computation of Collisionless Steady-State Plasma Flow Past a Disc, NASA Report CR-144159.

Contents

17. Shuttle Orbiter Charging in Polar Earth Orbit

by

A. G. Rubin
A. L. Besse
Air Force Geophysics Laboratory
Hanscom AFB, Mass. 01731

Abstract

Spacecraft in polar orbit are subject to charging by the intense electron stream that comprises the aurora. Charging is computed according to the Laframboise theory of plasma probes in which the variation of sheath thickness with potential is taken into account. In this environment spacecraft charge to potentials that depend on their size. It is shown that large spacecraft charge to higher potentials than small spacecraft. The shuttle orbiter being a large spacecraft, may charge to more than 6 kV passing through an intense beam of auroral electrons. Because of the deficiency of ambient ions in the near wake region, the rear of the vehicle will have the lowest threshold auroral current for charging and will charge to the highest potential.

1. INTRODUCTION

The Shuttle Orbiter based at Vandenberg will pass through the auroral oval during its flight. The aurora consists of intense current sheets or electron streams. The possibility exists of electrical charging in this environment. At the shuttle orbital altitude of 200 to 400 km, the ambient plasma temperature is in the range of a few tenths of an eV to several eV, and would not charge the shuttle to more than a few volts in the absence of the aurora.

Previous experimental measurements of spacecraft charging at ionospheric altitudes have encountered potentials of a few volts. The highest potential measured on an ionospheric satellite is -40 V. [1]

We shall make use of the Laframboise theory of spherical probes in a plasma to compute the charging of a spacecraft in the aurora. The Laframboise theory is a numerical analysis that takes space charge into account self-consistently, and is the most accurate theory available. In view of the drastic approximations already made, it might not seem important to use an accurate probe theory, but one of the key points in the analysis is the expansion of the plasma sheath with potential. The plasma sheath growth with potential provides the main result of this analysis, that the charging is higher for larger vehicles. It is also important to have the correct functional dependence of plasma sheath size with potential. Since the Laframboise theory is numerical, the results have been fitted to analytical forms by several authors for cases of interest. We shall use the analytical fit provided by Szuszczewicz and Takacs.

Potentials on large space structures in low earth polar orbit have previously been calculated applying spherical probe theories of Al'pert, [2] Langmuir and Blodgett, [3] and Parks and Katz. [4]

---

1. Sagalyn, R. C., and Burke, W. J. (1977) INJUN 5 observations of vehicle potential fluctuations at 2500 km, in Proceedings of the Spacecraft Charging Technology Conference, C. P. Pike and R. R. Lovell, Eds., AFGL-TR-77-0051, NASA TMX73537, AD A045459.

2. Al'pert, Ya. L. (1976) Wave-like phenomena in the near-earth plasma and interactions with man-made bodies, in Handbuch der Physik, Encyclopedia of Physics, Vol. XLIX V (5), Springer Verlag, Berlin, Heidelberg, New York.

3. Langmuir, I., and Blodgett, K. (1923) Currents limited by space charge between coaxial cylinders, Phys. Rev. 22:347; (1924) Currents limited by space charge between concentric spheres, Phys. Rev. 24:99.

4. Parks, D. E., and Katz, I. (1981) Charging of a large object in low polar earth orbit, in Spacecraft Charging Technology, 1980, AFGL-TR-81-0270, NASA CP 2182, AD A114426.

2. CHARGING CALCULATION

The Shuttle has a complex geometry with wingspan of 24 m and height of 17 m with a diversity of surface materials. To obtain an estimate of charging, and find out whether it is a real problem or not, the Shuttle will be modeled as a 10-m-radius sphere.

We wish to compute the charging of a spacecraft in polar earth orbit at low altitudes (200 to 400 km) when passing through intense auroral electron streams. The range of variables for the satellite and the environment are given in Table 1.

Table 1. Spacecraft Environment Parameters

Spacecraft Radius (m)	0.05, 0.5, 5.0, ∞
Ambient Plasma Density	$10^{10} - 10^{11}$ m^{-3}
Peak Auroral Electron Flux	$1.6 \times 10^{9}/cm^{2}sec$
Typical Debye Length	2 cm

Low-altitude satellites produce a wake, whose effects will be described later. Since the orbital velocity of 8×10^{5} cm/sec far exceeds the ion thermal velocity, ion current to the vehicle will be mostly ram current. Ram current is the current piled up on the leading surface by the vehicle in its forward motion.

The effects of $\vec{v} \times \vec{B}$ electric fields, small compared to the electric field due to charging, will be neglected. The effects of the magnetic field will be neglected as well. These effects will be discussed later. The spacecraft will charge negatively so that cold ambient electrons will be repelled. Their contribution to the current is negligible.

3. IONOSPHERIC PLASMA

The ion density and composition of the ionospheric plasma is shown in Figure 1, measured on an equatorial orbit by AE-E. In the 200 to 400 km region, the ion density varies from 10^{4} to $10^{5}/cm^{3}$ and is 99 percent O^{+} up to about 400 km where there is a few percent of H^{+}. We shall assume for simplicity that the plasma is entirely O^{+}.

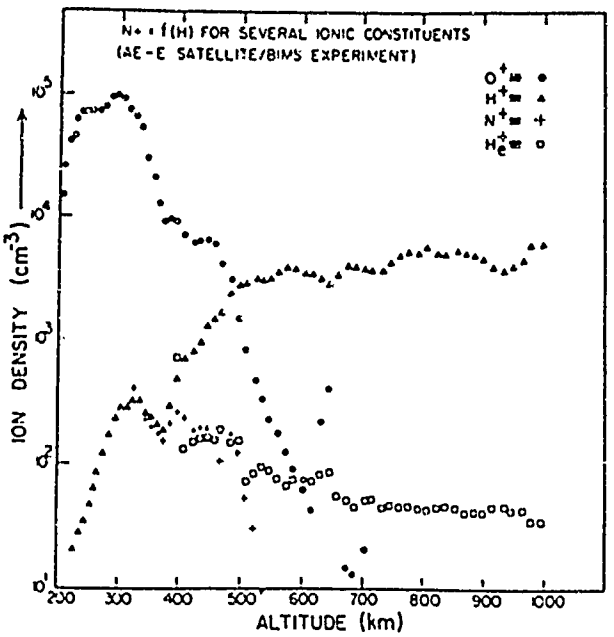

Figure 1. Composition of the F-Region Ionospheric Plasma

4. AURORAL ELECTRON FLUX

The aurora consists of streams of electrons and ions, with electrons carrying 99 percent of the current. Electron spectra in the aurora have been measured by rockets and satellites using particle spectrometers, and electron currents are measured by magnetometers. In addition, elèctron currents have been estimated by measuring X-ray fluxes on balloons. Bolyunova et al[5] measured electron fluxes of $1.6 \times 10^9/cm^2$ sec at 20 keV on the Electron 1 and Electron 3 satellites at 6000 to 7000-km altitude. Using data from DMSP, Shuman et al[6] measured a peak flux of 2.4×10^{10} electrons/cm^2 sec at 7 keV in a 26 March 1976 substorm. Tanskanen, Hardy, and Burke[7] measured an electron flux of $6 \times 10^{10}/cm^2$ sec at

5. Bolyunova, A.D., Vaisberg, O.L., Galperin, Yu.I., Potapov, B.P., Temny, V.V., and Shufskaya, F.K. (1966) Investigation of corpuscles on the Electron 1 and Electron 3 satellites - preliminary results, Space Research VI, McMillan, New York.

6. Shuman, B.M., Vancour, R.P., Smiddy, M., Saflekos, N.A., and Rich, F.J. (1981) Field-aligned current, convective electric field, and auroral particle measurements during a major magnetic storm, J. Geophys. Res. 86:5561.

7. Tanskanen, P.J., Hardy, D.A., and Burke, W.J. (1981) Spectral characteristics of precipitating electrons associated with visible aurora in the premidnight oval during periods of substorm activity, J. Geophys. Res. 86:1379.

840 km altitude in December 1977. This latter flux corresponds to a current of 100 $\mu A/m^2$. Whalen and McDiarmid,[8] using a rocket measurement, reported currents of 200 $\mu A/m^2$ in a moderate substorm. Burke, utilizing magnetometer measurements in the S3-2 satellite, reported an electron current of 200 $\mu A/m^2$ on 19 September 1976 at 1500-km altitude.[9]

Further information concerning electron fluxes in auroras is obtained from measurements of the energy flux of electrons. For example: 30 $ergs/cm^2$ sec are characteristic of bright, active arcs,[10] energy flux measurements on TIROS/NOAA show that more than 60 $ergs/cm^2$ sec are deposited on 5 percent of passes and that in rare events, 500 $ergs/cm^2$ sec are deposited.[11] For a spectrum characteristic of the most energetic events this corresponds to a current of 50 $\mu A/m^2$.

A plasma probe will charge to that floating potential at which the net current to the probe is zero. In the present case, the precipitating hot electron current and the ambient ram ion current are balanced. Secondary emission from surface materials by electrons and backscattering of electrons are important processes, and are taken into account approximately by using a secondary emission and backscattering coefficient.

The current balance equation is:

$$R_o^2 j_e (1 - S_p) \exp\left(-\frac{e\phi}{kTe}\right) = \pi R_c^2 j_r (1 + S_1)$$

where

j_e = hot electron current
j_r = ram ion current
S_p = total secondary yield from the hot electron current
S_i = the total secondary yield from ion current
R_o = vehicle radius
R_c = sheath radius ,

8. Whalen, B.A., and McDiarmid, I.B. (1972) Observations of magnetic-field aligned auroral electron precipitation, J. Geophys. Res. 77:191.
9. Burke, W.J. (1980) Electric fields, Birkeland currents, and electron precipitation in the vicinity of discrete auroral arcs, Proceedings of the Chapman Conference, Fairbanks, Alaska.
10. Meng, C.-I., Snyder, Jr., A.L., and Kroehl, H.W. (1978) Observations of auroral westward-traveling surges and electron precipitations, J. Geophys. Res. 83:575.
11. Evans, D.S. (1981) A study of exceptionally large auroral particle energy influxes, measured by the TIROS/NOAA total energy detector, EOS, 62(45):985.

where

$$R_c = R_p + \lambda_D \left(2.50 - 1.54 \exp\left(-0.32\, R_p/\lambda_D\right)\right) \cdot \left(e^{\phi}\, p/kT_e\right)^{1/2} \quad .$$

This is the Laframboise result for a spherical probe whose radius is large compared to the Debye length λ_D.

The hot electrons at 5 keV are substantially less affected by the plasma sheath than the ram ions at 5 eV.

5. RESULTS

Figure 2 shows the eclipse potential on spheres of radius 0.05, 0.5, and 5.0 m and for an infinitely large craft as a function of the ratio of precipitating electron to ram ion current densities in a plasma with ambient density $10^5/cm^3$. Sphere radii of 50 m and larger follow the charging curve for infinite radius.

The results here show a much higher threshold for charging of 0.5-m radius spacecraft than the Parks-Katz result and predict lower potentials for small spacecraft and higher potentials for large spacecraft.

6. DISCUSSION

In the calculation of charging several effects have been neglected which will be discussed here. Consider first the effects of the earth's magnetic field. Linson has argued that the effect of moderate levels of plasma turbulence in the sheath surrounding a probe is to increase the cross-field transport of particles to the limit that is expected for the case of space-charge-limited flow. In the present case, this mechanism is invoked for the hot electrons, where the Laframboise probe theory is employed in place of the Langmuir-Blodgett expression used by Linson. Magnetic field effects on ion motion can be safely ignored because the mean ion gyroradius is about 5 m in the ambient plasma at shuttle altitudes.

7. EFFECTS OF FLOW

In polar orbit at 200 to 400-km altitude, spacecraft velocities of 8×10^5 m/sec are much larger than thermal velocities of the ambient ionospheric plasma, which are typically 2×10^5 m/sec.

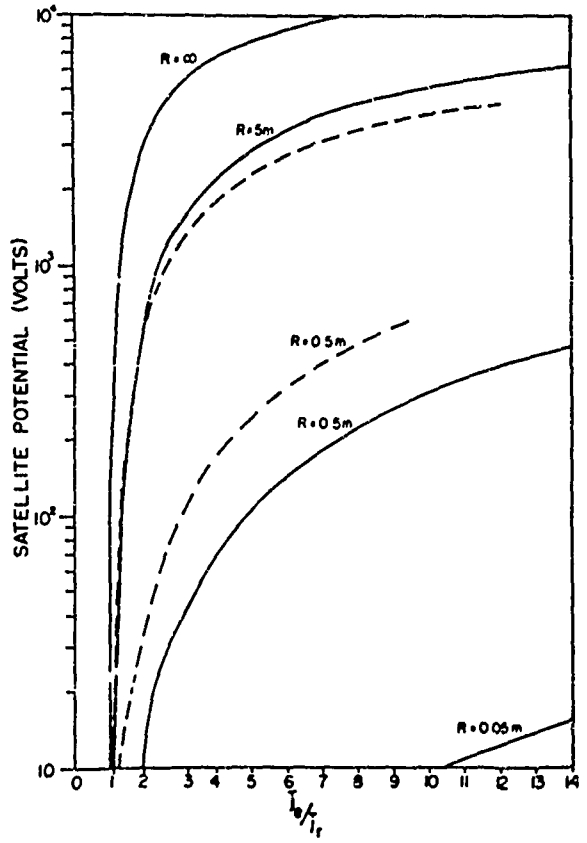

Figure 2. Eclipse Potential of Spheres of Radius 0.05, 0.5, 5.0, and Infinity vs the Ratio of Precipitating Hot Electron to Ram Ion Current Densities, Corrected for Backscattering and Secondary Emission

The potentials on the spacecraft surfaces are then determined by the flow of the ionospheric plasma around the vehicle. The main features of the flow are the ion ram current to the forward surface and the wake at the rear of the vehicle. The wake of a vehicle in the ionosphere has been studied theoretically (Bettinger and Chen,[12] Kanal,[13] Al'pert et al,[14] Woodroffe and Sonin,[15] Liu and Jew,[16] Gurevich et al,[17] Liu,[18,19] Gurevich and Pitaevskii,[20] Grabowsky and Fischer,[21] Call,[22] Fournier and Pigache,[23] Parker,[24] Al'pert[2]), and experimentally.[25,26,27]

Figure 3 shows the ratio of the ion current at the rear of Satellite S3-2 to the current on the forward surface.[27] In the range of altitudes from 300 to 400

Because of the large number of references cited above, they will not be listed here. See References, page 262.

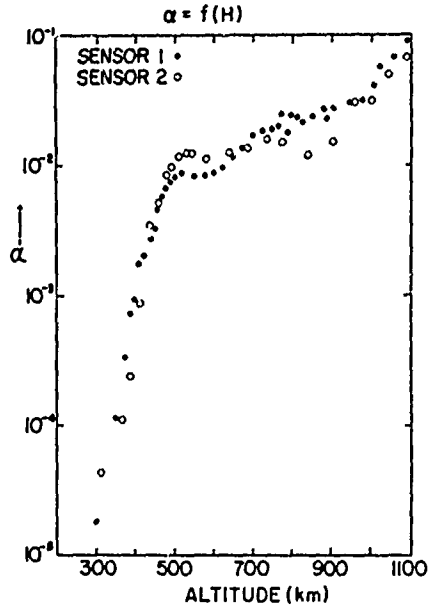

Figure 3. The Ratio of Wake to Ram Ion Current for S3-2 From 300- to 1100-km Altitude

km this ratio varies from 10^{-5} to 10^{-4}. This data was taken on several orbits for equatorial and middle latitudes. The dependence of this ratio (called α) on plasma parameters has been studied extensively. R_D, the ratio of vehicle radius to Debye length, is the parameter of interest.

α is an exponentially decreasing function of R_D, over the parameter range for which data is available.[26,28] In particular for an O^+ environment,[28]

$$\alpha = A_o \exp (A_1 R_D) \quad ,$$

where $A_o = 0.32$; $A_1 = -0.026$. At 300 km, the Debye ratio R_D of the Shuttle is 2000 and at 450 km, $R_D = 1200$. No experimental information exists in this parameter range.

28. Samir, U., Kaufman, Y.J., Brace, L.H., and Brinton, H.C. (1980) The dependence of ion density in the wake of the AE-C satellite on the ratio of body size to Debye length in an [O^+] -dominated plasma, J. Geophys. Res. 85:1769.

8. CHARGING IN THE WAKE

Using this information concerning the depletion of ions in the near wake, we can compute the expected potential. When auroral electron streams are at extremely high values, the forward part of the spacecraft will charge. For average auroral fluxes, however, the forward part of the vehicle will not charge, since $j_e/j_r < 1$. In the presence of the wake, the situation is different. At 300 km at 180° from the forward direction, $j_e/-j_r$ is now a factor of 10^5 higher, and charging can take place at much lower values of auroral flux than for the case where the wake is neglected. In particular, at 1 $\mu A/m^2$, a moderate auroral electron current, the asymptotic values of potentials in Figure 2 would apply, so that the stern will charge to more than 6 kV. This means that charging of the aft portion of the vehicle to multikilovolt potentials in an aurora will be common, although charging of the forward portion would be infrequent.

This differential charging is produced by the interplay of flow effects with precipitating auroral electrons. Differential potentials of this magnitude can lead to surface arcing or breakdown across insulating tiles.

Interestingly, the Shuttle will not necessarily fly in a nose-forward aspect. As an orbiting vehicle, for some applications it will fly with the bottom forward and with the experiment bay open and in the wake direction. We have seen that the maximum charging will take place on the aft surface, so that the experiment bay will sometimes be subject to the maximum effects of charging by the auroral electron beam, to potentials of 6 kV or more.

Using the Samir expression for j_r, the ion current at 180° is negligibly small at $R_D = 1200$. As an upper limit, the values found for S3-2 will be employed. Figure 3 shows the variation of X with altitude in the 300- to 1100-km range.[27] In the near wake, the charging is due entirely to the energetic electrons, to a good approximation.

Since the ion current is absent, in the 200- to 400-km region charging of the rear of the vehicle can take place with 4 to 5 orders of magnitude less hot electron current than the front. However, the rate of charging in the electron stream must be considered to determine the potential to which the vehicle could actually charge.

References

1. Sagalyn, R.C., and Burke, W.J. (1977) INJUN 5 observations of vehicle potential fluctuations at 2500 km, in Proceedings of the Spacecraft Charging Technology Conference, C.P. Pike and R.R. Lovell, Eds., AFGL-TR-77-0051, NASA TMX73537, AD A045459.

2. Al'pert, Ya.L. (1976) Wave-like phenomena in the near-earth plasma and interactions with man-made bodies, in Handbuch der Physik, Encyclopedia of Physics, Vol. XLIX V (5), Springer Verlag, Berlin, Heidelberg, New York.

3. Langmuir, I., and Blodgett, K. (1923) Currents limited by space charge between coaxial cylinders, Phys. Rev. 22:347; (1924) Currents limited by space charge between concentric spheres, Phys. Rev. 24:99.

4. Parks, D.E., and Katz, I. (1981) Charging of a large object in low polar earth orbit, in Spacecraft Charging Technology, 1980, AFGL-TR-81-0270, NASA CP 2182, AD A114426.

5. Bolyunova, A.D., Vaisberg, O.L., Galperin, Yu.I., Potapov, B.P., Temny, V.V., and Shufskaya, F.K. (1966) Investigation of corpuscles on the Electron 1 and Electron 3 satellites - preliminary results, Space Research VI, McMillan, New York.

6. Shuman, B.M., Vancour, R.P., Smiddy, M., Saflekos, N.A., and Rich, F.J. (1981) Field-aligned current, convective electric field, and auroral particle measurements during a major magnetic storm, J. Geophys. Res. 86:5561.

7. Tanskanen, P.J., Hardy, D.A., and Burke, W.J. (1981) Spectral characteristics of precipitating electrons associated with visible aurora in the premidnight oval during periods of substorm activity, J. Geophys. Res. 86:1379.

8. Whalen, B.A., and McDiarmid, I.B. (1972) Observations of magnetic-field aligned auroral electron precipitation, J. Geophys. Res. 77:191.

9. Burke, W.J. (1980) Electric fields, Birkeland currents, and electron precipitation in the vicinity of discrete auroral arcs, Proceedings of the Chapman Conference, Fairbanks, Alaska.

10. Meng, C.-I., Snyder, Jr., A.L., and Kroehl, H.W. (1978) Observations of auroral westward-traveling surges and electron precipitations, J. Geophys. Res. 83:575.

11. Evans, D.S. (1981) A study of exceptionally large auroral particle energy influxes, measured by the TIROS/NOAA total energy detector, EOS, 62(45):985.

12. Bettinger, R.T., and Chen, A.A. (1968) An end effect associated with cylindrical Langmuir probes moving at satellite velocities, J. Geophys. Res. 73:2513.

13. Kanal, M. (1964) Theory of current collection of moving cylindrical probes, J. Appl. Phys. 35:1697.

14. Al'pert, Ya.L., Gurevich, A.V., and Pitaevskii, L.P. (1965) Space Physics With Artificial Satellites, Consultant's Bureau, New York.

15. Woodroffe, J.A., and Sonin, Ain.A. (1974) Calculations for the wake of a small cylinder under ionospheric satellite conditions, Phys. Fluids 17:79.

16. Liu, V.C., and Jew, H. (1967) On the electrodynamic wake in a rarefied plasma, in Rarefied Gas Dynamics, Suppl. 4, Vol. II, C.L. Brundin, Ed., Academic Press, New York.

17. Gurevich, A.V., Pitaevskii, L.P., and Smirnova, V.V. (1970) Ionospheric aerodynamics, Soviet Phys. Usp. 99(1-2):595.

18. Liu, V.C. (1969) Ionospheric gas dynamics of satellites and diagnostic probes, Space Sci. Rev. 9:423.

19. Liu, V.C. (1975) On ionospheric aerodynamics, Prog. Aerosp. Sci. 16:273.

20. Gurevich, A.V., and Pitaevskii, L.P. (1975) Non-linear dynamics of rarefied ionized gas, Prog. Aerosp. Sci. 16(3):227.

21. Grabowsky, R., and Fischer, T. (1975) Theoretical density distribution of plasma streaming around a cylinder, Planet. Space Sci. 23:287.

22. Call, S.M. (1969) The Interaction of a Satellite With the Ionosphere, Report 46, Plasma Lab, Columbia University, New York.

23. Fournier, G., and Pigache, D. (1975) Wakes in collisionless plasmas, Phys. Fluids 18:1443.

24. Parker, L.W. (1978) Differential charging and sheath asymmetry of non-conducting spacecraft due to plasma flows, J. Geophys. Res. 83:4873.

25. Samir, U., Maier, E.J.R., and Troy, Jr., B.E. (1973) The angular distribution of ion flux around an ionospheric satellite, J. Atmos. Terr. Phys. 35:513.

26. Samir, U., Kaufman, Y.J., Brace, L.H., and Brinton, H.C. (1980) The near wake structure of the Atmosphere Explorer-C satellite: a parametric investigation, J. Geophys. Res. 85:1769.

27. Samir, U., Wildman, P.J., Rich, F., Brinton, H.C., and Sagalyn, R.C. (1981) About the parametric interplay between ionic mach number, body size and satellite potential in determining the ion depletion in the wake of the S3-2 satellite, J. Geophys. Res. 86(11):161.

28. Samir, U., Kaufman, Y.J., Brace, L.H., and Brinton, H.C. (1980) The dependence of ion density in the wake of the AE-C satellite on the ratio of body size to Debye length in an [O+] -dominated plasma, J. Geophys. Res. 85:1769.

18. Differential Charging

by

A. L. Besse
Air Force Geophysics Laboratory
Hanscom AFB, Mass. 01731

Based on a presentation by

Carolyn Purvis
NASA Lewis Research Center
Cleveland, Ohio 44135

Abstract

When electrically isolated surfaces have different material properties or are exposed to different environments, different potentials will be induced. The rates of charging are determined by the currents and the capacitances. The levels of charging are basically determined by the energies in the system--either the energies of the charged particles, whether they be natural or emitted, or from the applied voltages on the spacecraft.

Consider a geosynchronous spacecraft. The sheath is orders of magnitude larger than the spacecraft and much larger than the typical insulation thickness. Current densities are very small, a fraction of a nanoampere per square centimeter, but the particles are hot, with kilovolt energies. These numbers indicate that charging of the spacecraft with respect to the sheath should take place very rapidly, but that charging of various insulated surfaces with respect to the frame of the spacecraft should take place rather slowly. This implies that in eclipse there will be rapid charging of the whole structure, with slow differential

charging, while in sunlight, due to photoemission, the sun side does not charge but insulated surfaces on the dark side charge to high potential.

Data from the ATS-6 satellite showed that eclipse charging was as predicted. In sunlight, however, about 10 min after the injection of hot particles, main frame charging started and proceeded slowly, contrary to predictions. This can be explained by differential charging, as shown in a NASCAP simulation. Differential charging on the dark side creates a barrier of about 3.5 V on the sunlit side, suppressing photoelectron emission. The same simulation with spin added also shows charging, but at an even slower rate. Spacecraft that are spinning or have less dark area have to develop larger differentials to build barriers. The result in many cases is that differential charging is actually greater where the absolute potential is lower. On ATS-6, the emission of a neutral plasma seemed to lock the potential to a value close to zero and to destroy the barrier.

The ATS-5 satellite was equipped with a 'neutralizer' consisting of a hot wire filament emitting electrons. When it was turned on in eclipse to discharge the spacecraft, the potential dropped very rapidly at first, followed by a slow rise. Once again, this could be explained by differential charging.

In low earth orbit the situation is tremendously different. The main source of anisotropy in the environment is no longer solar radiation. Ambient electrons and ram ions exceed the current density of photoelectrons. The Debye length is comparable to other relevant thicknesses. These imply there should not be a tremendous gap between absolute and differential charging rates.

Contents

19. Potential Barriers and Multiple Roots in Spacecraft Charging

by

A. L. Besse
Air Force Geophysics Laboratory
Hanscom AFB, Mass. 01731

1. INTRODUCTION

This paper considers two phenomena that may be demonstrated with considerable rigor by computer modeling using a code such as NASCAP. The computer modeling, however, fails to give insight into the physics involved. This paper attempts to furnish such insight by use of simple barrier models and by sketching the history of multiple roots with emphasis on the necessary conditions.

Geosynchronous spacecraft in sunlight occasionally charge to negative potentials of a few hundred volts. The charging is of course driven by the flux of ambient energetic electrons striking the surface. However, the flux of low energy photoelectrons released from the surface exceeds the flux of ambient electrons arriving at the surface. Therefore, negative charging would appear to be impossible. A plausible model will be used to demonstrate that insulated surfaces on the dark side can, by charging to large negative potentials, create a potential barrier on the sun side. This barrier prevents the escape of photoelectrons. Unable to escape, these electrons return to the spacecraft. With the

photoelectron current nullified, negative charging of the spacecraft can take place in sunlight whenever the plasma is sufficiently energetic.

If half of the conducting surface on the dark side of a spacecraft is covered with an insulating material, one would expect that the net current between the plasma and that surface would be cut in half. This is not necessarily so. A second model will be used to demonstrate that potential barriers can form, blocking the escape of secondary electrons from the exposed dark side conducting surface. The result is that the net current to this surface is much more negative than would be expected.

Traditional plasma probe theory applied to spacecraft predicts a single stable floating potential at which the plasma-to-spacecraft current vanishes. This is not necessarily so for a non-Maxwellian plasma. The net current as a function of potential may have more than one root. The history of multiple roots will be reviewed, emphasizing the critical roles played by the emission of low energy secondary electrons and by non-Maxwellian electron distributions.

Multiple roots are possible not only for the main frame of a spacecraft, but also for differentially charged insulated surface areas. However, the differential charging creates potential barriers that can determine whether or not such multiple roots exist.

2. MONOPOLE-DIPOLE THEORY

Multidimensional effects leading to a saddle point in the potential near a plasma probe or spacecraft were first pointed out by Whipple and Parker.[1,2] The use of a combination of a monopole and a dipole field to model the formation of a saddle is due to Besse and Rubin.[3]

In an energetic plasma, insulated surfaces on the dark side of a spacecraft charge to large negative potentials. This creates a barrier and saddle point on the sun side blocking the escape of photoelectrons. The sun side then charges negatively until the barrier is weakened enough to allow the escape of most of the photoelectrons. The energy of the photoelectrons is only a few electron volts. The monopole-dipole field is modeled by

1. Whipple, Jr., E.C., and Parker, L.W. (1969) Theory of an electron trap on a charged spacecraft, J. Geophys. Res. 74:2962.
2. Whipple, Jr., E.C., and Parker, L.W. (1969) Effects of secondary electron emission on electron trap measurements on the magnetosphere and solar wind, J. Geophys. Res. 74:5763.
3. Besse, A.L., and Rubin, A.G. (1980) A simple analysis of spacecraft charging involving blocked photoelectron currents, J. Geophys. Res. 85:2324-2327.

$$\phi(r,\theta) = \frac{Q}{r_o}\left[\frac{r_o}{r} + A\left(\frac{r_o}{r}\right)^2 \cos\theta\right] \tag{1}$$

$$\frac{Q < 0}{r \geq r_o}$$

$$0.5 \leq A \leq 1.1$$

where

ϕ = potential
Q = net charge on spacecraft
r_o = spacecraft radius
r = radial position
A = dimensionless parameter
θ = zenith angle measured from midnight .

The parameter A specifies the strength of the dipole component relative to the monopole component. The limits imposed on Q, r, and A define the range where the theory is useful for explaining daylight charging. Equation (1) is readily manipulated to yield several useful quantities. The radial component of the electric field at the surface is given by

$$E(r_o,\theta) = -\frac{Q}{r_o^2} - \frac{2AQ}{r_o^3}\cos\theta \quad ; \quad Q < 0 \quad . \tag{2}$$

The first term represents the monopole contribution; the second term the dipole contribution. On the sun side the two terms have opposite polarities with the dipole term opposing the escape of photoelectrons. The area over which a retarding field (for escaping electrons) exists is given by:

$$\text{Area} = 2\pi\left[1 - \frac{1}{2A}\right] \quad , \quad A \geq \frac{1}{2} \quad . \tag{3}$$

The position of the saddle is given by:

$$r_s = 2Ar_o \quad , \quad A > \frac{1}{2} \quad . \tag{4}$$

The height of the barrier relative to the noon position on the surface is given by

$$|\phi\,(r_s,\pi) - \phi\,(r_o,\pi)| = \left|\frac{Q}{r_o}\left(A - \frac{1}{2}\right)\right| \quad ; \quad A \geq \frac{1}{2} \quad . \tag{5}$$

The predictions of the theory were calculated for a spacecraft of 1 m radius with an average surface potential of 1 kV negative. The results are given in Table 1.

Table 1. Predictions of the Monopole-Dipole Theory Applied to a Spherical Spacecraft of 1 m Radius With a Dielectric Surface Material Charged to an Average Potential of 1 kV Negative. The dimensionless parameter A determines the strength of the dipole component relative to the monopole component, both being measured at the surface at the midnight position

A→	1.1	1.0	0.9	0.8	0.7	0.6	0.5
θ	Surface Potentials (kV)						
0° (midnight)	-2.10	-2.00	-1.90	-1.80	-1.70	-1.60	-1.50
30°	-1.95	-1.87	-1.78	-1.69	-1.61	-1.52	-1.43
60°	-1.55	-1.50	-1.45	-1.40	-1.35	-1.30	-1.25
90° (dawn/dusk)	-1.00	-1.00	-1.00	-1.00	-1.00	-1.00	-1.00
120°	-0.45	-0.71	-0.55	-0.60	-0.65	-0.70	-0.75
150°	-0.05	-0.13	-0.22	-0.31	-0.39	-0.48	-0.57
180° (noon)	+0.10	0.00	-0.10	-0.20	-0.30	-0.40	-0.50
	Potentials at Saddle (kV)						
180° (noon)	-0.23	-0.25	-0.28	-0.31	-0.36	-0.42	-0.50
	Distance of Saddle from Surface (m)						
180° (noon)	1.20	1.00	0.80	0.60	0.40	0.20	0.00
	Surface Radial Electric Fields (kV/m)						
0° (midnight)	+3.20	+3.00	+2.80	+2.60	+2.40	+2.20	+2.00
30°	+2.91	+2.73	+2.56	+2.39	+2.21	+2.04	+1.87
60°	+2.10	+2.00	+1.90	+1.80	+1.70	+1.60	+1.50
90° (dawn/dusk)	+1.00	+1.00	+1.00	+1.00	+1.00	+1.00	+1.00
120°	-0.10	0.00	+0.10	+0.20	+0.30	+0.40	+0.50
150°	-0.89	-0.73	-0.56	-0.39	-0.21	-0.04	+0.13
180° (noon)	-1.20	-1.00	-0.80	-0.60	-0.40	-0.20	0.00
	Surface Area with Negative Field (m^2)						
180° (noon)	3.43	3.14	2.79	2.36	1.80	1.05	0.00

The monopole-dipole field satisfies Laplace's equation and thus is appropriate for spacecraft which are small compared to the Debye length. This includes geosynchronous spacecraft of existing dimensions but not larger spacecraft in low earth orbit, such as the shuttle.

The theory seeks to explain daylight charging and is needed only if the photoelectric current is larger than the ambient electron current. Norman and Freeman[4] measured the photoelectron current from a small gold spherical probe on OGO-5. They obtained a value of 22 $\mu A/m^2$ based on the total area of the probe. Garrett et al[5] measured a maximum electron number flux on ATS-6 of $1.7 \times 10^9/cm^2$ sec ster corresponding to 9 $\mu A/m^2$. Thus the photoelectron current is in general larger.

Data reported by Garrett et al[5] and Mullen et al[6] on ATS-5, ATS-6, and SCATHA show that if a spacecraft is charged to roughly 100 V negative in daylight it will charge to roughly 5 kV upon entering the earth's shadow. We may theorize that the dark side insulating surfaces are at roughly 5 kV negative both before and after entering eclipse. Assuming half of the dark side surface is insulated, this gives a 25:1 sun side to average dark side potential. This is considerably larger than predicted by this first order theory.

3. HARMONIC FIELD THEORY

Consider a spacecraft in sunlight whose conducting surfaces are charged to a small negative potential ϕ_A and whose insulated surfaces on the dark side are charged to a large negative potential ϕ_B. Assume that the insulated surfaces are in the form of strips of width W separated by areas of conducting surfaces also of width W and that W is small compared to both the radius of curvature and to the extent of the surface. The potential will be given approximately by:

$$\phi(x,y) = \frac{\phi_B+\phi_A}{2} + (\phi_B - \phi_A)\cos(\pi y/W)\, e^{-\pi x/W} \qquad (1)$$

4. Norman, K., and Freeman, R.M. (1973) Energy Distribution of Photoelectrons Emitted from a Surface on the OGO-5 Satellite, and Measurements of Satellite Potential, Photon and Particle Interactions with Surfaces in Space, Grard, S.J.L., Ed., D. Reidel Publishing Co., Holland.

5. Garrett, H.B., McInery, R.E., Deforest, S.E., and Johnson, B. (1979) Modeling of the Geosynchronous Plasma Environment - Part 3. ATS-5 and ATS-6 Pictorial Data Atlas, AFGL-TR-79-0015, AD A067843.

6. Mullen, E.G., Gussenhoven, M.S., and Garrett, H.B. (1981) A "Worst Case" Spacecraft Environment as Observed by SCATHA on 24 April 1974, AFGL-TR-81-0231, AD A108680.

where

x = distance from surface

y = distance parallel to surface and perpendicular to strips.

The component of the electric field normal to the surface will be, at the surface

$$E(y) = \frac{2\pi}{W} (\phi_B - \phi_A) \cos (\pi y/W) \quad . \tag{7}$$

If W is sufficiently small this harmonic field will be much larger in magnitude than the 1/R field due to the net charge on the spacecraft. It will block escape of secondary electrons from the dark side conducting surface. It will also cause some secondary electrons from the very negative insulated strips to go to the less negative conducting strips. The net effect will be a much larger negative current to the conducting surfaces on the dark side than would be expected.

The harmonic field at the surface can be fitted to any desired profile by adding the proper harmonics. The higher harmonics of course decay faster. Such harmonic fields obey Laplace's equation and are realistic provided that the strips are narrow compared both to other spacecraft dimensions and to the Debye length of the secondary electrons.

4. MULTIPLE ROOTS

A key factor in multiple root phenomena is the change in mean electron impact energy with change in object potential. If the electrons are monoenergetic, as in a vacuum tube, a negative potential will reduce their impact energy, that is, it will soften the spectrum. A key question is, how does the mean impact of electrons at geosynchronous altitude respond to the spacecraft potential? The answers can be found by examining pictorial spectra of eclipse charging events, in particular ATS-5 and ATS-6 pictorial spectra reported by Garrett et al,[5] by Deforest[7] and by Olsen.[8] In every case when the spacecraft enters eclipse and charges negatively, the electron spectrum at low energies is sharply attenuated while the spectrum at high energies is not noticeably affected. Clearly the retarding potential has increased the mean impact energy, that is, it has hardened the spectrum. The mean impact energy of a Maxwellian distribution

7. Deforest, S.E. (1972) Spacecraft charging at synchronous orbit, J. Geophys. Res. 77:652.

8. Olsen, R.C. (1980) Differential and Active Charging Results from the ATS Spacecraft, PH Dissertation Univ. of California, San Diego, pp. 125-126, Figure 1.

depends only on temperature and is independent of retarding potentials. Thus, vacuum tube and geosynchronous plasmas both exhibited non-Maxwellian behavior as far as mean impact energy vs potential is concerned.

The non-Maxwellian nature of the spectra having been established, the history of multiple roots will be reviewed, a history in which non-Maxwellian spectra play a key role. Also playing a key role is the copious emission of secondary electrons - more than one secondary per primary. The electronic age started with that triode vacuum tube amplifier. These tubes accelerate electrons to a few hundred electron volts. By coincidence, this is the range for copious emission of secondary electrons. However, in a triode the electric field at the output electrode (the "plate") is such as to prevent escape of the secondaries and thus they have no effect. No multiple roots exist for these tubes. The triode has negative internal feedback that limits the voltage amplification. To eliminate the feedback and to increase the amplification, an additional electrode known as a "screen" was introduced and the result was the tetrode. The unintentional result was to reverse the electric field at the plate over a portion of the operating range and to let the secondary electrons from the plate escape and be collected by the screen. Multiple roots appeared; two output levels for a single input level became possible. The mechanism has been explained by Alfrey.[9] Essentially what happens is that with the plate at its least positive potential the monoenergetic electrons strike it with an energy well below that at which secondary electron emission peaks. Less than one secondary electron per primary is emitted. The net effect is a negative current to the plate which holds its potential to a small positive value. On the other hand, with the plate at its most positive potential, the electrons striking it have sufficient energy to release more than one secondary electron per primary. The net effect is a positive current to the plate that holds its potential to a large positive value. Thus two output signals correspond to a single input signal. This was not acceptable for normal use. A fifth electrode was added, re-establishing a barrier to the escape of secondary electrons from the plate. The resulting tube, a "pentode", performed as intended. Early plasma probe theory developed by Mott-Smith and Langmuir[10] treated only Maxwellian distributions and neglected secondary electrons. The laboratory plasmas in which the probes were used were generally too cool for secondary electrons to be important. The early theory predicted a single root. When the theory was first applied to geosynchronous spacecraft, it failed to explain observations. Addition of secondary emission to probe theory resulted in better agreement

9. Alfrey, G.F. (1964) Physical Electronics, D. Van Nostrand, Princeton, N.J.
10. Mott-Smith, H.M., and Langmuir, I. (1926) The theory of collectors in gaseous discharges, Phys. Rev. 28:727-763.

between observation and theory. Still no multiple roots appeared in the theory. Only when the theory was extended to include non-Maxwellian distributions did multiple roots appear. The mechanism of dual Maxwellian distributions has been explained in some detail by Besse[11] making use of earlier work by Prokopenko and Laframboise[12] and of Sanders and Inouye.[13]

The essential mechanism for multiple roots for geosynchronous spacecraft will now be outlined. At zero potential the impacting electrons have a mean energy just a little above that at which maximum secondary electron emission occurs. Secondary electron emission is sufficient to prevent charging to negative potentials. The spacecraft cannot charge positively to more than a few volts because then the secondaries cannot escape. Therefore the spacecraft remains essentially at zero potential. Consider what may happen if the momentary operation of an ion gun causes the spacecraft to charge negatively. The effect of the negative potential is to increase the mean electron impact energy as previously discussed. As the mean impact energy originally was just above the energy for peak secondary emission, the effect is to move the energy further away from the peak. The number of secondaries per primary is reduced. There are no longer enough secondary electrons to prevent charging to a large negative potential. The spacecraft continues to charge negatively even after the gun is turned off.

Multiple roots and potential barriers can interact. If some surfaces on a spacecraft are at their positive roots and others at their negative roots, then the differential potentials are likely to create potential barriers in front of the positive root surfaces. The result is that the secondaries cannot escape and the positive roots cease to exist. Thus potential barriers tend to mandate that all surfaces possessing multiple roots be either at their positive roots or all be at their negative roots.

11. Besse, A. L. (1981) Unstable potential of geosynchronous spacecraft, J. Geophys. Res. 86:2443-2446.

12. Prokopenko, S. M. L., and Laframboise, J. G. (1977) Prediction of large negative shaded-side spacecraft potentials, Proc. Spacecraft Charging Technology Conf. NASA Tech Memo. 73537.

13. Sanders, N. L., and Inouye, G. T. (1978) Secondary Emission Effects on Spacecraft Charging: Energy Distribution Considerations, NASA Conf. Publ. 2071.

References

1. Whipple, Jr., E.C., and Parker, L.W. (1969) Theory of an electron trap on a charged spacecraft, J. Geophys. Res. 74:2962.
2. Whipple, Jr., E.C., and Parker, L.W. (1969) Effects of secondary electron emission on electron trap measurements on the magnetosphere and solar wind, J. Geophys. Res. 74:5763.
3. Besse, A.L., and Rubin, A.G. (1980) A simple analysis of spacecraft charging involving blocked photoelectron currents, J. Geophys. Res. 85:2324-2327.
4. Norman, K., and Freeman, R.M. (1973) Energy Distribution of Photoelectrons Emitted from a Surface on the OGO-5 Satellite, and Measurements of Satellite Potential, Photon and Particle Interactions with Surfaces in Space, Grard, S.J.L., Ed., D. Reidel Publishing Co., Holland.
5. Garrett, H.B., McInery, R.E., Deforest, S.E., and Johnson, B. (1979) Modeling of the Geosynchronous Plasma Environment - Part 3. ATS-5 and ATS-6 Pictorial Data Atlas, AFGL-TR-79-0015, AD A067843.
6. Mullen, E.G., Gussenhoven, M.S., and Garret, H.B. (1981) A "Worst Case" Spacecraft Environment as Observed by SCATHA on 24 April 1974, AFGL-TR-81-0231, AD A108680.
7. Deforest, S.E. (1972) Spacecraft charging at synchronous orbit, J. Geophys. Res. 77:652.
8. Olsen, R.C. (1980) Differential and Active Charging Results from the ATS Spacecraft, PH Dissertation Univ. of California, San Diego, pp. 125-126, Figure 1.
9. Alfrey, G.F. (1964) Physical Electronics, D. Van Nostrand, Princeton, N.J.
10. Mott-Smith, H.M., and Langmuir, I. (1926) The theory of collectors in gaseous discharges, Phys. Rev. 28:727-763.
11. Besse, A.L. (1981) Unstable potential of geosynchronous spacecraft, J. Geophys. Res. 86:2443-2446.

12. Prokopenko, S. M. L., and Laframboise, J. G. (1977) Prediction of large negative shaded-side spacecraft potentials, Proc. Spacecraft Charging Technology Conf. NASA Tech Memo. 73537.

13. Sanders, N. L., and Inouye, G. T. (1978) Secondary Emission Effects on Spacecraft Charging: Energy Distribution Considerations, NASA Conf. Publ. 2071.

Contents

20. Mechanisms That Limit Potentials on Ionospheric Satellites

by

D. E. Parks
I. Katz
S-Cubed Inc.
La Jolla, Calif. 92038

1. INTRODUCTION

Mechanisms that limit the electric potential on the body of an ionospheric satellite are considered. For spinning satellites with dielectric coatings it is shown that the currents of rotating charge embedded in the dielectric surface play a role in limiting the spacecraft ground potential relative to the surrounding plasma. Such currents can account for previous discrepancies of more than a factor of 2 between measured and calculated potentials of satellites in the region of the ionosphere where the effect of O^+ is dominant. The rotating current exceeds the neutral approximation current of O^+ to the wake side of the AE-C satellite, for example, by several orders of magnitude. More generally, dielectric conduction can also limit the satellite potential. The importance of such small currents as result from spin and conduction stems from the extremely small ion currents impinging on the wake side of the satellite. Theoretical estimates based on a newly described constant of the motion of a particle in a non-self-consistent electric potential indicates that the ion current density at the

wake side pole of a sphere with surface potentials such as those measured on AE-C, though substantially augmented by the electrical attraction of ions to the charged satellite, does not significantly affect the current balance. Field enhancement of wake side currents may be substantial, however, for large body potentials, and may play a significant role in limiting those potentials. Effects of combined electric and magnetic fields are not considered, but it is noted that in the absence of electric fields, the neutral approximation provides an upper bound on the current per unit area to any point on the surface of a convex body.

2. POTENTIAL CALCULATIONS

Consider an infinitely long metallic cylinder of radius a-d, uniformly coated by a dielectric with thickness d << a. The cylinder moves through the space plasma with velocity $\vec{V}_o$ and rotates with angular velocity ω about its axis of symmetry. We describe the physical situation from the perspective of a non-rotating space observer moving with the constant velocity $\vec{V}_o$. The potential at the dielectric-vacuum interface is denoted by $V(\alpha)$ and that of satellite ground by V_g.

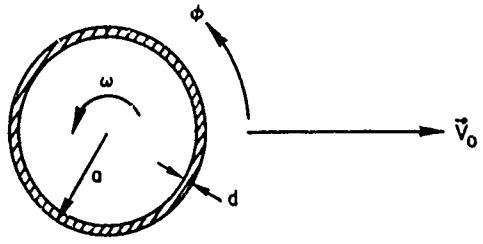

Figure 1. Geometry for Potential Calculations

An approximate equation for the current balance on the dielectric surface is given by

$$-j_i(\alpha) + j_o \exp[V(\alpha)/\theta] + j_e(\alpha) - j_\nu(\phi) + \frac{\omega \kappa \epsilon_o}{d} \frac{\partial V}{\partial \alpha} = 0 \quad . \tag{1}$$

The terms in this equation are, in their order of appearance, the current densities of plasma ions and electrons at position α on the surface, dielectric conduction, photoelectrons, and rotating dielectric-embedded charge.

Equation (1) is applied to the analysis of potentials on the AE-C satellite. For the case of the AE-C in eclipse, the rotating current

$$\frac{\omega\kappa\epsilon_o}{d}\frac{\partial V}{\partial \alpha} \simeq j_s = \frac{\omega\kappa\epsilon_o}{\pi d}\theta$$

plays the dominant role in limiting the negative charging of the wake-side surface at $\alpha = \pi$. The pertinent current densities (A/m^2) at $\alpha = \pi$ are

$$j_i \simeq 1.3 \times 10^{-21}$$
$$j_c \simeq 1 \times 10^{-16}$$
$$j_s \simeq 1.9 \times 10^{-11}$$

Table 1 summarizes the calculated satellite ground and peak surface potentials of a dielectric coated cylinder approximating the AE-C satellite.

Table 1. Ground (V_g) and Peak Surface Potentials for AE-C in Eclipse

AE-C		Model			Conductor
σ (mho/m)		0	0	10^{-17}	
ω (°/sec)	2	2	0	0	
$-V_g/\theta$	~9	8	14		4
-Vpeak		15	40	30	

Even without spin, dielectric conduction currents would limit the wake-side potential at $\alpha = \pi$ to a lesser value than that determined by ion-electron current balance.

3. ELECTRIC FIELD EFFECTS

The previously computed satellite potentials were based on the assumption that ion velocity was a constant of the motion (neutral approximation) and therefore not influenced by electric fields. This assumption is quite good on the front (upstream) surface for low satellite potentials ($\lesssim 5$ eV for O^+). For large potentials it is likely that good estimates can be made for the effective area for

front surface collection of ions. The situation is less clear on the wake-side surface (at $\alpha = \pi$) where electric fields may enhance particle and current densities by many orders of magnitude over their neutral approximation values.

The problem of field focusing is addressed by formulating upper bounds on the $j(\vec{r}_s)$ and $n(\vec{r}_s)$ at a position $\vec{r}_s$ on the satellite surface. The current density bound at $\vec{r}_s$ where the potential is $V(\vec{r}_s)$ given by

$$j_b(\vec{r}_s) = 2\int f_o(\vec{v}) \left(\frac{1}{2} v^2 - V(\vec{r}_s)\right) \quad v\, dv\, d\vec{\Omega} \quad ,$$

where $f_o(\vec{v})$ is the unperturbed (shifted Maxwellian) for plasma ions. The integration proceeds over all $v > 0$ and over a range of solid angle determined by the equations of motion. The validity of j_b as a bound requires that neighboring orbits emanating from $\vec{r}_s$ at a given energy diverge more at $r = \infty$ than at their point of origin.

The calculation of j_b (and n_b) can be carried out for axisymmetric model potentials of the form

$$V(r, \theta) = V_o(r) - f(\alpha)/r^2 \quad ,$$

where (r, α, ϕ) are spherical polar coordinates and $V_o(r)$ is spherically symmetric.

The utility of the above potential is that the quantity

$$C = \frac{L^2}{2} - f(\alpha) \quad ,$$

where L is the magnitude of the angular momentum about $r = 0$, as well as the total energy, and the axial component of angular momentum, are constants of the motion. The solution of the orbit equations is especially simple for particles that reach the poles of a sphere ($\alpha = 0, \pi$), for then the orbits are planar and the orbit determination is reducible to a quadrature.

Specific results for bounds were calculated for potentials of the form

$$V_o(r) = 0$$

$$f(\alpha) = \frac{4a^2}{3\pi^2} |V(\pi)| \left(\alpha^2 - \frac{\pi^2}{4}\right) ; \frac{\pi}{2} < \alpha < \pi$$

$$f(\alpha) = 0 \qquad 0 \leq \alpha \leq \pi/2 \quad ,$$

a form which approximates the surface potentials calculated on the AE-C. The table below summarizes the computed particle and current density bounds as a function of $|V(\pi)/\theta|$.

Table 2. Results for Density and Current Enhancement at Wake-Side Pole

$\lvert eV/\theta \rvert$	0	15	100	1000	10,000
$j/N_o v_{Te}$	7.9×10^{-17}	1.6×10^{-10}	2.3×10^{-6}	0.6	830
n/N_o	8.2×10^{-16}	2.6×10^{-11}	1.3×10^{-7}	1.3×10^{-2}	5.85

The entry in the first column is the actual neutral approximation value at $\alpha = \pi$ on the sphere.

4. CONCLUSIONS

Spin and conduction currents can be important in limiting satellite potentials. Electric fields can cause substantial focusing on wake-side surfaces. Though not an important effect for the AE-C satellite, it may be important for $V \gtrsim 100$ V. The importance of ion focusing for large potentials cannot be presently established, however, without considering departures from orbit-limited conditions.

Acknowledgment

This work was supported by the Air Force Geophysics Laboratory, Hanscom Air Force Base, Mass., under Contract No. F19628-82-C-0081.

Contents

21. The Importance of Neutrals, Transient Effects, and the Earth's Magnetic Field on Sheath Structure

by

L. M. Linson
Science Applications, Inc.
La Jolla, Calif. 92038

Abstract

Several aspects of theoretical treatments of the thickness of the sheath surrounding a large structure in low earth orbit that have received only minimal attention are discussed. It is suggested that the ionization of neutrals should be considered for potentials >> 15 V even though the mean free path for ionization in the ambient atmosphere is >> the structure size R_b. The effects of an enhanced local neutral density, the trapping of electrons in the magnetic field, and modification of the sheath space charge density due to ionization are estimated to support this suggestion. The importance of time scales associated with fluctuations in auroral fluxes, motion through inhomogeneous regions at orbital velocity, the motion of ions, ionization rates, and the response of the ionosphere is emphasized in terms of demonstrating understanding of fundamental physical processes. Lastly, criteria for determining when magnetic field effects cannot be neglected when estimating the sheath thickness S for $e\phi >> kT_e$ are derived and discussed. It is found that for moderate potentials $\phi < 220 R_b^2 V$, where R_b is the structure size in meters, magnetic effects cannot be neglected when the sheath size is comparable to or greater than the gyroradius of an electron of energy $e\phi$. Furthermore, it is found that magnetic effects invalidate cylindrical probe theoretic estimates $S \sim \lambda_D (e\phi/kT_e)^{1/2}$, where λ_D is the Debye length, when the electron density is less than $1.5 \times 10^5/cm^3$.

I. INTRODUCTION

An object or surface (henceforth termed structure) immersed in an ambient plasma disturbs the plasma. The nature of the disturbed region surrounding a structure in low earth orbit (LEO) in the ionosphere is a complicated, unsolved problem. At large potentials, the charged particle densities near the structure differ greatly from their ambient undisturbed values. We term this transition region between the structure and the quasi-neutral ambient (although nonequilibrium) plasma a sheath. The characteristics of this sheath depend on many factors (Whipple, Laframboise, these proceedings) and progress is often made by isolating a small subset of these factors and carrying out calculations of their effects. In this report we briefly discuss two aspects of this complicated problem: the role of neutrals and their ionization, and the importance of time-varying or transient phenomena; and give a criterion when the earth's magnetic field cannot be neglected when estimating sheath sizes for moderate potentials on large bodies.

There have been at least four complementary viewpoints that have generally been adopted when considering the electrical interactions that occur between a structure and an ambient plasma. They are:

(1) Probes as a diagnostic tool. This is the classical and most studied case. The viewpoint adopted here is to answer the following question: How does one interpret current-voltage characteristics in terms of the properties of the undisturbed ambient plasma?

(2) Equilibrium potential. The question here is: At what potential will a structure "float" in order that the net current to it will be zero?

(3) Current neutralization of rockets and satellites ejecting electron beams. The question to be answered here is: To what positive potential ϕ must a vehicle rise in order to collect a return current from the ambient plasma equal to the ejected beam current?

(4) Sheath geometry and thickness. This viewpoint is inherent in the previous three but tends to focus on the following question: How far away from a biased (either purposefully or inadvertently) instrument will one not disturb the ambient plasma very much?

The particular problem being addressed tends to influence the point of view and the main approach to a solution taken by an investigation. Yet these points of view are complementary. In (1) the question is what is the net current to the structure at a given potential. From one point of view, (2) and (3) are subsets of (1) asking for conditions near the floating potential, and in the electron current saturation regime at large positive potential, respectively. Yet (2) and (3) both

require zero net current to an isolated body in contact with the surrounding plasma, except in (3) one of the currents is under the control of the operator. The solution to all of these problems requires knowledge of the potential distribution surrounding the structure and how it merges with the plasma potential. The question posed in (4) has practical application for making measurements with instruments mounted on the RMS during active electron beam experiments when the shuttle is driven positive as was the case during the OSS-1 VCAP experiments (Shawhan and Murphy, Banks, Raitt and Williamson; these proceedings). All of the above problems are greatly impacted by the anisotropies introduced by the earth's magnetic field, the large orbital velocity of a structure in LEO, $\vec{V} \times \vec{B} \cdot \vec{L}$ potential variations (where $\vec{L}$ is the vector between the Langmuir probe and the engine nozzles on the shuttle), and different electrical characteristics of various surfaces. Here we will briefly mention the importance of some other factors.

In the next section we discuss the importance of neutrals, either ambient or emanating from the structure itself, and the resulting ionization that may be produced. In the following section we describe the importance of transients and time-variations in terms of factors that cause them and implications for the physics that describe them. In the last section we discuss a criterion for the conditions under which the earth's magnetic field must not be ignored when considering the sheath thickness.

2. THE IMPORTANCE OF NEUTRALS AND SECONDARY IONIZATION

The ionization cross section of atmospheric gases has a maximum $\sim 3 \times 10^{-16}$ cm^2 for electron energies of around 100 eV. At ambient neutral densities $n_n \lesssim 3 \times 10^9/cm^3$ (equivalent to $\sim 10^{-7}$ Torr) appropriate to altitudes above 250 km, the mean free path for ionization by electrons, λ_i, is $\gtrsim$ 10 km, a dimension much larger than most structure sizes. For this reason, the effects of ionization of neutrals have usually been ignored when examining the factors that control sheath thickness surrounding structures in low earth orbit (LEO).

There are several factors that indicate that the view outlined above is too simplistic. It is now apparent that a complex object like the space shuttle carries with it its own atmosphere. Measurements of 10^{-5} Torr, 2 orders of magnitude higher than ambient, were made on the recent OSS-1 flight by the plasma diagnostics package (PDP, Shawhan and Murphy, these proceedings). Such large neutral densities greatly shorten mean free paths for ionization and make ionization a more prominent factor.

When the potential on a structure exceeds some tens of volts, ionization may become important. An electron approaching such a structure may become

quasi-trapped due to the earth's magnetic field. For large enough electric fields and small enough structure sizes (to be discussed in more detail in Section 4 below), the electrons will perform $\vec{E} \times \vec{B}$ motion with a maximum velocity of 2E/B. In a 1/2 G field, an electric field strength > 100 V/m implies that the maximum kinetic energy of the electron exceeds 50 eV, sufficient to undergo ionizing collisions. Electric field strengths of this magnitude can be expected in the vicinity of meter-size appendages at potentials as low as 100 V. Indeed, these two factors, locally enhanced neutral densities and quasi-trapping of electrons in large electric fields, have been invoked to explain the presence of enhanced plasma densities and the collection of return current during electron beam ejection experiments from rockets.[1]

Furthermore, even a low ionization rate may have important effects on sheath structure. The reason is that ionization of ambient neutrals within a sheath provides a source of positive and negative space charge. If the ion density, n_i, becomes a fair-sized fraction of the electron density, n_e, the space charge distribution can be modified and affect the sheath structure. A qualitative order-of-magnitude estimate can be obtained from an approximation to the steady-state continuity equation for the secondary ions by setting the divergence of their flux, $\nabla \cdot n_i v_i \sim n_i v_i / S$, equal to their production rate, $\sim n_e v_e / \lambda_i$, where S is a sheath dimension;

$$n_i v_i \sim \frac{S}{\lambda_i} n_e v_e \quad .$$

If we set $v_{i,e} \sim (2e\phi/m_{i,e})^{1/2}$, we obtain

$$n_i \sim \left(\frac{m_i}{m_e}\right)^{1/2} \frac{S}{\lambda_i} n_e \quad .$$

This result suggests that secondary ionization can have an important effect even when the mean free path

$$\lambda_i \sim \left(\frac{m_i}{m_e}\right)^{1/2} S$$

is two or more orders of magnitude larger than the sheath size.

1. Cartwright, D.G., Monsoon, S.J., and Kellog, P.J. (1978) Heating of the ambient ionosphere by an artificially injected electron beam, J. Geophys. Res. 83:16.

The above estimate is not accurate but suggestive. The presence of secondary ionization in sheaths in the LEO regime has apparently received inadequate attention. The attempt by Galeev et al[2] to model these effects in the case of a rocket is little better than the above estimate because the expressions they derive are not solutions of the equations consistent with the model they describe.[3]

3. THE IMPORTANCE OF TRANSIENTS AND TIME VARIATIONS

Due to the complexity of the sheath problem, quasi-static models are very useful (Laframboise, these proceedings). These models have validity if changes in charging rates and ambient conditions occur more slowly than other time constants associated with the structure and its surroundings. Variations in auroral fluxes on time scales less than 100 msec are frequently observed, and traveling through auroral arc structures of ~ 800 m width at orbital velocity also gives a time scale ~ 100 msec for charging flux and ambient condition variations.

The charge state of the structure and its surroundings will have transients in response to these changing conditions. One factor that controls the charging rate is the capacitance C of the structure,

$$\frac{d\phi}{dt} = \frac{I}{C} \quad .$$

As an example, consider the shuttle whose capacitance is given predominantly by the dielectric-coated bay doors,

$$C = \frac{A}{d}\epsilon_o \quad ,$$

where $A \sim 300\ m^2$ is the total area of the bay doors which are open and exposed to the plasma (both sides) and $d \sim 3$ mils $= 75\ \mu$ is the thickness of the coating. These values give $C \sim 30\ \mu F$ for the shuttle capacitance. With this large capacitance, the time scale for a 100 V potential change is

$$\tau \sim \frac{CV}{\Delta I} = \frac{3 \times 10^{-3}}{\Delta I} \text{ sec} \quad .$$

2. Galeev, A.A., Mishin, E.V., Sagdeev, R.Z., Shapiro, V.D., and Shevchenko, V.I. (1976) Discharge in the region around a rocket following injection of electron beams into the ionosphere, Sov. Phys. Dokl. 21:641.

3. Drell, S.D., Foley, H.M., and Ruderman, M.A. (1965) Drag and propulsion of large satellites in the ionosphere: an Alfven propulsion engine in space, J. Geophys. Res. 70:3131.

If the change in charging current is carried by an auroral flux of $\sim 10^{-5}$ A/m^2 impinging on a collecting area of 300 m^2, the associated time-scale is $\sim$ 1 sec or 1000 msec, considerably longer than the time scale on which auroral fluxes may change.

There is a finite time to rearrange quasi-stationary sheath charges, which is dominated by the motion of ions. It takes $\sim$ 100 msec for an ambient thermal 0^+ ion to move a structure or sheath dimension of order 100 m. Furthermore, there is a similar time constant associated with the time that a given magnetic flux tube is in contact with the disturbed region of about 100 m radius surrounding a large potential.

Consideration of these time scales is important for several reasons. In the first place, they may determine the response of the system in some situations. Furthermore, this response depends critically on the physics and how it is modeled. Observations of time-varying phenomena provide critical tests of the degree of understanding of the mechanisms that control the sheath structure.

The time scales mentioned above are important for determining the response of the ionosphere to the disturbance created by the passage of an orbiting structure. As an example, Drell et al[3] suggested that the passage of a large orbiting structure could launch Alfven waves that may represent an appreciable drag. This mechanism is applicable only to large structures $R_b > V/\omega_{ci} \sim 30$ m in the ionosphere because the characteristic time must be longer than an inverse ion gyroradius $\omega_{ci}^{-1} \sim 0.004$ sec for Alfven waves to propagate. (This requirement reduces to $R_b > 2$ m at higher altitudes where H^+ is the dominant ion.)

The above mechanism is driven by the motional $\vec{V} \times \vec{B} \cdot \vec{L}$ potential difference with respect to the ambient plasma. It represents one approach to the more general problem of the closure of the current flows induced in the ionosphere. However, in their treatment, Drell et al[3] ignored the complicated sheath problem that controls the electrical coupling of the satellite to the ionosphere. The nature of the disturbance in the ionosphere, the closure of the currents, and the dependence of these effects on structure size is as yet an inadequately addressed problem.

4. CRITERION FOR MAGNETIC EFFECTS ON SHEATH SIZE

The nature of the sheath surrounding the noncoated portions of the shuttle, for example, the rocket motors or floating instruments, is still quite uncertain. A self-consistent solution for the electron saturation current to a finite-size structure in a magnetized, flowing plasma with structure radius $R_b \gg r_e, \lambda_D$ ($r_e = v_e/\omega_c \sim 2$ cm and $\lambda_D = v_e/\omega_p \sim 0.3$ cm are the electron gyroradius and

Debye length, respectively) has not yet been obtained. $v_e = (kT_e/m)^{1/2}$ is the electron thermal velocity, and $\omega_c = eB/m$ and $\omega_p = (e^2 n_e/m\epsilon_o)^{1/2}$ are the electron gyrofrequency and plasma frequency, respectively.

We investigate here a criterion to determine when the magnetic field cannot be neglected in calculations using cylindrical probe theory to estimate the sheath dimension.

The small gyroradius of ambient electrons, $r_e = v_e/\omega_c \sim 2\text{-}3$ cm, tends to keep the magnetic field lines as equipotentials, and the current collection has an axis of symmetry aligned with the magnetic field. Cylindrical probe theory should have some region of validity if the earth's magnetic field does not inhibit the flow of electrons to the probe. As we shall show, the sheath dimension S can be much larger than r_e without the magnetic field appearing to affect the result.

Several cylindrical probe theories for current collection in the electron saturation regime at potentials $\phi >> kT_e/e$ find that the sheath thickness S behaves as

$$\frac{S}{\lambda_D} \sim C\left(\frac{e\phi}{kT_e}\right)^{1/2} \tag{1}$$

for $R_b >> \lambda_D$ where C is a constant of order unity. As an example, Szuszczewicz and Takacs[4] find that $C \sim 2.5$ in the limits that we are considering.

The expression (1) is independent of R_b, T_e, and, of course, the magnetic field strength B. Indeed if we define the velocity of an electron having kinetic energy equal to $e\phi$ as

$$v_p = \left(\frac{2e\phi}{m}\right)^{1/2} , \tag{2}$$

Eq. (1) with $C = 2.5$ can be rewritten as

$$S = 1.8\,\frac{v_p}{\omega_p} = 5.9\left(\frac{10^5}{n_e}\right)^{1/2} \phi^{1/2} \text{ cm} . \tag{3}$$

This form explicitly demonstrates that for $e\phi >> kT_e$ and $R_b >> \lambda_D$, the sheath thickness in this model increases as $\phi^{1/2}$ and depends only on the ambient electron density. We are interested in knowing when the earth's magnetic field must modify this expression.

4. Szuszczewicz, E.P., and Takacs, P.Z. (1979) Magnetosheath effects on cylindrical Langmuir probes, Phys. Fluids 22:2424.

Consider a plane perpendicular to the magnetic field where the potential $\phi(r)$ in the sheath is positive and a monotonically decreasing function of r. In a very weak (or nonexistent) magnetic field, a stationary electron initially at a position $r_o > R_b$ will be attracted to the positive structure. In the opposite limit of a very strong magnetic field B, the electron at a position $r_o > R_b$ will initially accelerate radially towards the structure, but the Lorentz force will deflect the electron and prevent it from reaching the structure. Indeed, we label the minimum radius that it reaches r_m. In the limit that $r_o - r_m \ll S$, the electron performs a roughly cycloidal path whose average motion is circular at the radius r_o with a velocity E_o/B where E_o is the magnitude of the electric field, $|\partial\phi/\partial r|$, evaluated at $r = r_o$. The maximum velocity of the electron at r_m is $\sim 2E_o/B$.

It is obvious that when B is so strong that $r_o - r_m \ll S$, Eq. (3) is invalid. Linson and Papadopoulos[5] have integrated the equations of motion in cylindrical geometry including the effects of initial radial and angular velocities, v_{ro} and $v_{\theta o}$, respectively, at the position $r = r_o$. They define

$$\Delta\phi \equiv \phi(r_m) - \phi(r_o) > 0 \quad , \tag{4}$$

and find that the relation between the minimum and outer radii, r_m and r_o, can be expressed simply as

$$\left(1 + \frac{2v_{\theta o}}{r_o\omega_c}\right)\frac{r_o^2}{r_m^2} = 1 + 2\left(\frac{2e\Delta\phi}{m\omega_c^2 r_m^2}\right)^{1/2} \quad . \tag{5}$$

The initial kinetic energy plus change in potential energy, $e\Delta\phi$, has been converted entirely into kinetic energy in the theta direction at the minimum radius r_m.

We can now use Eq. (5) to determine when the magnetic field must invalidate Eq. (3). We ignore for simplicity the second term in brackets on the left-hand side of Eq. (5) when $v_{\theta o} \sim v_e$ because it is unimportant for $e\phi \gg kT_e$ and $r_e \ll R_b < r_o$. Consider an electron at the outer edge of the sheath

$$r_o \sim R_b + S \quad . \tag{6}$$

---

5. Linson, L. M., and Papadopoulos, K. (1981) Theoretical Support of the Spacelab Instrument/Experiment Definition of a Theoretical and Experimental Study of Beam-Plasma Physics (TEBPP), Report No. SAI-023-81-316LJ/LAPS-76, Science Applications, Inc., La Jolla, CA 92038.

Consider a plane perpendicular to the magnetic field where the potential $\phi(r)$ in the sheath is positive and a monotonically decreasing function of r. In a very weak (or nonexistent) magnetic field, a stationary electron initially at a position $r_o > R_b$ will be attracted to the positive structure. In the opposite limit of a very strong magnetic field B, the electron at a position $r_o > R_b$ will initially accelerate radially towards the structure, but the Lorentz force will deflect the electron and prevent it from reaching the structure. Indeed, we label the minimum radius that it reaches r_m. In the limit that $r_o - r_m \ll S$, the electron performs a roughly cycloidal path whose average motion is circular at the radius r_o with a velocity E_o/B where E_o is the magnitude of the electric field, $|\partial\phi/\partial r|$, evaluated at $r = r_o$. The maximum velocity of the electron at r_m is $\sim 2E_o/B$.

It is obvious that when B is so strong that $r_o - r_m \ll S$, Eq. (3) is invalid. Linson and Papadopoulos[5] have integrated the equations of motion in cylindrical geometry including the effects of initial radial and angular velocities, v_{ro} and $v_{\theta o}$, respectively, at the position $r = r_o$. They define

$$\Delta\phi \equiv \phi(r_m) - \phi(r_o) > 0 \quad , \tag{4}$$

and find that the relation between the minimum and outer radii, r_m and r_o, can be expressed simply as

$$\left(1 + \frac{2v_{\theta o}}{r_o\omega_c}\right)\frac{r_o^2}{r_m^2} = 1 + 2\left(\frac{2e\Delta\phi}{m\omega_c^2 r_m^2}\right)^{1/2} \quad . \tag{5}$$

The initial kinetic energy plus change in potential energy, $e\Delta\phi$, has been converted entirely into kinetic energy in the theta direction at the minimum radius r_m.

We can now use Eq. (5) to determine when the magnetic field must invalidate Eq. (3). We ignore for simplicity the second term in brackets on the left-hand side of Eq. (5) when $v_{\theta o} \sim v_e$ because it is unimportant for $e\phi \gg kT_e$ and $r_e \ll R_b < r_o$. Consider an electron at the outer edge of the sheath

$$r_o \sim R_b + S \quad . \tag{6}$$

5. Linson, L. M., and Papadopoulos, K. (1981) Theoretical Support of the Spacelab Instrument/Experiment Definition of a Theoretical and Experimental Study of Beam-Plasma Physics (TEBPP), Report No. SAI-023-81-316LJ/LAPS-76, Science Applications, Inc., La Jolla, CA 92038.

This electron will not impact the structure in falling through a potential $\Delta\phi \sim \phi$ unless $r_m \leq R_b$. It is convenient to define a characteristic potential

$$\phi_c = \frac{m}{2e}\omega_c^2 R_b^2 = 220\left(\frac{B}{0.5}\right)^2 R_b^2 \text{ V} \tag{7}$$

where B is in gauss and R_b is in meters. (The gyroradius of an electron with energy $e\phi_c$ is equal to the structure size R_b.) By combining Eqs. (5), (6), and (7), we find that the magnetic field will prevent an electron from reaching the structure unless the sheath size is small enough so that

$$\left(1 + \frac{S}{R_b}\right)^2 < 1 + 2\left(\frac{\phi}{\phi_c}\right)^{1/2} \equiv 1 + 2\,\frac{v_p}{\omega_c R_b} \quad . \tag{8}$$

For small $S \ll R_b$, this expression reduces to $S < v_p/\omega_c$.

Equation (3) for S cannot be valid if it violates condition (8). This condition places a restriction on the allowed values of ω_p/ω_c for which Eq. (3) may be valid;

$$\frac{\omega_p}{\omega_c} > 0.9\left(1 + \left[1 + 2(\phi/\phi_c)^{1/2}\right]^{1/2}\right) \quad . \tag{9}$$

For small $\phi \ll \phi_c$, this requirement reduces to $\omega_p > 1.8\omega_c$ while it becomes $\omega_p > 2.5\omega_c$ for $\phi = \phi_c$. With B = 0.5 G, this restriction requires $n_e > 1.5 \times 10^5/\text{cm}^3$. For $\phi \gg \phi_c$, the right-hand side of Eq. (9) varies as $1.3(\phi/\phi_o)^{1/4}$ but Eq. (3) for S is suspect for such large potentials.

The sheath thickness given by Eq. (3) may be written

$$S = 1.8\,\frac{\omega_c}{\omega_p}\left(\frac{\phi}{\phi_c}\right)^{1/2} R_b \quad . \tag{10}$$

For $\phi \lesssim \phi_c$ and ω_p satisfying Eq. (9), we have

$$S < 1.8\,\frac{\omega_c}{\omega_p} R_b < 0.7 R_b \quad , \tag{11}$$

that is, Eq. (3) is invalid for sheath thicknesses approaching or greater than the structure size R_b.

We summarize by saying that for B = 0.5 G and $\phi \leq 220R_b^2$ V, the expression (3) for the sheath thickness cannot be valid for $n_e < 1.5 \times 10^5$ cm^{-3}. Furthermore, when $S \ll R_b$, the criterion that determines when magnetic effects are important is that the gyroradius v_p/ω_c of an electron with energy $e\phi$ is comparable to or less than the sheath thickness.

References

1. Cartwright, D.G., Monsoon, S.J., and Kellog, P.J. (1978) Heating of the ambient ionosphere by an artificially injected electron beam, J. Geophys. Res. 83:16.
2. Galeev, A.A., Mishin, E.V., Sagdeev, R.Z., Shapiro, V.D., and Shevchenko, V.I. (1976) Discharge in the region around a rocket following injection of electron beams into the ionosphere, Sov. Phys. Dokl. 21:641.
3. Drell, S.D., Foley, H.M., and Ruderman, M.A. (1965) Drag and propulsion of large satellites in the ionosphere: an Alfven propulsion engine in space, J. Geophys. Res. 70:3131.
4. Szuszczewicz, E.P., and Takacs, P.Z. (1979) Magnetosheath effects on cylindrical Langmuir probes, Phys. Fluids 22:2424.
5. Linson, L.M., and Papadopoulos, K. (1981) Theoretical Support of the Spacelab Instrument/Experiment Definition of a Theoretical and Experimental Study of Beam-Plasma Physics (TEBPP), Report No. SAI-023-81-316LJ/LAPS-76, Science Applications, Inc., La Jolla, CA 92038.

Contents

22. The Threshold Temperature Effect in High-Voltage Spacecraft Charging

by

J. G. Laframboise
M. Kamitsuma
Physics Department and Centre for Research in Experimental Space Science
York University
Toronto, Canada M3J 1P3

Abstract

A new property of spacecraft surface materials, the "threshold temperature for high-voltage charging", is defined. A table of threshold temperatures, calculated for various spacecraft surface materials, is presented. This property explains and unifies several recently-identified phenomena affecting spacecraft charging, including: the existence of multiple floating potentials for certain spacecraft surfaces in certain external environments; "sensitivity" effects in the numerical prediction of spacecraft potentials; sudden jumps in both observed and simulated spacecraft potentials in slowly-varying environments; and observed "threshold" effects in high-voltage charging. In addition, knowledge of the threshold temperature for proposed or existing surface materials provides a simple, effective way to evaluate their charging behavior when exposed to various space environments.

1. INTRODUCTION

The high-voltage charging behavior of spacecraft surfaces displays a variety of unexpectedly complex features.

These features are most evident in the absence of photoemission (as on shaded surfaces of a spacecraft). One of them is the existence of multiple roots (zeros) in the current-voltage characteristic of various spacecraft materials exposed to certain kinds of ambient plasma environments. An example of such a current-voltage characteristic is shown in Figure 1. In this illustration, only the right- and left-hand roots, which are located at +1.9 and -4100 V, respectively, represent stable floating surface potentials, because the center root is an unstable one, in the sense that any voltage excursion from the indicated value (-500 V) would result in a net current of a sign that would cause the voltage excursion to increase, ultimately driving the voltage to the right- or left-hand roots.

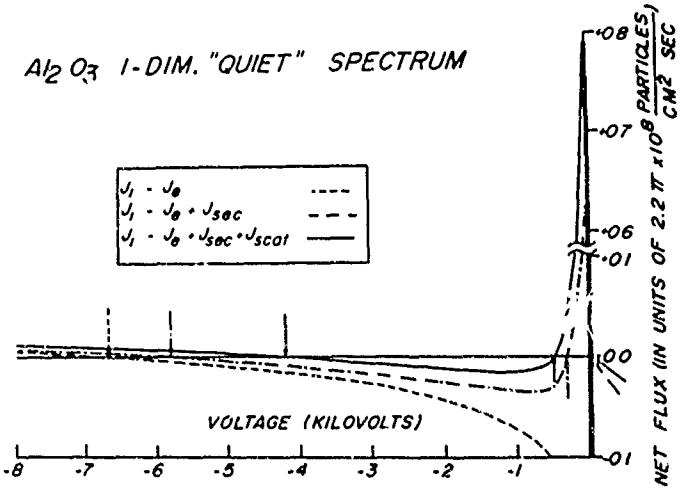

Figure 1. Current-voltage Characteristic for Aluminum Oxide in "Quiet" Magnetospheric Conditions, With a One-Dimensional Velocity-Space Cutoff for Collection of Ambient Charged Particles (after Prokopenko and Laframboise[2,3]). The zeros ("roots") of the characteristic are indicated by arrows. In calculating this characteristic, incident-angle dependence of secondary and backscattered electron yield has been ignored

The possibility of such triple-root situations was first proposed by Whipple.[1] Prokopenko and Laframboise[2,3] calculated current-voltage characteristics of various surface materials in outer-magnetospheric (including geostationary-orbit) plasma environments, and found numerous examples in which triple-root characteristics were actually obtained. Sanders and Inouye[4] did calculations to examine the ranges of conditions in which such characteristics would occur. Besse[5] examined the mechanisms underlying them. Meyer-Vernet[6,7] showed that they may also occur on dust grains in space, such as those in Saturn's rings. It is now generally recognized that in triple-root situations, the stable floating potential near space potential is the result primarily of a current balance between incident "primary" electrons and emitted (secondary and backscattered) electrons, with incident ion current making only a minor contribution, while at the more negative stable potential, the current balance is primarily between incident ion and electron currents, even though in this case also, both of these may be substantially modified by secondary or backscattered electron emission.

Another feature of the high-voltage charging phenomenon is the occurrence of "sensitivity" effects in the numerical prediction of spacecraft potentials,[8] in

1. Whipple, Jr., E.C. (1965) The Equilibrium Electric Potential of a Body in the Upper Atmosphere and in Interplanetary Space, Ph.D. Thesis, The George Washington Univ., Washington, D.C./Report No. X-615-65-296, NASA Goddard Space Flight Center, Greenbelt, Maryland.

2. Prokopenko, S.M.L., and Laframboise, J.G. (1977) Prediction of large negative shaded-side spacecraft potentials, in Proc. Spacecraft Charging Technology Conference, C.P. Pike and R.R. Lovell, Eds., Report No. AFGL-TR-77-0051, AD A045459, Air Force Geophysics Laboratory, Massachusetts/Report No. NASA TMX-73537, Lewis Research Center, Cleveland, Ohio, pp. 369-387.

3. Prokopenko, S.M.L., and Laframboise, J.G. (1980) High-voltage differential charging of geostationary spacecraft, J. Geophys. Res. 85(A8):4125-4131.

4. Sanders, N.L., and Inouye, G.T. (1979) Secondary emission effects on spacecraft charging: energy distribution considerations, in Spacecraft Charging Technology - 1978, NASA Conference Publication 2071/Report No. AFGL-TR-79-0082, AD A084626, Air Force Geophysics Laboratory, Massachusetts, pp. 747-755.

5. Besse, A.L. (1981) Unstable potential of geosynchronous spacecraft, J. Geophys. Res. 86(A4):2443-2446.

6. Meyer-Vernet, N. (1982) "Flip-flop" of electric potential of dust grains in space, Astron. Astrophys. 105:98-106.

7. Meyer-Vernet, N. (1982) Multivalued electrostatic potentials; "chance or necessity" for the charge of solid particles near Saturn?, in Proc. IAU Colloq. No. 75: Planetary Rings, Toulouse, France, August-September 1982.

8. Stannard, P.R., Schnuelle, G.W., Katz, I., and Mandell, M.J. (1981) Representation and material charging response of GEO plasma environments, in Spacecraft Charging Technology 1980, NASA Conference Publication 2182/Report No. AFGL-TR-81-0270, AD A114426, Air Force Geophysics Laboratory, Massachusetts, pp. 560-579.

which relatively small changes in assumed surface properties or ambient conditions can cause large changes in spacecraft floating potentials. Evidently, this phenomenon may frustrate attempts to make reliable predictions of spacecraft charging, and it is important to identify the parameter ranges in which such sensitivity effects occur.

This phenomenon is closely related to that of "threshold" effects, both predicted,[8] and observed,[9] in which no high-voltage charging occurs over a large range of environmental or surface conditions, but a small further change in conditions then results in a large change in surface potential from a small value (relative to space) to a value typically several kilovolts negative.

Another closely related effect is that of sudden large changes in surface potential in response to relatively slow temporal changes in ambient plasma conditions. This phenomenon was predicted by Prokopenko and Laframboise,[3] and Besse,[5] and subsequently observed both on the SCATHA (P78-2) satellite and in numerical simulations made using the NASA Charging Analyzer Program (NASCAP).[10,11]

In Sections 2 and 3, we introduce the concept of threshold temperature as a property of a spacecraft surface material, and we show that all of the above-mentioned phenomena are unified and explained by this concept.

A separate phenomenon, which often controls the differential charging of other surfaces, including sunlit ones, relative to the most highly-charged surface, is the "barrier" effect, which has been discussed by Fahleson,[12] Whipple,[13]

---

9. Gussenhoven, M.S., and Mullen, E.G. (1982) A "worst case" spacecraft charging environment as observed by SCATHA on 24 April 1979, paper No. 82-0271, Amer. Inst. Aeron. Astron. 20th Aerospace Sciences Mtg., January 1982, Orlando, Florida.

10. Schnuelle, G.W., Stannard, P.R., Katz, I., and Mandell, M.J. (1981) Simulation of charging response of SCATHA (P78-2) satellite, in Spacecraft Charging Technology 1980, NASA Conference Publication 2182/Report No. AFGL-TR-81-0270, AD A114426, Air Force Geophysics Laboratory, Massachusetts, pp. 580-591.

11. Stannard, P.R., Katz, I., Gedeon, L., Roche, J.C., Rubin, A.G., and Tautz, M.F. (1982) Validation of the NASCAP model using spaceflight data, Paper No. 82-0269, Amer. Inst. Aeron. Astron. 20th Aerospace Sciences Mtg., January 1982, Orlando, Florida, AFGL-TR-82-0108, AD A113440.

12. Fahleson, U. (1973) Plasma-vehicle interactions in space - some aspects on present knowledge and future development, in Photon and Particle Interactions with Surfaces in Space, R.J.L. Grard, Ed., D. Reidel, Dordrecht, Holland, pp. 563-569.

13. Whipple, Jr., E.C. (1976) Observation of photoelectrons and secondary electrons reflected from a potential barrier in the vicinity of ATS 6, J. Geophys. Res. 81(4):715-719.

Prokopenko and Laframboise,[2,3] Laframboise and Prokopenko,[14] Katz et al,[15] Besse and Rubin,[16] Purvis,[17] and Laframboise et al.[18]

2. THE THRESHOLD-TEMPERATURE PROPERTY

A typical secondary-electron yield curve is shown in Figure 2a. For most commonly-used spacecraft surface materials, there exists a region of this yield curve in which more than one secondary is produced on average per primary. This generally occurs for incident electron kinetic energies of a few hundred eV. In Figure 2b, energy-differential incident-electron flux (particle current density) curves are shown for Maxwellian electron velocity distributions at two representative values of electron temperature T_e. In the example shown, the peak of the lower-temperature curve is at almost the same energy as that of the secondary yield curve. In this situation, there is a large production of secondaries; in fact, the total secondary flux [which is given by an integral involving the product of these two functions; see Prokopenko and Laframboise,[2,3] Eq. (10)], will be greater than the incident primary flux if the maximum secondary yield δ_{max} per primary is greater than about 1.16 (Besse,[5] Figure 2). In contrast, the peak of the higher-temperature curve does not coincide closely with that of the secondary-emission curve, and in this case, the total secondary flux will be less than the incident flux. Evidently, a critical value of T_e must exist, intermediate between

14. Laframboise, J.G., and Prokopenko, S.M.L. (1977) Numerical simulation of spacecraft charging phenomena, in Proc. Spacecraft Charging Technology Conference, C.P. Pike and R.R. Lovell, Eds., Report No. AFGL-TR-77-0051, AD A045459, Air Force Geophysics Laboratory, Massachusetts/Report No. NASA TMX-73537, Lewis Research Center, Cleveland, Ohio, pp. 309-318.

15. Katz, I., Cassidy, J.J., Mandell, M.J., Schnuelle, G.W., Steen, P.G., and Roche, J.C. (1979) The capabilities of the NASA charging analyzer program, in Spacecraft Charging Technology 1978, NASA Conference Publication 2071/Report No. AFGL-TR-79-0082, AD A084626, Air Force Geophysics Laboratory, Massachusetts, pp. 101-122.

16. Besse, A.L., and Rubin, A.G. (1980) A simple analysis of spacecraft charging involving blocked photoelectron currents, J. Geophys. Res. 85(A5):2324-2328.

17. Purvis, C. (1982) Evolution of spacecraft charging technology, Paper No. 82-0273, Amer. Inst. Aeron. Astron. 20th Aerospace Sciences Mtg., January 1982, Orlando, Florida.

18. Laframboise, J.G., Godard, R., and Kamitsuma, M. (1982) Multiple floating potentials, "threshold-temperature" effects, and "barrier" effects in high-voltage charging of exposed surfaces on spacecraft, in Proc. Internat. Symp. on Spacecraft Materials in Space Environment, June 1982, Toulouse, France, European Space Agency, Paris, Publication No. ESA SP-178, pp. 269-275.

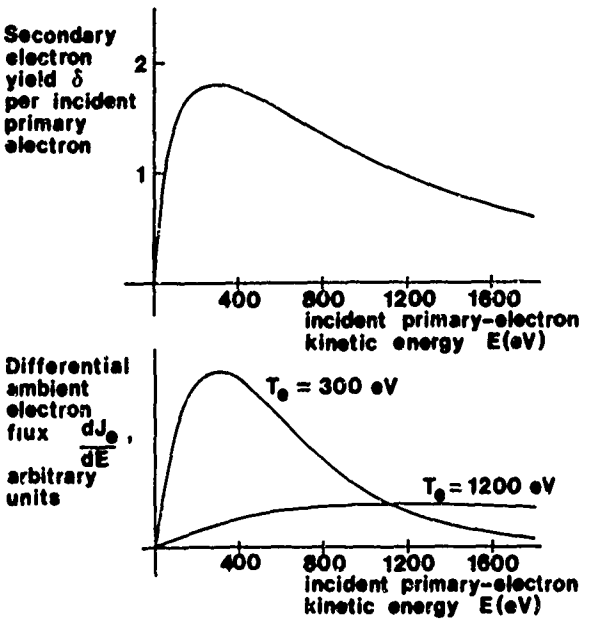

Figure 2. (a) Typical Form of Secondary-Electron Yield δ (Secondary Electrons Per Incident Primary Electron), as a Function of Incident Primary Kinetic Energy E, at Normal Incidence; (b) Energy-Differential Electron Flux dJ_e/dE for Maxwellian Ambient Electron Velocity Distributions at Two Different Temperatures. Total secondary-electron flux is obtained by integrating the product of these two functions [multiplied by another factor given in Eq. (10) of Prokopenko and Laframboise[2,3]] over energy E

the two values indicated, at which emitted flux would exactly balance incident flux.[19] (There will also be another such critical temperature, below the peak of the secondary yield curve, but this is not of importance here.)

Maxwellian ambient distributions also have the special property that if they are retarded by a repelling (negative) surface potential, the distribution of particle kinetic energies reaching the surface is independent of the value of this potential. Therefore, for a Maxwellian ambient distribution, the preceding conclusions have a special property: they are independent of spacecraft surface potential (Besse,[5] Cohen[19]) as long as this potential is negative (with respect to space). Therefore, if the ambient electrons were Maxwellian at the critical temperature, incoming and outgoing fluxes would balance each other for all negative values of surface potential, and the surface then "would not know at what

19. Cohen, H.A. (1982) Private communication.

potential to float", that is, the surface potential would become indeterminate, except for the (relatively small) current contribution from ambient ions. It is therefore evident that very large (negative) increases in floating potential will result for very small increases in ambient electron temperature in the neighborhood of this critical value, which is a property of the surface material only. We will therefore refer to this critical value as the threshold material temperature T* for high-voltage charging. In terms of this property, the first four effects mentioned in Section 1 can be immediately explained, as follows:

(1) Triple-root current-voltage characteristics have a simple explanation if the ambient electron velocity distribution can be approximated by a double Maxwellian. Such an approximation, although empirically based, is often a very good one (Garrett and DeForest,[20] Garrett et al[21]). In this case, a characteristic will have three roots if (i) the temperature T_1 of one Maxwellian is less than T*, but the other temperature T_2 is greater than T*, and (ii) the total emitted electron (secondary and backscattered) flux at space potential is greater than the incident flux.

This can be proved as follows. The roots of the current-voltage characteristic are given by the zeros of the function:

$$J_{net} = J_i - J_e + J_{sec} + J_{scat} \quad , \tag{1}$$

where J_i, J_e, J_{sec}, and J_{scat} are particle current densities (fluxes) for incident (ambient) ions and electrons, secondary electrons and backscattered electrons, respectively. Except at relatively large negative surface potentials ϕ_s relative to space, J_i is relatively small, and will be neglected in what follows. For $\phi_s < 0$, we then have, in this approximation:

$$\begin{aligned} J_{net} &= (J_{sec,1} + J_{scat,1} - J_{e,1}) \exp(e\phi_s/kT_1) \\ &\quad + (J_{sec,2} + J_{scat,2} - J_{e,2}) \exp(e\phi_s/kT_2) \\ &\equiv J_{net,1} \exp(e\phi_s/kT_1) + J_{net,2} \exp(e\phi_s/kT_2) \quad , \end{aligned} \tag{2}$$

20. Garrett, H.B., and DeForest, S. (1979) An analytical simulation of the geosynchronous plasma environment, Planet Space Sci. 27:1101-1109.

21. Garrett, H.B., Schwank, D.C., and DeForest, S.E. (1981) A statistical analysis of the low-energy geosynchronous plasma environment - I. electrons, Planet Space Sci. 29(10):1021-1044.

where $e > 0$ is the elementary charge, k is Boltzmann's constant, and all double-scripted J are space-potential values. A triple-root characteristic must have an unstable root, that is, a value of ϕ_s such that (a) $J_{net} = 0$, and (b) $dJ_{net}/d\phi_s > 0$. This can happen only for $\phi_s < 0$ because J_{sec} and J_{scat} both decrease rapidly at positive potentials (an exception to this, applicable at very small electron temperatures, has been found by Meyer-Vernet[6]). Condition (a) requires that $J_{net,1}$ and $J_{net,2}$ have opposite signs, that is, T* is between T_1 and T_2. Condition (b) implies that $J_{net} > 0$ for all ϕ_s values between this root and zero; this in turn implies that $J_{net,1} + J_{net,2} > 0$. This completes the proof of (i) and (ii). Even though this proof is only approximate for real velocity distributions, it will still be generally valid in terms of "temperatures" related in the usual way ($\bar{E} = 3/2\ kT$) to the mean energies obtained from a double-Maxwellian fit. Meyer-Vernet[6] has shown that triple roots can also occur with Maxwellian electrons, when the electron temperature is less than the "temperature" of emission of secondary electrons. The unstable root then occurs at a positive rather than negative value of ϕ_s.

Meyer-Vernet[7] has pointed out that in order for condition (ii) to be satisfied, T_1 must not only be less than T* but must also be greater than the lower critical temperature which we have mentioned in Section 1 but have not calculated in this paper. A. L. Besse (1982, private communication) has pointed out that ion collection will make a (usually small) negative contribution to $dJ_{net}/d\phi_s$ and may therefore in some cases prevent a triple-root situation by preventing (b) from being satisfied. This could be expected to happen for example if T_1 and T_2 were only slightly below and above T*, respectively, that is, if the electron distribution deviated only slightly from a single Maxwellian.

(2) For T (or $2\bar{E}/3k$) close to T*, most current-voltage characteristics will have both a very small value and small slope over a large range of potentials, and the floating potential(s) will then be subject to large changes when only small changes in conditions occur. This explains "sensitivity" effects.

(3) For T slightly less than T*, $J_{sec} + J_{scat} > J_e$ if $\phi_p < 0$, and the floating potential will generally be slightly positive. For T slightly greater than T*, $J_{sec} + J_{scat} < J_e$ and the floating potential will generally be very negative. Clearly T* is the temperature at which "threshold" effects may be expected.

(4) For a distribution which is (nearly) Maxwellian and has $T \approx T^*$, small (or gradual) changes in ambient conditions can cause the sign of $J_{sec} + J_{scat} - J_e$ to change, resulting in large, sudden changes in floating potential. For a distribution which may not be near-Maxwellian but which leads to a triple-root characteristic, changes in ambient conditions may cause two of the three roots to coalesce and disappear, also producing large, sudden potential changes.[3,5,6,7]

3. CALCULATION OF THRESHOLD TEMPERATURES; DISCUSSION

We have calculated threshold-temperature values (Table 1) for a variety of spacecraft surface materials. In order to do this we have calculated $J_{sec} + J_{scat} - J_e$ as a function of T for Maxwellian incident distributions, and searched numerically for the value T* at which this function changes from positive to negative as T increases.

For ambient electrons normally incident to a surface, we have used the secondary and backscattered flux expressions given by Prokopenko and Laframboise,[2,3] together with data given by Dekker,[22] Hachenberg and Brauer,[23,24] Gibbons,[25] Willis and Skinner,[26] Katz et al,[27] Schnuelle et al,[28] Leung et al,[29] and Krainsky et al.[30]

The increased yields for electrons incident at other angles have an important influence on our results (last three columns of Table 1). For both secondary

22. Dekker, A.J. (1958) Secondary electron emission, in Solid State Physics, F. Seitz and D. Turnbull, Eds., Vol. 6, Academic Press, New York, p. 251.

23. Hachenberg, O., and Brauer, W. (1959) Secondary electron emission from solids, Advan. Electron. Electron Phys. 11:413.

24. Hachenberg, O., and Brauer, W. (1962) Advan. Electron. Electron Phys. 16:145.

25. Gibbons, D.J. (1966) Secondary electron emission, in Handbook of Vacuum Physics, A.H. Beck, Ed., Pergamon, Oxford, p. 301.

26. Willis, R.F., and Skinner, D.K. (1973) Secondary electron emission yield behaviour of polymers, Solid State Commun. 13:685.

27. Katz, I., Parks, D.E., Mandell, M.J., Harvey, J.M., Brownell, Jr., D.H., Wang, S.S., and Rotenberg, M. (1977) A Three Dimensional Dynamic Study of Electrostatic Charging in Materials, NASA Contractor Report No. CR-135256, Lewis Research Center, Cleveland, Ohio.

28. Schnuelle, G.W., Parks, D.E., Katz, I., Mandell, M.J., Steen, P.G., Cassidy, J.J., and Rubin, A. (1979) Charging analysis of the SCATHA satellite, in Spacecraft Charging Technology - 1978, NASA Conference Publication 2071/Report No. AFGL-TR-79-0082, AD A084626, Air Force Geophysics Laboratory, Massachusetts, pp. 123-143.

29. Leung, M.S., Tueling, M.B., and Schnauss, E.R. (1981) Effects of secondary electron emission on charging, in Spacecraft Charging Technology 1980, NASA Conference Publication 2182/Report No. AFGL-TR-81-0270, AD A114426, Air Force Geophysics Laboratory, Massachusetts, pp. 163-178.

30. Krainsky, I., Lundin, W., Gordon, W.L., and Hoffman, R.W. (1981) Secondary electron emission yields, in Spacecraft Charging Technology 1980, NASA Conference Publication 2182/Report No. AFGL-TR-81-0270, AD A114426, Air Force Geophysics Laboratory, Massachusetts, pp. 179-197.

Table 1. Threshold Temperatures T* for Spacecraft Surface Materials

Material	Secondary		Backscattering				T* (keV)		
	E_{max} (keV)	δ_{max}	Z	A	B	C	TC1	TC2	TC3
Gold	0.80	1.45	79.0	0.4802	0.3566	0.6103	1.278	2.931	4.969
Aluminum	0.30	0.97	13.0	0.1568	0.0303	0.3431	0.000	0.000	0.601
Aluminum Oxide	0.30	2.60	10.0	0.1238	0.0172	0.3435	1.116	1.273	1.931
SIO2 (Quartz)	0.42	2.50	10.0	0.1238	0.0172	0.3435	1.496	1.713	2.621
Fused Silica	0.33	3.46	10.0	0.1238	0.0172	0.3435	1.645	1.847	2.707
Aquadag (Colloidal Graphite)	0.35	0.75	6.0	0.0800	0.0000	0.0000	0.000	0.000	0.000
Beryllium-Copper	0.30	2.20	29.0	0.3136	0.0692	0.6207	0.918	1.349	2.157
Beryllium-Copper (Activated)	0.40	5.00	29.0	0.3136	0.0692	0.6207	2.764	3.692	5.423
Teflon	0.30	3.00	8.0	0.0900	0.0000	0.0000	1.299	1.427	2.102
Kapton (Willis and Skinner)[26]	0.15	2.10	5.3	0.0700	0.0000	0.0000	0.433	0.474	0.769
Kapton (Leung et al)[29]	0.25	1.80	5.3	0.0700	0.0000	0.0000	0.583	0.647	1.096
Indium Oxide	0.80	1.40	24.4	0.2750	0.0600	0.5400	1.184	2.010	3.596
Magnesium	0.25	0.92	12.0	0.1460	0.0250	0.3440	0.000	0.000	0.441
Magnesium Oxide	0.40	4.00	10.0	0.1238	0.0172	0.3435	2.280	2.548	3.686
Silver	0.80	1.00	47.0	0.3900	0.2890	0.6320	0.000	1.233	2.754
ITO on Kapton	0.35	2.55	15.3	0.1830	0.0370	0.3820	1.275	1.550	2.370
IO on 'FEP' Teflon	0.36	2.39	16.2	0.1920	0.0400	0.3990	1.217	1.507	2.329
ITO on Borosilicate Glass	0.35	2.35	16.9	0.2000	0.0420	0.4100	1.160	1.453	2.255
Ion-Sputtered ITO on Kapton	0.39	1.52	15.3	0.1830	0.0370	0.3820	0.684	0.921	1.587
MGF2	0.85	6.38	10.0	0.1238	0.0172	0.3435	7.141	7.889	11.054
NASCAP 'NPAI'	0.15	2.10	5.0	0.0600	0.0000	0.0000	0.433	0.468	0.747
NASCAP 'SOLA'	0.41	2.05	10.0	0.1238	0.0172	0.3435	1.147	1.338	2.123
NASCAP 'CPAI'	0.15	2.10	5.0	0.0600	0.0000	0.0000	0.433	0.468	0.747
NASCAP 'WHITEN'	0.15	2.10	5.0	0.0600	0.0000	0.0000	0.433	0.468	0.747
NASCAP 'BLACKC YELOWC'	0.15	2.10	5.0	0.0600	0.0000	0.0000	0.433	0.468	0.747
NASCAP 'GOLDPD'	0.72	1.03	70.1	0.4560	0.3380	0.6120	0.000	1.392	2.857
NASCAP 'YGOLDC'	0.48	1.49	42.0	0.3730	0.2760	0.6170	0.810	1.392	2.444
NASCAP 'BOOMAT'	0.59	1.86	63.4	0.4380	0.3250	0.6130	1.443	2.596	4.203
NASCAP 'ML12'	0.30	1.00	6.0	0.0800	0.0000	0.0000	0.000	0.000	0.602

TC1: Including Secondary Electrons.

TC2: Including Secondary and Backscattered Electrons.

TC3: Same as TC2 Except That Angular Dependence of Yield is Included.

(Dekker,[22] Salehi and Flinn,[31] Krainsky et al,[30]) and backscattered (Darlington and Cosslett,[32] Krainsky et al[30]) electrons, it is found experimentally that the dependence of yield (average number of emitted electrons per incident electron) $\delta(E,\theta)$ on angle of incidence θ relative to the surface normal can be usefully approximated by a relation of the form

$$\ln \delta(E,\theta) = \ln \delta(E,0) + \beta(1-\cos\theta) \quad . \tag{3}$$

For secondary emission, the coefficient β appears to depend primarily on E/E_{max}, where E_{max} is the energy at which δ is largest when $\theta = 0^{o}$. For backscattered emission, β appears to depend most strongly on the atomic number Z of the surface material, and only weakly on incident energy E. Also, available information on E dependence is fragmentary, and in any case, secondary emission predominates over backscattered emission at smaller values of E. For these reasons, we have ignored the E dependence.

The dependence given by Eq. (3) has the special advantage that for any isotropic ambient velocity distribution, the integration over angle in the emitted flux expression can be done analytically. In this case, we have:

$$J_{sec} \text{ or } J_{scat} = \int f \delta v_n \, d^3\vec{v}$$

$$= \iiint f(E) \delta(E,\theta) (v\cos\theta)(v^2 \sin\theta \, dv \, d\theta \, d\psi)$$

$$= 2\pi \int_0^{\infty} f(E) \delta(E,0) v^3 dv \int_0^{1/2\pi} e^{\beta(E)(1-\cos\theta)} \cos\theta \sin\theta \, d\theta \quad , \tag{4}$$

where (v,θ,ψ) are spherical coordinates in velocity space with polar axis normal to the surface, $f \equiv d^6N/d^3\vec{r}\, d^3\vec{v}$ is the velocity distribution of ambient electrons, $E = 1/2mv^2$, and v_n is the normal component of incident electron velocity.

The integral over θ yields $[\exp(\beta)-\beta-1]/\beta^2$, which has the value 1/2 when $\beta = 0$. After β is specified as a function of E, multiplication of $\delta(E,0)$ by the factor $\Gamma = (2/\beta^2)[\exp(\beta)-\beta-1]$ then corrects $\delta(E,0)$ to include angle dependence

31. Salehi, M., and Flinn, E.A. (1981) Dependence of secondary-electron emission from amorphous materials on primary angle of incidence, J. Appl. Phys. 52(2):994-996.

32. Darlington, E.H., and Cosslett, V.E. (1972) Backscattering of 0.5 - 10 keV electrons from solid targets, J. Phys. D: Appl. Phys. 5:1969-1981.

of the secondary or backscattered yield [see also Whipple,[33] Eq. (3.11)]. To obtain the resulting dependence of $\delta \equiv \delta_{sec} + \delta_{scat}$ on E, we require that E_{max} and δ_{max} for normal-incidence secondary yield be specified, together with Z. Our complete yield algorithm then is:

$$\xi = \ell n(E/E_{max}); \; \eta = 0.2755(\xi - 1.658) - \sqrt{[0.2755(\xi - 1.658)]^2 + 0.0228};$$

$$\beta_{sec} = e^{\eta}; \; \Gamma_{sec} = (2/\beta_{sec}^2)\,[\exp(\beta_{sec}) - \beta_{sec} - 1] \; ;$$

$$\beta_{scat} = 7.37Z^{-0.56875}; \; \Gamma_{scat} = (2/\beta_{scat}^2)\,[\exp(\beta_{scat}) - \beta_{scat} - 1] \; , \quad (5)$$

where the above expressions for β_{sec} and β_{scat} have been obtained by fits to the data of Dekker,[22] Darlington and Cosslett,[32] Salehi and Flinn,[31] and Krainsky et al.[30] Finally,

$$\delta(E) = \left[7.4\delta_{max} \frac{E}{E_{max}} \exp\left(-2\sqrt{\frac{E}{E_{max}}}\right) \right] \Gamma_{sec} + [A - Be^{-CE}]\,\Gamma_{scat}, \quad (6)$$

where the factors multiplying Γ_{sec} and Γ_{scat} are, respectively, the secondary-yield curve of Sternglass,[34] and an empirical factor given by Prokopenko and Laframboise[3] [Eq. (9)], in which the coefficients A, B, and C are functions of Z obtained from the data of Sternglass[35] and Palluel.[36] These coefficients are also displayed in Table 1. $J_{sec} + J_{scat}$ is then given by 2π times the integral over v in Eq. (4) with f replaced by the Maxwellian distribution corresponding to temperature T, or more generally, by Eqs. (10) to (14) of Prokopenko and Laframboise.[2,3] $J_e = n_\infty (kT/2\pi m_e)^{1/2}$, that is, the usual random flux for a Maxwellian distribution (where n_∞ is ambient electron density and m_e is electron mass), or more generally, J_e is given by Eqs. (1) to (3) of Prokopenko and Laframboise.[2,3]

---

33. Whipple, Jr., E.C. (1981) Potentials of surfaces in space, Rep. Prog. Phys. 44:1197-1250.

34. Sternglass, E.J. (1954) Theory of Secondary Electron Emission, Sci. Pap. 1772, Westinghouse Res. Lab., Pittsburgh, Pa.

35. Sternglass, E.J. (1954) Backscattering of kilovolt electrons from solids, Phys. Rev. 95:345-358.

36. Palluel, P. (1947) Composante rediffusée du rayonnement electronique secondaire des métaux, C.R. Acad. Sci. 224:1492.

The resulting threshold temperatures T* (labeled "TC3") appear in the last column of Table 1. Corresponding values of T* for simplified forms of $\delta(E)$ as indicated (labeled "TC1" and "TC2") appear in the two adjacent columns. It is clear from these results that angle dependence of δ_{sec} and δ_{scat} has an important effect on values of T*. The values labeled "TC1" can also be inferred from Figure 2 of Besse.[5]

Clearly, those surface materials having the largest values of T* will be the "most resistant" to high-voltage charging (leaving aside the effects of material conductivity) because the ambient environment will exceed their threshold temperature the least often. From this viewpoint, and using the data of Table 1, MgF_2 is the "most resistant" material, followed by activated beryllium-copper, gold, and NASCAP 'BOOMAT', a spatially-averaged representation of a composite surface consisting of kapton partly covered with platinum strips, used on the SCATHA satellite (Schnuelle et al[28]). The zero entries for T* in Table 1 are those for which $J_{sec} + J_{scat} < J_e$ at all values of T.

Our discussion in this paper has been almost completely concerned with "absolute" or "overall" surface charging, and has been based only on calculations of local currents to and from surfaces. Calculations of this type are usually sufficient to determine the floating potential of the most highly (usually negatively) charged portion of a spacecraft surface, which is usually in a shaded or partly-shaded region of the spacecraft. However, the most damaging effects of high-voltage charging are "differential" effects involving large potential differences between adjacent parts of a spacecraft. These effects are frequently dominated by the "barrier" effect, a non-local phenomenon that we mentioned briefly in Section 1.

Acknowledgments

The central idea in this paper arose out of a conversation with H.A. Cohen. We have become aware of work that was done subsequent to the same conversation by H.A. Cohen and Shu Lai, and which parallels much of what is contained in this paper. A joint paper containing the combined results of all of this work is to be published.

We are also indebted to R.H. Prince and A.L. Besse for valuable discussions and comments. This work was supported by the United States Air Force Office of Scientific Research under grant AFOSR-76-2962, and by the Natural Sciences and Engineering Research Council of Canada under grant A-4638.

References

1. Whipple, Jr., E.C. (1965) The Equilibrium Electric Potential of a Body in the Upper Atmosphere and in Interplanetary Space, Ph.D. Thesis, The George Washington Univ., Washington, D.C./Report No. X-615-65-296, NASA Goddard Space Flight Center, Greenbelt, Maryland.

2. Prokopenko, S.M.L., and Laframboise, J.G. (1977) Prediction of large negative shaded-side spacecraft potentials, in Proc. Spacecraft Charging Technology Conference, C.P. Pike and R.R. Lovell, Eds., Report No. AFGL-TR-77-0051, AD A045459, Air Force Geophysics Laboratory, Massachusetts/Report No. NASA TMX-73537, Lewis Research Center, Cleveland, Ohio, pp. 369-387.

3. Prokopenko, S.M.L., and Laframboise, J.G. (1980) High-voltage differential charging of geostationary spacecraft, J. Geophys. Res. 85(A8):4125-4131.

4. Sanders, N.L., and Inouye, G.T. (1979) Secondary emission effects on spacecraft charging: energy distribution considerations, in Spacecraft Charging Technology - 1978, NASA Conference Publication 2071/Report No. AFGL-TR-79-0082, AD A084626, Air Force Geophysics Laboratory, Massachusetts, pp. 747-755.

5. Besse, A.L. (1981) Unstable potential of geosynchronous spacecraft, J. Geophys. Res. 86(A4):2443-2446.

6. Meyer-Vernet, N. (1982) "Flip-flop" of electric potential of dust grains in space, Astron. Astrophys. 105:98-106.

7. Meyer-Vernet, N. (1982) Multivalued electrostatic potentials; "chance or necessity" for the charge of solid particles near Saturn?, in Proc. IAU Colloq. No. 75: Planetary Rings, Toulouse, France, August-September 1982.

8. Stannard, P.R., Schnuelle, G.W., Katz, I., and Mandell, M.J. (1981) Representation and material charging response of GEO plasma environments, in Spacecraft Charging Technology 1980. NASA Conference Publication 2182/Report No. AFGL-TR-81-0270, AD A114426, Air Force Geophysics Laboratory, Massachusetts, pp. 560-579.

9. Gussenhoven, M.S., and Mullen, E.G. (1982) A "worst case" spacecraft charging environment as observed by SCATHA on 24 April 1979, paper No. 82-0271, Amer. Inst. Aeron. Astron. 20th Aerospace Sciences Mtg., January 1982, Orlando, Florida.

10. Schnuelle, G.W., Stannard, P.R., Katz, I., and Mandell, M.J. (1981) Simulation of charging response of SCATHA (P78-2) satellite, in Spacecraft Charging Technology 1980, NASA Conference Publication 2182/Report No. AFGL-TR-81-0270, AD A114426, Air Force Geophysics Laboratory, Massachusetts, pp. 580-591.

11. Stannard, P.R., Katz, I., Gedeon, L., Roche, J.C., Rubin, A.G., and Tautz, M.F. (1982) Validation of the NASCAP model using spaceflight data, Paper No. 82-0269, Amer. Inst. Aeron. Astron. 20th Aerospace Sciences Mtg., January 1982, Orlando, Florida, AFGL-TR-82-0108, AD A113440.

12. Fahleson, U. (1973) Plasma-vehicle interactions in space - some aspects on present knowledge and future development, in Photon and Particle Interactions with Surfaces in Space, R.J.L. Grard, Ed., D. Reidel, Dordrecht, Holland, pp. 563-569.

13. Whipple, Jr., E.C. (1976) Observation of photoelectrons and secondary electrons reflected from a potential barrier in the vicinity of ATS 6, J. Geophys. Res. 81(4):715-719.

14. Laframboise, J.G., and Prokopenko, S.M.L. (1977) Numerical simulation of spacecraft charging phenomena, in Proc. Spacecraft Charging Technology Conference, C.P. Pike and R.R. Lovell, Eds., Report No. AFGL-TR-77-0051, AD A045459, Air Force Geophysics Laboratory, Massachusetts/Report No. NASA TMX-73537, Lewis Research Center, Cleveland, Ohio, pp. 309-318.

15. Katz, I., Cassidy, J.J., Mandell, M.J., Schnuelle, G.W., Steen, P.G., and Roche, J.C. (1979) The capabilities of the NASA charging analyzer program, in Spacecraft Charging Technology 1978, NASA Conference Publication 2071/Report No. AFGL-TR-79-0082, AD A084626, Air Force Geophysics Laboratory, Massachusetts, pp. 101-122.

16. Besse, A.L., and Rubin, A.G. (1980) A simple analysis of spacecraft charging involving blocked photoelectron currents, J. Geophys. Res. 85(A5):2324-2328.

17. Purvis, C. (1982) Evolution of spacecraft charging technology, Paper No. 82-0273, Amer. Inst. Aeron. Astron. 20th Aerospace Sciences Mtg., January 1982, Orlando, Florida.

18. Laframboise, J.G., Godard, R., and Kamitsuma, M. (1982) Multiple floating potentials, "threshold-temperature" effects, and "barrier" effects in high-voltage charging of exposed surfaces on spacecraft, in Proc. Internat. Symp. on Spacecraft Materials in Space Environment, June 1982, Toulouse, France, European Space Agency, Paris, Publication No. ESA SP-178, pp. 269-275.

19. Cohen, H.A. (1982) Private communication.

20. Garrett, H.B., and DeForest, S. (1979) An analytical simulation of the geosynchronous plasma environment, Planet Space Sci. 27:1101-1109.

21. Garrett, H.B., Schwank, D.C., and DeForest, S.E. (1981) A statistical analysis of the low-energy geosynchronous plasma environment - I. electrons, Planet Space Sci. 29(10):1021-1044.

22. Dekker, A.J. (1958) Secondary electron emission, in Solid State Physics, F. Seitz and D. Turnbull, Eds., Vol. 6, Academic Press, New York, p. 251.

23. Hachenberg, O., and Brauer, W. (1959) Secondary electron emission from solids, Advan. Electron. Electron Phys. 11:413.

24. Hachenberg, O., and Brauer, W. (1962) Advan. Electron. Electron Phys. 16:145.

25. Gibbons, D.J. (1966) Secondary electron emission, in Handbook of Vacuum Physics, A.H. Beck, Ed., Pergamon, Oxford, p. 301.

26. Willis, R.F., and Skinner, D.K. (1973) Secondary electron emission yield behaviour of polymers, Solid State Commun. 13:685.

27. Katz, I., Parks, D.E., Mandell, M.J., Harvey, J.M., Brownell, Jr., D.H., Wang, S.S., and Rotenberg, M. (1977) A Three Dimensional Dynamic Study of Electrostatic Charging in Materials, NASA Contractor Report No. CR-135256, Lewis Research Center, Cleveland, Ohio.

28. Schnuelle, G.W., Parks, D.E., Katz, I., Mandell, M.J., Steen, P.G., Cassidy, J.J., and Rubin, A. (1979) Charging analysis of the SCATHA satellite, in Spacecraft Charging Technology - 1978, NASA Conference Publication 2071/Report No. AFGL-TR-79-0082, AD A084626, Air Force Geophysics Laboratory, Massachusetts, pp. 123-143.

29. Leung, M.S., Tueling, M.B., and Schnauss, E.R. (1981) Effects of secondary electron emission on charging, in Spacecraft Charging Technology 1980, NASA Conference Publication 2182/Report No. AFGL-TR-81-0270, AD A114426, Air Force Geophysics Laboratory, Massachusetts, pp. 163-178.

30. Krainsky, I., Lundin, W., Gordon, W.L., and Hoffman, R.W. (1981) Secondary electron emission yields, in Spacecraft Charging Technology 1980, NASA Conference Publication 2182/Report No. AFGL-TR-81-0270, AD A114426, Air Force Geophysics Laboratory, Massachusetts, pp. 179-197.

31. Salehi, M., and Flinn, E.A. (1981) Dependence of secondary-electron emission from amorphous materials on primary angle of incidence, J. Appl. Phys. 52(2):994-996.

32. Darlington, E.H., and Cosslett, V.E. (1972) Backscattering of 0.5 - 10 keV electrons from solid targets, J. Phys. D: Appl. Phys. 5:1969-1981.

33. Whipple, Jr., E.C. (1981) Potentials of surfaces in space, Rep. Prog. Phys. 44:1197-1250.

34. Sternglass, E.J. (1954) Theory of Secondary Electron Emission, Sci. Pap. 1772, Westinghouse Res. Lab., Pittsburgh, Pa.

35. Sternglass, E.J. (1954) Backscattering of kilovolt electrons from solids, Phys. Rev. 95:345-358.

36. Palluel, P. (1947) Composante rediffusée du rayonnement electronique secondaire des métaux, C.R. Acad. Sci. 224:1492.

23. Plasma Interaction of Negative Metal/Positive Dielectric Configurations

by

R. C. Chaky
G. T. Inouye
TRW, Inc.
Los Angeles, Calif.

Abstract

Large space structures in polar earth orbit (PEO) will have high power, high voltage solar arrays and possibly other high voltage equipment or components that are capable of interacting with the ambient plasma. The negative metal-positive dielectric configuration has been identified as a possible source of low voltage arc discharges, a corona-like zenering effect on the determination of the spacecraft potential, and a possible source of EMI noise. This paper is an interim presentation of studies of this configuration that demonstrate the enhanced emission of electrons at voltages under a kilovolt, as well as arc discharges and the noisy character of the electron emission currents. Samples of solar arrays, thermal blankets and second-surface mirrors have been studied.

24. Models of the Ionospheric Environment

by

R. W. Schunk
Center for Atmospheric and Space Sciences
Utah State University
Logan, Utah 84322

During the last decade our understanding of the physical processes that control ionospheric behavior has greatly increased. As a consequence, comprehensive, large-scale, quasi-static models of the high-latitude ionosphere have been developed to describe the aurora,[1-4] the E-region conductivity and currents,[2-5] the F-region,[3-7] and the polar wind.[8-12] In addition, 2-D particle-in-a-cell computer codes have been developed to study the microphysics connected with auroral acceleration processes. These studies involve models of double layers and anomalous resistivity to explain auroral electron precipitation as well as models describing the stochastic acceleration of ionospheric ions by both electrostatic ion cyclotron waves and lower hybrid waves to explain ion beams and conics.

The large-scale models of the high-latitude F-region are capable of producing time-dependent, 3-D ion density distributions for six ion species (NO^+, O_2^+, N_2^+, O^+, N^+, He^+) and electrons. The models take account of numerous high-latitude processes, including field-aligned diffusion, thermospheric winds,

Because of the large number of references cited above, they will not be listed here. See References, page 318.

electrodynamic drifts, polar wind escape, energy dependent chemical reactions, magnetic storm induced neutral composition changes, thermal conduction, diffusion-thermal heat flow, local heat sources and sinks, and ion production due to solar EUV radiation and energetic particle precipitation.

One of the early results to emerge from the use of these large-scale models is that high-latitude ionospheric features, such as the "main trough", the "ionization hole", the "tongue of ionization", the "aurorally produced ionization peaks", and the "universal time effects", are a natural consequence of the competition between the various chemical and transport processes known to be operating in the high-latitude ionosphere. In addition, the model studies have shown that the electron density at F-region altitudes displays a significant variation with season, solar cycle, convection pattern, and universal time.

Several interesting ionospheric features occur in winter for weak convection (Figure 1). A deep ionization hole occurs in the dawn sector poleward of the auroral oval. The hole is a result of slow antisunward convection in combination with ordinary ionic recombination. At 300 km, the electron density in the hole can be as low as $5 \times 10^2/cm^3$.[13] However, a short horizontal distance away, in the auroral oval, the densities can be more than three orders of magnitude larger, $5 \times 10^5/cm^3$. Another interesting ionospheric feature is the main or mid-latitude electron density trough. This trough, which is situated just equatorward of the nocturnal auroral oval, is a region of low electron density that has a narrow latitudinal extent but is extended in longitude. For winter solstice and slow convection, the electron density in the trough can be as low as $10^3/cm^3$ at 300 km.

When the plasma convection pattern changes, the high-latitude F-region can undergo major changes in a relative short time. For example, for strong convection in winter (Figure 2), the increased antisunward plasma drift sweeps the daytime high density plasma into the polar cap, producing an extended tongue of ionization. This tongue of ionization fills in the polar hole, with the electron density at 300 km increasing from $5 \times 10^2/cm^3$ to about $10^5/cm^3$. Likewise, for strong convection the density in the main trough is increased by more than an order of magnitude. Also, in summer the electron density in the high-latitude F-region is typically more than an order of magnitude greater than in winter (Figure 3). This results because most of the polar cap is sunlit in summer, while most of it is in darkness in winter.

There are some interesting thermal features in the high-latitude F-region. Elevated electron temperatures are found in the polar cusp and nocturnal auroral

13. Brinton, H.C., Grebowsky, J.M., and Brace, L.H. (1978) The high latitude winter F region at 300 km; thermal plasma observables from AE-C, J. Geophys. Res. 83:4767.

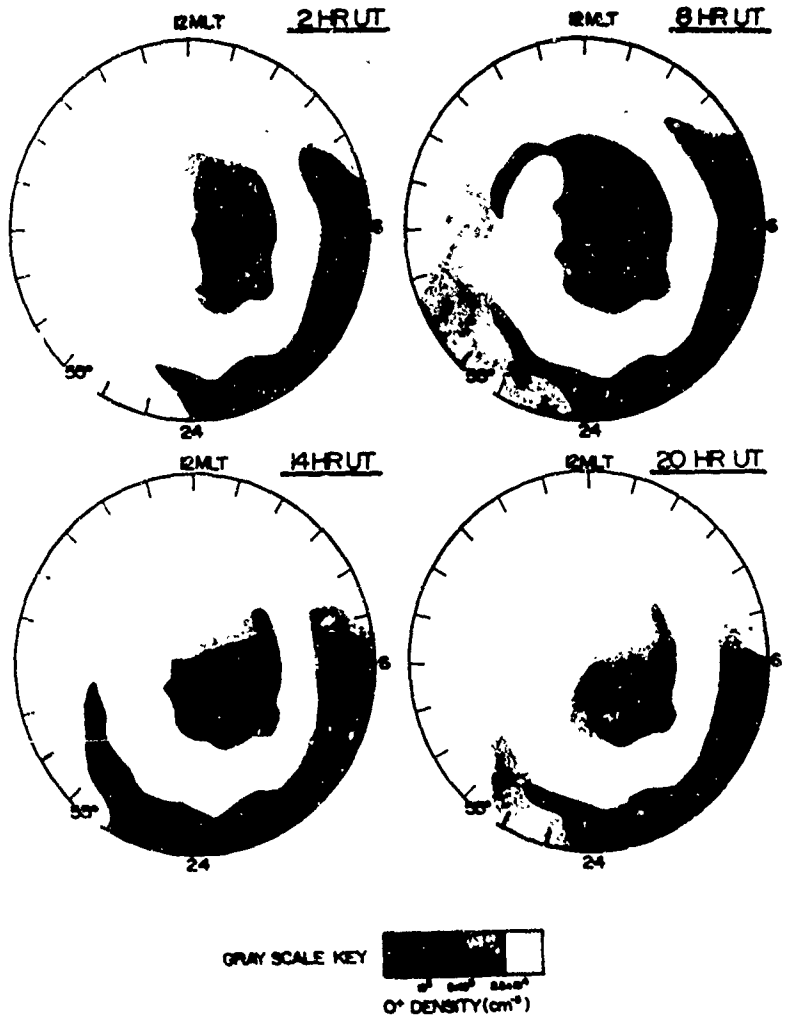

Figure 1. O^+ Density Contours at 300 km for Weak Convection in Winter. The contours are shown at four universal times in a magnetic quasi-inertial reference frame. The contour range was chosen to highlight the low density regions. From Sojka et al[6]

zone (4000 to 8000K). Also, ion temperature hot spots can appear in the dusk and/or dawn sectors depending on the plasma convection pattern (Figures 4 and 5). The hot spots are associated with strong plasma convection cells and the elevated ion temperatures are a result of an increased ion-neutral frictional heating rate. In the hot spot, the ion temperature is greatest at low altitudes (T_i > 4000 K) and decreases with altitude throughout the F-region. This behavior

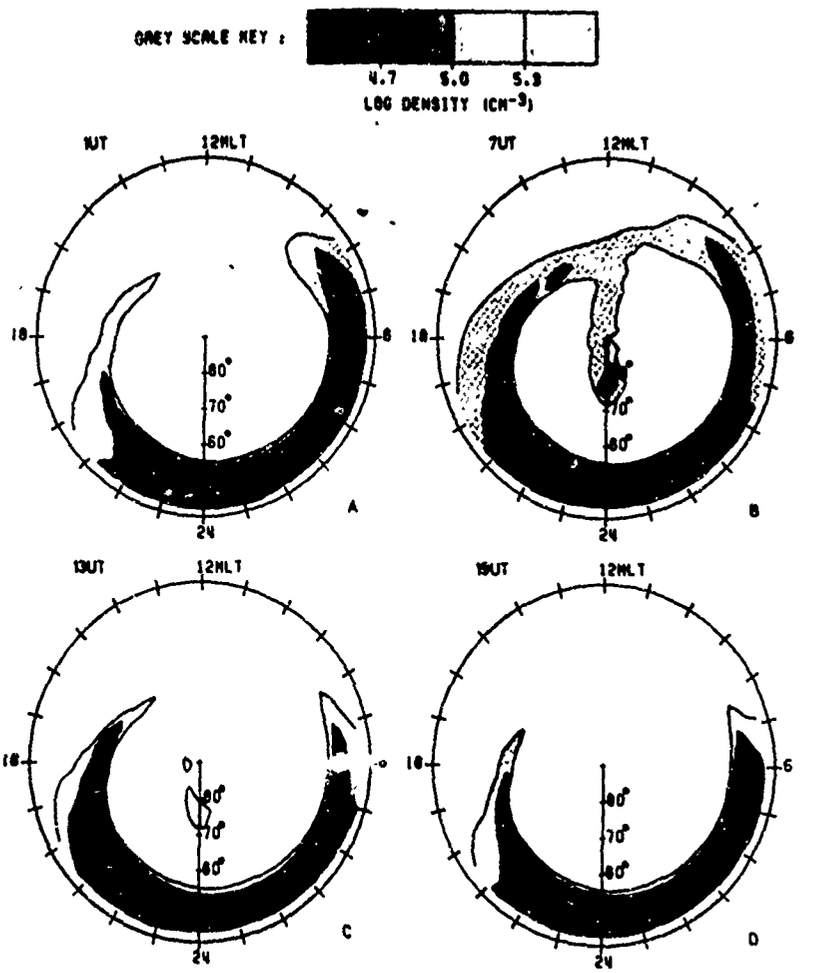

Figure 2. O^+ Density Contours at 300 km for Strong Convection in Winter. The contours are shown at four universal times in a magnetic quasi-inertial reference frame. From Sojka et al[14]

14. Sojka, J.J., Raitt, W.J., and Schunk, R.W. (1981) Plasma density features associated with strong convection in the winter high-latitude F region, J. Geophys. Res. 86:6908.

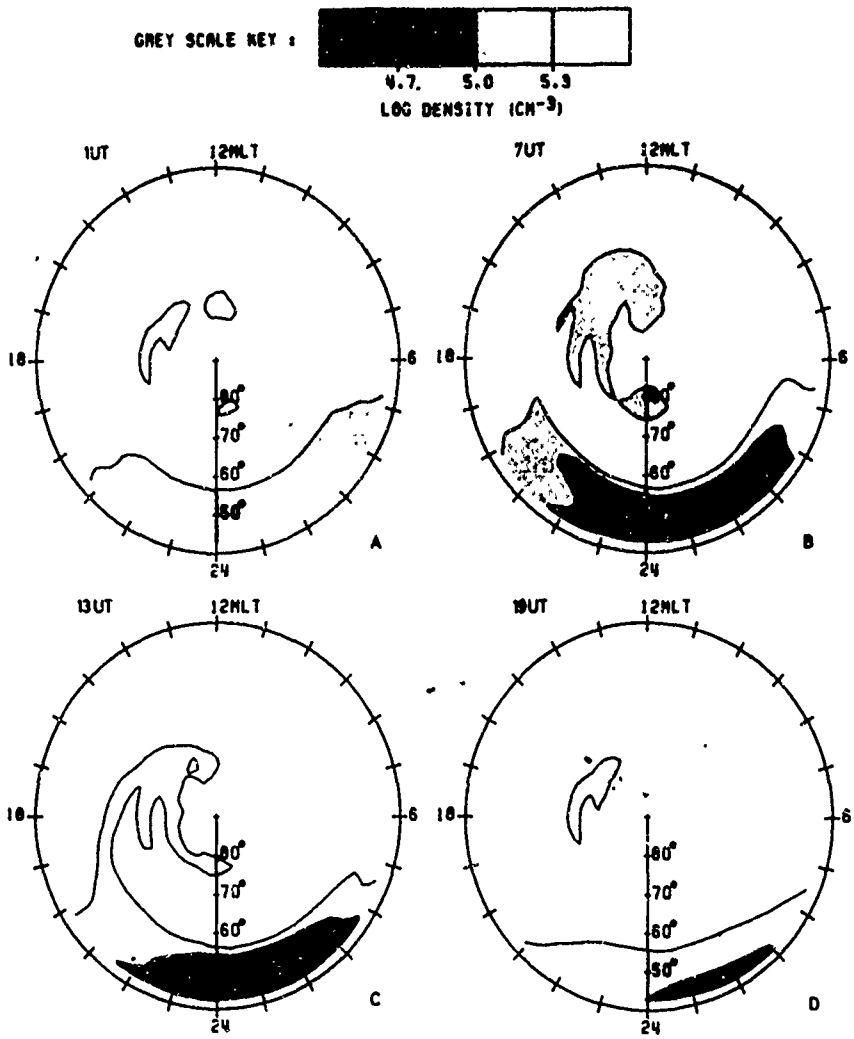

Figure 3. O^+ Density Contours at 300 km for Strong Convection in Summer. The contours are shown at four universal times in a magnetic quasi-inertial reference frame. From Sojka et al[15]

15. Sojka, J.J., and Schunk, R.W., J. Geophys. Res. (submitted 1982).

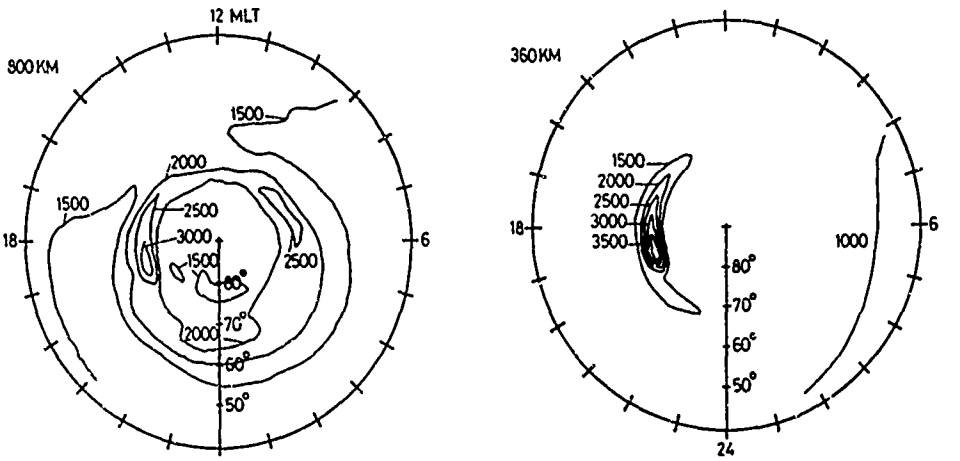

Figure 4. Contours of the Ion Temperature (^{o}K) in a Magnetic Quasi-inertial Reference Frame for Altitudes of 360 km (Right Panel) and 800 km (Left Panel). From Schunk and Sojka[16]

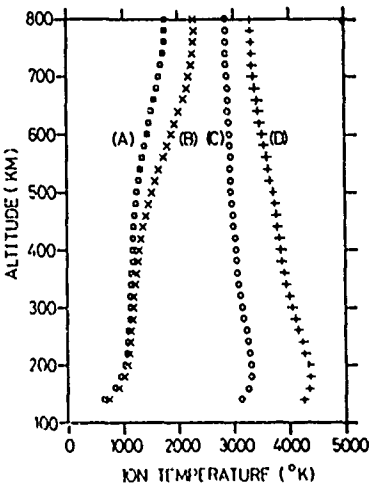

Figure 5. Ion Temperatures as a Function of Altitude at Selected Locations in the High-latitude Ionosphere. The locations are: (A) dayside, equatorward of auroral oval; (B) dayside, auroral oval; (C) edge of hot spot; and (D) center of hot spot. From Schunk and Sojka[16]

16. Sojka, J.J., Schunk, R.W., and Raitt, W.J. (1982) Seasonal variations of the high latitude F region for strong convection, J. Geophys. Res. 87:187.

is in sharp contrast with that found outside of the hot spot and at middle and low latitudes, where the ion temperature increases with altitude in the F-region.

Some theoretical work has been done on modeling magnetic storms.[17] In particular, these authors studied the response of the high-latitude F-region to an idealized magnetic storm for winter solstice and solar maximum conditions. The model storm was assumed to build in intensity over a 1-h time period, persist at full intensity for about 1.5 h, and then decay over a 3-h time period. During the buildup, the auroral oval expands, plasma convection velocities increase, and particle precipitation is significantly enhanced. The main result that was obtained from this study was that the ionospheric response time is a strong function of altitude. The lower F-region responds on a time scale of only minutes to the storm associated changes in the auroral precipitating electron flux, owing to the dominance of chemistry production-loss mechanisms over transport processes. At higher altitudes, in the vicinity of h_mF_2, the chemistry is balanced by both plasma diffusion along field lines and horizontal plasma convection, which acts to prolong the effect of the storm for many hours after it has ceased. The peak density responds only slowly to increased precipitation and may not reach its maximum enhanced value until over an hour after the storm main precipitation has passed. However, the F-region peak can be drastically altered on a time scale of minutes if large vertical transport velocities are associated with the storm electric field distribution. In the topside ionosphere the density variations are not correlated with the morphology of the storm auroral precipitation or the temporal variation of the storm electric field pattern. Time delays of up to 3 or 4 h occur at high altitudes for "peak" densities to be reached after a storm, and the subsequent recovery is on the order of 5 h. These long delays at altitudes above 400 km reflect the long time constants associated with plasma diffusion from low altitudes, where the plasma is created, to high altitudes.

Above the F-region, light ions are capable of flowing up and out of the ionosphere along the "open" geomagnetic field lines. Over the last decade various theoretical models have been developed to describe this light ion outflow, including hydrodynamic, hydromagnetic, kinetic, and generalized transport models. From these model studies the polar wind should have the following characteristics: (1) The H^+ flux should vary from 10^7 to $5 \times 10^8/(cm^2\ sec)$ and the He^+ flux from 10^5 to $10^7/(cm^2\ sec)$, depending on the geophysical conditions; (2) The ion temperature should be less than 8000K, that is, less than 1 eV; (3) The H^+ temperature should be anisotropic, with the temperature parallel to the magnetic field greater than the perpendicular temperature for supersonic H^+ outflow and the reverse for subsonic H^+ outflow; (4) The H^+ velocity distribution should be

17. Schunk, R.W., and Sojka, J.J. (1982) J. Geophys. Res. (in press).

asymmetric, with an elongated tail along the magnetic field in the upward direction; and (5) The electron temperature distribution should be anisotropic if the H^+ outflow is supersonic. In addition, recent numerical simulations indicate that an expanding polar wind should produce energetic H^+ and O^+ ions (~ 10 eV). These energetic ions are produced over the entire polar region, not just on auroral field lines.

References

1. Roble, R.G., and Rees, M.H. (1977) Time-dependent studies of the aurora: Effects of particle precipitation on the dynamic morphology of ionospheric and atmospheric properties, Planet Space Sci. 23:1103.
2. Matsushita, S., and Xu, W.-Y. (1982) Equivalent ionospheric current systems representing IMF sector effects on the polar geomagnetic field, Planet Space Sci. 30:641.
3. Knudsen, W.C., Banks, P.M., Winningham, J.D., and Klumpar, D.M. (1977) Numerical model of the convection F_2 ionosphere at high latitudes, J. Geophys. Res. 82:4784.
4. Watkins, B.J. (1978) A numerical computer investigation of the polar F region ionosphere, Planet Space Sci. 26:559.
5. Schunk, R.W., and Raitt, W.J. (1980) Atomic nitrogen and oxygen ions in the daytime high latitude F region, J. Geophys. Res. 85:1255.
6. Sojka, J.J., Raitt, W.J., and Schunk, R.W. (1981) A theoretical study of the high-latitude winter F region at solar minimum for low magnetic activity, J. Geophys. Res. 86:609.
7. Schunk, R.W., and Sojka, J.J. (1982) Ion temperature variations in the daytime high-latitude F region, J. Geophys. Res. 87:5169.
8. Holzer, T.E., Fedder, J.A., and Banks, P.M. (1971) A comparison of kinetic and hydrodynamic models of an expanding ion-exosphere, J. Geophys. Res. 76:2453.
9. Lemaire, J., and Scherer, M. (1973) Kinetic models of the solar and polar winds, Rev. Geophys. Space Phys. 11:427.
10. Raitt, W.J., Schunk, R.W., and Banks, P.M. (1975) A comparison of the temperature and density structure in high and low speed thermal proton flows, Planet Space Sci. 23:1103.
11. Schunk, R.W., and Watkins, D.S. (1981) Electron temperature anisotropy in the polar wind, J. Geophys. Res. 86:91.

12. Schunk, R.W., and Watkins, D.S. (1982) Proton temperature anisotropy in the polar wind, J. Geophys. Res. 87:171.

13. Brinton, H.C., Grebowsky, J.M., and Brace, L.H. (1978) The high latitude winter F region at 300 km; thermal plasma observables from AE-C, J. Geophys. Res. 83:4767.

14. Sojka, J.J., Raitt, W.J., and Schunk, R.W. (1981) Plasma density features associated with strong convection in the winter high-latitude F region, J. Geophys. Res. 86:6908.

15. Sojka, J.J., and Schunk, R.W., J. Geophys. Res. (submitted 1982).

16. Sojka, J.J., Schunk, R.W., and Raitt, W.J. (1982) Seasonal variations of the high latitude F region for strong convection, J. Geophys. Res. 87:187.

17. Schunk, R.W., and Sojka, J.J. (1982) J. Geophys. Res. (in press).

25. Polar Code Development

by

I. Katz
D. L. Cooke
M. J. Mandell
D. E. Parks
J. R. Lilley
J. H. Alexander
A. G. Rubin
S-Cubed, Inc.
La Jolla, Calif. 92038

This paper outlines

Possible charging of large space structures in polar orbit has been examined analytically for simple spherical objects. The major questions of the probability of such events and the magnitude of charging given a particular vehicle in a specified auroral flux remain unanswered. The POLAR code is being developed to address the latter question. ~~We will outline~~ the physical models being incorporated in the program and the status of the code development.

The phenomenon of charging may be divided into three processes: (1) the accumulation of charge on the object resulting from collection of charged particles from the space environment; (2) the resultant change in overall and differential potentials on the venicle; and (3) the formation of a sheath and wake due to the presence of a charged object. Of course, some degree of mutual consistency is required in modeling these processes. For example, the sheath and wake structure has a substantial effect on charged particle collection. Presently the POLAR

code contains well-established models for some processes and newly developed models for others. A few processes are modeled by tentative algorithms pending development of more adequate techniques.

The charged particle currents of importance are energetic (~ 10 keV) electrons precipitating along field lines, and the cool ambient ions attracted by the vehicle. The energetic electrons provide the impetus for charging; cooler ions are the counter current which quenches the charging. Since we are initially interested in seeing if potentials as large as 1000 V can develop on large vehicles, the first version of the POLAR code will assume that the directions of motion of the energetic electrons are unmodified, but that their energy in the potential field is conserved. The energy and angular distributions of these electrons are critical in the charging analysis. An examination of tile response to representative environments will be made using a material charging code such as MATCHG prior to any POLAR calculation. If the electron environment in the absence of ions is not strongly charging there is no possibility of developing high potentials.

The ion currents from the ambient cool low earth orbit plasma will be determined by tracking trajectories in from the plasma sheath surface. This technique has proved very successful when applied to non-flowing plasmas, and the modification to include finite Mach effects is under way. The formulations presented in "Mechanisms That Limit Potentials on Ionospheric Satellites" (D. E. Parks and I. Katz, these proceedings) should prove very useful in appropriately accounting for presheath focusing.

The accumulation of charge and change in potentials due to prescribed incident ion and electron currents is the area where the models being put in the POLAR code have the greatest reliability. With the possible exception of the floating potential with respect to plasma ground, both the physics and the numerics of the charging processes are well understood and tested. The surface interactions are essentially unchanged from those in NASCAP/GEO. New effects such as $\vec{V} \times \vec{B}$ and asymmetric ion currents will be included. A major improvement in the numerical treatment is the simultaneous solution of the space potentials and normal electric field boundary conditions that will make the approach to equilibrium far easier to calculate than it is with NASCAP/GEO.

The third major component of the charging calculation is the sheath and wake. Combined with the feedback on ion currents this is by far the most difficult problem both theoretically and computationally. In POLAR these problems are much more difficult, because of flow and magnetic field effects, than calculations of high voltage collection from non-flowing plasmas. For the first cut we are neglecting magnetic field effects and are concentrating on electric field and wake phenomena. Recent calculations have shown that there are simple models that

provide an adequate model of each of these effects separately. The NASCAP/LEO results have shown the validity of the accelerated plasma model for charge density in space charge limited collection. The study by Parks and Katz has shown the dominance of finite current effects in determining equatorial satellite potentials and has provided bounds on the current enhancement possible from electric field focusing. The first POLAR model will not include focusing effects in the ion density when determining potentials (they will be included in the currents, of course), however, it is an area where intensive effort is being spent to improve the formulation. The goal is to incorporate the focusing effect in the space charge by the use of analytical formulas.

The POLAR code presently consists of three major modules. The first is for object and mesh definition. The object definition is much along the lines of NASCAP but more restrictive - there are no plans to include booms. The space around the object is broken up into discrete cells. Since the important regions to include are located along the flow direction, the mesh "slices" are staggered so that most of the cells are used to resolve wake and sheath phenomena. The concept of the sliced bread staggered mesh has been implemented and tested for several simple objects. Figure 1 shows the silhouette of an object as it is located in the computational space. The grid is constructed, and the object transformed, so that the wake is most nearly parallel to the positive Z-axis. Diagnostic graphics are, for the moment, extremely primitive, but do show that the concept as designed is presently functioning.

The second module calculates the "neutral approximation" for the ion density. This is done by calculating the shadowing of straight line orbits by the object. The neutral approximation to the density is particularly simple to calculate for two reasons. First, the straight line orbits allow trajectories to be "traced" instantly, and second, the orbits, and thus shadowing factors, are independent of particle kinetic energy. For every point in space the basic algorithm finds the perimeter of each object surface in solid angle space and eliminates all orbits within the perimeter from contributing to the local phase space density. While using only discrete directions this technique has proven extremely fast and quite accurate. The major approximations are the discretization of the angles and the interpolation in solid angle space of the surface perimeters. Typically the solid angle space is gridded 36×180 and a few extra points are added along each surface edge to minimize interpolation errors. The algorithm has been tested by comparing it with analytical results for densities near a surface. Figures 2 to 4 are of diagnostic plots showing the portion of solid angle space shadowed by a flying brick. This neutral approximation to the ion density is only used for the charge formulation when solving for the space electric potential.

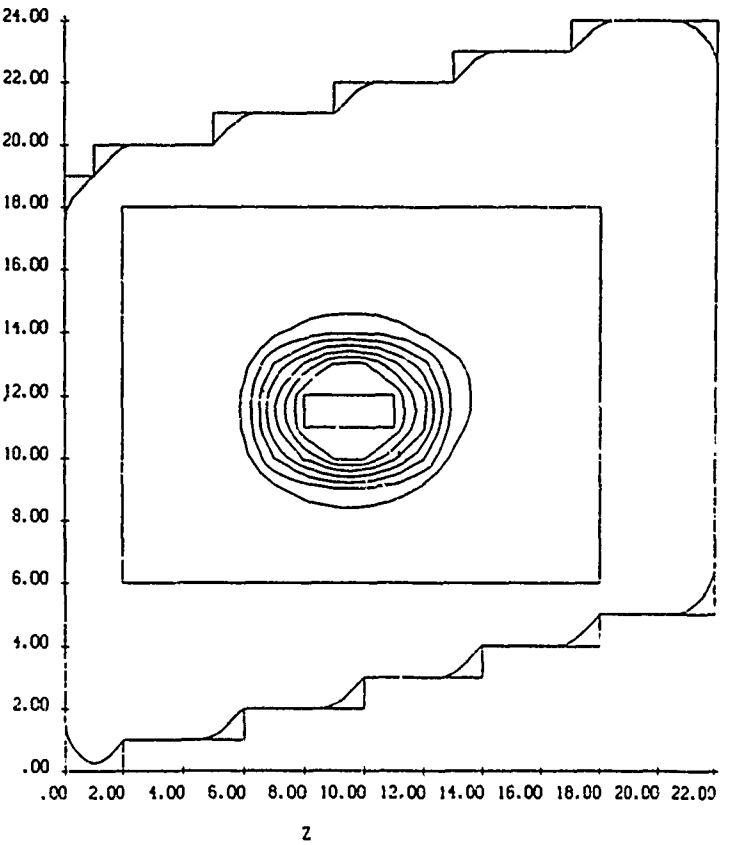

Figure 1. Flying Brick in a Staggered Grid

Sheath potential calculations are performed in the third module. The potentials are found by solving Poisson's equation

$$\nabla^2\phi = -\rho/\epsilon_o \quad ,$$

where the approximations are all contained in the determination of the charge density ρ. For the flying octagon we used a barometric approximation for the electron density and the neutral ion density

$$\rho = -n_o e^{\phi/kT} + n_i \text{ (neutral)} \quad .$$

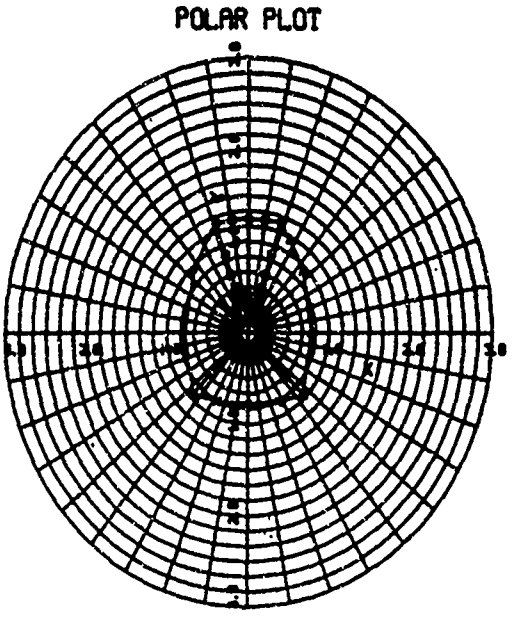

Figure 2. Neutral Approximation Phase Space Map of a Flying Brick Blocking the Ram Direction

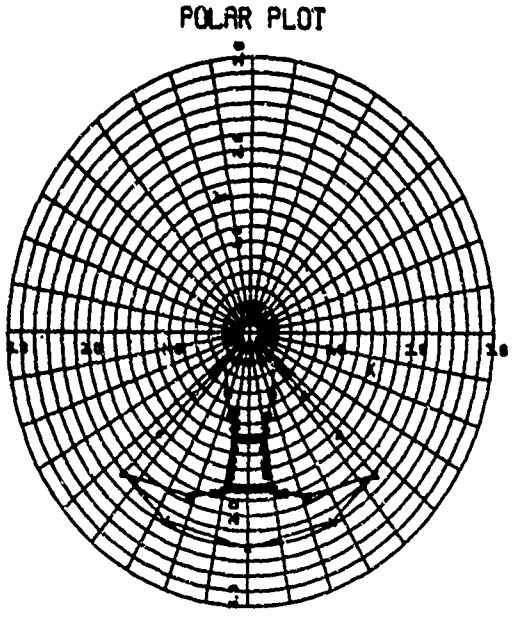

Figure 3. Neutral Approximation Phase Space Map of a Flying Brick at Right Angles to the Ram Direction

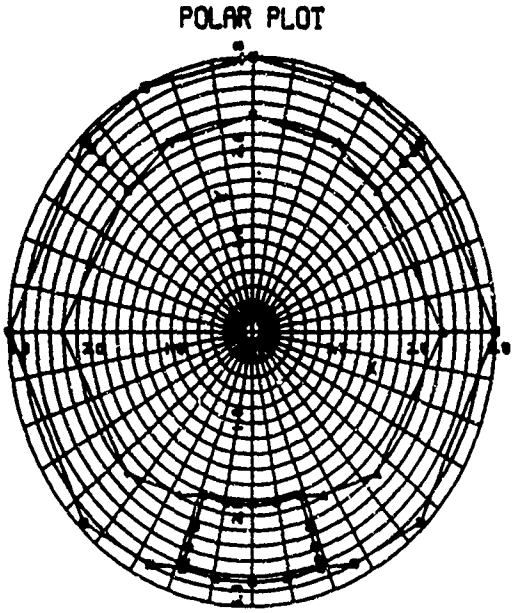

Figure 4. Flying Brick in the Anti-ram Direction

For high voltages this expression will be modified to include acceleration and focusing contributions to the ion density term. The acceleration contribution will add an asymptotic $(\phi/\theta)^{-1/2}$ to the ion density while the focusing terms are expected to be large only for near-orbit-limited regimes and should not dominate high voltage charging calculations. The average focusing expected can be estimated from the ratio of the sheath area to the satellite area. The local variation of the focusing is a much more difficult problem but should be amenable to some of the analytical approaches described by Parks and Katz.

Numerically, the nonlinear Poisson's equation is solved using the finite element approach previously employed in the NASCAP codes, although all the computer routines are new since the grid slicing algorithms force the computations to be performed in a very specific order. A new approach has been generated to handle surface potentials that will allow for faster convergence and for slanted thin plates. The writing and testing of the "forward fill - back fill" routines to handle surface potentials was a substantial task and there now exists the computational machinery to get surface potential information to geometrically complex cells. The residual matrices have been constructed for cubes, wedges, and cubes with a triangle surface. Matrices for cells with other geometries should be constructed and integrated into POLAR within the next few months.

The first sequence of calculations performed has been for a Mach 8 octagon whose potential is -1 kT. The ion density around such an object with an asymmetric Mach vector is shown in Figure 5. Potentials around the octagon for the Mach vector perpendicular to the spin axis are shown in Figures 6 and 7. An interesting physical effect, the deepening of an electrostatic well in the wake as the ratio of the satellite radius to the Debye length increases, can be seen in Figures 8, 9, and 10.

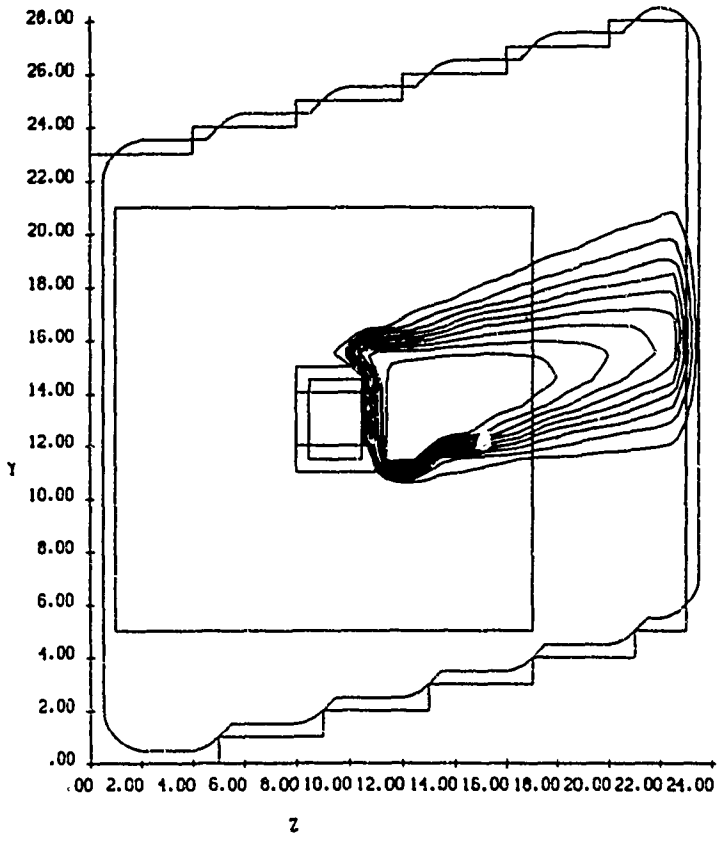

Figure 5. Wake Density Contours for Flying Octagon; $V_{Mach} = 8$

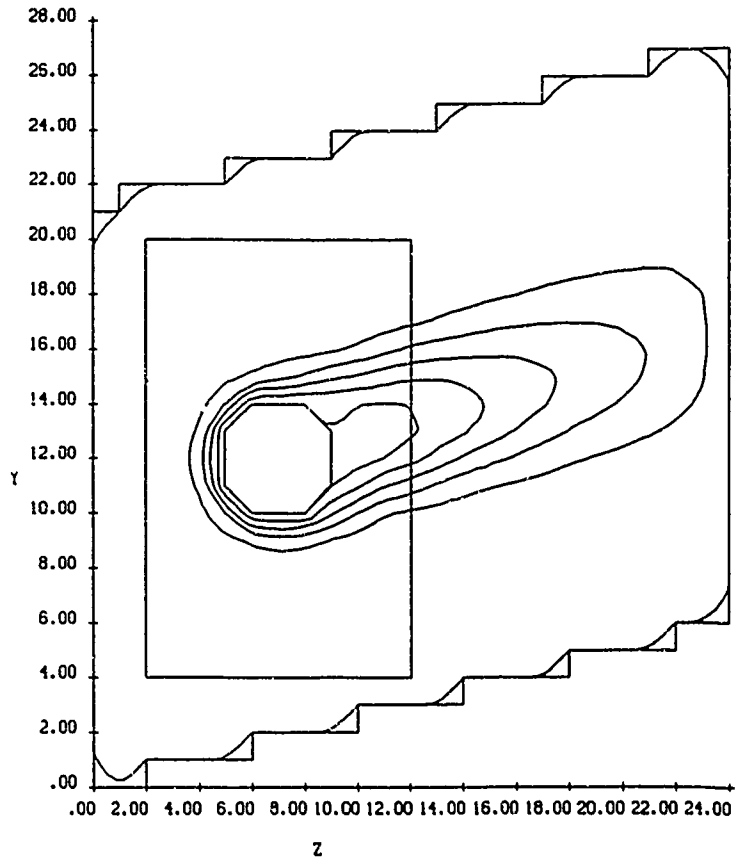

Figure 6. Potential Contours for Flying Octagon; R_s/λ^D = 2.5; V_s/kT = -1; V_{max} = -1.1

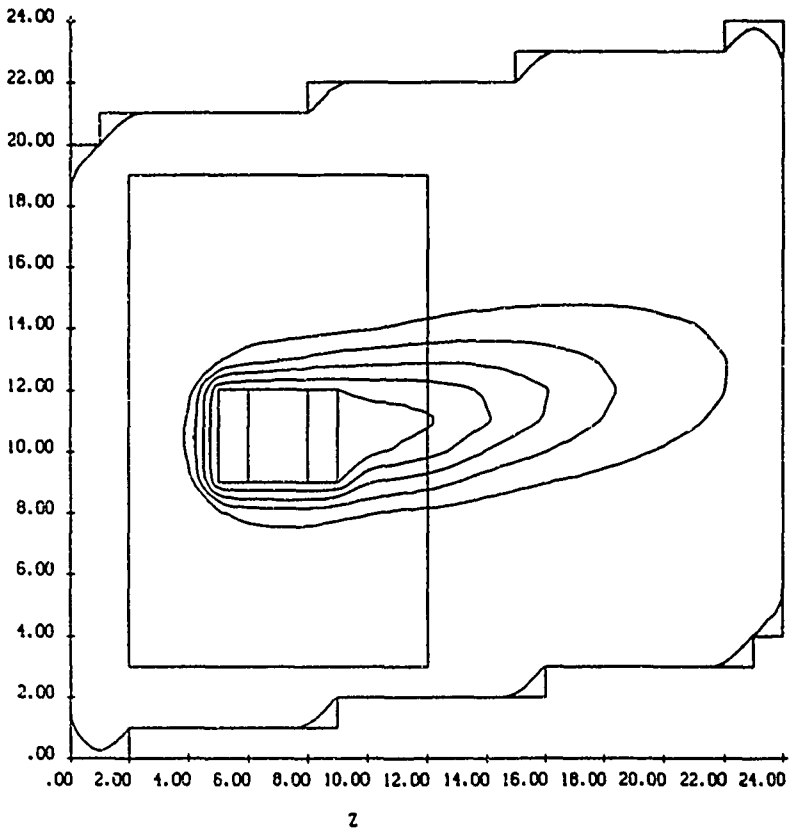

Figure 7. Potential Contours for Flying Octagon; $R_s/\lambda_D = 2.5$; $V_s/kT = -1$; $V_{max}/kT = -1.1$

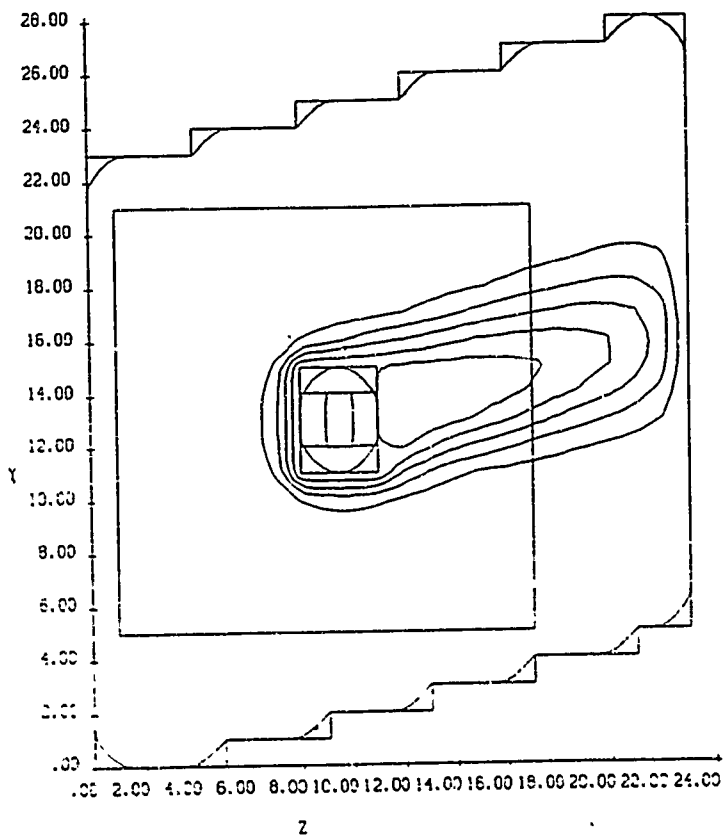

Figure 8. Potential Contours for Flying Octagon; R_s/λ_D = 2.5; V_s/kT = -1; V_{max}/kT = -1.2

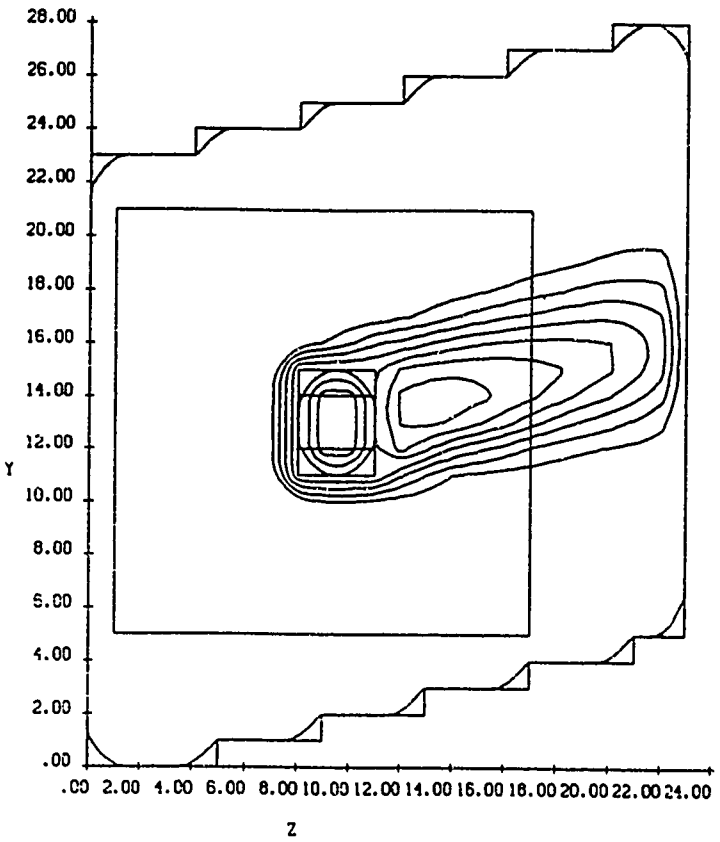

Figure 9. Potential Contours for Flying Octagon; R_s/λ_D = 3.5; V_s/kT = -1; V_{max} = -1.5

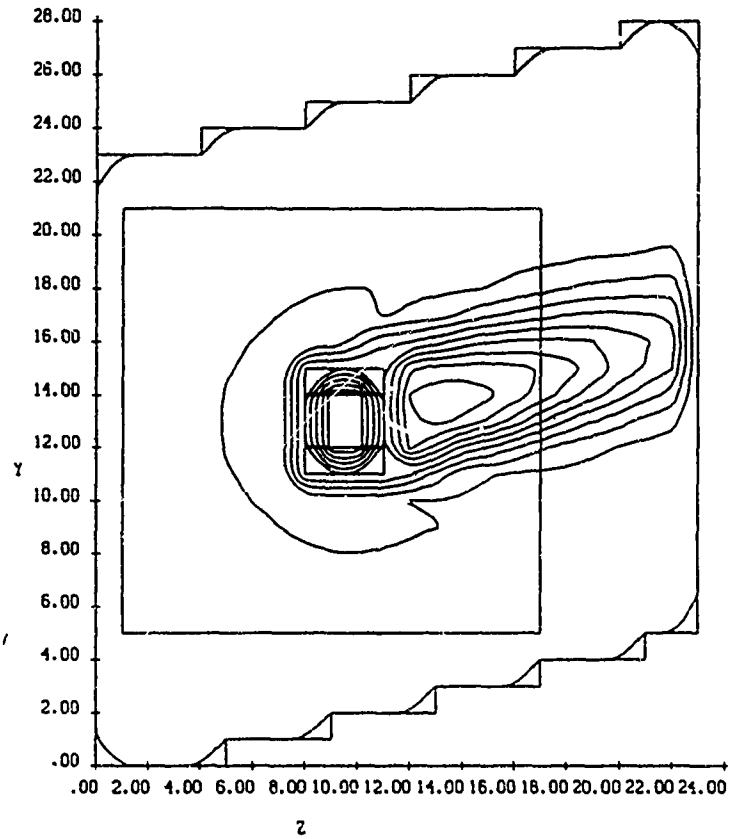

Figure 10. Potential Contours for Flying Octagon; R_s/λ_D = 5; V_s/kT = -1; V_{max} = -2

Acknowledgement

This work was supported by the Air Force Geophysics Laboratory, Hanscom Air Force Base, Mass., under Contract No. F19628-82-C-0081.

Contents

26. High Voltage Solar Array Models and Shuttle Tile Charging

by

A. Rubin
Air Force Geophysics Laboratory
Hanscom AFB, Mass. 01731

based on a presentation by

N. J. Stevens*
NASA Lewis Research Center
Cleveland, Ohio 44135

1. SOLAR ARRAY CHARGING

This paper describes

NASCAP/LEO (NASA Charging Analyzer Program/Low Earth Orbit) is a 3-D computer code that simulates the interaction of space plasma with high-voltage solar arrays in the thin plasma sheath regime. The code requires information about the object and the ambient plasma. The geometric description, the material composition and the voltage distribution versus time of a solar array are the data required about the object. The plasma properties needed are the composition, density, and temperature. NASCAP/LEO will then provide the time-dependent current to each element of area of the array from the external plasma. The NASCAP/LEO output is provided in both three-dimensional computer graphics

more

*Presently at Hughes Aircraft Co., Space Communications Group, Los Angeles, CA 90009

and in numerical form. NASCAP/LEO is user-oriented and will provide potential distributions around the object, the currents to each of the conductors, and graphical details of the sheaths and particle trajectories.

NASCAP/LEO, which is still in a preliminary state, is a tool for analyses of experimental data. We are now trying to compare the code predictions with data from ground simulation experiments on solar arrays. After verifying the code prediction capabilities on the ground, we will qualify the code against spaceflight data. The code will be used for extrapolation to solar arrays of various sizes and different power supplies. The present code treats biased surfaces in dielectric surroundings, and will eventually include all material properties and their influence on current-collection capabilities of the solar arrays.

Ground simulation tests of the collection capabilities of a disc, with bias voltages applied, were carried out. NASCAP/LEO predictions of current collection were within a factor of 2 of the data, within the uncertainty of the experiment.

NASCAP/LEO has been used to model current collection by a solar-cell array. To model current collection correctly at less than 100-V bias, the code must compute the potentials on the glass and the dielectrics. This is not allowed in the present form of the code. In the "Snapover" regime above 100 V where the whole panel starts collecting (see previous paper by N. J. Stevens) the predicted current is a factor of 2 less than the actual data. In the snap-over regime, more accurate modeling of the dielectric boundaries should improve the agreement.

2. SHUTTLE TILE CHARGING

In a cooperative program with AFGL/PHK, shuttle tile charging is being measured. The tests use white and black tile samples, about 12 in. square, made up exactly as they are to be put onto the shuttle. The samples are 0.5 to 3 in. thick. The material is 3 in. thick on the leading edges of the wings and the tail, where the heating is greatest, and tapers back to 0.5 in. at the tail end of the wings. The experiment has been run with the substrate grounded, using a monoenergetic electron beam of 1 to 25 kV at current densities of 0.1 and 1.0 nA/cm^2. Time-integrated photographs show many discharges at the gaps between the tiles.

Figure 1 shows the charging characteristic of the tiles, which is similar to glass. There is an offset of about 2000 V. Above 15 000 V there is some leakage, which causes a deviation from a straight line in the charging characteristic.

Figure 2 shows the charging rates, which are flux dependent. Although the tile is substantially charged in 10 sec, it takes about 100 sec to reach equilibrium.

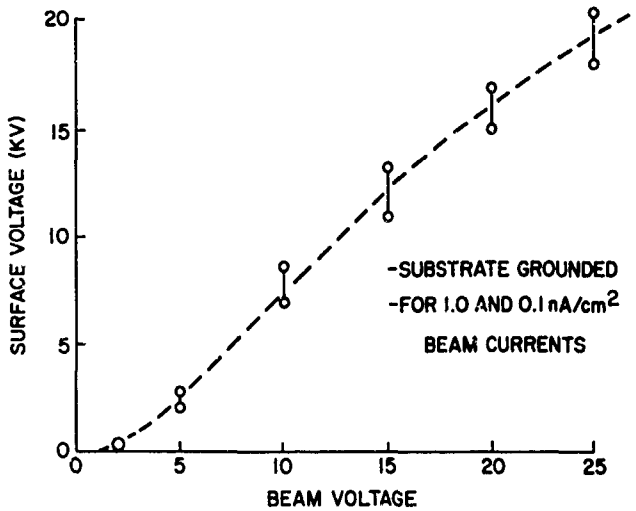

Figure 1. Equilibrium Shuttle Tile Surface Voltage at Electron Beam Energies to 25 kV. Equilibrium voltages are the same for charging currents of 1.0 and 0.1 nA/cm^2

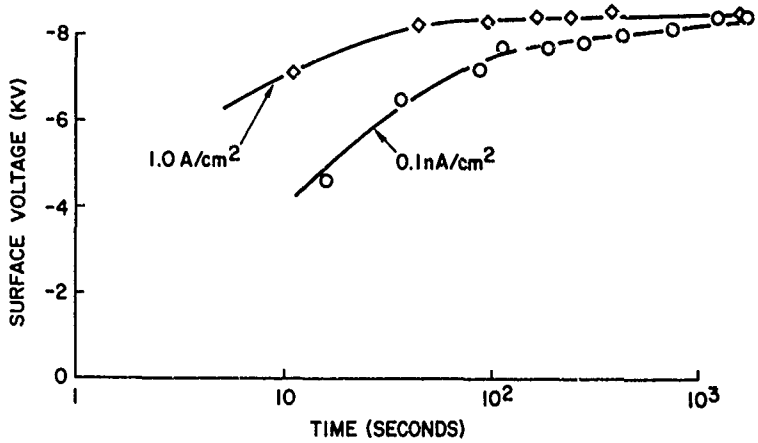

Figure 2. Shuttle Tile Charging vs Time, Due to 10-keV Electron Beams of 1.0 and 0.1 nA/cm^2

At higher energies it charges more rapidly, and quickly reaches equilibrium. The study is continuing, with investigations of thicker samples, and the effects of atomic oxygen concentration.

Contents

27. Sheath Shapes: A 3-D Generalization of the Child-Langmuir Sheath Model for Large High-Voltage Space Structures in Dense Plasmas

by

L. W. Parker
E. G. Holeman
Lee W. Parker, Inc.
252 Lexington Road
Concord, Mass. 01742

and

J. E. McCoy
Space Environment Office
NASA Johnson Space Center
Houston, Tex. 77058

Abstract

A new approach to computing sheaths of large high-voltage space structures in dense Low Earth Orbit/Polar Earth Orbit plasmas is described. The method solves the Poisson equation numerically, using a flexible-finite-element mesh that allows sheath shapes to be described through an extension of the well-known Child-Langmuir-Blodgett 1-D sheath model to three dimensions. Space charge is computed by following trajectories. This approach is potentially more

efficient for 3-D sheath and wake problems than other approaches presently available.

The code (CLPH3D) is applied to a number of problems, mostly concerning sheath shapes and ion focusing effects associated with dielectric borders on large high-voltage rectangular panels (in one case a long circular cylinder) interacting with a dense plasma, with and without flows. The plasma is assumed to have temperature 0.4 eV, density $10^6/cm^3$, and flow Mach number 7. The sheath shapes and ion focus patterns (producing "hot spots" where, for example, solar cells can be damaged) vary with the body and border geometry, body voltage, and plasma-flow velocity and direction. The meter-sized bodies are large compared with the Debye length (200 to 250 Debye lengths), and the voltages are large (200 to 2000 V) compared with kT/e.

In other applications (without flows), (1) an analytic space charge assumption of the type used by NASCAP/LEO is tested and found to overestimate sheath sizes, and (2) a small low-voltage probe introduced into the high-voltage sheath is found to produce a large disturbance of sheath shape and ion focus pattern.

1. INTRODUCTION

Interest has risen rapidly in recent years in problems of spacecraft interacting with plasmas, particularly at the high voltages associated with high-energy charging effects, in low earth orbits, or polar orbits passing through the auroral zone. Computer modeling of the associated effects requires innovative, sophisticated techniques.

We have formulated a new computer model (CLPH3D) capable of predicting detailed sheath parameters, generally in 3-D geometries. Some comparisons of computer solutions with solar-array-simulation experiments in the JSC Chamber A[1, 2, 3] have been made, and further comparisons are underway. Such comparisons not only serve to improve and validate the models, but are expected to suggest appropriate further experiments. The model can then be applied with confidence to (1) direct computations of, and to (2) scaling the experimental results for, predictions of the behavior of high-voltage structures in the ionosphere.

---

1. McCoy, J. E., and Konradi, A. (1979) Sheath effects observed on a 10-meter high-voltage panel in simulated low-earth-orbit plasma, in Spacecraft Charging Technology – 1978, R. C. Finke and C. P. Pike, Eds., NASA Conference Publication 2071, AFGL-TR-79-0082, AD A084626, pp. 315-340.
2. McCoy, J. E. (1980) High-voltage space plasma interactions, Proceedings of the Solar Power Satellite Program Review, DOE/NASA, available from NTIS, Springfield, VA 22161.
3. McCoy, J. E., Konradi, A., and Garriott, O. K. (1980) Current leakage for low altitude satellites, in Progress in Astronautics and Aeronautics, Vol. 71 (Space Systems and their Interactions with Earth's Space Environment), H. B. Garrett and C. P. Pike, Eds., AIAA, pp. 523-553.

To our knowledge, this model is capable of predicting, more accurately and economically than other models presently available, the trajectory-controlled space-charge-sheath electrical interactions of large high-voltage structures with high-density plasmas (particularly large high-voltage structures in the LEO/PEO ionosphere environment). We developed this model to fill the need for modeling high-voltage sheath and wake effects in dense plasmas, where the Debye length is small compared with the (large) body size. It evolved from a series of computer models specifically designed to handle space-charge-dominated sheaths and wakes in LEO, in axially symmetric but relatively simple geometries (see references by Parker and co-workers). The large and complex NASCAP/LEO code presently being developed by Katz and his co-workers(see reference), on the other hand, is based on the NASCAP space-charge-less code, which was designed for geosynchronous earth orbit conditions. NASCAP primarily provides Laplace-equation potential solutions for complex 3-D geometries, and runs trajectories to calculate surface currents using the Parker "inside-out" trajectory method. To apply NASCAP/LEO to dense plasmas where Poisson's equation must be solved, NASCAP/LEO models the space charge term by an assumed, overly simplified, function of local potential. This simplification avoids the running of trajectories that are actually required to evaluate space charge correctly, which is computationally costly in 3-D. CLPH3D evaluates space charge correctly in 3-D, but has not yet been applied to complex geometries, as has NASCAP. On the other hand, NASCAP handles complex 3-D geometries, but in dense plasmas, its offshoot, NASCAP/LEO, is constrained essentially to assume a formula for space charge. Hence, the two codes have complementary advantages. It is important to determine the error incurred in using the NASCAP/LEO approximation for space charge. Hence, one section of this paper is concerned with a comparison of the approximate vs rigorous evaluations of space charge.

An important experimental configuration is a dielectric object located within the sheath of a high-voltage panel. It is shown in this paper that a nonconducting border on the panel produces a significant disturbance of the sheath structure. This field structure leads to an ion focusing phenomenon on the surface of the panel,[1, 2, 3] that is, the impinging ion trajectories are concentrated (focused) within sharply defined areas. At the sharp edges of these areas, the current density is high. The size and shape of the focus area varies with panel voltage, size and shape of the nonconducting area, and plasma flow velocity. Computer predictions of these effects are discussed throughout much of this paper. Effects involving changes of sheath structure and modifications of the ion optics are expected to occur whenever dielectric objects are placed within the sheath. These effects should be taken into account in engineering design studies, whether the dielectric "incursion" is deliberate or inadvertent.

Another important experimental configuration is a probe in the sheath of the panel.[1,3] This is important not only because of the necessity to interpret the probe current-voltage characteristics in terms of the sheath and plasma parameters, but because the probe can by its presence strongly perturb the sheath. The perturbation will depend on the probe location as well as its voltage. It is shown in Section 4 that the probe within the sheath disrupts the sheath shape, the field structure, and the ion focusing pattern caused by the dielectric border. The probe disturbance effect is similar to that of an additional dielectric object placed within the sheath. This is an occurrence normally unavoidable in laboratory experiments (for example, probe supports do this) and is typically neglected in ground-based experiments (for example, solar array sheath experiments[4]). This disturbance effect may also be expected to occur in space; for example, whenever a piece of trash, cable, or wiring inadvertently enters the sheath, it can produce a pronounced disturbance. Even astronauts in EVA within say, a multi-kilovolt sheath can represent a 2-m dielectric object producing a disturbance.

This paper deals with the 3-D generalization of the Child-Langmuir sheath model, for application to the interactions of large high-voltage space structures with dense plasmas. A number of examples are presented. In most cases, the body potential is 500 to 5000 kT/e, where T is the temperature of the plasma, and the body dimension is about 200 or 250 plasma Debye lengths. Some of the results given in this paper were previously reported in preliminary form.[5,6]

To justify the approach taken in this paper, we test the Child-Langmuir sheath model by solving the following bench-mark case rigorously. (The computer program used exclusively for this section, called PARKSS, is used only for problems with spherical symmetry, and is distinctly different from the 2-D and 3-D programs discussed in the remainder of this paper.

Assume a spacecraft of scale dimension 1 m, in an ionospheric plasma with a temperature of 0.1 eV and a density $6 \times 10^4/cm^3$. (The Debye length is 1 cm, so that the body dimension is 100 Debye lengths.) Assume that 40-keV ions are emitted by an on-board accelerator and that the return current consists of ionospheric O^+ ions. The maximum beam current that can escape is equal to the return

---

4. Stevens, N.J. (1980) Space environmental interactions with biased spacecraft surfaces, Progress in Astronautics and Aeronautics, Vol. 71 (Space Systems and Their Interaction with Earth Space Environment), H. B. Garrett and C. P. Pike, Eds., AIAA, pp. 455-476. (See also adjacent paper.)

5. Parker, L.W. (1981) Trajectory-Controlled Space-Charge-Sheath Computer Models, NASA Contract NAS9-15934, Lee W. Parker, Inc.

6. Cooke, D.L., Parker, L.W., and McCoy, J.E. (1981) Three-dimensional space charge model for large high-voltage satellites, in Spacecraft Charging Technology 1980, N.J. Stevens and C.P. Pike, Eds., NASA Conference Publication 2182, AFGL-TR-81-0270, AD A114426, pp. 957-978.

current collected when the spacecraft is 40 kV negative. This voltage is 4×10^5 times kT/e of the plasma. Modeling the body by a sphere allows us to obtain self-consistent numerical sheath solutions by the rigorous methods of Parker[7, 8] and LaFramboise.[9] For a dimensionless sphere potential of 400,000 (the largest value treated to date, for a large sphere radius of 100 Debye lengths), Parker[7] calculates a current collection factor of 490 times ambient, or about 20 mA return current, which is equal to the maximum beam current that can escape. This return current corresponds to a sheath radius of about 22 sphere radii. The corresponding ratio of sheath radius to sphere radius predicted by the Child-Langmuir model is 20.4, using data of Langmuir and Blodgett[10] as fitted by Parker.[7] Hence we conclude that the Child-Langmuir sheath model is a reasonably good approximation under conditions where the body is large and at high voltage. Thus, a 3-D generalization should provide a reasonably good approximation in 3-D problems.

Figure 1 shows how the potential varies within the sheath. The attracted-particle density within the sheath (not shown here but presented in Figure 4 of Ref. 7), has a value about 0.2 times ambient at the sphere surface, drops off with increasing radius, and rises again to its normal value in the vicinity of 20 sphere radii.

It is of interest to compare the results of this strictly spherically symmetric but rigorous calculation with those of a simpler but more approximate spherically symmetric model, namely, one using linearized space charge, as represented by Eq. (17) and discussed by Parker.[7, 11] (This leads to the "Debye potential" model, used, fo example, by Whipple.[12]) With the Debye potential function given by

---

7. Parker, L.W. (1960) Plasmasheath-photosheath theory for large high-voltage space structures, in Progress in Astronautics and Aeronautics, Vol. 71 (Space Systems and Their Interaction With the Earth's Space Environment), H.B. Garrett and C.P. Pike, Eds., AIAA, pp. 477-522. Parker's method was reviewed by Garrett[8]

8. Garrett, H.B. (1981) The charging of spacecraft surfaces, Rev. Geophys. Space Phys. 19:577.

9. Laframboise, J.G. (1966) Theory of Spherical and Cylindrical Probes in a Collisionless Maxwellian Plasma at Rest, Univ. of Toronto Report UTIAS No. 100, June.

10. Langmuir, I., and Blodgett, K.B. (1924) Currents limited by space charge between concentric spheres, Phys. Rev. 24:49-59.

11. Parker, L.W. (1972) Computation of Ion Collection by a Large Rocket-Mounted Mass-Spectrometer Plate at a Large Drawing-In Potential, AFCRL-72-0524, AD 750483, Contract F19628-71-C-0200, Mt. Auburn Research Associates, Inc.

12. Whipple, E.C., Jr., Warnock, J.M., and Winkler, R.H. (1974) Effect of satellite potential on direct ion density measurements through the plasma-pause, J. Geophys. Res. 79:179.

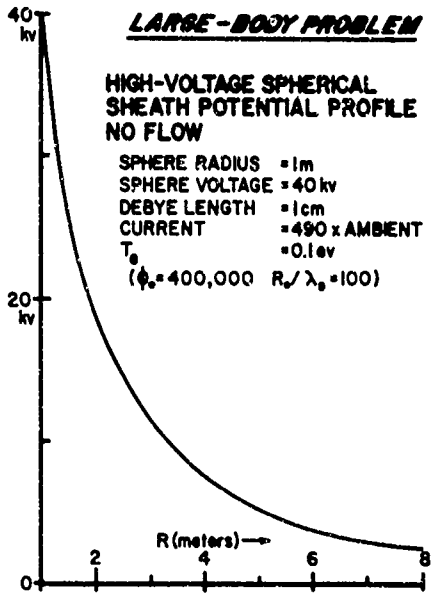

Figure 1. Large Body at Extremely High Voltage (40 kV in $6 \times 10^4/cm^3$, 0.1-eV Plasma). Self-consistent solution

$(\phi_o/r) \exp [(1 - r)/\lambda_D]$, where ϕ_o is the dimensionless sphere potential (in units of sphere radius), and λ_D is the Debye number (Debye length divided by sphere radius), one may use the "Turning-Point" formulation of Parker[7] to show that the current enhancement is given by

$$j/j_o = \text{least value of } \left[r^2 E_o + r|\phi_o| \exp((1 - r)/\lambda_D)\right]$$

$$= \text{least value of } \left[r^2 + 4 \times 10^5 \, r \exp(100 - 100r)\right]$$

$$= 1.39 \text{ (absorption radius = 1.16803)} .$$

[Here we have assumed monoenergetic attracted ions of thermal energy $E_o = 1$ (energy = kT).] Hence the current enhancement (1.39) is negligible compared with the rigorous value (490). The linearized-space-charge model is therefore grossly in error for conditions of interest in this paper. Thus, the 2-D and 3-D extensions of this linear model (for example, Parker[11] in an E-region rocket

problem, and by Katz et al[13] in their NASCAP-LEO model), although frequently used, are of limited interest and are confined to qualitative calculations. NASCAP/LEO, however, uses it as the limit of a more sophisticated analytic expression. [See Eq. (16)].

The structure of the remainder of this paper is as follows:

Section 2: Description of computer model.

Section 3: Discussion of 3-D problems.

Section 4: Studies of ion focusing and probe within a sheath.

Section 5: Studies of plasma flow effects.

Section 6: Surface current distributions associated with ion focusing.

Section 7: Concluding remarks.

Appendix A: Derivation of shape functions used for the tetrahedral finite elements.

2. COMPUTER MODEL

The CLPH3D (Child-Langmuir-Parker-Holeman) code is computationally inexpensive compared to other methods. It is based on assumptions similar to those of the familiar Child-Langmuir diode models in one-space-dimensional symmetry[10, 14] (planar, cylindrical, or spherical). Our 3-D generalization assumes that (a) there is a sharp sheath boundary (surface in 3-D) on which the potential is zero, that (b) the field is zero at all points on this boundary, and that (c) the attracted particles are accelerated inward (while creating space charge) toward the body surface starting with low or negligible energy. In the classical Child-Langmuir problems with symmetry, the shape of the sheath boundary is known, and the charge density can be represented by a simple analytical function of the local potential. As opposed to this, in a 3-D problem, the shape of the sheath boundary is unknown a priori, and in addition, the space charge density depends generally on the distribution of potential in space and not simply on the local potential. This implies that numerical procedures would be required, to determine (1) the space-charge density from analysis of particle trajectories, and (2) the geometry of the sheath boundary itself.

---

13. Katz, I., Mandell, M.J., Schnuelle, G.W., Parks, D.E., and Steen, P.G. (1980) Plasma Collection by High-Voltage Spacecraft at Low Earth Orbit, Paper AIAA-80-0042, AIAA 18th Aerospace Sciences Meeting.

14. Langmuir, I., and Blodgett, K.B. (1923) Currents limited by space charge between coaxial cylinders, Phys. Rev. 22:347-56.

The CLPH3D model accomplishes these tasks, using the Outside-In approach.[15, 16] The geometry of the sheath surface is obtained self-consistently as part of the solution, subject to the condition that the electric field vanish at all points on the surface. The sharp-sheath-boundary assumption is of course an approximation (which appears to be justifiable a priori because the panel voltages of interest are large compared with kT/e and the body dimensions are large compared with the plasma Debye length, and because reasonably good agreement was obtained with the rigorous bench-mark calculation discussion in Section 1).

The reason for setting up this type of grid, whose accuracy in 3-D would be comparable to that of the well-known Child-Langmuir solutions in 1-D, is that of computational economy, which is difficult to achieve for space charge problems in 3-D. Since the sheath boundary is part of the grid, one is always sure to have a high density of grid points where they are most important, namely, where the variations are strongest, even though only relatively few grid points are required. To obtain comparable accuracy with a fixed grid would require orders-of-magnitude more points and computer time. The fundamental grid or mesh skeletal structure for CLPH3D consists of a "base" representing the body, with lines radiating from it, much like pins protruding from a pincushion. The sheath surface is defined by the outer nodes (end points) of the lines, like the fabric of an umbrella stretched over the end points of the ribs. The interior nodes are distributed proportionally along the lines. The nodes are interconnected by straight lines, forming grid cells. Since the grid cells consist of deformable finite elements (tetrahedra here), the base can be deformed into various body shapes with some degree of arbitrariness.

Previous computer models have been developed by Parker using fixed grids in axisymmetric r-z geometry,[11, 16-25] and fixed grids in 3-D Cartesian geometry using the PANEL model.[6, 26, 27] For large high-voltage structures in dense plasmas, these are rigorous models, but are computationally relatively expensive to run. The new CLPH3D model may prove sufficiently generalizable (by adding quasineutral and transition regions) and efficient to eventually replace PANEL as a generalized rigorous 3-D model. A quasineutral approach for 3-D problems with flows suitable for adaptation was developed by Parker.[18]

Before the tetrahedral finite elements are considered, the method of obtaining the sheath shape is discussed.

Because of the large number of references cited above, they will not be listed here. See References, page 384.

2.1 2-D Child-Langmuir Sheath of Conducting Panel (The "Dynamic Pincushion" Mesh)

Figure 2 shows a 2-D cross-sectional view of the sheath of a long conducting panel, 1.0 m wide, with 200 V on the panel and plasma parameters $n_o = 10^6/cm^3$ and $kT/e = 0.4$ eV. The panel is represented by the heavy horizontal line. It is surrounded by the sheath, the volume of which is divided into a mesh of triangularized "boxes" or finite elements. A "finite-element" variational method (described below) is used to approximate the Poisson equation by discrete elements.[28] The mesh is a flexible "dynamic pincushion mesh" with sliding grid points. Its structure is formed by lines radiating from the panel surface (and from one or more points in the same plane) as shown. The points slide along the lines, which terminate on the sheath boundary. The entire mesh is defined by and contained within the sheath. The outer bounding surface of the grid represents the sheath "edge," formed by connecting the ends of the lines with straight-line segments. The bounding surface can expand or contract, acquiring whatever shape is required, to fulfill the boundary conditions of zero potential and zero gradient at all points of the boundary, for the given body shape and body surface potential distribution. The finite elements, which expand and contract, changing their shapes and density to accommodate changes in the sheath boundary, are used to achieve the flexibility required to accommodate an arbitrarily-curved body shape and sheath shape.

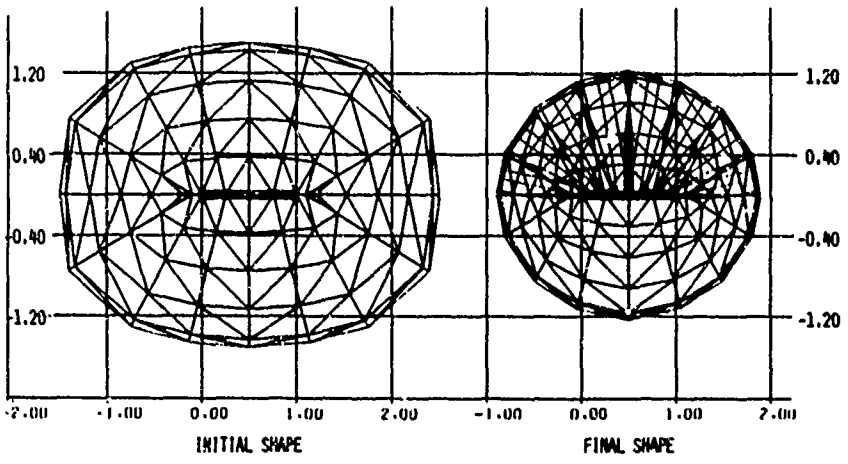

Figure 2. Long Bare Conducting Panel Child-Langmuir Sheath ("Dynamic Pinchusion" Grid)

28. Zienkiewicz, O.C. (1971) The Finite Element Method in Engineering Science, McGraw-Hill.

In three dimensions the mesh consists of tetrahedral boxes. The sheath boundary and body surfaces are flexible triangular areas. Three-dimensional results will be described later.

Trajectories are launched from many points along the sheath boundary, moving initially normal to this boundary (no-flow case), and space charge density is calculated within the elements by summing the contributions of the trajectories as they pass through the elements. Within any given element, the contribution of any one trajectory is proportional to (1) the time spent by that trajectory within the element, and to (2) the current density associated with the launch position of the trajectory. (Note that the current density can be nonuniform, for example, due to a flow velocity, and that emission trajectories can also be launched from the body surface.) This method is indifferent to whether trajectories cross one another, and in this sense it is superior to the simpler method of "flux tubes," in which the density contribution is inversely proportional to the flux tube area and hence becomes infinite when the defining trajectories cross.

The method requires iteration to determine the sheath shape. One begins with an initial guess and the boundary is moved in successive steps until convergence is achieved. Figure 2 shows both the initial assumed sheath shape (left-hand side of figure) and the final converged shape (right-hand side of figure). The dimensions shown are in units of the panel width. (Here the unit of length is 1 m. Later, we will discuss bordered as well as non-bordered panels. In those cases the unit length will be the panel width including the border, if any.) The final sheath thickness at the center is about 1.2 m, approximately equal to the value given by the planar Child-Langmuir formula. Note that the converged sheath shape is more nearly circular than the initial guess. Some ion trajectories are shown in the upper half of the converged sheath. No strong focusing effects are predicted for the bare panel. (A relatively coarse grid has been used; in some subsequent figures to be shown, finer grids were used.) However, strong focusing effects will be shown to occur when there is a nonconducting border. These are important because the power loss would be non-uniform over an array surface, and there would be "hot spots" (burning out solar cells) where the focusing is more intense. Also, the hot spots would move to different locations as the direction or velocity of plasma flow changes or as foreign objects (such as probes or stray "trash" insulation) are introduced into the sheath volume (see p. 366).

If the plasma has an isotropic velocity distribution, one may calculate the current collected simply from the sheath area depicted in the figure. In the 2-D view of Figure 2, one may measure the sheath perimeter and the panel length with a ruler, using any scale. Dividing the (upper) perimeter by the panel length gives the perimeter in meters (4.0 m in Figure 2). Multiplying this by the plasma

ion thermal current density in A/m^2 gives the current collected (per unit length in the direction perpendicular to the page) in A/m.

When there is a plasma flow (Maxwellian with drift) characterized by a Mach vector of magnitude M, and if M_1 and M_2 denote the components of the Mach vector perpendicular and parallel, respectively, to the sheath surface at a given position on this surface, then one may define factors F_1 and F_2 at this position, namely:

$$F_1 = \exp\left(-M_1^2\right) + \pi^{1/2} M_1(1 + \operatorname{erf} M_1)$$

$$F_2 = \pi^{1/2} M_2(1 + \operatorname{erf} M_1) \quad .$$

An "average" trajectory launched from this position may be assigned perpendicular and parallel components of velocity, given by the random thermal velocity multiplied, respectively, by F_1 and F_2. The current density associated with this trajectory is the random thermal value multiplied by F_1. Thus, the current collected may be calculated by integrating the weighted sheath area, where the weight factor is F_1, before multiplying by the ion random thermal current density. It can be shown (derivation not included here) that functions F_1 and F_2 may be obtained by integrating analytically over a Maxwellian velocity distribution with drift, where the drift velocity components are perpendicular and parallel to the surface of interest. The integration is straightforward.

2.2 Other Shapes

The mesh can deform to accommodate other shapes. For example, the flat panel of Figure 2 could be deformed to become a long circular cylinder. The cylinder and its sheath would be defined by a number of straight-line segments. A corresponding sphere in 3-D would be defined by a surface consisting of triangles.

2.3 Variational Method for Poisson Equation (Zienkiewicz[28])

Consider the Poisson equation:

$$\frac{\partial^2\phi}{\partial x^2} + \frac{\partial^2\phi}{\partial y^2} + \frac{\partial^2\phi}{\partial z^2} = -g \qquad (1)$$

with boundary conditions $\phi = \phi_D$ on R_D (Dirichlet).

$$\text{Let } J_1 = \iiint (1/2)(\Delta\phi)^2 \, dx\, dy\, dz \text{ (volume integral)} \quad . \tag{2}$$

$$\text{Let } J_2 = \iiint g\phi \, dx\, dy\, dz \text{ (volume integral)} \quad . \tag{3}$$

According to the variational method, the functional to be minimized is:

$$J = J_1 - J_2 \quad . \tag{4}$$

The variational principle may be written:

$$\delta J = \delta J_1 - \delta J_2 = 0 \quad , \tag{5}$$

where

$$\delta J_1 - \delta J_2 = -\iiint (\nabla^2\phi + g)\, \delta\phi \, dx\, dy\, dz \text{ over the volume} \tag{6}$$

where the $\delta\phi$ variations are arbitrary, so that one recovers the original boundary-value problem when the coefficients of $\delta\phi$ are set to zero.

2.4 Construction of J Using Tetrahedral Finite Elements

Consider one element, and relative nodes 1, 2, 3, 4. Let L_1, L_2, L_3, L_4 denote the "shape functions" (see Appendix A).

Let $\phi = \phi_1 L_1(x, y, z) + \phi_2 L_2(x, y, z) + \phi_3 L_3(x, y, z) + \phi_4 L_4(x, y, z)$.

Now construct J_1 and J_2 as functions of ϕ_1, ϕ_2, ϕ_3, ϕ_4. Then

$$J_1 = \frac{1}{2} \sum_i^4 \sum_j^4 \phi_i \phi_j \iiint \left[\left(\frac{\partial L_i}{\partial x}\right)\left(\frac{\partial L_j}{\partial x}\right) + \left(\frac{\partial L_i}{\partial y}\right)\left(\frac{\partial L_j}{\partial y}\right) + \left(\frac{\partial L_i}{\partial z}\right)\left(\frac{\partial L_j}{\partial z}\right)\right] dx\, dy\, dz$$

$$= \frac{1}{2} \sum_{i}^{4} \sum_{j}^{4} \phi_i (K_1)_{ij} \phi_j = \frac{1}{2} \underset{\sim}{\phi}^T \underset{\sim}{K}_1 \underset{\sim}{\phi} \quad . \tag{7}$$

Where the ($\sim$) symbol denotes a vector or a matrix, and the superscript "T" denotes the transpose.

For a linear tetrahedron, L = const + ax + by + cz, so that

$$\partial L/\partial x = a \quad , \quad \partial L/\partial y = b \quad , \quad \partial L/\partial z = c \quad .$$

Thus,

$$(K_1)_{ij} = (a_i a_j + b_i b_j + c_i c_j)/36V \quad , \tag{8}$$

where V is the volume of the element.

Next, if g is constant over the element,

$$J_2 = g \sum_{j=1}^{4} \phi_j \iiint L_j \, dx \, dy \, dz \tag{9}$$

$$= \underset{\sim}{\phi}^T \underset{\sim}{Q}_2 \quad , \tag{9}$$

where

$$(Q_2)_j = g \iiint L_j \, dx \, dy \, dz = gV/4 = q/4 \tag{10}$$

where q is the total charge. If g is defined at the nodes, however,

$$J_2 = \sum_{i}^{4} \sum_{j}^{4} \phi_i g_j \iiint L_i L_j \, dx \, dy \, dz \tag{11}$$

$$= \underset{\sim}{\phi}^T \underset{\sim}{G} \underset{\sim}{g} \quad , \tag{11}$$

where $\underset{\sim}{G}$ is the matrix defined by

$$(G)_{ij} = \iiint L_i L_j \, dx \, dy \, dz = \begin{cases} (2/20)V & \text{if } i = j \\ (1/20)V & \text{if } i \neq j \end{cases} . \tag{12}$$

Hence,

$$(Q_2)_j = \sum_{i=1}^{4} g_i(1 + \delta_{ij})/20 \quad ; \quad (\delta_{ij} = \text{Kronecker delta}) \tag{13}$$

Collecting all terms, the functional to be minimized is linear/quadratic in the ϕ_j:

$$J = \frac{1}{2} \underset{\sim}{\phi}^T \underset{\sim}{K}_1 \underset{\sim}{\phi} - \underset{\sim}{\phi}^T \underset{\sim}{Q}_2 \quad . \tag{14}$$

Hence, setting to zero the derivatives with respect to the components of $\underset{\sim}{\phi}$ (namely, ϕ_l) results in the desired matrix equation (= system of linear equations) representing the Poisson equation plus boundary conditions:

$$\underset{\sim}{K}_1 \underset{\sim}{\phi} = \underset{\sim}{Q}_2 \quad . \tag{1}$$

With this formulation, the gradient is defined to be zero at all surfaces at which the potentials are not defined. Thus, symmetry planes are automatically taken into account. Solution of the linear system [Eqs. (15)] yields the values of the potentials at the nodes.

3. THREE-DIMENSIONAL PROBLEMS

3.1 Pincushion Grid in Three Dimensions

The fundamental pincushion grid in 3-D consists of an inner "block", surrounded by a family of concentric shells. The inner block is topologically similar to one of the shells. Lines radiate from it like pins protruding from a pincushion. The sheath surface is defined by the positions of the outer nodes (at the end-points of the lines), similar to the way in which an umbrella fabric is stretched over the end points of its skeletal ribs. The interior nodes are distributed with proportional spacings along the lines. The nodes are interconnected, forming grid cells. Since the grid cells consist of deformable finite elements (cuboids divided into tetrahedra), the base can be deformed into various 3-D body shapes defined by triangles. The 2-D configuration shown in Figure 2 is a special case. The 3-D

problem uses three planes of symmetry and one octant. This is not an essential restriction but is governed by computer storage and time considerations. It is straightforward to remove two of the symmetry planes and to deform the base into a more complex structure, for example, the Shuttle-Orbiter. On the x-z or y-z planes, the grid is essentially identical to (one-half of) that shown in Figure 2.

Since the lines are "tracks" along which the nodes slide, the outer-surface (or sheath) nodes slide in or out to produce the appropriate sheath shape.

3.2 Bare Conducting 3-D Square Panel (36 in. = 0.914 m = 1 Unit)

Figures 3 through 8 show, in three different views, the sheath-shape solutions obtained for a 36 in. flat square bare conducting panel, biased to 200 V negative with respect to a plasma with the parameters $n_o = 10^6/cm^3$ and $kT/e = 0.4$ eV. The 36 in. size is chosen in accord with sizes used in experiments by Konradi et al.[29]

A rather coarse mesh is used here. The base (panel) is defined by 25 nodes arranged in a 5 × 5 square array, in the x-y plane. It is centered on the origin, and extends from -0.5 to +0.5 unit, in both the x and y directions. (The unit of length is the actual panel width, 0.914 m, or 36 in.). Since we are treating one quarter of the panel by symmetry, the computational panel extends from the origin to +0.5 unit in the x and y directions, with the corner at x = y = 0.5. For computational purposes the panel is assigned a small thickness, 0.02 unit (the magnitude of the small thickness is not important). Although the figures are not all drawn to the same scale, the relative dimensions may be inferred by referring them to the panel width.

Solutions were obtained, both with "true" space charge (using trajectories to calculate space charge rigorously, shown in Figures 3, 5, and 7) and "false" space charge (using an assumed analytic function, shown in Figures 4, 6, and 8).

Figures 3, 5, and 7 show three different views of the sheath shape and solution mesh, where the solutions were obtained using the "true" space charge (trajectory-controlled). In this set of figures (bare panel, as opposed to the bordered panel treated next) the sheath is roughly an oblate spheroid, with semi-major axis 1.03 units, and semi-minor axis (height) 0.73 units. Figure 7 shows clearly the 34 nodes on the sheath surface, at the ends of the 34 lines radiating from the panel surface. The sheath area shown is 1.39 units squared (= 5.6 times the panel area shown). The total sheath area is 8 times that shown, or 11.12 units squared. The total current collected is proportional to the sheath area, since essentially all trajectories launched from the sheath surface are

---

29. Konradi, A., McIntyre, B., and Potter, A.E. (1983) Experimental studies of scaling laws for plasma collection at high voltages, J. Spacecraft and Rockets (in press).

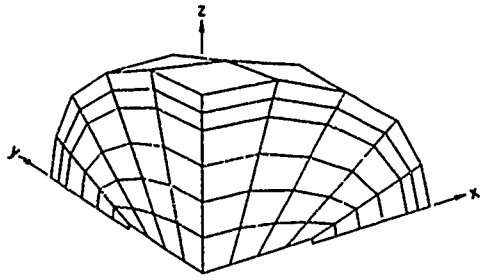

Figure 3. Bare Conducting Square Panel (36 in. × 36 in., View A). True space charge (1 unit = 36 in.)

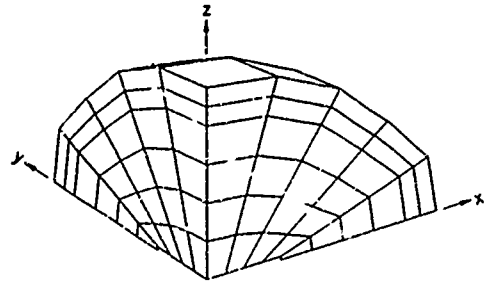

Figure 4. Bare Conducting Square Panel (36 in. × 36 in., View A). False space charge (1 unit = 36 in.)

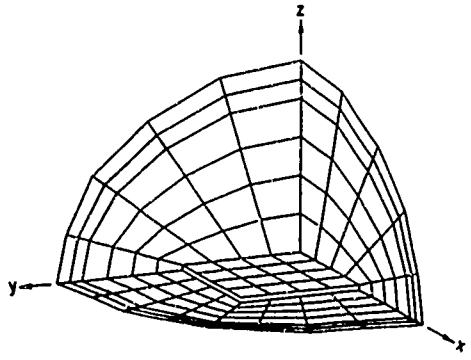

Figure 5. Bare Conducting Square Panel (36 in. × 36 in., View B). True space charge (1 unit = 36 in.)

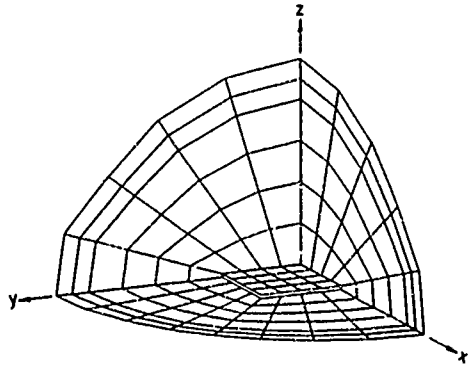

Figure 6. Bare Conducting Square Panel (36 in. × 36 in., View B). False space charge (1 unit = 36 in.)

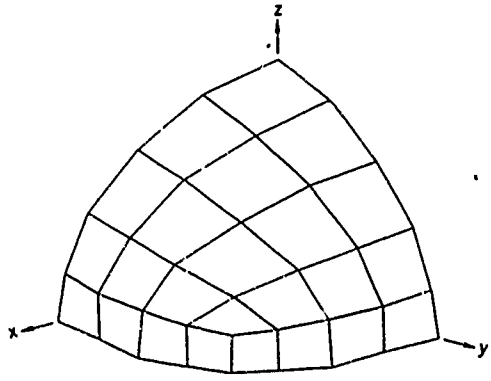

Figure 7. Bare Conducting Square Panel (36 in. x 36 in., View C). True space charge (1 unit = 36 in.)

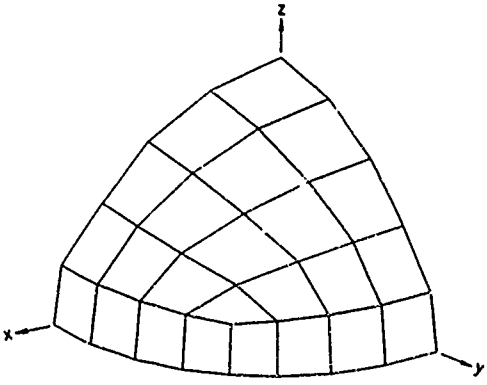

Figure 8. Bare Conducting Square Panel (36 in. × 36 in., View C). False space charge (1 unit = 36 in.)

collected. Assuming the value 0.144 mA/m^2 for ion current, given by Konradi et al[29] for their experiment, yields an estimated current of 1.35 mA.

Figures 4, 6, and 8 show a set of views corresponding, respectively, to Figures 3, 5, and 7. Here, however, the solutions were obtained using the "false" space charge given by the analytic assumed formula

$$\frac{\phi}{(1 + 2\pi^{1/2}\,\phi^{3/2})\,\lambda_D^2} \tag{16}$$

for dimensionless space charge density, where ϕ is the dimensionless local potential and λ_D is the Debye number. This formula reduces to the purely linear form ϕ/λ_D^2 in the small ϕ limit [Eq. (17)], and to the Child-Langmuir space-charge-limited-current form $(2\,\pi^{1/2}\,\phi^{3/2}\,\lambda_D^2)^{-1}$ in the large ϕ limit. This assumption, and variations thereof, have been used in the NASCAP/LEO code.[13,30] The sheath calculated using this formula has semi-major and semi-minor axes of 1.8 and 1.6 units, respectively, and a total sheath area of 37.7 units squared. The total current collected is estimated to be 4.5 mA. Hence, the false-space-charge calculation overestimates the sheath area and current collection by a factor of about 3, compared with CLPH3D.

We are comparing here two computational approaches to the space charge problem that do not agree with each other. One is the "true" space charge model that requires numerically computed trajectories for evaluating space charge. It is more rigorous than the "false" space charge model. The latter is simpler and more economical because no trajectories are computed, but is also necessarily less accurate. Equation (16) on which it is based is a more elaborate assumption than the still simpler linear model (p. 358), but appears also to be considerably in error. This error is related to the sheath size alone here. It would be still worse in modeling flow and focusing problems. However, such a simple model would be desirable for computational economy in large and extremely complex codes such as NASCAP/LEO. A possible suggestion is that Eq. (16) or similar forms presently used by NASCAP/LEO be improved by suitable fudge factors obtained through comparisons with "true" space charge calculations such as CLPH3D.

---

30. Mandell, M.J., Katz, I., Steen, P.G., and Schnuelle, G.W. (1980) The effect of solar array voltage patterns on plasma power losses, IEEE Trans. Nucl. Sci. NS-27.

Note: The true-space-charge sheath is insensitive to the precise value of the small potential assigned to the sheath boundary for numerical purposes. In contrast to this, however, the false-space-charge [Eq. (16)] sheath size is quite sensitive to the assumed value of sheath boundary potential. For the false-space-charge calculations reported here, the sheath boundary potential was assigned the value 0.16 eV (=0.4 kT/e of the assumed plasma).

3.3 Bordered Conducting 3-D Square Panel (48 in. = 1.22 m = 1 Unit)

Figures 9 through 14 show the sheath shape solutions for a 48-in. square panel, with 6-in. nonconducting borders, biased to 200 V negative with respect to the same plasma. The 48-in. size is used in the experiments of McCoy et al[1, 2, 3] with a bordered panel. (It should be noted that the "bordered" panel used by McCoy et al is actually a 36-in. conducting panel surrounded by a 6-in. nonconducting border, and may nominally be considered a 36-in. panel to be compared with the 36-in. "bare" panel. However, for the purposes of the computer model it is more convenient to consider it a 48-in. panel. Hence the "unit" will be 48 in.) In contrast to the bare panel, strong ion focusing occurs because of the transverse fields near the panel surface, in the vicinity of the border between the conducting (200 V) and nonconducting (0 V) surfaces. (See, for example, Figure 17 and subsequent figures for trajectories and more details concerning this important effect, which is evident in the experiments of McCoy et al.)

The mesh used is similar to that of Figures 3 through 8, except that the nodes on the panel are shifted slightly to accommodate the jump in potential at the conducting/nonconducting border. The symmetric computational panel again extends from the origin to x = +0.5 and y = +0.5 unit, and has the same small thickness.

Figures 9, 11, and 13 show the sheath shape as computed with true space charge. The sheath is smaller than in the bare-panel case (its height is only 0.5 unit, vs 0.73 unit in the bare-panel case (see Figures 15 and 16, and is "pinched in" at the "equator" region near the plane of the panel. This "pinch" brings its side surface in so strongly that it contacts the panel border at all of its x-y plane points, as shown in Figure 16. Figure 13 shows clearly how the sheath has come in over the border at the corner. The sheath area shown is 0.59 unit squared, or 2.4 times the panel area shown (0.25 unit squared).

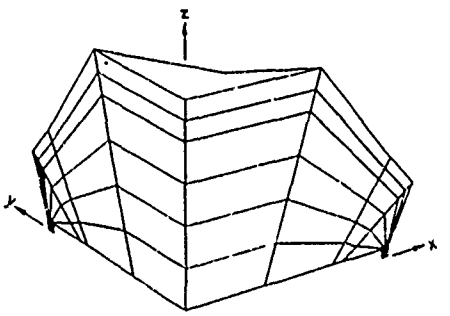

Figure 9. Square Panel (48 in. X 48 in., With 6 in. Nonconducting Border, View A). True space charge (1 unit = 48 in.)

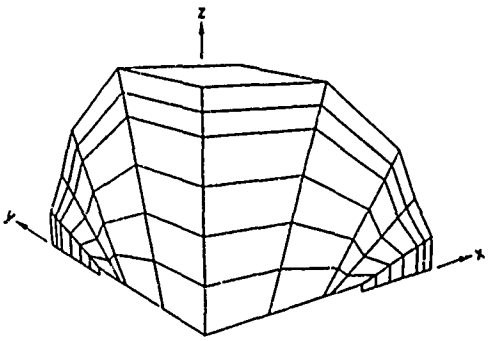

Figure 10. Square Panel (48 in. X 48 in., With 6 in. Nonconducting Border, View A). False space charge (1 unit = 48 in.)

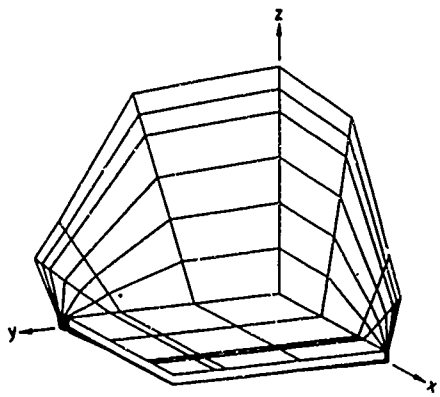

Figure 11. Square Panel (48 in. × 48 in., With 6 in. Nonconducting Border, View B). True space charge (1 unit = 48 in.)

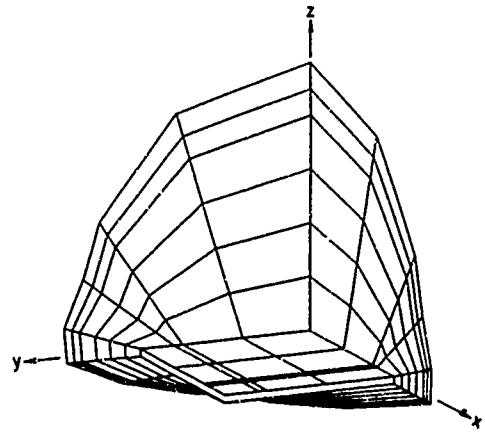

Figure 12. Square Panel (48 in. × 48 in., With 6 in. Nonconducting Border, View B). False space charge (1 unit = 48 in.)

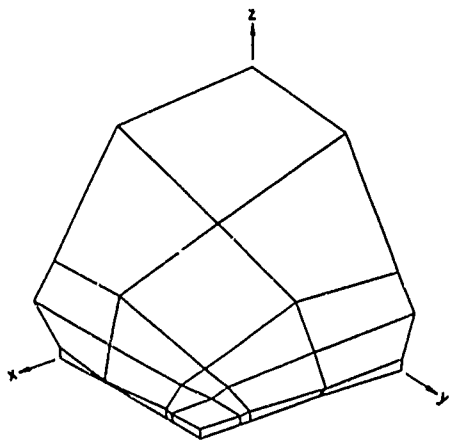

Figure 13. Square Panel (48 in. × 48 in., With 6 in. Nonconducting Border, View C). True space charge (1 unit = 48 in.)

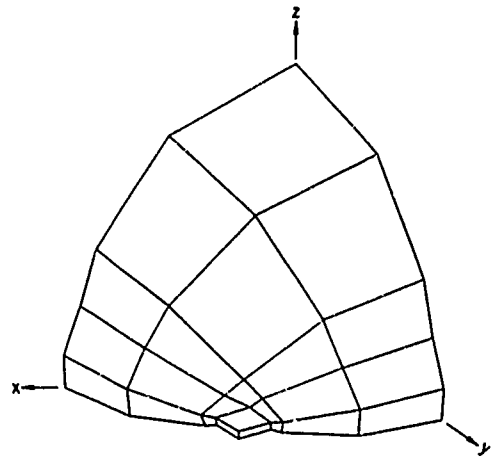

Figure 14. Square Panel (48 in. × 48 in., With 6 in. Nonconducting Border, View C). False space charge (1 unit = 48 in.)

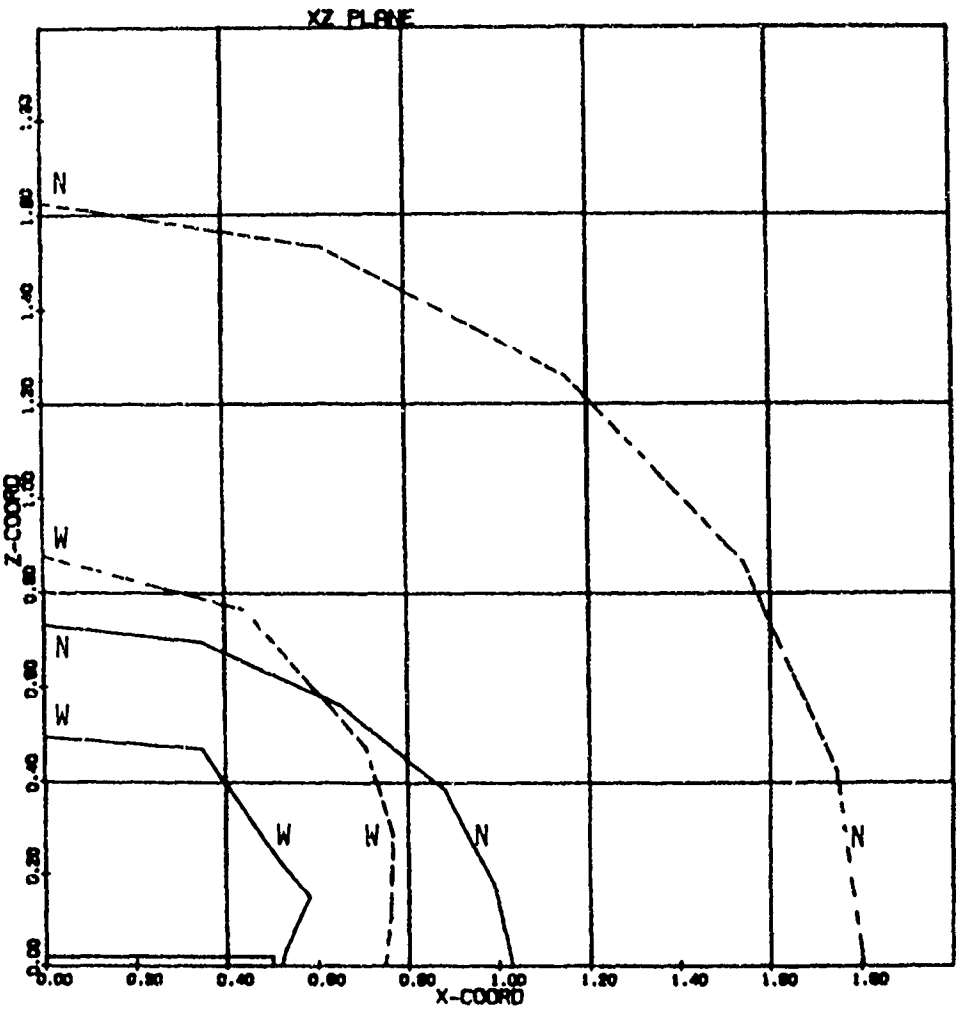

Figure 15. Summary of 200-V Square Panel Sheath Contours (x-z Plane). N = no border (bare panel). W = with 6 in. border. ——— = true space charge. ----- = false space charge. (10^6/cm^3, 0.4 eV plasma; all dimensions in units of panel width) (1 unit = 48 in.)

For comparison, Figures 10, 12, and 14 show the results for false space charge, corresponding, respectively, to Figures 9, 11, and 13 for true space charge. By comparison, the false-space-charge sheath is larger (see Figures 15 and 16), with height about 0.8 unit. Its radius at the equator is also about 0.8 unit, so that its x-z cross-section is approximately circular. In the x-z and y-z planes, it remains away from the border. However, as Figure 14 shows, the false-space-charge sheath is pulled in over the corner like the true-space-charge sheath (Figure 13). The false-space-charge sheath area shown is 1.08 units

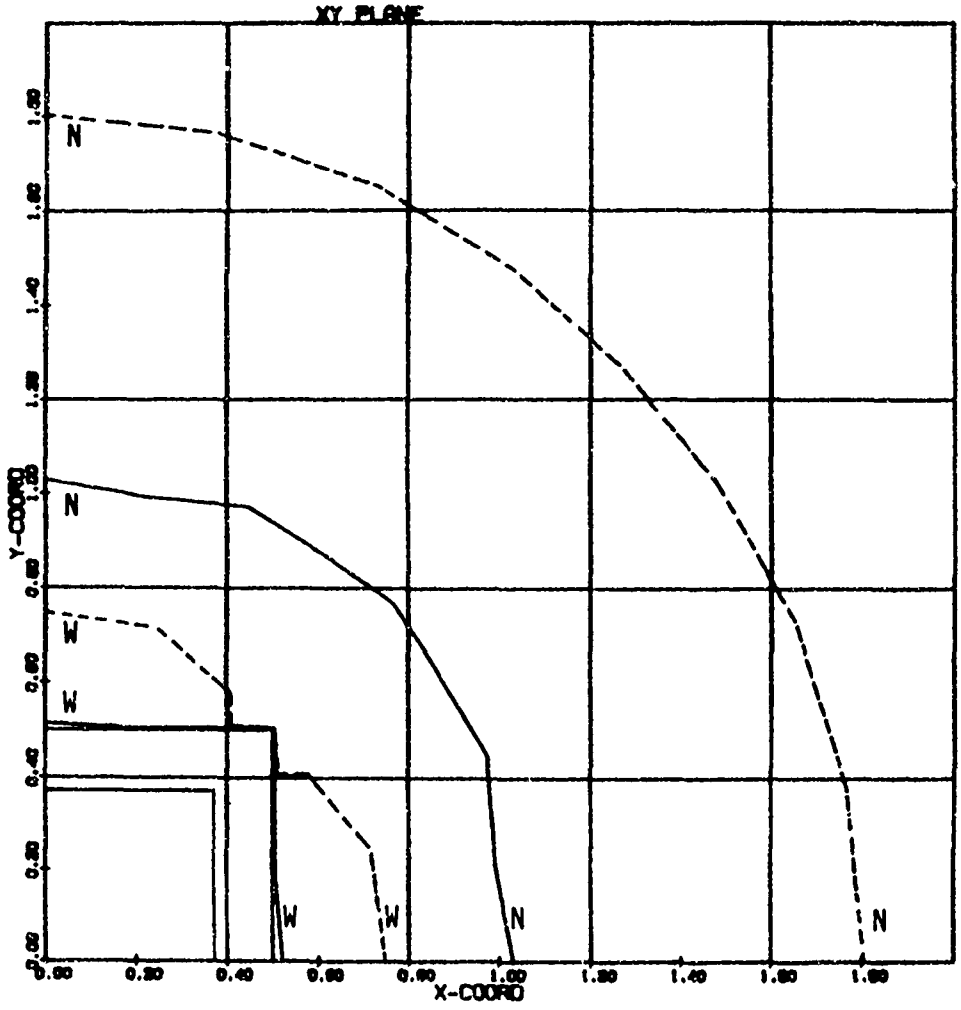

Figure 16. Summary of 200-V Square Panel Sheath Contours (x-y Plane). N = no border (bare panel). W = with 6 in. border. ——— = true space charge. ----- = false space charge. (10^6/cm^3, 0.4 eV plasma; all dimensions in units of panel width) (1 unit = 48 in.)

squared, or 4.3 times the panel area shown (compared with 2.3 using true space charge). (The "panel area shown" here denotes the conducting area plus the nonconducting bor ler.) Hence the false-space-charge model would overestimate the bordered-panel current collection by a factor of about 2, compared with CLPH-3D.

3.4 Summaries of Sheath Contours for Figures 3 Through 8 and 9 Through 14

Figure 15 summarizes the sheath contours discussed above, in the x-z vertical plane. The curves labelled N are for the bare panel ("no border"), and those labelled W are for the bordered panel ("with border"). The true and false-space-charge results are denoted by solid and dashed curves, respectively. The false-space-charge contours tend to be further away from the panel than their true-space-charge counterparts. The "pinched-in-at-the-waist" behavior of the true-space-charge sheath is evident for the bordered panel.

Figure 16 summarizes the contours in the x-y plane (plane of the panel). The "pinching-in" at the corner is evident for both true and false space charge, as is the tendency for the true-space-charge sheath to stay close to the border at all of its x-y plane points.

3.5 Focusing of Ion Trajectories on Bordered Square Panel in 3-D (1 Unit = 48 in.)

Figure 17 and 18 show some ion focusing effects due to the zero-volt border of the bordered panel. The panel impact points ("footprints") of approximately 2000 trajectories launched from the true-space-charge sheath surface (Figures 9, 11, and 13), are shown in Figure 17. The footprint pattern is "horn-shaped," with the "horn" extending toward the corner. Such a horn-shaped pattern is consistent with experiments.[1, 2, 3] Away from the corner, the currents are confined to an approximately square area of half-width 0.33 unit. By contrast, Figure 18a shows the ion focusing for trajectories launched from the false-space-charge sheath surface (Figures 10, 12, and 14). Here the pattern is narrower; away from the corner the currents are confined to an approximately square area of half-width 0.25 unit. This narrower pattern is associated with the large sheath area generated by the false space charge.

A similar narrow pattern (0.16 unit half-width, as shown in Figure 18b) is generated if the false-space-charge dimensionless density is assumed to be given by the "linearized space charge" term

$$\phi/\lambda_D^2 \quad , \tag{17}$$

which is the small-potential limit of Eq. (16). The Poisson equation then becomes a linear "Helmholtz" equation (appellation first applied by Parker[11] with the realization that the Helmholtz equation is actually a wave equation) where the Debye number plays the role of imaginary wave number. A parameter "HELM" is used in this case in place of the actual Debye number (HELM = 0.5 for Figure 18b). The relation between HELM and the true Debye number is unknown,

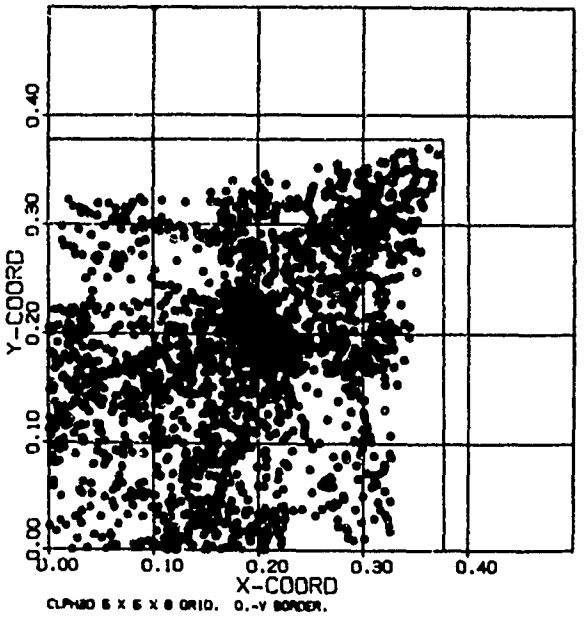

Figure 17. Ion Focusing Impact Pattern ("Footprints") on Bordered Square 200-V Panel. True space charge (1 unit = 48 in.)

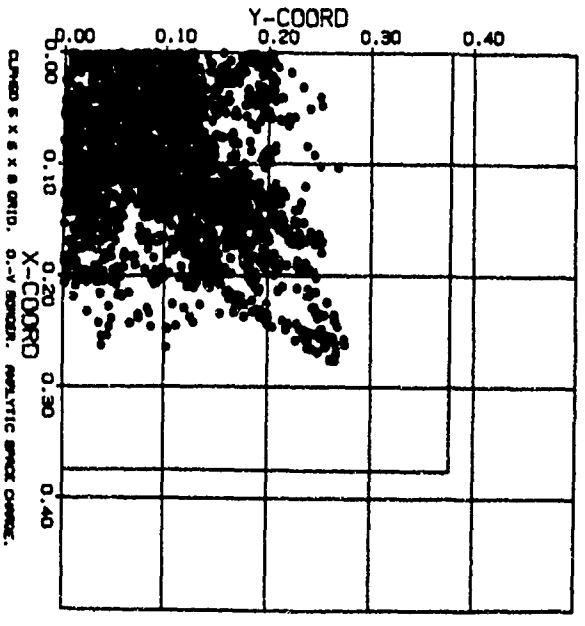

Figure 18a. Ion Focusing Impact Pattern ("Footprints") on Bordered Square 200-V Panel. False space charge (1 unit = 48 in.)

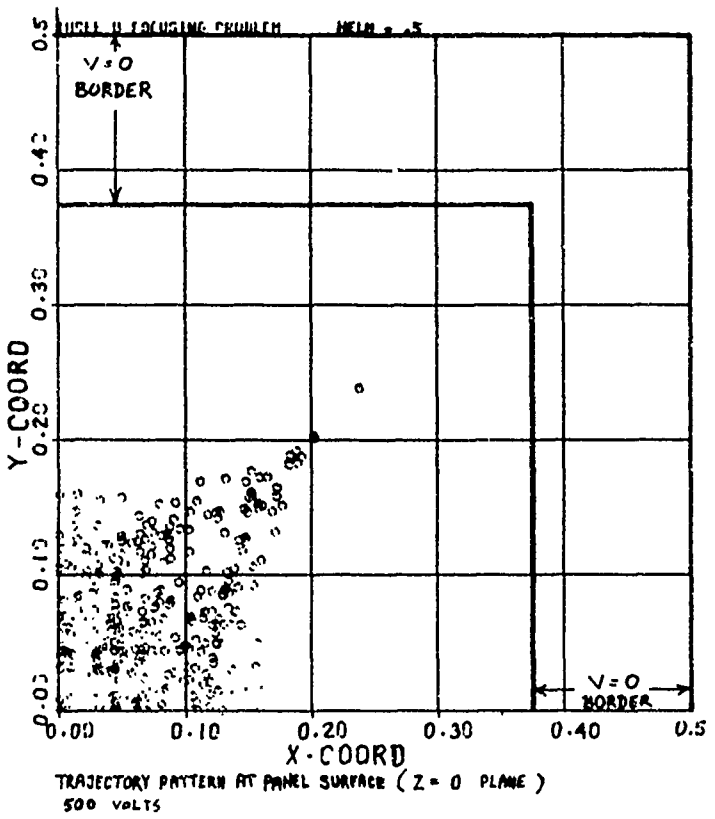

Figure 18b. Ion Focusing Impact Pattern ("Footprints") on Bordered Square 500-V Panel. False linear space charge (HELM = 0.5) (1 unit = 48 in.)

although attempts have been made theoretically to establish this relation.[7, 11] In spherical symmetry, the linear "Helmholtz" equation yields the familiar "Debye potential" function. (Figure 18b was obtained by launching about 500 trajectories from a plane five units above the panel plane, rather than from a self-consistent sheath surface.)

Parker[5] also applied Eq. (17) to a long panel (1 m × 10 m) in accord with the McCoy et al experiments, and predicted a thin focusing strip along the panel, with horns near the end corners. Incidentally, the value used for HELM (0.5) was chosen because it gave an optimum focusing effect (Ref. 26: HELM results presented but not included in proceedings).

3.6 Aircraft in 3-D

As a conceivable application of the pincushion mesh idea to more complex 3-D problems, Figure 19 shows a computer model representation of a large aircraft (C-130) used in electromagnetic scattering studies. This geometric representation of the surface is achieved by a collection of quadrilateral areas or "patches," and is used in obtaining solutions of Laplace's equation. Assuming that one wished, for example, to model the sheath around the Shuttle-Orbiter, a geometric representation such as that of Figure 19 could serve as the base of our "dynamic pincushion" mesh, with lines radiating from the nodes on the Shuttle-Orbiter surface, where the nodes are those defining the corners of the quadrilateral areas. Subsequent tetrahedralization of the mesh converts the surface quadrilaterals into surface triangles.

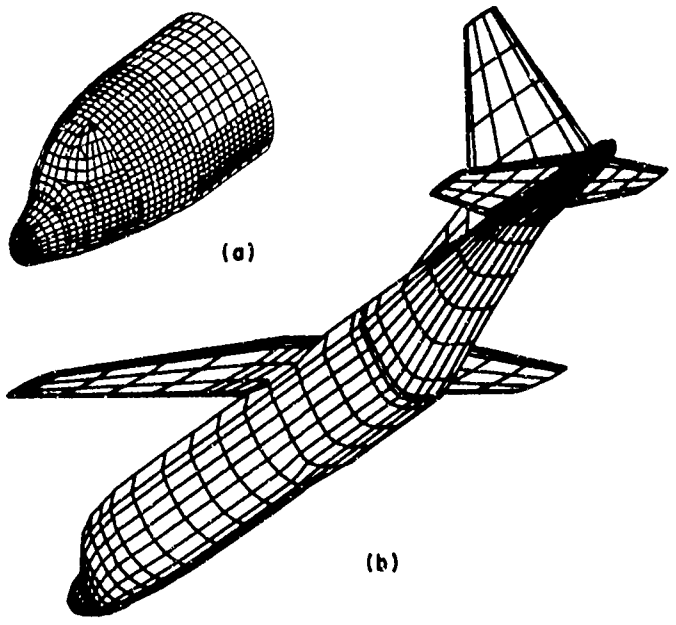

Figure 19. Computer Model Constructed of Quadrilateral Patches. (a) Fuselage front section in 3-D. (b) Fuselage in 3-D

4. ION-FOCUSING AND PROBE-WITHIN-SHEATH STUDIES

4.1 Ion Focusing on Long High-Voltage Panels With Nonconducting Borders (in 2 D) (1 Unit = 48 in.)

Ion focusing patterns observed to occur in experiments[1, 2, 3] can be attributed to the fact that there are nonconducting borders on the edges of the panel. These borders tend to equilibrate to the potential of the plasma and thus create strong transverse electric field components near the panel surface in the vicinity of the border between the conducting and nonconducting surfaces. Figure 20 shows a series of three solutions (2-D cross-sectional views) obtained for a long panel, for three different panel voltages, 400, 1200, and 2000 V. Here, the panel width is 48 in. (or 1.22 m), with 6 in. insulated borders, and with the same plasma parameters, $n_o = 10^6/cm^3$ and kT = 0.4 eV. Each problem is symmetric, with trajectories shown in the upper half, and the grid used shown in the lower half. The sheath clearly grows in size with increasing voltage. At 1200 V, the sheath thickness at the panel center is about 1.3 units, or about 1.6 m.

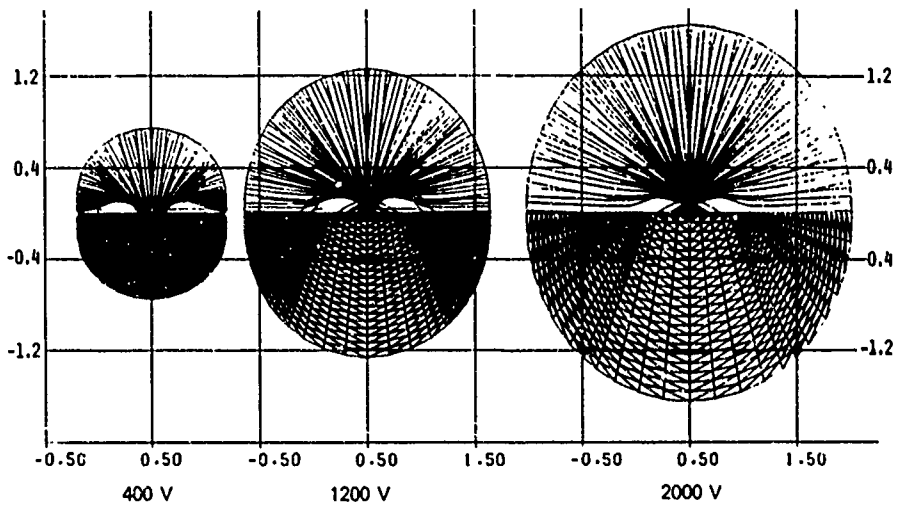

Figure 20. Long Bordered Panel Sheath Shapes (48 in. Width With 6 in. Nonconducting Border). Three Voltages: 400, 1200, 2000 V ($10^6/cm^3$, 0.4 eV plasma). Upper half = trajectories. Lower half = grid (1 unit = 48 in.)

The "focal voltage" is about 1200 V (center of figure). At this voltage the focus occurs on the panel. At lower voltages (for example, 400 V at the left-hand side of figure) the focus appears to be behind the panel ("under-focused") and the

surface current densities are concentrated within a strip along the center of the panel. The focusing strip becomes narrower as the voltage increases. At 400 V, the strip width is about 0.3 m. At 200 V (see below) the width is about 0.4 m. The highest surface current densities occur at the edges of the strip. These are "hot spots" where large localized power losses will occur.

At voltages below 400 V, the sheath shape is somewhat "pinched in" at the equator (in the plane of the panel). At 1200 V, the sheath is oval, with slightly larger vertical than horizontal dimension, but nearly circular. At higher voltages (for example, 2000 V at right-hand side of figure) the focus occurs in front of the panel ("over-focused"). The sheath is larger than the 1200 V sheath but similar in shape.

The sheath shape can also be quite circular (not shown). When the panel is at 200 V but narrower (0.5 m or about 20 in.), with proportionally narrower (about 2.5 in.) borders, and with the same plasma parameters as in Figure 20, the sheath is a circle of radius 1.0 panel widths (0.5 m). (See Ref. 5.)

4.2 Long Panel at 1200 V, With Nonconducting Borders (1 Unit = 48 in.)

Consider a long panel at the focusing voltage 1200 V, in a plasma with parameters $n_o = 10^6/cm^3$ and $kT/e = 0.4$ eV, with panel width 48 in. (1.22 m) and with 6 in. borders, as before. Figure 21 shows (in 2-D cross-section) a set of trajectories (upper half) and a set of potential contours (lower half). (The slight differences between this figure and the center part of Figure 20 are due to minor differences in the mesh and trajectories used. The sheath surface is essentially unchanged, an oval 2.6 units vertical length by 2.3 units horizontal width.) The potential contours include saddle point contours.

Figure 22* shows the potential contours in greater detail, labelled A through U. The saddle points are in the panel plane at about 0.2 unit off the edge and have a value of about 140 V. Two more contours are plotted at ± 0.4 V from this value.

Another solution (not shown) shows the effect of a narrower insulated border (3.6 instead of 6 in. in width). The effect of the narrower border is to allow the sheath to expand (to new height 1.4 units vs 1.3 units above the plane, and to new half-width 1.3 units vs 1.2 units in the plane of the panel.) The saddle points become stronger and approach closer to the panel edge.

*Editor's Note: The curves in Figures 22, 23, 24, 25, 30, 31, 39, and 40 were originally plotted in volts. They are actually in units of kT/e, and any legend on any of these figures in conflict with the caption should be multiplied by 0.4, to get the correct voltage.

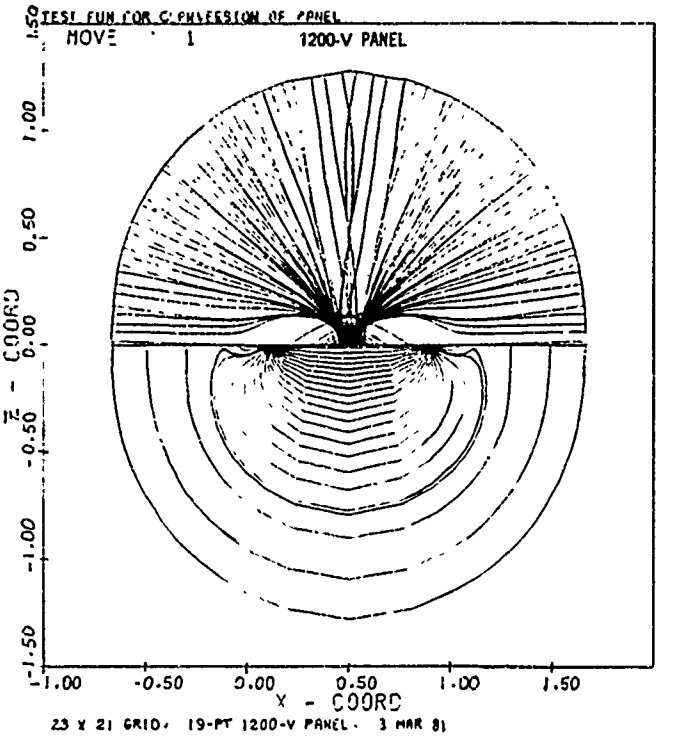

Figure 21. Long Bordered Panel at 1200 V. Upper half = trajectories. Lower half = equipotential contours (1 unit = 48 in.)

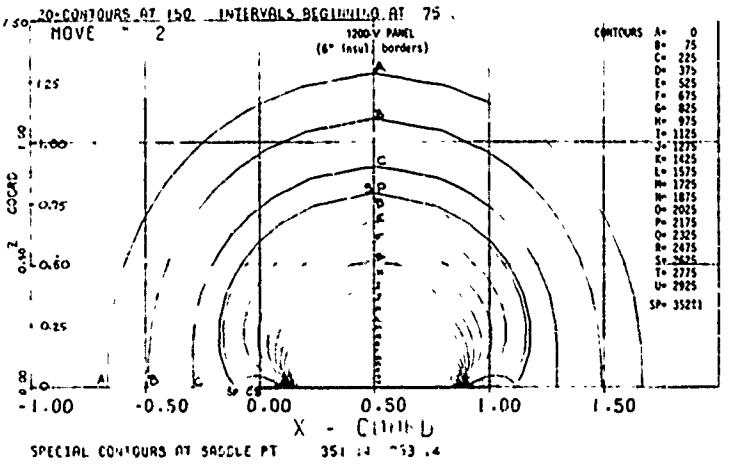

*Figure 22. Long Bordered Panel at 1200 V. Detailed equipotential contours (1 unit = 48 in.) (The contours are in units of kT and should be multiplied by 0.4 to determine voltages)

4.3 Probe Within Sheath of 1200-V Panel With Nonconducting Borders (1 Unit = 48 in.)

Figures 23 through 25 deal with the problem of a probe in the sheath, and show the interaction between the sheaths of the two bodies. The panel is at 1200 V, with 6 in. borders, and the probe is located at 0.5 unit above the center of the panel, at a voltage of 40 V of opposite sign. The plasma parameters are the same as before. Figure 23 shows trajectories (upper half) and equipotential contours (lower half). The trajectory plots now show the deflecting effect of the probe field. The relatively sharp focus pattern (of which Figure 21 is one example) is broken up. The sheath has shrunk in area, with a significant perturbation (indentation) in the central region. The potential contours show a significant compression of the "original" contours, between the probe and the panel. An additional saddle point appears, above the probe. Figure 24 depicts the contours in greater detail. The original "side" saddle point value was about 140 V and the new value is about 115 V. The additional saddle point, above the probe, has a value about 26 V.

The interaction illustrated in Figures 23 and 24 could also apply to a piece of dielectric material within the sheath. Figure 25 shows a set of associated field lines.

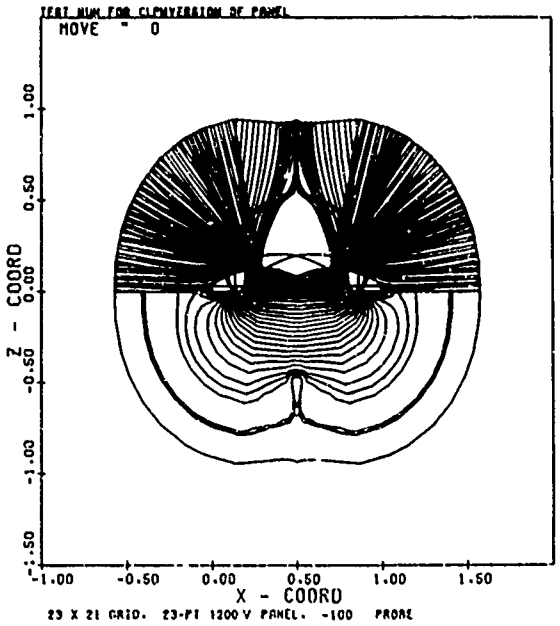

*Figure 23. 40-V Small Probe Within Sheath of 1200-V Bordered Panel. Upper half = trajectories. Lower half = equipotential contours (1 unit = 48 in.)

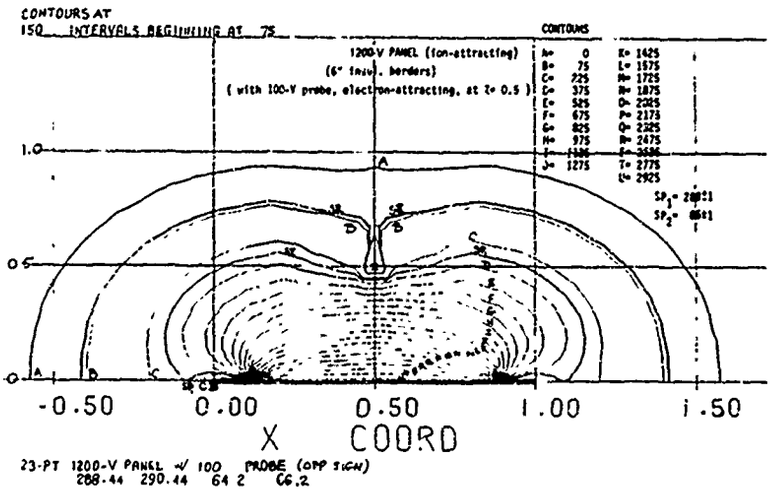

*Figure 24. 40-V Small Probe Within Sheath of 1200-V Bordered Panel. Detailed equipotential contours. (Cross marks location of probe. There are two saddle points, on x-axis and on z-axis. There are two 25.6-V contours, outer and inner (1 unit = 48 in.)) (The contours are in units of kT and should be multiplied by 0.4 to determine voltages. For example, the probe, marked 100, is at a potential of 40 V)

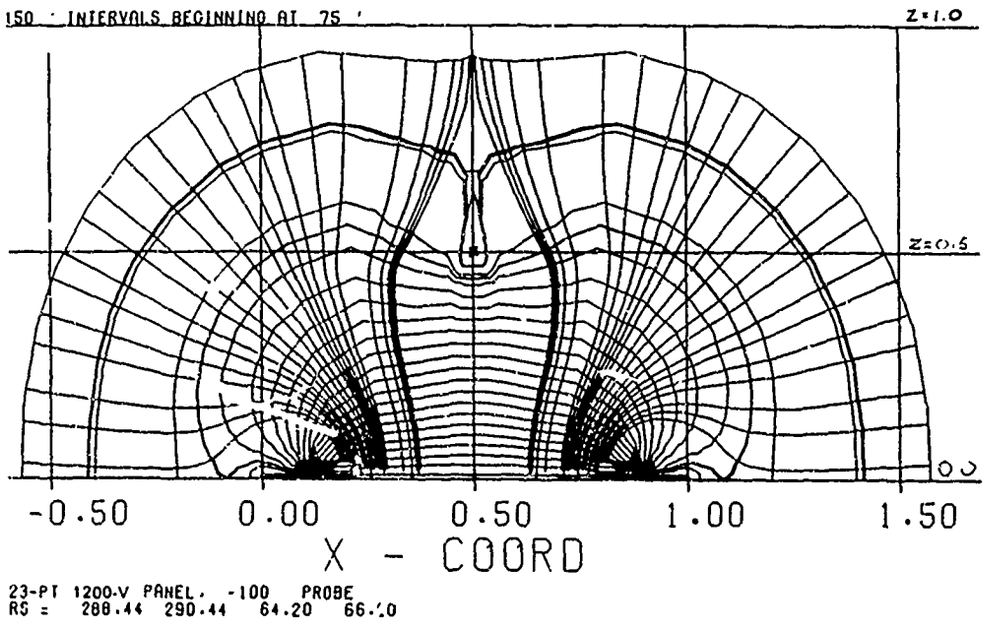

*Figure 25. 40-V Small Probe Within Sheath of 1200-V Bordered Panel. Field lines added. (Cross marks location of probe) (1 unit = 48 in.)

5. PLASMA FLOW EFFECTS

5.1 Effects of Plasma Flow on 1200-V Panel With Nonconducting Borders (1 Unit = 48 in.)

Up until now, we have considered only quiescent plasmas. In this section we consider the effects of a flowing plasma on the sheath shape of the negative 1200-V long panel (48 in. = 1.22-m width) with 6 in. nonconducting borders. The plasma parameters are $n_o = 10^6/cm^3$, $kT/e = 0.4$ eV in the frame of reference moving with the plasma, where the plasma drift velocity corresponds to a directed ion energy of 20 eV. Thus the Mach number of the flow is $(20/0.4)^{1/2} = 50^{1/2} = 7.07$. We consider a cross-section of the long panel in a cross-flow, and hence a 2-D problem. Three types of flows are treated, (1) no flow (Figure 26), (2) flow at 90^o, perpendicular to the panel surface (from top toward bottom, in Figure 27), and (3) flow at 0^o, parallel to the panel surface (from left to right, in Figure 28).

Figure 26 shows the sheath shape with no flow, and is similar to Figure 21 except that more trajectories are depicted (upper half of figure). The equipotential contours in the lower half of the figure are identical to those defined in Figure 22. From the sheath shape in the figure, one may compute the current collected, per meter of length in the direction perpendicular to the page, from the length of the sheath perimeter. If one measures this length with a ruler (upper half, using any scale), and divides by the length of the panel using the same scale (panel outlined by a box between x = 0 and x = 1), one obtains about 3.9 panel lengths, or 4.8 m. Assuming a thermal ion current density of $0.144\ mA/m^2$ (Ref. 29 value), the total current collected (upper surface) is 0.7 mA/m. Of course, this is concentrated at the center by the focusing effect. We will discuss the current distributions later.

Figure 27 shows the sheath shape when there is a Mach 7.07 flow of the same plasma, normal to the surface. The sheath, drawn to the same scale as Figure 26, has shrunk considerably, to a perimeter (upper half) of 1.8 panel lengths, or about 2.2 m. The current calculation, however, is complicated by the fact that there is a weight factor that depends on sheath position, because of the anisotropy of the flow. Thus, the current is higher than $2.2 \times 0.144 = 0.32$ mA/m. The current distribution is now spread over a wider strip, with high concentrations at the edges. These occur at positions about x = 0.26 and x = 0.74 on the panel surface. (Note that the insulating borders run from x = 0 to x = 0.125 and from x = 0.875 to x = 1.0.)

Figure 28 shows the distortion of the sheath shape when the Mach 7.07 flow is parallel to the surface, from left to right. Here, the sheath is compressed somewhat but mostly shifted to the right. It is pinched-in toward the border, on

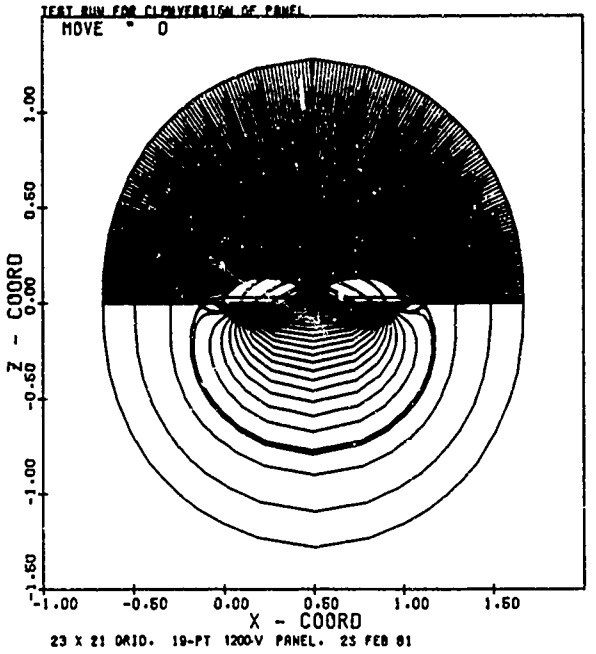

Figure 26. Long Bordered Panel at 1200 V. No flow ($10^6/cm^3$, 0.4 eV plasma). (More trajectories than in Figure 21.) (1 unit = 48 in.)

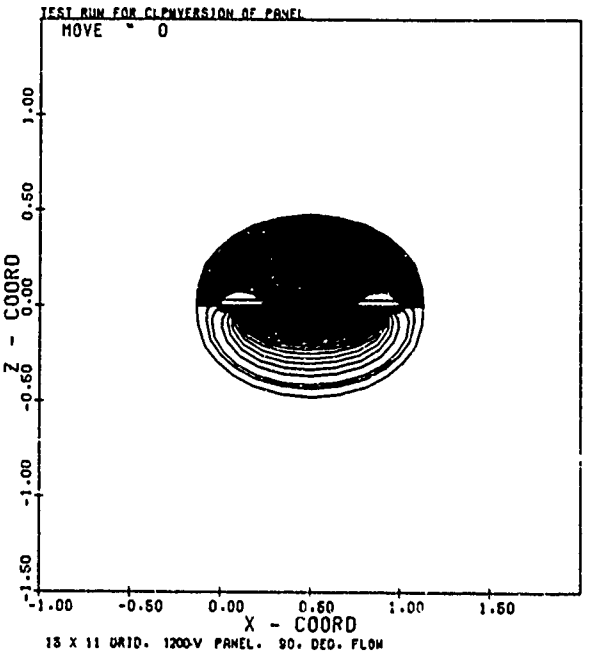

Figure 27. Long Bordered Panel at 1200 V. Mach 7 flow at 90^0 (normal to panel surface). (1 unit = 48 in.)

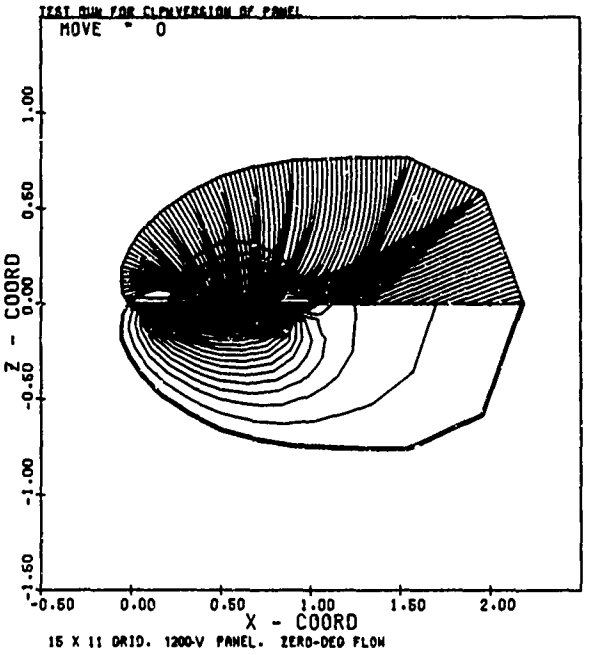

Figure 28. Long Bordered Panel at 1200 V. Mach 7 flow at 0° (parallel to panel surface). (1 unit = 48 in.

the left hand side. The sheath, drawn to the same scale as in Figure 26, has a perimeter of about 3.0 units (upper half), or about 3.8 m. The sheath volume is nearly the same as, though slightly smaller than, the no-flow volume. The current calculation again depends on the position-dependent weight factor. The current exceeds $3.8 \times 0.144 = 0.55$ mA/m. The current is distributed between the points $x = 0.33$ and $x = 0.81$ on the panel surface. Some of the trajectories from the rear surfaces of the sheath are not directly collected, and may not actually be ultimately collected. Because of their tendency to circulate around the panel, they were not followed very far and their contributions (mostly based on extremely small weights) were neglected. However, the wake region mesh was rather coarse. These contributions should be investigated using finer meshes. Figure 29a summarizes the sheath shapes for the three flow cases for the 1200-V panel.

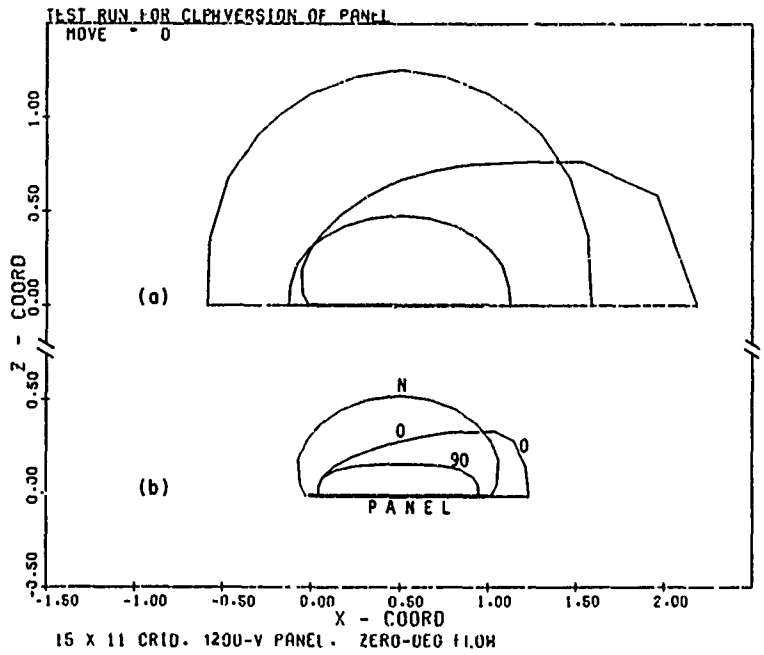

Figure 29. Summary of Panel (48-in. Width) Sheath Shapes ($10^6/cm^3$, 0.4 eV Plasma). N = No flow, 90° = 90° Mach 7.07 flow (normal to panel), 0° = 0° Mach 7.07 flow (parallel to panel). (a) 1200 V, (b) 200V

5.2 Effects of Plasma Flow on 200-V Panel With Nonconducting Borders (1 Unit = 48 in.)

In this section, the same panel and plasma are treated as in Figures 26 through 29, but the panel now is biased to 200 V. The same three types of flows are considered.

Figure 29(b) summarizes the sheath shapes for the three flow cases for the 200-V panel.

Figure 30 defines the equipotential contours to be shown in the succeeding figures.

Figure 31(a) shows the sheath shape for no flow, quite pinched-in at the sides near the panel borders. The upper sheath perimeter is 1.8 units, or 2.2 m. Using 0.144 mA/m^2 for ion thermal current density yields 0.32 mA/m. This current is distributed on a strip between x = 0.31 and x = 0.69, with concentrations at these values of x. We will discuss this current distribution later.

Figures 31(b) and 31(c) treat Mach 7.07 plasma flows, normal to (90°) and parallel to (0°) the surface, respectively (as in Figures 27 and 28). The upper sheath perimeters are 1.18 and 1.60 units, respectively, or 1.4 and 2.0 m. An

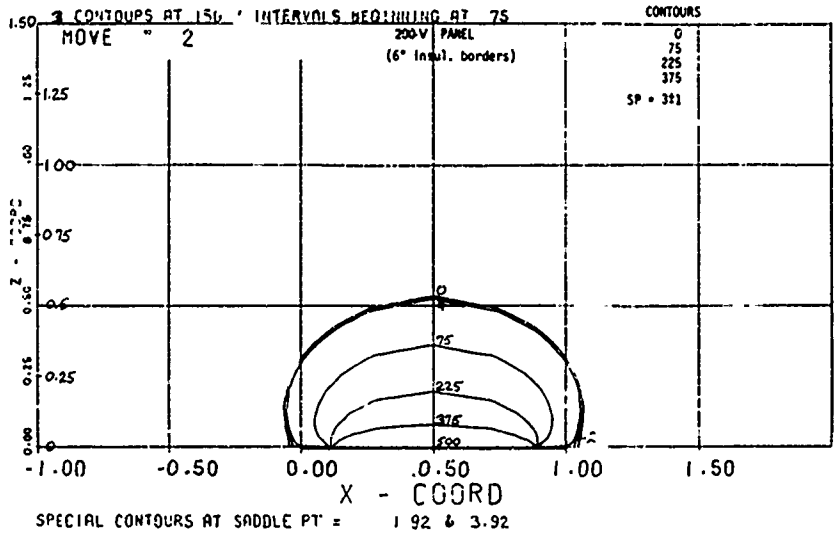

*Figure 30. Long Bordered Panel at 200 V. Detailed equipotential contours. (1 unit = 48 in.)

important feature of these sheaths is that they are attached to the nonconducting border of the panel. Both sides of the sheath are within the border in the case of the 90° flow, and the left side is within the border in the case of the 0° flow. All of the trajectories are collected. A small fraction impacts the border insulation in both cases. Aside from these impacts, the current is confined to the strip $x = 0.15$ to $x = 0.85$ in the 90°-flow case, with concentrations at these locations. In the 0°-flow case, the confinement is within the strip $x = 0.16$ to $x = 0.85$, with concentrations at these locations. At $x = 0.85$, however, the current is weak because of the reduced weight factors associated with these trajectories.

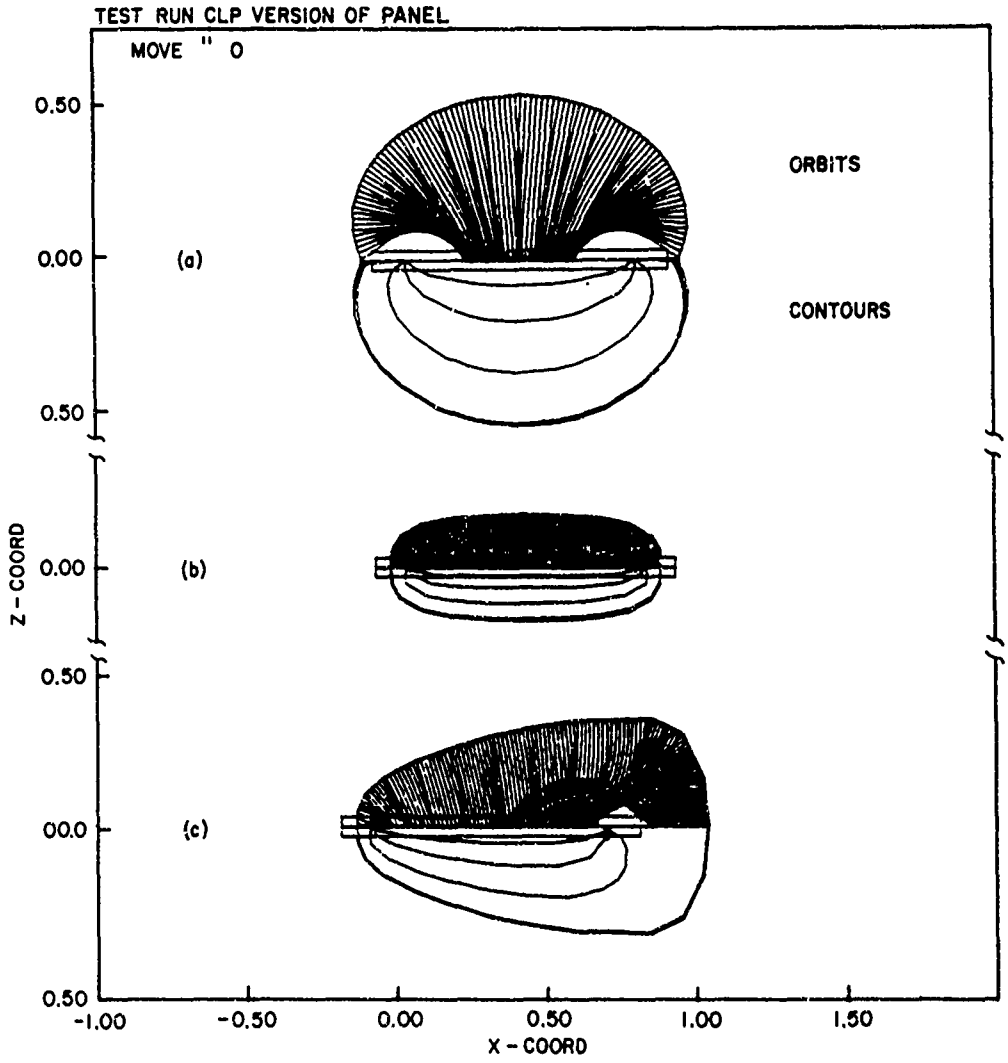

*Figure 31. Long Bordered Panel at 200 V (1 Unit = 48 in.). (a) No flow. (10^6/cm^3, 0.4 eV plasma.) (b) Mach 7 flow at 90° (normal to panel surface). (c) Mach 7 flow at 0° (parallel to panel surface)

6. SURFACE CURRENT DISTRIBUTIONS AND "HOT SPOTS" ASSOCIATED WITH ION FOCUSING AND PLASMA FLOWS

6.1 200-V Long Panel With Nonconducting Borders (No-flow, 1 Unit = 48 in.)

In this section the surface current distributions due to ion focusing and flow effects will be considered in greater detail. First we discuss the 200-V bordered panel, treated in Section 5.2, where Figure 31(a) shows the trajectories for the no-flow case. The current is distributed between positions x = 0.31 and x = 0.69 on the panel surface, with strong concentrations of the trajectories evident at these two points. (The panel is defined to lie between x = 0 and x = 1.) These strong concentrations are associated with high current densities. It is of interest to determine the ion current density distribution (or equivalently, the distribution of power density impacting on solar cells, for example). The high-concentration positions are "hot spots."

One way of predicting the current distribution is to divide the panel computationally into many small sections or "bins," and to count the relative numbers of trajectories hitting them. Good accuracy requires large numbers of trajectories and a fine grid to achieve statistically significant values. Using of the order of 1000 trajectories, and bins of width 0.01 on the panel results in a somewhat irregular histogram, as illustrated in Figure 32. The information obtainable from the histogram shown is relatively limited. (The solid curves are obtained from analytic fitting, as described next.)

If one instead plots the x-positions of the points of impact of individual trajectories vs their launch position on the sheath surface (arc length s, in this case), one obtains the "mapping" function shown in Figure 33. The scalloped structure is due to the use of the finite mesh structure defining the potential distribution and sheath boundary. This function is symmetric about the horizontal line at x = 0.5, because of the geometric symmetry of the problem. To compute current density from this function, one may assume $jdx = j_o ds$, from which we derive the relation,

$$j/j_o = F(s_1)/\left|dx/ds\right|_1 + F(s_2)/\left|dx/dx\right|_2 \quad , \tag{18}$$

where j is the local current density on the surface, j_o is the incident (random thermal) current density at the sheath surface, and F(s) is a weighting function for cases where the current density is nonuniformly distributed at the sheath surface. For the no-flow case, F(s) = 1. There are two terms in the equation, one from each branch of the mapping function.

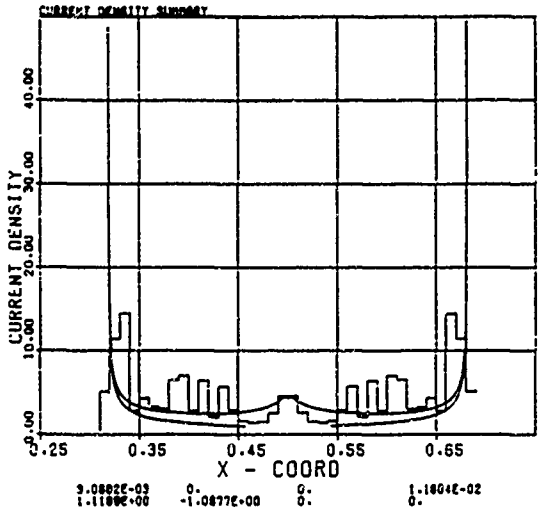

Figure 32. Current Density Distribution on 200-V Long Bordered Panel (Dimensionless, in Units of Random Thermal Current Density). No flow. Histogram vs analytical fit. Hot spots at x = 0.31 and 0.69. (Numbers are mapping function fit coefficients - see text) (1 unit = 48 in.)

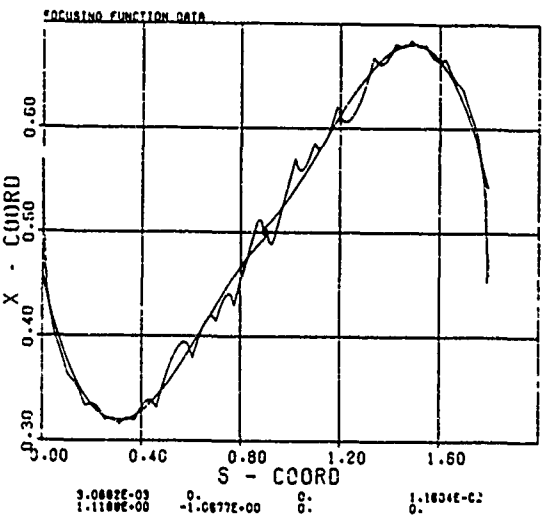

Figure 33. Analytic Fit and Trajectory Mapping Function for 200-V Bordered Panel. No flow. (Numbers are mapping function fit coefficients - see text) (1 unit = 48 in.)

It is obviously computationally unfeasible to use in Eq. (18) the mapping function shown in Figure 33, because the numerous zeros of dx/ds give rise to many infinite spikes (numerical artifacts) in the current density. However, even from the gross behavior of the mapping function it is clear from Figure 33 that no trajectories reach the panel outside of the strip between x = 0.30 and x = 0.70. If we replace the function in the figure by a smooth function, the smooth function should have a minimum near x = 0.30 and a maximum near x = 0.70. The derivatives dx/ds are zero at these positions, giving rise to two infinite spikes ("hot spots"). (The actual current density is finite due to several effects, including diffuse sheath boundaries and thermal velocity distributions.) It is convenient, therefore, to fit the numerical curve with an analytic function, and then derive the current density using the derivatives of the fitting function.

Figure 33 also shows a fit to the mapping function. The fitting curve is assumed to have the polynomial form:

$$x - x_o = A_o + A_{-2}(s - s_o)^{-2} + A_{-1}(s - s_o)^{-1} + A_1(s - s_o) + A_2(s - s_o)^2 + A_3(s - s_o)^3 + A_4(s - s_o)^4 + A_5(s - s_o)^5 \qquad (19)$$

The coefficients A_o, A_{-2}, A_{-1}, and A_1 of the fit are shown in the first row of numbers below the graph; and A_2, A_3, A_4 and A_5 are shown in the second row. Here, x_o and s_o denote the coordinates of the minimum (or maximum) chosen by the operator. There is such a fit for each branch, but by symmetry in this case they are assumed to be identical.

Taking the reciprocals of the derivatives results in the solid curves shown in Figure 32. There is one contribution from each branch. Hence, j/j_o is given by the sum of these.

A simpler fit for this case was given previously by Parker,[5] with $x_o = 0.316$ and $s_o = 0.3125$, and keeping only the A_2 term, where $A_2 = 0.856$. Taking the reciprocal derivative and multiplying by 2 (for 2 identical branches) gives the current density function: (implying hot spots at x = 0.316 and x = 0.684).

$$j/j_o = 1.081/(x - 0.316)^{1/2} \quad . \qquad (20)$$

It is of interest also to show a corresponding "optical" mapping function (Figure 34). This arises purely from the shape of the sheath and is obtained by assuming that all trajectories remain straight lines after being launched from the sheath surface. This results in a much smoother function. One may readily infer from Figure 34 that "optically" one would predict a narrower focusing strip where the current is confined between hot spots at x = 0.4 and x = 0.6.

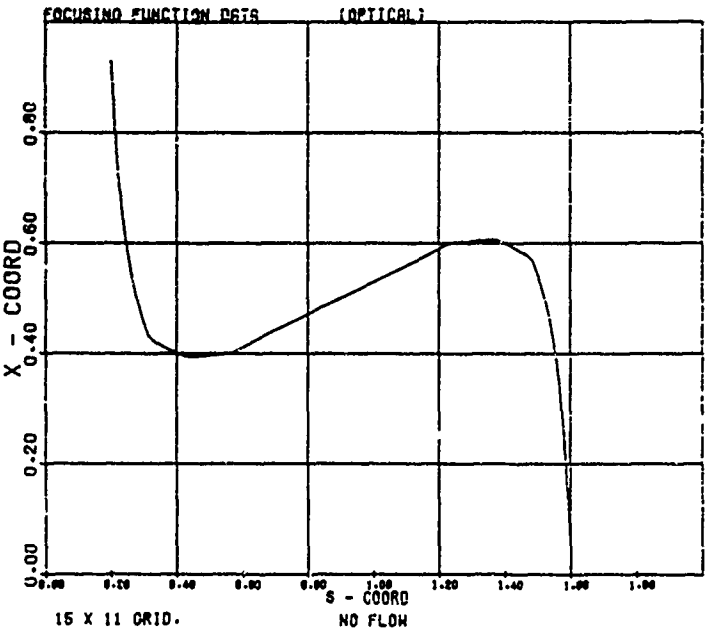

Figure 34. Optical Mapping Function for 200-V Bordered Panel. No flow. (Straight line trajectories from sheath launch position) (1 unit = 48 in.)

6.2 200-V Long Panel With Nonconducting Borders (90° and 0° Flows, 1 Unit = 48 in.)

In the flow problems presented here, the trajectories were launched in directions normal to the sheath surface. The associated current densities were represented by weight factors $F[M_n(s)]$, depending on the normal component of the Mach flow vector where M_n denotes the product of the Mach number with the cosine of the angle between the flow vector and the normal to the sheath at position s. That is, F(M) was defined as the "planar approximation" function:

$$F(M) = \exp(-M^2) + \pi^{1/2} M(1 + \text{erf } M) \quad .$$

The sheath and trajectories for the 200-V bordered long panel in a 90° flow (Mach 7.07 flow normal to the surface) are depicted in Figure 31b. The flow Mach number is 7.07. For the 90° flow, the current is distributed within the focusing strip between the hot spots at x = 0.15 and x = 0.85. Both sides of the sheath are within the border in this case. Figure 35 shows the resulting mapping function. The initial and final portions (steep rises near s = 0.008 and s = 1.12 are associated with trajectories impacting the nonconducting border, and will not

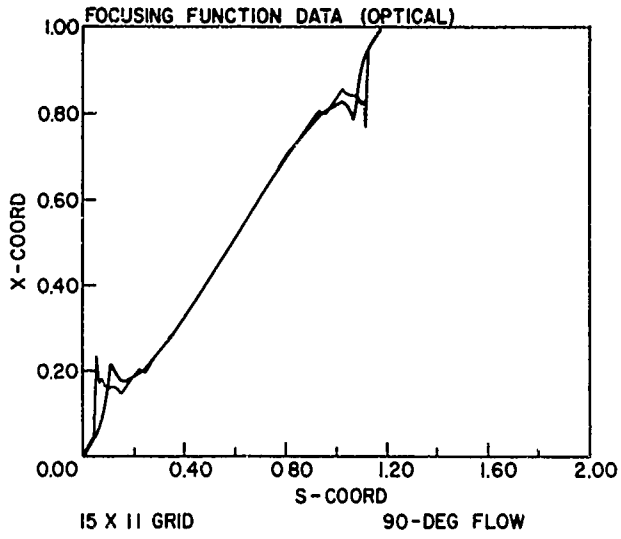

Figure 35. Trajectory Mapping Function and Optical Mapping Function for 200-V Bordered Panel. Mach 7 flow at 90° (normal to panel surface) (1 unit = 48 in.)

be discussed here. The remaining portion of the function begins with a minimum (x = 0.15) near s = 0.20, rises almost linearly with s until about s = 0.8, and then has a maximum (x = 0.85) near s = 1.00. There will therefore be hot spots at these x-locations. Note, incidentally, that they are further apart, that is, closer to the panel edges, than in the no-flow case.

An analytic fit was not made, but is a straightforward process. In view of the symmetry it would be similar to that of the no-flow case. The central linear portion of the mapping function is associated with constant current density, as might be expected from the flattened appearance of the sheath center section shown in Figure 31b. Figure 35 also shows the corresponding optical mapping function. This indicates a slightly narrower focusing strip with "optical" hot spots near x = 0.17 and x = 0.83.

The sheath and trajectories in a 0° flow (Mach 7.07 flow parallel to the surface) are depicted in Figure 31c. For the 0° flow, the current is distributed within the focusing strip between hot spots at x = 0.16 and x = 0.85. These are predictable from the minimum and maximum of the mapping function depicted in Figure 36 (neglecting the initial sharp-rise portion associated with impacts on the left border). The fairly linear central portion of the mapping function is associated with constant current density. According to Figure 31c, the sheath is approximately wedge-shaped, and the trajectories producing the constant current density originate on the side of the wedge. An analytic fit was not made but would

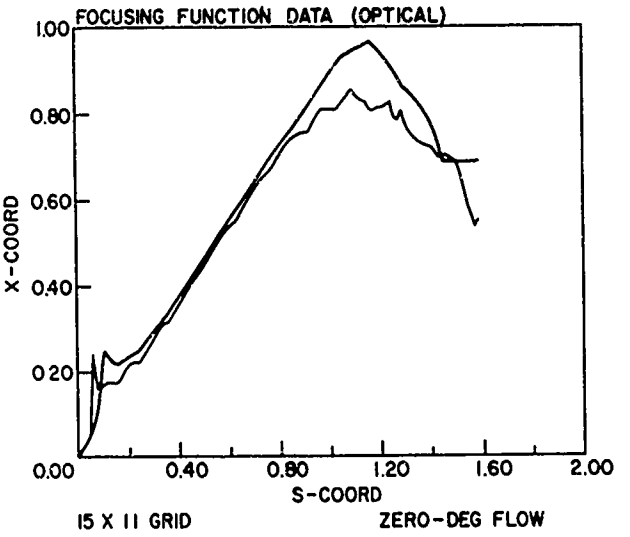

Figure 36. Trajectory Mapping Function and Optical Mapping Function for 200-V Bordered Panel. Mach 7 flow at 0^{o} (parallel to panel surface) (1 unit = 48 in.)

be straightforward. Figure 36 also presents the optical analog of the mapping function indicating that current would be confined between "optical" hot spots near x = 0.22 (minimum) and x = 0.97 (maximum), that is, a strip of almost the same width but shifted to the right.

6.3 1200-V Long Panel With Nonconducting Borders (Three Flow Cases, 1 Unit = 48 in.)

Here we discuss the three flow cases of the 1200-V bordered long panel, treated in Section 5.1 and shown in Figures 26 through 28 for the no-flow case, the 90^{o} flow case (Mach 7.07 flow normal to the surface), and the 0^{o} flow case (Mach 7.07 flow parallel to the surface), respectively. (As in the 200-V case, the panel is defined to lie between x = 0 and x = 1, with one part of the border lying between x = 0 and x = 0.125, and the other part lying between x = 0.875 and x = 1.0).

For the no-flow case (sheath and trajectories in Figure 26) the current is concentrated essentially at one point, namely, the center of the panel (x = 0.5). This case is actually slightly "under-focused," however. Its mapping function and the analytical fit depicted in Figure 37 show this. There is some resemblance here to the mapping function of Figure 32 for the under-focused 200-V no-flow case, namely a minimum followed by a maximum, at x-values close to one another, indicating two hot spots in close proximity to one another. (Here we

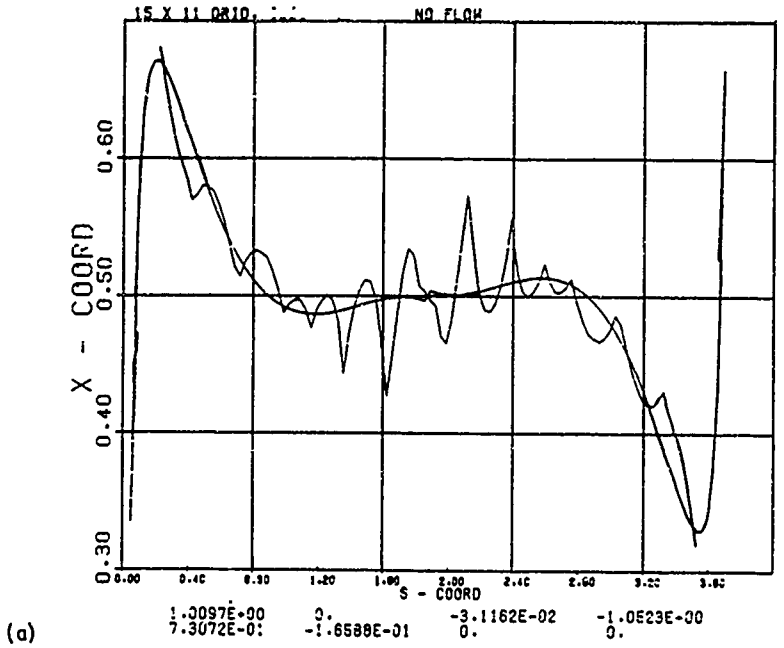

(a)

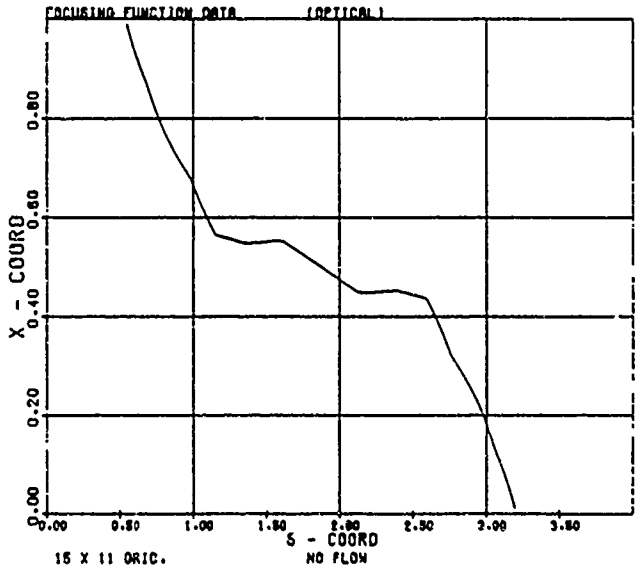

(b)

Figure 37. Analytic Fit, Trajectory Mapping Function and Optical Mapping Function for 1200-V Bordered Panel. No flow. (Impact position x on panel vs sheath launch positions.) (Numbers are mapping function fit coefficients - see text.) (1 unit = 48 in.)

ignore the steep initial and final rise portions of the fit in Figure 37 as artifacts.) Figure 37 also shows the corresponding optical mapping function, which is of interest because it erroneously indicates an "over-focused" situation. Figure 38 presents the histogram corresponding to impacts collected by bins of width 0.01. Also shown is the current density curve resulting from the analytical fit, indicating the superposition of two hot spots in close proximity to one another. The two branches should be added to obtain the current.

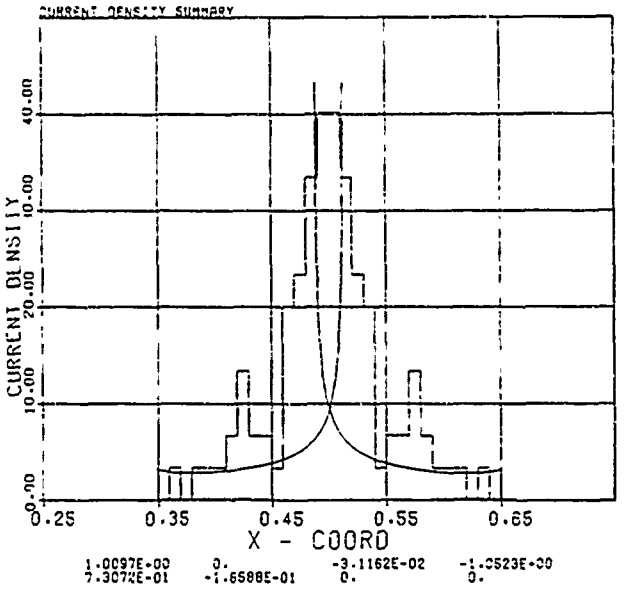

Figure 38. Current Density Distribution on 1200-V Long Bordered Panel (Dimensionless, in Units of Random Thermal Current Density). No flow. Histogram vs analytical fit. Merged hot spots at x = 0.51 and 0.49. (Numbers are mapping function fit coefficients - see text.) (1 unit = 48 in.)

For the 90° flow case (Mach 7.07 flow normal to the surface; sheath and trajectories shown in Figure 27), the surface current is confined between hot spots at x = 0.26 and x = 0.74. This is corroborated by the associated mapping function given by Figure 39. The corresponding optical mapping function (not shown) is similar in shape, and indicates hot spots at almost the same locations. No fit was made.

For the 0° flow case (Mach 7.07 flow parallel to the surface; sheath and trajectories shown in Figure 28), the surface current is confined between hot spots

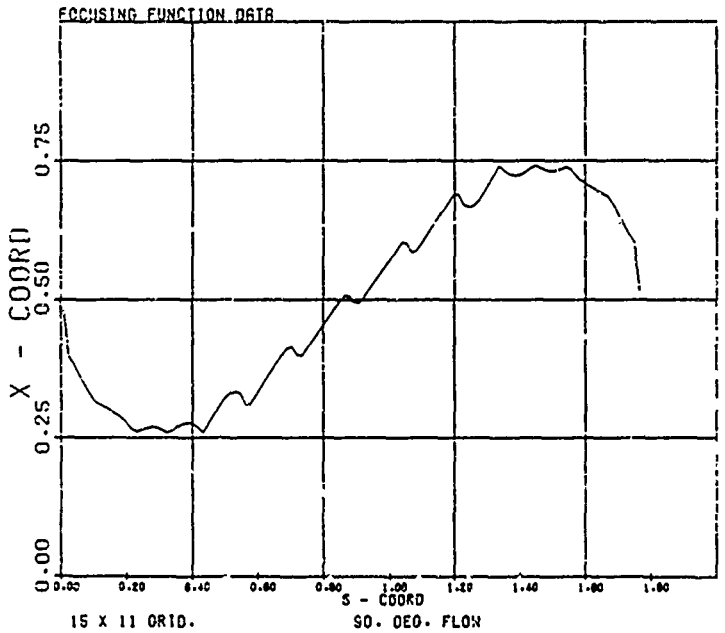

*Figure 39. Trajectory Mapping Function for 1200-V Bordered Panel. Mach 7 flow at 90^{o} (normal to panel surface) (1 unit = 48 in.)

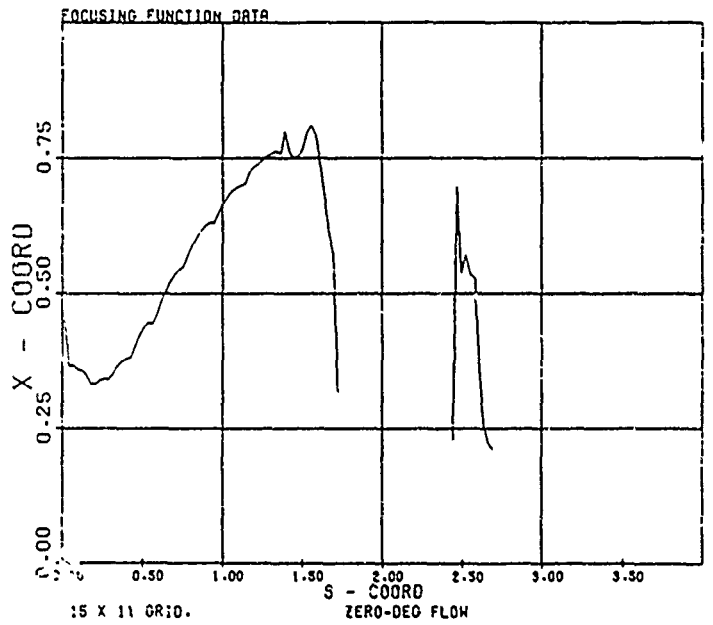

*Figure 40. Trajectory Mapping Function for 1200-V Bordered Panel. Mach 7 flow at 0^{o} (parallel to panel surface) (1 unit = 48 in.)

at x = 0.33 and x = 0.81. Figure 40 presents the mapping function. This function shows the minimum and maximum associated with the two hot spots, but has a gap between about s = 1.75 and s = 2.45. This is followed by a narrow peak with "spiky" behavior. The gap is associated with trajectories that are truncated as they cross the horizontal plane of symmetry. They may ultimately be collected, but they have mostly negligible weights. The peak is associated with trajectories from the far-wake region, but having negligible weights (see Figure 28). The corresponding optical mapping function (not shown) has a single minimum (hot spot) near x = 0.5.

7. CONCLUDING REMARKS

A new approach to computing sheaths of large high-voltage space structures in dense plasmas is described. This approach extends the Child-Langmuir sheath model to 3-D sheaths and body shapes. It uses a finite element method for the 3-D Poisson equation based on deformable tetrahedral elements that allow arbitrary sheath and body shapes to be described. The computational mesh consists of lines emanating from the body, suggestive of a pincushion. The entire mesh is contained between the body and the sheath surface. The tetrahedra are formed from the mesh nodes that slide along the lines whose lengths define nodes on the sheath surface. During the establishment of the solution by iteration, the sheath surface adjusts its shape (and the sliding nodes accommodate to this shape, so that the mesh is "dynamically" self-adjusting). The criterion for the final sheath shape is that both the potential and its normal gradient vanish at all sheath points. This is the 3-D extension of the familiar Child-Langmuir criterion. Space charge within the elements is calculated by following trajectories launched from the sheath surface, depositing charge as they move through the sheath, according to the time spent at points along their paths.

The 3-D generalization of the Child-Langmuir sheath method is supported by a rigorous self-consistent spherically-symmetric solution in which the body radius is 100 Debye lengths and the dimensionless potential is 400,000 (the highest value solved self-consistently to date).

The code is applied to a number of problems, mostly concerning ion focusing effects associated with dielectric borders on large high-voltage rectangular panels interacting with dense plasmas and with plasma flows characteristic of low earth orbit. The sheath shapes vary with the body and border geometry, body voltage, and plasma-flow velocity and direction. In all cases the bodies are large compared with the Debye length (ratios of 200 to 250), and the voltage is large compared to kT/e (dimensionless potentials 500 to 5000). In one case (long circular cylinder) the body dimension is 100 Debye lengths.

Square panels (of size 1 m, at 200 V negative bias) are treated in three dimensions, both with and without a nonconducting border, in a plasma with density $10^6/cm^3$ and temperature 0.4 eV. The sheath is roughly spheroidal without the border, but with a border it contracts in size and is "pinched-in" in the plane of the panel, coming in over the nonconducting surface at the corner. The focusing pattern ("footprints") of trajectories is such that the ion impacts are confined to a roughly square region with "horns" on the panel surface. An analytic approximation ("false space charge") of the type used by NASCAP/LEO is tested and found to significantly overestimate sheath sizes when compared with the sheaths obtained using rigorous (trajectory-controlled) space charge.

Ion focusing and surface current distributions are studied on long meter-sized bordered panels, at 200 and 1200 V negative bias, and with and without a Mach 7 plasma flow. Due to the focusing the current distributions are non-uniform, with intense "hot spots" where, for example, solar cells can be damaged. The hot spots move with changes in panel voltage and plasma flow direction. When the flow direction is perpendicular to the panel the sheath is compressed toward the panel, making it thinner. Its lateral extent is also diminished. The focusing strip on the panel surface broadens (the hot spots move further apart). When the flow is parallel to the panel the sheath is shifted in the direction of the flow; the sheath is compressed in the upstream and lateral regions, but flares out in the wake region. Also, the hot spots on the surface shift in the direction of the flow.

When a low-voltage probe is placed within the high-voltage sheath, an unexpectedly large disruption of sheath shape and surface current distribution is found to occur.

Acknowledgements

This work was supported by the National Aeronautics and Space Administration Lyndon B. Johnson Space Center. The assistance of D. K. Yue in the finite element formulation is gratefully acknowledged.

References

1. McCoy, J. E., and Konradi, A. (1979) Sheath effects observed on a 10-meter high-voltage panel in simulated low-earth-orbit plasma, in Spacecraft Charging Technology - 1978, R. C. Finke and C. P. Pike, Eds., NASA Conference Publication 2071, AFGL-TR-79-0082, AD A084626, pp. 315-340.

2. McCoy, J. E. (1980) High-voltage space plasma interactions, Proceedings of the Solar Power Satellite Program Review, DOE/NASA, available from NTIS, Springfield, VA 22161.

3. McCoy, J. E., Konradi, A., and Garriott, O. K. (1980) Current leakage for low altitude satellites, in Progress in Astronautics and Aeronautics, Vol. 71 (Space Systems and their Interactions with Earth's Space Environment), H. B. Garrett and C. P. Pike, Eds., AIAA, pp. 523-553.

4. Stevens, N. J. (1980) Space environmental interactions with biased spacecraft surfaces, Progress in Astronautics and Aeronautics, Vol. 71 (Space Systems and their Interaction with Earth Space Environment), H. B. Garrett and C. P. Pike, Eds., AIAA, pp. 455-476. (See also adjacent paper.)

5. Parker, L. W. (1981) Trajectory-Controlled Space-Charge-Sheath Computer Models, NASA Contract NAS9-15934, Lee W. Parker, Inc.

6. Cooke, D. L., Parker, L. W., and McCoy, J. E. (1981) Three-dimensional space charge model for large high-voltage satellites, in Spacecraft Charging Technology 1980, N. J. Stevens and C. P. Pike, Eds., NASA Conference Publication 2182, AFGL-TR-81-0270, AD A114426, pp. 957-978.

7. Parker, L. W. (1980) Plasmasheath-photosheath theory for large high-voltage space structures, in Progress in Astronautics and Aeronautics, Vol. 71 (Space Systems and their Interaction with the Earth's Space Environment), H. B. Garrett and C. P. Pike, Eds., AIAA, pp. 477-522.

8. Garrett, H. B. (1981) The charging of spacecraft surfaces, Rev. Geophys. Space Phys. 19:577.

9. Laframboise, J.G. (1966) Theory of Spherical and Cylindrical Probes in a Collisionless Maxwellian Plasma at Rest, Univ. of Toronto Report UTIAS No. 100, June.

10. Langmuir, I., and Blodgett, K.B. (1924) Currents limited by space charge between concentric spheres, Phys. Rev. 24:49-59.

11. Parker, L.W. (1972) Computation of Ion Collection by a Large Rocket-Mounted Mass-Spectrometer Plate at a Large Drawing-in Potential, AFCRL-72-0524, AD 750483, Contract F19628-71-C-0200, Mt. Auburn Research Associates, Inc.

12. Whipple, E.C., Jr., Warnock, J.M., and Winkler, R.H. (1974) Effect of sateilite potential on direct ion density measurements through the plasma-pause, J. Geophys. Res. 79:179.

13. Katz, I., Mandell, M.J., Schnuelle, G.W., Parks, D.E., and Steen, P.G. (1980) Plasma Collection by High-Voltage Spacecraft at Low Earth Orbit, Paper AIAA-80-0042, AIAA 18th Aerospace Sciences Meeting.

14. Langmuir, I., and Blodgett, K.B. (1923) Currents limited by space charge between coaxial cylinders, Phys. Rev. 22:347-56.

15. Parker, L.W. (1964) Numerical Methods for Computing the Density of a Rarefied Gas About a Moving Object, AFCRL-64-193, Contract AF19628-2782, Allied Res. Assoc. Inc.

16. Parker, L.W. (1976) Computation of Collisionless Steady-State Plasma Flow Past a Charged Disk, NASA CR-144159, Lee W. Parker, Inc.

17. Parker, L.W. (1970) Theory of the External Sheath Structure and Ion Collection Characteristics of a Rocket-Borne Mass Spectrometer, AFCRL-71-0105, AD 720833, Contract F19628-70-C-0053, Mt. Auburn Research Associates, Inc.

18. Parker, L.W. (1973) Computation of Ion Collection by a Rocket-Mounted Mass Spectrometer in the Limit of Vanishing Debye Number, AFCRL-TR-73-0735, AD 783625, Contract F19628-73-C-0065, Mt. Auburn Research Associates, Inc.

19. Parker, L.W. (1973) Computer Solutions in Electrostatic Probe Theory II. Two-Electrode Systems in r, z Geometry, AFAL-TR-72-222, Mt. Auburn Research Associates, Inc.

20. Parker, L.W. (1977) Calculation of sheath and wake structure about a pillbox-shaped spacecraft in a flowing plasma, in Proceedings of the Spacecraft Charging Technology Conference, C.P. Pike and R.R. Lovell, Eds., AFGL-TR-77-0051, AD A045459, NASA TMX-73537, pp. 331-366.

21. Parker, L.W. (1978) Differential charging and sheath asymmetry of non-conducting spacecraft due to plasma flows, J. Geophys. Res. 83: 4873-4876.

22. Parker, L.W. (1979) Time-Dependent Computer Model of Plasma Space Charge Interactions With a Finite-Cylindrical Spacecraft, AFGL-TR-80-0018, AD A084892, Lee W. Parker, Inc.

23. Parker, L.W., and Whipple, Jr., E.C. (1970) Theory of spacecraft sheath structure, potential, and velocity effects on ion measurements by traps and mass spectrometers, J. Geophys. Res. 75:4720.

24. Parker, L.W., and Holeman, E.G. (1981) Electrostatic charging and sheath structure of the Halley probe spacecraft due to impact-generated plasmas, in Proceedings of the Halley Probe Plasma Environment Workshop, European Space Technology Center Report ESA-SP-155, The Netherlands, pp. 67-80.

25. Grard, R.J.L., Parker, L.W., and Young, D.T. (1981) Interaction between a body and its environment during a cometary fly-by, Adv. Space Res. (COSPAR) 1:403-407.

26. Parker, L.W. (1979) Plasma sheath effects on equilibrium voltage distributions of large high-power satellite solar arrays, in Spacecraft Charging Technology - 1978, R.C. Finke and C.P. Pike, Eds., NASA Conference Publication, AFGL-TR-79-0082, AD A084626, pp. 341-357.

27. Parker, L.W. (1980) Effects of plasma sheath on solar power satellite array, J. Energy 4(No. 6):241.

28. Zienkiewicz, O.C. (1971) The Finite Element Method in Engineering Science, McGraw-Hill.

29. Konradi, A., McIntyre, B., and Potter, A.E. (1983) Experimental studies of scaling laws for plasma collection at high voltages, J. Spacecraft and Rockets (in press).

30. Mandell, M.J., Katz, I., Steen, P.G., and Schnuelle, G.W. (1980) The effect of solar array voltage patterns on plasma power losses, IEEE Trans. Nucl. Sci. NS-27.

Appendix A

Tetrahedral Shape Functions

Let 1, 2, 3, 4 denote relative node indices for the nodes of a linear tetrahedron. Let:

x_1, y_1, z_1 = coordinates of node 1

x_2, y_2, z_2 = coordinates of node 2

x_3, y_3, z_3 = coordinates of node 3

x_4, y_4, z_4 = coordinates of node 4 .

Define shape functions L_1, L_2, L_3, and L_4 such that:

$$1 = L_1 + L_2 + L_3 + L_4 \tag{A1}$$

$$x = L_1x_1 + L_2x_2 + L_3x_3 + L_4x_4 \tag{A2}$$

$$y = L_1y_1 + L_2y_2 + L_3y_3 + L_4y_4 \tag{A3}$$

$$z = L_1z_1 + L_2z_2 + L_3z_3 + L_4z_4 \quad . \tag{A4}$$

Thus, the properties of the shape functions are such that:

At node 1, $L_1 = 1$, $L_2 = L_3 = L_4 = 0$

At node 2, $L_2 = 1$, $L_1 = L_3 = L_4 = 0$

At node 3, $L_3 = 1$, $L_1 = L_2 = L_4 = 0$

At node 4, $L_4 = 1$, $L_1 = L_2 = L_3 = 0$. (A5)

Then for any function of x, y, z, such as potential ϕ defined by its nodal values ϕ_1, ϕ_2, ϕ_3, ϕ_4 at the respective nodes, an interpolation formula is provided. Namely, at any point x, y, z within the tetrahedron the value of ϕ is given by

$$\phi = L_1\phi_1 + L_2\phi_2 + L_3\phi_3 + L_4\phi_4 \quad . \tag{A6}$$

The shape functions are now obtained by solving Eqs. (A1) through (A4) for L_1, L_2, L_3, L_4. Let $\underset{\sim}{A}$ denote the matrix of coefficients in these equations. Then the matrix $\underset{\sim}{A}$ may be inverted to give

$$L_1 = d_1 + (a_1x + b_1y + c_1z)/6V \tag{A7}$$

$$L_2 = d_2 + (a_2x + b_2y + c_2z)/6V \tag{A8}$$

$$L_3 = d_3 + (a_3x + b_3y + c_3z)/6V \tag{A9}$$

$$L_4 = d_4 + (a_4x + b_4y + c_4z)/6V \quad , \tag{A10}$$

where V denotes the volume of the tetrahedron, and 6 V is the value of the determinant of $\underset{\sim}{A}$, namely:

$$6V = \begin{vmatrix} 1 & 1 & 1 & 1 \\ x_1 & x_2 & x_3 & x_4 \\ y_1 & y_2 & y_3 & y_4 \\ z_1 & z_2 & z_3 & z_4 \end{vmatrix} \tag{A11}$$

$$= \sum_{j=1}^{4} x_j a_j = \sum_{j=1}^{4} y_j b_j = \sum_{j=1}^{4} z_j c_j \quad . \tag{A12}$$

The values of a_j, b_j, c_j are given by determinants as follows (j = 1, 2, 3, 4):

$$a_j = \begin{vmatrix} 1 & 1 & 1 \\ q_1 & q_2 & q_3 \\ r_1 & r_2 & r_3 \end{vmatrix} ; \; b_j = \begin{vmatrix} 1 & 1 & 1 \\ p_1 & p_2 & p_3 \\ r_1 & r_2 & r_3 \end{vmatrix} ; \; c_j = \begin{vmatrix} 1 & 1 & 1 \\ p_1 & p_2 & p_3 \\ q_1 & q_2 & q_3 \end{vmatrix} , \tag{A13}$$

where

	for j = 1	for j = 2	for j = 3	for j = 4
(p_1, p_2, p_3) represents	(x_2, x_3, x_4)	(x_1, x_3, x_4)	(x_1, x_2, x_4)	(x_1, x_2, x_3)
(q_1, q_2, q_3) represents	(y_2, y_3, y_4)	(y_1, y_3, y_4)	(y_1, y_2, y_4)	(y_1, y_2, y_3)
(r_1, r_2, r_3) represents	(z_2, z_3, z_4)	(z_1, z_3, z_4)	(z_1, z_2, z_4)	(z_1, z_2, z_3) .

(A14)

Finally, these values of a_j, b_j, c_j are used in the evaluation of the matrix K_1 [Eq. (A8)].

Contents

28. Space Systems Environmental Interactions Technology Program

by

C. P. Pike
D. A. Guidice
R. A. Davis, Captain, USAF
A. L. Chesley, Captain, USAF
W. N. Hall
B. M. Shuman
Air Force Geophysics Laboratory
Hanscom AFB, Mass. 01731

Abstract

Exploitation of space for military purposes will increase in the Shuttle era when large, high-powered space systems will be deployed by military astronauts. The space environment will be a critical factor in the deployment, operation, and survivability of these new systems. A major concern is that a new system might be fielded in space with a costly environmental failure mode engineered into the basic design. The technology program described here addresses space environmental interactions on large-dimension high-power satellites to provide technology solutions that will insure against potential system failure.

1. INTRODUCTION

The objective of the Space Systems Environmental Interactions Technology Program is to develop technology to control interactions between large spacecraft systems and the earth's space environment. This effort will identify, investigate, and mitigate interactions that limit, degrade, or destroy the effectiveness of current and planned space systems. This program is the Air Force Advanced Development portion of a joint NASA - AF Space Technology Investigation.

As new, large, high-power space systems are designed and deployed, spacecraft-environment interactions will be of increasing concern. In the mid-1980s, DoD Space Shuttle flights will enter regions of the earth's space environment where naturally occurring electron beams exist. In the late 1980s, a large, high-power Space Based Radar could begin operational tests in the space plasma environment. High-power laser or particle beam weapon systems may also be placed in orbit in the future. The adverse effects of interactions between these systems and the space environment may disrupt or damage space vehicle systems, limit the application of in-orbit construction techniques, limit the use of large space structures, limit the power levels available to space-based systems from solar cell sources (see Figure 1), and pose hazards to astronauts performing extra-vehicular activities.

In the past, space systems were deployed without sufficient information for understanding the interaction of the system with the space environment. The adverse effects of the earth's environment on space systems have generated hundreds of operating anomalies in communications and surveillance satellites, including one catastrophic failure.

The large volume and weight launch capabilities of the Space Shuttle make possible a new class of spacecraft. These vehicles will be larger and have higher power requirements than existing space vehicles, introducing an entirely new set of design problems and operational constraints. The large dimensions of these spacecraft will cause environmental interactions previously ignored to have important impacts on system design and development. Some potentially significant interactions are described below:

(1) Spacecraft charging may become a significant problem, especially in the electron beam environment found in polar earth orbit. The size of the vehicles and the materials used in their construction will play an important part in defining the differential potentials seen on-board the craft. Arcing may disrupt vehicle operations, causing electronic malfunctions and damage to vehicle subsystems. Charging may develop to the point of causing significant vehicle distortion, especially when large, thin surfaces are involved.

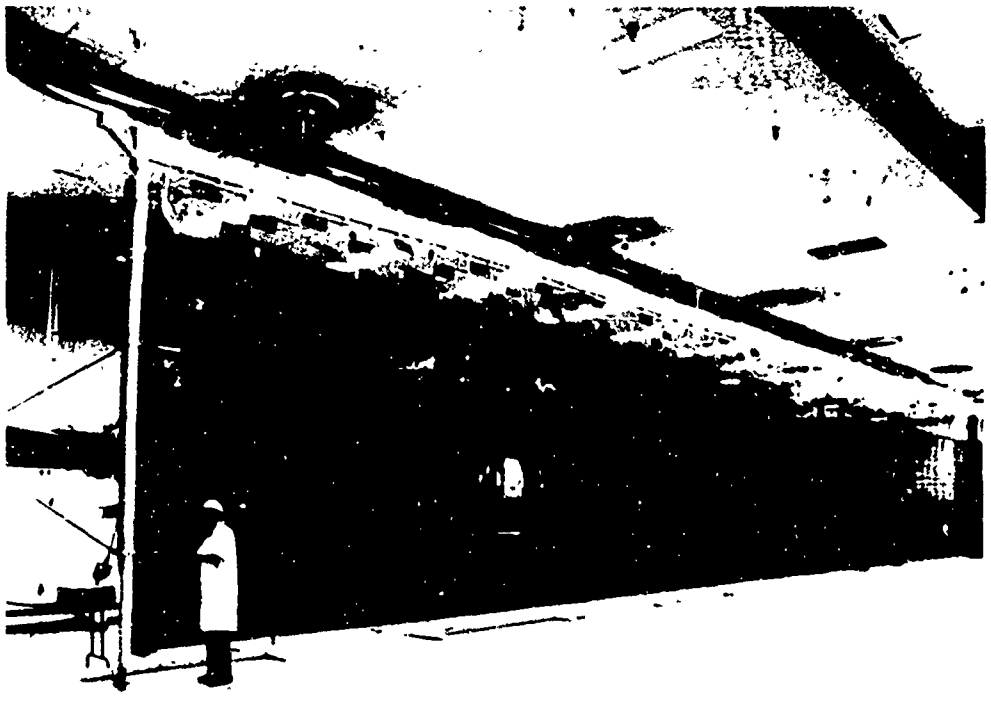

Figure 1. Solar Cells for Space-based Systems

(2) EVA (Extra-Vehicular Activity) operations may be hazardous to astronauts if they take place in the auroral electron environment near the poles, especially during an intense auroral event. Spacecraft charging may result in large potential differences between the astronaut and the shuttle. The resulting arc discharges could disrupt life-support equipment.

(3) Higher power consumption, with an accompanying increase in solar-cell voltages, will present further areas of difficulty: arcing between high voltage points may prove damaging, and the presence of high plasma densities at low altitudes may act as a conductive path and drain power away from the array. Thus, the use of high-power, high-voltage, solar arrays may be jeopardized.

(4) Gravity will cause the longest dimension of the vehicle to be nearly aligned with the earth. If this longest dimension is made of a conducting material, then the interaction of the vehicle velocity with the earth's magnetic field can cause torques on the craft, resulting in an instability in vehicle attitude.

Considering the immense cost and complexity of future space systems, spacecraft-environment interactions must be understood, evaluated, and neutralized in the design phase of system development.

2. AF/NASA PROGRAM

This joint AFSC/NASA research and technology program on spacecraft-environmental interactions began in FY81. The program was approved on 15 May 1980 by AFSC/DL and NASA/OAST and is outlined in the "Agreement for NASA/OAST - USAF/AFSC Space Interdependency on Spacecraft Environmental Interaction". The Air Force Geophysics Laboratory, acting as the focal point and prime coordinator for the Air Force effort, will work with other Air Force Laboratories (Air Force Wright Aeronautical Laboratories, Rome Air Development Center) and Space Division/YL to develop programs that will identify spacecraft-environment interaction problems and develop the technology that will enable designers to minimize or eliminate adverse effects (see Figure 2). The NASA research centers will actively participate in this space technology investigation.

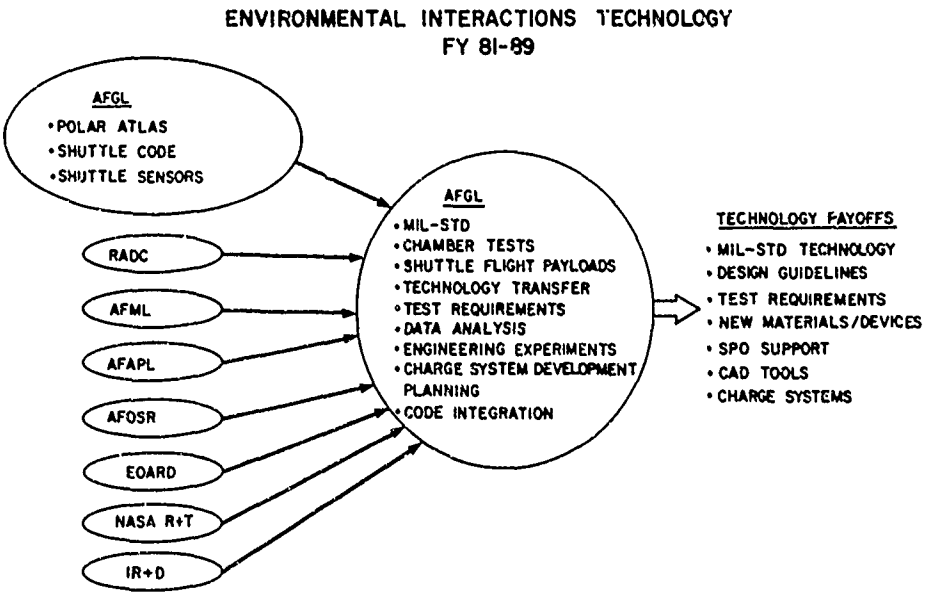

Figure 2. Outline of Spacecraft Environmental Interactions Technology Program

The Space Systems Environmental Interactions Technology Program will transfer the products of NASA and AF spacecraft-environment interaction research to the design, development, and operation of DoD-planned large, high-power space systems. The program will investigate the physical processes that couple space systems to the earth's space environment, develop Military Standard design guidelines and test specifications for space systems, and provide techniques and flight hardware to minimize or eliminate system interactions with the space environment. The technology developed in this investigation will support proposed AF-NASA space mission concepts into the 1990s.

3. PROGRAM STRUCTURE

The program is composed of three projects with the following objectives:

3.1 Space Systems Design and Test Standards Project

The project objective is to develop Military Standard engineering design guidelines and test procedures to mitigate the adverse interactions of large, high-power space systems with the earth's space environment.

The Military Standard Engineering design guidelines, shown in Figure 2, will combine the knowledge of spacecraft-environment interactions and proven mitigation techniques (developed under the other two projects) with the results of NASA and AF exploratory development programs. The guidelines, engineering "rules of thumb" to be followed in the design of large, high-power, advanced space systems, will be supplemented with a well documented and validated library of computer-aided design tools. These computer simulations will be applied to identify environmental weaknesses in space system designs.

Ground-based and on-orbit testing requirements for space systems and their components will also be developed. This product will assure that design guidelines, aimed at mitigating spacecraft-environment interactions, are incorporated and actively employed in the final space system design.

3.2 Interactions Measurement Payload for Shuttle (IMPS) Project

The project objective is to develop a Shuttle payload (shown in Figure 3) of appropriate engineering experiments to measure the interactive effects of the low altitude polar-auroral environment on large-structure, high-power space systems expected for Air Force operations in the 1990s. The new technology that emerges from this investigation will prevent failure and alleviate the degradation of advanced space systems due to adverse interactions with the earth's space environment.

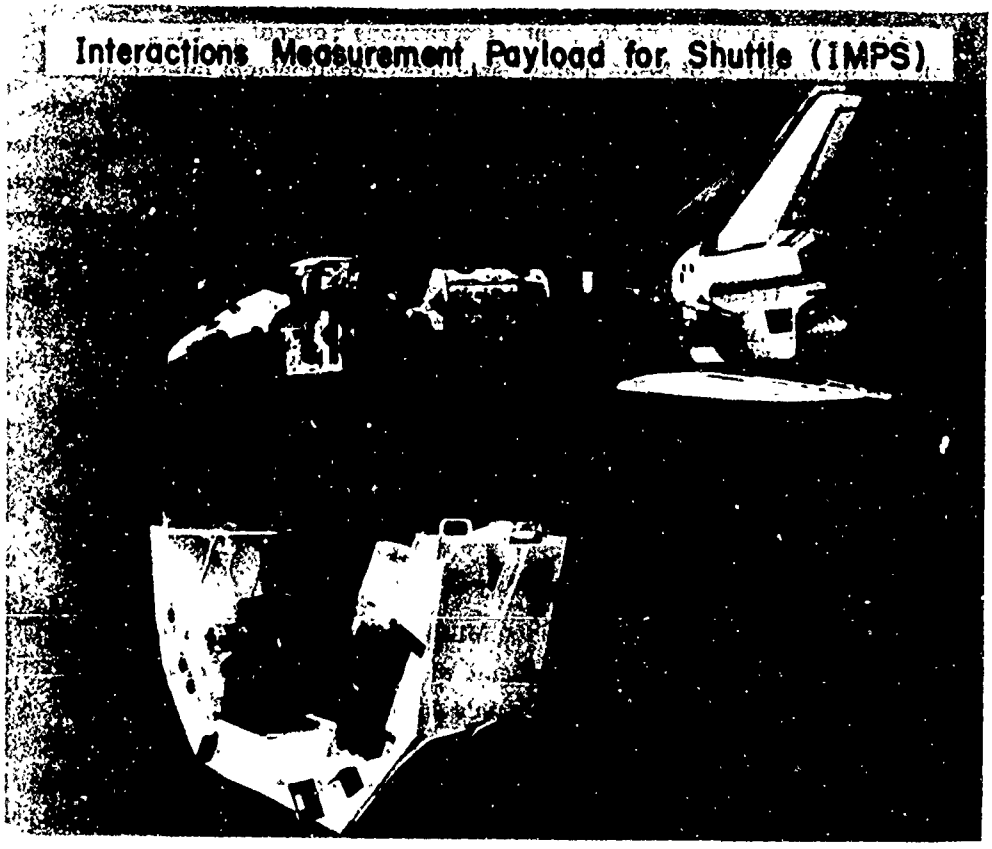

Figure 3. Shuttle Payload to Measure the Interactive Effects of the Low Altitude Polar-auroral Environment on Large-structure, High-power Space Systems

Typical effects to be investigated include:

(1) Interaction of the auroral plasma and current sheets on high-voltage solar arrays, resulting in power leakage or arc breakdown,

(2) Interactions of large currents and polar magnetic fields on large space structures, causing torques and structural deformations, thereby reducing the gain or pointing accuracy of large antennas,

(3) Interactions that increase electromagnetic interference, reducing the effectiveness of space communication and surveillance systems,

(4) Interactions that degrade the properties or performance of materials or electronic circuitry, resulting in operations errors or subsystem failures, and

(5) Interactions that pose a threat to the astronaut, especially during extra-vehicular activity (causing malfunctions in the astronaut's Manned Manipulator Unit during EVA, for example).

A baseline of engineering experiments, required to investigate the space environment interactions that affect Air Force space system operations, will be defined. A complete Science Team will be organized, composed of Air Force and NASA representatives, contractor personnel, and industry consultants. This working group will be chartered to design and develop the complete IMPS payload within the budgetary constraints. This process will require an extensive examination of the potential problem areas that could be encountered as large, high-power space systems are deployed. Experiments, capable of measuring the impact of these interactions on the Space Shuttle, will be designed. Based on budgetary constraints and a prioritized list of potential engineering experiments, the final IMPS payload will be determined. Mechanical, electrical, and managerial interfaces will be designed for maximum flexibility, reliability and cost benefit. Arrangements would be made to develop (design, fabricate, and test) the selected engineering experiments. The completed package of experiments will be combined with AFGL's active, automatic Charge Control System and a set of environment sensors to form the IMPS payload. The experimental payload will be flown on a late 80's Shuttle flight under the Air Force's Space Test Program (STP).

3.3 Charge Control System Project

The project objective is to develop a Flight Model Discharge System capable of monitoring and successfully controlling the potentials induced on space vehicles. This system will be capable of "autonomous" operation. The unit will monitor vehicle potential, determine when spacecraft charging is present, and operate a discharge device to eliminate potentials and maintain the vehicle in a neutral charge state.

The Flight Model Discharge System is designed to be incorporated into the household functions of any vehicle that may develop spacecraft charging. This autonomous (except for power) "black-box" system will require no control from the ground. While full ground-command capability will be retained for redundancy, only a "power on" command will be required to activate the system. It will detect charging, operate to neutralize that charging, and return to the passive mode.

4. PROGRAM SUMMARY

The program consists of combined contractual and in-house efforts aimed at understanding spacecraft-environment interaction phenomena, performing ground and space-based research, developing concepts and flight hardware to mitigate

adverse environmental effects, and combining the results of NASA and AF spacecraft-environment interaction research into a Military Standard document.

This research and technology program will provide the following products:

(1) Military Standard Design Guidelines and Test Specifications for Space Systems will summarize the technology, specify test criteria, and provide techniques to minimize or eliminate system interactions with the earth's space environment. Included will be a library of Computer-Aided Engineering tools for the evaluation of space system concepts and preliminary designs.

(2) The IMPS Shuttle payload of engineering experiments will provide direct, experimental input to the development of Design Guidelines for Space Systems.

(3) The space-flight qualified Flight Model Discharge System will be capable of monitoring and successfully controlling the potentials induced on space vehicles.

As a result of this program, techniques, concepts, and flight hardware will be developed and demonstrated to ensure the reliability and survivability of AF systems in the presence of the adverse environmental effects encountered in space.

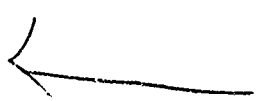

29. Summary of Experimental Results

by

J. F. Fennell
Space Sciences Laboratory
The Aerospace Corporation
P. O. Box 92957
Los Angeles, Calif. 90009

This session on experimental results provided both a review of satellite charging and laboratory results plus a discussion of new data with emphasis on the recent shuttle test flights. This panel provided, in essence, the type of basic input data required for modeling efforts. Most of the results were new to the modeling community and some of them are not understood even at a rudimentary level at this point. Some results require only changes in data bases of existing models. The highlights of the presentations are summarized in the following paragraphs.

The speakers emphasized those areas that were either orbit independent or specific to low altitude polar orbits. For example, Hardy presented results from a statistical study of auroral electron precipitation which showed that current densities in excess of tens of μ A/m^2 with energies in excess of 1 keV were possible in Near Earth Polar Orbits. Large variations in the currents were observed over 1-10 km sized regions. The minimum scale size is unknown. Such currents would readily charge surfaces in the wake region of a satellite.

Grard and Fennell both made presentations which related material properties to charging. Grard emphasized the secondary emission effect of both ions and electrons as a factor that controlled whether a particular surface charged or not in a given particle environment. Fennell's review showed that the conductivity of Kapton changed on orbit, Teflon showed a general increase in a "permanent" level of charging, and the level of quartz cloth charging was dependent on the magnitude of the charging current. The possibility that the higher concentration of oxygen present at Near Earth Polar Orbit might quench the Kapton conductivity changes was mentioned. It was pointed out that such material effects must be considered independent of orbit, and will make life difficult for the modeling community.

Johnstone and Raitt described some observed vehicle charging effects. Johnstone interpreted the Meteosat data (synchronous orbit) in terms of differential charging of surfaces with the satellite frame charging very rapidly compared to other surfaces. The shuttle charging picture, presented by Raitt, showed that the shuttle and the sensors responded in a very complicated manner to the FPEG (electron gun) operations. The charging levels and sensor differences depended upon whether operations occurred in daylight or dark and the orientation of the vehicle relative to the ram direction. Murphy presented results from the PDP (Plasma Diagnostic Package) that were equally complicated. The shuttle attitude control thrusters were seen to change structure charging levels. The shuttle was also seen to generate waves, probably ion acoustic, by its motion through the plasma. The electron beam operations also produced plasma waves. The plasma measurements characterized the electron beam spectrum at a distance from the shuttle and showed much beam scattering and heating.

The optical observations of the shuttle FPEG beams, described by P. Banks, showed the problems of making such observations in the shuttle bay, the control of the beam by the geomagnetic field, and the impact of the electron beam on shuttle surfaces. They also showed the strong optical brightening caused by attitude thruster firings.

The shuttle data analysis is only in the preliminary stages, but one of the most impressive revelations was the deterioration of organic surfaces that were exposed to the ram. The coatings on the PDP spherical probes and the Kapton blankets were damaged. Such effects will be equally important in Near Earth Polar Orbit and have not been properly considered to date for any proposed missions.

The many particle beam emissions from rockets and the ability to maintain relatively low vehicle potential while emitting amperes of electron current were summarized by Winkler. A beam-plasma interaction that increased the local

charge density and enabled the rocket frame to collect high currents was invoked as the mechanism which kept potentials low. This process has been duplicated in the laboratory environment but is not yet fully understood.

Wilkenfeld reviewed the relationship between arc discharge energy and possible malfunction or damage of electronic circuits. Integrated circuit upset, for example, can occur if only nanojoules of energy are coupled into the devices. A summary of the discharge specification presently being considered for the MIL standard was also reviewed. This area of spacecraft charging related discharges, their specification, and coupling to vehicle systems is not well understood at this time. Attempts are being made to perform laboratory testing on a SCATHA-like object to reproduce the observations made on orbit.

Discussion among the workshop participants highlighted several items that must be considered when analyzing the Near Earth Polar Orbit vehicle charging problem. For example, the wake regions of large structures will charge in the presence of auroral currents. The spatial scales and magnitudes of these currents need better definition, although it is expected that they are similar in scale size to optical arcs. In fact, the wake effect is a dominant factor in low altitude charging. Many standard dielectric materials will be degraded and their electrical properties can change on orbit, thus more investigation in the area of materials effects (including paints) is necessary.

Operations involving particle beams can give rise to differential charging and noise generation. The physics of beam-plasma discharge is still not well understood. More work is needed in this area if electron beam operations are to be carried out on large structures. Ion beams must be neutralized since the plasma cannot always provide the necessary replacement ion currents. The shuttle's attitude thrusters have a large but undefined effect on differential charging. The thruster effects should be examined in the available data. The present low earth orbit shuttle data must be used as a stepping stone to define new experiments for future flights and changes in the way experiments are done.

Acknowledgment

This work was supported by the U.S. Air Force Systems Command's Space Division under Contract F04701-82-C-0063.

30. Questions That Need to be Answered

by

H. A. Cohen
Air Force Geophysics Laboratory
Hanscom AFB, Mass. 01731

In the proceedings of the 1980 Spacecraft Charging Conference, Parks and Katz used space-charge-limited flow theory to show that large vehicles in a low polar orbit could charge to high potentials due to auroral energetic electrons. The implications of high potentials on spacecraft are serious. From ~~my~~ experience with studying the charging and discharging of spacecraft ~~I have~~ prepared a series of questions about large potentials on spacecraft in low polar orbit.

(1) Will large space vehicles in low polar orbits charge to high potentials due to the natural environment?

(a) To extend the previously formulated theory of probes in a stationary plasma to the case of a moving object, Parks and Katz determined an "equivalent" isotropic temperature for the streaming ions by setting the current entering a sheath in the isotropic case equal to the directed flow. Using this equivalent temperature they obtained an equivalent Debye length for the streaming ions by using the traditional formulation for Debye length, and the numerical density of the streaming ions. How valid are these assumptions?

(b) How does the presence of neutrals and metastable species influence both the charging and discharging of surfaces?

(c) Is there experimental evidence with the appropriate range of nondimensional variables that show such high potentials can be obtained?

(d) Is there experimental evidence with large objects in vacuum chambers that show high potentials can be obtained?

(2) What would be the consequences of large potential differences between the ambient plasma and surfaces on a large space structure?

There has been little or no evidence of discharging to the ambient from highly charged spacecraft.

(a) Would the charging and discharging of conducting and dielectric surfaces by processes from the ambient plasma cause problems on spacecraft? Examples of such problems are electromagnetic pulses that would affect electronic components both on the outside and inside of spacecraft, degradation of surfaces due to energetic ion sputtering, blow off during arc discharge, or large ion-flux contamination.

(b) What would be the time scale for charging and discharging a large structure?

(3) What would be the time scale for large differential charging?

The theory that has been mentioned was for absolute charging. We are pretty sure that the troubles that occur on charged vehicles are due to differential charging of surfaces with respect to spacecraft ground. We know that capacitive coupling between dielectrics and spacecraft frame ground surfaces prevents large differential charging in short time scales. Would the large space structure stay in a charging environment for a time period required for differential charging?

(4) What is the nature of the arcing from large dielectric surfaces?

(a) There is good laboratory evidence that some properties of pulses due to arcing from dielectrics to grounded conducting surfaces are monotonic with the area of the dielectric. Such properties include pulse width, amplitude, and energy. If these properties can be scaled to large space structure dimensions the results would be awesome. Is such scaling valid for large surfaces?

(b) Is it necessary or sufficient to break up large dielectric surfaces to reduce the effects of arcing?

(5) How should the resources available to study this problem be expended? If large potentials on large space structures in orbit are plausible, let alone probable, something must be done. How should we divide our encouragement and support of

(a) further analytical studies,

(b) simple one- or two-dimensional modeling,

(c) three-dimensional modeling with simple structures,

(d) three-dimensional modeling of actual space vehicle geometries,

(e) laboratory experiments with small models but for the proper range of non-dimensional variables,

(f) large vacuum chamber tests of large surfaces,

(g) sounding rocket tests with large surfaces, and

(h) shuttle tests and measurements?

31. Requirements for Validating System Models

by

M. S. Gussenhoven
Boston College
Chestnut Hill, Mass. 02167

As computer models become larger and more complex we have to do some hard thinking about how they can be validated, and then how they can become a permanent part of our collective scientific thinking. Until recently, the only form of quantitative expression was in explicit manipulation of mathematical functions. This form of expression probably reached its pinnacle in the 1950s in quantum field theory. It was also accompanied by great activity on the part of philosophers (initiating the new discipline, philosophy of science), who were concerned with validation of theory. In any case, we have had many years in which to grow accustomed to presentation of scientific theory analytically, and to become comfortable with its epistemological conundrums. So what ~~I would like to do~~ the author does here is make an analogy between the development and presentation of analytic scientific theory and that of computer models in order to suggest that there are additional requirements to be made on computer models to test their validity.

There are many types of computer codes and models. I limit my considerations to those which attempt to advance physical theory through system modeling; that is, those in which the code developer acts as theorist, and uses the

computer's numerical flexibility and speed to deal with larger systems and more complex interactions than he could without the computer. He applies established physical principles to a large, but finite number of units that comprise the whole system. He exercises considerable choice, in deciding where to inject causal links, when to make simplifying assumptions, and how to assess the importance of components of the interactions at key points in the model. The purpose of his effort is to so understand a physical situation that he can predict a final state from a given initial state. Assessment of the degree of accuracy of the prediction constitutes an assessment of the validity of the computer model (theory).

Not all system models fall into this category. At one extreme are algorithms. To my mind algorithms are ways of dealing with complicated sets of calculations, or large data sets, or both. The physics is done outside the algorithm, and is validated without appealing to the results of the algorithm. The algorithm only allows the physics, or the application of the statistics, or the survey of the data to be done more accurately and more quickly than can be done by hand. An algorithm test is essentially a test that the computer code, and it may be a very intricate one, runs correctly.

At the other end of the spectrum are codes that are really experiments in solving systems of complex mathematical equations. Often they begin as a genuine effort to model a physical system, but the internal intricacies of finding solutions eventually overwhelm. These codes are typically beset with problems of convergence, of multiple branches of solutions, and of iterations requiring extensive computer time. They are important for their potential use, but in their present state are hard to repeat, let alone validate. These types of codes are not meant to form an exhaustive list, but are described to help define the kind of computer effort that is the subject of validation; that is, computer models whose proper place is the domain of theoretical physics.

Before examining the differences between analytically-developed and computer-code developed theory let me make two points. First, I suggest that the standards we use for validating computer models be the same as those we use for validating analytic theory. In brief, we require of new theories that they account for the results predicted by existing theories and that, in addition, they predict new results. The extent to which these requirements are satisfied leads to real epistemological problems that we feel most urgently in the midst of major scientific breakthroughs, or revolutions (Thomas Kuhn's word). But even in normal times the scientific community sets rigorous standards for judging theory. We must neither increase nor decrease these standards when we assess computer models. It is hard to resist both tendencies. On the one hand the territory of large computer codes is new, and can be uncomfortably strange,

like the presence of a good magician. On the other hand, great expense is often required for code development and when this is the case, everyone, from the developer to the funding agency, is loath to show no real result. It is a great irony that the common ground of approval for those who condemn too quickly and those who forgive too easily is computer graphics. This aid to 3-D imagination obscures the proper theoretical use of the computer.

Second, it is imperative that theoretical constructs that are inputs or outputs of the model have uniquely defined equivalents in the body of measurement used to validate the model. It is not necessary that the measurements be already made, or even that they be state of the art. But to validate models both the theorist and the experimenter must cooperate in achieving a true intersection between the set of quantities that are measured and the set of theoretical concepts. A persistent problem with ionospheric and magnetospheric models is the near-uniform use, by theorists, of the concept temperature to describe plasma populations, instead of, say, average energy over a given energy range. It is well known that for these populations the notion of temperature is a poor one, but more important for our purposes, there is no unique way to make a temperature assignment from actual particle measurements. The lack of uniqueness is then used to justify data handling that obtains the best results. These questionable methods are used both in analytic and computer theoretical models. However, there is real opportunity in computer modeling to improve the theoretical-experimental match-up precisely because the modeling does not depend on use of tractable analytical functions, such as Maxwellian distribution functions.

A brief examination of how analytic theory is presented in a journal such as Physical Review shows the kind of problem we are confronted with when we attempt to place parallel validation requirements on computer models. Figure 1 is a schematic diagram of how both kinds of theoretical presentations are made. The first three steps are the same for both: the problem is stated, the physical principles to be used are listed, and the adaptation to the particular system modeled described. For the latter step there will be parametric values a, b, c... that are needed to describe the specific system; and initial conditions, x_i, y_i, z_i... that define the state of the system of interest.

The differences begin with what is the heart of the presentation: the development, or solving of the equations. Finding the solution is generally accompanied by the need for additional adaptation to the specific system. In an analytical presentation the development of the equations and the additional assumptions are explicitly given. True, there may be many steps "left to the reader" that are not as "easily shown" as is stated. Nevertheless, we can see the logic, and have full purview of the approximations and assumptions. The corresponding

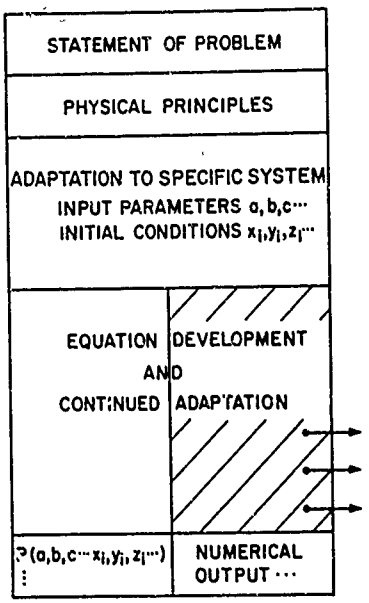

Figure 1. Schematic Diagram of the Presentation of Theoretical Results Analytically (Left-hand Side) and Numerically (Right-hand Side)

development when done with a computer constitutes the code. For most of us the code is a black box, and I have cross-hatched this part of the presentation in Figure 1 to suggest this. Thus, the first requirement we can make of computer model developers is that they devise methods for making their codes transparent.

The second major difference is in the form of the solution. The analytical theorist gives his solutions in functional form that depend on the system parameters and the initial conditions: P (a, b, c..., x_i, y_i, z_i...). The answer is more general than the specific application used in the presentation. If at a future time, differing initial conditions or different systems can be realized and measured, they also pertain to and contribute to the validation of the theoretical model.

The developer's computer model is far more temporally encapsulated. His solution, or output, is numerical. It is only the developer/programmer who is able to generalize the model results. The computer model cannot (unless by exceptional documentation, advertisement, and luck) lie fallow for some future researcher to apply in new and revealing ways. Thus, the second requirement for preparing a computer model for validation is that it be exercised over the entire physical range of each of the variables. For large codes this can be an

extremely difficult requirement, but I see no way around it. Close cooperation with experimenters who understand what mutual restrictions exist among measured variables can reduce the magnitude of the effort.

An examination of a simple analytic presentation shows how accessible and manipulative it is and illustrates the need for placing the two additional requirements on numerical models. Since we are concerned here with spacecraft charging let us look at a theory for eclipse charging presented by Garrett and Rubin.[1] They start with a two-species plasma, electrons and protons, each of which is described by a Maxwellian distribution having densities and temperatures n_e, T_e; n_i, T_i, respectively. They require current balance to the satellite from the incident ambient currents J_{e0}, J_{i0}, and the backscattered and secondary currents. Energy is conserved for the plasma distributions as they fall through the satellite-to-plasma potential difference, ϕ_{sc}. For negative potentials the expression they obtain for ϕ_{sc} is:

$$\phi_{sc} = -\frac{kT_e}{q} \ln \left[\frac{J_{e0}(1-a-c)}{(1+b)J_{i0}\left[1 - \frac{q\phi_{sc}}{kT_i}\right]} \right] ,$$

where

$$J_{e,i} = \frac{n_{e,i}}{(2\pi)} \left(\frac{2\pi\, kT_{e,i}}{m_{e,i}} \right)^{1/2} ,$$

and k, q, and m are the Boltzmann constant, the electronic charge, and the mass of the particle, respectively. The values a, b, and c are proportionality constants between the backscattered (c) and secondary (a,b) electron currents and the ambient electron (a, c) and ion (b) currents. The constants are assumed to be independent of the temperatures of the ambient electron and ion populations.

The first thing one notices is that the expression for ϕ_{sc} is a nonlinear one: ϕ_{sc} appears on both sides of the equation. Presumably, one could develop an iterative scheme to solve for ϕ_{sc}. Instead the authors take the approximation $q\phi_{sc}/kT_i \ll 1$, thereby linearizing the equation. These are the conditions under which they choose to "exercise" their solution. If we feel the approximation is not physically realistic, or we wish to apply the theory in the presence of a large cold-ion population, the analyticity of the solution gives us the freedom to

1. Garrett, H. B., and Rubin, A. G. (1978) Spacecraft charging at geosynchronous orbit-generalized solution for eclipse passage, Geophys. Res. Lett. 5:865.

determine its validity under other circumstances. For a numerical solution with similar nonlinearity, an iterative scheme would, no doubt, have been used. To exercise his solution the code developer has two strikes against him. First, there may be no way of his knowing that the relationship between ϕ_{sc} and T_i can help order the whole regime of solutions. Second, if he does make application only to relatively hot ion populations and small spacecraft potential he still must satisfy our legitimate curiosity about his results for the whole range of the ratio $q\phi_{sc}/kT_i$.

The Garrett-Rubin solution now has the form:

$$\phi_{sc} = -\frac{kT_e}{q} \ln\left[\frac{J_{e0}(1-a-c)}{J_{i0}(1+b)}\right] .$$

The assumption about the ion temperature has reduced the number of independent variables from four to two: the electron temperature and the ratio of the ambient electron current to the ambient ion current. Thus, for a given spacecraft, for which a value of the ratio $(1-a-c)/(1+b)$ can be assigned, validation of the Garrett-Rubin theory has been reduced to a simple matter. For a given ratio of J_{e0}/J_{i0} the satellite potential should vary linearly with kT_e, having a zero intercept. Garrett and Rubin assume for the ATS satellites that $(1-a-c)/(1+b) \simeq 1/10$; and find that for the cases for which they find charging $J_{e0}/J_{i0} \sim 25$. Thus,

$$\phi_{sc} \simeq -kT_e/q .$$

In this manner the validation procedure has been collapsed from a very complicated one involving four independent variables, to focus on simply one.

What can the numerical modeler do that similarly reduces the scope of exercising his model and at the same time maintains the confidence of the scientific community that the exercise has full physical merit? Appeal to the results of simpler analytic models can clearly be made in some instances. But also enlistment of the help of the experimental community must be sought. For instance, to know the ranges of the number fluxes of ions and electrons, one as a function of the other, is clearly a legitimate request by spacecraft charging theorists. Figure 2 shows this dependence for 100 days of data at near geosynchronous orbit which has recently been compiled in the SCATHA Atlas.[2] Lines have been drawn showing various values of the ratio of the electron-to-ion flux (equal to the current ratio for isotropic distributions). Almost all cases have

2. Mullen, E.G., and Gussenhoven, M.S. (1983) SCATHA Environmental Atlas, AFGL-TR-83-0002.

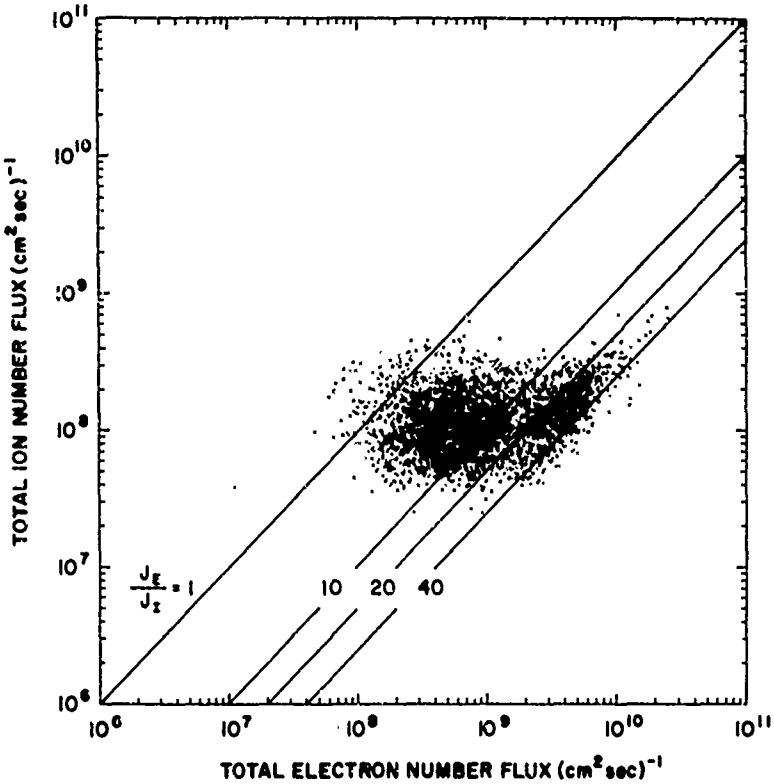

Figure 2. Scatter Plot of the Electron Number Flux as a Function of Ion Number Flux at Near-geosynchronous Orbit. Straight lines are for values of the ratio of the electron to the ion flux equal to 40, 20, 10, and 1 (taken from Mullen and Gussenhoven[2])

ratios between 1 and 40. For Garrett and Rubin, negative charging is not predicted for ratios less than 10 (for more than half the cases) and 20 (or 25) is a good middle value between 10 and 40.

Finally, we look briefly at how good the Garrett-Rubin prediction was: $q\phi_{sc} \sim kT_e$. Figure 3 shows the prediction (straight line) and the electron temperature as a function of ATS spacecraft potential. The agreement, at first glance, is quite good. However, inspection of the potentials for temperatures of 3 keV or less shows a systematic trend away from linear behavior. In fact, the potential goes to zero for $kT_e \sim 1.5$ to 2 keV. The Garrett-Rubin theory predicts that this should not be the case. The proportionality to kT_e is direct, regardless of the ratio of the currents. Because the theory is developed analytically we can go back and examine the assumptions made in developing the theory to try to repair this aspect of the solution. We see that the solution was reached

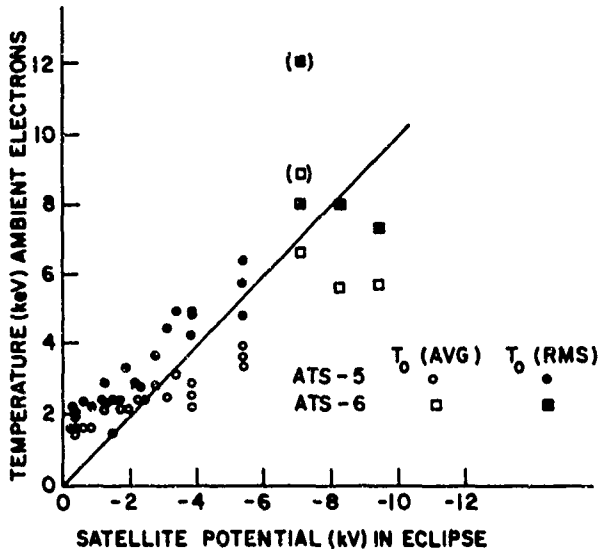

Figure 3. Ambient Electron Temperature Plotted as a Function of the Satellite Potential at Geosynchronous Altitude (Taken From Garrett and Rubin[1])

under the assumption that $1 - a - c \neq 0$, and, in fact, that it is greater than 1. We know that this is not always a good assumption. The dependence of a and c on the temperature of the incoming electrons must be taken into account, and for typical satellite materials, $1 - a - c = 0$ at precisely that temperature for which the Garrett-Rubin theory fails. At this temperature, called by Laframboise et al in these proceedings the threshold temperature, the outgoing backscattered and secondary electron currents exactly balance the incoming ambient electron current. It is only because the analytic theory is transparent in its assumptions that the source of the disagreement with measurement can be identified and possibly reworked. If the internal outputs and predictions of numerical models are not displayed or otherwise made subject to check by measurement, that is, if the internal workings of the model are not made transparent, computer models will have little chance of surviving comparison with wide ranges of measured values, and will not be able to be extended and refined as a result of such comparisons. They will have little chance of validation.

To summarize, we are looking for ways in which large computer models of physical systems can be established as legitimate theoretical efforts. Reference to the amount of exposition required of an analytical theory for its validation is useful. In preparation for validation a code or model must be exercised: the

range of output for the entire multiple ranges of inputs displayed. In the validation process the code must be made transparent: access to measurable or testable internal outputs made available.

Acknowledgments

This work was supported by the Air Force Geophysics Laboratory under Contracts F19628-82-K-0011 and F19628-81-K-0032. I would like to thank E.G. Mullen, H.A. Cohen, and D.A. Hardy for stimulating discussions on this topic.

☆ U. S. GOVERNMENT PRINTING OFFICE: 1983--600-000- 42